Designing Iron Oxide Nanoparticles for Enhanced Polymer Nanocomposites: Synthesis, Characterization, and Performance Optimization

Sakina Meftah

Université de Technologie de Compiègne

Roberval laboratory – Mechanical Engineering Department

Sorbonne Université

Monaris laboratory (CNRS UMR 8233) – Chemistry Department

Doctoral School No. 71: ENGINEERING SCIENCES

Doctoral dissertation of Mechanical and Material Engineering

Designing Iron Oxide Nanoparticles for Enhanced Polymer Nanocomposites

Synthesis, Characterization, and Performance Optimization

Funded by :

Institut de Science des Matériaux de Sorbonne Université

Chaire LEEGO: Challenges and Opportunities in Connecting Length and Time Scales in Nanostructured Materials

Sakina MEFTAH

The thesis was defended on 02/07/2025 before the following jury:

	Name	Affiliation
Reviewers	Dr. Katerina SOULANTICA	DR-CNRS | Institut National des Sciences Appliquées de Toulouse
	Prof. Laurent CHAZEAU	Institut National des Sciences Appliquées de Lyon
Examiners	Dr. Edith PEUVREL-DISDIER	CR-CNRS | École des Mines de Paris
	Dr. Layella ZIYANI	Université de Technologie de Compiègne
President	Prof. Xavier COLLIN	École Nationale Supérieure d'Arts et Métiers
Supervisors	Prof. Fahmi BEDOUI	Université de Technologie de Compiègne
	Dr. Isabelle LISIECKI	DR-CNRS | Sorbonne Université
	Dr. Anh-Tu NGO	Sorbonne Université
Invited	Prof. Djimédo KONDO	Sorbonne Université

Acknowledgements

This thesis marks the close of a long and winding journey. I am deeply thankful to everyone who walked beside me, whether just a few steps or all the way.

I sincerely thank my jury members for their time and contributions. I am grateful to my reviewers, Dr. Katerina Soulantica and Prof. Laurent Chazeau, for their careful reading and valuable insights that improved the manuscript. I also appreciate the constructive feedback and engaged discussions from my examiners, Dr. Edith Peuvreil-Disdier and Dr. Layella Ziyani. Finally, I thank Prof. Xavier Collin, president of the jury, for chairing the defense and for his support.

I gratefully acknowledge the Institut des Sciences des Matériaux at Sorbonne University for funding this thesis. I also thank Professors Christophe Petit and Lahouari Krim, directors of the MONARIS laboratory, for their support, and Professor Jérôme Favergeon, director of the Roberval laboratory, for facilitating my integration into the team.

To my supervisors, Fahmi, Isabelle, Tao (Anh-Tu), and Djim—thank you. Fahmi, your trust, your guidance, and the freedom you gave me to explore, stumble, and grow shaped both this thesis and the researcher I've become. Since my master's days, your thoughtful advice and long discussions helped me see beyond the data. Isabelle, thank you for your guidance and sharp insights, which always helped me move forward. Tao, I appreciated your support and encouragement, even from a distance. And Djim, your calm and quiet presence was a steady support, always there when it mattered most.

At MONARIS, science was a collaborative and joyful pursuit, where shared curiosity and camaraderie transformed even failed experiments into valuable learning experiences for young researchers.

Sonia HADAOUI guided me through the complexities of chemistry in the lab. She patiently explained difficult concepts, helped me fix the TEM after a late-night accident, and always seemed to know when I was struggling. She made chemistry accessible and enjoyable, and I still owe her several Mascotte Nutellas from our favorite bakery.

To Baptiste, Zohreh, and Hina: your chaotic laughter and questionable jokes were perfectly timed. To Cheriehan, Nada, Yinan, Ashkan, Sathapana, Konstantin, Charles, Vassim, Yuxuan, Abby, and Serkan: our lunch debates, from politics to love, were unmatched. Our shared burnout forged strong bonds, and our spontaneous, if culturally inappropriate, dabke breaks are unforgettable. Celebrating Zohreh and Konstantin's journey from colleagues to partners with all of you is a cherished memory.

I later joined the Roberval lab in Compiègne. Though Compiègne feels a world away from Paris's hustle, we quickly found our rhythm. Lina Achouri, with whom I first shared an office before our "working" styles led us to separate spaces, Nadine, Jeanne, Jean, Théo, Alla, Ouardia, Marcia, Ghessen, Elise, Loan, Daoming, and Jamal, thank you for turning the lab into a place of laughter, card games, and enjoyable distractions. As the "resident chemist" among mechanical engineers even if I technically am one, science talk was occasional, but team bonding over games and collaborative experiments was plentiful. Unlike the MONARIS crew, most of you are still in the trenches, so I'll leave it at that, out of both empathy and legal prudence.

I also want to thank the Fahmi family group: Stiliyana, Vigila, Baba Lohitha, Holy Father Roland, Viviana, Abhishek, Nadine, Zeynep, and Maïssa. Some of the best moments came just before our meetings, in those silent glances asking, "Who's the sacrifice this week?" Somehow, as the senior PhD student, I always managed to dodge the bullet. But it was never just about the presentations; it was about having each other's backs, no matter what. Nadine, who began as an intern, quickly became a pillar of this work, helping me through experiments and supporting me beyond the lab, including our memorable trip after my defense. I'm deeply grateful for her presence and collaboration.

I would also like to warmly thank the professors and researchers who supported this work through enriching discussions, opportunities, or practical help. Some generously shared materials, others offered valuable insights, or gave me the chance to grow through teaching. I am especially grateful to Prof. Erwann Guénin, whose scientific generosity and openness were deeply appreciated. To Dr. Layella Ziyani, thank you not only for your role as an examiner but also for your continued support and thoughtful guidance. I am equally thankful to Prof. Laurent Bouteiller, whose perspective helped sharpen my scientific reasoning. To Dr. Walid Harizi, thank you for your patience and availability, especially when I had questions during my teaching duties. A special thank-you to Dr. Delphine Brancherie for trusting me with teaching hours in her course. I also gratefully acknowledge Dr. Jinkai Yuan, Dr. Andres Jaramillo-Botero, and Prof. William A. Goddard for their scientific input and for the stimulating exchanges that broadened my perspective. These gestures, whether brief or sustained, left a meaningful mark on my path.

A big thank you to the Service d'Analyses Physico-Chimiques (SAPC) team at UTC—my unofficial third lab, considering how often I was there. To François Oudet, thank you for your trust and for letting me use the instruments on my own. Caroline Lefebvre, your patience and humor while training me on the TEM made all the difference. Adama Konaté, the DRX whisperer—thank you for never giving up on my confusing samples. And Frédéric Nadaud, thanks for the SEM support and your good spirits.

To the technical and administrative staff who kept the wheels turning: at MONARIS, Mylène, thank you for your warmth and efficiency, Patrick for your humor, Raoul for managing my endless supply requests with grace (even when the delivery wasn't your fault, I still had to ask). At Roberval, thank you, Maryline, for handling my mission forms despite my late emails, and to Nathalie, Valérie, Loïc, and Isabelle for your quiet but essential help.

To Zineb, Sana, Cilia, Nisrine, and Khadija—friends I met during the unusual COVID times as a master's student. Living together turned us from strangers into a tight-knit group. As proud members of the Tajine Ber9o9 Lovers ♡, we survived lockdown with endless tajine talks, late-night Omegle chats, and some surprisingly improved Arabic. Zineb's midnight philosophical questions kept us laughing for hours. Our spontaneous Ryanair trips were wild, unpredictable, and exactly what we needed. Thanks, girls, for all the memories.

And finally, my family. To my father, whose steady presence—even from miles away—was a quiet anchor I could always lean on. To my mother, who might not have followed every detail of what I was doing, yet never failed to show up in the ways that mattered most: a warm meal, a gentle nudge, or simply care. To Lina, my sister and confidante—thank you for your endless support, for knowing when to listen, when to stay silent, and even for keeping me company on the phone during those long, annoyed walks after missing the bus. To Zina and Youmi, the youngest and coolest siblings one could wish for—you probably thought "PhD" stood for "Postpone Holidays Drastically," but you always knew I'd make it back in time for our summers by the sea. And to Younes and Mona, my flatmates in the final stretch—thank you for turning an ordinary apartment into a home filled with laughter, midnight conversations, good food, and calm.

I could tell you the story behind each name, but instead, let's catch up soon—over coffee or a sunlit walk. ^ ^ .

Contents

Notations

AMF	Alternating Magnetic Fields
DLS	Dynamic Light Scattering
DSC	Differential Scanning Calorimetry
EDX	Energy Dispersive X-ray
FeST	Iron Stearate
HSP	Hansen Solubility Parameter
HST	Hansen Solubility Theory
IONPs	Iron Oxide Nanoparticles
NPs	Nanoparticles
OA	Oleic Acid
PIB	Polyisobutylene
SAR	Specific Absorption Rate
SAXS	Small-Angle X-ray Scattering
TEM	Transmission Electron Microscopy
TGA	Thermogravimetric Analysis
VSM	Vibrating Sample Magnetometry
WAXS	Wide-Angle X-ray Scattering
XRD	X-ray Diffraction

General Introduction

0.1 General Introduction

The development of nanoreinforced polymers holds significant promise for advanced materials, offering superior mechanical, thermal, and functional properties. Realizing this potential begins with the precise optimization of nanoparticle synthesis, continues through effective mixing and dispersion within polymer matrices, and ultimately depends on successfully scaling up production while linking nanoscale features to macroscopic performance.

A foundational step in this endeavor is the optimization of nanoparticle synthesis. For instance, iron oxide nanoparticles (IONPs) are pivotal components in designing multifunctional nanocomposites, as they combine mechanical reinforcement with magnetic and magnetothermal capabilities. The synthesis of IONPs demands meticulous control over particle size, crystallographic phase (e.g., magnetite Fe_3O_4 or maghemite γ-Fe_2O_3), and surface chemistry. These parameters directly affect not only the structural role of the nanoparticles within the polymer matrix but also their superparamagnetic behavior—a phenomenon characterized by zero coercivity below a critical size, which prevents magnetic agglomeration and facilitates rapid magnetization switching under external fields, an essential attribute for applications such as magnetic hyperthermia.

Following synthesis, the process of mixing or dispersing the nanoparticles into the polymer matrix is equally critical. Uniform nanoparticle dispersion governs the efficiency of stress transfer and enhances the composite's overall mechanical performance. Inadequate solvation of either the nanoparticles or the polymer can lead to aggregation, negatively impacting both interfacial bonding and functional properties. Surface modifications, such as the application of organic coatings, enhance nanoparticle-polymer compatibility, thereby mitigating aggregation and preserving the material's robustness.

Another persistent challenge is the multiscale characterization of these nanocomposites. Advanced analytical techniques are essential for establishing a clear relationship between the nanoscale microstructure and the macroscopic properties of the final product. Techniques such as transmission electron microscopy (TEM), small-angle X-ray scattering (SAXS), and wide-angle X-ray scattering (WAXS) enable detailed analysis of nanoparticle size, morphology, and spatial arrangement within the polymer matrix. These are complemented by dynamic mechanical analysis (DMA), which provides insights into the bulk mechanical behavior of the composites. In parallel, magnetic characterization techniques are indispensable in elucidating the superparamagnetic dynamics of IONPs, effectively linking nanoscale magnetic performance to overall magnetothermal efficiency.

This manuscript is devoted to the engineering of IONP-polymer composites through precise control over nanoparticle synthesis, optimized dispersion techniques, and strategic scale-up, all integrated with comprehensive multiscale characterization. In this context, the

present thesis aims to tackle the identified challenges by focusing on:

- Mastering the synthesis of iron oxide nanoparticles (IONPs) and investigating the key parameters that influence their growth, including particle size, crystallographic phase, and surface chemistry.
- Developing innovative fabrication methods to enhance the dispersion of nanoparticles within polymer matrices and optimize their interactions with the host polymer.
- Conducting a comprehensive analysis of the multiscale properties of the nanocomposites—from nanoparticle dispersion (characterized by techniques such as TEM, SAXS, and WAXS) and bulk mechanical behavior (studied by DMA) to nanoscale magnetic performance.

By systematically addressing these interrelated challenges, this work aims to establish robust design principles for next-generation multifunctional materials, in which enhanced mechanical properties converge with advanced magnetic and magnetothermal functionalities. Ultimately, the goal is to advance the field of nanoreinforced polymers and pave the way for their broader application in industrial and scientific domains.

0.2 Manuscript Structure

This thesis is organized into three major parts, each addressing crucial aspects of the study of iron oxide nanoparticles and polymer nanocomposites. The structure is designed to guide the reader through a comprehensive journey—from theoretical foundations and literature context to experimental investigations and the development of advanced materials.

Part I: Literature Review

This part lays the foundation for the study by discussing key background information and the state-of-the-art in the field. It comprises two chapters that critically examine previous research related to IONPs and polymer nanocomposites.

- **Chapter 1:** This chapter provides an in-depth review of the structure, properties, synthesis, and characterization of IONPs. It focuses on critical aspects such as particle size, surface chemistry, and the challenges associated with nanoparticle dispersion. Topics include colloidal stability, techniques to prevent aggregation in various solvents or media, and the issues related to reproducibility in nanoparticle production.
- **Chapter 2:** This chapter explores polymer nanocomposites. It discusses various processing methods and examines how the incorporation of IONPs affects the mechanical

performance and interfacial properties of the composite materials. The discussion is contextualized within the broader framework of advanced functional materials.

Part II: Synthesis and Control of Iron Oxide Nanoparticles

The second part of the thesis presents detailed experimental investigations on the synthesis and characterization of IONPs. This section is critical for establishing the parameters necessary for reproducible nanoparticle production and for understanding the growth mechanisms in different systems.

- **Chapter 3:** This chapter details the synthesis of IONPs with sizes below 20 nm. It emphasizes the role of surface chemistry control—particularly through the use of carboxylic ligands—and how it influences growth mechanisms and thermal decomposition processes. The chapter highlights the importance of precise synthetic control to tailor nanoparticle attributes.
- **Chapter 4:** The focus of this chapter is on the impact of reagent impurities on the reproducibility of IONP synthesis. It critically examines the challenges in achieving consistent size, morphology, and shape control, providing insight into the factors that can lead to variability in nanoparticle production.

Part III: Polymer Nanocomposites

This part of the thesis is dedicated to the integration of IONPs into polymer matrices and the study of the resulting nanocomposite properties. Special attention is given to the in situ synthesis of IONPs within polyisobutylene (PIB) and how this process influences the overall performance of the composite.

- **Chapter 5:** This chapter investigates the growth kinetics of IONPs within a PIB environment. It examines the interplay between nanoparticle formation and the polymer matrix, focusing on how synthesis conditions affect both the mechanical and magnetothermal properties of the resulting composites.
- **Chapter 6:** This final work provides an in-depth analysis of the structure–property relationships in PIB-based nanocomposites. It discusses strategies for optimizing nanoparticle dispersion and enhancing material functionality.

Conclusions and Perspectives

The final section summarizes the key findings of this work and proposes future research directions for advancing polymer nanocomposites.

Overall, this manuscript systematically addresses the challenges associated with nanoparticle synthesis, dispersion, and scale-up while establishing a clear connection between microstructural features and the macroscopic properties of nanocomposites. By bridging these scales, the work aims to contribute robust design principles for the next generation of multifunctional materials.

Part I

State of The Art

Chapter 1

Nanoparticles: Synthesis, Properties, and Challenges

Contents

1.1 The nanoworld

In a time marked by rapid technological miniaturization, the scientific community has increasingly focused on the nanoscale—a realm where particles are less than 100 nanometers in at least one dimension. One of the key features of nanoparticles is their **high surface area-to-volume ratio**, which significantly differs from bulk materials. As the size of the particles decreases, a greater proportion of atoms are located on the surface (Figure 1.1). This results in increased chemical reactivity, which drives enhanced catalytic activity and other surface-related phenomena. These characteristics—such as their increased reactivity, strength, and ability to exhibit new interactions—make nanoparticles crucial for controlling and enhancing the properties of materials and enabling new functionalities.

These particles, smaller than viruses, have the potential to revolutionize various fields, including medicine and electronics. To put this into perspective, a 1-nanometer particle is about the size of an orange compared to the Earth's diameter, which is approximately 12,742 kilometers. As research progresses, the range of applications for nanoparticles continues to expand, leading to significant breakthroughs in areas such as drug delivery systems, targeted cancer treatments, and energy-efficient technologies. The ability to manipulate matter at the nanoscale allows for exceptional precision in material engineering, resulting in functionalities that were once considered unattainable.

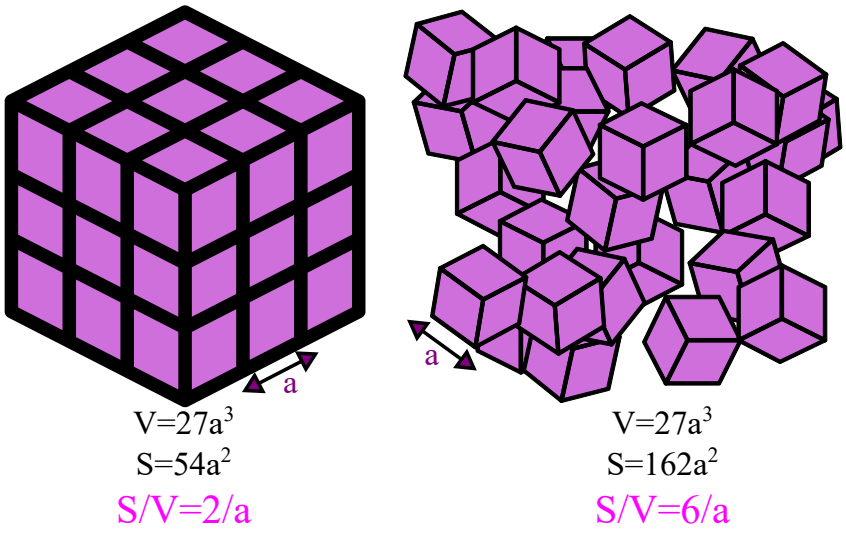

Figure 1.1 – *A visual comparison between a single large cube and multiple smaller cubes of equal total volume : Highlighting the Increase in Surface Area*

At the nanoscale, the properties of materials undergo significant changes due to their small size. Below a critical size threshold, the material properties—such as electronic, optical, and magnetic behavior—are governed by quantum effects, but more importantly, by the

dominance of surface interactions and the high surface area-to-volume ratio. As the size of the particles decreases, the ratio of surface atoms increases, which leads to enhanced reactivity, altered electronic states, and changes in optical absorption. This size-dependent behavior is why the properties of materials can differ dramatically when the particles reach the nanoscale.

For example, in semiconductor nanoparticles, known as quantum dots, the *light emission* can be tuned by adjusting their size. This size-dependent tunability is one of the key reasons why quantum dots have found applications in fields like bioimaging, displays, and solar cells [1] [2]. Similarly, metallic nanoparticles such as gold and silver exhibit *plasmonic properties*, where their interaction with light generates strong electromagnetic fields. This phenomenon is beneficial for advances in photothermal therapy, sensors, and energy-efficient devices [3].

In the case of magnetic materials, when their size falls below a critical threshold, they behave like a macromagnetic moment (or macrospin). This results in a characteristic phenomenon known as *superparamagnetism*, where the nanoparticles can spontaneously flip their magnetization due to thermal fluctuations in the absence of an external magnetic field. This feature is particularly useful for biomedical applications such as magnetic resonance imaging (MRI) and hyperthermia treatments [4]. However, because the magnetic moment of superparamagnetic nanoparticles is unstable at room temperature, they are generally unsuitable for long-term data storage, which requires stable magnetic states.

The exceptional properties and diverse applications of nanomaterials, such as nanoparticles, nanowires, and nanotubes, have been extensively validated through rigorous research and practical implementation, as demonstrated by the statistical analysis shown in Figure 1.2. However, the field remains dynamic, with ongoing efforts focused on three critical areas: (i) refining synthesis methods to achieve precise control over the size, shape, and composition of nanoparticles; (ii) advancing characterization techniques to better understand complex nanoscale phenomena, such as atomic structure, surface interactions, and quantum effects; and (iii) developing novel applications to further expand the potential of these materials. This iterative process of synthesis, characterization, and application drives continuous innovation in nanotechnology, revealing new properties and leading to groundbreaking applications across various industries. As our understanding of nanoscale behavior—both in terms of synthesis and properties—deepens and fabrication technologies advance, the scope of nanotechnology broadens, offering pioneering solutions to some of the most pressing scientific and technological challenges of our time.

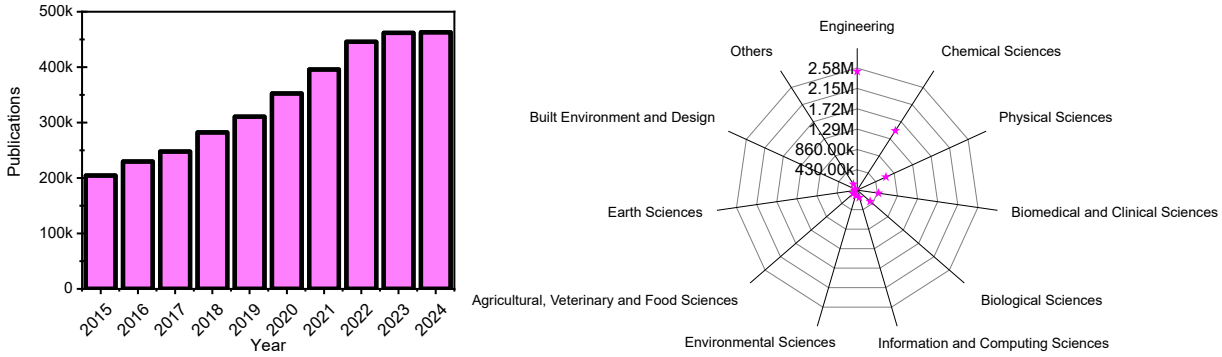

Figure 1.2 – *Publications related to the keyword nano from 2015 to 2023: histogram by year (left) and radar chart by research category (right). Data were extracted from the Dimensions.ai database and exported on November 30, 2024. The graphs illustrate the annual growth in research output and the distribution across research categories within the field of nanotechnology.*

1.2 The Rise of Iron Oxide Nanoparticles

Among the various materials explored at the nanoscale, iron oxide nanoparticles have garnered significant interest due to their remarkable properties and versatile applications [5]. Within this family of compounds, maghemite (γ-Fe_2O_3), magnetite (Fe_3O_4), and hematite (α-Fe_2O_3) are particularly notable for their different characteristics and widespread use in scientific and industrial fields [6] [7].

A data-driven analysis of the research activity in this field highlights the growing interest in iron oxide nanoparticles over time, as shown in Figure 1.3.

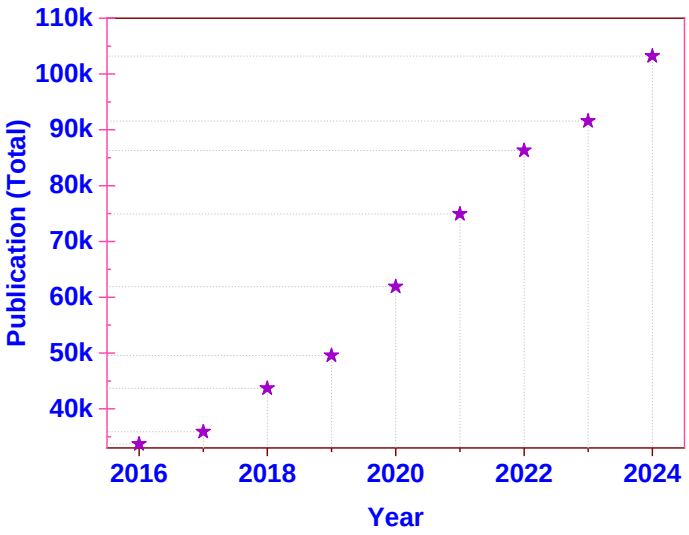

Figure 1.3 – *Data visualization of the search criteria 'iron oxide nanoparticles' from the Dimensions® database.*

Magnetite (Fe_3O_4) has garnered significant interest, particularly for its applications in magnetic resonance imaging and magnetic hyperthermia, thanks to its high saturation magnetization. Magnetite's composition includes both Fe^{2+} and Fe^{3+} ions, contributing to its strong magnetic properties. However, this composition also renders it more susceptible to oxidation, limiting its long-term stability in some applications [7] [8] .

In contrast, hematite (α-Fe_2O_3) is not magnetically active but is renowned for its thermal and chemical stability. These properties make it valuable in applications such as pigments and catalysis. Hematite's chemical composition and stability set it apart, particularly in high-temperature or reactive environments [7].

Between these two iron oxides lies maghemite (γ-Fe_2O_3), a material that combines advantageous traits from both magnetite and hematite. Maghemite, sharing the same crystal structure as magnetite, is fully oxidized, comprising only Fe^{3+} ions. This oxidation state enhances its chemical stability and reduces its toxicity compared to magnetite. The name "maghemite" coined in 1927, reflects its intermediary nature between magnetite and hematite [8].

The combination of magnetic properties and chemical stability in maghemite makes it a crucial material for enhancing the capabilities of iron oxide nanoparticles in various fields.

1.2.1 Crystalline Structure

The crystalline structure of maghemite, equivalently ($Fe_{2.67}O_4$), is fundamental to its properties. It has a cubic inverse spinel structure, which is similar to that of magnetite (Fe_3O_4) [8]. In both structures, oxygen anions create a face-centered cubic lattice, while iron cations occupy tetrahedral and octahedral interstitial sites. A key distinction between the two phases lies in their cation distribution and oxidation states [9].

In maghemite, all iron cations are in the trivalent state (Fe^{3+}), and the structure maintains charge neutrality through cation vacancies in the octahedral sites. Specifically, maghemite's cation distribution is represented as follows [9] (Figure 1.4):

$$(Fe^{3+})_8[Fe^{3+}_{40/3}\square_{8/3}]O_{32} \tag{1.1}$$

where $\square$ denotes a vacancy. Here, 8 Fe^{3+} ions occupy the tetrahedral sites, $\frac{40}{3}$ Fe^{3+} ions occupy the octahedral sites, and $\frac{8}{3}$ octahedral positions remain vacant. This cation arrangement contributes to maghemite's enhanced chemical stability and reduced magnetic properties compared to magnetite [9].

In contrast, the cation distribution in magnetite includes both divalent and trivalent iron ions:

$$(Fe^{3+})_8[Fe_8^{2+}Fe_8^{3+}]O_{32} \tag{1.2}$$

In this configuration, 8 Fe^{3+} ions occupy the tetrahedral sites, while 8 Fe^{2+} and 8 Fe^{3+} ions occupy the octahedral sites. The presence of both Fe^{2+} and Fe^{3+} ions in magnetite contributes to its strong ferrimagnetic properties.

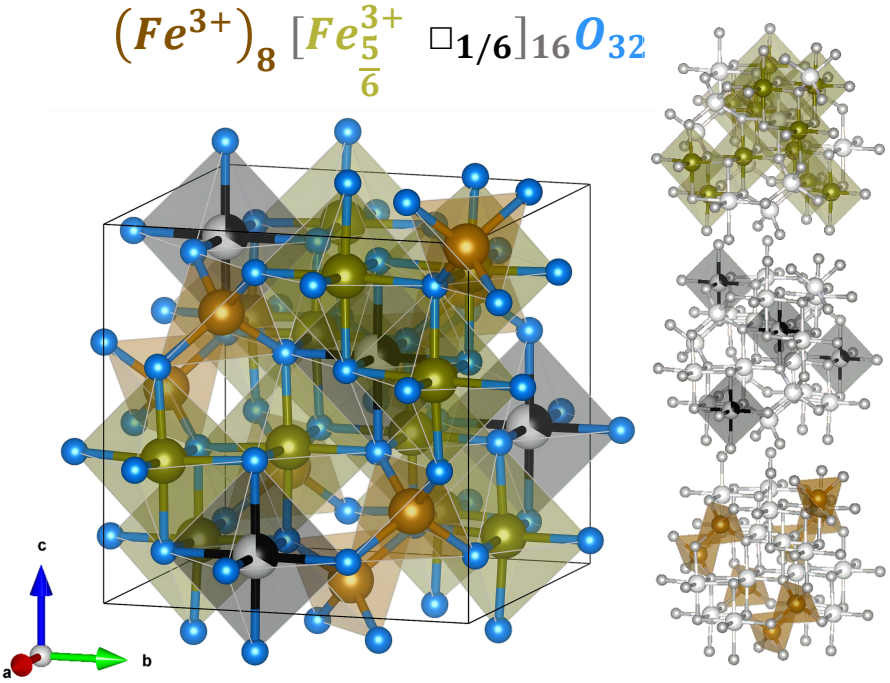

Figure 1.4 – *Unit cell of maghemite showing 8 Fe^{3+} atoms in tetrahedral (4-fold) coordination, 12 Fe^{3+} atoms in octahedral (6-fold) coordination, and 4 vacancies. Illustration generated using VESTA software based on data from [10]. For comparison, magnetite also contains 8 Fe atoms in tetrahedral (4-fold) coordination, but all octahedral sites are occupied: 16 atoms are distributed equally, with half being Fe^{2+} and the other half Fe^{3+}.*

The structural relationship between magnetite and maghemite is also of particular interest. Under oxidizing conditions, magnetite transforms into maghemite through the conversion of Fe^{2+} ions to Fe^{3+}. To maintain charge neutrality during this process, some iron ions are removed, creating the characteristic vacancies in maghemite. This transformation underscores the chemical and structural similarity between the two materials.

Despite their nearly identical crystalline structures, subtle differences in physical properties distinguish magnetite from maghemite. For example, the lattice parameter a is slightly larger for magnetite (0.8394 nm) than for maghemite (0.8346 nm), due to the larger ionic radius of Fe^{2+} ions compared to Fe^{3+} ions [11]. These distinctions, though minor, are crucial in understanding the functionalities of each material [12].

1.2.2 Magnetic Properties

Ferro-, Ferri-, and Antiferromagnetic States of Iron Oxides

The crystal structures of maghemite and magnetite contribute to their magnetic properties, classifying them as ferrimagnetic materials. Ferrimagnetic materials exhibit a distinct type of magnetic behavior where the magnetic moments (or spins) of ions align in opposite directions, known as antiparallel alignment. However, in these materials, the magnetic moments do not completely cancel each other out due to an unequal distribution of these moments, resulting in a net magnetization (see Figure 1.5).

In maghemite's inverse spinel structure, the magnetic moments of Fe^{3+} ions located at tetrahedral and octahedral sites align oppositely, yet they do not negate one another, which leads to a net magnetization, even in the absence of Fe^{2+} ions (refer to Figure 1.5). The presence of vacancies in the octahedral sites contributes to a strong magnetic response, although this response is slightly weaker than that of magnetite [13].

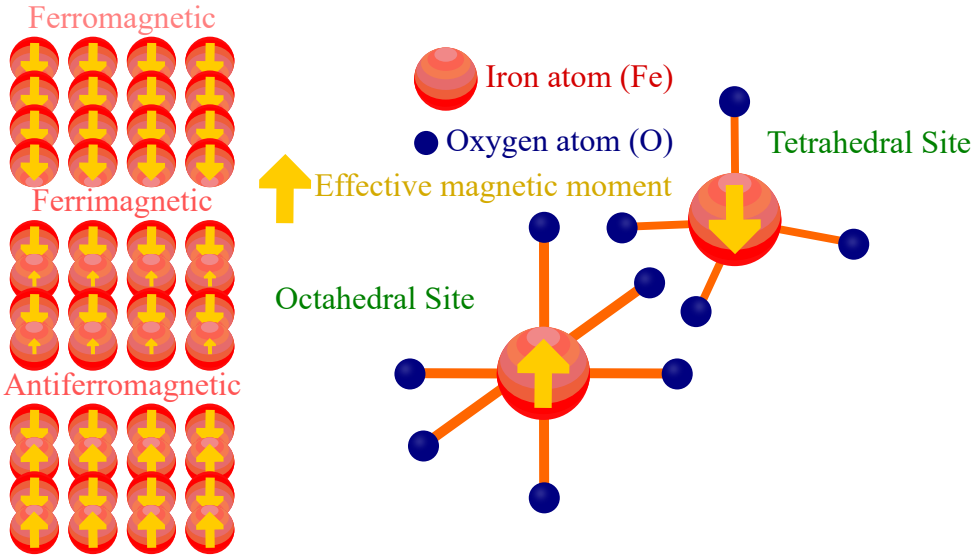

Figure 1.5 – *Illustration of magnetic structures and atomic arrangements: ferrimagnetic and antiferromagnetic configurations (left) and the ferric spinel structure (right), showing iron (Fe) and oxygen (O) atoms at tetrahedral and octahedral sites, which contribute to the net magnetic moment.*

In the inverse spinel structure of magnetite (Fe_3O_4), the magnetic moments of Fe^{2+} and Fe^{3+} ions are arranged in an antiparallel configuration, but the Fe^{2+} ions contribute stronger magnetic interactions, resulting in a higher net magnetic moment[14]. This arrangement leads to a higher saturation magnetization for magnetite compared to its oxidized counterpart, maghemite (γ-Fe_2O_3) [8].

Regarding hematite (α-Fe_2O_3), it exhibits a corundum-type hexagonal crystal structure

and is characterized by its antiferromagnetic behavior. In this structure, the magnetic moments of Fe^{3+} ions align antiparallel, effectively canceling each other out and resulting in no net magnetization at room temperature [14].

Superparamagnetism in Nanoparticles

Magnetic domains are fundamental to the behavior of ferromagnetic materials. In bulk materials, these domains consist of aligned magnetic moments of atoms, each acting as a small magnet. However, as the size of a ferro or ferrimagnetic particle decreases to the nanoscale, its magnetic properties change significantly. When particles become sufficiently small, typically at the nanoscale, they can form a single magnetic domain. In this state, all magnetic moments within the particle align in a single direction, resulting in unique magnetic characteristics. These nanoparticles enter a state called superparamagnetism below a critical size, usually 20-30 nanometers [15]. Superparamagnetic particles become magnetized when exposed to an external magnetic field. Upon removal of the external field, they lose their net magnetic moment [4] (Figure 1.6).

This magnetic behavior was first predicted theoretically by Néel [16], who proposed that for sufficiently small nanoparticles, spin thermal agitation induced by thermal energy prevents the existence of a stable magnetization. This results in the effective loss of resistance to changes in magnetization. The superparamagnetic state occurs when the thermal energy ($k_B T$, where T is the temperature and k_B is the Boltzmann constant) becomes comparable to or greater than the energy barrier for magnetic moment reversal, known as the anisotropy energy, (KV where K and V are the anisotropy energy constant and the volume of the particle).

Superparamagnetic particles are similar to paramagnetic materials in that both types of materials only exhibit magnetization when subjected to an external magnetic field. However, superparamagnetic particles demonstrate significantly stronger magnetization compared to paramagnetic material. This enhanced behavior occurs because superparamagnetic particles act as single magnetic domains with large effective magnetic moments and high magnetic susceptibility. In contrast, paramagnetic materials have weak and random alignment of unpaired electrons, resulting in low magnetization.

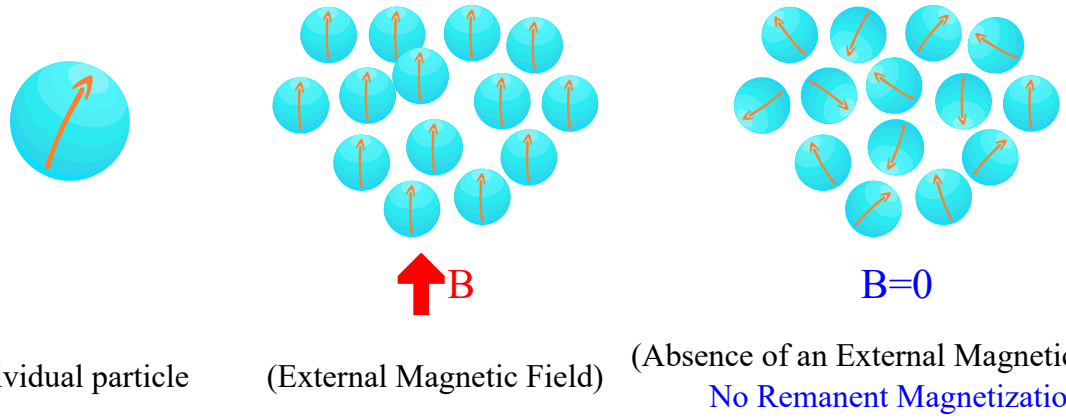

Figure 1.6 – *Superparamagnetism: (Left) Individual particle with random orientation of magnetic moments. (Middle) Alignment of magnetic moments under an external magnetic field (B). (Right) In the absence of an external magnetic field (B=0), no remanent magnetization is observed.*

Concepts of Ferromagnetic and Ferrimagnetic Magnetic Materials

Understanding ferromagnetic and ferrimagnetic materials requires examining several key conceptual parameters that describe their magnetic behavior under different conditions. The following concepts provide a comprehensive framework for analyzing the magnetic characteristics of these materials:

Magnetization Saturation (M_s) Magnetic saturation is the maximum magnetization a material can achieve when exposed to a sufficiently high external magnetic field. At this point, all magnetic moments are aligned with the field direction. Further increases in the field strength do not change the magnetization.

- M_s depends on the chemical nature and density of magnetic moments in the material.
- In nanoparticles, M_s can be reduced due to the presence of a non-magnetic surface layer or size effects.

Coercivity (H_c) Coercivity is the strength of the magnetic field required to reduce a material's net magnetization to zero after saturation. It measures the material's resistance to demagnetization.

- Materials with high coercivity are called hard magnets (used in permanent magnets).
- Materials with low coercivity are called soft magnets (used in electromagnetic cores).
- Superparamagnetic nanoparticles exhibit near-zero coercivity at room temperature due to thermal fluctuations of their magnetization.

Remanence (M_r) Remanence is the magnetization that remains in a material after the external magnetic field has been removed. It reflects the material's ability to retain residual magnetization.

- In bulk ferromagnetic and ferrimagnetic materials, remanence is related to the alignment of magnetic domains.
- In superparamagnetic nanoparticles, remanence is negligible at a temperature with greater thermal energy than the anisotropy energy.

Blocking Temperature (T_b) The blocking temperature is the temperature below which magnetic nanoparticles remain in a stable magnetic state, where their magnetic moments no longer fluctuate thermally.

- Above T_b, particles become superparamagnetic, and their magnetic moments fluctuate rapidly between different orientations under the influence of thermal energy ($k_B T$).
- T_b depends on particle size, magnetic anisotropy (K), and measurement time scale.

Magnetic Anisotropy (K) Magnetic anisotropy describes the dependence of magnetic energy on the orientation of magnetic moments relative to certain preferred directions in the material. Main sources of anisotropy include:

- Magnetocrystalline anisotropy: related to the symmetry of the crystal lattice.
- Surface anisotropy: significant in nanoparticles where the surface represents a large fraction of the total volume.
- Shape anisotropy: due to particle geometry (e.g., spherical or elongated).

The magnetic anisotropy energy with axial symmetry ($E = KV \sin^2 \theta$) determines the stability of magnetic moments against thermal fluctuations, where V is the particle volume and θ is the angle between the magnetic moment and the easy axis. In this equation, K represents the anisotropy constant, which is a material-specific property. The easy axis is the energetically favorable direction of spontaneous magnetization in a magnetic material. It is the direction along which the material is most easily magnetized, requiring the least amount of external energy to align its magnetic moments. The angle θ measures how far the magnetic moment deviates from this preferred orientation. When $\theta = 0$ or 180, the magnetic moment aligns perfectly with the easy axis, resulting in the lowest energy state. As θ increases, the energy required to maintain that orientation also increases, making the magnetic moment less stable against thermal fluctuations.

Hysteresis Loop The hysteresis loop describes the variation of magnetization (M) of a material as a function of the applied magnetic field (H). It provides key information:

- Saturation magnetization (M_s), coercivity (H_c), and remanence (M_r).

An example of a hysteresis loop will be illustrated later in the characterization techniques section (1.7), specifically when discussing the vibrating sample magnetometer technique (1.7.5) and Figure 1.29.

1.2.3 Biocompatibility

Following their magnetic properties, a key feature of iron oxide nanoparticles worth highlighting is their biocompatibility, attributed to several important characteristics. Their chemical stability, mainly maghemite, in biological environments ensures minimal release of toxic ions, safeguarding cellular health [17]. Furthermore, their surfaces can be functionalized with biocompatible coatings, such as polyethylene glycol (PEG) or natural biomolecules, to improve interactions with biological systems [18]. The typical size of IONPs, around 10 nanometers, facilitates efficient processing and elimination by the body [19]. Some IONPs also possess antioxidant properties, aiding in the neutralization of harmful reactive oxygen species within cells [20]. Additionally, IONPs can be engineered to be biodegradable, enabling their gradual breakdown and safe clearance from the body [18]. Studies consistently demonstrate that well-designed IONPs exhibit low cytotoxicity and provoke minimal inflammatory responses, even at relatively high concentrations [21].

1.2.4 Applications and Current Research Directions

The physicochemical properties of maghemite nanoparticles, including their high surface area-to-volume ratio, superparamagnetism, and biocompatibility, have prompted extensive research into their potential applications. The sections below summarize some of these promising uses.

Biomedical Applications IONPs are increasingly recognized for their versatility in various biomedical applications (Figure 1.7). Their superparamagnetic properties and the ease of surface functionalization make them suitable for a range of uses, including hyperthermia, magnetic resonance imaging, immunoassays, drug delivery, and cell separation (Figure 1.7). In therapeutic applications, IONPs are particularly effective for **Targeted drug delivery** [12] [22]. By modifying their surfaces with specific ligands, these nanoparticles can direct therapeutic agents to particular tissues or cells, enhancing treatment efficacy while minimizing side effects. This is especially important in cancer therapy, where magnetic nanoparticles can be utilized in **hyperthermia treatments**. When exposed to an alternating magnetic field, they generate localized heat that can selectively destroy cancer cells [23] [24]. In diagnostics, IONPs enhance imaging techniques such as **Magnetic Resonance Imaging** by improving contrast and resolution. This capability allows for better visualization of tissues and the identification of pathological conditions [25] [26] [27]. Additionally, IONPs are valuable in **Immunoassays** for the rapid detection of biomolecules, enhancing sensitivity and enabling the identification of low-abundance targets like viral antigens in COVID-19 diagnostics [28]. Their remarkable properties improve detection limits, making IONPs es-

sential tools for accurate biomolecule identification [29]. The integration of therapeutic and diagnostic functions—known as theranostics—is another area where magnetic NPs are making significant contributions. This approach allows for real-time monitoring of treatment responses [30], enabling adjustments based on individual patient needs. Furthermore, magnetic NPs are effective in **Isolating specific biomolecules** like DNA, proteins, and cells. This functionality is useful for both biomedical research and industrial purification processes [31] [32]. Their efficiency in binding biomolecules offers advantages over traditional methods such as chromatography.

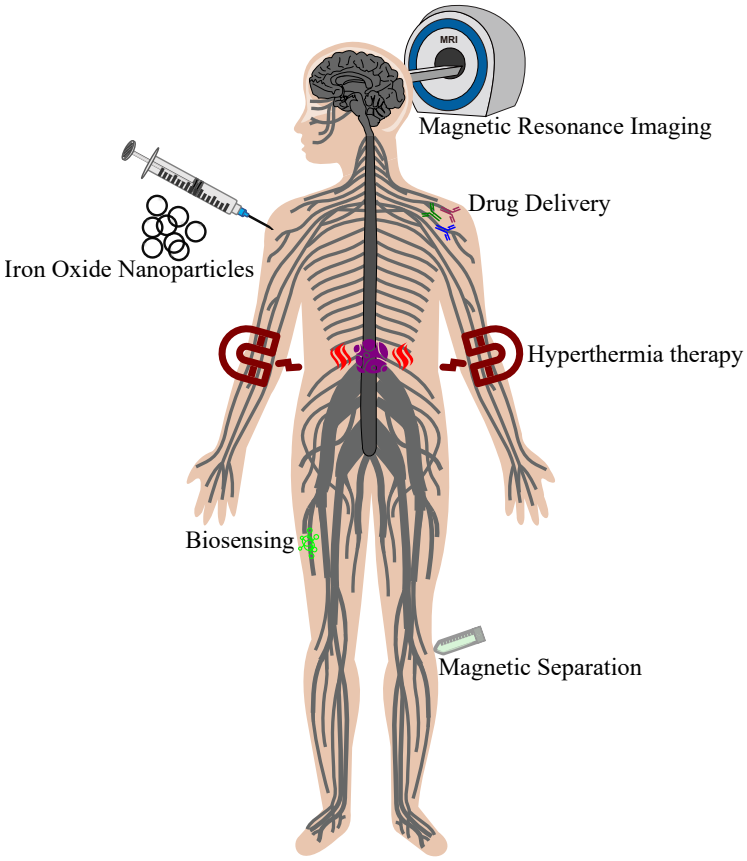

Figure 1.7 – *Biomedical applications of superparamagnetic iron oxide nanoparticles*

Environmental Applications IONPs are also proving effective in environmental remediation. In **water treatment** (Figure 1.8), IONPs serve as powerful adsorbents and catalysts for the removal of pollutants such as heavy metals and organic compounds [33]. Their high surface area allows for efficient binding to target contaminants, facilitating their removal from contaminated water sources [34]. Research has demonstrated that IONPs can effectively reduce concentrations of toxic substances like arsenic, chromium, and copper [35] [36] [37]. The functionalization of IONPs with materials such as chitosan further enhances their

adsorption capacity and selectivity for specific pollutants [38]. This adaptability makes IONPs a promising solution for addressing emerging contaminants in water treatment systems. IONPs also play a significant role in air **filtration technologies**. By integrating IONPs into nanofiber filters, researchers have achieved particle collection efficiencies of up to 97%, significantly outperforming traditional filtration methods [39]. This high efficiency is crucial for improving air quality in urban environments where particulate matter and other pollutants pose health risks. The incorporation of IONPs into electrospun nanofiber membranes not only enhances pollutant removal but also allows for the development of lightweight and flexible filter materials that can be easily deployed in various settings [40]. In **soil remediation**, IONPs contribute to the immobilization of heavy metals and the degradation of organic pollutants [41] [42] [43]. Their magnetic properties enable easy recovery after treatment, which minimizes environmental impact. Additionally, by enhancing the bioavailability of nutrients in contaminated soils, IONPs can promote the growth of plants that aid in phytoremediation efforts [44]. This dual functionality helps clean up contaminated sites while supporting ecological restoration initiatives.

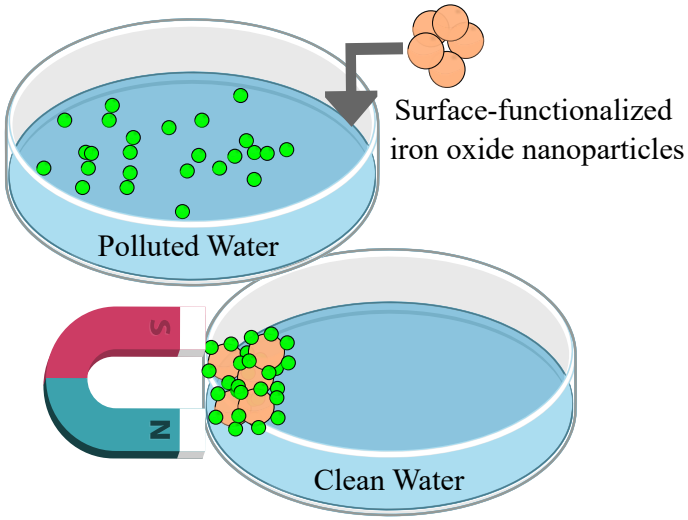

Figure 1.8 – *Iron oxide nanoparticles application in wastewater treatment*

Industrial Applications Besides their biomedical and environmental applications, these nanoparticles have also found roles in various industrial sectors. In ferrofluids, they help create magnetic fluids for uses like seals in rotating machinery and improving heat dissipation in audio devices [45] [46]. In the storage industry, magnetic nanoparticles enable smaller data bits without losing stability, increasing storage capacity in hard drives and other magnetic media [47]. They are also explored for use in inductors and transformers in high-frequency electronics, where their low energy loss at high frequencies is important for efficient power

electronics [47].

1.3 Structural Characteristics Versus Functionality

The effectiveness and diverse applications of IONPs are not solely reliant on their intrinsic properties. Instead, their performance and potential across various fields are greatly influenced by important structural factors, such as particle size, surface modifications, and morphology (Figure 1.9).

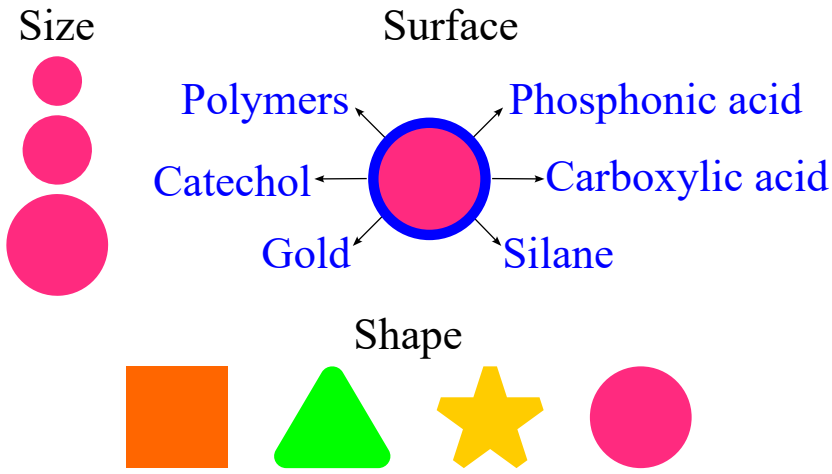

Figure 1.9 – *Main Features of Nanoparticles*

Mastering the size, composition, and morphology of nano-objects is a critical step for enhancing their properties and ensuring the success of their applications. Several examples illustrating this are provided below:

1.3.1 Effect of Structural Characteristics of IONPs on Their Magnetic Properties

Among these structural characteristics, size is one of the most critical factors. A fundamental magnetic property that varies with size is the blocking temperature, which, as discussed earlier, refers to the temperature at which the magnetic moments of nanoparticles become "blocked." At this temperature, the magnetic moments no longer relax on the timescale of measurement [48]. Smaller nanoparticles exhibit lower blocking temperatures, which significantly affects their magnetic behavior, even at room temperature [49] [50].

A major property dictating the magnetic behavior of iron oxide nanoparticles is also their crystallinity. The high crystallinity of the nanoparticles, or the strong order of atoms, increases the magnetocrystalline anisotropy, which describes the preferred orientation of magnetic moments in the crystal lattice [51]. This higher level of anisotropy results in a stronger

overall magnetic response. The anisotropy energy, critical to the stability of the magnetic moment, determines whether nanoparticles exhibit ferromagnetic or superparamagnetic characteristics [52]. It represents the energy barrier that thermal energy must overcome to spontaneously flip magnetic moments. Thus, crystallinity not only amplifies the magnetic response but also governs IONP behavior across various temperatures and magnetic fields.

The balance between size and crystallinity engenders rich magneto-physical phenomenology. In this context, small magnetic nanoparticles have low blocking temperatures and tend to be superparamagnetic. Nevertheless, highly crystalline nanoparticles can preserve their ferromagnetic properties down to relatively small sizes due to their increased magnetocrystalline anisotropy, which confers greater thermal stability to their magnetic moments [53].

The high surface-to-volume ratio in smaller nanoparticles amplifies surface effects, which stem from incomplete atomic coordination and broken lattice symmetry at the surface [54]. At the nanoparticle surface, uncompensated spins create a magnetically disordered layer, typically 0.54–1 nm thick, exhibiting canted spins or spin-glass-like behavior [55]. This magnetically disordered layer disrupts the uniform spin alignment characteristic of bulk materials, reducing overall saturation magnetization. As particle size diminishes further, the relative influence of this disordered layer becomes more pronounced, progressively weakening the magnetic properties of nanoparticles smaller than 10–20 nm.

Moreover, a concept introduced by Kaiser and Miskolczy underscores the possible existence of a magnetically dead layer at the nanoparticle surface [56]. They proposed a model for the superparamagnetic magnetization curve that fit experimental data by incorporating a thin, nonmagnetic layer about one unit cell thick. Subsequent studies have consistently observed that magnetic diameters, determined through magnetic measurements, are significantly smaller than physical diameters, with discrepancies often attributed to such magnetically dead layers [54].

Surface modification further influences these magnetic properties. The interaction between surface capping agents and the nanoparticle surface can alter the thickness or characteristics of the magnetically dead layer, thereby enhancing or suppressing surface magnetization. In one study, oleic acid functionalization in 6, 10, and 17 nm Fe_3O_4 nanoparticles increased saturation magnetization to near bulk values, attributed to covalent bonding that reduced surface spin disorder [57]. In another study, dopamine-functionalized nanoparticles showed improved magnetic properties (Ms increased from 38 emu/g Fe to 60 emu/g Fe), while oleic acid-functionalized nanoparticles still exhibited an Ms far below the bulk value. These findings highlight the critical role of surface capping agents in tailoring the magnetic response of nanoparticles [58].

In addition to size, crystallinity, and surface structure, the shape of IONPs is another

important factor influencing their magnetic behavior and suitability for various applications. Different shapes—such as nanospheres, nanorods, nanocubes, nanoplates, and nanoflowers—impart unique properties [59] [60]. The shape determines how easily magnetization occurs along specific directions. For example, nanorods exhibit easier magnetization along their long axis due to shape anisotropy, while nanocubes and nanooctopods are known for their superior heating capabilities, making them particularly effective for applications like magnetic hyperthermia [61] [62]. By carefully tailoring nanoparticle shapes, researchers can optimize IONPs for specific uses.

1.3.2 Effect of Structural Characteristics of IONPs on Reactivity

While the magnetic properties of IONPs are profoundly influenced by their structural characteristics, these same features also play a crucial role in determining their reactivity. As particle size decreases, the dramatically increased surface-to-volume ratio exposes more atoms with unsaturated coordination, creating highly reactive sites primed for chemical interactions [63]. This enhanced reactivity, however, comes with a potential trade-off of reduced stability and increased aggregation tendency.

The crystallinity of IONPs further modulates this reactivity landscape. While highly crystalline particles typically demonstrate lower chemical activity due to their stable atomic arrangements, less crystalline or amorphous structures rich in defects become catalytic hotspots. These defect-laden regions serve as ideal platforms for electron transfer, ion exchange, and heterogeneous catalysis, transforming structural imperfections into chemical opportunities [64].

Surface structure adds another layer of complexity, with under-coordinated surface atoms experiencing lattice distortions that create reactive sites. Functional groups like hydroxyl ions, commonly present in aqueous environments, can participate in acid-base reactions or influence contaminant adsorption [65].

Particle morphology, such as whether they are nanospheres, nanorods, or nanocubes, reveals different crystallographic facets that have distinct chemical activities, allowing for directional reactivity. The shape and crystal phase of iron oxides determine how surface iron (Fe) and oxygen (O) atoms are arranged, which is closely related to the active sites for catalysis [66].

1.4 Synthesis of Iron Oxide Nanoparticles

To control these key features of the nanoparticles, it is essential to consider the synthesis process employed. To achieve precise control over these attributes, a range of synthesis methods has been developed in the literature [5] [67]. These methods can be broadly classified into two categories: Top-Down and Bottom-Up approaches.

1.4.1 Top-Down vs. Bottom-Up

The **top-down approach** for synthesizing iron oxide nanoparticles involves breaking down larger bulk materials into nanosized particles. One effective technique within this approach is laser ablation, which uses focused laser beams to vaporize material from a solid target, resulting in the formation of nanoparticles in a liquid medium [68]. Other top-down methods include crushing, milling, or grinding, which also contribute to the production of nanoparticles [67]. In contrast, the **bottom-up approach** involves synthesizing materials molecule by molecule, atom by atom, or cluster by cluster. Common techniques in this category include co-precipitation, sol-gel synthesis, microemulsion methods, and thermal decomposition [5].

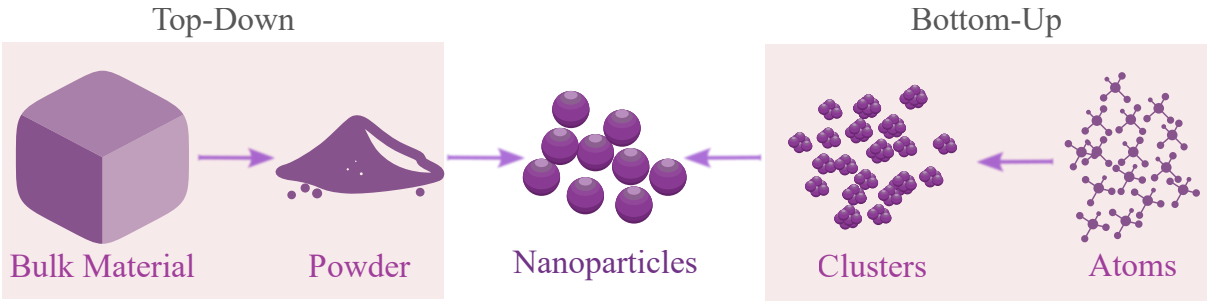

Figure 1.10 – *Scheme of top-down and bottom-up synthesis of nanoparticles*

Both the top-down and bottom-up approaches offer specific advantages and limitations when synthesizing iron oxide nanoparticles [69]. The top-down method allows good control over the size and shape of the nanoparticles produced, as it involves breaking down larger particles into nanoscale sizes. This approach utilizes well-established mechanical processes, making it easier to implement in industrial settings. However, it is energy-intensive, requiring significant energy input due to mechanical milling and crushing processes. Additionally, nanoparticles produced via this method are often larger compared to those produced by bottom-up techniques, which may limit their applications. A key drawback of the top-down approach is its inability to passivate nanoparticles with specific surface ligands during production, which can hinder their stability and functionality in applications requiring tailored surface chemistries. In contrast, the bottom-up method can produce nanoparticles

with superior geometric structures and size ranges due to the atomic-molecular interactions involved in the synthesis. This method is often more scalable and versatile, allowing for the production of nanoparticles with specific properties tailored for various applications. However, it can involve complex chemical processes that require careful control of reaction conditions to achieve desired outcomes, and there is a risk of introducing contaminants during the chemical synthesis processes, which can affect the purity and functionality of the nanoparticles. Ultimately, the choice between these two approaches depends on the specific requirements of the application, including factors such as desired particle size, shape, purity, and scalability.

In this study, we prefer a bottom-up approach because it allows for precise control over the size, shape, and surface chemistry of the materials. This level of control is essential for optimizing their performance and enhancing our understanding of how these characteristics affect material behavior.

1.4.2 Bottom-Up Synthesis

a. Liquid-Phase Synthesis: A Central Focus

Among bottom-up techniques, liquid-phase synthesis stands out due to its versatility and the high degree of control it offers over particle characteristics such as size, shape, and composition. Methods such as thermal decomposition, hydrothermal synthesis, and microemulsion, which operate in solution, offer significant advantages [5]. Reaction parameters, including temperature, precursor concentration, and pH, can be precisely tuned to direct nanoparticle formation. These processes are also energy-efficient and safer, typically requiring mild conditions such as lower temperatures and atmospheric pressure compared to gas-phase methods, such as chemical vapor deposition [70]. However, unlike the relatively mature field of organic synthesis, the chemical synthesis of nanocrystals remains largely empirical. This gap highlights the need for quantitative theories to guide the transformation.

b. Theoretical Frameworks

The fundamental processes of nanoparticle formation in liquid-phase synthesis — nucleation and growth — are described by two key theoretical models: the LaMer model and the Gibbs free energy framework. While these models offer valuable explanations, they do not account for all aspects of the nanoparticle formation process.

The **LaMer model** provides a structured approach to understanding the synthesis of nanocrystals, describing their formation in three distinct stages [71]:

1. **Monomer Generation**: Initially, monomers are generated through the reduction or

a physical transformation of molecular precursors. As the reaction progresses, the monomer concentration increases, reaching the saturation concentration (C_s), which represents the maximum concentration of monomers that can dissolve in the solution. This concentration defines the solubility limit.

2. **Nucleation**: Once the concentration surpasses a minimum nucleation concentration (C_{min}), supersaturation occurs, which triggers the spontaneous formation of nuclei. Only those nuclei that reach a critical size become stable and thermodynamically favorable. The C_{min} represents the concentration at which rapid nucleation starts, as the monomer concentration exceeds the saturation limit.
3. **Growth**: Once stable nuclei form, they begin to grow irreversibly as monomers are added to their surfaces. The growth continues until the concentration of monomers falls below the saturation concentration (C_s), halting further nucleation, as there are not enough monomers to create new nuclei. The concentration profile during this phase is shown in the LaMer-Dinegar diagram (Figure 1.11), which illustrates the evolution of precursor concentration over time.

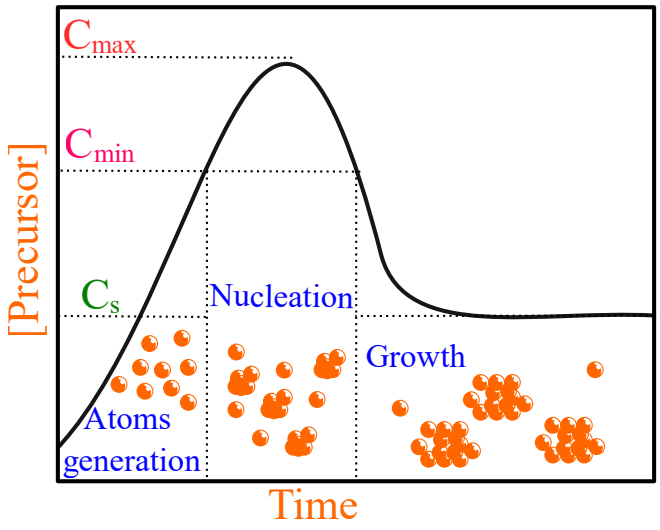

Figure 1.11 – *LaMer-Dinegar Diagram: Schematic representation of crystal growth kinetics showing the evolution of precursor concentration over time, based on the Lamer model. The process is divided into three distinct phases: atom generation (initial phase with individual atoms), nucleation (formation of small clusters), and growth (development of larger crystal structures). The concentration profile highlights characteristic points: maximum concentration (C_{max}), minimum concentration (C_{min}), and saturation concentration (C_s).*

The separation of nucleation and growth stages is critical for achieving size-homogeneous colloids, as overlapping these stages leads to polydispersity (a wide size distribution). This understanding lays the foundation for designing processes to control nanocrystal size and shape.

While the LaMer model provides a comprehensive kinetic picture of nanocrystal formation, it primarily focuses on the concentration dynamics of monomers. However, Classical Nucleation Theory (CNT) adds a thermodynamic perspective by incorporating energy considerations to explain the stability of forming nuclei [72]. In CNT, the formation of a stable nucleus depends on the interplay between two competing factors:

- **Surface Energy**: The energy required to form the surface of the nanoparticle, opposing growth.
- **Bulk Energy**: The energy gained when monomers transition from the solution phase to the solid phase, favoring growth.

This balance leads to the **Gibbs free energy equation** [73], which quantifies the total energy change during nucleation:

$$\Delta G = 4\pi\gamma R^2 + \frac{4}{3}\pi R^3 \rho_s \Delta\mu \tag{1.3}$$

Where:

- γ is the surface tension at the solid/liquid interface.
- R is the radius of the nucleus.
- ρ_s is the density of the solid material.
- $\Delta\mu$ is the chemical potential difference between the monomers in solution and the bulk material.

This equation captures the competing roles of surface and bulk energies:

- The **surface term** ($4\pi\gamma R^2$) makes nucleus growth energetically unfavorable at small sizes, as the energy cost of creating surface area increases.
- The **volume term** ($\frac{4}{3}\pi R^3 \rho_s \Delta\mu$) favors growth by releasing energy as monomers are incorporated into the nucleus.

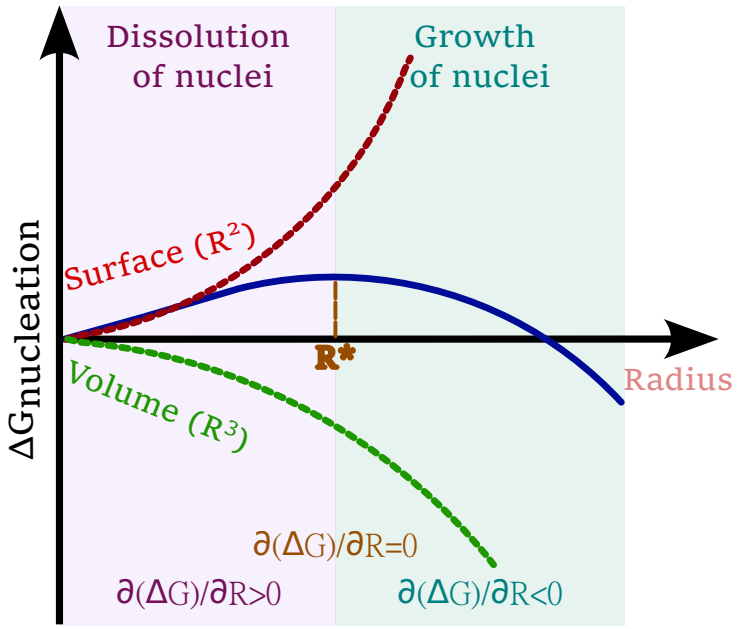

Figure 1.12 – *Diagram of the system's free energy evolution as a function of nucleus size. The violet area on the left corresponds to the range of nucleus sizes where dissolution is favored; the green area on the right corresponds to the size range where nucleus growth is favored.*

When the nucleus reaches a critical size, both terms balance, and the nucleus becomes stable (See Figure 1.12). Nuclei that surpass the **critical radius** (R^*) continue to grow, while smaller nuclei dissolve back into the solution. The critical radius is determined by setting the derivative of the total Gibbs free energy change (ΔG) with respect to the nucleus radius (R) to zero, i.e.,

$$\frac{\delta \Delta G}{\delta r} = 0, \tag{1.4}$$

This condition gives:

$$R^* = -\frac{2\gamma}{\Delta G_V}, \tag{1.5}$$

Interestingly, nucleation can also be heterogeneous, which means it may occur on an external site to the system, such as a surface, an impurity, or even a nanoparticle. In this scenario, the kinetic barrier for nucleation is reduced, and the critical radius decreases. This occurs because nucleation on a heterogeneous site reduces surface tensions, as it limits the formation of liquid-solid interfaces.

c. Temporal Coupling of Nucleation and Growth

The growth stage in the LaMer diagram corresponds, as previously explained, to the

expansion of the nuclei. In the LaMer-Dinegar model, this phase begins once nucleation has occurred and when a sufficient amount of metallic atoms or monomers have been utilized in the nucleation process. At this point, the concentration of monomers drops below the critical level at which nucleation can occur.

Following this, the monomers in the solution contribute to the enlargement of the pre-existing nuclei: this process is referred to as growth via monomer diffusion within the solution.

In this framework, where nucleation and growth unfold in two separate sequential steps from a time perspective, the rate of NP growth depends solely on the diffusion rate of the monomers. This mechanism promotes size uniformity because smaller NPs, being less stabilized due to a higher surface-to-volume ratio and greater surface energy, will experience accelerated growth. As a result, the overall NP size will approach a specific critical size, with a minimal size distribution. This phenomenon is known as size homogenization or size focusing.

However, nucleation and growth are not always temporally independent. Figure 1.13 demonstrates a scenario where multiple nucleation events may occur over time, running concurrently with the growth of previously formed NPs. This situation arises when monomers are consumed quickly and incompletely. In particular, it can occur if: i) the diffusion rate is greater than or comparable to the nucleation rate; ii) the reduction rate is slower than the nucleation rate.

It is worth mentioning that while the Lamer diagram and Gibbs free energy provide useful frameworks, they cannot fully explain or predict the intricate details of nanoparticle formation. These models have limitations when it comes to capturing the complexities of the synthesis process. Although they offer insights into nucleation and growth, they primarily focus on equilibrium conditions and do not account for kinetic factors, precursor interactions, and the dynamic nature of growth mechanisms. The chemical synthesis of nanocrystals remains, in many ways, an art form, as there is currently no quantitative theory capable of precisely predicting how to obtain new materials with controlled size and shape from a molecule [74].

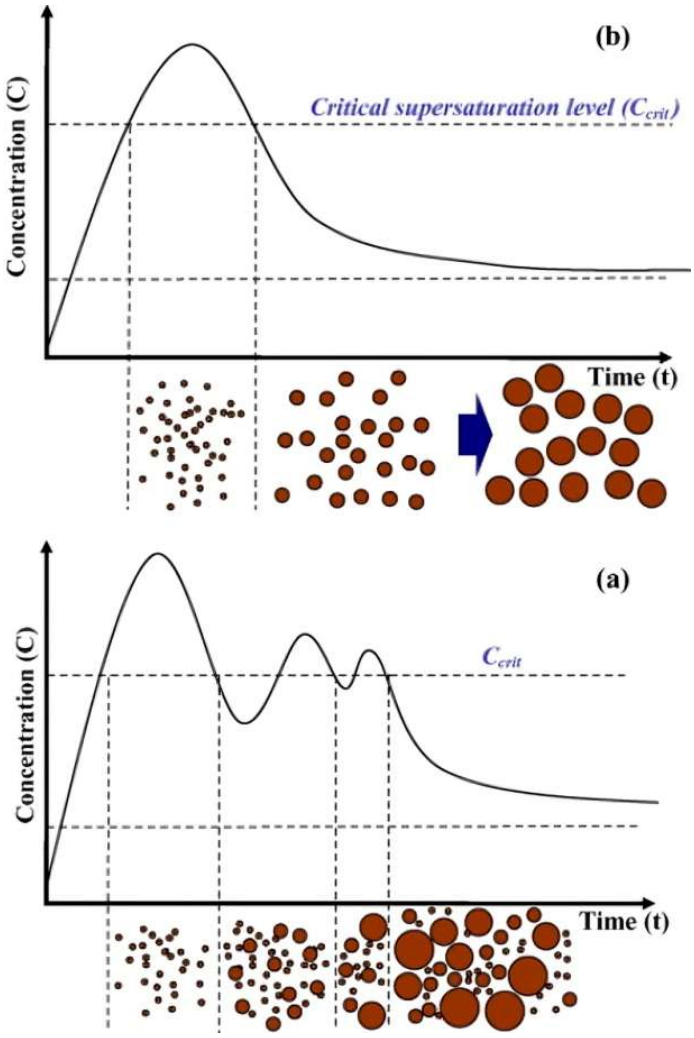

Figure 1.13 – *Schematic illustrating the size distribution of NP populations according to the LaMer model: (top) a single, discrete nucleation event over time; (bottom) multiple successive nucleation events over time [75].*

d. Crystallinity during Growth

The crystal structure of the nanoparticles is shaped by several key factors during the growth process. According to the literature on the crystallinity of iron oxide nanoparticles, temperature plays a significant role, with higher temperatures generally enhancing crystallinity. This is because elevated temperatures speed up the transformation from amorphous to crystalline structures, allowing atoms to arrange more precisely and form well-ordered crystal lattices [76] [77] [78]. The concentration of precursors also has a major impact on nucleation and growth rates, which ultimately determine the final crystalline structure of the nanoparticles. Lower precursor concentrations usually result in slower, more controlled particle formation, often leading to higher crystallinity, while higher concentrations can cause

faster reactions that may introduce structural irregularities [79]. The solvent chosen for the reaction is crucial as it affects both the reaction kinetics and the mechanisms of particle formation. For example, high-boiling point organic solvents enable high-temperature reactions, which promote the growth of more perfect crystal structures [80]. Reaction time is another important factor; longer synthesis periods provide more opportunities for atoms to align and correct structural defects, gradually refining the internal structure of the nanoparticles [78] [79]. Finally, the chemical environment—such as the presence of ligands, the oxidation state of iron, and oxygen partial pressure—further influences the crystallization process. These subtle chemical factors can determine whether magnetite or maghemite forms, each with distinct crystallographic properties [81] [82].

e. Morphology during Growth

The shape of nanoparticles is fundamentally influenced by the principle of surface energy minimization, which drives the system toward the most stable configuration. Without external modifiers, nanoparticles adopt morphologies dictated by the Wulff construction, a geometric model that predicts equilibrium shapes by balancing the surface energies of different crystallographic facets [83]. For iron oxide nanoparticles, low-energy facets like 111 and 100 of the spinel structure often dominate in these thermodynamic states, resulting in isotropic or irregular shapes due to uncontrolled growth [84][85]. Depending on the relative growth rates of each facet in the reaction medium, the final nanoparticle shape is determined, as illustrated in Figure 1.14.

During nanoparticle synthesis, ligands play a critical role in shaping particles by altering surface energy balance. Ligands can selectively bind to specific crystallographic facets via coordination bonds, van der Waals interactions, or hydrogen bonding [85] [86]. By adsorbing to these facets, ligands reduce their surface energy, thereby stabilizing them and suppressing growth along those directions (Figure 1.15). This selective inhibition introduces kinetic control into the system, favoring anisotropic growth and enabling the formation of well-defined shapes that deviate from thermodynamic equilibrium [59] [85] .

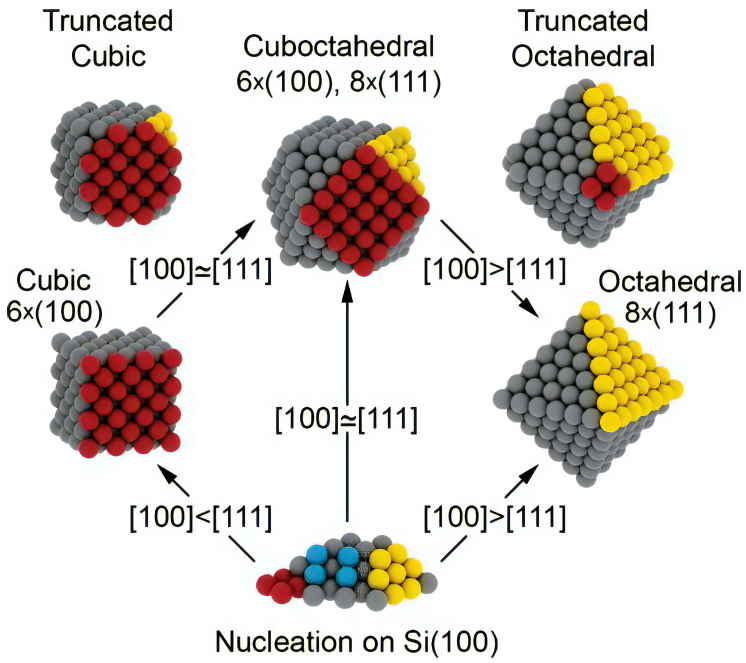

Figure 1.14 – *Schematic diagram illustrating the concept of shape evolution in nanoparticles, where different relative growth rates along specific crystallographic directions ([100] and [111]) lead to distinct morphologies. This principle is exemplified by the shape transformation observed in Cu nanoparticles under varying growth conditions [87].*

Under standard conditions, spherical iron oxide nanoparticles are typically obtained when oleic acid is used as the sole surfactant, suggesting that oleic acid acts as a general stabilizer across all facets [85]. In contrast, amine-based ligands such as oleylamine can influence growth in different ways, allowing for alternative shapes like nanocubes or rods.[88] [89]. The combination of ligands and synthesis parameters (e.g., temperature, solvent, precursor concentration) allows precise tuning of nanoparticle morphology [59]. Without ligands, the uncontrolled growth of iron oxide nanoparticles leads to larger, irregular structures, driven solely by the system's drive to minimize total surface energy [90]. This lack of regulation can also result in poor reproducibility, undermining applications where uniformity is critical. Researchers have also demonstrated that thermal energy plays a significant role in controlling the distribution of shapes in populations of nanoparticles, with a strong dependence on particle size, further highlighting the complexity of nanoparticle shape determination [91].

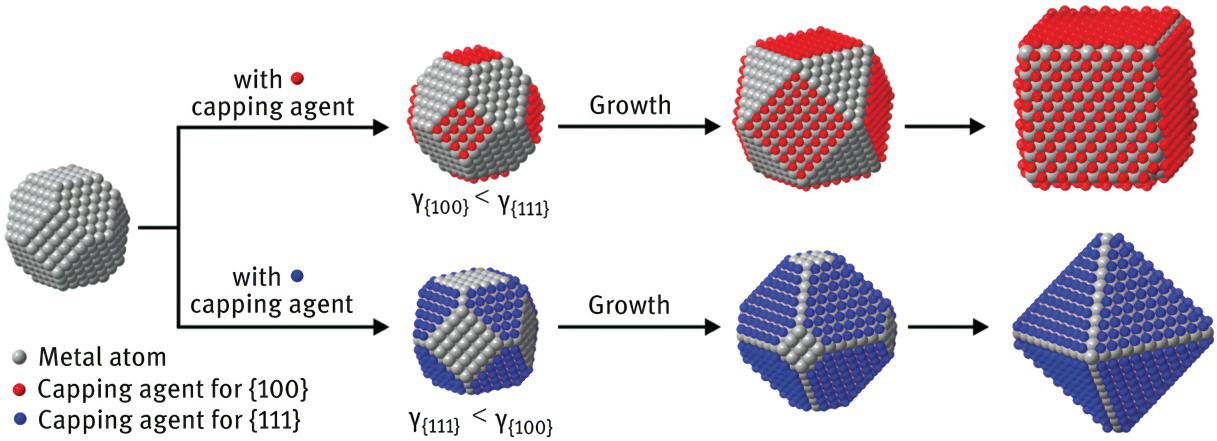

Figure 1.15 – *Schematic depicting morphology control from a cubo-octahedral seed through the selective passivation of (100) or (111) facets, highlighted in red and blue, respectively, leading to cubic or octahedral morphologies [92].*

f. Ostwald Ripening

After the initial growth phase, when all available monomers in the system are consumed, nanoparticles can further develop through maturation processes. A significant mechanism in this context is Ostwald ripening, which influences the size and morphology of these nanoparticles [93]. In Ostwald ripening, larger particles grow at the expense of smaller ones due to differences in solubility. The smaller nanoparticles dissolve because they are thermodynamically unstable, and their monomers redeposit onto larger particles, leading to a more uniform size distribution. This gradual process contributes to the homogenization of nanoparticle sizes. As smaller particles dissolve into the growth solution, the resulting monomers facilitate the growth of larger particles. Recent studies indicate that employing techniques like inductive heating can enhance this ripening process, allowing for the production of larger iron oxide nanoparticles with narrow size distributions while maintaining their magnetic properties [94].

g. Stabilization Mechanisms of Nanoparticles

After the synthesis process, nanoparticles tend to aggregate due to their high surface energy. To prevent this, they can be stabilized using two main types of repulsive forces: electrostatic and steric repulsion [95], illustrated in Figure 1.16.

Electrostatic stabilization occurs when charged species adsorb onto the nanoparticle surfaces, creating a layer of like charges that repel each other. For iron oxide nanoparticles, this happens through different processes. For example, the surface hydroxyl groups (Fe-OH) can protonate or deprotonate depending on the pH of the solution, or charged ions and

molecules can adsorb onto the surface from the surrounding medium. This gives the nanoparticle surface a charge, which attracts counter-ions from the solution, forming an electric double layer. This layer consists of a Stern layer of tightly bound counter-ions and a more diffuse layer of loosely associated ions. Common stabilizers that use this mechanism include sodium citrate, which imparts a negative charge, and tetramethylammonium hydroxide, which provides a positive charge [96].

Steric stabilization, on the other hand, relies on physical barriers created by adsorbed molecules. These molecules are often long and flexible, and they extend into the surrounding medium, effectively separating the nanoparticles from each other. When two particles come close together, the stabilizing layer on each nanoparticle overlaps, creating steric repulsion that keeps the particles apart. Common steric stabilizers for iron oxide nanoparticles include polyvinyl alcohol and oleic acid [97] [98].

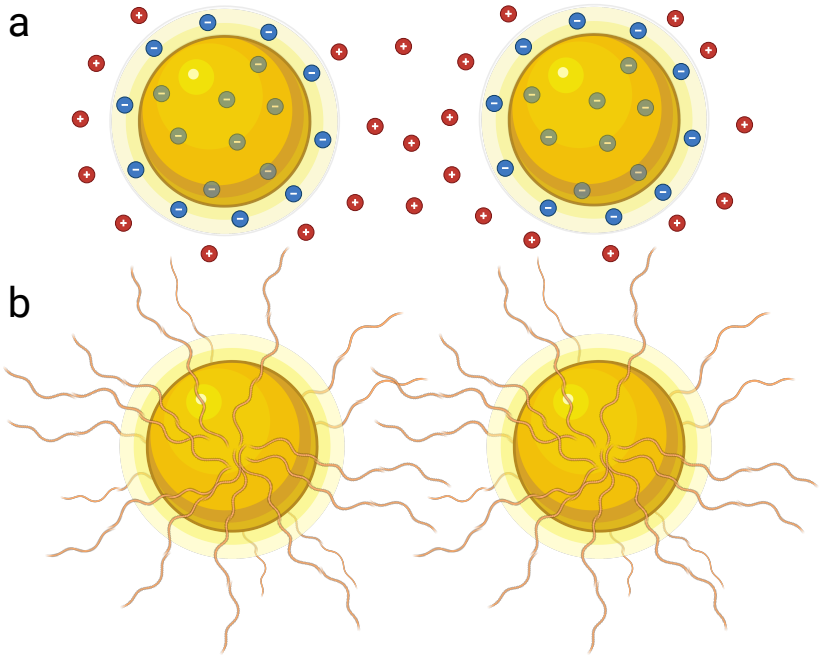

Figure 1.16 – *Schematic representation of (a) particles stabilized by the electrostatic layer and (b) particles stabilized by steric repulsion*

h. Purification of Nanomaterials

After synthesis, nanoparticles often exist in a complex colloidal solution that contains various chemical components. This mixture may include leftover solvents, excess stabilizers, and byproducts from the reactions that produced the nanoparticles. These impurities can influence the properties of the nanoparticles. To address this issue, synthesis protocols typically incorporate purification steps to remove unwanted substances.

To extract the nanoparticles from the synthesis solution, the colloidal balance must

be disrupted to induce precipitation or reversible aggregation. This can be achieved by introducing a solvent that interacts poorly with the surface molecules of sterically stabilized nanoparticles. This process encourages flocculation, resulting in nanoparticle aggregation. Following these adjustments, centrifugation is employed to separate the nanoparticles from the rest of the solution. The resulting pellet contains the purified nanoparticles, which can then be re-dispersed in a suitable solvent that ensures their stability (Figure 1.17).

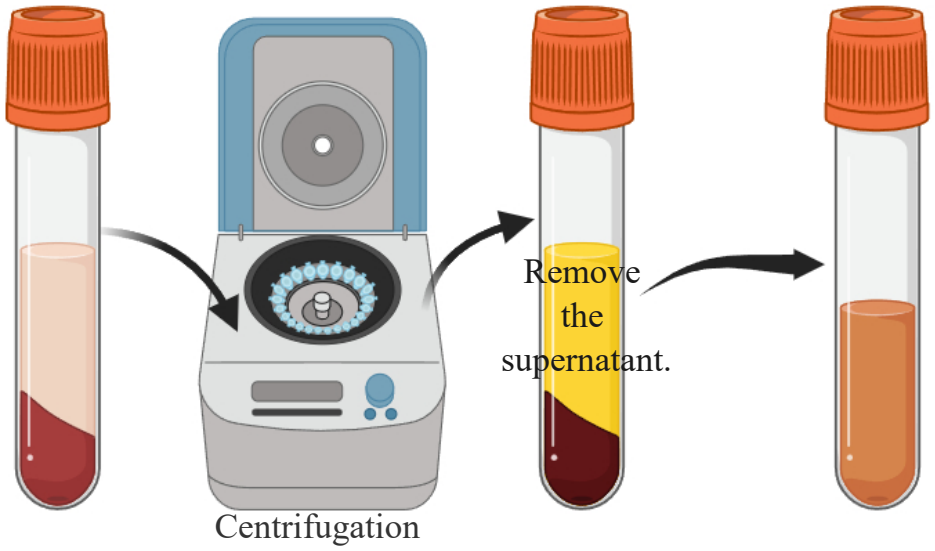

Figure 1.17 – *Schematic representation of the nanoparticle washing process. Nanoparticles are dispersed in a poor solvent to promote aggregation, followed by centrifugation to separate them from the supernatant. The aggregated nanoparticles are then redispersed in a good solvent to achieve a stable colloidal suspension*

Purification is not just about removing impurities, it also provides an opportunity to sort nanoparticles based on size and shape. By understanding how these structural factors influence solubility, researchers can enhance the quality and functionality of their final products.

1.5 Overview of Synthesis Methods

Building on the fundamental principles of bottom-up synthesis in liquid phases, which include precursor atom concentration, nucleation, and morphology control during growth, this section delves into the specific synthesis methods of iron oxide nanoparticles in liquid phase. We will examine a range of synthesis methods, highlight their particular advantages, and discuss recent advancements in the field.

1.5.1 Early Synthesis Methods: Coprecipitation

The coprecipitation method, originally developed by Massart in 1981 [99], is one of the first and most widely used techniques for synthesizing iron oxide nanoparticles. Valued for its robustness and ability to produce large volumes of nanoparticle suspensions in a single synthesis step. The Massart method, illustrated in Figure 1.18, involves the coprecipitation of ferrous (Fe^{2+}) and ferric (Fe^{3+}) ions in an alkaline medium using common precursors like iron(II) chloride ($FeCl_2$) and iron(III) chloride ($FeCl_3$). These precursors are mixed typically in a 2:1 molar ratio and then precipitated by adding a base, such as sodium hydroxide (NaOH) or ammonium hydroxide (NH_4OH).

The size and morphology of the nanoparticles can be adjusted by controlling various parameters during the synthesis, such as pH, temperature, ionic strength, and the nature of the salts (e.g., chlorides, sulfates, or nitrates). For instance, increasing the pH and temperature generally results in smaller particle sizes. The Fe^{2+}/Fe^{3+} ratio is a key factor in determining the final iron oxide phase, and surface properties can be tuned by adding stabilizing agents during or after synthesis [100], as well as through post-synthesis treatments. These modifications enhance the colloidal stability of the nanoparticles and enable further functionalization for specific applications.

The coprecipitation reaction for producing magnetite (Fe_3O_4) nanoparticles occurs under basic conditions, with ferrous and ferric ions reacting to form magnetite in a one-pot synthesis [5]:

$$Fe^{3+} + 2Fe^{2+} + 8OH^- \rightarrow Fe_3O_4\ (\text{solid}) + 4H_2O$$

This process can be carried out at room temperature or elevated temperatures, with factors like the rate of base addition, temperature, and stirring rate influencing the nanoparticle characteristics. For maghemite ($\gamma - Fe_2O_3$) nanoparticles, an additional oxidation step is typically required to convert magnetite into maghemite by oxidizing the Fe^{2+} ions to Fe^{3+} within the structure [101]. Alternatively, maghemite can also be synthesized by coprecipitating only ferric ions (Fe^{3+}), followed by thermal or hydrothermal treatment that promotes crystallization and structural rearrangement. Note that ferric ions cannot be oxidized further; thus, the process does not involve oxidation in the redox sense, but rather a structural transformation leading to maghemite formation.

While the coprecipitation method is highly flexible and cost-effective for producing iron oxide nanoparticles on a large scale, it does face limitations. Achieving a narrow size distribution and high crystallinity remains challenging, as the method does not allow for precise control over nanoparticle size and shape. Variations in reaction conditions can lead to differences in the final nanoparticle characteristics, making reproducibility an issue.

Additionally, nanoparticles produced by coprecipitation tend to agglomerate over time, which can reduce their effectiveness for certain applications. Despite these challenges, the coprecipitation method remains a cornerstone in the field of nanomaterial synthesis, especially when scalability and simplicity are prioritized.

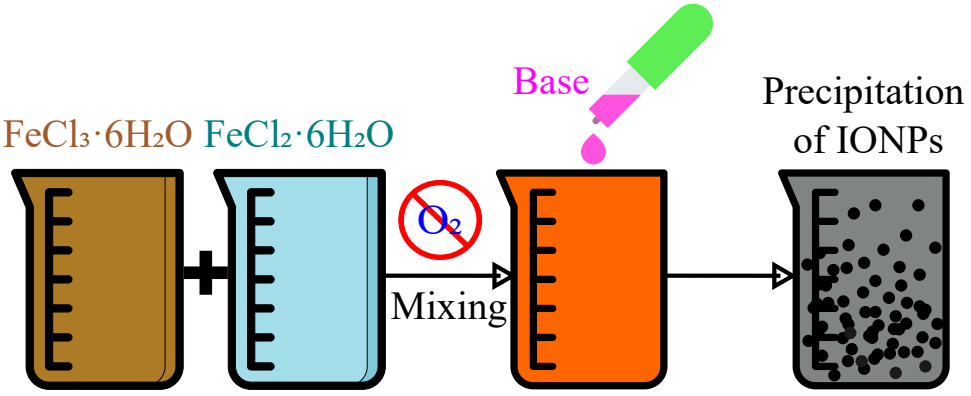

Figure 1.18 – *Schematic Representation of the Co-precipitation Process for Synthesizing Iron Oxide Nanoparticles*

1.5.2 Advanced Synthesis Methods

To achieve greater control over the properties of iron oxide nanoparticles, researchers have developed advanced synthesis techniques. Methods such as microemulsion, sol-gel processes, hydrothermal synthesis, and thermal decomposition enable precise tailoring of particle size, shape, and crystallinity. These techniques offer distinct advantages, facilitating the production of high-quality iron oxide materials optimized for diverse applications.

1. Microemulsion Synthesis

Microemulsions are thermodynamically stable colloidal systems that enable two immiscible liquids, such as oil and water, to coexist in a single phase due to surfactants, which reduce interfacial tension [102]. These systems serve as nanoreactors, providing a controlled environment for nanoparticle synthesis. The process, as visualized in Figure 1.19, begins with the preparation of a stable dispersion, where the oil phase acts as the continuous medium, and water droplets, encapsulated by surfactants such as sodium dodecyl sulfate, form micelles. These micelles confine the metal precursors, such as ferric chloride ($FeCl_3$) and ferrous chloride ($FeCl_2$), creating isolated reaction zones. To synthesize iron oxide nanoparticles [103], a basic solution like ammonia or a second emulsion is introduced into the microemulsion system. This step disrupts the micelles, allowing the confined precursors to mix and react, initiating controlled nucleation and growth of the nanoparticles. Surfactants play a critical role in stabilizing the nanoparticles, reducing agglomeration, and ensuring

uniform particle size. The micelles also help regulate the reaction by limiting the nucleation and growth phases, providing precise control over the process [104]. Once the nanoparticles are formed, they are extracted from the system using organic solvents to remove excess surfactant and impurities. The final properties of the magnetic nanomaterials, such as size, crystallinity, and surface characteristics, depend significantly on the type and structure of the surfactant used [105]. This method offers significant advantages, including the production of highly crystalline nanoparticles with tunable sizes and properties under mild and easily controlled conditions [106].

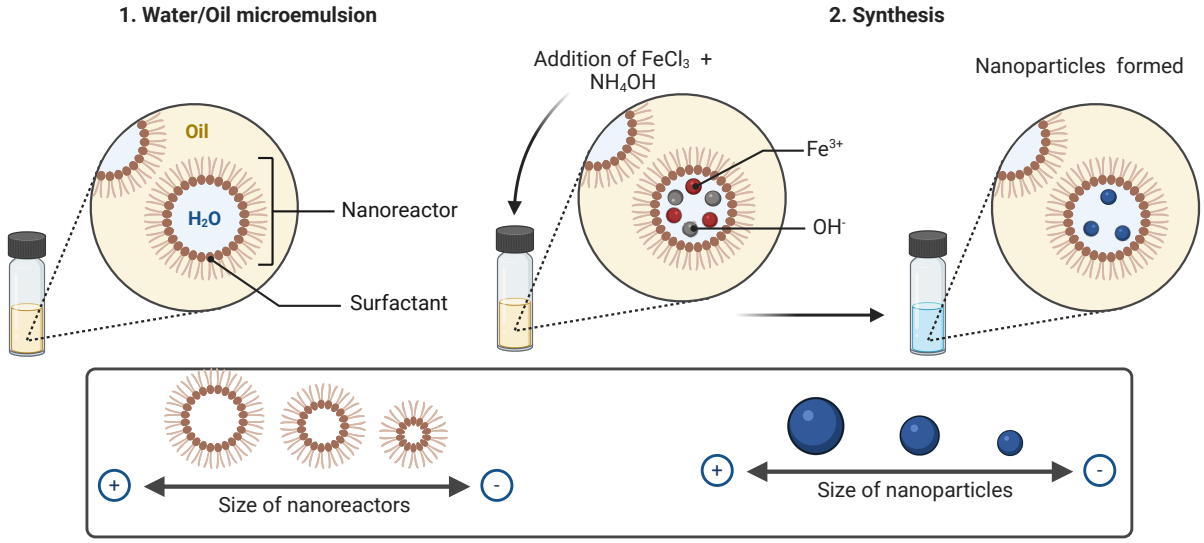

Figure 1.19 – *Schematic representation of the microemulsion synthesis process. [Created with BioRender.com]*

2. Sol-Gel Processes

The sol-gel process is a method that transforms a liquid solution (called a sol) into a solid gel through two main chemical reactions: hydrolysis and condensation. Hydrolysis involves the use of water to break down chemical bonds in a compound, while polycondensation refers to a type of polymerization process that links smaller molecules into larger, more complex structures.

In the context of synthesizing iron oxides using the sol-gel method, various precursors can be employed, including ferric nitrate, ferric chloride, and iron alkoxides [107] [108] [109].

The key steps in the Sol-Gel process are the following :

1. **Formation of the Sol**: The process begins by dissolving an iron precursor, such as

ferric nitrate ($Fe(NO_3)_3$), in water to form a sol.

2. **Hydrolysis**: Water molecules react with the iron ions, forming iron hydroxide complexes.
$$Fe^{3+} + 3\,H_2O \longrightarrow Fe(OH)_3 + 3\,H^+ \tag{1.6}$$
3. **Condensation**: The iron hydroxide complexes link together, forming a network structure.
$$2\,Fe(OH)_3 \longrightarrow Fe_2O_3 + 3\,H_2O \tag{1.7}$$
4. **Gelation**: As condensation continues, the sol transforms into a gel. This process is often initiated by adding a base like sodium bicarbonate or ammonium hydroxide.
5. **Drying and Annealing**: The gel is dried and then heated at high temperatures. This step is crucial for crystallization and forming the desired iron oxide structure.

The synthesis process is governed by various factors, including pH, the type and concentration of the salt precursor, reaction kinetics, temperature, agitation, and the properties of the gel [110]. Leveraging these parameters, the sol-gel method enables precise control over the size, morphology, and characteristics of the resulting iron oxide nanoparticles.

3. Hydrothermal Synthesis

The hydrothermal method was initially introduced by the German geologist Karl Emil von Schafhäutl in 1845, when he successfully grew microscopic quartz crystals using a pressure cooker [111]. This pioneering work laid the foundation for the development of hydrothermal synthesis techniques that are widely used today in various scientific and industrial applications. In the synthesis of iron oxide nanoparticles, the hydrothermal method involves preparing an aqueous solution of iron precursors, such as ferric chloride or ferric nitrate, often supplemented with reducing agents like hydrazine hydrate. Stabilizers or surfactants, such as polyvinylpyrrolidone, are added to prevent agglomeration and control particle growth. This mixture is then transferred to a sealed autoclave, where it is subjected to high temperatures (typically between 130°C and 250°C) and elevated pressure. These conditions promote the nucleation and growth of iron oxide nanoparticles. The size and morphology of the nanoparticles can be controlled by adjusting parameters such as temperature, pressure, reaction time, and the concentration of precursors and stabilizers [112]; for instance, higher temperatures generally lead to larger particles, while varying stabilizer concentrations can influence particle shape [113] [114]. After the reaction, the autoclave is cooled, and the resulting suspension is collected. The nanoparticles are subsequently washed to remove any unreacted precursors and dried to obtain a powder form. This method allows for precise control over the size and morphology of the nanoparticles, making it suitable for various

applications.

4. Thermal Decomposition

The thermal decomposition method is a sophisticated and highly effective technique for synthesizing iron oxide nanoparticles with exceptional control over their size, morphology, and crystalline properties. This approach, which has become a cornerstone in the field of nanoparticle synthesis, owes its prominence to the groundbreaking work of Park and colleagues in 2004 [97]. The method involves the controlled breakdown of carboxylate precursors in a carefully orchestrated environment, typically utilizing iron-based compounds such as iron acetylacetonate ($Fe(acac)_3$) or iron oleate as precursors (Figure1.20). These precursors undergo decomposition in the presence of surfactants and high-boiling organic solvent.

The reaction mechanism can be broadly divided into two the stages: nucleation and growth. During nucleation, the iron precursors decompose at high temperatures, forming iron oxide monomers that subsequently aggregate to form nuclei. In the growth stage, these nuclei expand into nanoparticles through the continuous addition of monomers from the solution. The thermal decomposition method offers remarkable tunability through the manipulation of several key parameters, including temperature (typically ranging from 250°C to 320°C), reaction time, surfactant-to-precursor ratio, heating rate, and precursor concentration.

Surfactants, like oleic acid, serve two key purposes during the synthesis process. First, they act as capping agents, helping to stabilize the growing nanoparticles and prevent them from agglomerating. Second, they play a role in controlling the size of the particles. The ratio of surfactant to precursor is especially important in determining the final size and uniformity of the nanoparticles [115] [97] [50].

The thermal decomposition method has several advantages, including excellent control over particle size and shape, high monodispersity of the resulting nanoparticles, and the ability to produce nanoparticles with high crystallinity. However, this method also presents certain challenges. It requires precise control of reaction conditions, involves the use of high-boiling organic solvents that may raise environmental concerns, and produces nanoparticles that are typically hydrophobic. As a result, additional surface modification is often necessary for biomedical applications.

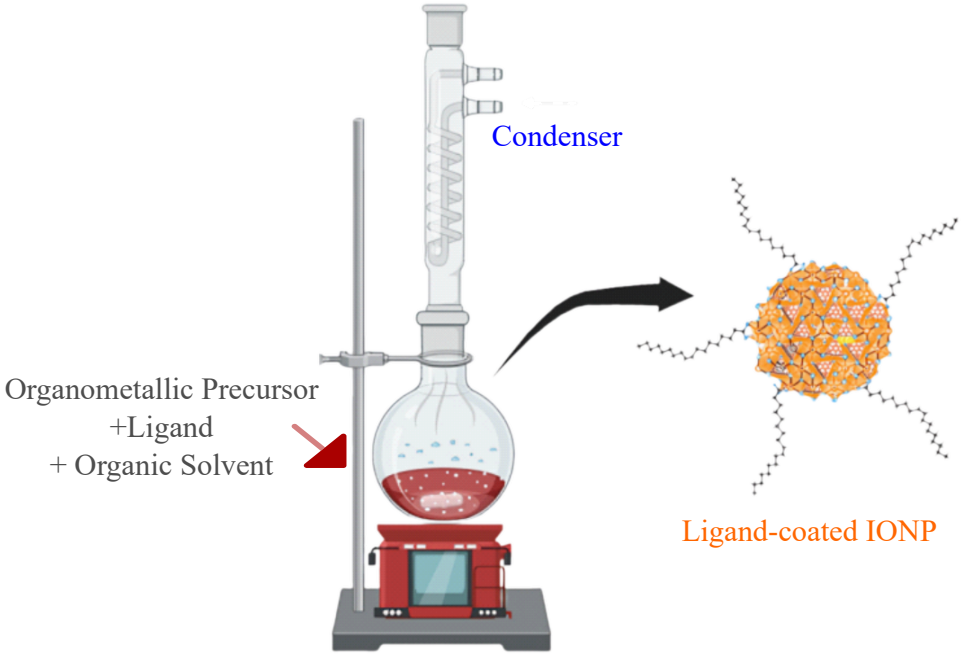

Figure 1.20 – *Schematic representation of the Thermal decomposition synthesis process [Created with BioRender.com]*

1.5.3 Comparison of Synthesis Methods

Following the discussion of the various synthesis methods for iron oxide nanoparticles, the table 1.1 below summarizes their key characteristics and differences. It highlights the advantages and challenges of each method in terms of particle size control, morphology, and scalability, providing a concise overview for comparison.

In this study, the thermal decomposition method was selected due to its effectiveness in producing high-quality iron oxide nanoparticles with precisely controlled size and shape. This control is essential for examining how the size of nanoparticles affects the mechanical properties of polymers, which will be addressed in the following chapter. This method offers a good balance between simplicity and the ability to create nanoparticles with adjustable dimensions. It provides a variety of parameters for precise control over the characteristics of the nanoparticles, presenting many opportunities for customization. However, this versatility also brings challenges in managing the complexity of the different parameters involved.

Table 1.1 – *Comparison of Iron Oxide Nanoparticle Synthesis Methods*

Method	Advantages	Disadvantages	Reproducibility Challenges
Co-precipitation	Simple and cost-effective; suitable for large-scale production; high yield.	Limited control over particle size and shape; broad size distribution.	Sensitive to pH, temperature, and precursor ratio fluctuations.
Microemulsion	Good control over size and shape; narrow size distribution; tunable particle properties.	Requires surfactants and organic solvents; low yield; not easily scalable.	Dependent on emulsion stability and composition.
Hydrothermal	High crystallinity and uniform size; environmentally friendly.	High-pressure and high-temperature conditions; batch process.	Variability in reaction time, temperature, and precursors affects reproducibility.
Sol-gel	Uniform and highly crystalline particles; control over composition and size.	Complex synthesis process; requires long processing times.	Sensitive to reaction conditions like gelation time and temperature.
Thermal decomposition	Excellent size and shape control; high crystallinity and monodispersity.	Expensive precursors and organic solvents; requires high temperatures.	Highly dependent on precursor type, temperature, and reaction time.

1.6 Challenges in Reproducibility

The reproducibility of nanoparticle synthesis, including for iron oxide nanoparticles, remains a significant challenge in nanoscience [116]. Studies reveal that approximately 70% of researchers struggle to replicate published results, with failure rates as high as 90% in chemistry and 80% in biology [117]. These statistics underscore the extent of the reproducibility crisis in scientific research. The synthesis of nanoparticles, such as IONPs, often involves multiple interdependent parameters. For instance, the reaction temperature not only affects particle size but also influences crystallinity and surface chemistry [79]. Such intricate dependencies make it difficult to standardize procedures or predict outcomes reliably. Moreover, small fluctuations in other factors, such as pH or precursor concentrations, can further amplify inconsistencies. This lack of reproducibility poses a considerable barrier to progress,

particularly in nanoscience, where material properties are highly sensitive to even minor variations in synthesis conditions. Addressing this issue requires a thorough understanding of these challenges to emphasize the limitations of current methodologies and to advocate for strategies aimed at achieving more reliable and consistent results in nanoparticle research.

1.7 Characterization Techniques

In order to understand the behavior and properties of nanoparticles, researchers have developed a variety of advanced characterization techniques that enable the analysis of morphology, crystallization, aggregation, and magnetic properties. The following sections detail the techniques employed in the experiments presented in this thesis.

1.7.1 TEM (Transmission Electron Microscopy)

Transmission Electron Microscopy (TEM) is an indispensable technique in nanoscience, offering unparalleled resolution to observe structures at the atomic scale. Invented in 1931 by Ernst Ruska and Max Knoll, TEM revolutionized the study of materials by allowing scientists to visualize details far smaller than what optical microscopes can resolve, thanks to the much shorter de Broglie wavelength of electrons compared to visible light [118].

Principle

The operation of a TEM relies on the interaction between a high-energy electron beam and a thin sample. When electrons pass through the specimen, they are scattered or transmitted based on the material's internal structure. These interactions provide critical information about the sample's morphology, crystal structure, and composition [118].

The core components of a TEM, , as shown in Figure 1.21, include:

- **Electron Source:** Generates a beam of high-energy electrons, typically from a tungsten filament or a field-emission gun.
- **Condenser Lenses:** Focus the electron beam onto the sample.
- **Condenser Aperture:** Limits beam divergence to improve coherence.
- **Sample Stage:** Holds the ultrathin sample for analysis, which is usually less than 100 nm thick to allow effective electron transmission.
- **Objective Lens:** Forms the first magnified image of the sample.
- **Objective Aperture:** Enhances contrast by selecting specific scattered electrons.
- **Selected Area Aperture:** Allows examination of a specific region of the sample.
- **Intermediate Lenses:** Further magnify the image.
- **Projective Lens:** Projects the final image onto the viewing system.
- **Fluorescent Screen:** Displays the electron image, which can also be captured digitally.

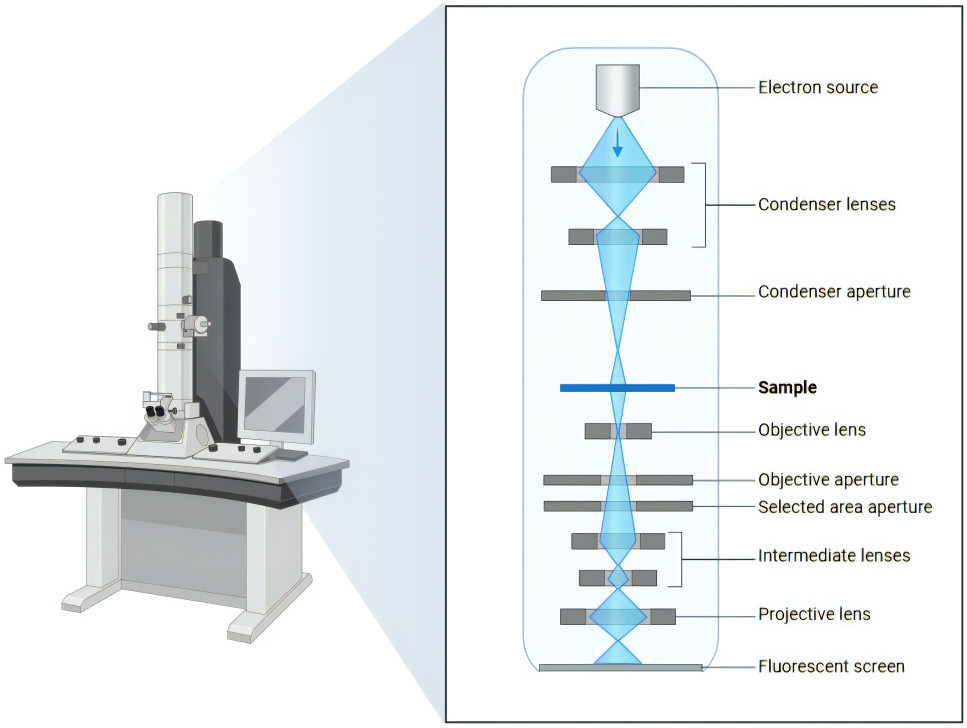

Figure 1.21 – *Schematic of a Transmission Electron Microscope showing its main components. [Created with BioRender.com]*

Sample preparation

Preparing samples for TEM requires ultrathin specimens, typically less than 100 nm. For nanoparticle suspensions, the process involves depositing the sample onto a carbon-coated grid (3 mm in diameter) as shown in Figure 1.22.

1. **Carbon-Coated Grid:** A small copper or nickel grid with an ultra-thin carbon layer supports the sample (Figure 1.22a).
2. **Sample Application:** Place a drop (3–5 μL) of a diluted nanoparticle suspension onto the grid (Figure 1.22b). The suspension is typically in water or ethanol, ensuring even dispersion.
3. **Drying:** Gently blot the edge of the grid with filter paper to remove excess liquid, then air-dry in a dust-free environment.

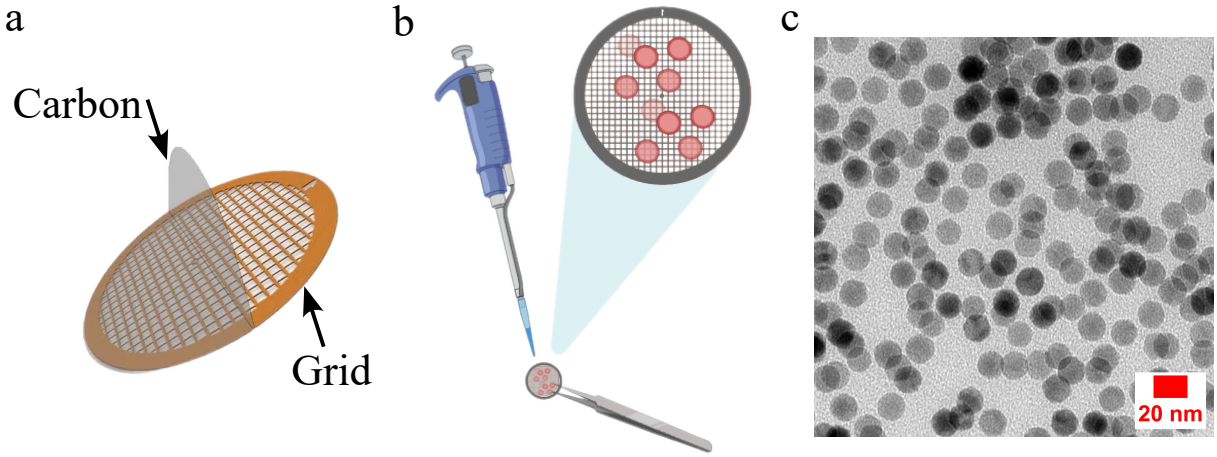

Figure 1.22 – *(a) A standard carbon-coated TEM grid. (b) Deposition of a sample droplet onto the grid. (c) A TEM image of the sample obtained during this thesis. [Created with BioRender.com]*

1.7.2 DLS (Dynamic Light Scattering)

While TEM provides powerful morphological insights, it does not provide information about the size distribution of particles in a liquid suspension. To address this gap, researchers often turn to Dynamic Light Scattering (DLS). DLS is a technique designed to measure the size distribution of particles in suspension. Unlike TEM, which requires the sample to be prepared as a solid film, DLS works with particles dispersed in liquids, such as water or organic solvents.

In a typical DLS experiment, a laser beam is passed through the sample, and the light scattered by the particles is detected at a specific angle, as shown in Figure 1.23. The primary principle is that the light scattering intensity is related to the size of particles suspended in a solution. The technique works by measuring how light scattered by particles fluctuates over time. These fluctuations are caused by the Brownian motion of the particles as they move through the solvent. The key relationship between scattering intensity and particle size lies in how quickly these intensity fluctuations occur. The faster the particles move, the quicker the fluctuations in the scattering intensity. Conversely, slower-moving particles (which are larger) cause slower fluctuations in the scattered light intensity.

To quantify the relationship between particle size and the rate of light scattering, DLS uses the Stokes-Einstein equation, which connects the diffusion coefficient (how fast particles move) with the size of the particle:

$$D = \frac{k_B T}{6\pi\eta r} \tag{1.8}$$

Where:

- D is the diffusion coefficient (related to how fast the particle moves),
- k_B is the Boltzmann constant,
- T is the temperature,
- η is the viscosity of the solvent,
- r is the hydrodynamic radius of the particle.

The size measured by DLS is the hydrodynamic diameter. This refers to the effective diameter of a particle in suspension, which includes the particle itself and any solvent or other molecules that are associated with it, such as a solvation shell. This size is important because it reflects the particle's behavior in solution, affecting properties like diffusion, stability, and how the particle interacts with its surrounding environment.

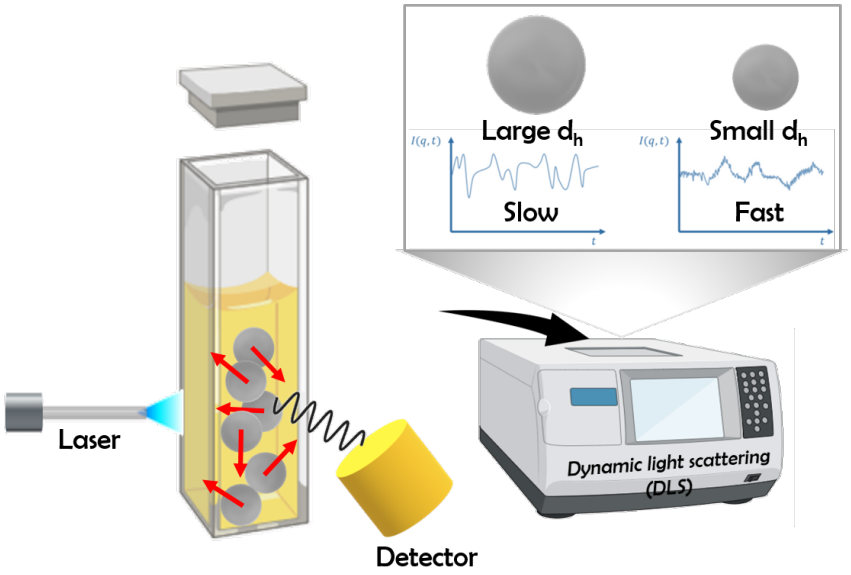

Figure 1.23 – *Dynamic Light Scattering analysis of particle sizes [Created with BioRender.com].*

1.7.3 XRD (X-ray Diffraction)

To further understand the properties of the nanoparticles, X-ray diffraction is employeds, a technique that reveals their crystallinity and phase composition [119]. XRD operates based on Bragg's law, which describes the diffraction of X-rays by the planes of atoms in a crystal lattice. X-rays are diffracted at specific angles when they interact with the crystalline structure. Bragg's law is expressed as [120]:

$$n\lambda = 2d\sin(\theta) \tag{1.9}$$

where:

- n is the diffraction order (typically 1),

- λ is the wavelength of the X-ray,
- d is the spacing between crystal planes, and
- θ is the angle of incidence (the angle between the X-ray beam and the crystal planes).

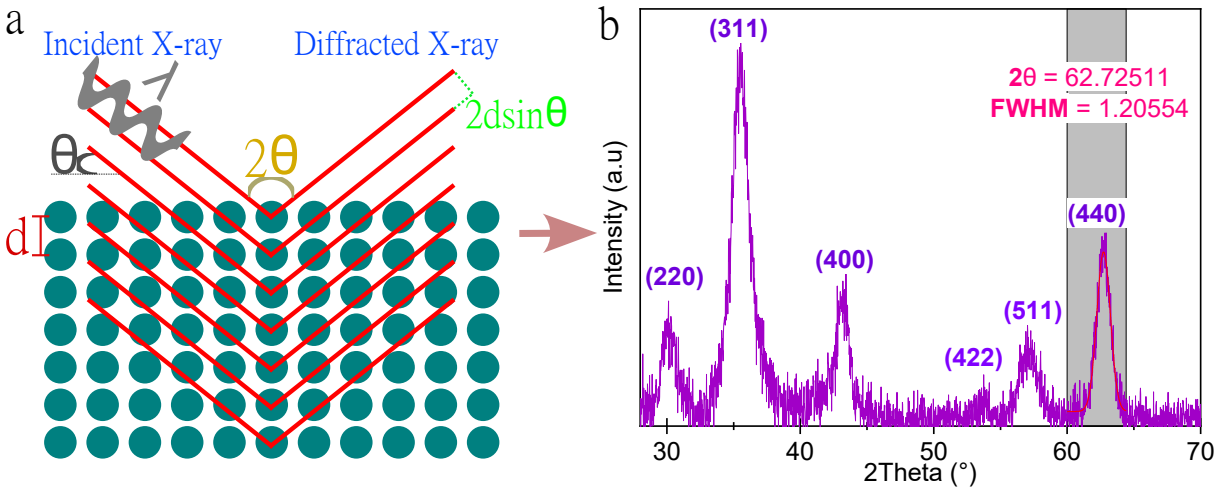

Figure 1.24 – *(a) Schematic representation of Bragg's Law showing X-ray diffraction from atomic planes with spacing d, where θ is the incident angle and $2d\sin\theta$ represents the path difference. (b) XRD pattern of iron oxide nanoparticles obtained during this thesis, showing characteristic diffraction peaks indexed as (220), (311), (400), (422), (511), and (440), with detailed peak analysis at $2\theta = 62.72511^\circ$ and FWHM = 1.20554, calculated using Origin software. The identification of the iron oxide phase was confirmed with the help of the ICDD PDF card 04-021-3968.*

As shown in Figure 1.24, constructive interference of X-rays occurs when waves reflected from adjacent planes in the crystal lattice combine in phase, leading to an amplification of the diffracted signal. For this to happen, the difference in the path traveled by the X-rays reflected from successive planes must equal an integer multiple (n) of the wavelength (λ), with the extra distance traveled by the X-rays given by $2d\sin(\theta)$. This condition results in a diffraction peak at the corresponding angle θ. Figure 1.25 depicts the X-ray diffractometer, provided by the Service Analyses Physico-Chimiques, during the diffraction process. The image highlights the setup, including the X-ray source, sample holder, and detector, which are essential for obtaining the diffraction data.

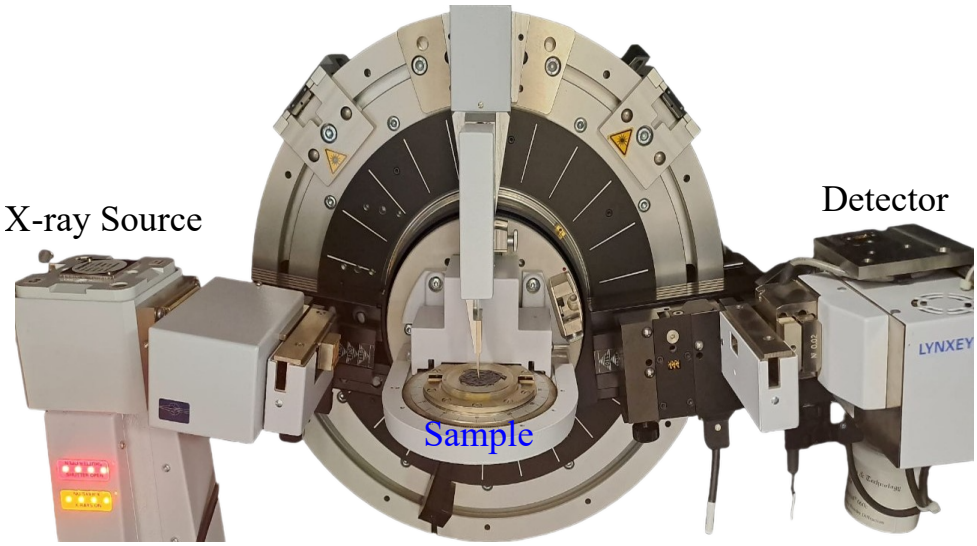

Figure 1.25 – *Advance X-ray diffractometer provided by the Service Analyses Physico-Chimiques, showing the X-ray source, sample holder, and detector during the diffraction process.*

This phenomenon results in a diffraction pattern where each peak corresponds to specific crystal plane spacings. The positions and intensities of these peaks provide information about the atomic arrangement and crystalline phases present in the material. For instance, in the case of iron oxide nanoparticles, XRD can distinguish maghemite (γ-Fe_2O_3) from other phases like magnetite (Fe_3O_4) or hematite (α-Fe_2O_3) by analyzing the diffraction peak positions and comparing them to standard reference patterns from the International Centre for Diffraction Data (ICDD). This is illustrated in Figure 1.26, which shows the step scan X-ray diffraction of the (5 1 1) peak from standard samples of mixed magnetite and maghemite.

To further quantify the structural properties, the crystallite size can be calculated using the Scherrer equation:

$$D = \frac{K\lambda}{\beta \cos(\theta)} \tag{1.10}$$

where:

- D is the crystallite size,
- K is the shape factor (typically 0.9 for spherical particles),
- λ is the wavelength of the X-ray,
- β is the full width at half maximum (FWHM) of the diffraction peak in radians, and
- θ is the Bragg angle.

Those parameters can be calculated using Origin software as shown in Figure 1.24b.

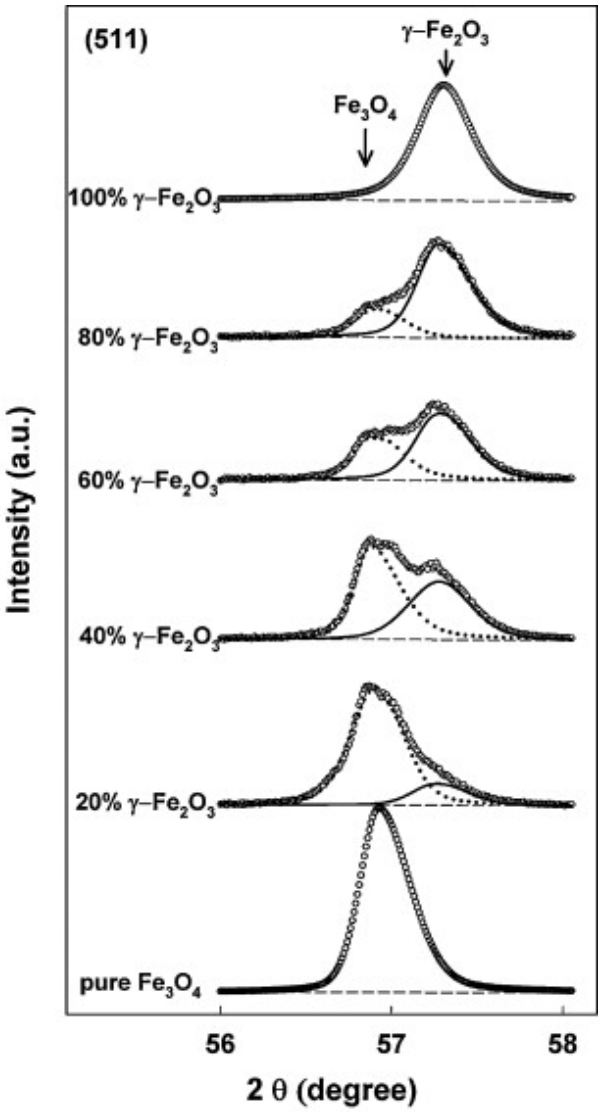

Figure 1.26 – *Step scan X-ray diffraction of (5 1 1) peak from standard samples of mixed magnetite (Fe_3O_4) and maghemite (γ-Fe_2O_3). Lower angle peak: magnetite; higher angle peak: maghemite [121].*

1.7.4 SAXS (Small-Angle X-ray Scattering)

SAXS (Small-Angle X-ray Scattering) is a technique that complements XRD by probing different structural aspects of materials, especially at larger distances. While XRD (or WAXS) focuses on atomic-scale crystallinity and phase composition, SAXS operates at much smaller scattering angles, typically below 5°, and is sensitive to structures on the nanoscale (Figure 1.27). It provides valuable information about the size, shape, and distribution of particles, as well as their spatial arrangement within a material.

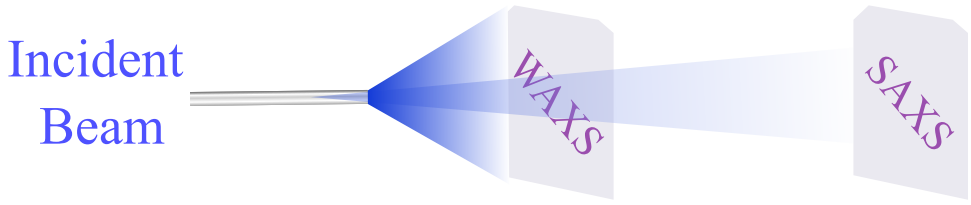

Figure 1.27 – *Comparison of Small-Angle X-ray Scattering (SAXS) and Wide-Angle X-ray Scattering (WAXS) techniques based on beam-to-detector distance and scattering angle ranges*

Guinier plot

The **Guinier plot** is a tool used in SAXS to analyze the size of nanoparticles or the radius of gyration (R_g) in a material. It is particularly useful for small, spherical particles. The plot is based on the following Guinier law at low q values:

$$I(q) \approx I(0) \exp\left(-\frac{q^2 R_g^2}{3}\right) \tag{1.11}$$

The scattering vector q is related to the scattering angle θ by the following equation:

$$q = \frac{4\pi}{\lambda} \sin\theta \tag{1.12}$$

where:

- q is the magnitude of the scattering vector, also referred to as the momentum transfer.
- λ is the wavelength of the incident radiation.
- θ is the scattering angle, which is half the angle between the incident and scattered beams.

To construct the plot, $\ln(I(q))$ is plotted against q^2 for low q values. A straight-line fit in the linear region of the plot provides the slope, from which R_g can be calculated as:

$$R_g = \sqrt{-3 \cdot \text{slope}} \tag{1.13}$$

For spherical particles, the radius of gyration R_g is related to the particle radius R by the following formula:

$$R_g = \frac{R}{\sqrt{5}} \tag{1.14}$$

This SAXS data analysis can be performed directly from data files using software such as *RAW* or similar tools, which allow the extraction of intensity vs. q data and the generation of Guinier plots.

Aggregation of nanoparticles can cause deviations from the expected linear Guinier behavior. If aggregates form, the plot may show curvature instead of a straight line, indicating that the particles are no longer individually dispersed. This change suggests the formation of larger clusters, which will affect both the size and the scattering intensity.

Form & Structure Factor

The intensity of a SAXS pattern arises from the combined contributions of two key components: **the form factor** and **the structure factor**. This relationship is described mathematically as:

$$I(q) \propto P(q) \cdot S(q) \tag{1.15}$$

where:

- $I(q)$ is the scattering intensity,
- $P(q)$ is the form factor,
- $S(q)$ is the structure factor, and
- q is the scattering vector.

This formulation enables researchers to simultaneously probe the properties of individual particles and their collective organization within a sample.

The **form factor** reflects the scattering contribution of individual particles in the sample, independent of how they are arranged. It reveals details such as:

- **Particle Size:** How large the particles are.
- **Particle Shape:** Whether the particles are spherical, rod-like, plate-like, or irregular.
- **Internal Structure:** Variations in electron density within the particle, such as core-shell structures.

In dilute systems, where particles are far apart and do not significantly interact, the scattering intensity is dominated by $P(q)$. This simplifies the interpretation and focuses on the inherent characteristics of the particles.

The **structure factor** accounts for interactions between particles and their spatial arrangement in the sample. It provides insights into:

- **Interparticle Interactions:** Forces such as attraction, repulsion, or steric hindrance that dictate particle spacing.
- **Order or Arrangement:** Whether particles are randomly distributed, in a regular lattice, or exhibit short-range order.

The structure factor becomes particularly important in concentrated systems, where particles are close enough to interact. At low q values (longer length scales), $S(q)$ highlights particle packing and arrangement, revealing features like aggregation, clustering, or crystalline ordering.

By fitting SAXS data, as shown in Figure 1.28, to both the form factor and structure factor models, a comprehensive understanding of the nanoparticle characteristics—ranging from their individual size and shape to their collective arrangement—can be obtained.

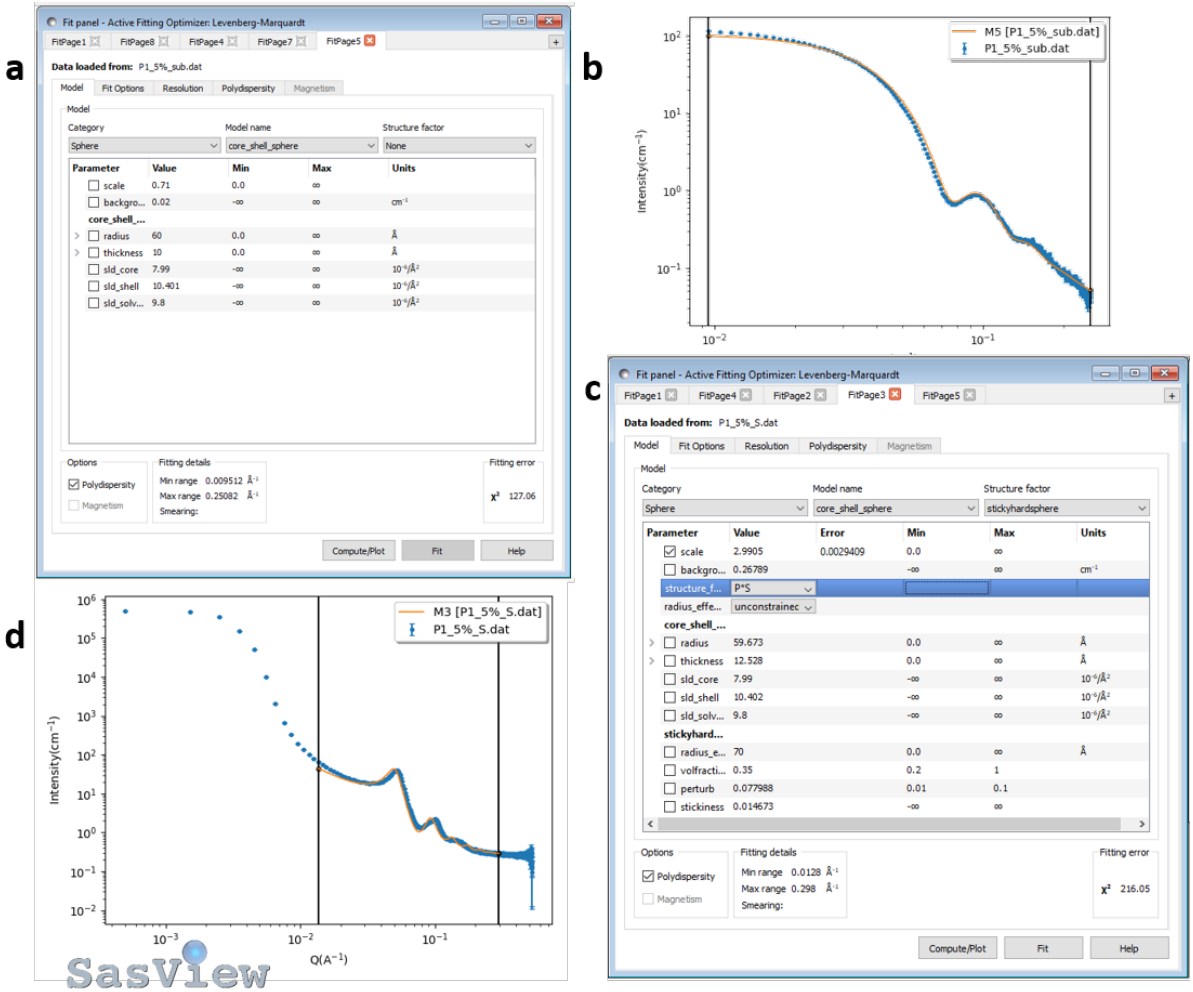

Figure 1.28 – *SasView software interface for SAXS analysis: Panel (a) shows the core-shell sphere model (Form factor) fit with polydispersity settings for nanoparticles in the dilute regime. Panel (b) presents a log-log plot of scattering intensity vs. Q, with experimental data and fitted curve. Panel (c) includes additional parameters for structure factor settings, and Panel (d) shows the concentrated sample fit.*

Spacial arrangement

In concentrated samples, the ratio of the peak positions in SAXS patterns can provide essential information about the type of **ordering** present in the system. These ratios are linked to the symmetry and periodicity of the particle arrangement. The following table 1.2 summarizes the typical peak ratios observed for different types of structures, which can help in identifying whether the material exhibits hexagonal, lamellar, or cubic arrangements.

Table 1.2 – *Diffraction Planes and Relative Positions of the Lattice Peaks of bcc, fcc, and hcp Lattices [122]*

BCC Body-Centered Cubic		FCC Face-Centered Cubic		HCP Hexagonal Close-Packed	
Diffraction plane (*hkl*)	Relative Position	Diffraction Plane (*hkl*)	Relative Position	Diffraction Plane (*hk.l*)	Relative Position
(110)	1	(111)	1	(10·0)	1
(200)	$2^{1/2}$	(200)	$(4/3)^{1/2}$	(00·2)	1.06
(211)	$3^{1/2}$	(220)	$(8/3)^{1/2}$	(10·1)	1.13
(220)	$4^{1/2}$	(311)	$(11/3)^{1/2}$	(10·2)	1.46
(310)	$5^{1/2}$	(222)	$4^{1/2}$	(11·0)	1.73
(222)	$6^{1/2}$	(400)	$(16/3)^{1/2}$	(10·3)	1.88
(321)	$7^{1/2}$	(331)	$(19/3)^{1/2}$	(11·1)	2.00
(400)	$8^{1/2}$	(420)	$(20/3)^{1/2}$	(11·2)	2.03
(411), (330)	$9^{1/2}$			(20·0)	2.07
(420)	$10^{1/2}$			(00·4)	2.12
				(20·2)	2.26
				(10·4)	2.34
				(20·3)	2.56
				(21·0)	2.64
				(21·1)	2.70

1.7.5 VSM (Vibrating Sample Magnetometry)

Vibrating Sample Magnetometry (VSM) is a powerful technique used to study the magnetic properties of materials. By measuring the magnetic moment of a sample in response to an applied magnetic field through the hysteresis loop (Figure 1.29a), VSM provides important insights into its magnetic behavior. This technique is especially useful for nanoparticle analysis, as it allows for the evaluation of key magnetic characteristics, such as saturation magnetization, coercivity, and remanence.

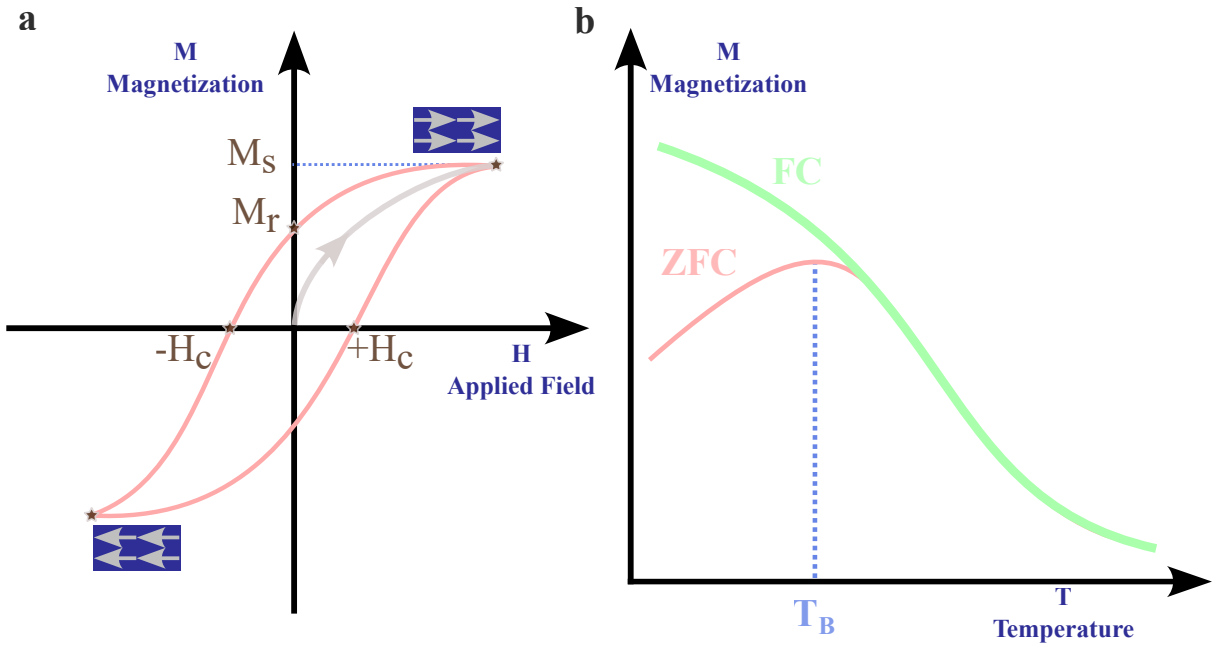

Figure 1.29 – *(a) Typical magnetic hysteresis loop showing saturation magnetization (M_s), remanent magnetization (M_r), and coercive field (H_c); (b) Temperature dependence of magnetization comparing Zero-Field-Cooled (ZFC) and Field-Cooled (FC) curves, with T_B indicating the blocking temperature.*

Before performing hysteresis measurements, a **Zero-Field Cooling (ZFC)** procedure is often conducted, especially for nanoparticles exhibiting **superparamagnetism** or **ferrimagnetism**. The sample is first cooled without an external magnetic field, ensuring the magnetic moments are disordered. After cooling, a small magnetic field is applied, and magnetic moment is measured as the temperature increases, helping study the transition from disordered to ordered magnetic behavior (Figure 1.29b).

The ZFC measurement determines the **blocking temperature (T_B)**, below which the magnetic moments become "frozen" due to insufficient thermal energy to align the magnetic moment with the small applied field. Above T_B, nanoparticles show **superparamagnetic** behavior (the megnetic moment of the NPs are disordered and the net magnetic moment of the sample is zero), and below T_B, they exhibit **ferrimagnetic** or **ferromagnetic** behavior. In contrast, **Field Cooling (FC)** involves applying a magnetic field while cooling, allowing the nanoparticles to align with the field as they become magnetically ordered.

It is important to note that after conducting the ZFC procedure, **hysteresis measurements** are typically performed at a temperature **below the blocking temperature (T_B)** generally at 3K. This ensures that the nanoparticles are in the ordered magnetic state, where their magnetic moments are aligned and the material shows magnetic hysteresis behavior (with remanence and coercivity).

1.7.6 SQUID Magnetometer (Superconducting Quantum Interference Device)

The Superconducting Quantum Interference Device (SQUID Magnetometer) is another highly effective technique for characterizing the magnetic properties of materials. It is known for its exceptional sensitivity, allowing the measurement of extremely small magnetic signals. SQUID operates based on quantum interference in superconducting loops, providing precise measurements of the magnetization of a sample. This technique is particularly valuable for studying weakly magnetic materials, such as superparamagnetic nanoparticles, as well as materials that undergo complex magnetic transitions. SQUID magnetometer can measure both direct current (dc) and alternating current (ac) magnetic properties, making it a versatile tool in the field of magnetism.

The key differences between VSM and SQUID magnetometer are based on sensitivity and the range of magnetic properties they can measure:

- **Sensitivity**: SQUID magnetometer offers much higher sensitivity than VSM.
- **Magnetic Properties**: SQUID magnetometer can measure both direct current (dc) and alternating current (ac) magnetic properties, whereas VSM typically focuses on dc measurements.

1.8 Conclusion

Throughout this chapter, we have explored the fundamental aspects of iron oxide nanoparticles, from their crystalline structure and magnetic properties to their diverse applications and synthesis methods.

We have highlighted the crucial relationship between structural characteristics and functionality, emphasizing how size, surface functionalization, and shape influence the properties and potential uses of these nanoparticles.

The synthesis methods discussed—ranging from coprecipitation to advanced techniques such as thermal decomposition and hydrothermal synthesis—demonstrate the flexibility available for tailoring IONPs for specific applications. Each method presents distinct advantages and challenges, allowing researchers to optimize nanoparticle features for their intended purposes. However, reproducibility remains a major challenge in the field, largely due to the complex interplay between synthesis parameters and their impact on the final product.

We have also reviewed a range of characterization techniques, including TEM, DLS, XRD, SAXS, SQUID magnetometry, and VSM. These powerful tools enable researchers to

thoroughly analyze and understand the properties of IONPs.

In summary, iron oxide nanoparticles represent a dynamic and rapidly evolving area within nanotechnology. The interplay between their structural properties, synthesis strategies, and characterization methods holds tremendous potential for innovation across multiple disciplines. As research advances, we can anticipate improvements in synthesis control, enhanced reproducibility, and the emergence of novel applications leveraging the unique characteristics of these nanoparticles.

Chapter 2

Polymer Nanocomposites: Design, Optimization, and Characterization

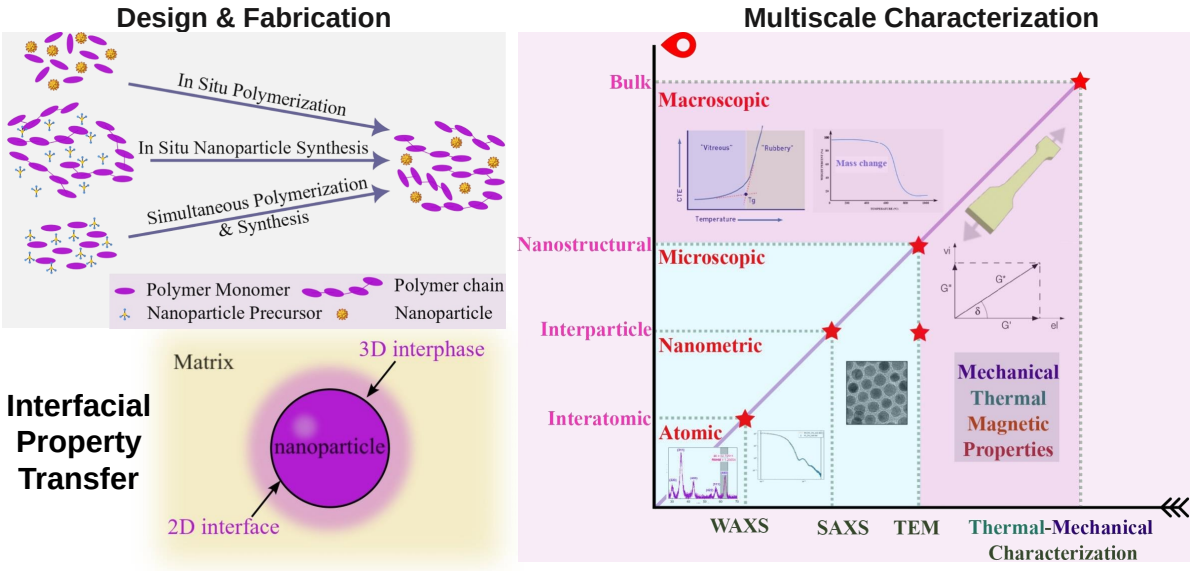

Contents

2.1 Introduction to Polymer Nanocomposites

In mechanical engineering, a significant challenge lies in developing materials that combine high strength with low weight. This combination is crucial in industries such as aerospace, automotive, and construction, where energy efficiency and structural optimization are essential [123] [124]. Polymers are widely appreciated in these sectors for their lightweight nature, versatility, and ease of processing. However, their inherent mechanical limitations often restrict their use in advanced applications requiring enhanced performance.

Recent advances in nanotechnology have offered a promising solution to these challenges. The precise synthesis and surface engineering of nanoparticles, as detailed in the previous chapter, are fundamental to unlocking their full potential as reinforcing agents in polymer matrices. By leveraging the high surface-to-volume ratio and tunable surface properties of nanoparticles, researchers have developed a new class of materials known as polymer nanocomposites. These materials combine the versatility of polymers with the exceptional mechanical, thermal, and sometimes magnetic properties imparted by nanoparticles. Both experimental and numerical studies have demonstrated that the inclusion of nanoparticles significantly enhances the strength, stiffness, and durability of the polymer while preserving its lightweight characteristics [125].

For instance, incorporating a small amount of nanoparticles (1–5%)—such as layered silicates or carbon nanotubes—can yield performance improvements comparable to those achieved with much higher loadings (15–40%) of traditional fillers like talc or glass fibers. This reduction in filler content not only simplifies processing but also reduces component weight and enhances energy efficiency during manufacturing [126].

The enhanced mechanical properties exhibited by polymer nanocomposites stem primarily from the efficient load transfer facilitated by nanofillers, *a term used to refer to nanoparticles when describing their role in reinforcing polymer matrices*. These nanofillers not only provide mechanical reinforcement but also confer additional functional benefits, creating a synergistic combination that enables the design of advanced materials with tailored properties for cutting-edge applications.

For instance, studies have demonstrated how specific nanofillers can enhance both the structural and functional performance of polymer matrices. In poly(lactic acid) (PLA)-based films, the addition of zinc oxide (nano-ZnO) nanofillers improved oxygen-gas and water-vapor permeability, enhancing both mechanical strength and barrier properties. This combination makes such materials ideal for food packaging applications [127].

Similarly, polyvinylidene fluoride (PVDF) nanocomposites with 6 wt.% carbon-based nanofillers, including graphene nanoplatelets, multi-walled carbon nanotubes (MWCNTs), and their hybrids, demonstrated significant enhancements. The nanofillers increased the

amorphous fraction in PVDF and enhanced the β-phase by up to 12%, particularly with MWCNTs. These composites showed self-regulating Joule heating behavior and improved resistive properties, making them suitable for self-regulated heating systems [128].

In another study, PLA/ethylene-vinyl acetate copolymer (EVA) composites containing just 1% carbon nanotubes (CNTs) exhibited a significant improvement in dielectric properties, with the dielectric constant increasing from 5.81 to 11.08. Despite a slight reduction in PLA's mechanical properties and crystallization ability, the composite's improved thermal stability made it well-suited for electronic applications [129].

Additionally, polyethylene oxide and sodium alginate films embedded with gold nanoparticles (Au NPs) demonstrated a reduction in the optical energy gap, from 4.73 eV to 2.92 eV in direct transition and from 2.95 eV to 1.50 eV in indirect transition. The films also exhibited improved dielectric and electrical properties, suggesting their potential for use in electroactive materials [130].

Finally, PVDF nanocomposites incorporating magnetite (Fe_3O_4) nanoparticles with hydroxyl-terminated surfaces showed significant enhancements in piezoelectric properties. These improvements were attributed to stronger interfacial interactions and localized polarization, underscoring the material's promise for advanced piezoelectric applications [131].

2.2 Polymer Classifications

Polymers are materials composed of long-chain macromolecules formed through the repetitive linkage of smaller units called monomers. These macromolecules develop via chemical reactions that establish the polymer's backbone. The diversity of polymers arises from variations in monomer structure, bonding types, and molecular arrangements, enabling the creation of materials with properties spanning rigid plastics to flexible rubbers. While polymers can be classified by origin (natural or synthetic) or polymerization mechanism (addition or condensation), the most common classification system categorizes them based on thermal behavior into three primary categories: **thermoplastics**, **thermosets**, and **elastomers**.

Among these, thermoplastics are widely used due to their ease of processing. Unlike thermosets, which undergo irreversible curing, thermoplastics can be repeatedly melted and reshaped, making them highly versatile for manufacturing applications. Thermoplastics are further divided into **amorphous** and **semicrystalline** polymers.

Amorphous thermoplastics lack a well-defined crystalline structure, resulting in transparency and relatively **high impact resistance**, as their disordered molecular arrangement allows for better energy dissipation during sudden mechanical shocks. However, they typically exhibit **lower mechanical strength** under sustained or tensile loading and are more susceptible to stress cracking under cyclic or long-term stress conditions.

In contrast, semicrystalline thermoplastics exhibit both crystalline and amorphous regions, leading to enhanced mechanical strength and chemical resistance.

Elastomers, distinct from thermoplastics, are characterized by their exceptional flexibility, which stems from their lightly cross-linked or physically entangled molecular structure. While some classification systems group elastomers with thermoplastics, they are more accurately classified as a separate class due to their unique mechanical properties and molecular architecture.

The primary objective of this study is to systematically investigate the size-dependent effects of nanoparticles on the mechanical properties of polymers. To isolate these effects and avoid confounding variables, elastomers (specifically polyisobutylene, PIB) were selected as the polymer matrix. In semicrystalline thermoplastics, nanoparticle reinforcement often induces changes in crystallization behavior (e.g., altered crystallinity, phase transitions), which could obscure the direct relationship between nanoparticle size and mechanical performance. By employing amorphous elastomers like PIB, crystallization-related complexities are entirely eliminated, ensuring that observed mechanical changes are exclusively attributable to nanoparticle interactions. PIB's amorphous molecular structure and low glass transition temperature (T_g = -64°C) further guarantee flexibility at physiological conditions, enabling precise analysis of how filler dimensions influence polymer reinforcement. This methodological approach ensures that the nanoparticle size effect remains the sole variable under investigation, providing unambiguous insights into reinforcement mechanisms.

2.3 Key Parameters in Nanocomposite Optimization

The performance of polymer nanocomposites is influenced by several interconnected factors that dictate the interactions between the nanofillers and the polymer matrix. Among these, the nanofiller mass fraction, their dimensionality, and their surface area-to-volume (S/V) ratio play pivotal roles. Each of these parameters contributes uniquely to the enhancement of mechanical, thermal, and electrical properties by modifying the interfacial characteristics and load transfer efficiency within the composite. The following sections provide a detailed discussion of these factors and their impact on nanocomposite performance.

2.3.1 Nanofiller Mass Fraction

The mass fraction of nanoparticles (w_f) plays a pivotal role in polymer nanocomposite design, directly influencing mechanical performance and material behavior [132]. Unlike conventional microparticles, nanoparticles exhibit unique reinforcement characteristics that depend critically on their concentration and dispersion quality [133]. Increasing nanoparticle content typically enhances stiffness, strength, and thermal stability due to the formation of interparticle networks that improve load transfer within the polymer matrix [134]. This contrasts with microparticles, which often degrade composite properties at high loadings [135]. However, excessive nanoparticle concentrations risk agglomeration, creating stress concentration points that reduce ductility and mechanical reinforcement [136]. Figure 2.1 illustrates this effect of nanoparticle volume fraction on the thermal conductivity of polymers (case of nanofluids), showing that an increase in filler content generally enhances thermal conductivity, as observed across different studies.

While nanoparticles offer superior reinforcement potential, their effectiveness depends on achieving uniform dispersion. Poor dispersion or agglomeration disrupts interfacial interactions, leading to nonuniform stress distribution and diminished performance [137] [136]. Processability also declines with excessive filler content, creating a trade-off between reinforcement benefits and practical limitations. Determining the optimal w_f requires balancing these competing factors [132].

To predict composite behavior, micromechanical models like the Halpin-Tsai equation are widely used [138] [139]. The model relates composite elastic modulus (E_c) to matrix modulus (E_m), nanoparticle volume fraction (ϕ_f), and reinforcement factor (η):

$$E_c = E_m \left(\frac{1 + \eta \phi_f}{1 - \xi \eta \phi_f} \right) \tag{2.1}$$

Here, η is defined as:

$$\eta = \frac{\left(\frac{E_f}{E_m}\right) - 1}{\left(\frac{E_f}{E_m}\right) + \xi} \tag{2.2}$$

where E_f is the nanoparticle modulus and ξ is a shape factor dependent on nanoparticle geometry. Experimental studies often report nanoparticle content as a mass fraction (w_f), requiring conversion to volume fraction (ϕ_f) using matrix (ρ_m) and nanoparticle (ρ_f) densities [140]:

$$\phi_f = \frac{w_f}{w_f + \left(\frac{\rho_f}{\rho_m}\right)(1 - w_f)} \tag{2.3}$$

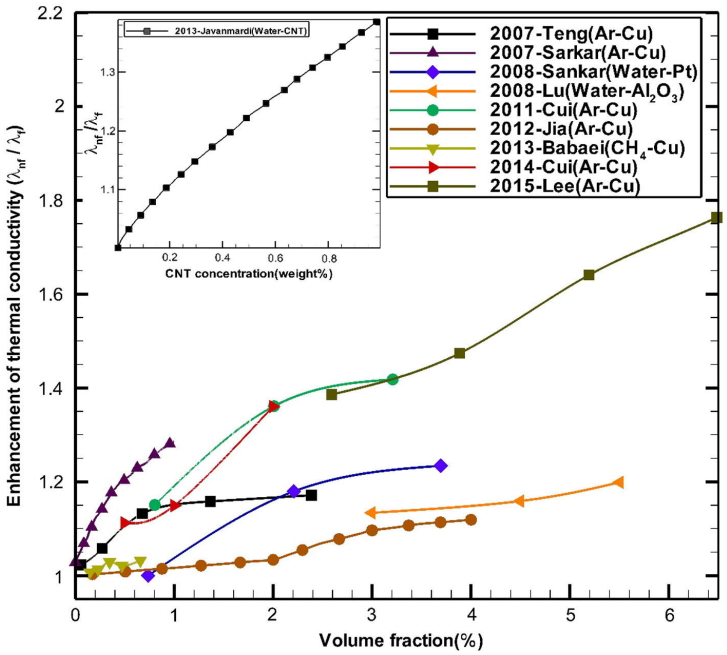

Figure 2.1 – *The variation of thermal conductivity with nanoparticle volume fraction across different studies, demonstrating that the thermal conductivity of nanofluids improves as the nanoparticle volume fraction increases. [141]*

2.3.2 Nanofiller dimensionality

Nanofillers are classified based on their dimensionality within the nanoscale range (1–100 nm). This classification encompasses structures ranging from zero-dimensional (0D) to three-dimensional (3D), as depicted in Figure 2.2.

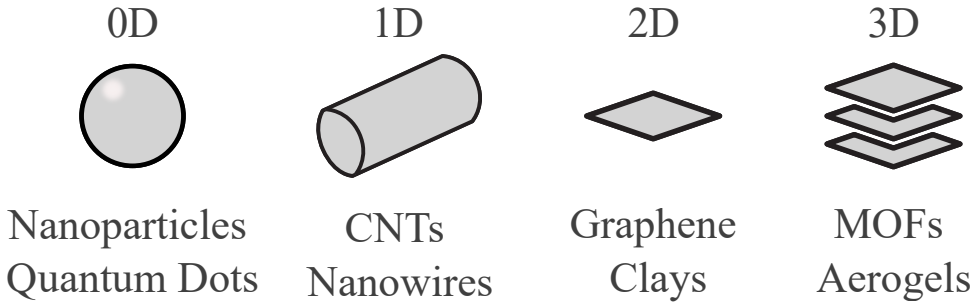

Figure 2.2 – *Nanofillers are classified by dimensionality: 0D (nanoparticles, quantum dots), 1D (CNTs, nanowires), 2D (graphene, clays), and 3D (MOFs, aerogels), each providing distinct structural properties for diverse applications in nanocomposite materials.*

0D nanofillers (e.g., nanoparticles, quantum dots) have all three dimensions in the nanoscale. Their isotropic properties (uniform behavior in all directions) and high surface area-to-volume ratio facilitate bonding with the matrix. However, they do not provide directional reinforcement, which may limit their use in applications requiring anisotropic strength.

1D nanofillers (e.g., carbon nanotubes, nanowires) have two dimensions in the nanoscale and one macroscopic dimension. Their elongated shape and high aspect ratio (length-to-width) allow directional reinforcement, making them suitable for applications where aligned strength is beneficial, such as lightweight composites.

2D nanofillers (e.g., graphene, clay sheets) have one dimension in the nanoscale (thickness) and two macroscopic dimensions. Their planar geometry contributes to in-plane stiffness and barrier properties, which can enhance flexural rigidity and environmental resistance.

3D nanofillers (e.g., metal-organic frameworks, aerogels) have all three dimensions in the nanoscale but often form interconnected or porous networks. Their low density and tunable structures enable either isotropic or anisotropic reinforcement, depending on their alignment, making them ideal for lightweight aerospace materials and energy-efficient designs. More broadly, materials that exhibit nanometric features despite having an overall size in the millimeter or micrometer range, or those constructed from nanosized building blocks, are classified as '3D nanomaterials' [142].

At identical mass or volumetric fractions of the nanofiller, their dimensionality influences the properties of the nanocomposite, as shown in Figure 2.3. This figure presents a comprehensive comparison of the dielectric properties of various PVDF (polyvinylidene fluoride)-based composites, each containing 2 wt% of a different conductive filler material (CB, MWCNT, SWCNT, rGO, and graphite).

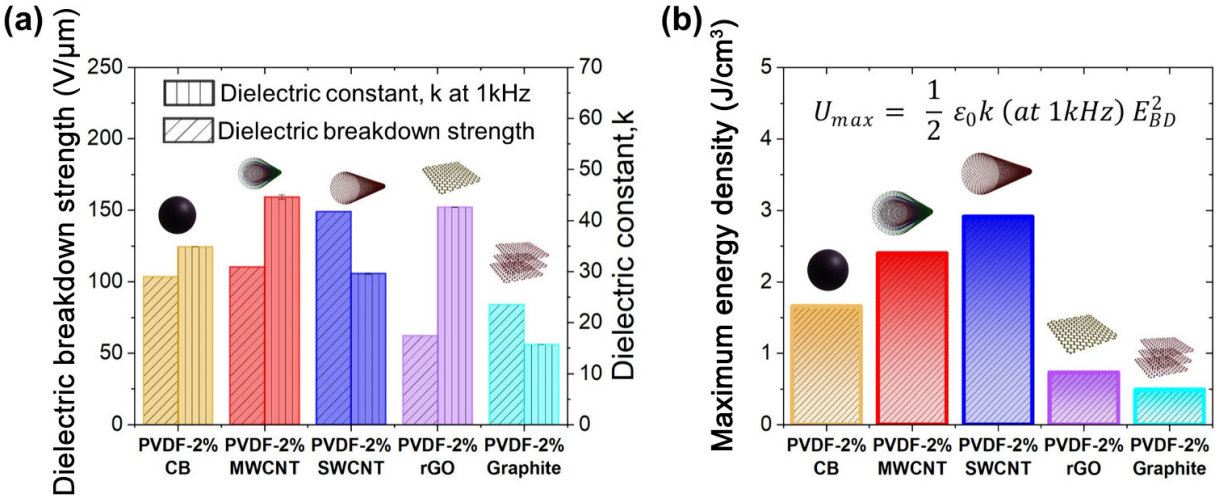

Figure 2.3 – *(a) Dielectric breakdown strength and dielectric constant at 10 kHz for PVDF films containing 2 wt% of CB, MWCNT, SWCNT, rGO, and graphite. (b) Maximum energy density of PVDF-2 wt% CB, PVDF-2 wt% MWCNT, PVDF-2 wt% SWCNT, PVDF-2 wt% rGO, and PVDF-2 wt% graphite films at 10 kHz [143].*

While dimensionality primarily dictates mechanical enhancement in nanocomposites (e.g., isotropic reinforcement in 0D vs. directional strength in 1D), shape introduces chemical

variability even within the same dimensional class. For instance, 0D fillers such as spherical and cubic nanoparticles exhibit isotropic mechanical behavior but differ chemically due to their exposed crystal facets. A spherical shape may reduce surface roughness and limit reactive sites, whereas a cubic shape exposes sharp edges and distinct crystallographic planes, thereby altering interactions with the polymer matrix. These geometric differences can impact dispersion, interfacial bonding, and reactivity, despite both shapes being classified as 0D. Thus, while dimensionality governs bulk mechanical properties, shape modulates chemical compatibility and interfacial dynamics.

2.3.3 Surface-to-Volume Ratio & Size Effects

The surface-to-volume ratio (SVR), defined as the ratio of a particle's surface area to its volume, emerges as a critical parameter for elucidating size-dependent effects in nanocomposites. For spherical nanoparticles, SVR scales inversely with size:

$$SVR = \frac{6}{d}$$

where d denotes the particle diameter. As particles transition into the nanoscale, SVR increases exponentially, amplifying surface-mediated phenomena such as interfacial bonding and aggregation tendencies. This relationship is illustrated in Figure 2.4, which shows how the SVR varies with particle volume for various shapes.

At identical mass fractions, SVR-driven differences in particle size directly influence mechanical performance as shown in Figure 2.5. For instance, 0D nanoparticles with identical chemical composition but varying sizes exhibit divergent mechanical properties due to SVR-dependent interfacial adhesion. Smaller particles (higher SVR) enhance filler-matrix interactions through increased surface contact, yet their reduced size elevates dispersion challenges, necessitating surfactants or functionalization to mitigate aggregation [145].

For 1D nanotubes, smaller diameters (higher SVR) improve mechanical reinforcement by increasing interfacial shear stress and load transfer efficiency. However, this benefit is contingent on maintaining alignment, as aggregation due to high SVR can negate reinforcement gains [147].

By strategically controlling SVR, researchers can balance enhanced interfacial interactions and aggregation risks [148] [149], enabling tailored mechanical properties for applications ranging from high-strength composites to lightweight structural materials.

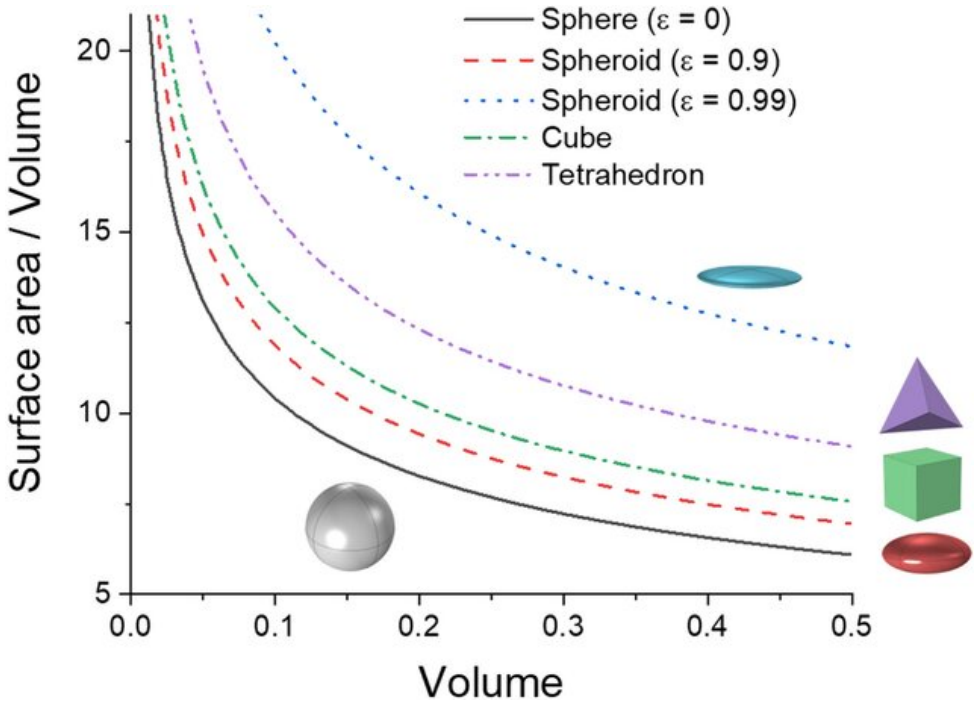

Figure 2.4 – *Relationship Between Surface-to-Volume Ratio and Volume for Various Shapes (ϵ, representing ellipticity, increases from 0 to 0.99) [144]*

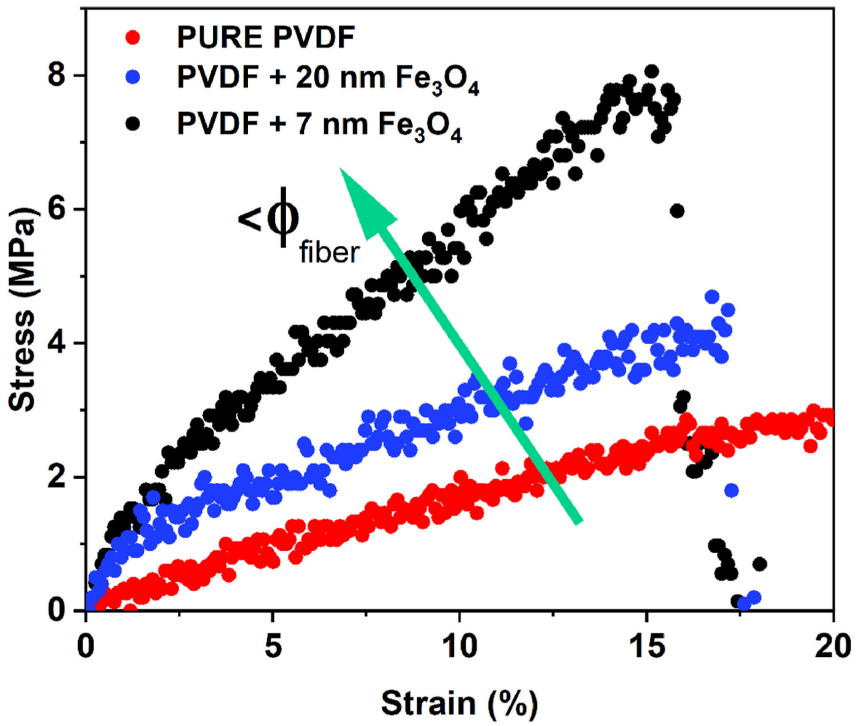

Figure 2.5 – *Size effect on tensile behavior. Stress–strain curves of pure PVDF, PVDF-20 nm Fe_3O_4, and PVDF-7 nm Fe_3O_4 electrospun films at 10 wt% loading, showing increased stiffness with decreasing nanoparticle size [146].*

2.4 Interface and Interphase in Nanocomposites

The influence of nanofillers in polymer nanocomposites extends beyond their intrinsic properties, as their high surface-to-volume ratio amplifies interfacial interactions. However, the impact of these interactions is not solely dictated by surface contact; rather, it is mediated by a transitional region known as the interphase. This region, which forms between the nanofillers and the bulk polymer, plays a decisive role in determining the macroscopic properties of the nanocomposite [150].

While the *interface* represents the immediate boundary where direct interactions occur between the nanofiller and polymer matrix, the *interphase* is a three-dimensional zone surrounding the nanofiller, where polymer chain mobility and molecular organization deviate from the bulk material. The characteristics of this interphase—such as its thickness, stiffness, and bonding dynamics—are strongly influenced by nanoparticle size, surface chemistry, and dispersion.

As the size of nanofillers decreases, their SVR increases, intensifying surface interactions. This enhanced surface effect modifies the polymer's local environment, reinforcing or weakening the material depending on how the interphase is structured. If well-controlled, the interphase can enhance mechanical strength, toughness, and thermal stability. Conversely, a poorly controlled interphase may lead to localized stress concentrations and mechanical failure.

Thus, the performance of polymer nanocomposites cannot be understood simply as an average of the polymer and nanofiller properties. Instead, it is largely governed by the molecular architecture of the interphase, which dictates how nanoscale interactions translate into macroscopic behavior, as illustrated in Figure 2.6 [151].

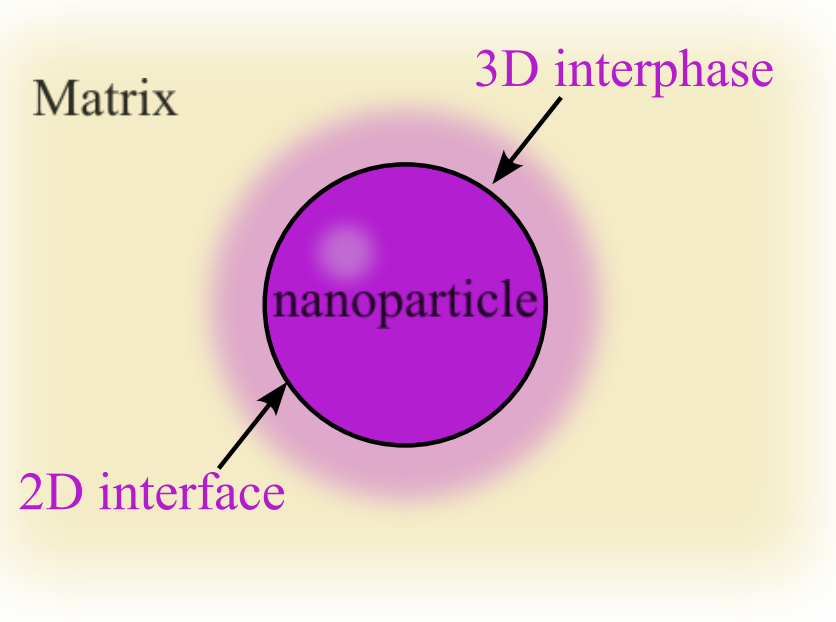

Figure 2.6 – *Visualization of the interface and interphase regions in nanocomposite materials.*

The formation of the interphase involves polymer chains adsorbing onto the nanoparticle surface through various interactions, including chemical, physical, long-range, and short-range interactions, which restrict their mobility [151]. These adsorbed chains form loop-like structures that provide sites for entanglement with nearby polymer chains (see Figure 2.7). The interphase emerges as surrounding polymer chains infiltrate these adsorbed structures, facilitating entanglement transfer and impacting the relaxation dynamics of the polymer chains in the bulk. This mechanism enhances the macroscopic mechanical properties of nanocomposites.

Using transmission electron microscopy (TEM), Priestley et al. were the first to visualize the interfacial adsorption layer around nanoparticles directly [152]. They also demonstrated a correlation between the structure of interfacial layers and their influence on the material's glass transition temperature (Tg), shedding light on the complex interplay between nanofillers, the interface, and the interphase.

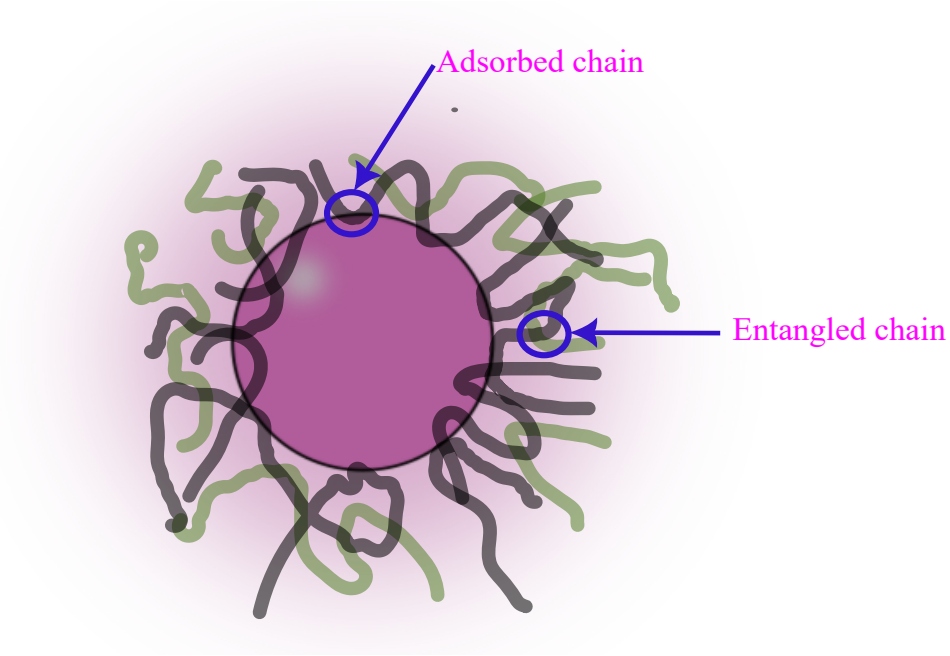

Figure 2.7 – *Illustration of the interphase in polymer nanocomposites, highlighting the formation and transfer mechanisms within the interfacial phase. It includes adsorbed chains on the surface and entangled chains connected to the adsorbed ones*

2.4.1 Inter-Particle Distance and Its Role in the Interphase

The correlation between the mechanical enhancement and the mass fraction of the nanofiller, as discussed previously, is associated with the inter-particle distance, τ. This distance is a critical parameter that determines the extent of interaction between nanoparticles and their surrounding matrix.

When the inter-particle distance decreases below a critical value, the interphase regions surrounding individual nanoparticles begin to overlap, forming a three-dimensional network rather than isolated transition zones. Within these interphase regions, the composite properties transition gradually from those of the nanofillers to those of the polymer matrix, leading to significant modifications in mechanical behavior. This overlap enhances stress transfer efficiency and influences polymer chain mobility on a larger scale, impacting properties such as stiffness, toughness, and overall reinforcement.

Under ideal dispersion conditions, the inter-particle distance τ can be expressed as a function of the mass fraction ϕ and the average particle size d [153]:

$$\tau = d\left(\left(\frac{\pi}{6\phi}\right)^{1/3} - 1\right) \tag{2.4}$$

The correlation between the inter-particle distance τ and the improvement in the mechanical properties of SiO_2/epoxy nanocomposites has been demonstrated in previous studies

[153]. Research indicates that a reduced τ correlates with enhanced stress transfer efficiency and mechanical reinforcement. However, as τ continues to decrease, the increased proximity of nanoparticles may also lead to interphase percolation or, in extreme cases, nanoparticle aggregation, which can hinder mechanical performance.

Thus, controlling the interparticle distance is crucial in optimizing the interphase structure to ensure effective reinforcement without inducing undesirable effects. Figure 2.8 illustrates the relationship between τ and the mechanical properties of nanocomposites, highlighting the importance of achieving a critical τ value to form a well-structured interphase network.

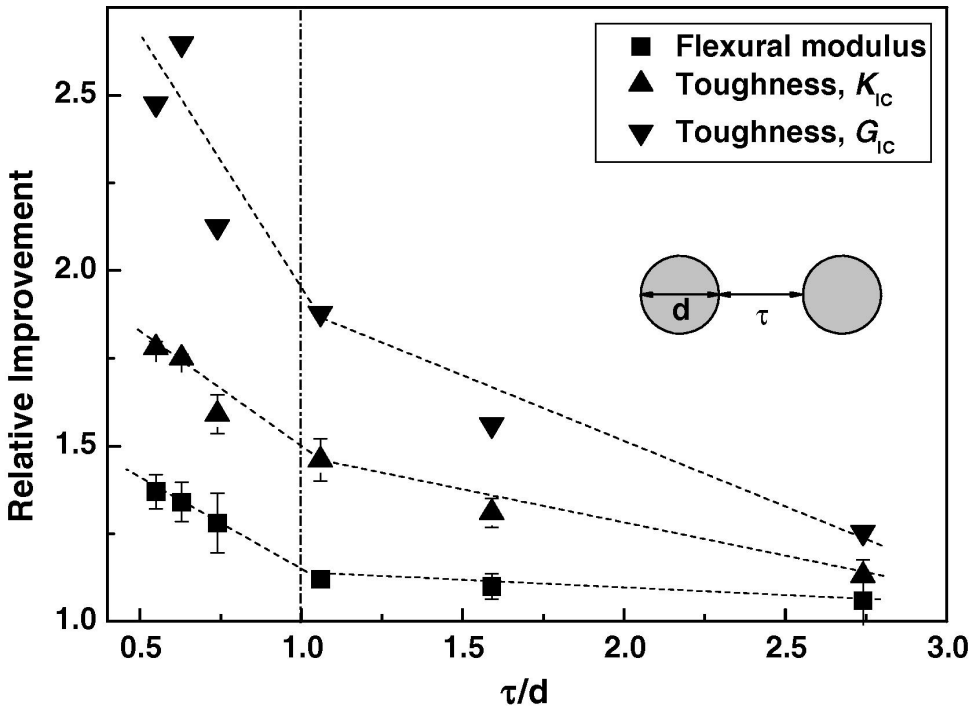

Figure 2.8 – *The correlation between the inter-particle distance τ and the improvement in the mechanical properties of SiO_2/epoxy nanocomposites has been demonstrated in previous studies [153].*

2.4.2 Propagation Distance

Another important distance to consider when discussing the interphase is the propagation distance. This parameter determines how far the nanofiller's influence extends into the polymer matrix. In simpler terms, it represents the thickness of the interphase region, which depends on several factors in addition to the nanoparticle loading, such as the strength and nature of polymer-nanofiller interactions, nanoparticle size, and surface characteristics.

Interestingly, research has also found a correlation between the molecular weight of the polymer chains and the thickness of the interphases. From various studies and different nanocomposite systems, this correlation has been defined as [154] [155] [156]:

$$h_{ads} = a \cdot R_g \tag{2.5}$$

where h_{ads} is the adsorption layer thickness, R_g is the radius of gyration of the polymer chains, and a ranges from 0.5 to 0.8. The adsorption layer thickness is closely related to the chain size, as characterized by R_g.

Along the chain length, the conformation of the adsorbed chains can also influence the thickness of the interface layer through topological interactions between structures in the adsorbed chains (e.g., loops) and those in adjacent unadsorbed chains [151]. This highlights the significance of adsorption chain conformation on the long-range interfacial effects. According to the research results the chains in the tightly bound adsorbed layers predominantly adopt a closely arranged loop conformation, which allows for high-density segment–solid contacts, thereby achieving a large enthalpy gain [157] [158] [159] [160].

Several studies have yielded valuable insights into the extent of interphase propagation. Using advanced characterization techniques such as neutron scattering, atomic force microscopy [161], and small-angle X-ray scattering [162], researchers can examine chain dynamics at varying distances from the nanofiller surface. These studies indicate that the interphase region can extend up to tens of nanometers in systems with strong interactions. In contrast, systems with weaker interactions may confine this range to only a few nanometers [151].

The impact of propagation distance on nanocomposite properties extends beyond mechanical reinforcement. It significantly influences other functional properties such as thermal and electrical conductivity. For instance, in polymer nanocomposites containing conductive fillers like carbon nanotubes or graphene, the propagation distance can affect the formation of conductive networks, thereby impacting the overall electrical properties of the material (Figure 2.9) [163] [164].

2.5 Polymer Nanocomposites Elaboration

2.5.1 Aggregation Challenges

Achieving uniform nanoparticle dispersion in polymer nanocomposites is essential for optimizing performance. Effective reinforcement relies on a homogeneous distribution that strengthens interfacial interactions with the polymer matrix and enhances stress transfer. However, the high surface-to-volume ratio of nanoparticles, which aids load distribution, also promotes agglomeration. This issue is illustrated in Figure 2.10, where iron oxide nanoparticles in PVDF aggregate due to their high surface energy and poor chemical compatibility

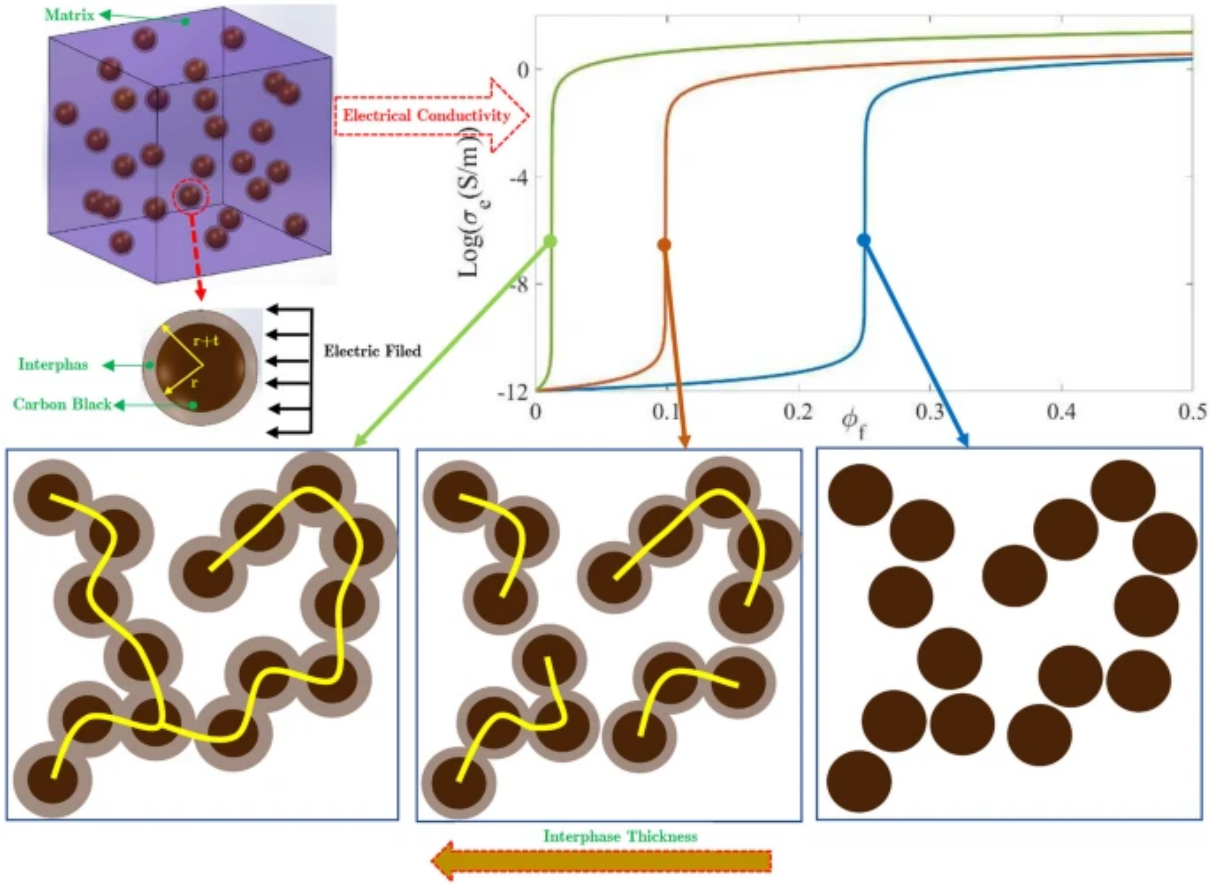

Figure 2.9 – *Analytical study on the electrical conductivity of conductive polymer nanocomposites (PNCs). The model accounts for quantum electron tunneling, interphase thickness, and conductivity contributions from the filler, interphase, and matrix. The graph shows conductivity evolution with filler volume fraction (ϕ_f), highlighting the percolation threshold. The bottom schematics illustrate how increasing interphase thickness influences the formation of conductive pathways [164].*

with both the polymer matrix and its solvents (DMF and acetone).

A similar trend is observed in TiO_2-reinforced polyester matrices (Figure 2.11), where dispersion quality varies with concentration. While well-dispersed at 1, 2, and 3 vol.%, significant agglomeration occurs at 4 vol.%, leading to reduced fracture toughness due to weak adhesion between titania particles and the polyester matrix [165].

Nanoparticle dispersion and aggregation depend on several factors, including particle size, shape, volume fraction, and polymer–filler interactions. High surface energy drives nanoparticle clustering [137], while weak interfacial adhesion exacerbates detachment or migration during processing [166]. Additionally, thermodynamic instability, particularly at elevated temperatures, sustains aggregation over time. These clusters act as stress concentrators, compromising mechanical strength, thermal stability, transparency, barrier performance, and resistance to environmental degradation [167]. The impact of poor dispersion extends

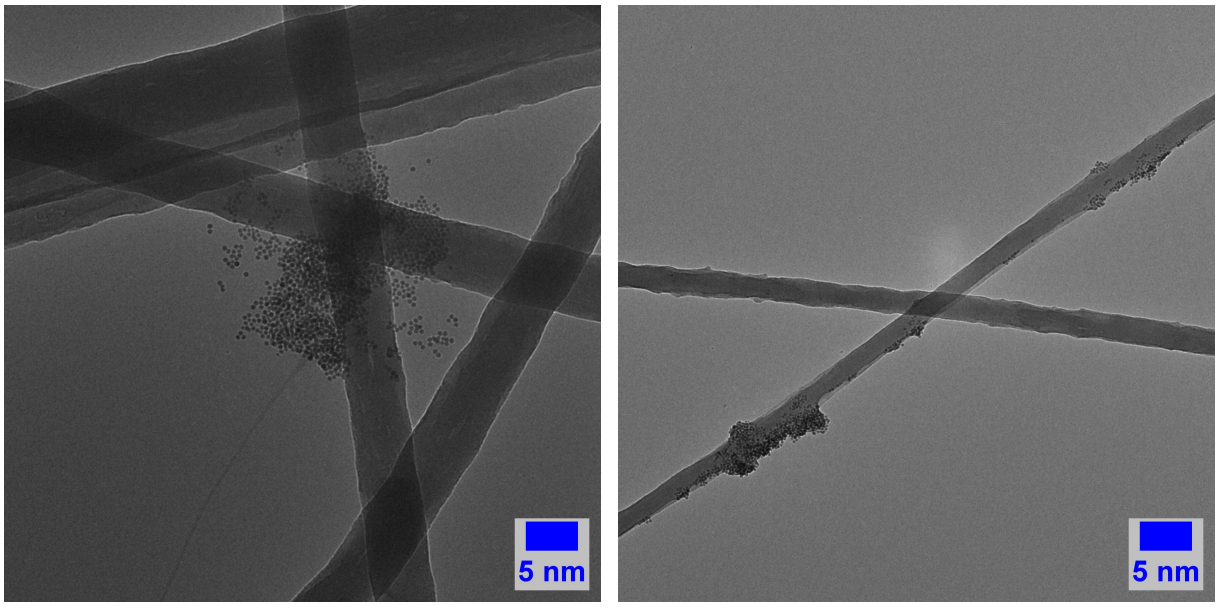

Figure 2.10 – *TEM images aggregation of maghemite nanoparticles within a PVDF polymer nanocomposite fabricated by coaxial electrospinning. This image highlights the difficulty in achieving uniform nanoparticle dispersion.*

beyond mechanical properties, influencing structural integrity and long-term stability under various environmental conditions.

2.5.2 Strategies for Reducing Aggregation

To address nanoparticle aggregation, several methods have been developed to mitigate their inherent tendency to agglomerate. These strategies enhance interfacial interactions and ensure homogeneous nanoparticle distribution within the polymer matrix:

- **Surface Modification**: Chemical functionalization tailors nanoparticle properties by grafting functional groups onto their surfaces. This enhances compatibility with the polymer matrix, reduces surface energy, minimizes agglomeration, and strengthens interfacial bonding [168].
- **Ultrasonication**: High-frequency sound waves generate cavitation effects that disrupt nanoparticle clusters in suspension. This method ensures uniform dispersion during polymer blending and remains effective when combined with other techniques [169] [170] .
- **Grafting Techniques**: Polymer chains are attached to nanoparticles via "grafting to" (preformed chains) or "grafting from" (in situ polymerization) methods. The resulting steric stabilization prevents nanoparticle contact and improves matrix compatibility, enhancing dispersion and interfacial adhesion [171] [172].

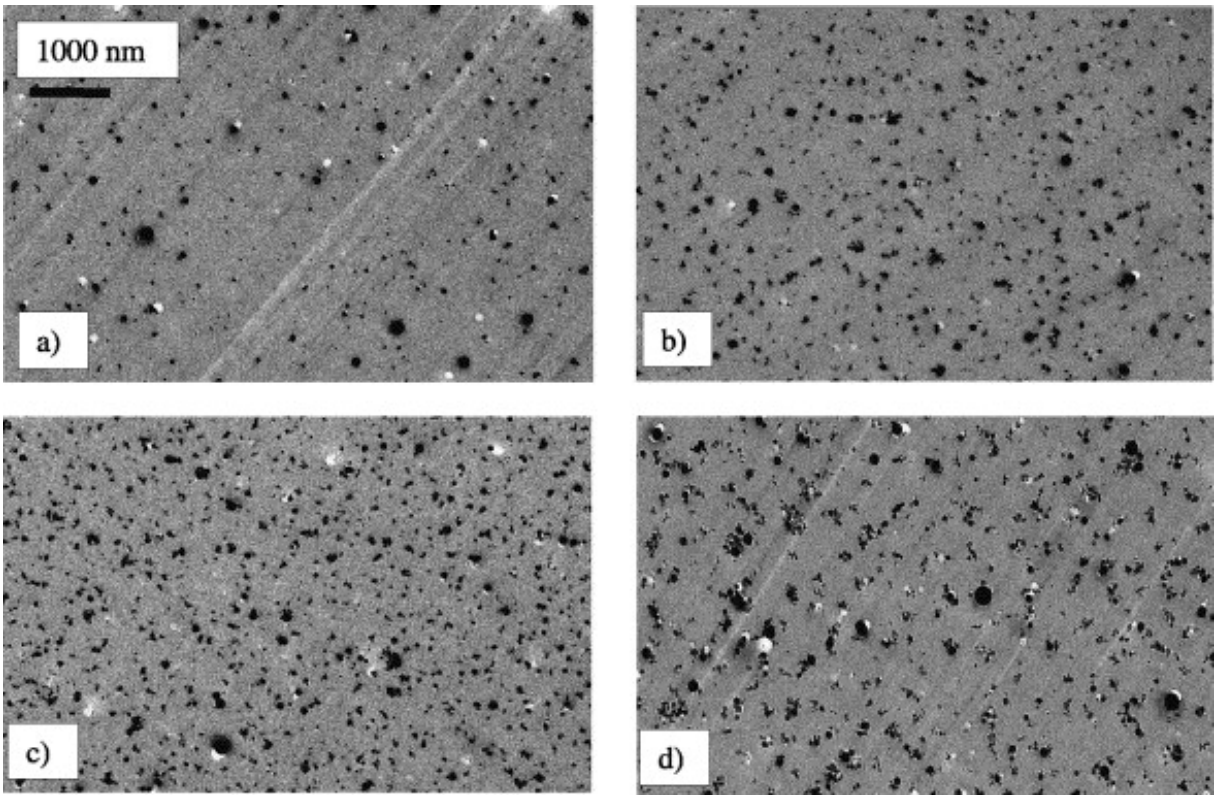

Figure 2.11 – *TEM micrographs illustrating the dispersion of TiO_2 nanoparticles within the polyester matrix at different volume fractions: (a) 1 vol.%, (b) 2 vol.%, (c) 3 vol.%, and (d) 4 vol.%. Excellent dispersion is observed in specimens with 1, 2, and 3 vol.% TiO_2, while significant agglomeration occurs in the 4 vol.% specimen [165].*

Optimizing fabrication processes further enhances dispersion efficiency, as discussed in the following section.

2.5.3 Fabrication Process

Polymer nanocomposites can be produced using two main strategies: **mixing pre-prepared components** or employing in **situ methods** [142].

Mixing Pre-prepared Components

The mixing of pre-prepared components involves using pre-synthesized polymers and nanoparticles, which are combined using techniques that enhance dispersion and interaction between the two components. Common methods include:

Melt mixing is a process that involves heating a polymer until it reaches its molten state, which makes it viscous enough to incorporate nanoparticles. During this process, the nanoparticles are mechanically blended into the molten polymer using equipment such as

an extruder or a mixer. This method is solvent-free, making it environmentally friendly, and is suitable for use with thermally stable polymers and nanoparticles.

In the **solution mixing** method, the polymer is dissolved in a suitable solvent to create a solution, into which the nanoparticles are dispersed. This dispersion can be achieved through techniques such as ultrasonication or stirring. Once a uniform mixture is achieved, the solvent is removed, typically through evaporation or precipitation, leaving behind a nanocomposite material. This method offers better control over nanoparticle dispersion and is suitable for polymers and nanoparticles that are sensitive to heat. However, the use of solvents raises environmental and cost concerns.

Electrospinning Electrospinning is a technique that produces nanofibers by stretching a polymer-nanoparticle solution into fine fibers using a high-voltage electric field. These fibers solidify once they reach the collector. Nanoparticles can either be embedded within the fibers or remain on their surface, making this method suitable for creating lightweight materials with a high surface area. However, achieving uniform dispersion of nanoparticles throughout the fibers poses a significant challenge.

A variation of this technique called coaxial electrospinning utilizes a coaxial needle to simultaneously spin two solutions, forming core-shell fibers, as illustrated in Figure 2.12. This approach allows for better encapsulation of nanoparticles.

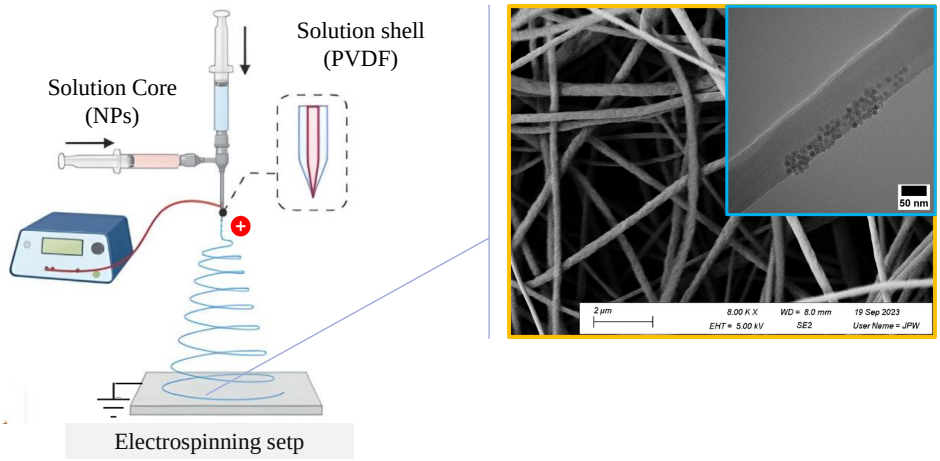

Figure 2.12 – *Schematic representation of the coaxial electrospinning setup used in experiments conducted during this PhD research, illustrating the formation of nanofibers with embedded nanoparticles. The figure includes SEM images showcasing the morphology of the resulting nanofibers and a TEM image highlighting the distribution of nanoparticles within the fiber structure [173].*

In-situ Methods

involve synthesizing either the polymer, the nanoparticles, or both directly in the presence of each other (Figure 2.13). These methods often result in better integration and enhanced properties due to the close interaction between components during synthesis, such as:

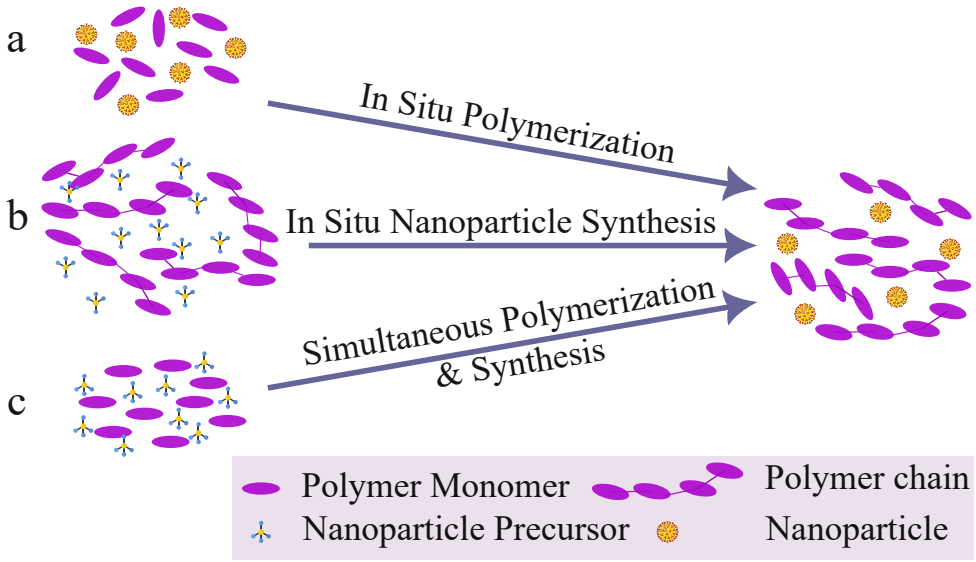

Figure 2.13 – *Schematic of polymer nanocomposite synthesis methods. (a) In situ polymerization with nanoparticles, (b) In situ nanoparticle synthesis within the polymer matrix, and (c) Simultaneous polymerization and nanoparticle synthesis. Adapted from [174], with modifications.*

In situ polymerization in nanoparticles that are dispersed in a solution of monomers (of polymers) or oligomers and then initiating the polymerization process. As the polymer forms around the nanoparticles, it creates strong interfacial bonding and ensures uniform dispersion. This method enhances compatibility and can be used with various monomers, including both thermosetting and thermoplastic polymers. However, it is essential to maintain a stable dispersion of nanoparticles and to carefully control the polymerization conditions [175].

Or, **In situ nanoparticle synthesis** that involves creating nanoparticles directly within a polymer matrix or solution. Precursors are dissolved in the polymer system, and chemical reactions—such as thermal decomposition or reduction—generate nanoparticles in situ. The polymer matrix stabilizes the nanoparticles during their formation, ensuring a uniform size and distribution. This method eliminates the need for surface modification of the nanoparticles but requires careful optimization of reaction conditions to prevent polymer degradation and the formation of unwanted by-products [176] [177].

The two described approaches can be performed simultaneously. **Simultaneous in situ synthesis and polymerization** combines nanoparticle formation and polymerization in a

single step. When optimized, this method can achieve uniform dispersion, strong interfacial bonding, and improved compatibility between the polymer matrix and nanoparticles [178].

2.6 Rationale for Nanocomposites *In-Situ* Synthesis

Among the fabrication methods for nanocomposites discussed earlier, in situ synthesis was chosen as the optimal approach. This decision aligns with the core objectives of this doctoral research, which focuses on synthesizing iron oxide nanoparticles while precisely controlling their size, surface chemistry, and shape to tailor their physical and chemical properties. The next step in this research is to extend this expertise to the development of nanocomposites, where the main challenge is optimizing the interactions between nanoparticles and the polymer to achieve the desired material properties.

The in situ method, where nanoparticles are synthesized directly within the polymer matrix, offers significant advantages. By integrating nanoparticle formation with the polymer processing, it ensures precise control over nanoparticle characteristics, such as size and surface functionality, while avoiding the dispersion issues typically encountered in post-synthesis mixing. This approach promotes better nanoparticle-polymer compatibility, leading to uniform dispersion and enhanced mechanical and functional properties in the final composite.

To further optimize this system, we focused on evaluating the solubility of the polymer in the synthesis mixture and analyzing its Hansen parameters. Improving nanoparticle dispersion within a polymer matrix requires considering the compatibility among the polymer, nanoparticles, their surface ligands, and the solvents used. Hansen Solubility Parameters (HSP) provide a systematic framework for analyzing these interactions and ensuring that the nanoparticle dispersion is optimized for the desired properties.

Hansen Solubility Theory divides the solubility parameter into three components: dispersive forces (δ_d), polar forces (δ_p), and hydrogen bonding forces (δ_h). By comparing the Hansen solubility parameters of the polymer, nanoparticles (including their surface ligands), and the solvents used for dispersion, we can identify the best combinations to promote uniform dispersion, which is crucial for enhancing the performance of the nanocomposite [179].

For example:

- The solvent chosen for the polymer should have HSP values that closely match those of the polymer to ensure effective dissolution and processing.
- The solvent used to disperse the nanoparticles should correspond to the HSP of the nanoparticle surface (including its ligand) to stabilize the dispersion and prevent

aggregation.

- Ensuring that the HSP of both solvents match can improve compatibility when combining the polymer and nanoparticles, promoting better integration during the fabrication of composites.
- By analyzing and matching these solubility parameters, Hansen Solubility Theory allows for the rational selection of solvents and surface ligands, reducing trial-and-error approaches and leading to improved nanoparticle dispersion and overall nanocomposite performance.

To illustrate the concept of HSP compatibility, we include a 3D representation of the Hansen Solubility Parameter space. As shown in Figure 2.14, the interaction radius (R_0) of a reference material (blue dot) is visualized within regions of good and poor solvents.

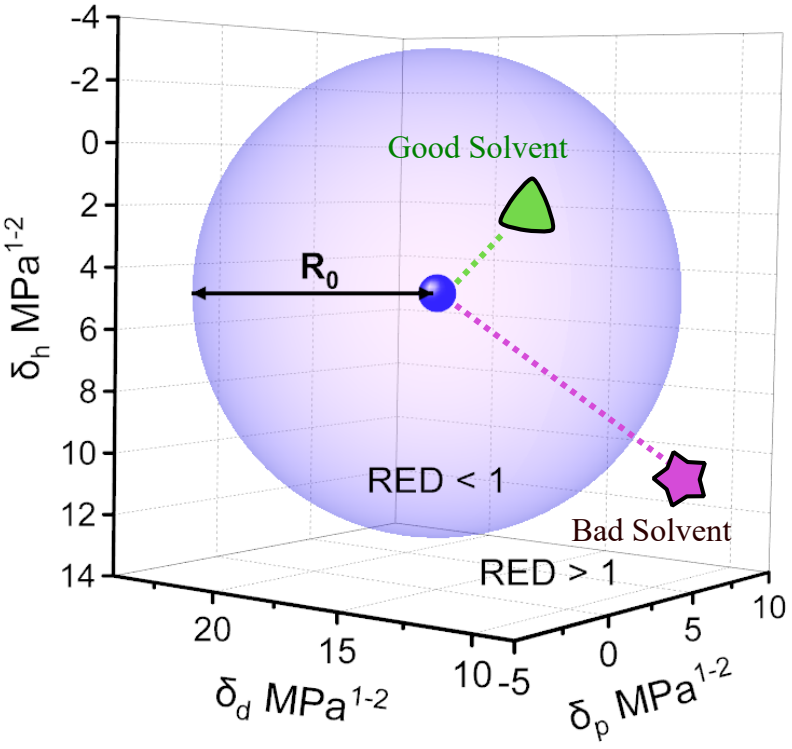

Figure 2.14 – *3D Hansen Solubility Parameter space showing the interaction radius (R_0) of a reference material (blue dot) with good solvent (green triangle) and bad solvent (pink star) regions. The sphere represents the solubility boundary where RED (Relative Energy Difference) = 1, with RED < 1 indicating good solvents and RED > 1 indicating poor solvents. The axes represent the three Hansen parameters: δ_d (dispersive), δ_p (polar), and δ_h (hydrogen bonding) in $MPa^{1/2}$ units.*

Hansen Solubility Theory (HST) is a valuable tool for predicting solubility behavior, especially in non-polar and moderately polar systems. However, it has its limitations. HST utilizes Hansen Solubility Parameters to model molecular interactions, but the variability in

reference data can sometimes lead to inconsistent predictions. The effectiveness of the theory decreases when applied to highly polar substances or complex molecules, and it struggles to accurately model intricate molecular interactions, such as those found in ionic liquids [180]. Additionally, HST operates under the assumption of ideal conditions, which may overlook real-world factors like temperature variations and concentration effects.

A comprehensive study assessing the performance of the Hansen solubility model using a dataset of 25 polymers found an accuracy rate of 67% for solvents and 76% for non-solvents. This underscores both its utility and its limitations in practical applications [181].

This approach was used for polyisobutylene, confirming the compatibility of this selected polymer with the synthesis process. The results will be presented in Chapter 5.

2.7 Characterization Techniques

The experimental characterization of nanocomposites adopts a multiscale approach, utilizing techniques that span different length scales to achieve a comprehensive understanding of their properties and performance. As illustrated in Figure 2.15, this approach integrates methods that complement one another, bridging the gap between nanoscale structural features and macroscopic properties. Such an integrated framework enables a thorough evaluation of nanocomposite behavior.

The previous chapter introduced techniques such as Wide-Angle X-ray Scattering (WAXS), Small-Angle X-ray Scattering (SAXS), and Transmission Electron Microscopy (TEM) for nanoparticle characterization. Primarily used for morphological analysis, these methods provide key information on nanoparticle size, shape, crystallinity, and spatial arrangement. While initially applied to individual nanoparticles, they remain crucial for investigating the structural features of nanocomposites.

Although the focus now extends to bulk-scale properties, **morphological characterization techniques** continue to play a key role in nanocomposite analysis. TEM, for example, provides insights into nanoparticle dispersion and morphology within the polymer matrix. Similarly, WAXS and SAXS contribute to understanding polymer and nanoparticle crystallinity as well as nanoparticle spatial distribution.

Beyond morphology, characterizing the **compositional aspects** of nanocomposites is essential. Quantifying the nanoparticle and polymer mass fractions enables correlation between structural and macroscopic properties, particularly mechanical and thermal behavior. Densitometry, for instance, allows for the determination of composite density. When combined with information on nanoparticle size and polymer density, it provides an estimate of the nanoparticle mass fraction, as discussed in the following section. Additionally, Thermogravimetric Analysis (TGA) serves as a complementary technique to confirm this

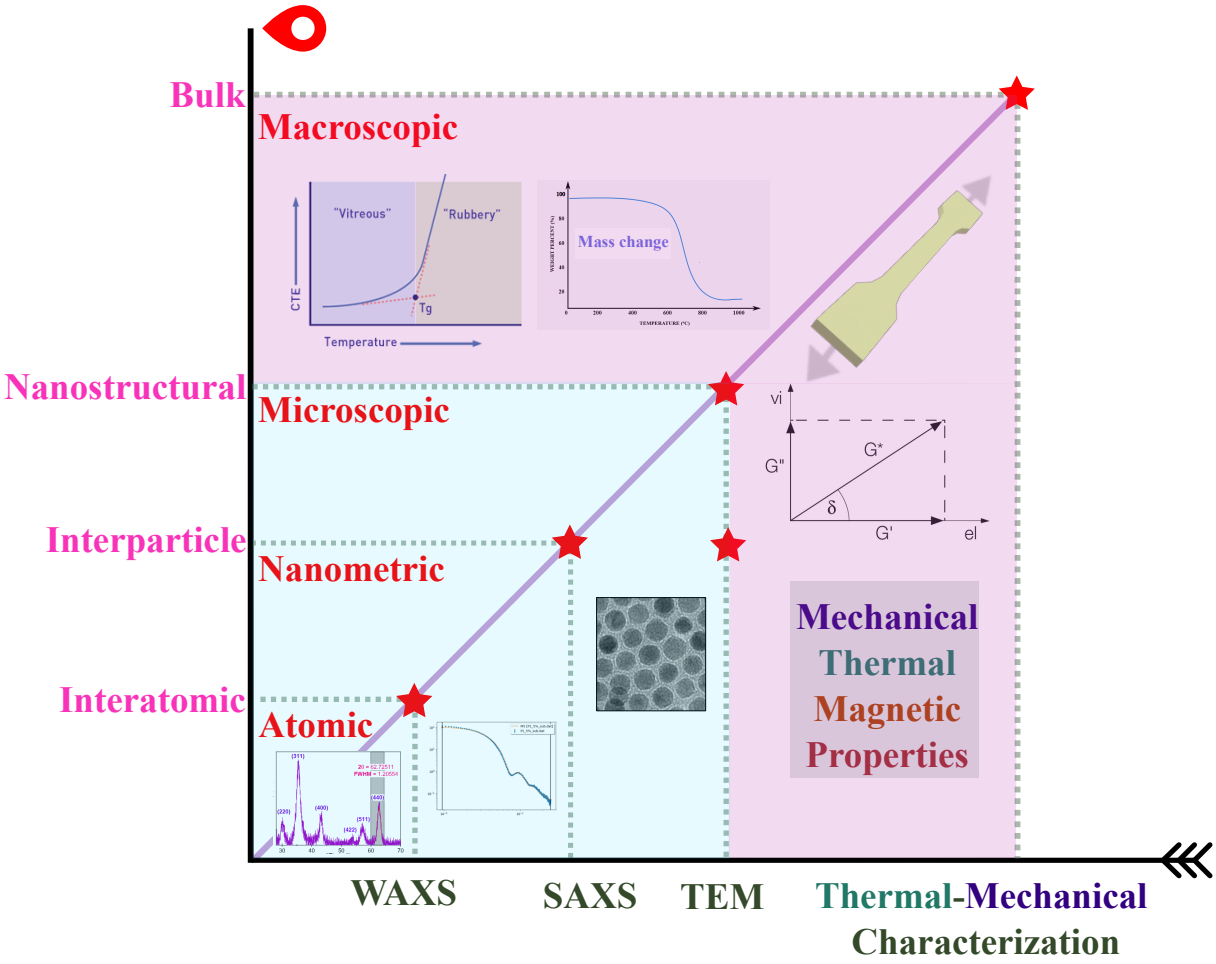

Figure 2.15 – *multi-scale characterization chart illustrating the relationship between the length scales (from atomic to bulk) and the corresponding characterization techniques, including WAXS, SAXS, TEM, Rheology, DMA, DSC, and TGA.*

information.

The evaluation of **macroscopic properties** relies on techniques tailored to specific aspects of material performance. **Mechanical properties** are analyzed using methods such as rheology and Dynamic Mechanical Analysis (DMA), which provide insights into viscoelastic behavior and stiffness. **Thermal properties** are investigated through Differential Scanning Calorimetry (DSC) to study thermal transitions and TGA to assess thermal stability.

2.7.1 Morphological Analysis

This section revisits the previously introduced techniques—TEM, WAXS, and SAXS—to highlight their relevance in nanocomposite characterization. While their fundamental principles remain unchanged, these methods are employed to analyze key morphological features, including nanoparticle dispersion, crystallinity, and spatial arrangement.

Transmission Electron Microscopy (TEM)

TEM is a critical tool for nanocomposite characterization, offering high-resolution imaging of internal structures. It enables:

- **Nanoparticle Dispersion Analysis:** Assessing the spatial distribution of nanoparticles within the polymer matrix.
- **Particle-Matrix Interface Evaluation:** Examining the interactions between nanoparticles and the surrounding polymer.
- **Agglomeration Detection:** Identifying nanoparticle clustering that may affect composite properties.
- **Morphological Changes Observation:** Monitoring alterations in nanoparticle shape or structure due to polymer interactions.

With nanoscale resolution, TEM provides direct insight into the structural organization of nanocomposites and the influence of processing conditions.

Wide-Angle X-ray Scattering (WAXS)

WAXS offers valuable information on the crystalline structure of nanocomposites at the atomic and molecular levels, including:

- **Polymer Crystallinity Analysis:** Assessing changes in polymer crystallinity upon nanoparticle incorporation.
- **Phase Identification:** Detecting new crystalline phases resulting from nanoparticle-polymer interactions.
- **Nanoparticle Crystallinity Monitoring:** Identifying potential structural modifications in nanoparticles within the composite.

Comparing WAXS data from pure components and nanocomposites helps elucidate the impact of nanoparticles on the overall crystalline structure.

Small-Angle X-ray Scattering (SAXS)

Complementing WAXS and TEM, SAXS probes larger-scale structures, providing insights into:

- **Spatial Distribution:** Investigating nanoparticle arrangement within the polymer matrix.
- **Hierarchical Structure:** Identifying multi-scale structural features in nanocomposites.
- **Interfacial Regions:** Analyzing interactions between nanoparticles and the polymer matrix.
- **Aggregation Behavior:** Detecting nanoparticle networks or clusters formed under specific conditions.

Together, these techniques provide a comprehensive morphological analysis, linking nanoscale structures to macroscopic properties.

2.7.2 Composition Analysis

Density Measurements

The density (ρ) of the nanocomposite can be determined using a precision density balance based on Archimedes' principle. The setup involves measuring the sample's mass in air (m_{air}) and then in a reference liquid (m_{liquid}) with a known density (ρ_{liquid}) at the measurement temperature, as shown in Figure 2.16. The density of the nanocomposite can be calculated using the following equation:

$$\rho = \frac{m_{\text{air}} \cdot \rho_{\text{liquid}}}{m_{\text{air}} - m_{\text{liquid}}} \tag{2.6}$$

This approach allows for precise density determination by accurately accounting for the displacement of the reference liquid during the measurement.

The density measurement can also be used to estimate the mass fraction of nanoparticles (w_m) in the nanocomposite, provided the densities of the nanocomposite (ρ_c), the matrix (ρ_m), and the filler (ρ_p) are known. The mass fraction can be calculated using the following equation:

$$w_m = \frac{\left(\frac{1}{\rho_c} - \frac{1}{\rho_p}\right)}{\left(\frac{1}{\rho_m} - \frac{1}{\rho_p}\right)} \tag{2.7}$$

This equation allows for determining the contribution of the nanoparticles to the composite's overall density.

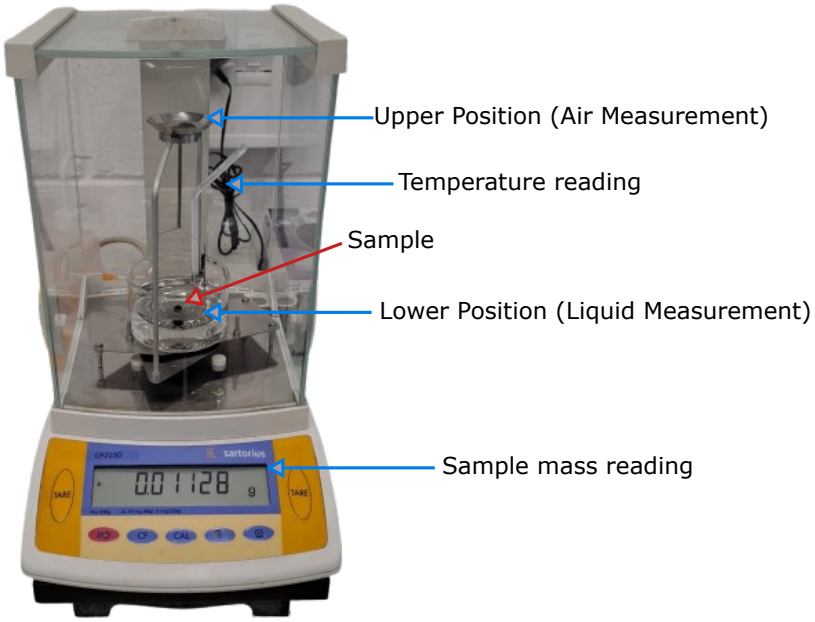

Figure 2.16 – *Precision density balance setup for accurate density measurements. The apparatus inside the glass chamber includes a suspension mechanism for measuring samples in air and a reference liquid. The balance utilizes Archimedes' principle to determine density through displacement.*

TGA (Thermogravimetric Analysis)

Thermogravimetric Analysis (TGA) is a technique that measures the mass loss of a sample as it is heated under a controlled atmosphere (e.g., air or nitrogen). The sample is subjected to a controlled heating rate, and the corresponding mass changes are recorded, providing insights into its composition.

TGA is commonly used to determine the composition of a material, but it is also employed to assess thermal degradation, quantify moisture or solvent content, and analyze volatile components. The occurrence of mass losses at specific temperatures enables the identification of different material phases based on their thermal behavior and provides quantitative information on the amount of each component present in a sample (Figure 2.17).

This technique is particularly useful for studying polymers, composites, and other complex materials. It is often complemented by other methods, such as Differential Scanning Calorimetry (DSC), to achieve a more comprehensive thermal characterization.

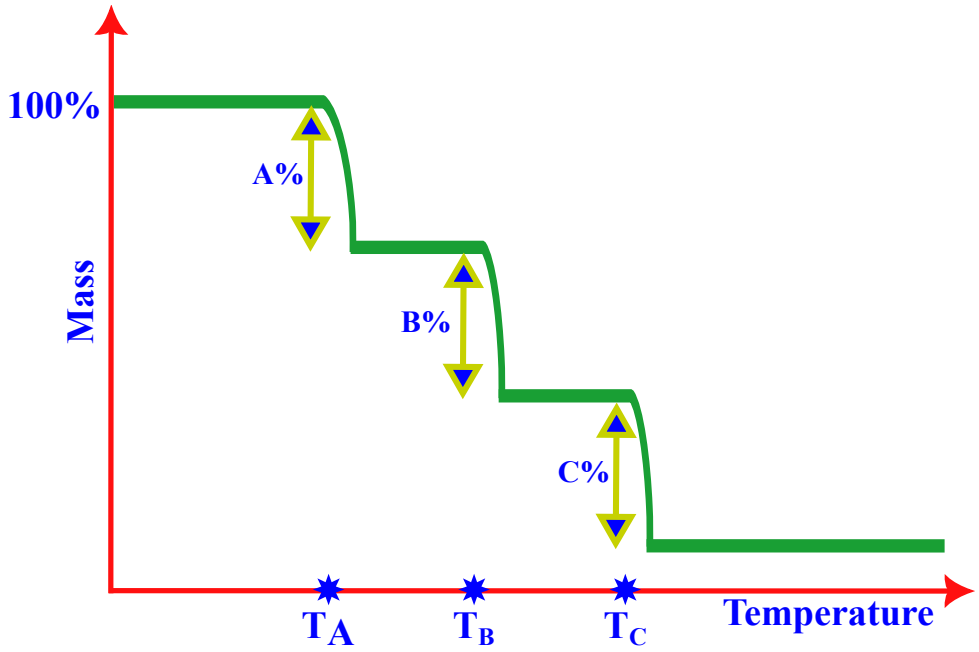

Figure 2.17 – *Thermogravimetric Analysis curve showing mass loss at different temperatures.*

2.7.3 Physical Characterization

Regarding the **physical properties** of nanocomposites, Thermogravimetric Analysis (TGA), mentioned earlier, serves not only as a technique for quantifying composition but also for analyzing physical properties such as thermal stability, degradation, and, in some cases, oxidation behavior.

To complement TGA, Differential Scanning Calorimetry (DSC), presented in the following section, provides additional insights into the thermal behavior of nanocomposites.

DSC (Differential Scanning Calorimetry)

Differential Scanning Calorimetry (DSC) is a thermal analysis technique used to measure thermal transitions, such as the glass transition temperature (Tg), in polymers. In DSC, a sample and a reference material are placed in separate pans (see Figure 2.18) and subjected to a controlled heating or cooling program. The heat flow into or out of the sample is continuously monitored and compared to that of the reference material, which has a known heat capacity and remains stable during the experiment.

DSC is especially effective for detecting changes in heat capacity during transitions such as the glass transition temperature. When a polymer reaches Tg, it transitions from a glassy state to a rubbery state, resulting in a change in heat capacity. This change can be observed as a step change in the heat flow curve, as illustrated in Figure 2.19.

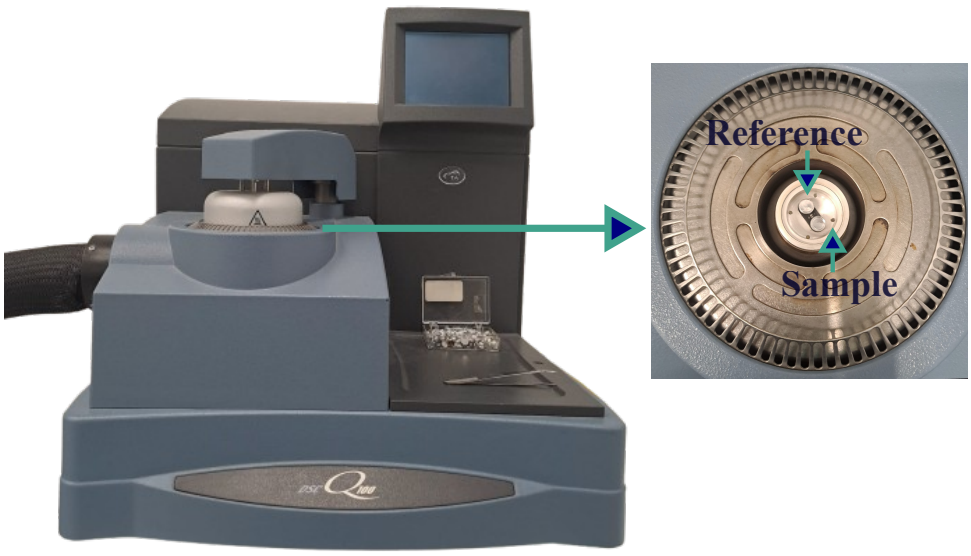

Figure 2.18 – *A Differential Scanning Calorimetry Q100 machine used for thermal analysis of materials in the Roberval Laboratory - UTC.*

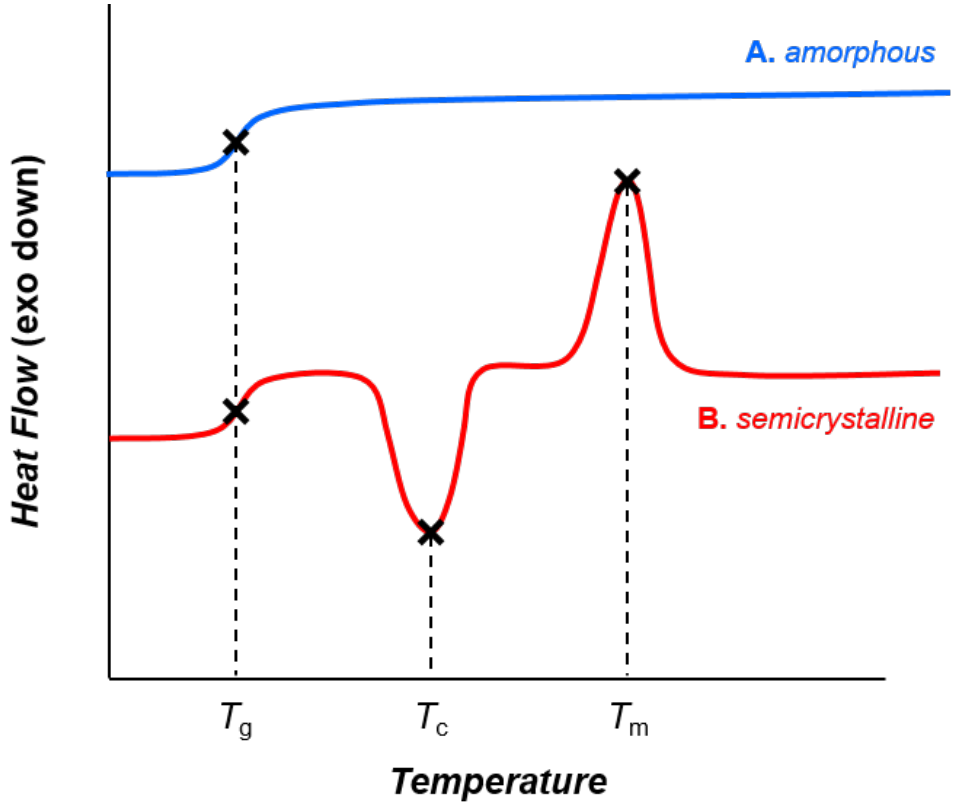

Figure 2.19 – *Thermal transitions in (A) amorphous and (B) semicrystalline polymers. As temperature rises, both amorphous and semicrystalline polymers experience the glass transition (Tg). Amorphous polymers (A) do not show any other phase transitions, whereas semicrystalline polymers (B) undergo crystallization and melting at temperatures Tc and Tm, respectively.*

In this thesis, DSC was also employed to analyze the thermal behavior and decomposition of carboxylate precursors used in nanoparticle synthesis, identifying key temperature points related to the dissociation of carboxyl groups.

2.7.4 Mechanical Characterization

Understanding the mechanical behavior of a material requires various testing techniques that evaluate stiffness, strength, and viscoelastic properties.

Tensile tests, DMA, and rheology are among the most commonly used methods to characterize mechanical performance. Each of these techniques provides complementary insights into different aspects of the material's response to mechanical stress.

Tensile Tests

Tensile testing is used to evaluate material properties like strength, elasticity, and ductility, with data typically shown as stress-strain curves. Young's modulus, which reflects stiffness, is derived from the linear portion of the curve using the formula:

$$E = \frac{F \cdot L_0}{A \cdot \Delta L} \tag{2.8}$$

where F is the applied force, A is the cross-sectional area, L_0 is the initial length, and ΔL is the elongation.

The experimental setup for tensile testing is illustrated in Figure 2.20, which shows an electrospun PVDF film being tested using a 300 N load cell. The red arrow indicates the direction of the applied force.

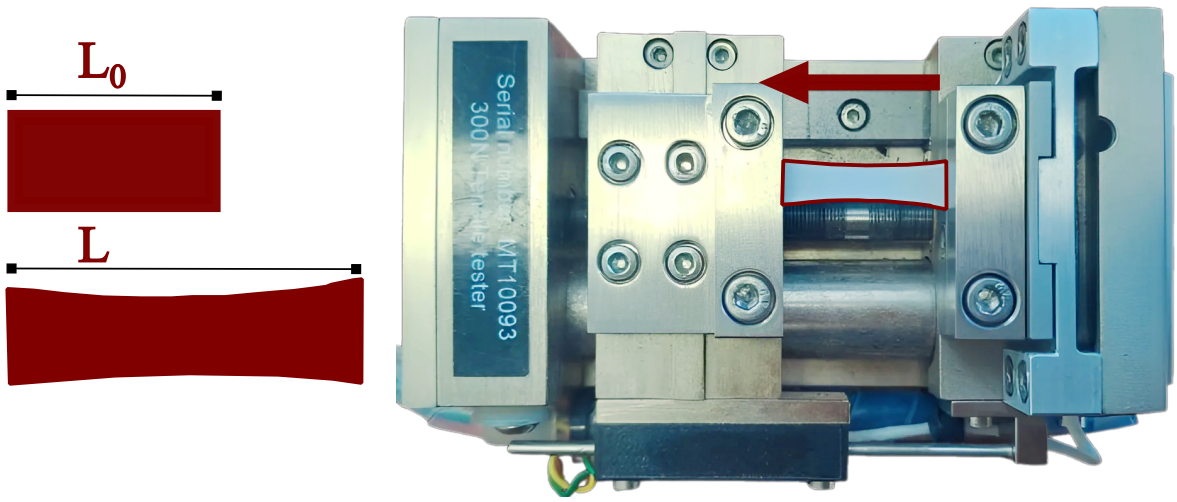

Figure 2.20 – *Tensile testing of an electrospun PVDF film using a 300 N load cell, with the red arrow indicating the direction of the applied force.*

(DMA) Dynamic Mechanical Analysis

Building on the mechanical properties obtained from tensile testing, Dynamic Mechanical Analysis (DMA) provides deeper insights into the viscoelastic behavior of materials under oscillatory stress. While tensile testing measures the Young's modulus (E) through static stress-strain experiments, DMA evaluates how materials respond to dynamic deformation, revealing their ability to store and dissipate energy.

The key properties derived from DMA are the storage modulus (E'), which quantifies the elastic response, the loss modulus (E''), which measures the viscous dissipation of energy, and the complex modulus (E^*), defined as the vector sum of E' and E''. The storage modulus can be expressed as:

$$E' = \frac{\sigma_0 \cos(\delta)}{\varepsilon_0}, \tag{2.9}$$

and the loss modulus is given by:

$$E'' = \frac{\sigma_0 \sin(\delta)}{\varepsilon_0}. \tag{2.10}$$

Here, σ_0 is the stress amplitude, ε_0 is the strain amplitude, and δ is the phase angle between the stress and strain. The complex modulus is represented as:

$$E^* = \sqrt{(E')^2 + (E'')^2}. \tag{2.11}$$

In DMA, the material is subjected to a sinusoidal strain:

$$\varepsilon(t) = \varepsilon_0 \sin(\omega t), \tag{2.12}$$

where ω is the angular frequency, and the resulting stress is:

$$\sigma(t) = \sigma_0 \sin(\omega t + \delta). \tag{2.13}$$

The phase angle δ reflects the viscoelastic nature of the material, where an elastic solid has $\delta = 0$ and a purely viscous fluid has $\delta = \pi/2$. The oscillatory stress and the response to it are shown in Figure 2.21.

DMA experiments are typically conducted under controlled conditions:

- **Strain amplitude**: Kept small, usually less than 1% of the sample dimension, to remain within the linear viscoelastic regime (LVER).
- **Temperature range**: Measurements can span from sub-ambient temperatures to over 300°C, depending on the instrument and material.

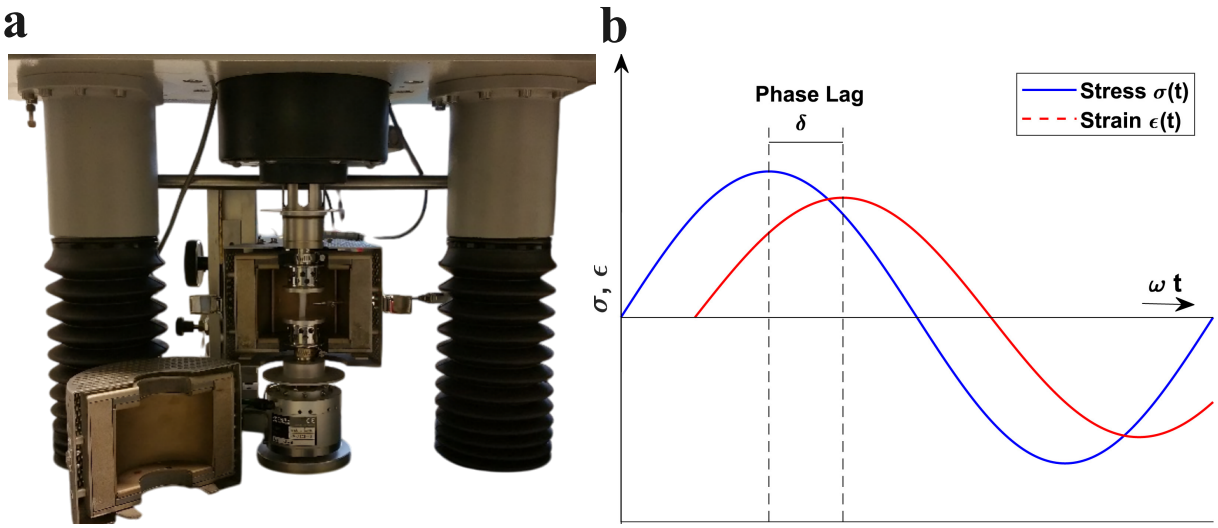

Figure 2.21 – *(a) Setup of the specimen mounted between two plates inside a thermal chamber for DMA testing at the Roberval Laboratory of UTC [182]. (b) Stress-strain relationship observed in DMA measurements [183].*

- **Frequency range**: Most instruments operate between 0.01 Hz and 200 Hz.

The technique can be performed in several modes, including tension, compression, and bending, with the choice of mode depending on the material and the desired insights.

By analyzing the storage modulus (E') and loss modulus (E'') over a range of temperatures or frequencies, DMA provides crucial information about the viscoelastic properties of materials. Additionally, the glass transition temperature (T_g) can be identified as the temperature at which E' drops significantly and E'' exhibits a peak, offering insights into the thermal behavior as shown in Figure 2.22.

Rheological Characterization

Expanding upon the principles of DMA, rheology delves into a broader spectrum of material states and deformation behaviors. Unlike DMA, which primarily examines solid materials, rheology explores the flow and deformation of materials across solid, liquid, and intermediate states, offering crucial insights into complex systems such as polymer melts, suspensions, and gels.

In rheology, materials' response is quantified using shear moduli: storage modulus (G'), which measures the elastic response, loss modulus (G''), which quantifies viscous energy dissipation, and complex shear modulus (G^*), which combines G' and G'' as:

$$G^* = G' + iG'' = \sqrt{G'^2 + G''^2} \tag{2.14}$$

The complex viscosity (η^*) relates to G^* via:

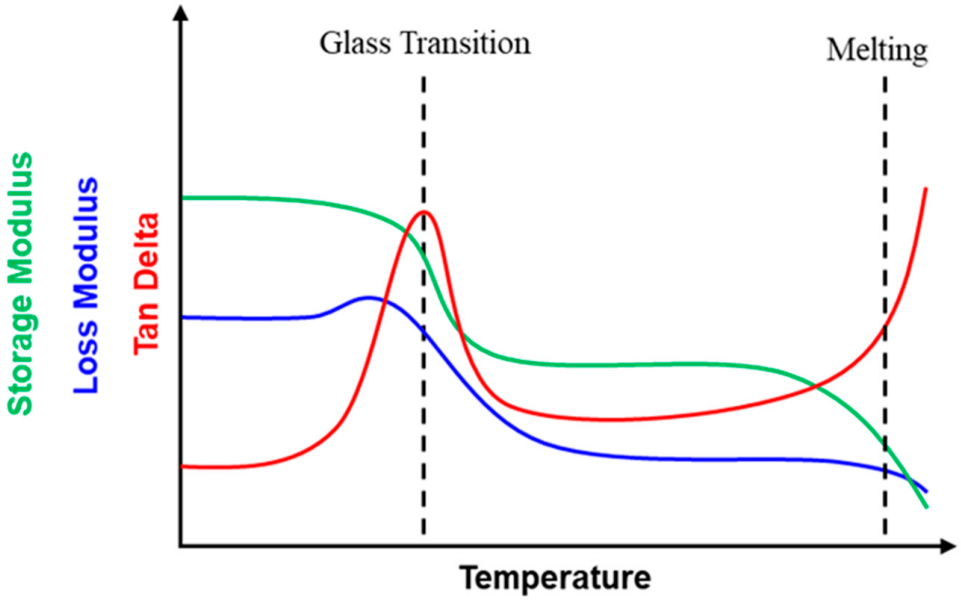

Figure 2.22 – *Example of a typical DMA thermogram for polymers. [184].*

$$\eta^* = \frac{G^*}{\omega} = \frac{\sqrt{G'^2 + G''^2}}{\omega} \tag{2.15}$$

where ω is the angular frequency.

Rheological tests typically involve sinusoidal strain $\gamma(t) = \gamma_0 \sin(\omega t)$, leading to a stress response $\tau(t) = \tau_0 \sin(\omega t + \delta)$, with a phase lag δ that characterizes the material's viscoelasticity. The storage and loss moduli can be expressed in terms of stress and strain amplitudes:

$$G' = \frac{\tau_0}{\gamma_0} \cos(\delta) \tag{2.16}$$

$$G'' = \frac{\tau_0}{\gamma_0} \sin(\delta) \tag{2.17}$$

To ensure accurate measurements, an amplitude sweep identifies the LVER, where G' and G'' are constant. Beyond this region, material behavior becomes nonlinear due to structural changes. Once the LVER is determined, a frequency sweep explores the material's response across a range of angular frequencies (ω), typically from 0.01 Hz to 100 Hz, providing insights into its time-dependent behavior and transitions between elastic (solid-like) and viscous (liquid-like) states.

G' and G'' measured during the frequency sweep can also be linked to mechanical

properties like the Young's modulus (E) using the relationship:

$$E \approx 2G'(1+\nu), \tag{2.18}$$

where ν is the Poisson's ratio.

By combining amplitude and frequency sweeps, rheology provides a comprehensive understanding of a material's viscoelastic and flow properties. A rotational rheometer showing its key components, is illustrated in Figure 2.23 below.

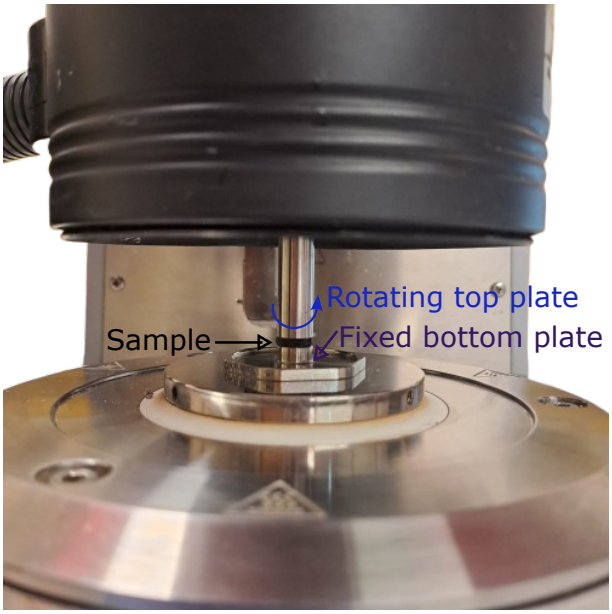

Figure 2.23 – *A rotational rheometer from the TIMR laboratory of UTC, showing its key components, including a stationary bottom plate, a rotating top geometry, and a sample material between them.*

2.7.5 Magnetothermal Characterization

An important property to characterize in iron oxide nanoparticle-based composites is their magnetothermal behavior. Before discussing the characterization techniques, we briefly present the mechanism underlying this property.

Iron oxide nanoparticles have the ability to convert electromagnetic energy into heat when subjected to an alternating magnetic field. This magnetothermal effect is governed by two primary relaxation mechanisms: **Néel** and **Brownian** relaxation. In both mechanisms, the continuous attempt of magnetic moments to realign with the oscillating external field leads to energy loss, which is dissipated in the form of heat. These processes are particularly significant in the superparamagnetic regime.

The overall heating efficiency is determined by the *effective relaxation time* τ_{eff}, which

combines the contributions of both mechanisms as follows [185]:

$$\frac{1}{\tau_{\text{eff}}} = \frac{1}{\tau_N} + \frac{1}{\tau_B} \tag{2.19}$$

- **Néel relaxation** (τ_N) involves the internal reorientation of the magnetic moment within a fixed nanoparticle, driven by thermal fluctuations that help overcome the anisotropy energy barrier. This reorientation, in response to the alternating field, results in energy dissipation due to internal magnetic friction. This mechanism dominates in smaller particles and depends on the magnetic anisotropy constant, particle volume, and temperature (Figure 2.24).
- **Brownian relaxation** (τ_B) refers to the physical rotation of the entire nanoparticle within its surrounding medium to align its magnetic moment with the external field. The resulting viscous drag from the medium resists this motion, converting part of the energy into heat. It is governed by the particle's hydrodynamic volume, the viscosity of the medium, and temperature (Figure 2.24).

Both relaxation mechanisms are only activated under an alternating magnetic field. In a static magnetic field, magnetic moments align and remain in equilibrium, resulting in negligible heat production.

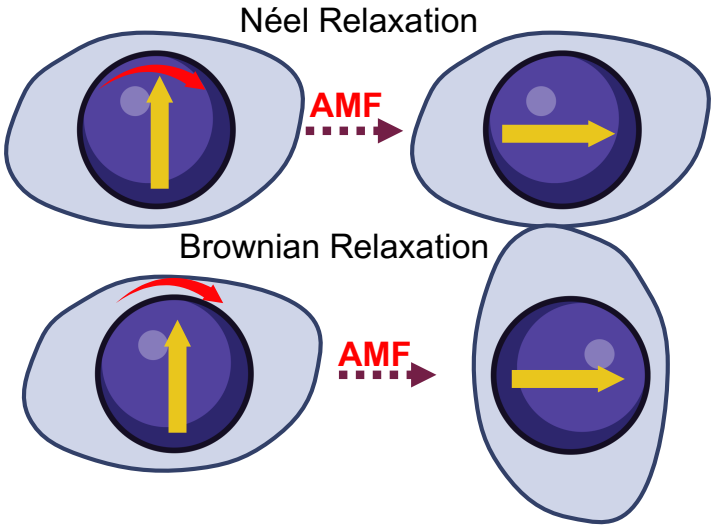

Figure 2.24 – *Magnetic nanoparticle relaxation under an alternating magnetic field: Néel relaxation (top) corresponds to internal magnetic moment rotation, while Brownian relaxation (bottom) corresponds to physical rotation of the nanoparticle.*

The heating ability of nanoparticles is quantified using the **specific absorption rate (SAR)**—an extrinsic parameter related to power dissipated per unit mass—and the **intrinsic loss parameter (ILP)**, which reflects the material's intrinsic heating capacity. The heating efficiency of IONPs under an alternating magnetic field is highly dependent on particle size.

In the superparamagnetic regime, heating arises from Néel and Brownian relaxation, both of which are sensitive to nanoparticle size. Smaller particles often exhibit lower magnetization due to spin-spin exchange interactions that lead to disordered, spin glass-like surface layers—features rarely observed in bulk magnetic materials [186] [187] [188]. Additionally, incomplete coordination of surface metal ions contributes to magnetic frustration and reduced magnetic moments [189].

Crystallinity is another key factor. Well-crystallized IONPs exhibit superior magnetic properties because structural defects and amorphous regions hinder magnetization reversal under AC fields. Nanoparticle morphology also plays a role: cubic IONPs generally outperform spherical ones due to their flat <100> facets, which reduce surface spin disorder [190]. In contrast, the curved surfaces of spherical IONPs enhance spin canting and reduce effective magnetization. Studies report that cubic IONPs can exhibit nearly double the specific loss power compared to spherical particles of similar size (356.2 vs. 189.6 W/g) [191].

Viscosity of the surrounding medium also significantly affects heating efficiency. Higher viscosity limits the rotational mobility of nanoparticles, suppressing Brownian relaxation and reducing the heating effect. In high-viscosity environments, such as intracellular or gel-like media, SAR values can decrease by up to 50% compared to those in aqueous solutions [192]. This is especially important for larger particles, where Brownian rotation significantly contributes to relaxation [193]. Conversely, smaller particles (typically <20 nm) primarily undergo Néel relaxation, which is independent of the medium's viscosity and thus maintains consistent heating performance. For intermediate to larger particles (20–37 nm), Brownian motion becomes more dominant, making the SAR strongly dependent on medium viscosity due to hindered rotational motion.

To investigate the magnetothermal behavior of magnetic nanoparticles, experiments are typically conducted using a dedicated hyperthermia setup such as the one provided by NanoScale Biomagnetics (Figure 2.25). This system includes a coil connected to an alternating current (AC) power source, which generates a well-controlled alternating magnetic field. When magnetic nanoparticles are exposed to this field, they convert electromagnetic energy into heat through magnetic relaxation mechanisms.

A fiber optic thermometer is commonly employed to measure the sample temperature with high accuracy. Being immune to electromagnetic interference, it ensures reliable data acquisition even in strong magnetic environments. The temperature sensor is immersed in the sample and connected to a digital acquisition system, enabling real-time recording and visualization of temperature versus time throughout the experiment.

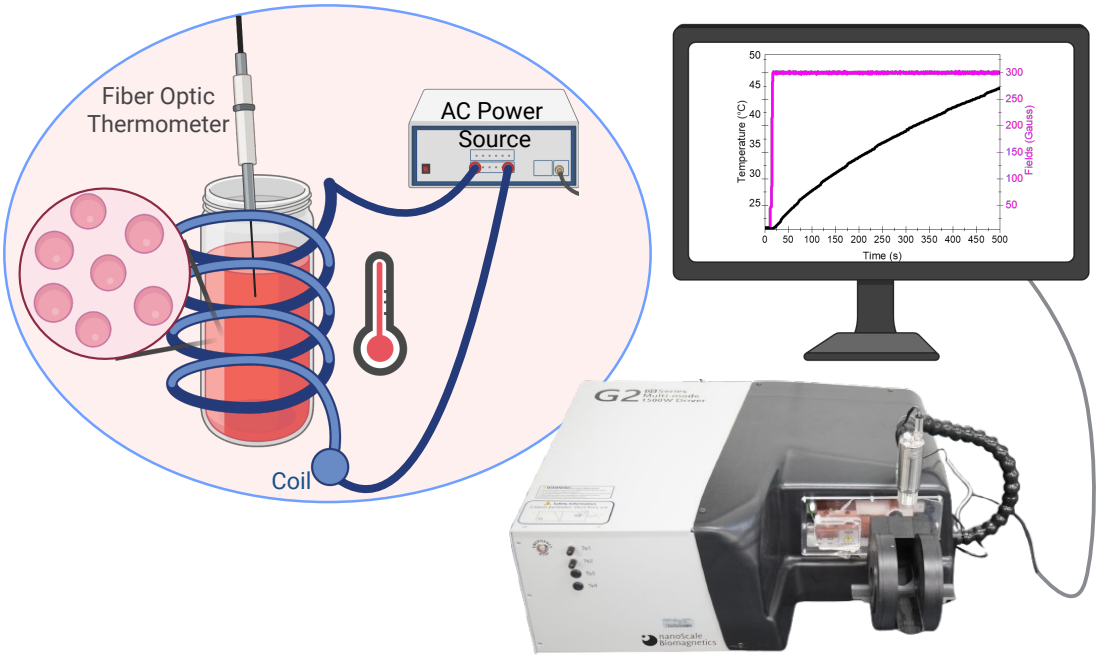

Figure 2.25 – *Setup of the hyperthermia test utilizing NanoScale Biomagnetics equipment (From Phénix Laboratory at Sorbonne Université). The system consists of an electromagnetic coil powered by an AC source, a sample container, and a fiber optic thermometer for precise temperature monitoring.*

2.8 Conclusion

This chapter has provided a comprehensive overview of polymer nanocomposites, encompassing their design principles, fabrication methods, and evaluation strategies. Particular emphasis was placed on the matrix–filler interface, which plays a pivotal role in dictating the ultimate performance of these materials.

A broad array of characterization techniques was presented, highlighting the importance of multiscale approaches to capture the structural, thermal, magnetic, and mechanical behaviors of nanocomposites. These techniques offer critical insights into the complex interactions occurring across multiple length scales, thereby elucidating the structure–property relationships that govern material performance.

Altogether, the interdisciplinary framework outlined in this chapter establishes a solid foundation for the rational design of advanced nanocomposites tailored to meet specific engineering requirements.

Bibliography

[1] B. A. Kairdolf, A. M. Smith, T. H. Stokes, M. D. Wang, A. N. Young, and S. Nie, "Semiconductor quantum dots for bioimaging and biodiagnostic applications," *Annual review of analytical chemistry*, vol. 6, no. 1, pp. 143–162, 2013.

[2] J. Tian and G. Cao, "Semiconductor quantum dot-sensitized solar cells," *Nano reviews*, vol. 4, no. 1, p. 22578, 2013.

[3] J. Boken, P. Khurana, S. Thatai, D. Kumar, and S. Prasad, "Plasmonic nanoparticles and their analytical applications: A review," *Applied Spectroscopy Reviews*, vol. 52, no. 9, pp. 774–820, 2017.

[4] n. Wahajuddin and S. Arora, "Superparamagnetic iron oxide nanoparticles: magnetic nanoplatforms as drug carriers," *International journal of nanomedicine*, pp. 3445–3471, 2012.

[5] A. Ali, H. Zafar, M. Zia, I. ul Haq, A. R. Phull, J. S. Ali, and A. Hussain, "Synthesis, characterization, applications, and challenges of iron oxide nanoparticles," *Nanotechnology, science and applications*, pp. 49–67, 2016.

[6] R. M. Cornell, U. Schwertmann, *et al.*, *The iron oxides: structure, properties, reactions, occurrences, and uses*, vol. 664. Wiley-vch Weinheim, 2003.

[7] P. Sangaiya and R. Jayaprakash, "A review on iron oxide nanoparticles and their biomedical applications," *Journal of Superconductivity and Novel Magnetism*, vol. 31, no. 11, pp. 3397–3413, 2018.

[8] H. Shokrollahi, "A review of the magnetic properties, synthesis methods and applications of maghemite," *Journal of Magnetism and Magnetic Materials*, vol. 426, pp. 74–81, 2017.

[9] N. A. Yousif, S. M. Al-Jawad, A. A. Taha, and H. Stamatis, "A review of structure, properties, and chemical synthesis of magnetite nanoparticles," *Journal of Applied Sciences and Nanotechnology*, vol. 3, no. 2, pp. 18–31, 2023.

[10] M. Coduri, P. Masala, L. Del Bianco, F. Spizzo, D. Ceresoli, C. Castellano, S. Cappelli, C. Oliva, S. Checchia, M. Allieta, *et al.*, "Local structure and magnetism of fe2o3 maghemite nanocrystals: The role of crystal dimension," *Nanomaterials*, vol. 10, no. 5, p. 867, 2020.

[11] A. Cervellino, R. Frison, G. Cernuto, A. Guagliardi, and N. Masciocchi, "Lattice parameters and site occupancy factors of magnetite–maghemite core–shell nanoparticles. a critical study," *Journal of Applied Crystallography*, vol. 47, no. 5, pp. 1755–1761, 2014.

[12] J. Estelrich, E. Escribano, J. Queralt, and M. A. Busquets, "Iron oxide nanoparticles for magnetically-guided and magnetically-responsive drug delivery," *International journal of molecular sciences*, vol. 16, no. 4, pp. 8070–8101, 2015.

[13] P. Vach, *Solution synthetis and actuation of magnetic nanostructures*. PhD thesis, Humboldt-Universität Berlin Berlin, 2014.

[14] F. Bødker, M. F. Hansen, C. B. Koch, K. Lefmann, and S. Mørup, "Magnetic properties of hematite nanoparticles," *Physical Review B*, vol. 61, no. 10, p. 6826, 2000.

[15] C. Bean and u. D. Livingston, "Superparamagnetism," *Journal of Applied Physics*, vol. 30, no. 4, pp. S120–S129, 1959.

[16] L. Néel, "Théorie du traînage magnétique des ferromagnétiques en grains fins avec application aux terres cuites," in *Annales de géophysique*, vol. 5, pp. 99–136, 1949.

[17] J. Li, Y. Liu, R. Cha, B. Ran, K. Mou, H. Wang, Q. Xie, J. Sun, and X. Jiang, "The biocompatibility evaluation of iron oxide nanoparticles synthesized by a one pot process for intravenous iron supply," *RSC advances*, vol. 6, no. 17, pp. 14329–14334, 2016.

[18] H. Nosrati, M. Salehiabar, M. Fridoni, M.-A. Abdollahifar, H. Kheiri Manjili, S. Davaran, and H. Danafar, "New insight about biocompatibility and biodegradability of iron oxide magnetic nanoparticles: stereological and in vivo mri monitor," *Scientific reports*, vol. 9, no. 1, p. 7173, 2019.

[19] Q. Feng, Y. Liu, J. Huang, K. Chen, J. Huang, and K. Xiao, "Uptake, distribution, clearance, and toxicity of iron oxide nanoparticles with different sizes and coatings," *Scientific reports*, vol. 8, no. 1, pp. 1–13, 2018.

[20] N. Singh, "Antioxidant metal oxide nanozymes: role in cellular redox homeostasis and therapeutics," *Pure and Applied Chemistry*, vol. 93, no. 2, pp. 187–205, 2021.

[21] D. Ling and T. Hyeon, "Chemical design of biocompatible iron oxide nanoparticles for medical applications," *Small*, vol. 9, no. 9-10, pp. 1450–1466, 2013.

[22] Y. Toropova, D. Korolev, M. Istomina, G. Shulmeyster, A. Petukhov, V. Mishanin, A. Gorshkov, E. Podyacheva, K. Gareev, A. Bagrov, *et al.*, "Controlling the movement of magnetic iron oxide nanoparticles intended for targeted delivery of cytostatics," *International Journal of Nanomedicine*, pp. 5651–5664, 2021.

[23] A. E. Deatsch and E. E. Evans, "Heating efficiency in magnetic nanoparticle hyperthermia," *Journal of Magnetism and magnetic Materials*, vol. 354, pp. 163–172, 2014.

[24] E. Múzquiz-Ramos, V. Guerrero-Chávez, B. Macías-Martínez, C. López-Badillo, and L. García-Cerda, "Synthesis and characterization of maghemite nanoparticles for hyperthermia applications," *Ceramics International*, vol. 41, no. 1, pp. 397–402, 2015.

[25] L. Li, W. Jiang, K. Luo, H. Song, F. Lan, Y. Wu, and Z. Gu, "Superparamagnetic iron oxide nanoparticles as mri contrast agents for non-invasive stem cell labeling and tracking," *Theranostics*, vol. 3, no. 8, p. 595, 2013.

[26] R. Qiao, C. Yang, and M. Gao, "Superparamagnetic iron oxide nanoparticles: from preparations to in vivo mri applications," *Journal of Materials Chemistry*, vol. 19, no. 35, pp. 6274–6293, 2009.

[27] A. Taylor, K. M. Wilson, P. Murray, D. G. Fernig, and R. Levy, "Long-term tracking of cells using inorganic nanoparticles as contrast agents: are we there yet?," *Chemical Society Reviews*, vol. 41, no. 7, pp. 2707–2717, 2012.

[28] Y. Ha and I. Kim, "Recent developments in innovative magnetic nanoparticles-based immunoassays: from improvement of conventional immunoassays to diagnosis of covid-19," *BioChip Journal*, vol. 16, no. 4, pp. 351–365, 2022.

[29] M. Pastucha, Z. Farka, K. Lacina, Z. Mikušová, and P. Skládal, "Magnetic nanoparticles for smart electrochemical immunoassays: a review on recent developments," *Microchimica Acta*, vol. 186, pp. 1–26, 2019.

[30] J. Wang, Z. Ali, N. Wang, W. Liang, H. Liu, F. Li, H. Yang, L. He, L. Nie, N. He, *et al.*, "Simultaneous extraction of dna and rna from escherichia coli bl 21 based on silica-coated magnetic nanoparticles," *Science China Chemistry*, vol. 58, pp. 1774–1778, 2015.

[31] Z. Saiyed, C. Ramchand, and S. Telang, "Isolation of genomic dna using magnetic nanoparticles as a solid-phase support," *Journal of Physics: Condensed Matter*, vol. 20, no. 20, p. 204153, 2008.

[32] C. Tang, Z. He, H. Liu, Y. Xu, H. Huang, G. Yang, Z. Xiao, S. Li, H. Liu, Y. Deng, *et al.*, "Application of magnetic nanoparticles in nucleic acid detection," *Journal of Nanobiotechnology*, vol. 18, pp. 1–19, 2020.

[33] N. Ferroudj, J. Nzimoto, A. Davidson, D. Talbot, E. Briot, V. Dupuis, A. Bee, M. S. Medjram, and S. Abramson, "4. maghemite nanoparticles and maghemite/silica nanocomposite microspheres as magnetic fenton catalysts for the removal of water pollutants," *Applied Catalysis B-environmental*, 2013.

[34] R. Bushra, M. Ahmad, K. Alam, F. Seidi, S. Shakeel, J. Song, Y. Jin, H. Xiao, *et al.*, "Recent advances in magnetic nanoparticles: Key applications, environmental insights, and future strategies," *Sustainable Materials and Technologies*, p. e00985, 2024.

[35] J. Hu, G. Chen, and I. M. Lo, "Selective removal of heavy metals from industrial wastewater using maghemite nanoparticle: performance and mechanisms," *Journal of environmental engineering*, vol. 132, no. 7, pp. 709–715, 2006.

[36] A. Nematollahzadeh, S. Seraj, and B. Mirzayi, "Catecholamine coated maghemite nanoparticles for the environmental remediation: Hexavalent chromium ions removal," *Chemical Engineering Journal*, vol. 277, pp. 21–29, 2015.

[37] A. Rehman, A. Naeem, I. Ahmad, F. Fozia, M. H. Almutairi, M. Aslam, M. Israr, B. O. Almutairi, and Z. Ullah, "Synthesis of plant-mediated iron oxide nanoparticles and optimization of chemically modified activated carbon adsorbents for removal of as, pb, and cd ions from wastewater," *ACS omega*, vol. 9, no. 1, pp. 317–329, 2023.

[38] A. Jawed, A. K. Golder, and L. M. Pandey, "Bio-based iron oxide nanoparticles forming bi-functional chitosan composite adsorbent for cr (vi) decontamination," *Chemical Engineering Journal*, vol. 481, p. 148411, 2024.

[39] D. Wang, B. Zhu, X. He, Z. Zhu, G. Hutchins, P. Xu, and W.-N. Wang, "Iron oxide nanowire-based filter for inactivation of airborne bacteria," *Environmental Science: Nano*, vol. 5, no. 5, pp. 1096–1106, 2018.

[40] J. Kim, S. Chan Hong, G. N. Bae, and J. H. Jung, "Electrospun magnetic nanoparticle-decorated nanofiber filter and its applications to high-efficiency air filtration," *Environmental Science & Technology*, vol. 51, no. 20, pp. 11967–11975, 2017.

[41] Y. Zou, X. Wang, A. Khan, P. Wang, Y. Liu, A. Alsaedi, T. Hayat, and X. Wang, "Environmental remediation and application of nanoscale zero-valent iron and its composites for the removal of heavy metal ions: a review," *Environmental science & technology*, vol. 50, no. 14, pp. 7290–7304, 2016.

[42] L. Xiang, J. D. Harindintwali, F. Wang, M. Redmile-Gordon, S. X. Chang, Y. Fu, C. He, B. Muhoza, F. Brahushi, N. Bolan, *et al.*, "Integrating biochar, bacteria, and plants for sustainable remediation of soils contaminated with organic pollutants," *Environmental Science & Technology*, vol. 56, no. 23, pp. 16546–16566, 2022.

[43] A. Karthick, B. Roy, and P. Chattopadhyay, "Comparison of zero-valent iron and iron oxide nanoparticle stabilized alkyl polyglucoside phosphate foams for remediation of diesel-contaminated soils," *Journal of environmental management*, vol. 240, pp. 93–107, 2019.

[44] M. Li, P. Zhang, M. Adeel, Z. Guo, A. J. Chetwynd, C. Ma, T. Bai, Y. Hao, and Y. Rui, "Physiological impacts of zero valent iron, fe3o4 and fe2o3 nanoparticles in rice plants and their potential as fe fertilizers," *Environmental Pollution*, vol. 269, p. 116134, 2021.

[45] M. Imran, A. R. Ansari, A. H. Shaik, S. Hussain, A. Khan, M. R. Chandan, *et al.*, "Ferrofluid synthesis using oleic acid coated fe3o4 nanoparticles dispersed in mineral oil for heat transfer applications," *Materials Research Express*, vol. 5, no. 3, p. 036108, 2018.

[46] O. Oehlsen, S. I. Cervantes-Ramírez, P. Cervantes-Avilés, and I. A. Medina-Velo, "Approaches on ferrofluid synthesis and applications: current status and future perspectives," *ACS omega*, vol. 7, no. 4, pp. 3134–3150, 2022.

[47] K. K. Kefeni, T. A. Msagati, and B. B. Mamba, "Ferrite nanoparticles: synthesis, characterisation and applications in electronic device," *Materials Science and Engineering: B*, vol. 215, pp. 37–55, 2017.

[48] W. Wu, Z. Wu, T. Yu, C. Jiang, and W.-S. Kim, "Recent progress on magnetic iron oxide nanoparticles: synthesis, surface functional strategies and biomedical applications," *Science and technology of advanced materials*, vol. 16, no. 2, p. 023501, 2015.

[49] A. Demortiere, P. Panissod, B. Pichon, G. Pourroy, D. Guillon, B. Donnio, and S. Bégin-Colin, "Size-dependent properties of magnetic iron oxide nanocrystals," *Nanoscale*, vol. 3, no. 1, pp. 225–232, 2011.

[50] S. Meftah, A.-T. Ngo, L. Bouteiller, V. Russier, D. Hrabovsky, A. Konaté, D. Kondo, F. Bedoui, and I. Lisiecki, "Synthesis and magnetic properties of spherical maghemite nanoparticles with tunable size and surface chemistry," *Langmuir*, 2024.

[51] M. D. Nguyen, L. Deng, J. M. Lee, K. M. Resendez, M. Fuller, S. Hoijang, F. Robles-Hernandez, C.-W. Chu, D. Litvinov, V. G. Hadjiev, *et al.*, "Magnetic tunability via control of crystallinity and size in polycrystalline iron oxide nanoparticles," *Small*, vol. 20, no. 43, p. 2402940, 2024.

[52] L. Maldonado-Camargo, M. Unni, and C. Rinaldi, "Magnetic characterization of iron oxide nanoparticles for biomedical applications," *Biomedical Nanotechnology: Methods and Protocols*, pp. 47–71, 2017.

[53] Q. Li, C. W. Kartikowati, S. Horie, T. Ogi, T. Iwaki, and K. Okuyama, "Correlation between particle size/domain structure and magnetic properties of highly crystalline fe3o4 nanoparticles," *Scientific reports*, vol. 7, no. 1, p. 9894, 2017.

[54] B. Issa, I. M. Obaidat, B. A. Albiss, and Y. Haik, "Magnetic nanoparticles: surface effects and properties related to biomedicine applications," *International journal of molecular sciences*, vol. 14, no. 11, pp. 21266–21305, 2013.

[55] Z. Shaterabadi, G. Nabiyouni, G. F. Goya, and M. Soleymani, "The effect of the magnetically dead layer on the magnetization and the magnetic anisotropy of the dextran-coated magnetite nanoparticles," *Applied Physics A*, vol. 128, no. 8, p. 631, 2022.

[56] R. Kaiser and G. Miskolczy, "Magnetic properties of stable dispersions of subdomain magnetite particles," *Journal of Applied Physics*, vol. 41, no. 3, pp. 1064–1072, 1970.

[57] P. Guardia, B. Batlle-Brugal, A. Roca, O. Iglesias, M. Morales, C. Serna, A. Labarta, and X. Batlle, "Surfactant effects in magnetite nanoparticles of controlled size," *Journal of Magnetism and Magnetic Materials*, vol. 316, no. 2, pp. e756–e759, 2007.

[58] D. K. Nagesha, B. D. Plouffe, M. Phan, L. H. Lewis, S. Sridhar, and S. K. Murthy, "Functionalization-induced improvement in magnetic properties of fe3o4 nanoparticles for biomedical applications," *Journal of Applied Physics*, vol. 105, no. 7, 2009.

[59] A. G. Roca, L. Gutiérrez, H. Gavilán, M. E. F. Brollo, S. Veintemillas-Verdaguer, and M. del Puerto Morales, "Design strategies for shape-controlled magnetic iron oxide nanoparticles," *Advanced drug delivery reviews*, vol. 138, pp. 68–104, 2019.

[60] P. Hugounenq, M. Levy, D. Alloyeau, L. Lartigue, E. Dubois, V. Cabuil, C. Ricolleau, S. Roux, C. Wilhelm, F. Gazeau, *et al.*, "Iron oxide monocrystalline nanoflowers for highly efficient magnetic hyperthermia," *The Journal of Physical Chemistry C*, vol. 116, no. 29, pp. 15702–15712, 2012.

[61] B. Freis, M. D. L. A. Ramirez, C. Kiefer, S. Harlepp, C. Iacovita, C. Henoumont, C. Affolter-Zbaraszczuk, F. Meyer, D. Mertz, A. Boos, *et al.*, "Effect of the size and shape of dendronized iron oxide nanoparticles bearing a targeting ligand on mri, magnetic hyperthermia, and photothermia properties—from suspension to in vitro studies," *Pharmaceutics*, vol. 15, no. 4, p. 1104, 2023.

[62] D. Lisjak and A. Mertelj, "Anisotropic magnetic nanoparticles: A review of their properties, syntheses and potential applications," *Progress in Materials Science*, vol. 95, pp. 286–328, 2018.

[63] W. Karim, A. Kleibert, U. Hartfelder, A. Balan, J. Gobrecht, J. A. van Bokhoven, and Y. Ekinci, "Size-dependent redox behavior of iron observed by in-situ single nanoparticle spectro-microscopy on well-defined model systems," *Scientific reports*, vol. 6, no. 1, p. 18818, 2016.

[64] M. Elmaalouf, M. Odziomek, S. Duran, M. Gayrard, M. Bahri, C. Tard, A. Zitolo, B. Lassalle-Kaiser, J.-Y. Piquemal, O. Ersen, *et al.*, "The origin of the high electrochemical activity of pseudo-amorphous iridium oxides," *Nature communications*, vol. 12, no. 1, p. 3935, 2021.

[65] M. D. Shultz, J. U. Reveles, S. N. Khanna, and E. E. Carpenter, "Reactive nature of dopamine as a surface functionalization agent in iron oxide nanoparticles," *Journal of the American Chemical Society*, vol. 129, no. 9, pp. 2482–2487, 2007.

[66] D. Zhou, Y. Zhou, Y. Li, and W. Shen, "Nanostructured iron oxides for heterogeneous catalysis," *EnergyChem*, p. 100124, 2024.

[67] V. Amendola, M. Meneghetti, G. Granozzi, S. Agnoli, S. Polizzi, P. Riello, A. Boscaini, C. Anselmi, G. Fracasso, M. Colombatti, *et al.*, "Top-down synthesis of multifunctional iron oxide nanoparticles for macrophage labelling and manipulation," *Journal of Materials Chemistry*, vol. 21, no. 11, pp. 3803–3813, 2011.

[68] L. Almásy, D. Creanga, C. Nadejde, L. Rosta, E. Pomjakushina, and M. Ursache-Oprisan, "Wet milling versus co-precipitation in magnetite ferrofluid preparation," *Journal of the Serbian Chemical Society*, vol. 80, no. 3, pp. 367–376, 2015.

[69] J. E. Ogbezode, U. S. Ezealigo, A. Bello, V. C. Anye, and A. P. Onwualu, "A narrative review of the synthesis, characterization, and applications of iron oxide nanoparticles," *Discover Nano*, vol. 18, no. 1, p. 125, 2023.

[70] R. Atchudan, T. N. J. I. Edison, S. Perumal, D. RanjithKumar, and Y. R. Lee, "Direct growth of iron oxide nanoparticles filled multi-walled carbon nanotube via chemical vapour deposition method as high-performance supercapacitors," *International Journal of Hydrogen Energy*, vol. 44, no. 4, pp. 2349–2360, 2019.

[71] V. K. LaMer and R. H. Dinegar, "Theory, production and mechanism of formation of monodispersed hydrosols," *Journal of the american chemical society*, vol. 72, no. 11, pp. 4847–4854, 1950.

[72] R. Becker and W. Döring, "Kinetische behandlung der keimbildung in übersättigten dämpfen," *Annalen der physik*, vol. 416, no. 8, pp. 719–752, 1935.

[73] J. W. Gibbs *et al.*, *On the equilibrium of heterogeneous substances*. The Academy New Haven, 1874.

[74] C. B. Whitehead, S. Özkar, and R. G. Finke, "Lamer's 1950 model of particle formation: a review and critical analysis of its classical nucleation and fluctuation theory basis, of competing models and mechanisms for phase-changes and particle formation, and then of its application to silver halide, semiconductor, metal, and metal-oxide nanoparticles," *Materials Advances*, vol. 2, no. 1, pp. 186–235, 2021.

[75] J. Park, J. Joo, S. G. Kwon, Y. Jang, and T. Hyeon, "Synthesis of monodisperse spherical nanocrystals," *Angewandte Chemie International Edition*, vol. 46, no. 25, pp. 4630–4660, 2007.

[76] P. Bhavani, C. Rajababu, M. Arif, I. V. S. Reddy, and N. R. Reddy, "Synthesis and characterization of iron oxide nanoparticles prepared hydrothermally at different reaction temperatures and ph," *International Journal of Materials Research*, vol. 107, no. 10, pp. 942–947, 2016.

[77] M. Tai, C. W. Lai, S. B. A. Hamid, D. D. Suppiah, K. Lau, W. Yehya, N. Julkapli, W. Lee, and Y. Lim, "Facile synthesis of magnetite iron oxide nanoparticles via precipitation method at different reaction temperatures," *Materials Research Innovations*, vol. 18, no. sup6, pp. S6–470, 2014.

[78] M. Tajabadi and M. Khosroshahi, "Effect of alkaline media concentration and modification of temperature on magnetite synthesis method using feso4/nh4oh," *International Journal of Chemical Engineering and Applications*, vol. 3, no. 3, p. 206, 2012.

[79] N. H. AbuTalib, A. P. LaGrow, M. O. Besenhard, O. Bondarchuk, A. Sergides, S. Famiani, L. P. Ferreira, M. M. Cruz, A. Gavriilidis, and N. T. K. Thanh, "Shape controlled iron oxide nanoparticles: inducing branching and controlling particle crystallinity," *CrystEngComm*, vol. 23, no. 3, pp. 550–561, 2021.

[80] P. K. Narnaware and C. Ravikumar, "Influence of solvents, reaction temperature, and aging time on the morphology of iron oxide nanoparticles," *Inorganic and Nano-Metal Chemistry*, vol. 52, no. 7, pp. 922–936, 2022.

[81] Z. Li, C. Chanéac, G. Berger, S. Delaunay, A. Graff, and G. Lefèvre, "Mechanism and kinetics of magnetite oxidation under hydrothermal conditions," *RSC advances*, vol. 9, no. 58, pp. 33633–33642, 2019.

[82] E. Demangeat, M. Pédrot, A. Dia, M. Bouhnik-le Coz, F. Grasset, K. Hanna, M. Kamagate, and F. Cabello-Hurtado, "Colloidal and chemical stabilities of iron oxide nanoparticles in aqueous solutions: the interplay of structural, chemical and environmental drivers," *Environmental Science: Nano*, vol. 5, no. 4, pp. 992–1001, 2018.

[83] G. Wulff, "Xxv. zur frage der geschwindigkeit des wachsthums und der auflösung der krystallflächen," *Zeitschrift für Kristallographie-Crystalline Materials*, vol. 34, no. 1-6, pp. 449–530, 1901.

[84] Z. Zhou, X. Zhu, D. Wu, Q. Chen, D. Huang, C. Sun, J. Xin, K. Ni, and J. Gao, "Anisotropic shaped iron oxide nanostructures: controlled synthesis and proton relaxation shortening effects," *Chemistry of Materials*, vol. 27, no. 9, pp. 3505–3515, 2015.

[85] M. V. Kovalenko, M. I. Bodnarchuk, R. T. Lechner, G. Hesser, F. Schäffler, and W. Heiss, "Fatty acid salts as stabilizers in size-and shape-controlled nanocrystal synthesis: the case of inverse spinel iron oxide," *Journal of the American Chemical Society*, vol. 129, no. 20, pp. 6352–6353, 2007.

[86] Y. Yin and A. P. Alivisatos, "Colloidal nanocrystal synthesis and the organic–inorganic interface," *Nature*, vol. 437, no. 7059, pp. 664–670, 2005.

[87] A. Radi, D. Pradhan, Y. Sohn, and K. Leung, "Nanoscale shape and size control of cubic, cuboctahedral, and octahedral cu- cu2o core- shell nanoparticles on si (100)

by one-step, templateless, capping-agent-free electrodeposition," *ACS nano*, vol. 4, no. 3, pp. 1553–1560, 2010.

[88] H. Yang, T. Ogawa, D. Hasegawa, and M. Takahashi, "Synthesis and magnetic properties of monodisperse magnetite nanocubes," *Journal of Applied Physics*, vol. 103, no. 7, 2008.

[89] Y. Wang and H. Yang, "Synthesis of iron oxide nanorods and nanocubes in an imidazolium ionic liquid," *Chemical Engineering Journal*, vol. 147, no. 1, pp. 71–78, 2009.

[90] D. Bonvin, D. T. Alexander, A. Millán, R. Piñol, B. Sanz, G. F. Goya, A. Martínez, J. A. Bastiaansen, M. Stuber, K. J. Schenk, *et al.*, "Tuning properties of iron oxide nanoparticles in aqueous synthesis without ligands to improve mri relaxivity and sar," *Nanomaterials*, vol. 7, no. 8, p. 225, 2017.

[91] R. Ding, I. M. P. Espinosa, D. Loevlie, S. Azadehranjbar, A. J. Baker, G. Mpourmpakis, A. Martini, and T. D. Jacobs, "Size-dependent shape distributions of platinum nanoparticles," *Nanoscale advances*, vol. 4, no. 18, pp. 3978–3986, 2022.

[92] L. García-Cruz, V. Montiel, and J. Solla-Gullón, "Shape-controlled metal nanoparticles for electrocatalytic applications," *Physical Sciences Reviews*, vol. 4, no. 1, p. 20170124, 2019.

[93] P. W. Voorhees, "The theory of ostwald ripening," *Journal of Statistical Physics*, vol. 38, pp. 231–252, 1985.

[94] J. G. Ovejero, M. d. P. Morales, and S. Veintemillas-Verdaguer, "Inductive heating enhances ripening in the aqueous synthesis of magnetic nanoparticles," *Crystal Growth & Design*, vol. 23, no. 1, pp. 59–67, 2022.

[95] S. Laurent, D. Forge, M. Port, A. Roch, C. Robic, L. Vander Elst, and R. N. Muller, "Magnetic iron oxide nanoparticles: synthesis, stabilization, vectorization, physicochemical characterizations, and biological applications," *Chemical reviews*, vol. 108, no. 6, pp. 2064–2110, 2008.

[96] M. A. Cândido, N. C. V. Rost, V. R. Ferreira, and L. Raniero, "Síntese de nanopartículas de óxido de ferro estabilizadas com citrato de sódio e tmaoh," *Research, Society and Development*, vol. 11, no. 16, pp. e139111637698–e139111637698, 2022.

[97] J. Park, K. An, Y. Hwang, J.-G. Park, H.-J. Noh, J.-Y. Kim, J.-H. Park, N.-M. Hwang, and T. Hyeon, "Ultra-large-scale syntheses of monodisperse nanocrystals," *Nature materials*, vol. 3, no. 12, pp. 891–895, 2004.

[98] A. Bakandritsos, G. C. Psarras, and N. Boukos, "Some physicochemical aspects of nanoparticulate magnetic iron oxide colloids in neat water and in the presence of poly (vinyl alcohol)," *Langmuir*, vol. 24, no. 20, pp. 11489–11496, 2008.

[99] R. Massart, "Preparation of aqueous magnetic liquids in alkaline and acidic media," *IEEE transactions on magnetics*, vol. 17, no. 2, pp. 1247–1248, 1981.

[100] L. Li, K. Mak, C. W. Leung, K. Chan, W. Chan, W. Zhong, and P. Pong, "Effect of synthesis conditions on the properties of citric-acid coated iron oxide nanoparticles," *Microelectronic Engineering*, vol. 110, pp. 329–334, 2013.

[101] A. Bee, R. Massart, and S. Neveu, "Synthesis of very fine maghemite particles," *Journal of Magnetism and Magnetic Materials*, vol. 149, no. 1-2, pp. 6–9, 1995.

[102] C. Solans, P. Izquierdo, J. Nolla, N. Azemar, and M. J. Garcia-Celma, "Nano-emulsions," *Current opinion in colloid & interface science*, vol. 10, no. 3-4, pp. 102–110, 2005.

[103] J. Vidal-Vidal, J. Rivas, and M. López-Quintela, "Synthesis of monodisperse maghemite nanoparticles by the microemulsion method," *Colloids and Surfaces A: Physicochemical and Engineering Aspects*, vol. 288, no. 1-3, pp. 44–51, 2006.

[104] M. Pileni, "Reverse micelles as microreactors," *The Journal of physical chemistry*, vol. 97, no. 27, pp. 6961–6973, 1993.

[105] A. B. Chin and I. I. Yaacob, "Synthesis and characterization of magnetic iron oxide nanoparticles via w/o microemulsion and massart's procedure," *Journal of materials processing technology*, vol. 191, no. 1-3, pp. 235–237, 2007.

[106] W. Wu, Q. He, and C. Jiang, "Magnetic iron oxide nanoparticles: synthesis and surface functionalization strategies," *Nanoscale research letters*, vol. 3, pp. 397–415, 2008.

[107] M. Klotz, A. Ayral, C. Guizard, C. Ménager, and V. Cabuil, "Silica coating on colloidal maghemite particles," *Journal of colloid and interface science*, vol. 220, no. 2, pp. 357–361, 1999.

[108] Y. Lu, Y. Yin, B. T. Mayers, and Y. Xia, "Modifying the surface properties of superparamagnetic iron oxide nanoparticles through a sol- gel approach," *Nano letters*, vol. 2, no. 3, pp. 183–186, 2002.

[109] K. Kojima, M. Miyazaki, F. Mizukami, and K. Maeda, "Selective formation of spinel iron oxide in thin films by complexing agent-assisted sol-gel processing," *Journal of Sol-Gel Science and Technology*, vol. 8, pp. 77–81, 1997.

[110] S. Akbar, S. Hasanain, N. Azmat, and M. Nadeem, "Synthesis of fe2o3 nanoparticles by new sol-gel method and their structural and magnetic characterizations," *arXiv preprint cond-mat/0408480*, 2004.

[111] K. Byrappa and M. Yoshimura, *Handbook of hydrothermal technology*. William Andrew, 2012.

[112] S. Ge, X. Shi, K. Sun, C. Li, C. Uher, J. R. Baker Jr, M. M. Banaszak Holl, and B. G. Orr, "Facile hydrothermal synthesis of iron oxide nanoparticles with tunable magnetic properties," *The Journal of Physical Chemistry C*, vol. 113, no. 31, pp. 13593–13599, 2009.

[113] W. Xie, Z. Guo, F. Gao, Q. Gao, D. Wang, B.-s. Liaw, Q. Cai, X. Sun, X. Wang, and L. Zhao, "Shape-, size-and structure-controlled synthesis and biocompatibility of iron oxide nanoparticles for magnetic theranostics," *Theranostics*, vol. 8, no. 12, p. 3284, 2018.

[114] B. Ankamwar, "Hydrothermal synthesis of rod shaped iron oxide nanoparticles," in *AIP Conference Proceedings*, vol. 2335, AIP Publishing, 2021.

[115] W. Baaziz, B. P. Pichon, S. Fleutot, Y. Liu, C. Lefevre, J.-M. Greneche, M. Toumi, T. Mhiri, and S. Begin-Colin, "Magnetic iron oxide nanoparticles: reproducible tuning of the size and nanosized-dependent composition, defects, and spin canting," *The Journal of Physical Chemistry C*, vol. 118, no. 7, pp. 3795–3810, 2014.

[116] D. B. Allison, A. W. Brown, B. J. George, and K. A. Kaiser, "Reproducibility: A tragedy of errors," *Nature*, vol. 530, no. 7588, pp. 27–29, 2016.

[117] M. Baker, "1,500 scientists lift the lid on reproducibility," *Nature*, vol. 533, no. 7604, 2016.

[118] D. B. Williams, C. B. Carter, D. B. Williams, and C. B. Carter, *The transmission electron microscope*. Springer, 1996.

[119] B. E. Warren, *X-ray Diffraction*. Courier Corporation, 1990.

[120] G. Jauncey, "The scattering of x-rays and bragg's law," *Proceedings of the national academy of sciences*, vol. 10, no. 2, pp. 57–60, 1924.

[121] W. Kim, C.-Y. Suh, S.-W. Cho, K.-M. Roh, H. Kwon, K. Song, and I.-J. Shon, "A new method for the identification and quantification of magnetite–maghemite mixture using conventional x-ray diffraction technique," *Talanta*, vol. 94, pp. 348–352, 2012.

[122] Y.-Y. Huang, H.-L. Chen, and T. Hashimoto, "Face-centered cubic lattice of spherical micelles in block copolymer/homopolymer blends," *Macromolecules*, vol. 36, no. 3, pp. 764–770, 2003.

[123] J. A. Njuguna, F. Silva, and S. Sachse, "Nanocomposites for vehicle structural applications," 2011.

[124] J. Baur and E. Silverman, "Challenges and opportunities in multifunctional nanocomposite structures for aerospace applications," *MRS bulletin*, vol. 32, no. 4, pp. 328–334, 2007.

[125] E. C. Demir, M. T. McDermott, C. l. Kim, and C. Ayranci, "Towards better understanding the stiffness of nanocomposites via parametric study of an analytical model modeling parameters and experiments," *Journal of Composite Materials*, vol. 57, no. 6, pp. 1087–1104, 2023.

[126] K. I. Winey and R. A. Vaia, "Polymer nanocomposites," *MRS bulletin*, vol. 32, no. 4, pp. 314–322, 2007.

[127] Z. Tang, F. Fan, Z. Chu, C. Fan, and Y. Qin, "Barrier properties and characterizations of poly (lactic acid)/zno nanocomposites," *Molecules*, vol. 25, no. 6, p. 1310, 2020.

[128] S. Stoyanova, E. Ivanov, L. R. Hegde, A. Georgopoulou, F. Clemens, F. Bedoui, and R. Kotsilkova, "Pvdf hybrid nanocomposites with graphene and carbon nanotubes and their thermoresistive and joule heating properties," *Nanomaterials*, vol. 14, no. 11, p. 901, 2024.

[129] P. Wang, T. Song, H. M. Abo-Dief, J. Song, A. K. Alanazi, B. Fan, M. Huang, Z. Lin, A. A. Altalhi, S. Gao, *et al.*, "Effect of carbon nanotubes on the interface evolution and dielectric properties of polylactic acid/ethylene–vinyl acetate copolymer nanocomposites," *Advanced Composites and Hybrid Materials*, vol. 5, no. 2, pp. 1100–1110, 2022.

[130] M. Farea, A. Abdelghany, and A. Oraby, "Optical and dielectric characteristics of polyethylene oxide/sodium alginate-modified gold nanocomposites," *RSC advances*, vol. 10, no. 62, pp. 37621–37630, 2020.

[131] M. Sahihi, A. Jaramillo-Botero, W. A. Goddard III, and F. Bedoui, "Interfacial interactions in a model composite material: Insights into $\alpha \rightarrow \beta$ phase transition of the magnetite reinforced poly (vinylidene fluoride) systems by all-atom molecular dynamics simulation," *The Journal of Physical Chemistry C*, vol. 125, no. 39, pp. 21635–21644, 2021.

[132] E. Alonso-Redondo, L. Belliard, K. Rolle, B. Graczykowski, W. Tremel, B. Djafari-Rouhani, and G. Fytas, "Robustness of elastic properties in polymer nanocomposite films examined over the full volume fraction range," *Scientific reports*, vol. 8, no. 1, p. 16986, 2018.

[133] A. Jabbarzadeh and B. Halfina, "Unravelling the effects of size, volume fraction and shape of nanoparticle additives on crystallization of nanocomposite polymers," *Nanoscale Advances*, vol. 1, no. 12, pp. 4704–4721, 2019.

[134] D. B. Subbappa, K. B. Kancherla, B. Raju, and D. R. Mahapatra, "Enhancing toughness and thermal stability using ysz nanoparticle in glass fabric composites," *Applied Composite Materials*, pp. 1–27, 2025.

[135] M. M. Ibrahim, N. El-Tayeb, M. Shazly, and M. El-Sayed Seleman, "An experimental study on the effect of graphite microparticles on the mechanical and tribological properties of epoxy matrix composites," *Functional Composite Materials*, vol. 5, no. 1, p. 2, 2024.

[136] M. A. Ashraf, W. Peng, Y. Zare, and K. Y. Rhee, "Effects of size and aggregation/agglomeration of nanoparticles on the interfacial/interphase properties and tensile strength of polymer nanocomposites," *Nanoscale research letters*, vol. 13, pp. 1–7, 2018.

[137] Y. Zare, "Study of nanoparticles aggregation/agglomeration in polymer particulate nanocomposites by mechanical properties," *Composites Part A: Applied Science and Manufacturing*, vol. 84, pp. 158–164, 2016.

[138] K. A. A. Halim, J. E. Kennedy, M. A. A. M. Salleh, A. F. Osman, M. F. Omar, and N. Sunar, "Micromechanical modeling of polyamide 11 nanocomposites properties using composite theories," *Archives of Metallurgy and Materials*, vol. 68, 2023.

[139] Y. Zare, "Development of halpin-tsai model for polymer nanocomposites assuming interphase properties and nanofiller size," *Polymer Testing*, vol. 51, pp. 69–73, 2016.

[140] N. KORDANI, A. S. VANINI, and v. p. y. ADIBIPOUR, REZVAN journal=Journal of Theoretical and Applied Mechanics, "New theory to predict the elastic modulus of carbon nanotube based-composites,"

[141] F. Jabbari, A. Rajabpour, and S. Saedodin, "Thermal conductivity and viscosity of nanofluids: A review of recent molecular dynamics studies," *Chemical Engineering Science*, vol. 174, pp. 67–81, 2017.

[142] R. K. Verma, S. Kesarwani, J. Xu, and J. P. Davim, *Polymer nanocomposites: Fabrication to applications*. CRC Press, 2023.

[143] F. H. Likhi, M. Singh, H. R. Potdukhe, P. M. Ajayan, M. M. Rahman, and A. Karim, "Tuning dielectric properties with nanofiller dimensionality in polymer nanocomposites," *ACS Applied Materials & Interfaces*, vol. 16, no. 42, pp. 57253–57267, 2024.

[144] J. Kim, S. K. Mohanty, and H. D. Yoo, "Modeling ionic intercalation and solid-state diffusion using typical descriptors of batteries," *Journal of Applied Electrochemistry*, vol. 51, pp. 703–713, 2021.

[145] R. Hong and Q. Chen, "Dispersion of inorganic nanoparticles in polymer matrices: challenges and solutions," *Organic-Inorganic Hybrid Nanomaterials*, pp. 1–38, 2015.

[146] F. S. N. Oliva, M. Sahihi, L. Lenglet, A. Ospina, E. Guenin, A. Jaramillo-Botero, W. A. Goddard III, and F. Bedoui, "Nanoparticle size and surface chemistry effects on mechanical and physical properties of nano-reinforced polymers: The case of pvdf-fe3o4 nano-composites," *Polymer Testing*, vol. 117, p. 107851, 2023.

[147] D. G. Papageorgiou, Z. Li, M. Liu, I. A. Kinloch, and R. J. Young, "Mechanisms of mechanical reinforcement by graphene and carbon nanotubes in polymer nanocomposites," *Nanoscale*, vol. 12, no. 4, pp. 2228–2267, 2020.

[148] W. Xu, Q. Duan, H. Ma, W. Chen, and H. Chen, "Interfacial effect on physical properties of composite media: Interfacial volume fraction with non-spherical hard-core-soft-shell-structured particles," *Scientific reports*, vol. 5, no. 1, p. 16003, 2015.

[149] W. Wang, *The Reinforcement of Nanocomposites by Boron Nitride Nanosheets and Nanotubes*. The University of Manchester (United Kingdom), 2021.

[150] D. Ciprari, K. Jacob, and R. Tannenbaum, "Characterization of polymer nanocomposite interphase and its impact on mechanical properties," *Macromolecules*, vol. 39, no. 19, pp. 6565–6573, 2006.

[151] J. Huang, J. Zhou, and M. Liu, "Interphase in polymer nanocomposites," *JACS Au*, vol. 2, no. 2, pp. 280–291, 2022.

[152] K. Randazzo, M. Bartkiewicz, B. Graczykowski, D. Cangialosi, G. Fytas, B. Zuo, and R. D. Priestley, "Direct visualization and characterization of interfacially adsorbed polymer atop nanoparticles and within nanocomposites," *Macromolecules*, vol. 54, no. 21, pp. 10224–10234, 2021.

[153] H. Zhang, Z. Zhang, K. Friedrich, and C. Eger, "Property improvements of in situ epoxy nanocomposites with reduced interparticle distance at high nanosilica content," *Acta materialia*, vol. 54, no. 7, pp. 1833–1842, 2006.

[154] C. Durning, B. O'shaughness, U. Sawhney, D. Nguyen, J. Majewski, and G. Smith, "Adsorption of poly (methyl methacrylate) melts on quartz," *Macromolecules*, vol. 32, no. 20, pp. 6772–6781, 1999.

[155] C. Housmans, M. Sferrazza, and S. Napolitano, "Kinetics of irreversible chain adsorption," *Macromolecules*, vol. 47, no. 10, pp. 3390–3393, 2014.

[156] Y. Fujii, Z. Yang, J. Leach, H. Atarashi, K. Tanaka, and O. K. Tsui, "Affinity of polystyrene films to hydrogen-passivated silicon and its relevance to the t g of the films," *Macromolecules*, vol. 42, no. 19, pp. 7418–7422, 2009.

[157] N. Jiang, J. Shang, X. Di, M. K. Endoh, and T. Koga, "Formation mechanism of high-density, flattened polymer nanolayers adsorbed on planar solids," *Macromolecules*, vol. 47, no. 8, pp. 2682–2689, 2014.

[158] P. Gin, N. Jiang, C. Liang, T. Taniguchi, B. Akgun, S. K. Satija, M. K. Endoh, and T. Koga, "Revealed architectures of adsorbed polymer chains at solid-polymer melt interfaces," *Physical review letters*, vol. 109, no. 26, p. 265501, 2012.

[159] S. Cheng, A. P. Holt, H. Wang, F. Fan, V. Bocharova, H. Martin, T. Etampawala, B. T. White, T. Saito, N.-G. Kang, *et al.*, "Unexpected molecular weight effect in polymer nanocomposites," *Physical review letters*, vol. 116, no. 3, p. 038302, 2016.

[160] B. Zuo, H. Zhou, M. J. Davis, X. Wang, and R. D. Priestley, "Effect of local chain conformation in adsorbed nanolayers on confined polymer molecular mobility," *Physical review letters*, vol. 122, no. 21, p. 217801, 2019.

[161] S. Aoyama, Y. T. Park, C. W. Macosko, T. Ougizawa, and G. Haugstad, "Afm probing of polymer/nanofiller interfacial adhesion and its correlation with bulk mechanical

properties in a poly (ethylene terephthalate) nanocomposite," *Langmuir*, vol. 30, no. 43, pp. 12950–12959, 2014.

[162] S. Cheng, B. Carroll, V. Bocharova, J.-M. Carrillo, B. G. Sumpter, and A. P. Sokolov, "Focus: Structure and dynamics of the interfacial layer in polymer nanocomposites with attractive interactions," *The Journal of chemical physics*, vol. 146, no. 20, 2017.

[163] Y. Zare and K. Y. Rhee, "An innovative model for conductivity of graphene-based system by networked nano-sheets, interphase and tunneling zone," *Scientific Reports*, vol. 12, no. 1, p. 15179, 2022.

[164] M. Mazaheri, J. Payandehpeyman, and S. Jamasb, "Modeling of effective electrical conductivity and percolation behavior in conductive-polymer nanocomposites reinforced with spherical carbon black," *Applied Composite Materials*, pp. 1–16, 2022.

[165] V. M. Evora and A. Shukla, "Fabrication, characterization, and dynamic behavior of polyester/tio2 nanocomposites," *Materials Science and Engineering: A*, vol. 361, no. 1-2, pp. 358–366, 2003.

[166] J. Liu, Y. Gao, D. Cao, L. Zhang, and Z. Guo, "Nanoparticle dispersion and aggregation in polymer nanocomposites: insights from molecular dynamics simulation," *Langmuir*, vol. 27, no. 12, pp. 7926–7933, 2011.

[167] J. E. Seppala, *The rheology and thermodynamics of polymer nanocomposites*, vol. 72. 2010.

[168] M. Rong, M. Zhang, and W. Ruan, "Surface modification of nanoscale fillers for improving properties of polymer nanocomposites: a review," *Materials science and technology*, vol. 22, no. 7, pp. 787–796, 2006.

[169] V. Díaz-Mena, X. F. Sánchez-Romate, M. Sánchez, and A. Ureña, "Effect of sonication batch on electrical properties of graphitic-based pvdf-hfp strain sensors for use in health monitoring," *Sensors*, vol. 24, no. 6, p. 2007, 2024.

[170] K. Yang, Z. Yi, Q. Jing, R. Yue, W. Jiang, and D. Lin, "Sonication-assisted dispersion of carbon nanotubes in aqueous solutions of the anionic surfactant sdbs: The role of sonication energy," *Chinese science bulletin*, vol. 58, pp. 2082–2090, 2013.

[171] S. K. Kumar, N. Jouault, B. Benicewicz, and T. Neely, "Nanocomposites with polymer grafted nanoparticles," *Macromolecules*, vol. 46, no. 9, pp. 3199–3214, 2013.

[172] C. Chevigny, F. Dalmas, E. Di Cola, D. Gigmes, D. Bertin, F. Boué, and J. Jestin, "Polymer-grafted-nanoparticles nanocomposites: dispersion, grafted chain conformation, and rheological behavior," *Macromolecules*, vol. 44, no. 1, pp. 122–133, 2011.

[173] S. Mefath, A.-T. Ngo, D. Kondo, I. Lisiecki, and F. Bedoui, "Enhancing mechanical properties of pvdf polymers through iron oxide nanoparticle reinforcement: An investigation into materials behavior," in *The 5th International Seminar on Advanced Mechanical Technologies*, 2024.

[174] X. Zhao, L. Lv, B. Pan, W. Zhang, S. Zhang, and Q. Zhang, "Polymer-supported nanocomposites for environmental application: a review," *Chemical engineering journal*, vol. 170, no. 2-3, pp. 381–394, 2011.

[175] J. A. LaNasa, V. M. Torres, and R. J. Hickey, "In situ polymerization and polymer grafting to stabilize polymer-functionalized nanoparticles in polymer matrices," *Journal of Applied Physics*, vol. 127, no. 13, 2020.

[176] A. Kelarakis, "In situ generation of nanoparticles on and within polymeric materials," *Polymers*, vol. 16, no. 11, p. 1611, 2024.

[177] Z. A. Nurakhmetova, A. N. Azhkeyeva, I. A. Klassen, and G. S. Tatykhanova, "Synthesis and stabilization of gold nanoparticles using water-soluble synthetic and natural polymers," *Polymers*, vol. 12, no. 11, p. 2625, 2020.

[178] A. Amini, M. Rahimi, M. Nazari, C. Cheng, and B. Samali, "One-pot facile simultaneous in situ synthesis of conductive ag–polyaniline composites using keggin and preyssler-type phosphotungstates," *RSC advances*, vol. 9, no. 5, pp. 2772–2783, 2019.

[179] C. M. Hansen, *Hansen solubility parameters: a user's handbook*. CRC press, 2007.

[180] S. Bapat, S. O. Kilian, H. Wiggers, and D. Segets, "Towards a framework for evaluating and reporting hansen solubility parameters: applications to particle dispersions," *Nanoscale advances*, vol. 3, no. 15, pp. 4400–4410, 2021.

[181] S. Venkatram, C. Kim, A. Chandrasekaran, and R. Ramprasad, "Critical assessment of the hildebrand and hansen solubility parameters for polymers," *Journal of chemical information and modeling*, vol. 59, no. 10, pp. 4188–4194, 2019.

[182] A. S. Blivi, *Effet de taille dans les polymères nano-renforcés: caractérisation multi-échelles et modélisation*. PhD thesis, Université de Technologie de Compiègne, 2018.

[183] I. Henriques, L. Borges, M. Costa, B. Soares, and D. Castello, "Comparisons of complex modulus provided by different dma," *Polymer Testing*, vol. 72, pp. 394–406, 2018.

[184] T. Wang, H. Chen, W. J. Liang, B. S. L. Ng, R. Lu, J. Qi, H. Wang, J. Zhang, H. Xie, R. Xiao, *et al.*, "Layered composites for high tan delta plateau over wide temperature range," *Polymers*, vol. 16, no. 24, p. 3587, 2024.

[185] E. C. Abenojar, S. Wickramasinghe, J. Bas-Concepcion, and A. C. S. Samia, "Structural effects on the magnetic hyperthermia properties of iron oxide nanoparticles," *Progress in Natural Science: Materials International*, vol. 26, no. 5, pp. 440–448, 2016.

[186] Y.-w. Jun, Y.-M. Huh, J.-s. Choi, J.-H. Lee, H.-T. Song, S. Kim, S. Yoon, K.-S. Kim, J.-S. Shin, J.-S. Suh, *et al.*, "Nanoscale size effect of magnetic nanocrystals and their utilization for cancer diagnosis via magnetic resonance imaging," *Journal of the American Chemical Society*, vol. 127, no. 16, pp. 5732–5733, 2005.

[187] M. Morales, C. Serna, F. Bødker, and S. Mørup, "Spin canting due to structural disorder in maghemite," *Journal of Physics: Condensed Matter*, vol. 9, no. 25, p. 5461, 1997.

[188] M. d. P. Morales, S. Veintemillas-Verdaguer, M. Montero, C. Serna, A. Roig, L. Casas, B. Martinez, and F. Sandiumenge, "Surface and internal spin canting in γ-fe2o3 nanoparticles," *Chemistry of Materials*, vol. 11, no. 11, pp. 3058–3064, 1999.

[189] R. Chen, M. G. Christiansen, and P. Anikeeva, "Maximizing hysteretic losses in magnetic ferrite nanoparticles via model-driven synthesis and materials optimization," *ACS nano*, vol. 7, no. 10, pp. 8990–9000, 2013.

[190] S.-h. Noh, W. Na, J.-t. Jang, J.-H. Lee, E. J. Lee, S. H. Moon, Y. Lim, J.-S. Shin, and J. Cheon, "Nanoscale magnetism control via surface and exchange anisotropy for optimized ferrimagnetic hysteresis," *Nano letters*, vol. 12, no. 7, pp. 3716–3721, 2012.

[191] L. M. Bauer, S. F. Situ, M. A. Griswold, and A. C. S. Samia, "High-performance iron oxide nanoparticles for magnetic particle imaging–guided hyperthermia (hmpi)," *Nanoscale*, vol. 8, no. 24, pp. 12162–12169, 2016.

[192] R. R. Shah, T. P. Davis, A. L. Glover, D. E. Nikles, and C. S. Brazel, "Impact of magnetic field parameters and iron oxide nanoparticle properties on heat generation for use in magnetic hyperthermia," *Journal of magnetism and magnetic materials*, vol. 387, pp. 96–106, 2015.

[193] E. Myrovali, K. Papadopoulos, G. Charalampous, P. Kesapidou, G. Vourlias, T. Kehagias, M. Angelakeris, and U. Wiedwald, "Toward the separation of different heating mechanisms in magnetic particle hyperthermia," *ACS omega*, vol. 8, no. 14, pp. 12955–12967, 2023.

Part II

Iron Oxide Nanoparticles Synthesis

Chapter 3

Size & Surface Chemistry Control

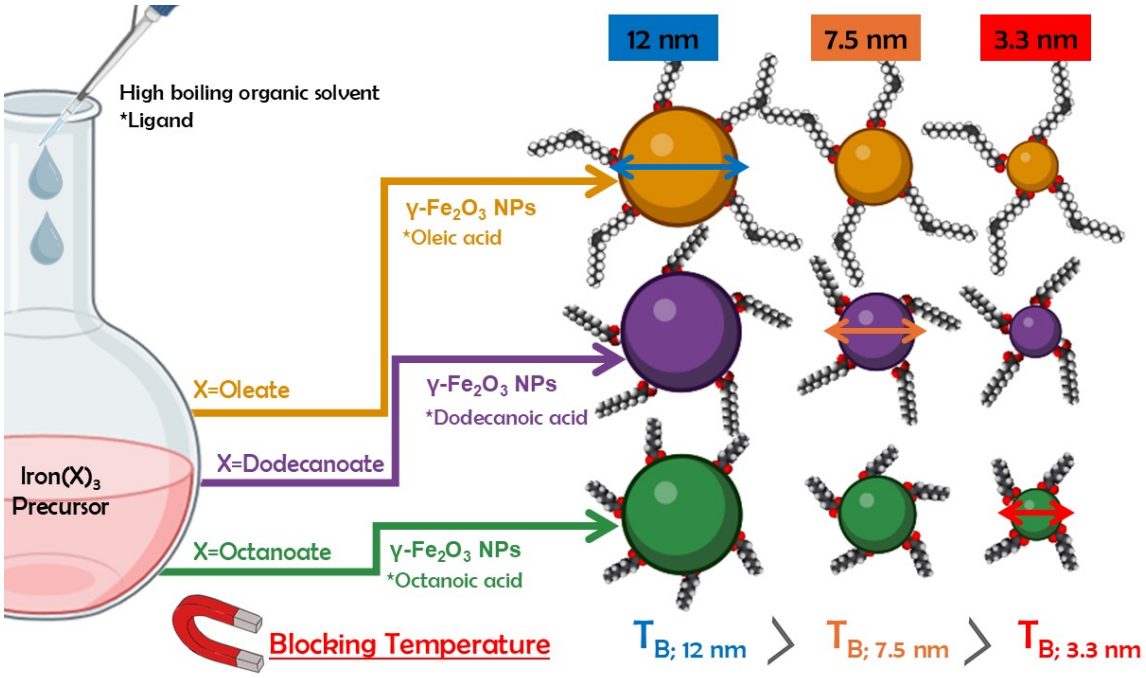

Contents

3.1 Introduction

The synthesis of maghemite nanoparticles with precise control over their size, shape, and surface chemistry remains a significant challenge. However, it offers immense potential for advancing a wide range of technological applications [1] [2] [3] [4]. As the demand for sophisticated nanomaterials continues to rise, achieving accurate control over nanoparticle properties has become increasingly critical.

Among the various chemical synthesis methods for iron oxide nanoparticles discussed in Chapter 1, Section 1.5, the thermal decomposition of carboxylate precursors stands out as particularly effective. This method is known for producing nanoparticles with low-size polydispersity. However, attaining such precise size control requires meticulous optimization of several synthesis parameters [5] [6] [7] [8] [9] [10] [11]. These include reaction conditions (such as heating rate, reaction time, and temperature), characteristics of the reagents (including precursors, surfactants, and solvents), as well as their concentrations and ratios [12] [13].

The complexity of nanoparticle synthesis arises not only from the numerous parameters involved but also from the intricate interplay between them. For instance, the ligand-to-precursor ratio significantly influences nanoparticle size. Conflicting findings in the literature add to this challenge: while some studies report that increasing this ratio leads to larger particles, others observe the opposite effect [14]. These inconsistencies reflect the multifactorial and nuanced nature of nucleation and growth processes.

As mentioned in the literature chapter, the synthesis of nanomaterials remains a field where no comprehensive theoretical framework currently exists to account for all these parameters simultaneously. Variations in a single parameter can significantly impact the role of others, further complicating the development of general rules for nanoparticle synthesis. This highlights the need for continued experimental and theoretical efforts to better understand and predict the dynamics of nanoparticle formation.

This chapter explores the synthesis parameters for maghemite nanoparticles with diameters smaller than 20 nm. This size range is chosen because nanoparticles of this size have a high surface-to-volume ratio, which notably increases the stiffness of polymers. As shown in Figure 3.1, this effect is evident when silica nanoparticles are incorporated into a PMMA matrix, where significant improvements in mechanical properties are observed for particles under 20 nm [15]. Additionally, nanoparticles in this size range exhibit superparamagnetic behavior, broadening their potential applications in diverse fields.

The surface chemistry of the maghemite nanoparticles was meticulously engineered through the application of carboxylic acids with varying alkyl chain lengths. This strategic selection of surface coatings plays a crucial role in modulating the nanoparticles' properties

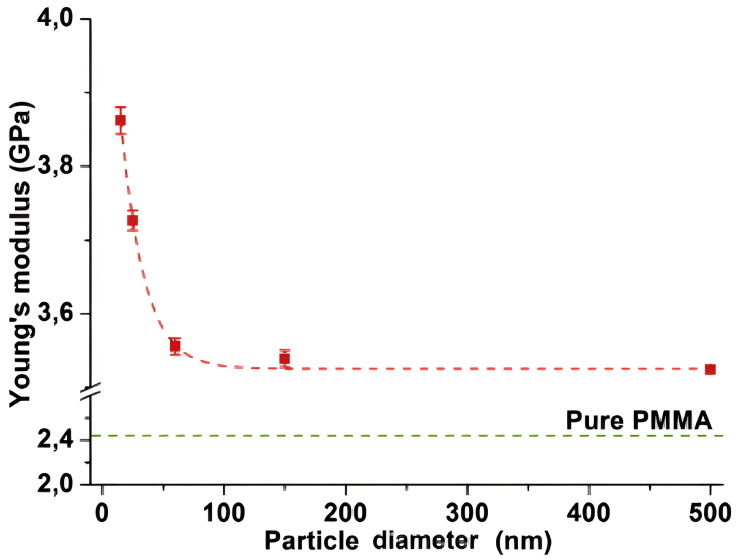

Figure 3.1 – *Young's modulus evolution as a function of silica nanoparticle diameter in PMMA nanocomposites. The graph demonstrates significant mechanical property enhancement for particles below 20 nm, with the highest Young's modulus values (approximately 3.8 GPa) achieved at the smallest particle diameters. The mechanical properties gradually decrease with increasing particle size until reaching a plateau, while remaining above the pure PMMA reference value (2.4 GPa). [15]*

and interactions with their environment. Three distinct carboxylic acids were chosen for this study:

- Oleic acid ($C_{18}H_{34}O_2$): A long-chain fatty acid with 18 carbon atoms and one double bond.
- Dodecanoic acid ($C_{12}H_{24}O_2$): Also known as lauric acid, a medium-chain saturated fatty acid with 12 carbon atoms.
- Octanoic acid ($C_8H_{16}O_2$): A short-chain saturated fatty acid, also called caprylic acid, containing 8 carbon atoms.

These carboxylic acids, depicted in Figure 3.2, represent a systematic variation in alkyl chain length, allowing for a comprehensive investigation of how ligand size influences nanoparticle characteristics.

Long-chain ligands, such as oleic acid (C18), offer enhanced steric protection, reducing aggregation and promoting uniform dispersion. However, these same long chains can hinder surface accessibility, as observed in Figure 3.3, where oleic acid prevents poly(vinylidene fluoride) (PVDF) from accessing the surface of iron oxide nanoparticles. This interaction inhibits the formation of the β-phase in PVDF, which is critical for its piezoelectric properties. Shorter chains, like octanoic acid with only 8 carbon atoms, allow closer interactions between particles and polymer matrices, potentially enhancing catalytic or functional properties but

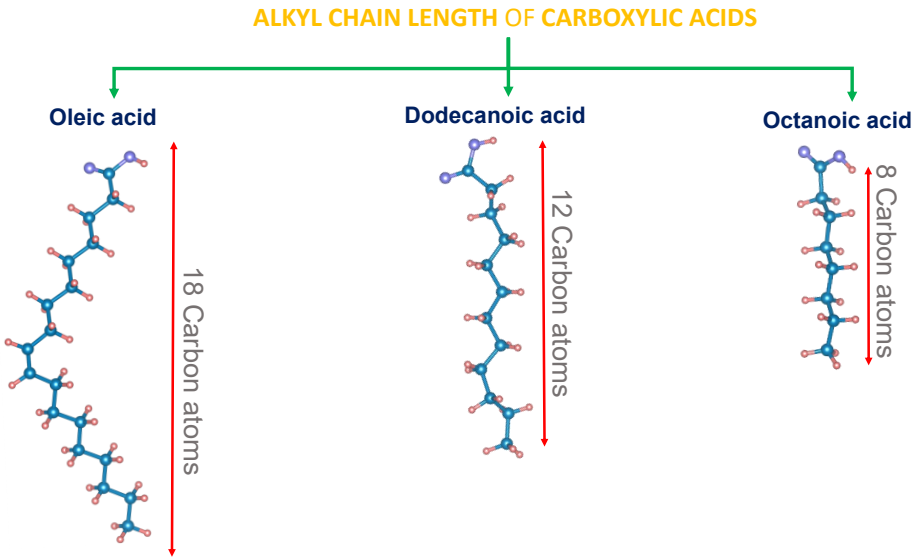

Figure 3.2 – *Alkyl chain length of the selected carboxylic acids: Oleic acid, Dodecanoic acid, Octanoic acid*

at the cost of dispersion stability. Intermediate chain lengths, such as dodecanoic acid (C12), can provide a balance, facilitating both effective dispersion and favorable interactions.

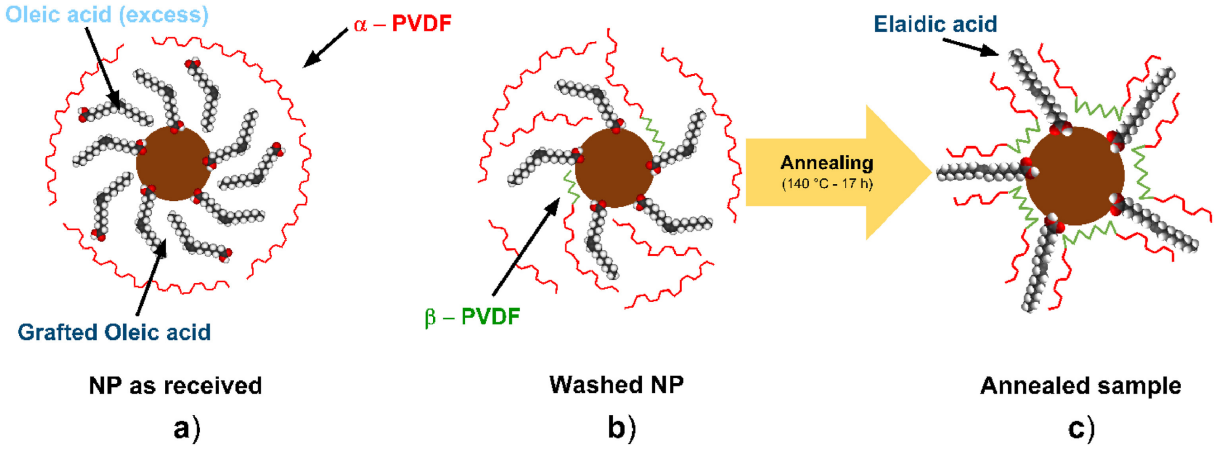

Figure 3.3 – *Schematic illustration of carboxylic acid surface ligands and their impact on nanoparticle-polymer interactions. (Top) Evolution of iron oxide nanoparticle surface chemistry showing: (a) as-synthesized NPs with grafted oleic acid (C18), where the long ligand chains reduce surface accessibility and inhibit β-PVDF formation, (b) washed NPs with partial surface modification, allowing limited β-PVDF interactions, and (c) annealed sample with elaidic acid formation, altering surface accessibility while maintaining steric stability. [16]*

The studies on surface accessibility and β-PVDF formation were further investigated by molecular dynamics simulations [17] [18], as shown in Figure 3.4. The average dipole moment of α-PVDF during 10 ns of molecular dynamics simulation was calculated in the absence and presence of magnetite slabs with different surface treatments. These treatments

included OH termination, 20% acetic acid termination, 20% hexanoic acid termination, 20% dodecanoic acid termination, and 20% oleic acid termination. The results indicated that OH termination exhibited the highest dipole moment, corresponding to a higher amount of β-phase formation.

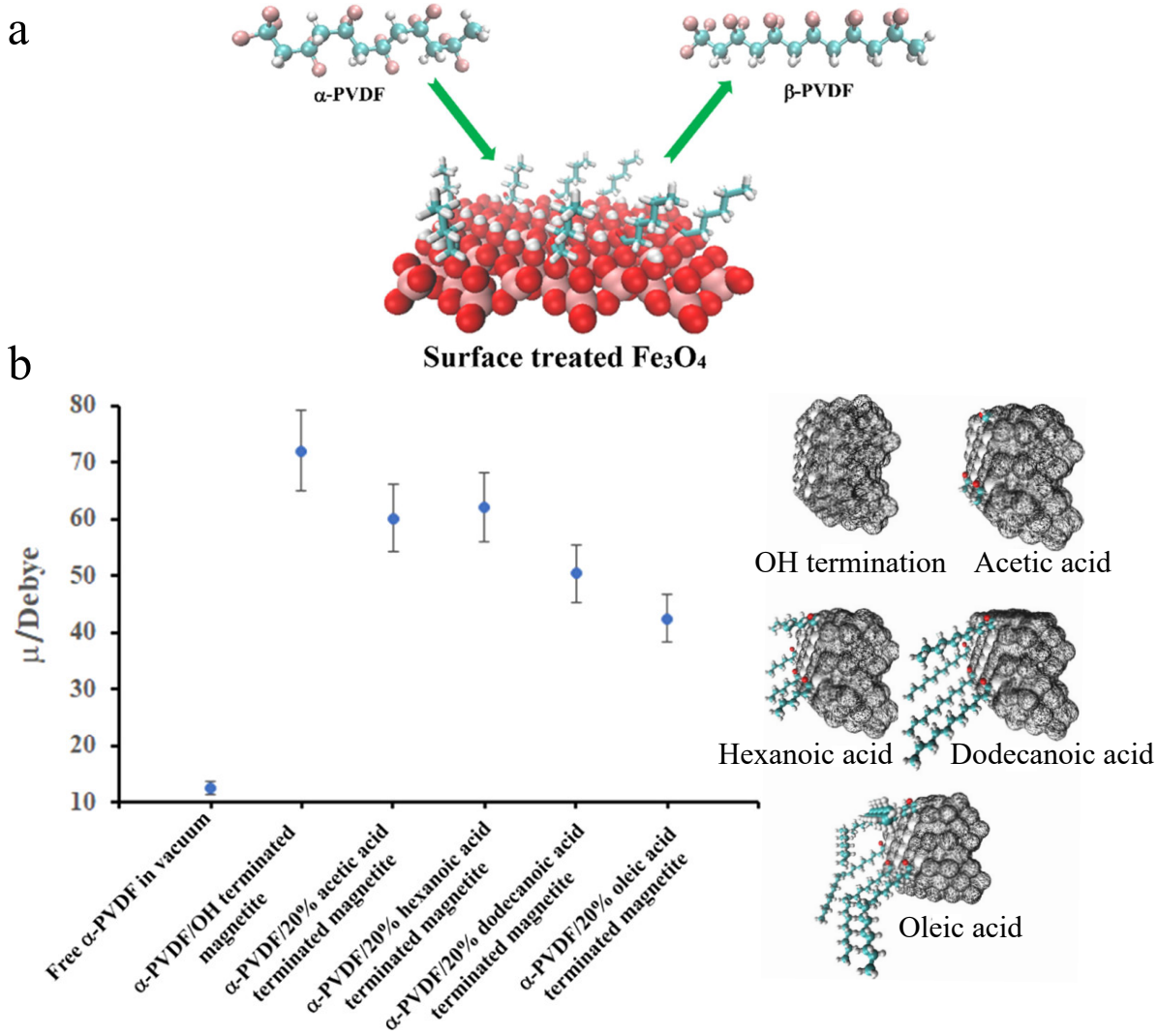

Figure 3.4 – *(a) Illustration of the transformation of α-PVDF into β-PVDF upon contact with the magnetite slab. (b) Average dipole moment of α-PVDF during 10 ns of molecular dynamics simulation in the absence and presence of magnetite slabs with different surface treatments, including OH termination, 20% acetic acid termination, 20% hexanoic acid termination, dodecanoic acid termination, and 20% oleic acid termination. [17]*

Building on insights into size range selection and surface coating choices in polymer nanocomposite properties, **this study aims to synthesize nanoparticles in three distinct sizes below 20 nm, each with the three selected coatings.** This method will produce a varied collection of nine distinct samples, aimed at facilitating future research on how nanoparticle size and surface chemistry affect interactions with polymers in the interphase

and their resulting properties.

We aim to develop and optimize synthesis protocols to achieve precise control over particle size and surface chemistry. Our research will focus on optimizing nanoparticle synthesis for specific sizes and surface characteristics. We will investigate growth kinetics and mechanisms, characterize the size distribution and surface chemistry, and correlate synthesis parameters with the resulting magnetic properties.

3.2 Samples Preparation & Characterization

3.2.1 Strategy for Size and Surface Chemistry Control

The synthesis of maghemite nanoparticles with precise control over both size and surface chemistry has remained a challenge in nanomaterials research. Traditional methods often struggle to achieve both consistent particle sizes and tailored surface properties using carboxylic acid ligands with varying chain lengths. This difficulty arises because conventional techniques for modifying surface ligands while maintaining a constant iron precursor frequently lead to mixed ligand passivation and unintended variability in particle size [10]. As a result, it becomes challenging to decouple the effects of ligand chain length from particle size, which is crucial for developing nanoparticles for specific applications.

To address these limitations, this chapter presents a novel, systematic approach to maghemite NP synthesis. The strategy involves examining the thermal decomposition of three distinct iron complexes—iron oleate (C_{18}), iron dodecanoate (C_{12}), and iron octanoate (C_8)—each paired with corresponding stabilizing ligands: oleic acid, dodecanoic acid, and octanoic acid. This innovative method aims to achieve three distinct size ranges within each precursor-ligand system, enabling simultaneous control over nanoparticle size and surface chemistry while offering a detailed investigation into growth mechanisms.

By systematically examining the relationships between precursor chemistry, ligand interactions, and synthesis conditions, this study provides valuable insights for the rational design of maghemite nanoparticles tailored for specific applications. The approach not only addresses longstanding challenges in NP synthesis but also paves the way for more precise control over nanomaterial properties.

3.2.2 Synthesis of Iron(X)$_3$ Precursors (X = oleate, dodecanoate, octanoate)

To synthesize the three selected precursors—iron oleate (C_{18}), iron dodecanoate (C_{12}), and iron octanoate (C_8)—we reacted iron(III) chloride ($FeCl_3$) with their corresponding sodium fatty acid salts: sodium oleate, sodium dodecanoate, and sodium octanoate. This synthesis followed a method reported by Park et al. [19] for the preparation of iron oleate and was adapted for the synthesis of iron dodecanoate (C_{12}) and iron octanoate (C_8). Specifically, iron chloride (10.8 g, 40 mmol) and sodium oleate (36.5 g, 120 mmol) were dissolved in a solvent mixture consisting of 80 mL ethanol, 60 mL distilled water, and 140 mL hexane. The reaction mixture was heated to 70 °C and maintained at this temperature for 4 hours to ensure completion. The upper organic phase containing the iron-oleate complex was separated using a funnel and washed three times with 30 mL of distilled water. Finally, the hexane was evaporated using a rotary evaporator, yielding the iron-oleate complex as a waxy red-brown paste. The process is illustrated in Figure 3.5.

For iron dodecanoate and iron octanoate, similar procedures were followed with their corresponding sodium salts: sodium dodecanoate (72.12 g, 120 mmol) and sodium octanoate (51.53 g, 120 mmol). These reactions also proceeded with the same solvent mixture and heating conditions, leading to the desired complexes.

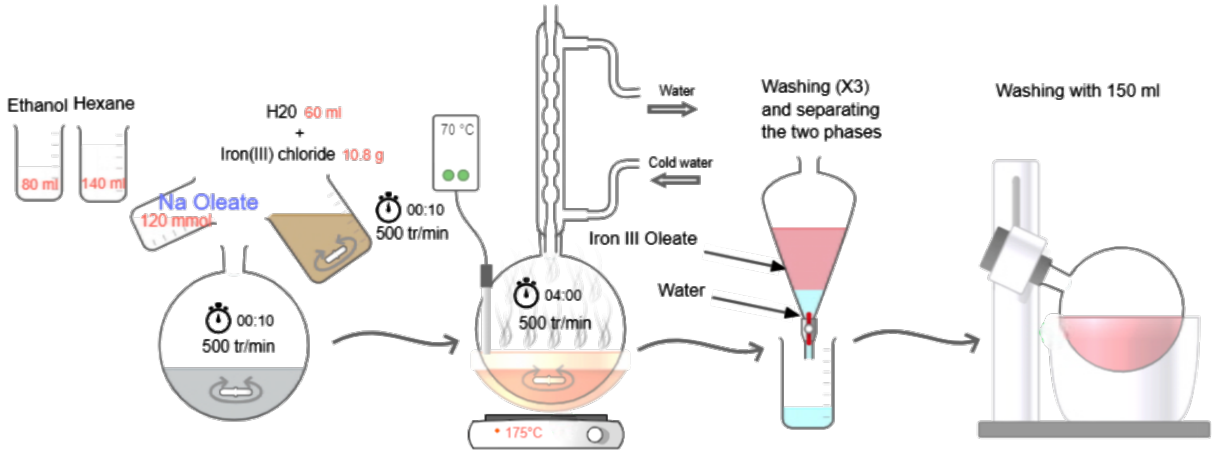

Figure 3.5 – *Illustration of the synthesis and isolation process of the iron oleate precursor.*

3.2.3 Synthesis of (Y) acid iron coated iron oxide NPs precursors (Y = oleic, dodecanoic, octanoic)

To produce spherical maghemite nanoparticles with three distinct average diameters, all below 20 nm and stabilized by carboxylic acids of varying chain lengths, we modified the synthesis method described by Park et al. [19]. Our approach utilized the thermal decomposition of iron oleate in the presence of oleic acid (C_{18}), which was dissolved in 1-octadecene. This process resulted in maghemite nanoparticles coated with oleic acid.

Building on this foundation, we expanded our synthesis to include two additional surface chemistries by replacing iron oleate with iron dodecanoate and iron octanoate, each paired with dodecanoic acid (C_{12}) and octanoic acid (C_8), respectively. This modification enabled us to investigate how the decomposition of different iron carboxylate precursors affects the properties of the synthesized nanoparticles.

To achieve the desired size ranges for each surface chemistry, we conducted a systematic study of synthesis parameters. Size control was accomplished through various strategies, including the well-documented solvent effect [10] [19]. Higher boiling point solvents, such as 1-octadecene (318°C), promote the growth of larger NPs. However, this approach has limitations, particularly for very small NPs (e.g., 3 nm). Additionally, we found that the decomposition behavior of the precursors was significantly influenced by the chain length of the carboxylic acids, affecting the nucleation and growth mechanisms.

The NPs synthesized in this study were categorized into three size ranges based on their average diameters.

- Small: approximately 3.3 nm
- Intermediate: approximately 7.5 nm
- Large: approximately 12.0 nm

3.3 Precursors and Nanoparticles Characterization

3.3.1 (DSC) Differential Scanning Calorimetry

Differential Scanning Calorimetry was employed to investigate the thermal decomposition behavior of the three iron carboxylate precursors used in our study. This technique has been previously utilized in the literature to analyze the thermal decomposition of iron oleate, allowing for the identification of endothermic peaks associated with the dissociation of oleic acid chains and their correlation with nucleation and growth temperatures [20].

We used the work referenced in [20] to (1) validate the results obtained for iron oleate and (2) extend this approach to analyze the thermal properties of iron dodecanoate and iron

octanoate precursors. The differential scanning calorimetry analysis was performed using a DSC instrument Q200 equipped with version 24.11 Build 124 software. Thermograms were acquired over a temperature range of 25 to 400°C, with a heating rate of 10°C/min. For sample preparation, approximately 1.3 mg of each precursor was placed in a Tzero Aluminum Hermetic pan under a nitrogen atmosphere.

This analysis provided valuable insights into the decomposition behavior of the different precursors, allowing us to:

- Identify the characteristic endothermic peaks for each precursor
- Compare the thermal decomposition of the precursors with varying carboxylic acid chain lengths.
- Correlate the observed thermal events with the nucleation and growth processes during nanoparticle synthesis

3.3.2 (EDS) Energy Dispersive X-ray Spectrometry

Prior to the DSC analysis, we employed Energy Dispersive X-ray Spectrometry to determine the chemical composition of the precursors. This step was added to ensure the purity of the components and to verify that the peaks observed in the DSC analysis were indeed related to the precursors and not to any present impurities.

The EDS analysis was conducted using a scanning electron microscope (Quanta FEG 250, Thermo Fisher) equipped with a Quantax X-Flash detector (Synergie4 Bruker). This analysis was performed at the Service Analyses Physico-Chimiques (SAPC) at the Université de Technologie de Compiègne.

By utilizing EDS, we were able to:

- Confirm the elemental composition of each precursor
- Detect and quantify any potential impurities
- Ensure the reliability of subsequent DSC measurements

3.3.3 (TEM) Transmission Electron Microscopy

To characterize the morphology of the synthesized nanoparticles, we conducted Transmission Electron Microscopy analysis. The TEM imaging was performed using a JEOL JEM-1011 microscope operated at an accelerating voltage of 100 kV.

Sample preparation for TEM analysis involved depositing drops of the colloidal nanoparticle solution onto amorphous carbon-coated TEM grids. To ensure statistical significance, we analyzed over 700 nanoparticles from the TEM images using ImageJ software. This analysis allowed us to determine:

- Average diameter of the nanoparticles
- Size distribution and polydispersity

The mean diameter was calculated as the arithmetic average of these measurements. Polydispersity was quantified using the standard deviation relative to the mean size, providing a measure of the size uniformity of the nanoparticle population.

3.3.4 (XRD) X-Ray Diffraction

To confirm the formation of maghemite nanoparticles and study their crystal structure, we employed X-Ray Diffraction analysis. This technique allowed us to identify the characteristic peaks of maghemite and calculate the unit cell parameters. XRD measurements were conducted using a Bruker D8 Advance X-ray diffractometer, provided by the Service Analyses Physico-Chimiques (SAPC) at the Université de Technologie de Compiègne. The instrument was operated under the following conditions:

- Voltage: 30 kV
- Current: 40 mA
- X-ray wavelength: 0.1506 nm
- Scanning range: 2θ from 25° to 70°
- Step size: 0.02°

All nanoparticle samples were analyzed in powder form. For the analysis, the samples were carefully deposited on a holder with a silicon monocrystal to minimize background interference.

3.3.5 (SQUID) Superconducting Quantum Interference Device

To characterize the magnetic behavior of the synthesized nanoparticles, we conducted comprehensive magnetic measurements using a commercial Superconducting Quantum Interference Device (SQUID) magnetometer (MPMS3, Quantum Design, USA). The measurements were performed on films of powdered iron oxide nanoparticles, with the applied field parallel to the nanoparticle film.

Our magnetic characterization included:

- Zero-field-cooled (ZFC) and field-cooled (FC) susceptibility curves:
  - ▷ Applied field: 1.59×10^3 A·m^{-1}
  - ▷ Temperature range: 3 K to 300 K
- Magnetization curves:

- ▹ Maximum applied field: 3.98×10^6 A·m^{-1}

The ZFC and FC measurements were conducted as follows:

- ZFC protocol: The sample was cooled from 300 K to 3 K without an applied field, then heated to 300 K in a field of 1.59×10^3 A·m^{-1} while recording the magnetization $M_{ZFC}(T)$.
- FC protocol: The sample was cooled again to 3 K under the same applied field, and the magnetization $M_{FC}(T)$ was recorded during heating.

For both ZFC and FC measurements:

- Heating rate: approximately 2 K·min^{-1} for each temperature step
- Measurement time: ∼5 s per data point

Additionally, hysteresis curves were obtained at 3 K to further elucidate the magnetic properties of the nanoparticles at low temperatures.

3.4 Precursors Decomposition Investigation

Thermal decomposition study by DSC

Iron (Oleate)$_3$

The thermal behavior of iron oleate (C_{18}) obtained DSC is presented in Figure 3.6a. The DSC pattern revealed several distinct endothermic peaks, each corresponding to specific thermal events.

A subtle endothermic peak was observed at 120 °C, indicating the elimination of crystal hydrate water from the precursor. At 230 °C, another endothermic peak signaled the dissociation of the first oleate group from the iron oleate complex, which is associated with the nucleation step in the formation of nanoparticles. A subsequent endothermic peak was detected at 320 °C, corresponding to the dissociation of the two remaining oleate ligands, an event linked to the growth phase of the nanoparticles. The final endothermic peak, occurring at approximately 380 °C, signifies the complete decomposition of the iron oleate precursor. These findings are consistent with previous research on the thermal decomposition of iron oleate complexes and their role in nanoparticle synthesis [19] [20] [21].

Importantly, the EDS analysis, presented in the insets of Figure 3.6 for the three precursors, revealed no detectable impurities, confirming that the peaks observed in the DSC analysis were related to the precursors themselves and not to any contaminants, such as chlorine or sodium, which could result from non-stoichiometric conditions during synthesis or an inadequate washing step [22].

Iron (Dodecanoate)$_3$

The DSC pattern of the iron dodecanoate (C_{12}) precursor, as shown in Figure 3.6b, exhibited distinct thermal characteristics compared to its oleate counterpart. A low-temperature peak was observed at approximately 77 °C, which can be attributed to the melting point of this precursor. Unlike iron oleate (C_{18}), iron dodecanoate is solid at room temperature, explaining this unique low-temperature feature. Two significant endothermic peaks were detected at 265 °C and 310 °C. Drawing parallels with the behavior of iron oleate, these peaks likely correspond to the nucleation and growth processes, respectively. Notably, the nucleation peak for iron dodecanoate occurred at a higher temperature (265 °C) compared to that of the oleic precursor (230 °C), indicating that the dodecanoate precursor requires substantially higher temperatures to initiate nucleation. The growth peak at 310 °C was observed at a slightly lower temperature than its oleic counterpart. A comparative analysis of the DSC patterns indicates that the distinction between nucleation and growth processes, which is important for producing nanoparticles with a narrow size distribution, is less pronounced when using the dodecanoic precursor compared to the oleic precursor. The complete decomposition of iron dodecanoate occurs at approximately 370 °C, which is lower than the decomposition temperature observed for the oleic precursor.

Iron (Octanoate)$_3$

The thermal behavior of the iron octanoate (C_8) precursor, as illustrated in Figure 3.6c, exhibits distinct characteristics compared to its longer-chain counterparts. A low-temperature endothermic peak is observed at 60 °C, which can be attributed to the melting point of the precursor, similar to the iron dodecanoate (C_{12}) precursor. However, the decomposition pattern of the iron octanoate precursor is notably more complex than that of the C_{18} and C_{12} precursors.

Unlike the C_{18} and C_{12} precursors, which displayed two distinct peaks associated with nucleation and growth steps, the iron octanoate precursor exhibits three endothermic peaks at 202 °C, 220 °C, and 270 °C. This tripartite peak structure suggests a more intricate dissociation pathway for the C_8 precursor. One possible interpretation is that each of these peaks corresponds to the sequential dissociation of an octanoate group from the precursor. However, the exact nature of these thermal events requires further investigation to be fully understood.

The complete decomposition of the iron octanoate precursor occurs at approximately 350 °C, which is lower than the decomposition temperatures observed for both the oleic (C_{18}) and dodecanoic (C_{12}) precursors. This lower decomposition temperature indicates that the iron octanoate precursor is less thermally stable compared to its longer-chain analogues.

The unique thermal behavior of the iron octanoate (C_8) precursor, marked by three endothermic events, indicates a complex decomposition mechanism that may affect nanoparticle nucleation, growth, size, shape, stability, and reproducibility.

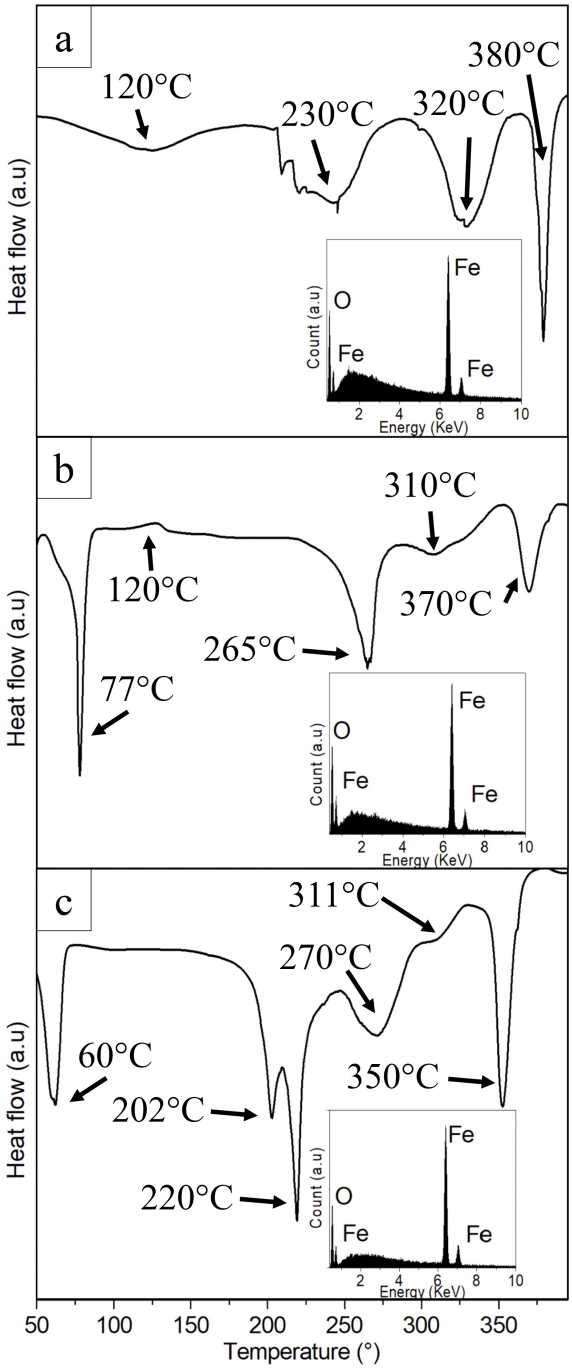

Figure 3.6 – *Differential scanning calorimetry (DSC) of the (a) iron oleate, (b) iron dodecanoate, and (c) iron octanoate precursors. Insets: corresponding energy dispersive X-ray spectrometry (EDS) patterns.*

3.5 TEM analysis of size and morphology

3.5.1 Synthesis of Oleic acid (C18)-coated maghemite nanoparticles

The synthesis of the larger maghemite nanoparticles coated with oleic acid (C_{18}) was adapted from the method described by Park and Co., with modifications primarily in scale and heating rate. The process involved dissolving 1.42 g (1.6 mmol) of iron oleate precursor and 0.22 g (0.8 mmol) of oleic acid in 10 ml of octadecene, resulting in a precursor-to-ligand concentration ratio (R) of 2. This mixture was heated to the boiling point of octadecene (318 °C), refluxed for 30 minutes, and then cooled to room temperature. The synthesis conditions are summarized in Table 3.1. The resulting black solution was purified by washing with excess acetone and centrifugation at 4900 rpm for 10 minutes. The oleic acid-coated NPs were then dispersed in chloroform. TEM analysis of the C_{18}-NPs, as shown in Figure 3.7a, revealed a population of highly uniform spherical nanoparticles. The inset of Figure 2a indicates that these NPs have a mean diameter of 12.6 nm with a narrow size polydispersity of 4%.

Table 3.1 – *Parameters used for the synthesis of maghemite nanoparticles by thermal decomposition approach with the TEM size measured.*

Sample	Precursor (mmol)	Ligand (mmol)	R = [P/L]	Solvent (Tbp °C)	Reflux Time (min)	TEM Diameter (nm)
C18-NPs	1.6	0.8	2.0	Octadecene (318°C)	30	12.6 (σ = 4%)
	1.6	0.8	2.0	Hexadecene (274°C)	30	7.8 (σ = 4%)
	4.0	2.0	2.0	Hexadecene (274°C)	30	3.4 (σ = 14.3%)
C12-NPs	1.6	3.2	0.50	Octadecene (318°C)	30	13.3 (σ = 5.7%)
	0.8	1.6	0.50	Hexadecene (274°C)	60	7.8 (σ = 6.7%)
	0.8	2.8	0.29	Hexadecene (274°C)	60	3.2 (σ = 14.5%)
C8-NPs	1.6	2.0	0.80	Hexadecene (274°C)	90	11.2 (σ = 13.7%)
	1.6	2.0	0.80	Hexadecene (274°C)	60	7.0 (σ = 13.4%)
	3.2	6.3	0.50	Hexadecene (274°C)	30	3.2 (σ = 12.3%)

The choice of solvent with a lower boiling point significantly influences the size of the synthesized nanoparticles [8] [10] [19] [23]. When hexadecene (boiling point: 274 °C) was used instead of octadecene, while keeping all other parameters constant, the mean diameter of the nanoparticles decreased from 12.6 nm to 7.8 nm. Notably, the size polydispersity remained low at 4%, as evidenced in Figure 3.7b and its inset. This reduction in nanoparticle size can be attributed to the lower growth activation resulting from the use of hexadecene, whose boiling point (274 °C) is below the growth peak temperature (300 °C) observed in the DSC analysis (Figure 3.6). In contrast, octadecene's higher boiling point (318 °C) allows for more extensive growth. The remarkably low nanoparticle size polydispersity (4% in both cases) is a consequence of the distinct separation between the nucleation and growth processes. The DSC measurement reveals a nucleation peak at approximately

230 °C, corresponding to the dissociation of the first oleate ligand from the iron oleate precursor. Subsequently, at around 320 °C, the remaining two oleate ligands dissociate, triggering nanoparticle growth (Figure 1a). This clear temporal and thermal separation of nucleation and growth stages contributes to the uniform size distribution of the synthesized nanoparticles.

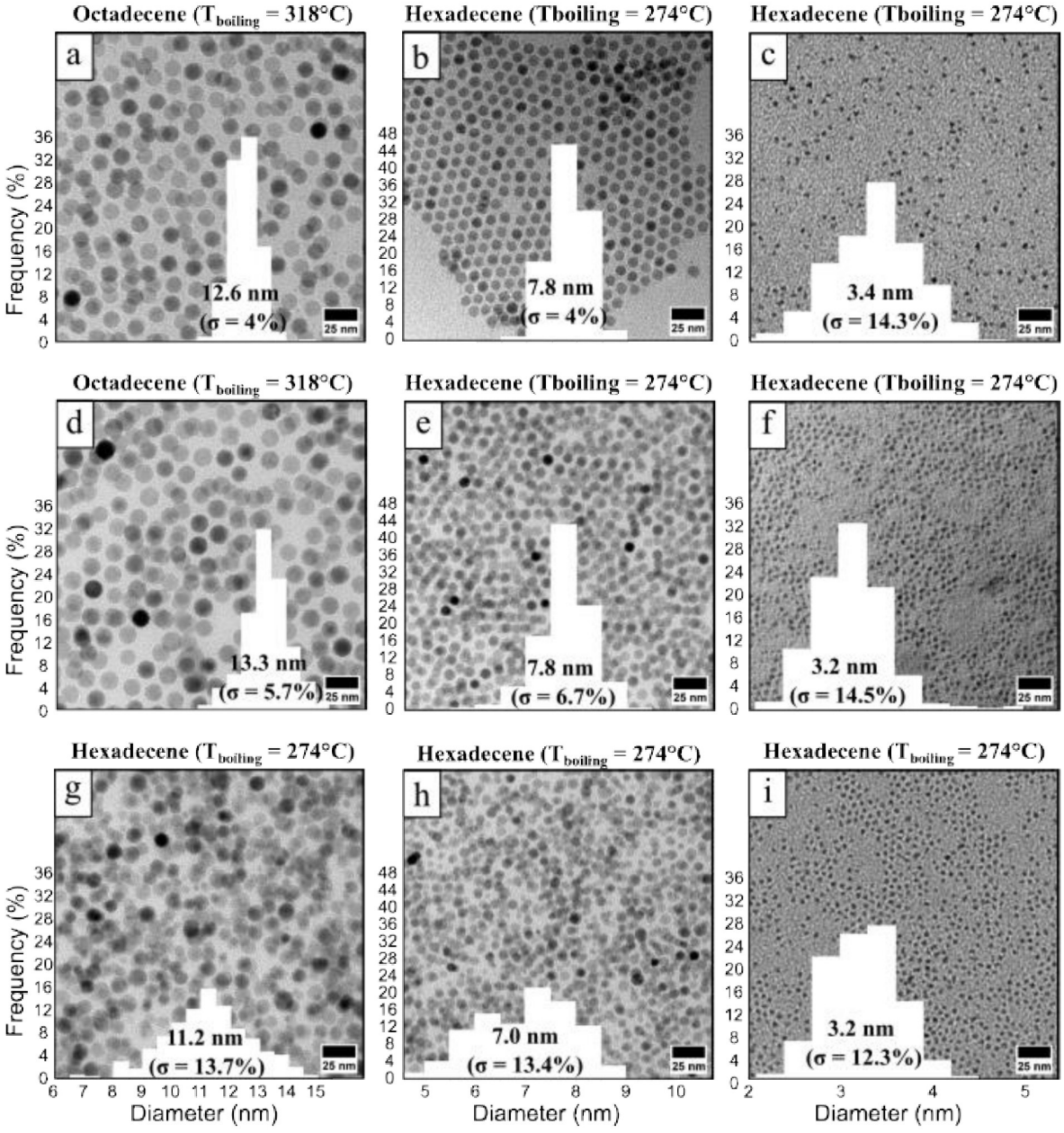

Figure 3.7 – *Transmission electron microscopy (TEM) images of maghemite nanoparticles synthesized from (a,b,c) iron oleate, (d,e,f) iron dodeconaoate, and (g,h,i) iron octanoate. The mean diameters are centered on (a,d,g) 12.0 nm, (b,e,g) 7.5 nm and (c,f,i) 3.3 nm.*

By lowering the reaction temperature to 251°C using tetradecene, a population of small

nanoparticles (∼2.6 nm) was obtained. However, the reaction exhibited a very low yield and high size polydispersity (20%), likely due to the reaction temperature being close to the nucleation peak, which limits complete precursor decomposition. Thus, the solvent strategy with tetradecene proved ineffective in consistently producing smaller nanoparticles.

To further reduce the nanoparticle size and achieve the smallest dimensions, we modified a second synthesis parameter: the precursor concentration. While maintaining other parameters that yielded the medium-sized 7.8 nm C18-NPs, we increased the precursor concentration from 1.6 mmol to 4 mmol in 10 ml of hexadecene. The ratio R remained at 2, and the reflux time was kept at 30 minutes (Table 3.1). As illustrated in Figure 3.7c, these conditions resulted in the formation of 3.4 nm NPs with a size polydispersity of 14.3%.

The observed decrease in mean NP size with increasing precursor concentration can be attributed to the enhancement of iron supersaturation before nucleation, as explained by the LaMer supersaturation theory. Figure 3.8 demonstrates the relationship between precursor concentration and nanoparticle size. When the concentration was increased from 1.6 to 3.2 mmol, nanoparticles with a diameter of 6 nm were obtained (Figure 3.8c). Conversely, decreasing the concentration to 0.8 mmol resulted in larger nanoparticles of 12 nm (Figure 3.8a).

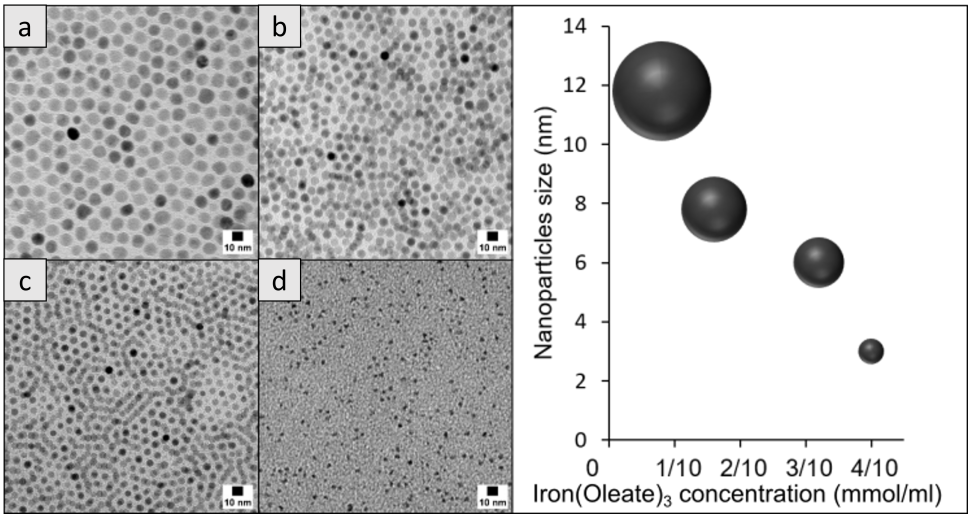

Figure 3.8 – *The size of iron oxide nanoparticles decreases with increasing concentration of iron oleate precursors in Hexadecene*

These results reveal a linear relationship between precursor concentration and nanoparticle size in the case of iron oleate: higher concentrations lead to smaller nanoparticles. This trend is consistent across the concentration range studied, from 0.8 mmol to 4 mmol, demonstrating the significant impact of precursor concentration on the final nanoparticle dimensions.

3.5.2 Synthesis of Dodecanoic acid (C12)-coated maghemite nanoparticles

Using iron dodecanoate as a precursor instead of iron oleate, while following the procedure for larger C_{18}-NPs, resulted in polydisperse C_{12}-NPs with a mean diameter of 14.0 nm and a size polydispersity (σ) of 17%. This outcome contrasts with the low polydispersity 12.6 nm NPs obtained with iron oleate. The difference in population quality can be attributed to the distinct decomposition processes of the two iron precursors. For iron oleate, nucleation and growth peaks occur at approximately 230 °C and 320 °C, respectively, whereas for iron dodecanoate, these peaks are observed at 265 °C and 310 °C (Figure 3.6).

To compensate for the differences in nucleation and growth dynamics between iron oleate and iron dodecanoate, and to produce uniform C_{12}-NPs with an average size close to 12 nm, we conducted multiple experiments involving various parameter adjustments. After numerous iterations and careful analysis of the results, we refined the protocol to modify the concentrations of both precursor and ligand. The optimized synthesis employed 1.045 g (1.6 mmol) of iron dodecanoate precursor combined with 0.64 g (3.2 mmol) of dodecanoic acid, establishing a precursor-to-ligand ratio (R) of 0.5. This ratio was established through systematic variation and represents the optimal balance for achieving the desired characteristics of the nanoparticles, while utilizing octadecene as the solvent (boiling point: 318 °C) and maintaining a reflux duration of 30 minutes, as outlined in Table 3.1.

The TEM imaging of the nanoparticles synthesized under these optimized conditions, along with the corresponding size distribution histogram (Figure 3.7d and inset), reveal the successful formation of C_{12}-NPs. These nanoparticles exhibit an average diameter of 13.3 nm and a narrow size distribution with a polydispersity of only 5.7%. This outcome demonstrates the effectiveness of our refined synthesis parameters, which were the result of extensive experimentation and careful optimization.

To synthesize intermediate-sized C_{12}-NPs, we adopted a strategy similar to that used for C_{18}-NPs, substituting the higher-boiling octadecene with hexadecene as the reaction solvent. Initially, this modification resulted in highly polydisperse C_{12}-NPs with a mean diameter of 6.3 nm and a size distribution of 16%. Recognizing the need for improvement, we refined our approach by adjusting key synthesis parameters. We halved the precursor concentration from 1.6 mmol to 0.8 mmol while maintaining the precursor-to-ligand ratio (R). Concurrently, we extended the reflux duration from 30 to 60 minutes. These strategic modifications yielded C_{12}-NPs with a mean diameter of 7.8 nm and a notably improved size polydispersity of 6.7%, as shown in Figure 3.7e and its inset. This process of optimization reveals the intricate relationship between precursor type and synthesis conditions in nanoparticle formation. It underscores the necessity for a nuanced approach when working with different iron

precursors to achieve desired nanoparticle characteristics.

By modifying the precursor-to-ligand ratio (R) from 0.5 to 0.28 for the 7.8 nm C_{12}-NPs synthesis, specifically by increasing the dodecanoic acid ligand concentration while keeping other parameters constant, we obtained C_{12}-NPs with a mean diameter of 3.2 nm and a size polydispersity of 14.5% (Figure 2f and inset of Figure 3.7f).

The impact of ligand concentration on nanoparticle growth has been extensively studied, with conflicting trends reported in the literature. Some studies have observed an increase in nanoparticle size with higher ligand concentrations [8] [24] [25] [26], while others have noted a decrease [10] [27] [28] [29]. This discrepancy can be attributed to whether the ligand primarily affects the nucleation or growth stage of nanoparticle formation.

In cases where nanoparticle size increases with ligand concentration, it is hypothesized that the ligands enhance the stability of the iron complex, thereby slowing nucleation. This results in fewer nuclei, ultimately leading to larger nanoparticles. Conversely, when excess ligands inhibit nanoparticle growth by covering active growth sites, smaller nanoparticles are produced.

The complex interplay between ligand concentration and other reaction parameters (such as reactant nature and concentration, solvent choice, heating rate, and reflux time) likely accounts for these divergent observations across different studies. In our specific case, the reduction in C_{12}-NP size from 7.8 nm to 3.2 nm, achieved by increasing the dodecanoic acid ligand concentration from 1.6 mmol to 2.8 mmol while maintaining other conditions, can be attributed to the inhibition of nanoparticle growth due to the excess ligands blocking active growth sites on the developing nanoparticles.

3.5.3 Synthesis of Octanoic acid (C8)-coated iron oxide nanoparticles

In our attempt to synthesize C_8-NPs, we initially applied the conditions established for larger C_{18}-NPs, substituting iron oleate with iron octanoate as the precursor. This approach resulted in highly polydisperse nanoparticles with a mean diameter of 20 nm and a size distribution of 15%. Recognizing the need for improvement, we systematically optimized several key parameters to achieve the desired nanoparticle population.

The refined synthesis protocol involved adjusting the solvent, ligand-to-precursor ratio, and reflux time. Specifically, we maintained the precursor concentration at 1.6 mmol but modified the ratio R to 0.8. We also switched to hexadecene (boiling point 274 °C) as the reaction medium and extended the reflux time to 90 minutes (Table 3.1).

These optimized conditions yielded significantly improved results. TEM analysis, as shown in Figure 3.7g and its inset, revealed C_8-NPs with a mean diameter of 11.2 nm and a size polydispersity of 13.7%. While the size distribution is broader than that achieved with

longer-chain precursors, these results represent a substantial improvement over the initial attempt and demonstrate the successful synthesis of C_8-NPs with controlled size.

By shortening the reflux time from 90 to 60 minutes while keeping other parameters constant, the average particle size decreased from 11.2 nm to 7.0 nm, with the polydispersity remaining almost unchanged at 13.4% (Figure 3.7h and its inset). This trend, observed using iron octanoate as the precursor and hexadecene as the solvent, highlights the time-dependent nature of the growth process during reflux at 274 °C, which corresponds to the growth temperature identified in the DSC study (Figure 3.6c).

The smallest C_8-NPs were obtained by adjusting the reflux time, *R*-value, and precursor concentration. Reducing the reflux time from 60 to 30 minutes, decreasing the *R*-value from 0.8 to 0.5, and increasing the octanoic acid concentration from 1.6 mmol to 3.2 mmol resulted in C_8-NPs with an average diameter of 3.2 nm and a size polydispersity of 12.3% (Figure 3.7i and its inset).

Notably, the C_8-NPs consistently display higher polydispersity than their C_{18} and C_{12} counterparts, irrespective of size. This phenomenon can potentially be attributed to a more intricate dissociation process of the iron octanoate precursor. Unlike the C_{18} and C_{12} precursors, which exhibit two endothermic events, the iron octanoate precursor demonstrates three such events, occurring in closer proximity to each other.

3.5.4 Effect of Ligand Saturation on Nanoparticle Growth and Colloidal Stability

After detailing the synthesis conditions and nanoparticle sizes obtained for each precursor, it is important to consider another key factor: the saturation of the ligands used. In our study, both unsaturated oleate (C_{18}) and saturated dodecanoate (C_{12}) and octanoate (C_8) ligands were employed, introducing differences not only in chain length but also in ligand saturation. Switching the precursor from unsaturated oleate (C_{18}) to saturated dodecanoate (C_{12}) or octanoate (C_8) alters two key parameters: chain length and ligand saturation.

Other experimental factors, such as precursor ratio, solvent boiling point, and reflux time, were also varied, making it difficult to isolate the specific effects of ligand unsaturation. However, literature indicates that unsaturation in ligands such as oleate introduces a bend in the alkyl chain, leading to less ordered ligand shells compared to the more linear and ordered shells formed by saturated ligands [30] [31] [32]. This bend disrupts tight packing, allowing for better solvent intercalation and improving colloidal stability. Consequently, unsaturated ligands can enhance nanoparticle solubility by promoting better interactions with the solvent.

In our study, despite the variation in ligand saturation, we did not observe significant

changes in colloidal stability, which remained consistently high. Based on the literature, we would expect that the enhanced solvent-ligand interactions, particularly the increased solubility of the ligand, should reduce ligand-ligand attractions within the ligand shell during nanoparticle growth. This reduction in ligand-ligand interactions is anticipated to weaken the integrity of the ligand shell, thereby promoting nanoparticle growth [33].

3.6 XRD analysis of crystal structure

The XRD patterns for nine iron oxide nanoparticle (NP) samples are presented in Figure 3.9, along with reference patterns for maghemite (γ-Fe_2O_3) and magnetite (Fe_3O_4) to facilitate comparison. The reference patterns correspond to maghemite (ICDD PDF card no. 04-021-3968), with a unit cell parameter of 8.336 Å, and magnetite (ICDD PDF card no. 00-019-0629), with a unit cell parameter of 8.396 Å. For the C12-coated NPs, additional peaks attributed to dodecanoic acid were observed, confirming the presence of the ligand on the nanoparticle surface. Moreover, a noticeable peak broadening was observed as the nanoparticle size decreased, which is consistent with the Scherrer equation. This broadening is primarily due to the reduced number of coherently diffracting lattice planes in smaller crystallites, resulting in broader and less intense diffraction peaks. The effect becomes more pronounced as the crystallite size approaches the nanoscale, where the limited long-range order in the crystal structure leads to a relaxation of the diffraction conditions.

The indexing of all samples, which differed in size (7 nm and 12 nm) and surface chemistry (C18, C12, and C_8), showed a predominant alignment with maghemite over magnetite. Given the striking similarity in the XRD patterns of these two crystalline phases, the unit cell parameters were determined by analyzing the position and broadening of the (311) reflection within the spinel structure, following established procedures [34]. To extract the lattice parameter, the Scherrer equation was applied:

$$D = \frac{k\lambda}{\beta \cos(\theta)} \tag{3.1}$$

where D is the crystallite size, k is the shape factor, λ is the X-ray wavelength, β is the full width at half maximum (FWHM) of the (311) peak, and θ is the Bragg angle. The unit cell parameters were then obtained by refining the position of the (311) peak within the spinel structure. The calculated unit cell parameters for the samples, summarized in Table 3.2, ranged from 8.334 Å to 8.346 Å, which closely matches the known lattice parameter of maghemite (γ-Fe_2O_3), typically around 8.33 Å. In contrast, magnetite (Fe_3O_4) has a slightly larger lattice parameter of approximately 8.396 Å, reinforcing the alignment of our samples with maghemite. These results suggest that, although surface chemistry and nanoparticle size

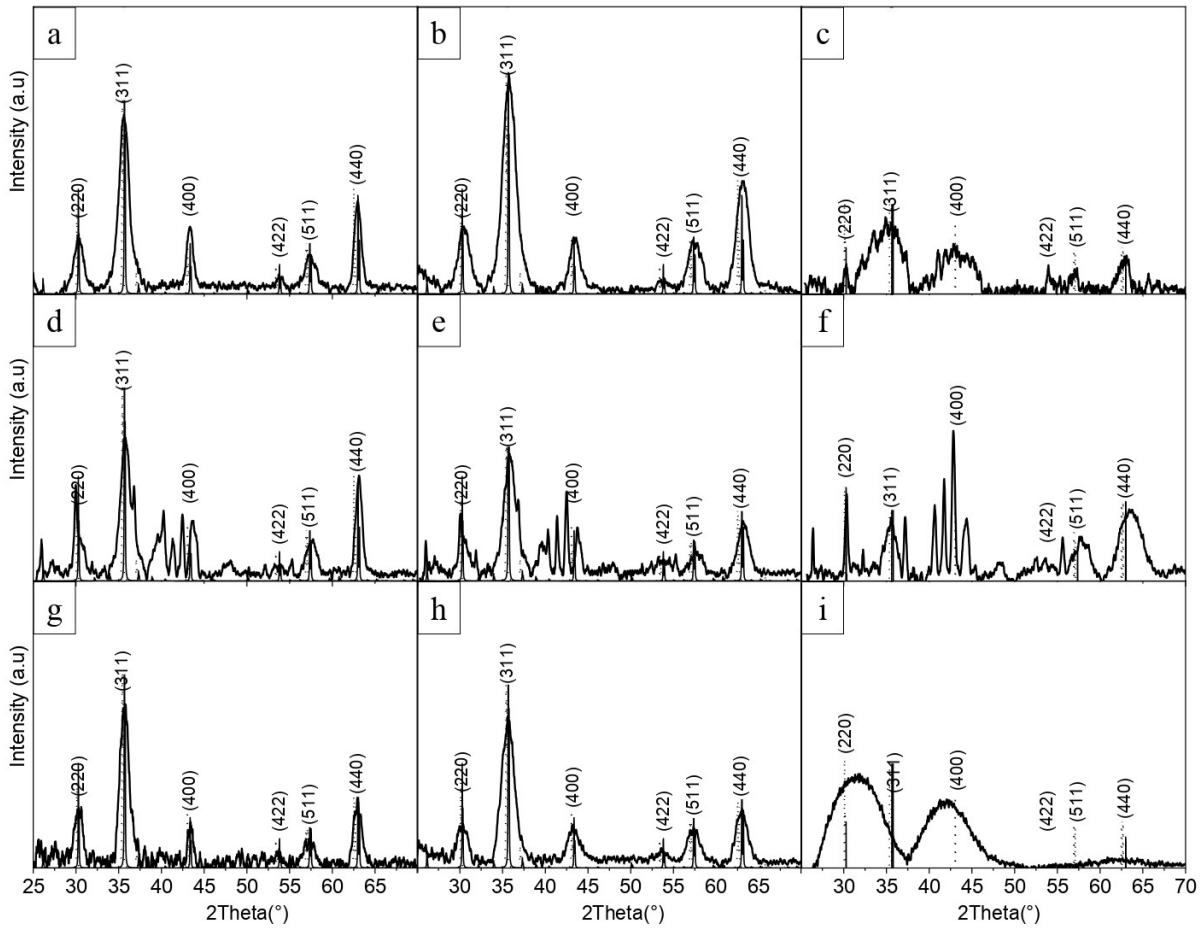

Figure 3.9 – *X-ray diffraction (XRD) patterns of iron oxide nanoparticles synthesized from (a,b,c) iron oleate, (d,e,f) iron dodeconoate, and (g,h,i) iron octanoate. The mean diameters are centered on (a,d,g) 12.0 nm, (b,e,g) 7.5 nm and (c,f,i) 3.3 nm. Solid lines: maghemite (Ref. 04-021-3968, PDF-5) reference pattern. Dotted lines: magnetite (Ref. 04-027-0607, PDF-5) reference patterns.*

may influence other properties, the crystal structure predominantly aligns with maghemite, as supported by the XRD analysis.

For the smallest nanoparticles (3 nm), the XRD peaks exhibited broader widths for the C_{18}-NPs and C_{12}-NPs, which is consistent with the expectations from the Scherrer equation [8] [35]. However, due to the low crystallinity and substantial noise in the XRD patterns, a clear distinction between maghemite and magnetite could not be made, preventing the precise calculation of the unit cell parameters for these small nanoparticles.

The analysis of the XRD pattern for the 3 nm C_8-coated nanoparticles revealed even more pronounced peak broadening, along with shifts in the peak positions. These shifts, along with the increased broadening, suggest that the diffraction patterns of the C_8-coated nanoparticles may be influenced by factors other than crystallinity, such as interactions

Table 3.2 – *TEM and XRD Size Analysis and Unit Cell Measurements of Iron Oxide Nanoparticles Using the (311) Plane Position and Broadening.*

Sample	TEM size (nm)	XRD size (nm)	Cell parameter (nm)
C18-NPs	12.6	6.0	8.345
	7.8	4.6	8.346
C12-NPs	13.3	5.1	8.335
	7.8	4.7	8.334
C8-NPs	11.2	6.8	8.336
	7.0	5.0	8.346

between the nanoparticles and their surface ligands, such as free carboxylates or iron complexes. These interactions can distort the crystal lattice, affecting the positions and shapes of diffraction peaks. Consequently, the XRD data for these nanoparticles may not offer a straightforward interpretation of their crystalline composition, making it more challenging to directly correlate the diffraction data with the exact phase composition.

Although the XRD analysis predominantly identifies maghemite as the main phase, it is important to recognize that the presence of magnetite, even if minimal, cannot be definitively excluded. The ability of XRD to distinguish between maghemite and magnetite is limited because of the similarity in their diffraction patterns. This overlap in their XRD spectra makes it difficult to quantify or conclusively identify minor phases, even if they are present in trace amounts. Therefore, while XRD provides valuable insights into the dominant phase, its precision in detecting and quantifying minor phases like magnetite is constrained by the structural similarities between these two iron oxide phases.

3.7 Magnetic Properties

3.7.1 Magnetization versus temperature measurements

The magnetic properties of the nine nanoparticle samples were investigated using field-cooled (FC) and zero-field-cooled (ZFC) magnetization versus temperature curves, as shown in Figure 3.10. These samples, depicted in Figure 3.7, vary in both size and surface chemistry. When cooled in the absence of an external magnetic field, the spins remain disordered at 3 K, resulting in negligible magnetization. However, upon applying a small magnetic field ($1.59 \times 10^3\,\mathrm{A\,m^{-1}}$), the spins begin to align with the field as the temperature increases. This alignment causes the magnetization to rise until it reaches a maximum at a temperature, $T_{\max}$, which corresponds to the blocking temperature, T_B.

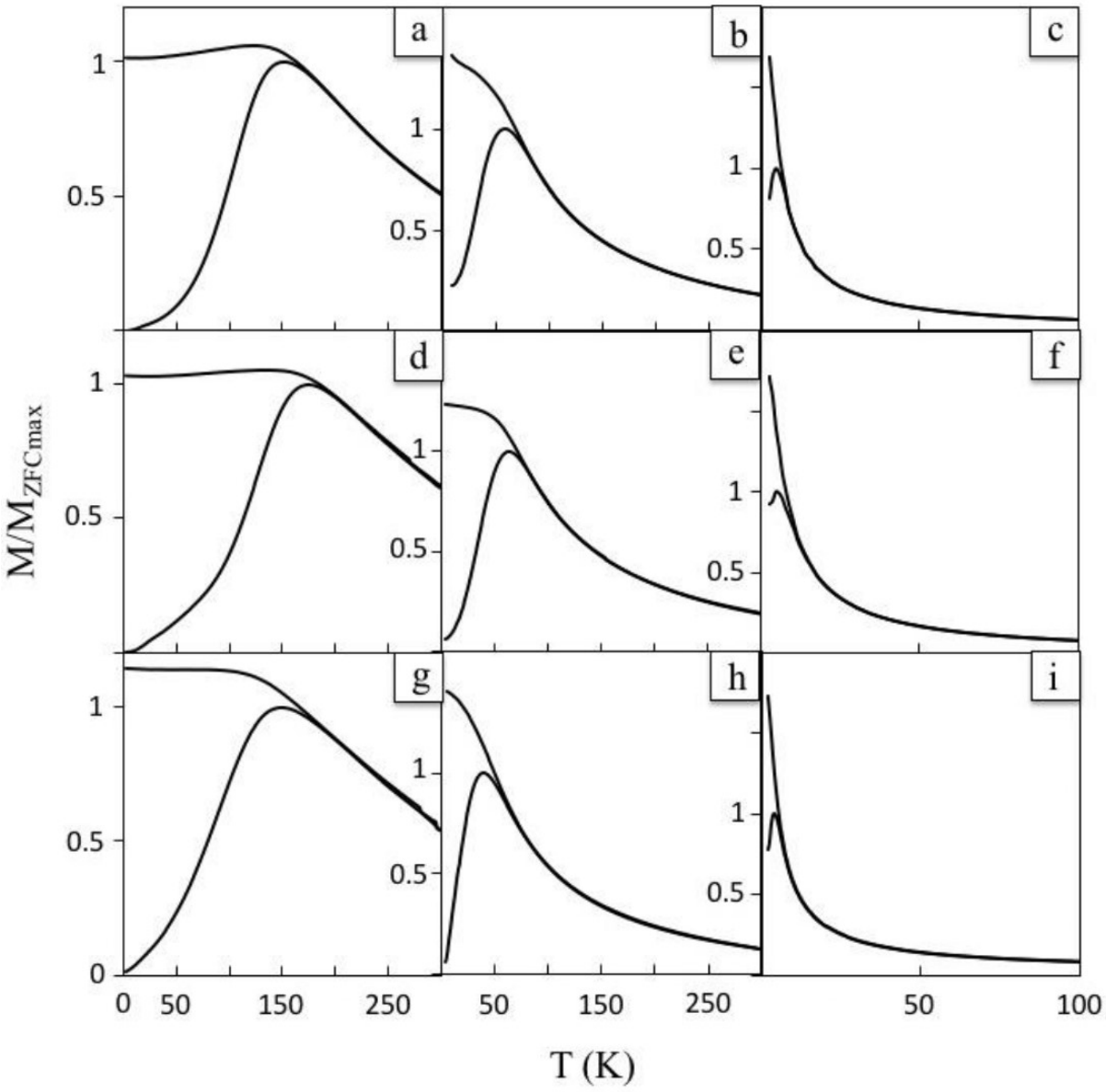

Figure 3.10 – *FC and ZFC magnetization versus temperature curves with applied field H = 1.59 x 103 Am-1, of maghemite nanoparticles synthesized from (a,b,c) iron oleate, (d,e,f) iron dodeconoate and (g,h,i) iron octanoate. The mean diameters are centered on (a,d,g) 12.0 nm, (b,e,g) 7.5 nm and (c,f, i) 3.3 nm.*

Above the blocking temperature (T_B), magnetic nanoparticles exhibit paramagnetic behavior. This means that as temperature increases, thermal energy becomes so high that it prevents the spins from aligning with the applied magnetic field, causing the magnetization to decrease.

For a system of identical particles (monodisperse), we define T_B using this equation:

$$T_B = \frac{KV}{k_B \ln\left(\frac{\tau_x}{\tau_0}\right)} \tag{3.2}$$

Where:

- K is the energy anisotropy constant
- V is the particle volume
- k_B is Boltzmann's constant
- τ_0 is the characteristic relaxation time (10^{-10} s for ferro- or ferrimagnetic materials)
- τ_x is the experimental time scale (60 s for susceptibility measurements)

In real systems with particles of different sizes (polydisperse), the situation becomes more complex. The temperature of maximum magnetization ($T_{\max}$) doesn't match T_B exactly. Instead, we need to consider a distribution of blocking temperatures related to the distribution of particle volumes. This deviation has been discussed in Refs. [36], [37], [38], and [39].

We can analyze this distribution using the derivative $\frac{d(M_{\mathrm{ZFC}}-M_{\mathrm{FC}})}{dT}$, which represents the T_B distribution. This distribution has two important points:

1. T_{IP} (inflection point): The maximum of $\frac{d(M_{\mathrm{ZFC}})}{dT}$
2. $T_{\max}$: Where $\frac{d(M_{\mathrm{ZFC}})}{dT} = 0$

The temperatures T_{IP} and $T_{\max}$, listed in Table 3.3, represent the lower and upper limits of the blocking temperature. These temperatures are associated with a characteristic volume, V_0, in the log-normal distribution of particle volumes, as described by Sappey [36].

Table 3.3 – *Magnetic parameters extracted from the ZFC magnetization and the hysteresis curves for the nine populations of maghemite nanoparticles, passivated with oleate (C18), dodecanoate (C12), and octanoate (C8) ligands. TB: blocking temperature, Mr/MHmax: ratio of remanent-to-magnetization at Hmax (Hmax = 3.98 x 106 Am-1), Hc: coercive field.*

Sample	**Diameter (nm)**	T_B **(K)**	M_r/M_{smax}	H_C **(10^4 Am^{-1})**
C18-NPs	12.6 ($\sigma = 4.0\%$)	117	0.44	4.18
	7.8 ($\sigma = 4.0\%$)	45	0.38	4.02
	3.4 ($\sigma = 14.3\%$)	5	0.06	0.99
C12-NPs	13.3 ($\sigma = 5.7\%$)	124	0.34	3.34
	7.8 ($\sigma = 6.7\%$)	42	0.38	3.70
	3.2 ($\sigma = 14.5\%$)	4	0.11	0.44
C8-NPs	11.2 ($\sigma = 13.7\%$)	83	0.37	4.02
	7.0 ($\sigma = 13.4\%$)	22	0.29	2.49
	3.2 ($\sigma = 12.3\%$)	4	0.03	0.48

For the very small nanoparticles, the distinction between blocking temperature (T_B) and the temperature of maximum magnetization (T_{max}) becomes less meaningful. This is due to two main factors:

- **Increased spin canting**: As particle size decreases, the spins at the surface become less aligned with the core, leading to a canted spin structure.
- **Higher prevalence of crystalline defects**: Smaller particles tend to have a higher proportion of surface atoms, which can lead to more structural imperfections.

These factors make the traditional models used to describe Zero-Field-Cooled (ZFC) and Field-Cooled (FC) magnetizations less accurate for such small particles. As a result, for these tiny nanoparticles, it is more appropriate to consider T_{max} as the temperature at which the entire distribution of particles enters the superparamagnetic regime.

In other words, T_{max} represents a more reliable indicator of the magnetic behavior transition for these extremely small nanoparticles, rather than trying to distinguish between T_B and T_{max}, which becomes problematic at this scale.

The larger oleic acid (C18)-coated maghemite nanoparticles (12.6 nm) showed a blocking temperature ($T_B(\nu_0)$) of 117 K, which is consistent with literature values for similar-sized C18-coated maghemite nanoparticles [10] [19]. The C12-coated NPs (13.3 nm) exhibited a $T_B(\nu_0)$ of 124 K, while the C8-coated NPs (11.2 nm) had a $T_B(\nu_0)$ of 83 K. For these larger nanoparticles, a trend is evident: as the mean particle size increases, the blocking temperature also increases, which aligns with the theoretical relationship between blocking temperature and particle volume presented in equation 3.2.

For the intermediate-sized nanoparticles, the trend of decreasing blocking temperature with smaller particle size continues. The C18-NPs (7.8 nm), C12-NPs (7.8 nm), and C_8-NPs (7.0 nm) had $T_B(\nu_0)$ values of 45 K, 42 K, and 22 K, respectively. This suggests that both the nanoparticle size and surface coating influence the blocking temperature, with larger particles generally having higher T_B values.

For the smaller nanoparticles with a diameter of around 3.3 nm, the blocking temperature (T_B) was found to be around 5 K (Table 3.3). This low T_B value is mainly due to their very small volume. However, it is also likely influenced by spin canting, which becomes more pronounced as the particle size decreases and further lowers the blocking temperature.

The ZFC curves for the larger and intermediate-sized nanoparticles, passivated with C18, C12, and C8 ligands and normalized to T_{max}, are presented in Figure 3.11. For all nanoparticle sizes, the curve for the C8-NPs appears broader compared to those of the C18 and C12 NPs. This suggests a wider distribution of magnetic anisotropy energy, which can be attributed to the broader size distribution of the C8-NPs in comparison to the C12 and C18 NPs (Table 3.1).

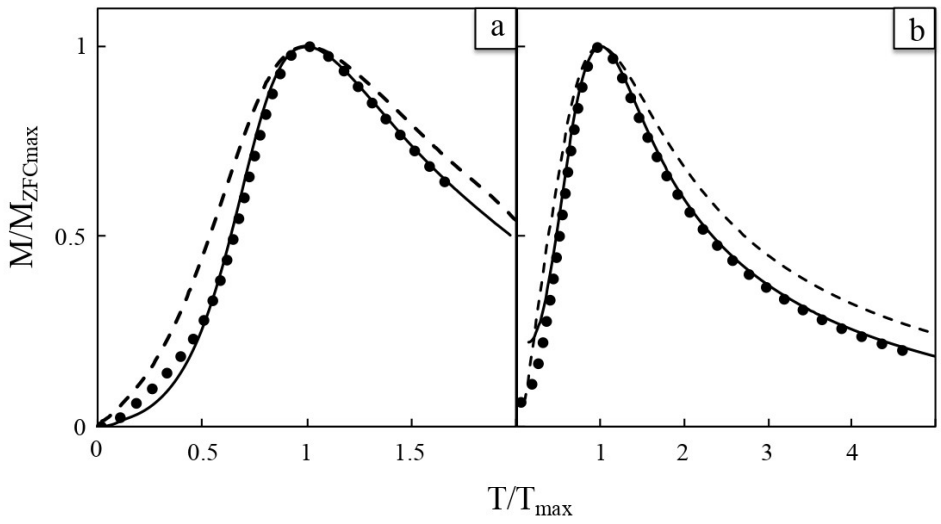

Figure 3.11 – *Zero field magnetization versus temperature curves normalized to Tmax of maghemite nanoparticles synthesized from iron oleate (solid line), iron dodeconoate (full circles), and iron octanoate (dashed line). (a) large-nanoparticle sizes, (b) intermediate-nanoparticle sizes.*

In the FC curves, the magnetization remains higher than in the ZFC curves between 3 K and the blocking temperature (T_B). Once the temperature exceeds T_B, the magnetization begins to decrease and eventually aligns with the ZFC curve. For the larger nanoparticles (Figures 3.10a, d, and g), the FC curves show a relatively flat trend at temperatures below T_B, which suggests the presence of strong dipolar interactions. On the other hand, for intermediate-sized nanoparticles (Figures 3.10b, e, and h) and the small nanoparticles (C18, C12, and C_8) (Figures 3.10c, f, and i), the FC curves demonstrate a more consistent decrease before merging with the ZFC curve above T_B. This indicates that dipolar interactions are less influential in these samples [40]. The stronger dipolar interactions in the larger maghemite nanoparticles, compared to the intermediate and small-sized particles, can be explained in two ways. Firstly, the larger particles underwent a more thorough washing process at the end of the synthesis, which minimized the presence of by-products (such as excess surfactant) in the colloidal solution and reduced the interparticle distance. Secondly, it is well established that dipolar interactions in nanoparticle assemblies become stronger as the particle volume increases [41].

3.7.2 Magnetic Hysteresis Measurements

Hysteresis curves for nine distinct populations of maghemite nanoparticles, varying in both size and surface chemistry, reveal intriguing magnetic properties. These curves, obtained following zero-field-cooled (ZFC) measurements, illustrate how the material's magnetization (M) changes in response to an applied magnetic field (H), as shown in Figure 3.12. Notably, none of the samples achieve saturation magnetization—the maximum possible magnetization of a material—at the maximum applied field ($H_{\max}$) of 3.98×10^6 A·m^{-1}. The larger and intermediate-sized NPs exhibit magnetization curves that approach saturation, while the smallest particles remain far from saturation even at this high field strength. This behavior in the smallest NPs is likely due to a more pronounced spin canting effect, where the magnetic moments of atoms are not perfectly aligned, and the presence of crystalline defects, both of which would require much higher fields to reach saturation.

The magnetic properties of these NPs are further characterized by two key parameters: the ratio of remanent magnetization (the magnetization remaining when the applied field is removed) to magnetization at $H_{\max}$ ($M_r/M_{H_{\max}}$) and the coercive field (H_c, the field strength required to reduce the magnetization to zero after saturation), both of which are listed in Table 3.3. For the larger and intermediate-sized NPs, the $M_r/M_{H_{\max}}$ ratio is found to be approximately 0.4, which closely aligns with the expected value of 0.5 for materials exhibiting uniaxial anisotropy—a property indicating that the material has a preferred direction of magnetization. This alignment with uniaxial anisotropy provides insight into the magnetic behavior and structure of these larger NPs, suggesting a more uniform magnetic orientation compared to their smaller counterparts.

This magnetic behavior aligns well with findings from earlier studies [8] [42]. Regardless of the type of ligand coating, the smaller nanoparticles exhibit a very low remanent magnetization ratio ($M_r/M_{H_{\max}}$), ranging from 0.03 to 0.11. This low ratio can be explained by the fact that the measurement temperature (3 K) is very close to their blocking temperature, which is around 5 K. At this temperature, most of the nanoparticles are in a superparamagnetic state, meaning their magnetic moments fluctuate rapidly and do not remain aligned when the external magnetic field is removed.

The small size of the nanoparticles has two key effects: (1) the measurement temperature is very close to the blocking temperature, and (2) spin canting becomes more significant. These effects can be modeled by adding a component of non-anisotropic NPs ($K_{\text{eff}} = 0$) to the overall distribution. This non-anisotropic component accounts for two factors: the presence of an ultra-soft magnetic phase caused by spin canting and the smallest NPs, which remain in the superparamagnetic regime ($T < T_B$).

To illustrate this concept, we performed Monte Carlo simulations of the hysteresis loop,

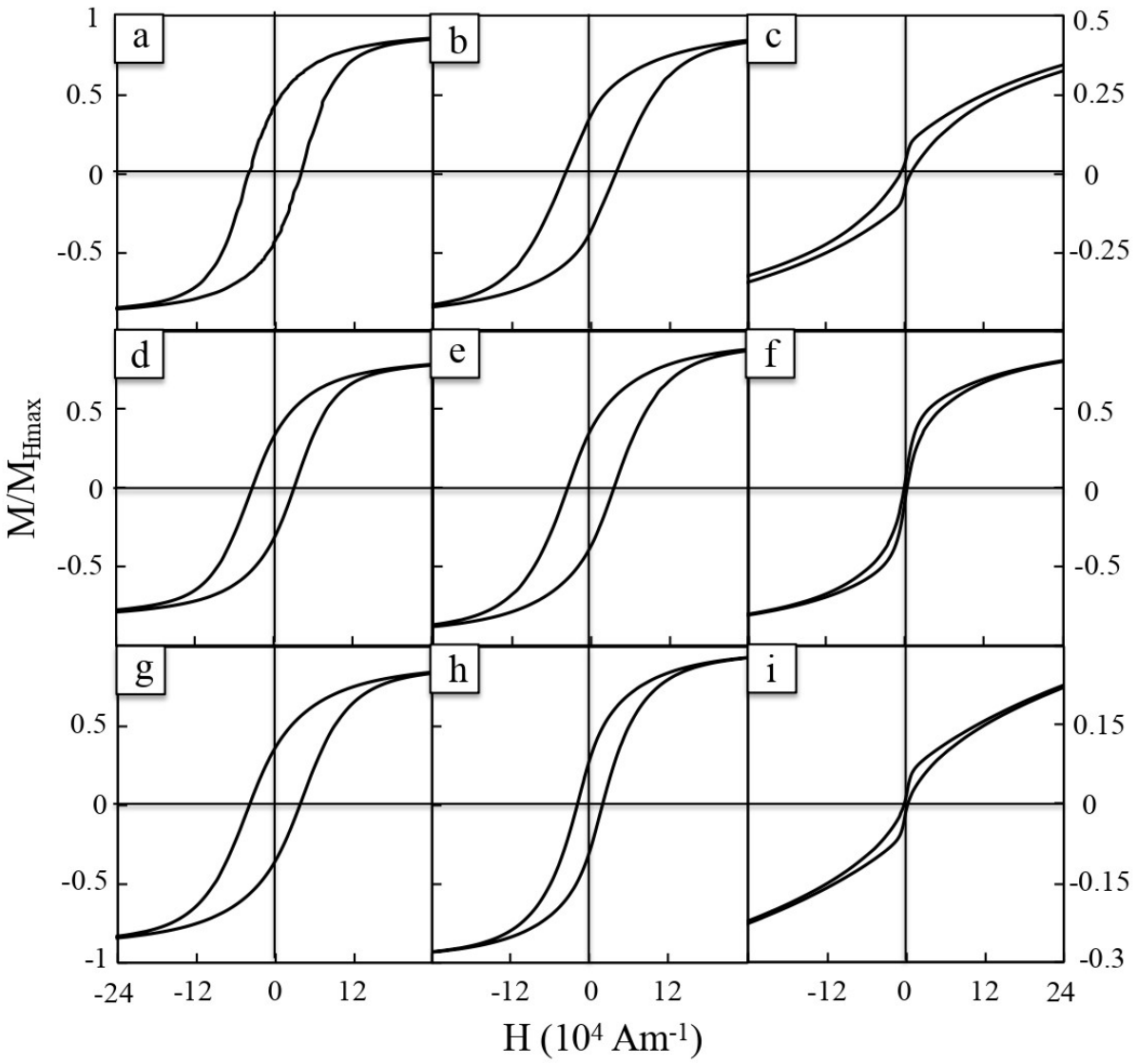

Figure 3.12 – *Hysteresis curves performed at 3 K, of maghemite nanoparticles synthesized from (a,b,c) iron oleate, (d,e,f) iron dodeconoate, and (g,h,i) iron octanoate. The mean diameters are centered on (a,d,g) 12.0 nm, (b,e,g) 7.5 nm and (c,f, i) 3.3 nm.*

presented in Figure 3.13. We compared two cases: one with a single Stoner-Wohlfarth component (representing uniform anisotropy) and another that included a non-anisotropic component. These simulations revealed two key outcomes. First, both the remanent magnetization ratio (M_r/M_s) and coercivity (H_c) are reduced. Second, the hysteresis curves for the C8 and C18 samples could be qualitatively reproduced.

This suggests that the sharp decrease in H_c and the "shoulder" feature observed in the magnetization curves ($M(h)$) of the C8 and C18 samples are signatures of a magnetic multiphase system. In other words, these NP assemblies contain regions with different magnetic behaviors. A similar explanation has been proposed for the hysteresis behavior of

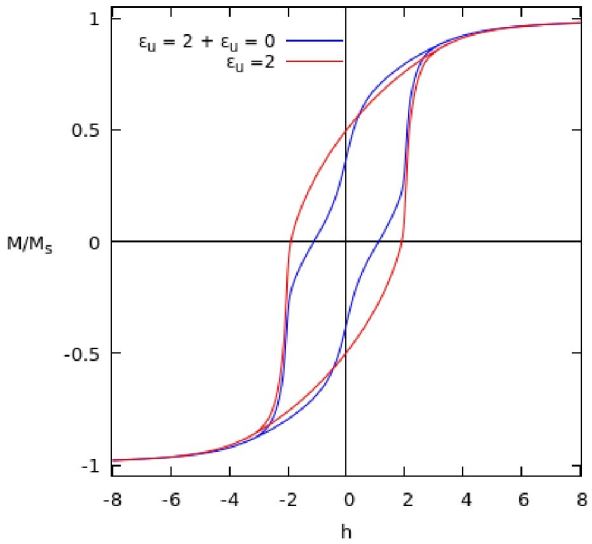

Figure 3.13 – *Monte Carlo simulation of the hysteresis curve of a single Stoner-Wolfarth model with reduced uniaxial anisotropy eu = 2 and mixture including a non-anisotropic component (eu = 0). This model is given only for a qualitative purpose as the value chosen for the reduced anisotropy energy (eu = 2) is not fitted to the experimental samples. The reduced field h is H/Hr where Hr is the reference field Hr = Hk/(2eu) and Hk the usual anisotropy field (2K/(μ_0.Ms)).*

CoPt NPs during annealing [43] [44].

3.8 Conclusion

In this chapter, we presented the first demonstration of low-size polydisperse spherical maghemite nanoparticles synthesized via the thermal decomposition of iron precursors with precise control over both their surface chemistry and diameter.

This was achieved using three types of iron complexes—iron oleate (C18), iron dodecanoate (C12), and iron octanoate (C8)—in combination with fatty acid ligands of matching alkyl chain lengths: oleic acid (C18), dodecanoic acid (C12), and octanoic acid (C8). This dual approach allowed us to systematically explore the influence of precursor and ligand chemistry on nanoparticle formation and properties.

Optimal conditions were identified for the growth of nanoparticles with diameters centered at approximately 3.3 nm, 7.5 nm, and 12.0 nm, depending on the precursor chain length and its thermal decomposition kinetics. These findings underline the significant role of precursor decomposition behavior in controlling NP size.

The magnetic properties of the nine distinct maghemite NP populations, characterized by SQUID magnetometry, provided further evidence of the precise size control achieved in this study. These magnetic characterizations reveal how nanoparticle dimensions influence

their blocking temperature, coercivity, and magnetic anisotropy, adding valuable insights into the interplay between size, surface chemistry, and magnetic behavior.

Looking ahead, future research could explore the impact of ligands with varying chemical structures and chain lengths on the interactions of maghemite NPs with their environment, particularly in applications such as polymer nanocomposites, as highlighted in the introduction. Tailoring ligand chain length not only influences nanoparticle dispersion within a polymer matrix but is also crucial in engineering supercrystals of maghemite NPs. The ability to fine-tune interparticle distances and the three-dimensional crystalline structure of these superlattices could open new avenues in the design of advanced nanomaterials.

Such well-ordered magnetic superlattices hold significant potential for exploring phenomena associated with dipolar interactions in dense assemblies. For instance, highly packed supercrystals may exhibit dipolar superferromagnetism (SFM), a phenomenon that bridges the gap between fundamental physics and advanced materials science. These findings could lead to innovative applications in data storage, spintronics, and other fields relying on controlled magnetic behavior at the nanoscale.

Chapter 4

Reproducibility & Morphology Control

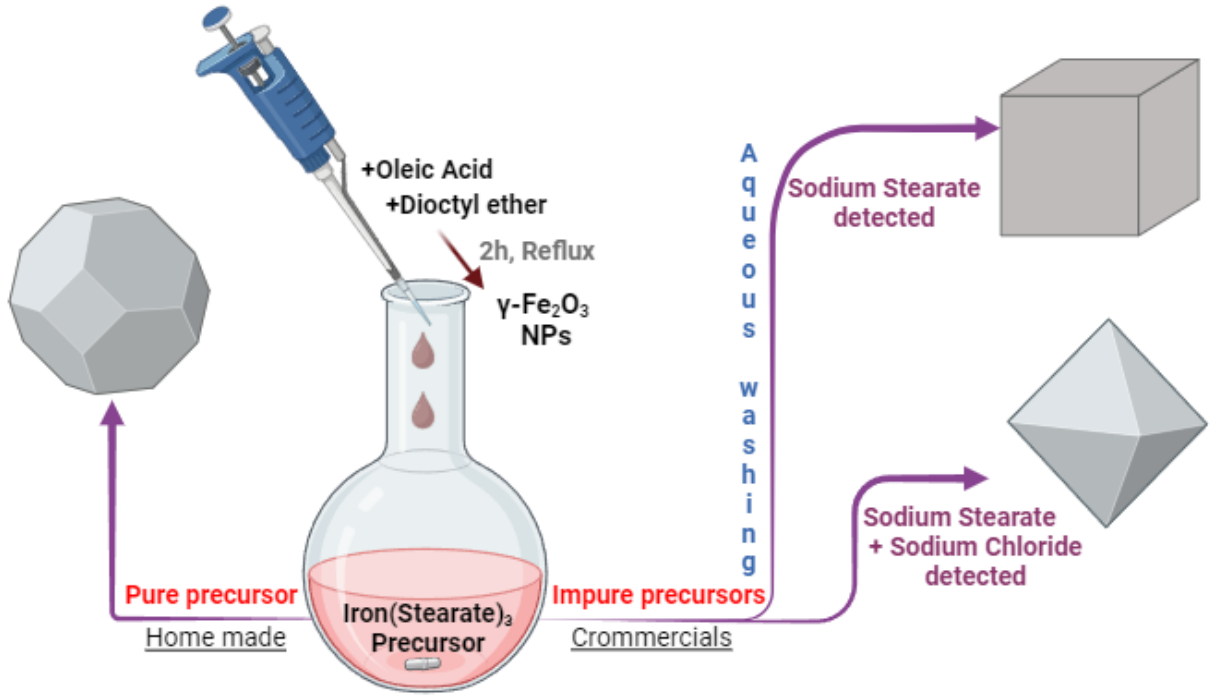

Contents

4.1 Introduction

The synthesis of iron oxide nanoparticles has undergone significant advancements, yet reproducibility remains one of the most persistent challenges in the field. While the primary parameters influencing nanoparticle size and surface chemistry—such as precursor concentration, reaction temperature, and ligand ratios—are well-documented as presented in the previous chapter, many secondary and often-overlooked factors continue to introduce variability. This variability complicates efforts to replicate results, both across different laboratories and within the same experimental conditions. For example, subtle variations in stirring speed or reaction time can lead to discrepancies in nanoparticle size and shape, underscoring the difficulty of standardizing synthesis protocols across the community [45].

Ensuring reproducibility requires meticulous control over a multitude of interdependent parameters, spanning processes at both the atomic and nanoscale. At the atomic scale, factors such as precursor decomposition, solvation of reactants, and adsorption of ligands and salts play critical roles. At the nanoscale, processes like nucleation, growth, and particle aging determine the final morphology and properties of the nanoparticles. A comprehensive understanding of these mechanisms is therefore essential—not only for improving synthesis reliability but also for enabling the discovery of novel nanomaterials.

This chapter focuses on an often-overlooked parameter in IONP synthesis: the origin and purity of precursors. Specifically, it examines how commercially sourced, washed, and homemade iron stearate precursors influence the growth of maghemite nanoparticles. Detailed characterization reveals that impurities present in commercial precursors—such as sodium stearate and sodium chloride—play a decisive role in determining nanoparticle morphology. Depending on the precursor used, the resulting nanoparticles exhibit spherical, cubic, or triangular shapes. These findings highlight a critical issue: attempts to reproduce published synthesis protocols frequently yield inconsistent morphologies due to unaccounted-for impurities.

Additionally, this study emphasizes the importance of identifying and understanding precursor impurities, an aspect rarely addressed in the literature. Such impurities, often introduced during precursor fabrication, significantly alter the nucleation and growth mechanisms of nanoparticles. These findings underscore the need for a more systematic approach to precursor preparation and characterization within the field.

Importantly, the formation of triangular nanoparticles under the synthesis conditions described in this work has not been reported previously. This novel observation adds a new dimension to the understanding of morphology control in IONP synthesis and demonstrates how even seemingly minor variations in precursor composition can lead to unexpected results.

This chapter aims to illuminate the multifactorial and nuanced nature of IONP synthesis, with a particular focus on the hidden variables that must be addressed to overcome reproducibility challenges and advance the field.

4.2 Samples Preparation

4.2.1 Iron Stearate: Commercial and Laboratory-Synthesized Precursors

In this study, we employed a synthesis protocol for iron oxide nanoparticles that utilized iron stearate (FeSt) as the precursor. Iron stearate is an iron carboxylate complex coordinated with stearic acid, a saturated carboxylic acid with an 18-carbon chain. Five types of iron stearate precursors were examined:

1. A commercial iron(II) stearate precursor from Strem Chemicals (9% Fe), as received (P_1);
2. The same iron(II) stearate after an aqueous washing (P_1^W);
3. A commercial iron(III) stearate precursor from TCI (5.8–7% Fe), as received (P_2);
4. The same iron(III) stearate after washing (P_2^W);
5. A laboratory-synthesized iron(III) stearate precursor (P_3).

The laboratory-synthesized iron(III) stearate ($FeSt_3$), referred to as P_3, was prepared through the reaction of sodium stearate (NaSt) with iron(III) chloride ($FeCl_3$) in an aqueous solution, following the protocol reported by Cotin et al. [46]. The synthesis procedure is as follows:

Sodium stearate (9.8 g, 32 mmol) was transferred into a two-necked round-bottom flask and dissolved in 320 mL of ultrapure water. The solution was heated to reflux at 120 °C and stirred for 30 minutes to ensure complete dissolution of the stearate. Separately, iron(III) chloride (2.9 g, 10.7 mmol) was dissolved in 160 mL of ultrapure water and added dropwise to the sodium stearate solution under vigorous stirring. Upon mixing, a light orange precipitate formed immediately.

The reaction mixture was maintained at 120 °C with continuous stirring for an additional 25 minutes before being allowed to cool to room temperature. The precipitate was then thoroughly washed with 4 L of ultrapure water to remove any unreacted salts or impurities. After filtration using a Büchner funnel, the precipitate was oven-dried at 64 °C for 22 hours to yield the final product.

This approach ensured the production of a high-purity iron(III) stearate precursor, serving as a reliable benchmark for comparing the properties and behavior of commercially sourced

precursors.

4.2.2 Synthesis of oleic acid-coated iron oxide nanoparticles

Synthesis of oleic acid-coated γ-Fe_2O_3 nanoparticles was based on the thermal decomposition approach reported in a previous study by Begin-Colin et al., [9] [10] however some with slight modification i.e., a smaller volume of dioctyl ether (10 mL instead of 20 mL) and a higher heating rate (45 °C/min instead of 5 °C/min).

Specifically, 0.69 g (1.1 mmol) of iron (II) stearate ($FeSt_2$) precursor (or 1 g (1.1 mmol) of iron (III) stearate ($FeSt_3$) precursor), and 0.63 g (2.2 mmol) of oleic acid are dissolved in 10 mL of dioctyl ether. This mixture is heated to the boiling point of dioctyl ether (287 °C) with a heating rate of 45 °C/min, refluxed for 2 h, and then cooled to room temperature. A black solution is formed and washed with a large excess of acetone followed by centrifugation (4900 rpm, 5 min). The oleic acid-coated NPs are finally dispersed in chloroform.

Five oleic acid-coated γ-Fe_2O_3 NP syntheses were performed with the same recipe described above with P_1, P_1^w, P_2, P_2^w, and P_3.

The commercial $FeSt_2$ and $FeSt_3$ precursors are washed as follows: 10 g of precursor in powder form is mixed with 150 mL of ultrapure water under vigorous stirring and is heated to 65 °C for 15 min. Then the mixture is cooled to room temperature. The precursor is then washed with 4 L of ultrapure water and filtrated with a Buchner funnel and oven-dried at 64 °C for 22 h.

4.2.3 Precursors and Nanoparticles Characterization

(TEM) Transmission electron microscopy

TEM study is performed using a JEOL JEM-1011 microscope at 100 kV. For this study, some drops of the colloidal solution are deposited on an amorphous carbon-coated TEM grid. The average diameter and the polydispersity of NPs are determined from more than 500 NPs using ImageJ.

(EDS) Dispersive X-ray Spectrometry

The chemical compositions were determined by energy dispersive X-ray spectrometry (EDS) analysis using a scanning electron microscope (SEM, JEOL 5510 LV, Ltd, Tokyo, Japan) with IXRF Systems 500 digital processing.

(XRD) X-ray Diffraction

Powder X-ray diffraction (PXRD) diffractograms were recorded on a D8 DISCOVER of a Bruker XRD machine with a copper tube operating at 40 kV. All the samples were in the form of powder by which low background silicon sample holders were filled.

(VSM) Vibrating Sample Magnetometry

Magnetic measurements were conducted using a Quantum Design vibrating sample magnetometer (VSM) with a field of 20 Oe for the zero-field-cooled (ZFC) and field-cooled (FC) susceptibility curves, and with fields up to 5 T for the magnetization curves. All magnetic measurements were performed on a film of powdered iron oxide nanoparticles (NPs). During the measurement, the applied field was parallel to the iron oxide NP film.

For the ZFC measurements, the sample was cooled from 300 to 3 K with no field and then heated to 300 K in a field of 20 Oe to record the magnetization $M_{\mathrm{ZFC}}(T)$ of the sample. For the FC measurements, the sample was cooled again to 3 K under the same applied field, and the magnetization $M_{\mathrm{FC}}(T)$ was recorded. In both cases, the measurements were performed during heating with a heating rate on the order of 1 K min^{-1}. The measurement time was approximately 1 s. The hysteresis curves were obtained at 3 K.

4.3 TEM analysis for Size and Morphology

4.3.1 Synthesis of IONPs using precursors $\mathbf{P}_1$ and $\mathbf{P}_1^w$

Figure 4.1a and 4.1b show the TEM images of γ-Fe_2O_3 NPs synthesized using commercial grade iron (II) stearate ($FeSt_2$), P_1. Low and high-magnification images reveal a population composed of almost uniform NPs with triangular shape. The corresponding size histogram Figure 4.1d, shows a mean triangle height and a size polydispersity of 9.7 nm and 16% respectively. Surprisingly, the synthesis performed with the same precursor but after being washed, P_1^w, leads to a single population of nanocubes. As shown in Figure 4.1e and 4.1f, they are characterized by flat facets and sharp edges and their mean side diagonal is 10.5 nm. Thanks to a very low size polydispersity, 11% Figure 4.1h, they tend to self-organize in 2D superlattices.

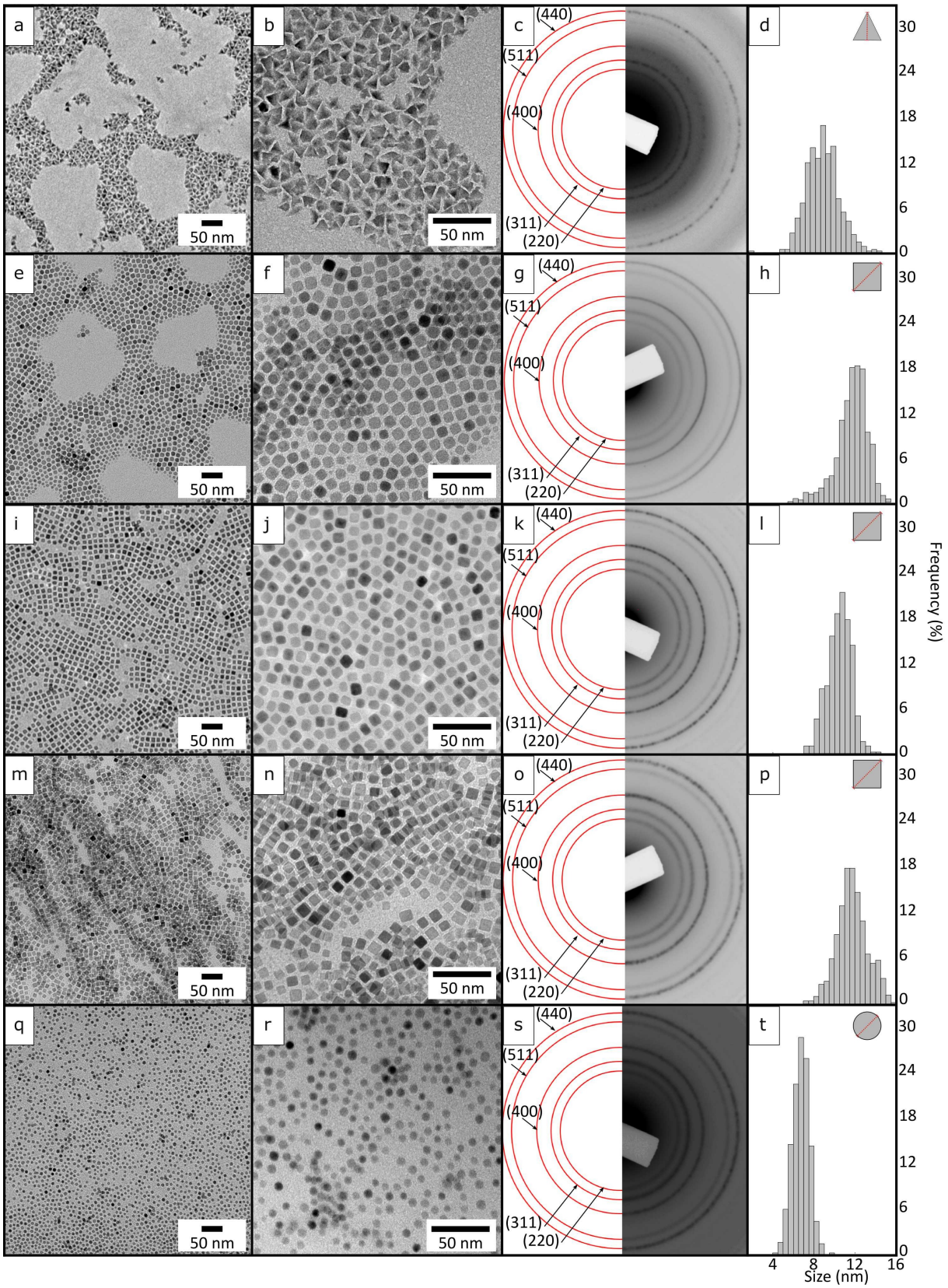

Figure 4.1 – *TEM images, corresponding electron diffraction patterns, and size histograms of maghemite (γ-Fe_2O_3) nanoparticles synthesized with P_1 (a,b,c,d), P_1^w (e,f,g,h), P_2 (i,j,k,l), P_2^w (m,n,o,p) and P_3 (q,r,s,t) precursors.*

4.3.2 Synthesis of IONPs using precursors P_2 and P_2^w

Replacing iron (II) stearate ($FeSt_2$) precursor P_1 with iron (III) stearate ($FeSt_3$) precursor P_2, while keeping other chemical components the same, results in a drastic change in the NP shape. Considering the as-received precursor (not washed), Figure 4.1i and 4.1j clearly show that the population is made of nanocubes and not nanotriangles, which have rather similar characteristics compared to the sample prepared with the precursor P_1, i.e., a mean side diagonal and size polydispersity of 11.7 nm and 13% respectively Figure 4.1l. In this case, no washing effect on this precursor is observed as the population obtained with P_2^w, remains composed of nanocubes Figure 4.1m and 4.1n with similar mean side diagonal and size polydispersity of 11.7 nm and 11.7% respectively (Figure 4.1p).

4.3.3 Synthesis of IONPs using NPs using precursor P_3

Finally, using a precursor we synthesized in the laboratory iron (III) stearate ($FeSt_3$), P_3, a single population of spherical γ-Fe_2O_3 NPs form Figure 4.1q and 4.1r. The size histogram (Figure 4.1t) shows a mean diameter of 6.7nm with a size polydispersity of 12%.
From previous studies reported in the literature [8] [9] [10] [11] [46], a similar approach used to synthesize maghemite NPs induces the formation of spherical ones. In our study, we find that spherical NPs are only formed with the use of the home-made precursor P_3 and never with the commercial ones (as-received and washed). In addition, our results clearly evidence a drastic impact of both the supplier and the washing of the commercial product in the anisotropic shape of NPs. To understand this puzzling result, elemental analysis and X-ray diffraction studies have been performed for the different precursors to determine the possible impurities qualitatively and quantitatively, which could explain the differences we observe in the NP growth that in turn their final shape.

4.4 SAED and XRD Analysis of the IONPs Crystal Structure

4.4.1 Selected Area Electron Diffraction

The crystalline structure of the five populations of NPs obtained with P_1, P_2, P_1^w, and P_2^w and P_3 precursors have been investigated by the selected area electron diffraction (SAED). Whatever the precursor used and the shape of the NPs are, the electron diffraction patterns Figure 4.1c,g,k,o and s show five rather thin diffraction rings at 1.47, 1.60, 2.08, 1.51, and 2.95 Å corresponding to the (440), (511), (400), (311), and (220) planes of a maghemite iron oxide phase according to the JCPD 39–1346 database. However, it is important to note

that the lattice spacings of the maghemite and magnetite phases are very close. This is thus difficult to conclude that our samples consist of pure maghemite. To address this uncertainty, the X-ray diffraction technique has been used to gain a more comprehensive understanding of the crystal structures of our NPs.

4.4.2 X-ray Diffraction

To discriminate between magnetite and maghemite phases of the iron oxide nanoparticles synthesized by using the different precursors P_1^w, P_2, P_2^w and P_3, we follow the method developed by Kim et al. [47] based on the X-ray analysis. The X-ray corresponding patterns are presented in Figure 4.2. For all the samples, we detect the peaks characteristic of maghemite or magnetite, i.e., while peaks corresponding to hematite and wüstite are noticeably absent. The two peaks (210) and (211), which are the signature of exclusive maghemite are observed for the spherical and cubic NPs obtained with the precursors P_3 and P_2^w respectively. The cubic NPs synthesized with P_2 precursor show the (210) peak but not the (211) peak while the cubic NPs obtained with the P_1^w show the opposite trend. The presence of the (210) and/or (211) peaks, coexisting with the others ((220), (311), (400), (422), (511), (440)), is indicative of either pure maghemite or a mixture of maghemite and magnetite. However, as reported by Kim et al. [47], the position of the peak (511) is essential as it allows to discriminate between magnetite and maghemite phases. Indeed, they show that the (511) peak shifts from 57° to 57.3° from pure magnetite to pure maghemite phase. In the case of a combination of both phases, they observe a larger peak, with a shoulder, composed of the lower and the higher angle peak [47]. As shown in the inset of 4.2, which represents the magnified regions between 50° and 60° of the diffraction patterns, all the (511) peaks are found at a value 2 Theta of 57.3° and appear symmetric. No shoulder characteristic of a mixture of maghemite and magnetite is observed. This feature, which agrees with the presence of the (210) and/or (211) peaks, allows us to conclude the formation of pure maghemite NPs for the spherical and cubic NPs obtained with the P_1^w, P_2, P_2^w, and P_3 precursors. Unfortunately, the triangular colloidal NP solution obtained with the P1 precursor, could not be studied by XRD. This is explained by the too-low concentration of the colloidal solution. Indeed, we noticed that the triangular NP powder appears light red, in contrast to the black color of the other shape samples. This color variation is attributed to the presence of the precursor (color and texture). The low concentration of this population is explained by the low yield of this thermal decomposition reaction. However, the electron diffraction signature of the triangle NPs is like that of the spherical and cubic NPs. This permits us to conclude the formation of maghemite triangular NPs.

In summary, thanks to a comprehensive structural study with both electron and/or X-ray

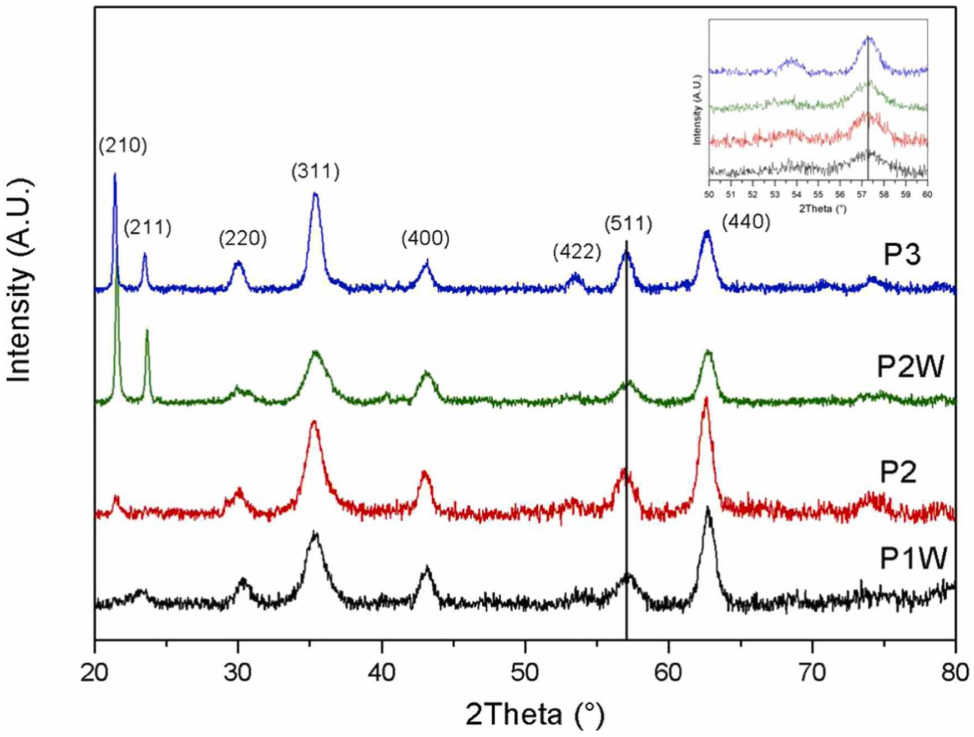

Figure 4.2 – *XRD patterns of nanoparticles synthesized with P_1^w, P_2, P_2^w, and P_3 precursors. Inset: magnified regions between 50° and 60° of the diffraction patterns.*

diffraction techniques, we conclude the formation of pure maghemite for the spherical, cubic, and triangular NPs synthesized with the P_1, P_1^w, P_2, P_2^w, and P_3 precursors. This result evidences that the impurities involved in the reaction, through the precursor, do not impact the crystalline structure of the iron oxide NPs. Conversely, it has a drastic effect on NP growth and therefore on the final shapes.

4.5 Elemental Analysis of P_1, P_1^w, P_2, P_2^w, and P_3 Precursors

Elemental analysis spectra performed for the five precursors are shown in Figure 4.3. In addition to the iron, and while not expected, sodium and chlorine elements are detected for the commercial precursors. The relative atomic composition of the three elements obtained by quantification of the spectra is reported in Table 4.1. If we focus on the precursor P_1 from Strem Chemicals, it appears that it contains a high atomic percent of sodium elements, 48%. After its washing, (P_1^w), this value remains almost unchanged, 49%. Besides, 27% of chloride is detected on the as-received precursor while this value drops to 3% after its washing (P_1^w). Concerning the TCI commercial precursor, P_2, it also contains a high atomic percent of sodium elements, 34%, however only 14% of chloride is detected. P_2 washing mainly induces the drop of this last value to 4%. The same analysis performed on the home-made

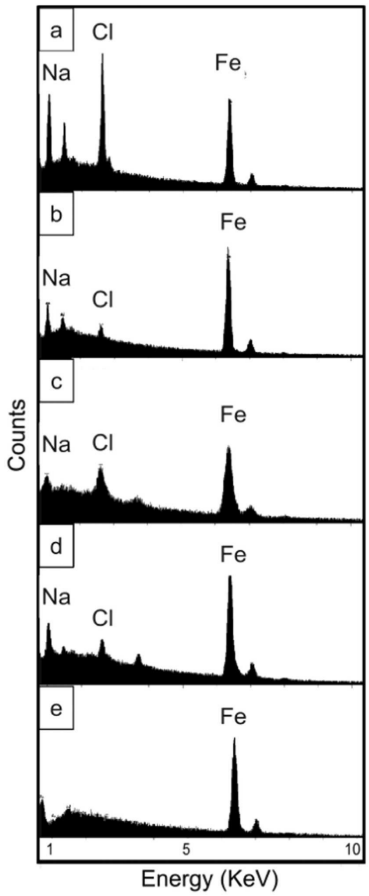

Figure 4.3 – *EDX patterns of P_1 (a), P_1^w (b), P_2 (c), P_2^w (d), and P_3 (e) precursors*

precursor (P_3) clearly shows that neither sodium nor chloride are detected.

	Atom%		
Precursor	Fe	Na	Cl
P_1	25	48	27
P_1^W	48	49	3
P_2	52	34	14
P_2^W	58	38	4
P_3	100	0	0

Table 4.1 – *Relative atomic percentage of Fe, Na and Cl of P_1, P_1^w, P_2, P_2^w, and P_3 precursors.*

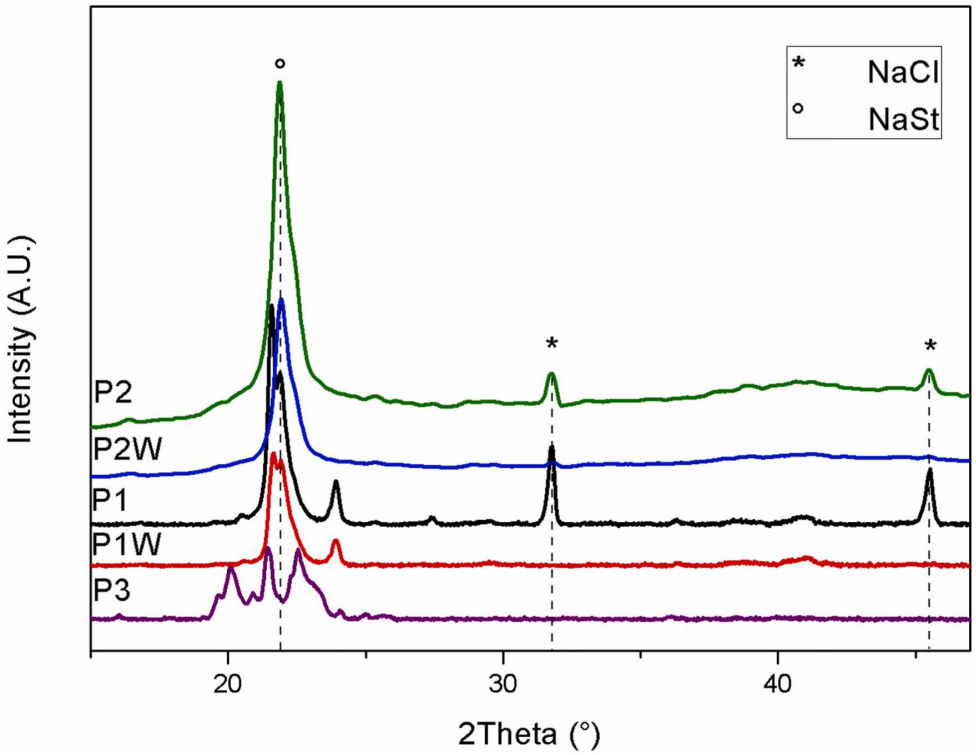

Figure 4.4 – *XRD patterns of P_1, P_1^w, P_2, P_2^w, and P_3 precursors.*

4.6 X-ray Diffraction Analysis of P_1, P_1^w, P_2, P_2^w, and P_3 Precursors

To determine the nature of the compounds present in the commercial P_1, P_1^w, P_2, P_2^w, and P_3 precursors, an X-ray diffraction study has been performed. The XRD diffractograms are shown in Figure 4.4.

For P_1 and P_2 precursors, one can detect two peaks at 31.7°, and 45.5° (marked with *) corresponding to the (200) and (220) plane reflections respectively, of NaCl salt [48]. After their washing, (P_1^w, P_2^w), these peaks are not anymore observed. If we focus on the smaller angle diffraction pattern, and for all the commercial precursors, P_1, P_1^w, P_2, and P_2^w, one intense peak at around 22° (marked with °) is observed. This peak is attributed to NaSt [49]. The XRD pattern of the home-made precursor (P_3) is characteristic of the pure lamellar structure $Fe(St)_3$ without any evidence of the presence of neither NaCl nor NaSt.
This XRD study is in good agreement with the elemental analysis. The presence of NaCl and NaSt is evidenced in the two as-received commercial precursors. After their washing, NaCl salt disappears. Finally, the home-made precursor is characterized by pure $FeSt_3$.

4.7 How to explain the presence of the detected impurities in the commercial precursors?

The results obtained by chemical and XRD analyses are interpreted as the following. The home-made precursor, P_3, has been synthesized in the stoichiometric conditions of the reaction:

$$FeCl_3 + 3NaSt \rightarrow FeSt_3 + 3NaCl$$

i.e., 3 sodium stearates for 1 iron chloride (see experimental section). Once the iron precursor is obtained, the solution is washed with a large amount of ultrapure water (4L) to remove the totality of the amount of sodium and chloride ions by-products. Considering the chemical analysis Table 4.1, the absence of detection of these two by-products confirms that the iron precursor P_3 obtained is pure.

Conversely, for the as-received (not washed) commercial precursor P_1, a large amount of sodium and chloride ions are detected Table 4.1. In addition, we note that the amount of sodium (48%) is higher compared to that of chloride ions (27%). This result makes us suggest that first, P_1 synthesis has not been performed in the stoichiometric conditions of the reaction but with a ratio of the sodium stearate to the chloride iron concentration higher than 3, leading to the presence of remaining sodium stearate and sodium chloride as by-products. Second, the washing step of the solution has not been optimal, otherwise, chloride ions would not be present. Our explanation is confirmed through the analysis of the precursor after its washing with 4L of ultrapure water P_1^w. The amount of detected chloride drops from 27% to 3%, while that of sodium ions remains high (49%) Table 4.1. Conversely to the chloride ions, sodium ions cannot be removed during the washing with water as it forms the sodium stearate complex, which is not soluble in water. So, one can conclude that the P_1^w precursor contains a mixture of iron and sodium stearate in almost equal concentrations.

For the as-received commercial precursor P_2 (not washed), sodium (34%) and chloride (14%) are also detected Table 4.1. After its washing, the amount of chloride drops to 4%. Similar findings as for P_1 apply. However, the lower amount of sodium and chloride compared to P_1 suggests that P_2 has been produced in closer stoichiometric conditions compared to the synthesis of P_1 .

4.8 Interpretation of the γ-Fe_2O_3 nanoparticle shape, in light of the nature of the impurities detected in the commercial iron stearate precursors

In light of the chemical and XRD analyses, the variety of maghemite NP shapes obtained can only be explained in terms of the purity of the iron precursors. All the other synthesis conditions are equal (ligand, solvent, heating rate, temperature, and reflux time).

When the synthesis is performed with the home-made iron stearate precursor (pure), oleic acid plays the role of universal stabilizer on each facet of the NPs, and the final NPs are spherical. In the literature, this behavior is well illustrated in several papers [9] [10] reporting the formation of spherical iron oxide NPs by the thermal decomposition of iron stearate in the presence of oleic acid, without any additives. Begin-Colin et al. have evidenced that, regardless of the number of stearate chains of the iron precursor, $FeSt_2$ or $FeSt_3$ leads to spherical NPs [46] [50] . It is noteworthy that spherical iron oxide NPs have also been obtained with oleate precursors, always in the presence of oleic acid and without any additives [6] [19] .

Conversely, when additives are present in the reaction medium, anisotropic NP growth can occur, resulting from their selective adsorption on the NP facets. For example, the addition of sodium oleate is expected to lead to cubic iron oxide NPs [23] [51] [52] [53] [54] . In this case, nanocubes are induced by the selective adsorption of the sodium oleate on the 100 facets of iron oxide. This induces the faster growth of the NP along the [111] direction over the [100] leading to surfaces composed of 100 facets. Comparative studies show, without any ambiguity, that the same approach performed in the absence and the presence of sodium oleate, gives rise to spherical and cubic NPs respectively [23] [54] . Therefore, one can conclude that cubic NP growth formed by using the commercial precursors (P_1^w, P_2, and P_2^w), could be determined by the key role played by the sodium stearate.

The formation of the triangular NPs (tetrahedral geometry), is more puzzling. Chemical analysis indicates that the precursor P_1, yielding this shape, contains both sodium stearate and NaCl salt. Sodium stearate, here, is expected to bind to the 100 facets of iron oxide to form cubic NPs and then, does not seem to play a role in the formation of triangular NPs. However, it has been reported by Kovalenko et al. [23] that the thermal decomposition of iron oleate in the presence of sodium oleate gives rise to either nanocubes or a mixture of nanocubes and bipyramidal NPs. The first ones are obtained with a $NaOL/Fe(OL)_3$ molar ratio of 1 and a heating rate of 3.3°C/min. The second ones are formed using similar growth conditions as for cubes, but by decreasing the NaOL/Fe(OL)3 molar ratio to 0.67 and by reducing the heating rate to 1°C/min. Besides, using the same approach with iron

oleate precursor and sodium oleate ligand, Zhou et al. [52] observed, in mild conditions (with octadecene as solvent), the formation of Fe3O4 111 facet exposed tetrahedrons, while in a higher boiling temperature solvent (tri-n-octylamine), they form nanocubes. These two examples indicate that sodium oleate may play various roles in different conditions. Concerning our study, the question is "Does the presence of NaCl in the commercial precursor P_1, could favor such a versatility of the role of sodium stearate?" At this moment, this question remains open. Otherwise, another question arises regarding the role played by Cl^- or Na^+ ions, in excess in the precursor P_1. Gao et al. [55] have shown that Cl^- adsorbs on the 100 facets of magnetite-yielding nanocubes. If we focus on the tetrahedral geometry, one hypothesis is that Na^+ ions selectively adsorb on the 111 facets of maghemite. This strategy is not excluded in a previous study reported by Liz-Marzan [54]. Besides, in a previous study performed in the laboratory, the use of Cl^- and Br- ions has been shown to control the shape of copper NPs from nanorods to nanocubes [56]. Therefore, it is reasonable to think that either sodium stearate and/or Na^+, Cl^- ions, could be the key parameters in the growth of the triangular maghemite NPs.

4.9 Does the nature of the precursor, $FeSt_2$ and $FeSt_3$ play a role in the growth of cubic and triangular maghemite nanoparticles?

In recent papers, Begin-Colin et al. have reported the role played by the number of stearate chains (2 and 3) of the iron stearate precursors on the growth of iron oxide nanoparticles [46] [50] [57] [58] . They have studied the influence of the ratio sodium oleate (NaOL) / oleic acid (OA) with $FeSt_2$ and $FeSt_3$ iron stearate precursors differing by their hydration state, on the shape of nanoparticles. The authors demonstrate clearly, the important role played by the presence of NaOL on the NP shape. Nanospheres are obtained in the absence of NaOL, i.e., with only OA. Facetted shapes are obtained, when NaOL is added, even at low concentration. They also show that the evolution of the shape with the amount of NaOL can depend on the nature of the precursor, $FeSt_2$ and $FeSt_3$, and on their hydration degree. For the NaOL/OA ratio (20/80), less-rounded NPs are obtained for all precursors. When this ratio increases, $FeSt_2$ and dehydrated $FeSt_2$ are allowed to obtain nanoplates while $FeSt_3$ and dehydrated $FeSt_3$ lead to nanocubes. The change in the NP shape is explained in terms of the thermal stability of the precursors, which differs from $FeSt_2$ to $FeSt_3$ iron stearate precursors.

In our study, we evidence that maghemite nanocubes are obtained with both $FeSt_2$ washed (P_1^w) and $FeSt_3$ washed and not washed (P_2^w, P_2) precursors. In addition, for all three cases, we identify a constant environment, i.e., the presence of sodium stearate (see 4.7), which

is known to drive the nanoparticle growth toward the cubic shape. This result thus does not allow us to conclude an effect of the nature of the stearate precursor on the NP shape. However, it evidences the crucial role played by the presence of sodium stearate in the formation of maghemite nanocubes.

Focusing on the triangular maghemite NPs, we show in this paper that they are obtained with $FeSt_2$ not washed (P_1) precursor in the presence of NaSt, Na^+, and Cl^- ions. However, the same precursor, $FeSt_2$ washed (P_1^w) leads to nanocube growth. In addition, the triangular NPs are only obtained in the presence of NaSt, Na^+, and Cl^- while the nanocubes are obtained in the presence of NaSt. This behavior makes us conclude with the importance of the "impurities" in the formation of the triangles rather than the role played by the nature of the precursor.

Therefore, from the study presented in this paper, a possible impact of the nature of the precursor on the growth of anisotropic shape NPs cannot be evidenced.

This study clearly shows that the supplier, i.e., the purity of the iron stearate, must be considered in the reproducibility of maghemite NP syntheses. This constitutes another key parameter in the formation of NPs. Such finding has already been reported for other colloidal syntheses for example [59] and constitutes an impediment to the development of NPs as well as to the understanding of the growth mechanisms involved in these syntheses.

4.10 18-Carbon Chain Precursors: Nanoparticle Size Reproducibility of Iron Oleate versus Iron Stearate

In contrast to the approach described in Chapter 3—where iron oleate, dodecanoate, and octanoate were employed to investigate the effect of carbon chain length (with only oleate containing a double bond) on nanoparticle growth mechanisms and characteristics—this chapter introduces the use of homemade iron stearate.

Preliminary observations indicated that the synthesized iron stearate was of high purity and generally produced nanoparticles with a spherical morphology. However, the resulting nanoparticle sizes showed poor reproducibility across different synthesis batches. It is important to note that the origin of this lack of reproducibility was not systematically investigated in the present work.

By contrast, iron oleate demonstrated more reliable control over particle size under comparable synthesis conditions. Therefore, iron oleate was preferred for experiments where reproducibility in nanoparticle size was essential.

4.11 Conclusion

In the literature, the thermal decomposition of commercial iron stearate precursors in the presence of oleic acid and in the absence of additives typically yields spherical iron oxide nanoparticles. This provides a well-established baseline for nanoparticle morphology under standard synthesis conditions.

However, our study reveals that using similar commercial iron precursors—whether washed or unwashed—no longer leads to spherical nanoparticles. Instead, we observe the formation of uniform and monodisperse populations of cubic or triangular maghemite nanoparticles. This demonstrates that subtle variations in precursor purity can drastically affect nanoparticle shape.

Through precise chemical and structural analyses (including XRD), we identified the presence of sodium stearate and sodium chloride as "impurities" in the precursors. Their presence explains not only the formation of cubic nanoparticles but also introduces a novel route toward the synthesis of triangular maghemite nanoparticles—a morphology rarely documented and poorly understood in the literature.

These triangular nanoparticles hold strong potential due to their unexplored magnetic behavior, which could lead to new applications. Future work will aim to decipher their growth mechanism in detail to finely tune their structural properties and gain insight into their unique magnetic features.

Bibliography

[1] S. Sheng, W. Liu, K. Zhu, K. Cheng, K. Ye, G. Wang, D. Cao, and J. Yan, "Fe3o4 nanospheres in situ decorated graphene as high-performance anode for asymmetric supercapacitor with impressive energy density," *Journal of colloid and interface science*, vol. 536, pp. 235–244, 2019.

[2] F. Rajabi, A. Pineda, S. Naserian, A. M. Balu, R. Luque, and A. A. Romero, "Aqueous oxidation of alcohols catalysed by recoverable iron oxide nanoparticles supported on aluminosilicates," vol. 15, no. 5, pp. 1232–1237. Number: 5 Publisher: The Royal Society of Chemistry.

[3] M. D. Nguyen, H.-V. Tran, S. Xu, and T. R. Lee, "Fe3o4 nanoparticles: Structures, synthesis, magnetic properties, surface functionalization, and emerging applications," vol. 11, no. 23, p. 11301. Number: 23 Publisher: Multidisciplinary Digital Publishing Institute.

[4] R. G. D. Andrade, S. R. S. Veloso, and E. M. S. Castanheira, "Shape anisotropic iron oxide-based magnetic nanoparticles: Synthesis and biomedical applications," vol. 21, no. 7, p. 2455. Number: 7 Publisher: Multidisciplinary Digital Publishing Institute.

[5] S. Sun and H. Zeng, "Size-controlled synthesis of magnetite nanoparticles," *Journal of the American Chemical Society*, vol. 124, no. 28, pp. 8204–8205, 2002.

[6] N. R. Jana, Y. Chen, and X. Peng, "Size-and shape-controlled magnetic (cr, mn, fe, co, ni) oxide nanocrystals via a simple and general approach," *Chemistry of materials*, vol. 16, no. 20, pp. 3931–3935, 2004.

[7] F. X. Redl, C. T. Black, G. C. Papaefthymiou, R. L. Sandstrom, M. Yin, H. Zeng, C. B. Murray, and S. P. O'Brien, "Magnetic, electronic, and structural characterization of nonstoichiometric iron oxides at the nanoscale," *Journal of the American Chemical Society*, vol. 126, no. 44, pp. 14583–14599, 2004.

[8] A. Demortiere, P. Panissod, B. Pichon, G. Pourroy, D. Guillon, B. Donnio, and S. Bégin-Colin, "Size-dependent properties of magnetic iron oxide nanocrystals," *Nanoscale*, vol. 3, no. 1, pp. 225–232, 2011.

[9] M. Pauly, B. P. Pichon, P. Panissod, S. Fleutot, P. Rodriguez, M. Drillon, and S. Begin-Colin, "Size dependent dipolar interactions in iron oxide nanoparticle monolayer and multilayer langmuir–blodgett films," *Journal of Materials Chemistry*, vol. 22, no. 13, pp. 6343–6350, 2012.

[10] W. Baaziz, B. P. Pichon, S. Fleutot, Y. Liu, C. Lefevre, J.-M. Greneche, M. Toumi, T. Mhiri, and S. Begin-Colin, "Magnetic iron oxide nanoparticles: reproducible tuning of the size and nanosized-dependent composition, defects, and spin canting," *The Journal of Physical Chemistry C*, vol. 118, no. 7, pp. 3795–3810, 2014.

[11] W. Baaziz, B. P. Pichon, J.-M. Grenèche, and S. Begin-Colin, "Effect of reaction environment and in situ formation of the precursor on the composition and shape of iron oxide nanoparticles synthesized by the thermal decomposition method," *CrystEngComm*, vol. 20, no. 44, pp. 7206–7220, 2018.

[12] J. Park, J. Joo, S. G. Kwon, Y. Jang, and T. Hyeon, "Synthesis of monodisperse spherical nanocrystals," *Angewandte Chemie International Edition*, vol. 46, no. 25, pp. 4630–4660, 2007.

[13] L. Wu, A. Mendoza-Garcia, Q. Li, and S. Sun, "Organic phase syntheses of magnetic nanoparticles and their applications," *Chemical reviews*, vol. 116, no. 18, pp. 10473–10512, 2016.

[14] H. S. Dehsari, A. H. Ribeiro, B. Ersöz, W. Tremel, G. Jakob, and K. Asadi, "Effect of precursor concentration on size evolution of iron oxide nanoparticles," *CrystEngComm*, vol. 19, no. 44, pp. 6694–6702, 2017.

[15] A. Blivi, F. Benhui, J. Bai, D. Kondo, and F. Bédoui, "Experimental evidence of size effect in nano-reinforced polymers: Case of silica reinforced pmma," *Polymer Testing*, vol. 56, pp. 337–343, 2016.

[16] F. S. N. Oliva, M. Sahihi, L. Lenglet, A. Ospina, E. Guenin, A. Jaramillo-Botero, W. A. Goddard III, and F. Bedoui, "Nanoparticle size and surface chemistry effects on mechanical and physical properties of nano-reinforced polymers: The case of pvdf-fe3o4 nano-composites," *Polymer Testing*, vol. 117, p. 107851, 2023.

[17] M. Sahihi, A. Jaramillo-Botero, W. A. Goddard III, and F. Bedoui, "Interfacial interactions in a model composite material: Insights into $\alpha \rightarrow \beta$ phase transition of the magnetite reinforced poly (vinylidene fluoride) systems by all-atom molecular dynamics simulation," *The Journal of Physical Chemistry C*, vol. 125, no. 39, pp. 21635–21644, 2021.

[18] F. Bedoui, M. Sahihi, A. Jaramillo-Botero, and W. A. Goddard III, "Enhancing multifunctionality: Optimal properties of iron-oxide-reinforced polyvinylidene difluoride unveiled through full atom molecular dynamics simulations," *Langmuir*, vol. 40, no. 15, pp. 8067–8073, 2024.

[19] J. Park, K. An, Y. Hwang, J.-G. Park, H.-J. Noh, J.-Y. Kim, J.-H. Park, N.-M. Hwang, and T. Hyeon, "Ultra-large-scale syntheses of monodisperse nanocrystals," *Nature materials*, vol. 3, no. 12, pp. 891–895, 2004.

[20] L. M. Bronstein, X. Huang, J. Retrum, A. Schmucker, M. Pink, B. D. Stein, and B. Dragnea, "Influence of iron oleate complex structure on iron oxide nanoparticle formation," *Chemistry of materials*, vol. 19, no. 15, pp. 3624–3632, 2007.

[21] T. Balakrishnan, M.-J. Lee, J. Dey, and S.-M. Choi, "Sub-nanometer scale size-control of iron oxide nanoparticles with drying time of iron oleate," *CrystEngComm*, vol. 21, no. 27, pp. 4063–4071, 2019.

[22] S. Meftah, A.-T. Ngo, A. Shahmanesh, A. Courty, D. Kondo, F. Bedoui, and I. Lisiecki, "Striking effect of the iron stearate purity on the shape and size of maghemite nanoparticles," *Colloids and Surfaces A: Physicochemical and Engineering Aspects*, vol. 680, p. 132689, 2024.

[23] M. V. Kovalenko, M. I. Bodnarchuk, R. T. Lechner, G. Hesser, F. Schäffler, and W. Heiss, "Fatty acid salts as stabilizers in size-and shape-controlled nanocrystal synthesis: the case of inverse spinel iron oxide," *Journal of the American Chemical Society*, vol. 129, no. 20, pp. 6352–6353, 2007.

[24] R. Hufschmid, H. Arami, R. M. Ferguson, M. Gonzales, E. Teeman, L. N. Brush, N. D. Browning, and K. M. Krishnan, "Synthesis of phase-pure and monodisperse iron oxide nanoparticles by thermal decomposition," *Nanoscale*, vol. 7, no. 25, pp. 11142–11154, 2015.

[25] W. Y. William, J. C. Falkner, C. T. Yavuz, and V. L. Colvin, "Synthesis of monodisperse iron oxide nanocrystals by thermal decomposition of iron carboxylate salts," *Chemical communications*, no. 20, pp. 2306–2307, 2004.

[26] Y. Zhu, F. Jiang, K. Chen, F. Kang, and Z. Tang, "Size-controlled synthesis of monodisperse superparamagnetic iron oxide nanoparticles," *Journal of alloys and compounds*, vol. 509, no. 34, pp. 8549–8553, 2011.

[27] P. Guardia, N. Pérez, A. Labarta, and X. Batlle, "Controlled synthesis of iron oxide nanoparticles over a wide size range," *Langmuir*, vol. 26, no. 8, pp. 5843–5847, 2010.

[28] J. M. Vargas and R. D. Zysler, "Tailoring the size in colloidal iron oxide magnetic nanoparticles," *Nanotechnology*, vol. 16, no. 9, p. 1474, 2005.

[29] C. Moya, X. Batlle, and A. Labarta, "The effect of oleic acid on the synthesis of fe 3- x o 4 nanoparticles over a wide size range," *Physical Chemistry Chemical Physics*, vol. 17, no. 41, pp. 27373–27379, 2015.

[30] J. J. Calvin, A. S. Brewer, and A. P. Alivisatos, "The role of organic ligand shell structures in colloidal nanocrystal synthesis," vol. 1, no. 2, pp. 127–137. Number: 2 Publisher: Nature Publishing Group.

[31] R. Tadmor, R. E. Rosensweig, J. Frey, and J. Klein, "Resolving the puzzle of ferrofluid dispersants," vol. 16, no. 24, pp. 9117–9120. Number: 24 Publisher: American Chemical Society.

[32] A. K. Gupta and M. Gupta, "Synthesis and surface engineering of iron oxide nanoparticles for biomedical applications," vol. 26, no. 18, pp. 3995–4021. Number: 18.

[33] S. Costanzo, G. Simon, J. Richardi, P. Colomban, and I. Lisiecki, "Solvent effects on cobalt nanocrystal synthesis—a facile strategy to control the size of co nanocrystals," vol. 120, no. 38, pp. 22054–22061. Number: 38 Publisher: American Chemical Society.

[34] A. G. Roca, J. F. Marco, M. d. P. Morales, and C. J. Serna, "Effect of nature and particle size on properties of uniform magnetite and maghemite nanoparticles," vol. 111, no. 50, pp. 18577–18584. Number: 50 Publisher: American Chemical Society.

[35] A. Patterson, "The scherrer formula for x-ray particle size determination," *Physical review*, vol. 56, no. 10, p. 978, 1939.

[36] R. Sappey, E. Vincent, N. Hadacek, F. Chaput, J. P. Boilot, and D. Zins, "Nonmonotonic field dependence of the zero-field cooled magnetization peak in some systems of magnetic nanoparticles," vol. 56, no. 22, pp. 14551–14559. Publisher: American Physical Society.

[37] I. J. Bruvera, P. Mendoza Zélis, M. Pilar Calatayud, G. F. Goya, and F. H. Sánchez, "Determination of the blocking temperature of magnetic nanoparticles: The good, the bad, and the ugly," vol. 118, no. 18, p. 184304.

[38] K. L. Livesey, S. Ruta, N. R. Anderson, D. Baldomir, R. W. Chantrell, and D. Serantes, "Beyond the blocking model to fit nanoparticle ZFC/FC magnetisation curves," vol. 8, no. 1, p. 11166. Publisher: Nature Publishing Group.

[39] C. Schmitz-Antoniak, "X-ray absorption spectroscopy on magnetic nanoscale systems for modern applications," vol. 78, no. 6, p. 062501. Publisher: IOP Publishing.

[40] E. Tronc, P. Prene, J. Jolivet, F. d'Orazio, F. Lucari, D. Fiorani, M. Godinho, R. Cherkaoui, M. Nogues, and J. Dormann, "Magnetic behaviour of γ-fe 2 o 3 nanoparticles by mössbauer spectroscopy and magnetic measurements," *Hyperfine Interactions*, vol. 95, pp. 129–148, 1995.

[41] D. Kechrakos and K. Trohidou, "Magnetic properties of self-assembled interacting nanoparticles," *Applied Physics Letters*, vol. 81, no. 24, pp. 4574–4576, 2002.

[42] A. T. Ngo and M. P. Pileni, "Assemblies of ferrite nanocrystals: partial orientation of the easy magnetic axes," vol. 105, no. 1, pp. 53–58. Publisher: American Chemical Society.

[43] N. Sehdev, R. Medwal, and S. Annapoorni, "Enhanced phase stabilization of CoPt in the presence of ag," vol. 110, no. 3, p. 033901.

[44] J. H. Kim, J. Kim, K. H. Baek, D. H. Im, C. K. Kim, and C. S. Yoon, "Fabrication of CoPt nanoparticles with high coercivity on a polymer film," vol. 301, no. 1, pp. 419–424.

[45] A. Avasthi, C. Caro, M. L. Garcia-Martin, and M. P. Leal, "Deciphering the parameters to produce highly reproducible and scalable iron oxide nanoparticles," *Reaction Chemistry & Engineering*, vol. 8, no. 7, pp. 1638–1653, 2023.

[46] G. Cotin, C. Kiefer, F. Perton, M. Boero, B. Ozdamar, A. Bouzid, G. Ori, C. Massobrio, D. Begin, B. Pichon, *et al.*, "Evaluating the critical roles of precursor nature and water content when tailoring magnetic nanoparticles for specific applications," *ACS Applied Nano Materials*, vol. 1, no. 8, pp. 4306–4316, 2018.

[47] W. Kim, C.-Y. Suh, S.-W. Cho, K.-M. Roh, H. Kwon, K. Song, and I.-J. Shon, "A new method for the identification and quantification of magnetite–maghemite mixture using conventional x-ray diffraction technique," *Talanta*, vol. 94, pp. 348–352, 2012.

[48] M. Rabiei, A. Palevicius, A. Dashti, S. Nasiri, A. Monshi, A. Vilkauskas, and G. Janusas, "Measurement modulus of elasticity related to the atomic density of planes in unit cell of crystal lattices," *Materials*, vol. 13, no. 19, p. 4380, 2020.

[49] J. Liang, Y. Ma, Y. Zheng, H. T. Davis, H.-T. Chang, D. Binder, S. Abbas, and F.-L. Hsu, "Solvent-induced crystal morphology transformation in a ternary soap system: sodium stearate crystalline fibers and platelets," *Langmuir*, vol. 17, no. 21, pp. 6447–6454, 2001.

[50] F. Perton, G. Cotin, C. Kiefer, J.-M. Strub, S. Cianferani, J.-M. Greneche, N. Parizel, B. Heinrich, B. Pichon, D. Mertz, *et al.*, "Iron stearate structures: An original tool for nanoparticles design," *Inorganic Chemistry*, vol. 60, no. 16, pp. 12445–12456, 2021.

[51] M. Pauly, B. P. Pichon, P.-A. Albouy, S. Fleutot, C. Leuvrey, M. Trassin, J.-L. Gallani, and S. Begin-Colin, "Monolayer and multilayer assemblies of spherically and cubic-shaped iron oxide nanoparticles," *Journal of Materials Chemistry*, vol. 21, no. 40, pp. 16018–16027, 2011.

[52] Z. Zhou, X. Zhu, D. Wu, Q. Chen, D. Huang, C. Sun, J. Xin, K. Ni, and J. Gao, "Anisotropic shaped iron oxide nanostructures: controlled synthesis and proton relaxation shortening effects," *Chemistry of Materials*, vol. 27, no. 9, pp. 3505–3515, 2015.

[53] A. Shavel, B. Rodríguez-González, M. Spasova, M. Farle, and L. M. Liz-Marzán, "Synthesis and characterization of iron/iron oxide core/shell nanocubes," *Advanced functional materials*, vol. 17, no. 18, pp. 3870–3876, 2007.

[54] A. Shavel and L. M. Liz-Marzán, "Shape control of iron oxide nanoparticles," *Physical Chemistry Chemical Physics*, vol. 11, no. 19, pp. 3762–3766, 2009.

[55] Z. Xu, C. Shen, Y. Tian, X. Shi, and H.-J. Gao, "Organic phase synthesis of monodisperse iron oxide nanocrystals using iron chloride as precursor," *Nanoscale*, vol. 2, no. 6, pp. 1027–1032, 2010.

[56] A. Filankembo, S. Giorgio, I. Lisiecki, and M. Pileni, "Is the anion the major parameter in the shape control of nanocrystals?," *The Journal of Physical Chemistry B*, vol. 107, no. 30, pp. 7492–7500, 2003.

[57] G. Cotin, C. Kiefer, F. Perton, D. Ihiawakrim, C. Blanco-Andujar, S. Moldovan, C. Lefevre, O. Ersen, B. Pichon, D. Mertz, *et al.*, "Unravelling the thermal decomposition parameters for the synthesis of anisotropic iron oxide nanoparticles," *Nanomaterials*, vol. 8, no. 11, p. 881, 2018.

[58] G. Cotin, F. Perton, C. Petit, S. Sall, C. Kiefer, V. Begin, B. Pichon, C. Lefevre, D. Mertz, J.-M. Greneche, *et al.*, "Harnessing composition of iron oxide nanoparticle: Impact of solvent-mediated ligand–ligand interaction and competition between oxidation and growth kinetics," *Chemistry of Materials*, vol. 32, no. 21, pp. 9245–9259, 2020.

[59] D. K. Smith and B. A. Korgel, "The importance of the ctab surfactant on the colloidal seed-mediated synthesis of gold nanorods," *Langmuir*, vol. 24, no. 3, pp. 644–649, 2008.

LANGMUIR

pubs.acs.org/Langmuir Article

Synthesis and Magnetic Properties of Spherical Maghemite Nanoparticles with Tunable Size and Surface Chemistry

Sakina Meftah, Anh-Tu Ngo, Laurent Bouteiller, Vincent Russier, David Hrabovsky, Adama Konaté, Djimédo Kondo, Fahmi Bedoui, and Isabelle Lisiecki*

Cite This: *Langmuir* 2024, 40, 22673−22683 Read Online

ACCESS | Metrics & More | Article Recommendations

ABSTRACT: We report the synthesis of uniform populations of spherical maghemite nanoparticles by thermal decomposition of iron precursors with tunable diameters centered at 3.3, 7.5, and 12.0 nm and tunable surface chemistry. The three stabilizing ligands were fatty acids with three different alkyl chain lengths (18, 12, and 8 carbon atoms). The unprecedented accurate control of the surface chemistry is made possible by the use of three types of iron complexes, that is, iron oleate (C18), iron dodecanoate (C12), and iron octanoate (C8), associated with fatty acid ligands having the same alkyl chain length, that is, oleic acid (C18), dodecanoic acid (C12), and octanoic acid (C8). Since the thermal decomposition of the iron precursor varies with the chain length, no general rules can be applied to control the nanoparticle size, but optimal synthesis conditions have been investigated to induce the growth of nanoparticles with three different surface chemistries, keeping the diameters centered at 3.3, 7.5, and 12.0 nm. Finally, structural characterization of the nine populations of maghemite nanoparticles was performed by transmission electron microscopy and X-ray diffraction, and magnetic properties were determined by using SQUID magnetometry.

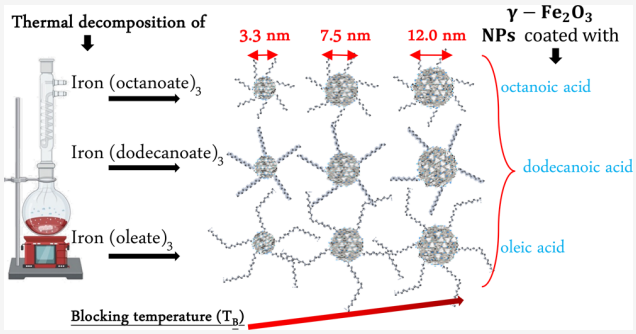

1. INTRODUCTION

Over the past two decades, the synthesis of iron oxide nanoparticles (NPs) has seen significant advance, driven by their potential in a wide range of technological applications, including data recording,[1] catalysis,[2] wastewater treatment,[3] and biomedicine.[4]

Among these iron oxides, magnetite (Fe_3O_4) has been prominently featured in the literature, particularly for its use in magnetic resonance imaging (MRI) and magnetic hyperthermia due to its high saturation magnetization. However, maghemite (γ-Fe_2O_3), a closely related iron oxide, exhibits distinct properties. Unlike magnetite, maghemite is fully oxidized and contains only Fe^{3+} ions, which provides superior chemical stability. This increased stability is valuable for applications requiring long-term performance, such as environmental remediation and drug delivery.[5] Furthermore, the surface chemistry of maghemite is more conducive to uniform functionalization, thereby improving its effectiveness. In addition, the absence of Fe^{2+} ions in maghemite results in lower toxicity, making it a safer choice for biomedical applications.[6] These unique properties of maghemite underscore its importance in advancing the capabilities of iron oxide NPs in various fields.

Further accurate control of their structural and chemical characteristics (size, shape/geometry, nanocrystallinity, composition, and surface chemistry) is fundamental to continuously improving their performance. Among the numerous chemical routes developed to produce iron oxide NPs,[7] the thermal decomposition of organometallic precursors is the most suitable for inducing NPs with low polydispersity. However, many key parameters must be controlled to successfully prepare well-defined populations of iron-oxide NPs with tunable size[8−15] and shape.[3,16−24] These key parameters include the reaction parameters (heating rate, reaction time, and reaction temperature), the nature of the reagents (precursors, stabilizing surfactant, solvent), the concentration of reagents, the surfactant-to-precursor ratio, and the possible presence of additives.[25,26] The purity of the reagents is another key parameter for the reproducibility of these syntheses. For example, it has been shown that

Received: July 1, 2024
Revised: September 9, 2024
Accepted: September 30, 2024
Published: October 15, 2024

https://doi.org/10.1021/acs.langmuir.4c02495
Langmuir 2024, 40, 22673−22683

commercial iron precursors have been successfully used for several years to form spherical maghemite NPs, while the "same" purchased precursor now yields anisotropic-shaped NPs because of the presence of impurities that strongly affect particle growth.[27]

The complexity of these syntheses is due to not only the full set of involved parameters but also the intricate interplay between these parameters. For instance, there are still controversies in the literature regarding the effect of the ligand/precursor ratio, which, according to different studies, can promote an increase or decrease in the final size.[28] When one parameter differs from one synthesis to another, this may impact the role played by others, avoiding, in this case, the establishment of general rules concerning the nucleation and growth processes of the NPs.

This can explain why the synthesis of maghemite NPs coated with tunable carboxylic acid chain lengths through the thermal decomposition of iron carboxylic acid complexes, keeping their size unchanged, has never been reported. Indeed, in this case, varying the nature of the coating ligands surrounding the particles implies a change similar to that of the precursor and that of the stabilizing ligand, which can drastically impact the nucleation and/or growth process and, in turn, the NP size and/or shape. Most of the time, only the nature of the ligand is changed while keeping the iron precursor unchanged, which results in the mixing of the two ligands, taking part in the passivation of the NPs.[14]

From a fundamental point of view, controlling the surface chemistry of NPs is crucial. On the one hand, this allows for the control of interactions between NPs during the growth of their 2D and 3D assemblies. Hence, the alkyl chain length has been shown to dictate the crystalline structure,[29,30] interparticle distance,[31] and coherence length[32] in plasmonic NPs supercrystal, allowing fine control of their physical properties. On the other hand, when the coated NPs are incorporated in a soft matrix (e.g., a polymer), the ligand plays a paramount role in achieving optimal dispersion as well as in the properties of the matrix, which can be influenced by the interaction ligand/matrix.[33,34] Whether NPs interact with each other in supercrystals or in a specific environment to form nanocomposites, accurate control of both the size and surface chemistry is crucial.

This paper reports the synthesis of spherical maghemite NPs of three different sizes, centered at 3.3, 7.5, and 12.0 nm, and three different coating agents characterized by different alkyl chain lengths (18, 12, and 8 carbons). An unprecedented series of nine NP populations were obtained by investigating the thermal decomposition of three iron complexes, that is, iron oleate (C18), iron dodecanoate (C12), and iron octanoate (C8), in the presence of stabilizing ligands with the same alkyl chain length, that is, oleic acid (C18), dodecanoic acid (C12), and octanoic acid (C8).

The structural characterizations performed by transmission electron microscopy (TEM), X-ray diffraction (XRD), and magnetic properties performed by SQUID magnetometry of the nine populations of maghemite NPs are presented.

2. EXPERIMENTAL SECTION

2.1. Chemical Products. All of the materials were used as purchased without further purification. Iron(III) chloride ($FeCl_3.6H_2O$, 99%, VWR), sodium oleate (>97.0%, TCI), sodium dodecanoate (>97%, TCI), sodium n-octanoate (>99%, TCI), 1-hexadecene (for synthesis, Sigma-Aldrich), 1-octadecene (technical grade, 90%, Sigma-Aldrich), oleic acid (technical grade, 90%, Sigma-Aldrich), dodecanoic acid (99%, Thermo Scientific), and octanoic acid (99%, Thermo Scientific) were used.

2.2. Synthesis of Iron(X)$_3$ Precursors (X = Oleate, Dodecanoate, and Octanoate). Three iron(X)$_3$ precursors (*X = oleate, dodecanoate, and octanoate*) were prepared by the reaction of an iron(III) chloride salt ($FeCl_3$) with the corresponding sodium fatty acid salts, sodium oleate, sodium dodecanoate, and sodium octanoate. The synthesis of the iron (oleate)$_3$ precursor was based on a method reported by Park et al.[11] Iron chloride (10.8 g, 40 mmol) and sodium oleate 36.5 g (120 mmol) were solubilized in a mixture of solvents composed of 80 mL of ethanol, 60 mL of distilled water, and 140 mL of hexane. The reaction mixture was heated to 70 °C and maintained at that temperature for 4 h until the reaction was complete. The upper phase containing the iron-oleate complex was then collected using a separating funnel and subjected to three washing steps with 30 mL of distilled water. Subsequently, hexane was evaporated using a rotary evaporator, yielding an iron-oleate complex in a waxy, red-brown paste form. A similar method was used to prepare iron(dodecanoate)$_3$ and iron(octanoate)$_3$ by replacing sodium oleate with sodium dodecanoate and octanoate, respectively.

2.3. Transmission Electron Microscopy (TEM). TEM was performed using a JEOL JEM-1011 microscope operated at 100 kV. For the TEM analysis, drops of the colloidal solution were deposited onto an amorphous carbon-coated TEM grid. The average diameter and polydispersity of the NPs were determined by measuring the diameters of over 700 NPs from the TEM images using ImageJ software. The mean diameter was calculated as the average of these measurements, and polydispersity was assessed based on the standard deviation relative to the mean size.

2.4. X-Ray Diffraction (XRD). XRD of the NPs was carried out using a Bruker D8 Advance X-ray diffractometer provided by the Service Analyses Physico-Chimiques (SAPC) at the Université de Technologie de Compiègne. The instrument was operated at 30 kV and 40 mA with an X-ray wavelength of 0.1506 nm. The scanning encompassed a 2θ range of 25−70°, with increments of 0.02°. All of the NP samples were in powder form. For the analysis, the samples were deposited on a holder with a silicon monocrystal.

2.5. Energy Dispersive X-ray Spectrometry (EDS). The chemical compositions of the iron precursors were determined using energy dispersive X-ray spectrometry (EDS) analysis, conducted on a scanning electron microscope (Quanta FEG 250, Thermo Fisher) equipped with a Quantax—X-Flash (Synergie4—Bruker). This analysis was performed at the Service Analyses Physico-Chimiques (SAPC) at the Université de Technologie de Compiègne.

2.6. Differential Scanning Calorimetry (DSC). DSC analysis was performed to investigate the thermal properties of iron (oleate)$_3$, iron (dodecanoate)$_3$, and iron (octanoate)$_3$. The analysis was performed using a DSC Q200 instrument with version 24.11 Build 124 software. DSC thermograms were obtained in the temperature range of [25−400 °C] at a heating rate of 10 °C/min. For the sample preparation, approximately 1.3 mg of the product was used, and measurements were conducted with a Tzero Aluminum Hermetic pan under a nitrogen atmosphere.

2.7. Magnetic Measurements. Magnetic measurements were carried out on a commercial superconducting quantum interference device (SQUID) magnetometer (MPMS3, Quantum Design, USA) with a field of $1.59 \times 10^3 Am^{-1}$ for the zero-field-cooled (ZFC)/field-cooled (FC) susceptibility curves and with fields of up to $3.98 \times 10^6 Am^{-1}$ for the magnetization curves. All magnetic measurements were performed on a film of powdered iron oxide NPs. During the measurement, the applied field was parallel to the iron-oxide NP film. For the ZFC measurements, the sample was cooled from 300 to 3 K with no field and then heated to 300 K in a field of $1.59 \times 10^3 Am^{-1}$ to record the magnetization $M_{ZFC}(T)$ of the sample. For the FC measurements, the sample was cooled again to 3 K under the same applied field, and the magnetization M_{FC} (T) was recorded. In both cases, the measurements were performed on heating with a heating rate on the order of 2 K min^{-1} for each temperature step. The

https://doi.org/10.1021/acs.langmuir.4c02495
Langmuir 2024, 40, 22673−22683

measurement time was ∼5 s. The hysteresis curves were obtained at 3 K.

3. RESULTS AND DISCUSSION

To synthesize spherical maghemite NPs with three different diameters, centered at 3.3, 7.5, and 12.0 nm, and stabilized with three different carboxylic acid chain lengths, we adapted the procedure reported by Park et al., which involves the thermal decomposition of iron oleate in the presence of oleic acid (C18),[11] giving rise to oleic acid-coated maghemite NPs. The unprecedented accurate *control of the NP surface chemistry* we present here was obtained thanks to the use of three types of precursors, iron oleate, iron dodecanoate, and iron octanoate complexes, associated with their corresponding carboxylic acids, that is, oleic acid (C18), dodecanoic acid (C12), and octanoic acid (C8). For the three types of surface chemistry, that is, by using the three associated types of precursors, the *control of the NP size* is obtained by using various strategies including the well-known solvent effect.[11] Indeed, it is now well established that the higher the boiling point of the solvent, for instance, tetradecene (251 °C), hexadecene (274 °C), or octadecene (318 °C), the larger the NPs. However, this strategy is somewhat limited, particularly for the synthesis of smaller NPs (∼3 nm) (see below). In addition, the thermal decomposition of the three precursors was strongly dependent on the carboxylic acid chain length. This means that the nucleation and growth processes differ from one precursor to another, which, in turn, requires the adaptation of the synthesis conditions from one precursor to another. Therefore, the size control of maghemite NPs stabilized with C18, C12, and C8 ligands involves not only the solvent effect strategy but also other strategies adapted to the different types of precursors. For convenience, NPs with mean diameters centered at 3.3, 7.5, and 12.0 nm are named small-, intermediate-, and large-size NPs, respectively.

The dependence of the thermal decomposition of the precursors with the carboxylic acid chain length is illustrated by DSC analysis. TEM and XRD studies were performed to characterize the structural parameters of the nine populations of maghemite NPs with diameters centered at 3.3, 7.5, and 12.0 nm and stabilized with C18, C12, and C8 carboxylic acids. The magnetic properties of the nine populations were investigated.

3.1. Thermal Decomposition Study of the Iron Precursors by DSC. The thermal decomposition of the precursors, iron oleate (C18), iron dodecanoate (C12), and iron octanoate (C8), was analyzed by using DSC to elucidate the differences in their decomposition behavior as influenced by the carboxylic acid chain length. DSC was chosen for its ability to precisely capture the enthalpic changes associated with the decomposition process, thereby providing detailed insight into the distinct thermal characteristics of each precursor.[11,35] The results are shown in Figure 1.

The DSC pattern of iron oleate (C18; Figure 1a) showed a weak endothermic peak at 120 °C, which can be attributed to the removal of crystal hydrate water. In good agreement with previous studies,[11,35,36] an endothermic peak was observed at 230 °C, which corresponds to the dissociation of the first oleate group from the precursor, whereas the next peak, at 320 °C, was assigned to the dissociation of the two remaining ligands. The former was associated with the nucleation step, whereas the latter was associated with the growth step. At

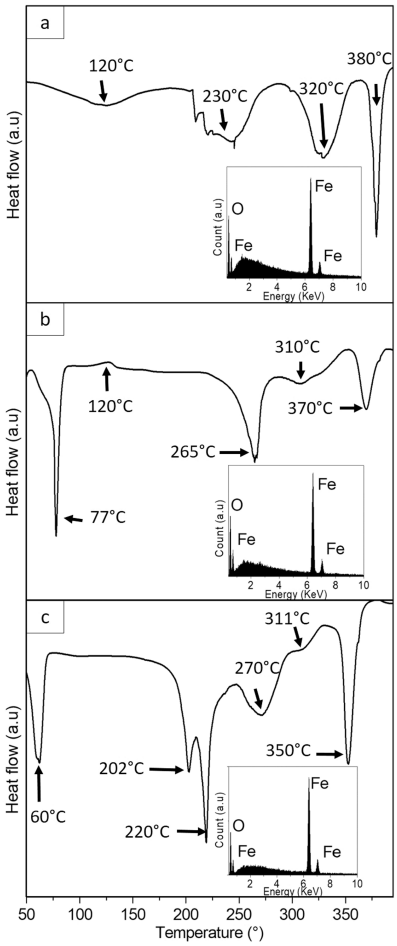

Figure 1. Differential scanning calorimetry (DSC) of (a) iron oleate, (b) iron dodecanoate, and (c) iron octanoate precursors. Insets: corresponding energy dispersive X-ray spectrometry (EDS) patterns.

higher temperatures (approximately 380 °C), the last peak corresponds to complete decomposition of the precursor.

The DSC pattern of the iron dodecanoate (C12) precursor (Figure 1b) showed low-temperature peaks at approximately 77 °C. Elemental analysis revealed that only iron was present. The absence of other elements such as chlorine or sodium reveals the absence of impurities such as sodium dodecanoate, which could result either from nonstoichiometric conditions during their synthesis or from a nonoptimal washing step.[27] The peak obtained at low temperatures can only be assigned to the melting point of this precursor, which is solid at room temperature, unlike iron oleate (C18). Two endothermic peaks were observed at 265 and 310 °C. Because of the similar behavior observed for iron oleate, it can be assumed that these two endothermic peaks correspond to the nucleation and growth peaks, respectively. However, the nucleation peak was found at higher temperatures compared to that of the oleic precursor (265 vs 230 °C). This indicates that the nucleation step requires a significantly higher temperature for the dodecanoate precursor than that for the oleic precursor. The second endothermic peak at 310 °C occurred at a temperature slightly lower than that of the oleic precursor. Comparative measurements of the DSC patterns of oleic and dodecanoic precursors show that the effective separation of the nucleation and growth processes taking place at different temperatures is

https://doi.org/10.1021/acs.langmuir.4c02495
Langmuir 2024, 40, 22673−22683

Table 1. Parameters Used for the Synthesis of Maghemite Nanoparticles by the Thermal Decomposition Approach with the TEM Size Measured

	precursor (mmol)	ligand (mmol)	R = IP/LJ	solvent (T_{bp} °C)	reflux time (min)	TEM diameter (nm)
C18-NPs	1.6	0.8	2.0	Octadecene (318 °C)	30	12.6 (σ = 4.11%)
	1.6	0.8	2.0	Hexadecene (274 °C)	**30**	7.8 (σ = 4.0%)
	4.0	2.0	2.0	Hexadecene (274 °C)	30	3.4 (σ = 14.3%)
C12-NPs	1.6	3.2	0.50	Octadecene (318 °C)	30	13.3 (σ = 5.7%)
	0.8	1.6	0.50	Hexadecene (274 °C)	60	7.8 (σ = 6.7%)
	0.8	2.8	0.29	Hexadecene (274 °C)	60	3.2 (σ = 14.5%)
C8-NPs	1.6	2.0	0.80	Hexadecene (274 °C)	90	11.2 (σ = 13.7%)
	1.6	2.0	0.80	Hexadecene (274 °C)	60	7.0 (σ = 13.4%)
	3.2	6.3	0.50	Hexadecene (274 °C)	30	3.2 (σ = 12.3%)

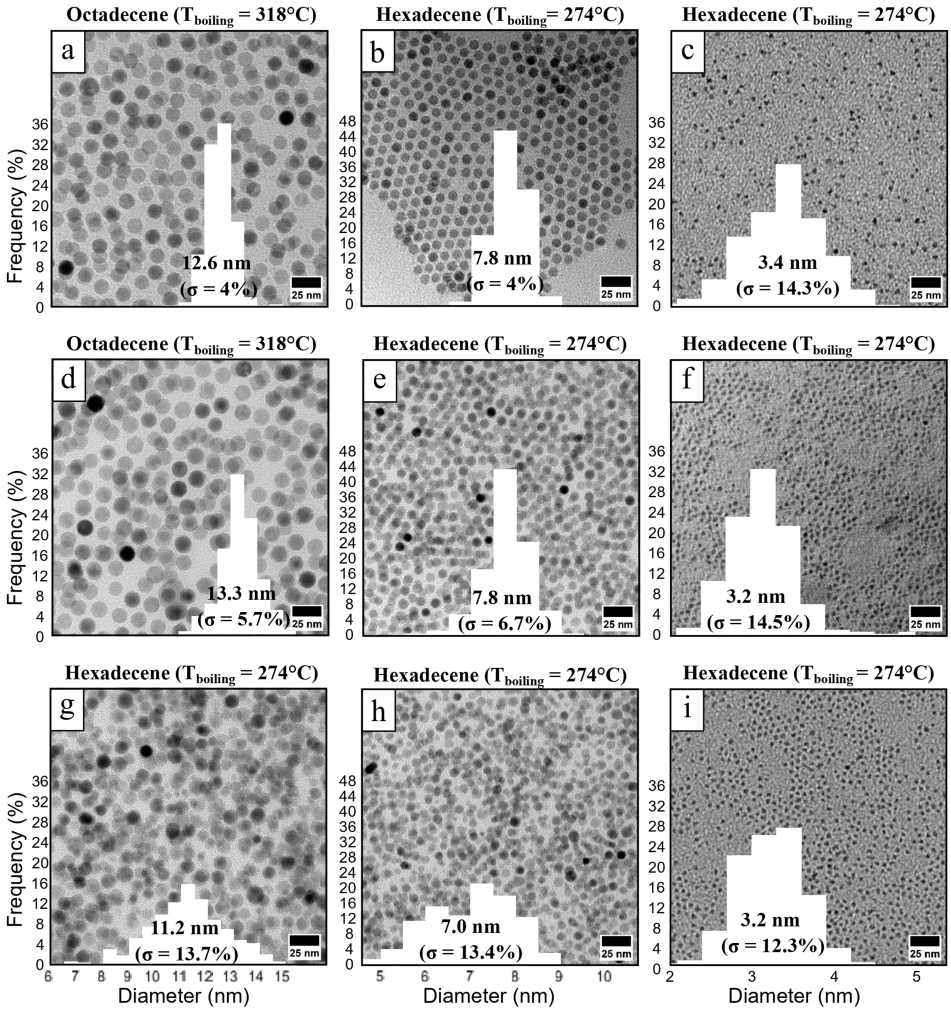

Figure 2. Transmission electron microscopy (TEM) images of maghemite nanoparticles synthesized from (a–c) iron oleate, (d–f) iron dodeconaoate, and (g–i) iron octanoate. The mean diameters are centered on (a,d,g) 12.0 nm, (b,e,h) 7.5 nm, and (c,f,i) 3.3 nm.

less in the latter than in the former. Complete decomposition occurs at approximately 370 °C, which is lower than that of the oleic precursor.

Focusing on the iron octanoate (C8) precursor (Figure 1c), a low-temperature peak is observed at 60 °C. As for the precursor iron dodecanoate (C12), this peak could be attributed to its melting point. However, unlike the behavior observed for the C18 and C12 precursors, which displayed two peaks attributed to the nucleation and growth steps, three peaks at 202, 220, and 270 °C were obtained for the C8 precursor. It is possible that each of these three peaks corresponds to the dissociation of an octanoate group from the precursor; however, in any case, they reveal a more complex dissociation pathway than in the case of C18 and C12 precursors. Finally, complete decomposition occurs at approximately 350 °C, which is lower than the temperatures of the oleic and dodecanoic precursors.

3.2. TEM Study. *3.2.1. Size Control of Oleic Acid (C18)-Coated Maghemite NPs.* The synthesis of larger oleic acid (C18)-coated maghemite NPs was based on the procedure reported by Park and Co.[11] 1.42 g (1.6 mmol) of the iron oleate precursor and 0.22 g (0.8 mmol) of oleic acid were

https://doi.org/10.1021/acs.langmuir.4c02495
Langmuir 2024, 40, 22673–22683

dissolved in 10 mL of octadecene. The precursor-to-ligand concentration ratio R was equal to 2. This mixture was heated to the boiling point of octadecene (318 °C), refluxed for 30 min, and cooled to room temperature (Table 1). A black solution was formed, which was washed with a large excess of acetone followed by centrifugation at 4900 rpm for 10 min. Oleic acid-coated NPs were dispersed in chloroform. Figure 2a shows the TEM image of the resulting C18-NPs, revealing a population composed of highly uniform spherical NPs, with a mean diameter and a size polydispersity of 12.6 nm and 4%, respectively (inset of Figure 2a).

Using a lower boiling point (bp) solvent, hexadecene (bp: 274 °C), other things being equal, the mean diameter decreases from 12.6 to 7.8 nm, keeping a low size polydispersity of 4% (Figure 2b and inset of Figure 2b). This behavior is explained by the lower growth activation resulting from the use of a solvent, whose boiling point (274 °C) is lower than the growth peak (300 °C) (Figure 1) compared to the octadecene (318 °C).[11,12,14,16]

The very low NP-size polydispersity (4% for both cases) is explained by the specific separation of the nucleation and growth processes. Indeed, the DSC measurement shows a nucleation peak at approximately 230 °C, corresponding to the first oleate ligand dissociation from the iron oleate, while at approximately 320 °C, the remaining two oleate ligands dissociate in their turns, inducing NP growth (Figure 1a).

By further decreasing the reaction temperature through the use of tetradecene (251 °C), other things being equal, a population of small NPs (~2.6 nm) was obtained; however, a very low reaction yield and high size polydispersity (20%) were observed. This behavior is attributed to the fact that the reaction temperature is close to the nucleation peak, thus hindering the decomposition of all precursors. The solvent strategy, through the use of tetradecene, being unsuccessful in producing the smaller NPs, we kept the procedure giving the 7.8 nm C18-NPs with the following modifications: the precursor concentration is increased from 1.6 to 4 mmol, keeping unchanged the ratio R equal to 2, as well as the solvent, hexadecene, and the reflux time, 30 min (Table 1). As shown in Figure 2c, these conditions led to the formation of 3.4 nm with a size polydispersity of 14.3%. The decrease in the mean NP size with increasing precursor concentration results from the enhancement of iron supersaturation before nucleation and is explained by the LaMer supersaturation theory.[37,38]

3.2.2. Size Control of Dodecanoic Acid (C12)-Coated Maghemite NPs. By repeating the procedure used to obtain the larger C18-NPs (see Section 3.2.1), with iron dodecanoate as a precursor instead of iron oleate, we obtained polydisperse C12-NPs (σ = 17%) with a mean diameter of 14.0 nm instead of low polydisperse 12.6 nm NPs. As before, the change in the quality of the populations can be explained by the change in the decomposition processes of the two iron precursors. For iron oleate, the nucleation and growth peaks are at around 230 and 320 °C, respectively, compared to 265 and 310 °C for iron dodecanoate (Figure 1). To overcome the variation of the nucleation and growth kinetics from the iron oleate to the iron dodecanoate and then successfully obtain uniform C12-NPs with a mean diameter centered on 12 nm, the precursor and ligand concentrations have been modified as follows: 1.045 g (1.6 mmol) of iron dodecanoate precursor and 0.64 g (3.2 mmol) of dodecanoic acid have been used, giving a ratio, R, of 0.5. The solvent used remained unchanged, that is, octadecene (318 °C), as well as the reflux time 30 min (Table 1). Under optimized conditions, the TEM image and size histogram (Figure 2d and inset of Figure 2d) illustrate the formation of 13.3 nm C12-NPs with a low polydispersity of 5.7%.

Similar to the synthesis of the intermediate C18-NP size, we used a lower-boiling solvent, hexadecene, instead of octadecene, to form the intermediate C12-NP size. The resulting C12-NPs were highly polydispersed (16%) with a mean diameter of 6.3 nm. By adjusting the conditions, i.e., by decreasing the precursor concentration from 1.6 to 0.8 mmol, keeping unchanged the ratio R, and increasing the reflux time from 30 to 60 min, low-size polydispersity C12-NPs (6.7%) with a mean diameter of 7.8 nm were obtained (Figure 2e and the inset of Figure 2e). This behavior illustrates the importance of the nature of the Fe precursor.

By adjusting the ratio, R, to 0.28 (instead of 0.5 for the 7.8 nm C12-NPs), that is, by increasing the dodecanoic acid ligand concentration, other things being equal, 3.2 nm C12-NPs with a size polydispersity of 14.5% were obtained (Figure 2f and inset of Figure 2f). The effect of the increase in the ligand concentration on NP growth has been investigated by several groups, and trends of either (1) increasing[12,37,39,40] or (2) decreasing[14,19,38,41] size have been observed. This effect can be the opposite of whether it affects the nucleation or the growth step. In the first case, an increase in ligand concentration tended to induce a higher stabilization of the iron complex. This stabilization slows the nucleation step, which in turn lowers the number of nuclei, leading to a larger NP size. In the second case, excess ligands tend to inhibit NP growth by covering the growth sites, resulting in a smaller NP size. The intricate interplay between the ligand concentration and the other reaction parameters (the nature and concentration of the reactants, solvent, heating rate, and reflux time), which differ from one study to another, likely explains the two opposite trends reported in the literature. In our case, the decrease in the C12-NP size from 7.8 to 3.2 nm with increasing the dodecanoic ligand from 1.6 to 2.8 mmol, other things being equal, can be explained by the blocking of the NP growth of the growing NPs.

3.2.3. Size Control of Octanoic Acid (C8)-Coated Maghemite NPs. Starting again from the synthesis conditions established for the larger C18-NP size and replacing the iron oleate precursor with an iron octanoate precursor, we obtained highly polydispersed NPs (15%) with a mean diameter of 20 nm. To obtain the desired NP population, the nature of the solvent, the ligand/precursor ratio, and the reflux time were optimized as follows: the precursor concentration was 1.6 mmol, the ratio, R, was 0.8, and the synthesis occurred in hexadecene (b.p.). 274 °C), with a reflux time of 90 min (Table 1). As shown in the TEM image and size histogram (Figure 2g and inset of Figure 2g), the resulting C8-NPs were characterized by mean size and size polydispersity of 11.2 nm and 13.7%, respectively.

Decreasing the reflux time from 90 to 60 min, other things being equal, the mean size decreases from 11.2 to 7.0 nm, keeping almost unchanged the size polydispersity, 13.4% (Figure 2h and inset of Figure 2h). This behavior observed under our conditions, that is, with an iron octanoate precursor and hexadecene as a solvent, illustrates the time dependence of the growth process during the reflux performed at 274 °C, which corresponds to the growth temperature according to the DSC study (Figure 1c).

https://doi.org/10.1021/acs.langmuir.4c02495
Langmuir 2024, 40, 22673−22683

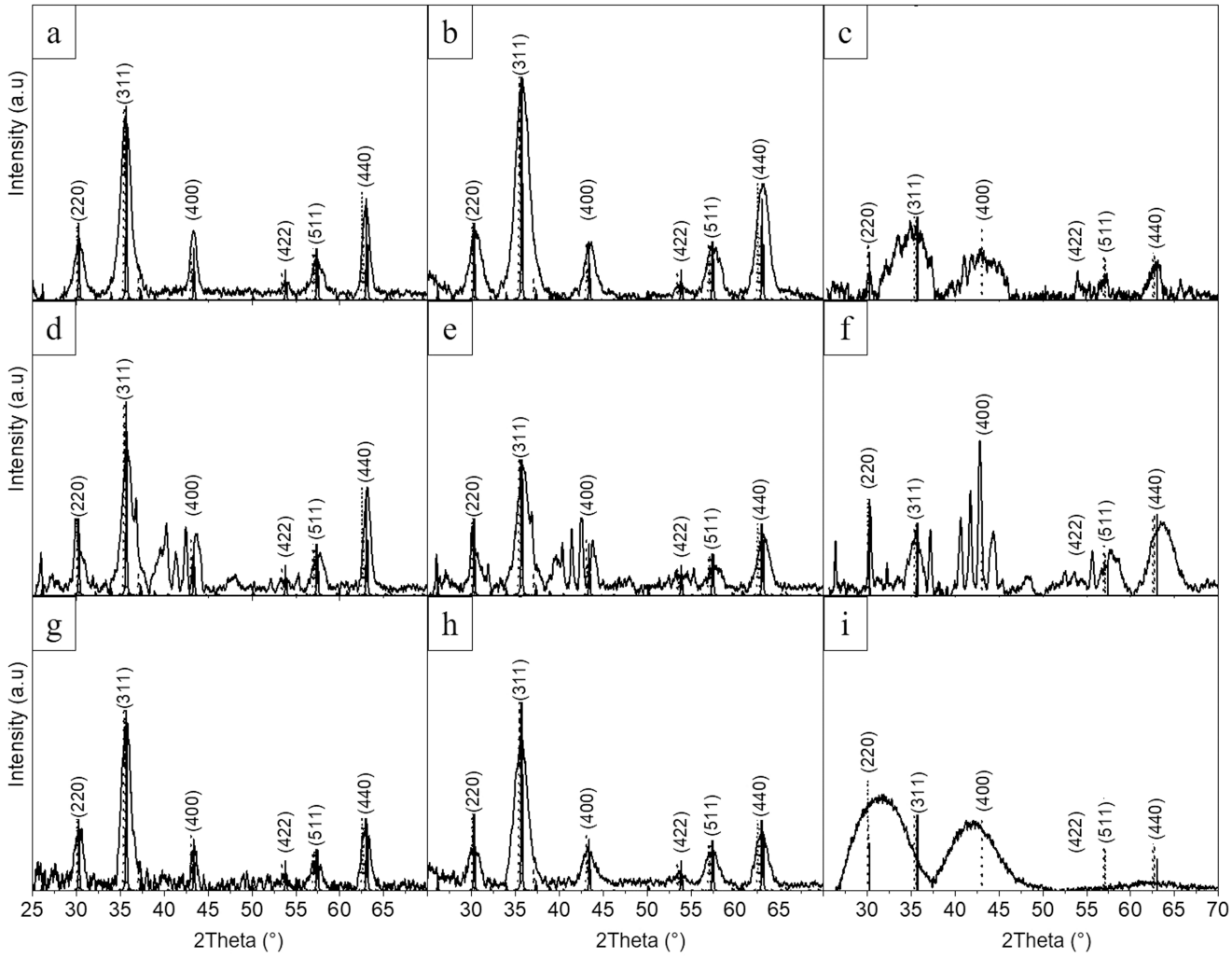

Figure 3. X-ray diffraction (XRD) patterns of iron oxide nanoparticles synthesized from (a−c) iron oleate, (d−f) iron dodeconoate, and (g−i) iron octanoate. The mean diameters are centered on (a,d,g) 12.0 nm, (b,e,h) 7.5 nm, and (c,f,i) 3.3 nm. Solid lines: maghemite (*ref. 04-021-3968, PDF-5*) reference pattern. Dotted lines: magnetite (*ref. 04-027-0607, PDF-5*) reference patterns.

The smallest C8-NPs were obtained by combining the reflux time, the *R*-value, and the precursor concentration effects. Hence, by decreasing both the reflux time from 60 to 30 min, the *R*-value from 0.8 to 0.5, and by increasing the octanoic acid concentration from 1.6 to 3.2 mmol, C8-NPs with a mean diameter and size polydispersity of 3.2 nm and 12.3%, respectively, have been obtained (Figure 2i and inset of Figure 2i).

It is noteworthy that whatever the size is, the C8-NPs have a higher polydispersity compared to their C18- and C12-counterparts. This behavior may be explained by a more complex dissociation process of the iron octanoic precursor revealed by three endothermic events (instead of two for the C18 and C12 precursors), which are, furthermore, close to each other.

After detailed details of the synthesis conditions and three NP sizes obtained from each precursor, it is worth considering another intriguing parameter: saturation of the ligands used. In our study, both unsaturated oleate (C_{18}) and saturated dodecanoate (C_{12}) and octanoate (C_8) ligands were employed, introducing differences not only in chain length but also in ligand saturation. When the precursor is switched from unsaturated oleate (C_{18}) to saturated dodecanoate (C_{12}) or saturated octanoate (C_8) ligands), two key parameters are altered: chain length and ligand saturation. In addition, other experimental conditions, including the precursor ratio, solvent boiling point, and reflux time, were also modified. Therefore, isolating the specific effects of ligand unsaturation is challenging because of these simultaneous changes.

However, the literature indicates that unsaturation in ligands such as oleate introduces a bend in the alkyl chain, leading to less ordered ligand shells compared to the more linear and ordered shells formed by saturated ligands.[42−44] This bend disrupts the tight packing, allowing for better solvent intercalation and enhanced colloidal stability. As a result, unsaturated ligands can influence the solubility of NPs by facilitating better interactions with the solvent. In our study, regardless of the degree of saturation of the ligand, no significant changes in colloidal stability were observed, and the stability remained consistently high.

These differences in solvent−ligand interactions due to ligand saturation are also expected to affect the growth mechanism of the NPs. Indeed, the enhanced solvent−ligand interactions, specifically the increased solubility of the ligand, led to a reduction in the ligand−ligand attractions within the ligand layer surrounding the NPs during their growth. This

https://doi.org/10.1021/acs.langmuir.4c02495
Langmuir 2024, 40, 22673−22683

reduction weakened the integrity of the ligand layer, thereby promoting particle growth.[45]

3.3. XRD Study. Figure 3 presents the XRD patterns for nine iron oxide NP samples, with reference patterns for maghemite (γ-Fe_2O_3) and magnetite (Fe_3O_4) employed for comparative analysis. The reference patterns correspond to maghemite (ICDD PDF card 04-021-3968) with a unit cell parameter of 8.336 Å and magnetite (ICDD PDF card 00-019-0629) with a unit cell parameter of 8.396 Å. The XRD patterns of the C12-coated NPs exhibit additional peaks that can be attributed to dodecanoic acid. Peak broadening was observed as the NP size decreased, which is consistent with the Scherrer equation. Indexation of all samples, varying in size (7 and 12 nm) and surface chemistry (C18, C12, and C8), indicated a predominant alignment with maghemite rather than magnetite. Given the close similarity of the XRD patterns for these two crystalline phases, the unit cell parameters were determined by analyzing the position and broadening of the (311) reflection within the spinel structure following established procedures.[46] The unit cell parameter values for the samples summarized in Table 2 ranged from 8.334 to 8.346 nm, which closely matched the known lattice parameter of maghemite (γ-Fe_2O_3), typically at approximately 8.330 nm. In contrast, magnetite (Fe_3O_4) has a slightly larger lattice parameter of approximately 8.396 nm. The calculated cell parameter values for these samples (C18-NPs, C12-NPs, and C8-NPs) suggested that the crystal phase present in these NPs was predominantly maghemite rather than magnetite. This conclusion aligns with the characteristic slight reduction in the lattice parameter expected for maghemite, likely due to the presence of vacancies in the iron sites compared with the fully occupied iron sites in magnetite.

Table 2. TEM and XRD Size Analysis and Unit Cell Measurements of Iron Oxide Nanoparticles Using the (311) Plane Position and Broadening

	TEM size (nm)	XRD size (nm)	Cell parameter (nm)
C18-NPs	12.6	6.0	8.345
	7.8	4.6	8.346
C12-NPs	13.3	5.1	8.335
	7.8	4.7	8.334
C8-NPs	11.2	6.8	8.336
	7.0	5.0	8.346

For the smallest NPs (3 nm), the XRD peaks become larger for the smaller C18-NPs and C12-NPs, which is in line with the Scherrer equation,[12,47] but the low crystallinity and significant noise in the patterns precluded a clear distinction between maghemite and magnetite, preventing the calculation of the unit cell parameters. Further analysis of the XRD pattern for the 3 nm C8-coated NPs revealed more pronounced peak broadening and shifts in peak positions compared to those of the C18- and C12-coated samples. These shifts and broadening indicate that the diffraction patterns of the C8-coated NPs may be influenced by factors other than crystallinity such as interactions with free carboxylates or iron complexes. Consequently, the XRD pattern may not provide a straightforward interpretation of the composition. Although XRD analysis predominantly identified maghemite as the main phase, it is important to note that the negligible presence of magnetite cannot be conclusively ruled out. The precision of XRD in distinguishing and quantifying minor phases is limited because of the similar diffraction patterns of maghemite and magnetite.

3.4. Magnetic Properties of Maghemite NPs with Tunable Size and Surface Chemistry. *3.4.1. Magnetization versus Temperature Measurements.* Figure 4 shows the field-cooled (FC) and zero-field-cooled (ZFC) magnetization versus temperature curves for the nine populations of maghemite NPs presented in Figure 2, differing in both their size and surface chemistry. As the sample has been cooled in zero field, there is no net alignment of the spins at 3 K; hence, the magnetization is close to zero. A small magnetic field ($1.59 \times 10^3 Am^{-1}$) was applied. As the temperature increases, the spins become progressively "unblocked," aligning toward the field direction, and the magnetization increases until it reaches a maximum at a temperature T_{max} related to the blocking temperature T_B. Above T_B, the behavior is paramagnetic, i.e., the thermal energy increases to such an extent that the increased dynamic rotation of the spins prevents alignment in the field direction, and the magnetization decreases with increasing temperature. In a monodisperse assembly, T_B is typically defined using eq 1:

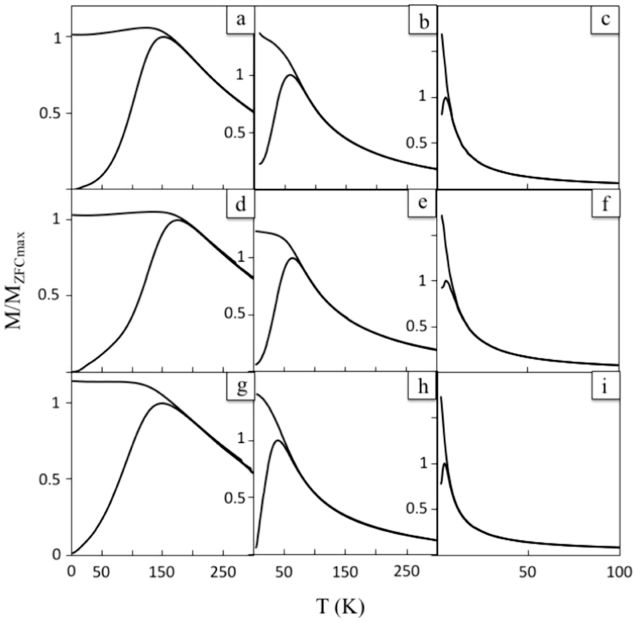

Figure 4. FC and ZFC magnetization versus temperature curves with applied field $H = 1.59 \times 10^3 Am^{-1}$, of maghemite nanoparticles synthesized from (a–c) iron oleate, (d–f) iron dodeconoate, and (g–i) iron octanoate. The mean diameters are centered on (a,d,g) 12.0 nm, (b,e,h) 7.5 nm, and (c,f,i) 3.3 nm.

$$T_B = KV/[k_B \ln(\tau_x/\tau_0)] \quad (1)$$

where K, V, and k_B are the energy anisotropy constant, particle volume, and Boltzmann's constant. τ_0 is a characteristic relaxation time of 10^{-10} s for ferro- or ferrimagnetic materials, and $\tau_x = 60$ s is the experimental time scale of the susceptibility measurement. When the size polydispersity cannot be neglected, T_{max} does not coincide with T_B, as has already been discussed in refs 48–51 and the distribution of T_B must be related to the distribution of particle volumes. The derivative $d(M_{ZFC} - M_{FC})/dT$ can be seen as the T_B distribution presenting two characteristic temperatures, namely, T_{IP} for the inflection point, defined as the maximum

https://doi.org/10.1021/acs.langmuir.4c02495
Langmuir 2024, 40, 22673–22683

value of $d(M_{ZFC})/dT$ (and equivalently of $d(M_{ZFC} - M_{FC})/dT$), and T_{max} where $d(M_{ZFC})/dT = 0$. Clearly, T_{IP} and T_{max} are the lower and upper bounds, respectively, of the blocking temperature corresponding to the characteristic value, $V_{0,}$ of the volume log-normal distribution, as introduced by Sappey et al.[48] (see Table 3). For the smallest particles, <V> c.a. 3.3 nm,

Table 3. Magnetic Parameters Extracted from the ZFC Magnetization and Hysteresis Curves for the Nine Populations of Maghemite Nanoparticles Passivated with Oleate (C18), Dodecanoate (C12), and Octanoate (C8) Ligands[a]

	diameter (nm)	T_B (K)	M_r/M_{Hmax}	H_c (10^4 Am^{-1})
C I 8-NPs	12.6 (σ = 4.0%)	117	0.44	4.18
	7.8 (σ = 4.0%)	45	0.38	4.02
	3.4 (σ = 14.3%)	5	0.06	0.99
C I 2-NPs	13.3 (σ = 5.7%)	124	0.34	3.34
	7.8 (σ = 6.7%)	42	0.38	3.70
	3.2 (σ =14.5%)	5	0.11	0.44
C8-NPs	11.2 (σ = 13.7%)	83	0.37	4.02
	7.0 (σ = 13.4%)	22	0.29	2.11
	3.2 (σ = 12.3%)	4	0.03	0.48

[a] T_B: blocking temperature, M_r/M_{Hmax}: ratio of remanent-to-magnetization at Hmax (Hmax = 3.98 × $10^6 Am^{-1}$), H_c: coercive field.

such a distinction is much less meaningful because of the increasing influence of spin canting and crystalline defects, making the models used for the introduction of ZFC/FC magnetizations inaccurate. Hence, in this case, we consider T_{max} as the temperature at which the entire distribution reaches the superparamagnetic regime as a more representative one.

The larger oleic acid (C18)-coated maghemite NPs (12.6 nm) were characterized by a $T_B(v_0)$ value of 117 K (Table 3). This value is in good agreement with the values reported in the literature for similar-sized C18-coated maghemite NPs.[11,14] The C12-NPs (13.3 nm) and C8-NPs (11.2 nm) were characterized by $T_B(v_0)$ values of 124 and 83 K, respectively, similar to that of C18-NPs with sizes of the same order. For the series of larger NPs, it is noticeable that the higher the mean diameter, the higher the T_B, which is consistent with an increase in the particle volume (see eq 1). This magnetic trend is further illustrated for the intermediate-sized NP (Table 3). Whatever the ligand is, it is characterized by a lower T_B compared to the larger NPs. The C18-NPs (7.8 nm), C12-NPs (7.8 nm), and C8-NPs (7.0 nm) were characterized by $T_B(v_0)$ values of 45, 42, and 22 K, respectively. By focusing on the smaller NPs with a diameter of approximately 3.3 nm, we found T_B values around 5 K (Table 3). This low value of T_B is explained by their very small volume but not only. Indeed, it is likely that spin canting, which is all the more important as the particle size is small, significantly contributes to lowering the blocking temperature. The ZFC curves for the series of larger and intermediate-sized NPs passivated with C18, C12, and C8 ligands, normalized to $T_{max,}$ are presented in Figure 5. Whatever the NP size, it appears that the curve for the C8-NPs is broadened concerning those of the C18 and C12 NPs. This reflects a larger distribution of the magnetic anisotropy energy due to a larger size distribution for the C8-NPs compared to the C12- and C18-NPs (Table 1).

In the FC curves, the magnetization is larger than that of the ZFC curves from 3 K to T_B. Above T_B, the magnetization

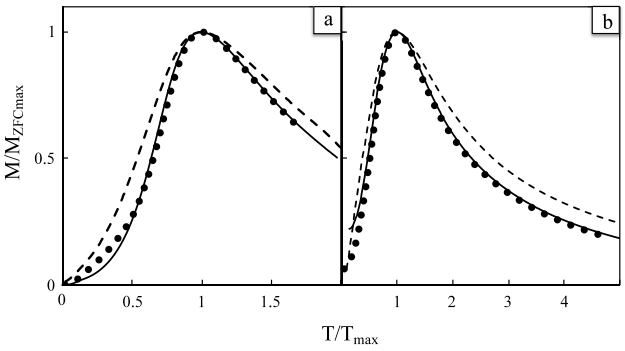

Figure 5. Zero field magnetization versus temperature curves normalized to T_{max} of maghemite nanoparticles synthesized from iron oleate (solid lines), iron dodeconoate (solid circles), and iron octanoate (dashed line). (a) Large-nanoparticle sizes, (b) intermediate-nanoparticle sizes.

decreases with increasing temperature and joins the ZFC curve.

The FC curves obtained for the series of the large-size NPs (Figure 4a,d,g) show a rather flat FC curve at a temperature below T_B, which is indicative of strong dipolar interactions. However, for the intermediate- and small-sized (C18, C12, and C8) NPs (Figure 4b,c,e,f,h,i), the FC curves show an almost uniform decay before joining the ZFC curve above T_B, which suggests that the dipolar interaction effect for these samples is not predominant.[52] The stronger interactions between the larger maghemite NPs compared to those of the intermediate and small-size NPs can be explained in two ways. First, the washing of the larger particles, at the end of the synthesis, was more efficient compared to the intermediate- and small-size particles, ensuring a very low amount of byproducts (e.g., an excess of surfactant) in the colloidal solution and then a decrease in the interparticle distance for the larger particles compared to the intermediate- and small-size NPs. Second, it is well established that dipolar interactions in the assembly of NPs increase with the volume of the NPs.[53]

3.4.2. Magnetic Hysteresis Measurements. Figure 6 shows the corresponding hysteresis curves for the nine populations of maghemite NPs, differing by both their size and surface chemistry. Regardless of the sample, saturation magnetization is never attained with a field H_{max} of 3.98 × 10^6 Am^{-1}. The magnetization curves for the larger NPs and the intermediate-sized NPs are close to saturation, while the smallest particles, owing to the more important spin canting effect and crystalline defects, likely saturate at much higher fields. The ratio of remanent-to-magnetization at H_{max} (M_r/M_{Hmax}) and the coercive field (H_c) are listed in Table 3. For the larger NPs as well as for the intermediate-size NPs, the (M_r/M_{Hmax}) is found to be approximately 0.4, which is close to the value of 0.5, expected for uniaxial anisotropy.[54]

This magnetic behavior is in good agreement with previously reported studies.[12,14,55] However, regardless of the ligand coating, the smaller particles are characterized by a very low value (M_r/M_{Hmax}) between 0.03 and 0.11. This behavior is attributed to the fact that the measurement temperature (3 K) is very close to their blocking temperature, around 5 K; i.e., a majority of the NPs display a superparamagnetic behavior. Moreover, due to the small NP size, one expects that the spin canting will take a much more relative importance than in the case of the larger NPs. In a first approximation, both

https://doi.org/10.1021/acs.langmuir.4c02495
Langmuir 2024, 40, 22673−22683

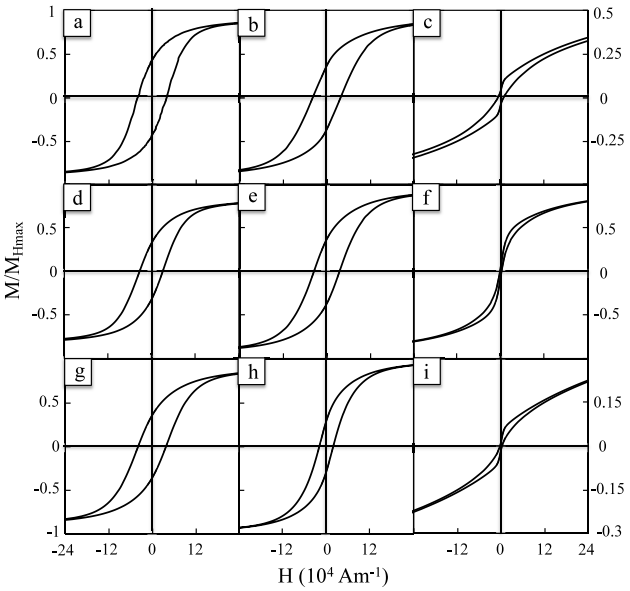

Figure 6. Hysteresis curves performed at 3 K, of maghemite nanoparticles synthesized from (a−c) iron oleate, (d−f) iron dodeconoate, and (g−i) iron octanoate. The mean diameters are centered on (a,d,g) 12.0 nm, (b,e,h) 7.5 nm, and (c,f,i) 3.3 nm.

consequences of the small NP size, namely the small deviation between the measuring and blocking temperatures and the relative importance of the spin canting, can be modeled by adding to the distribution of NPs a component of non-anisotropic NP ($K_{eff} = 0$) representing either an ultrasoft phase due to the spin canting or the distribution of the smallest NPs, which are in the superparamagnetic regime ($T < T_b$). As a qualitative example, we performed Monte Carlo simulations (see Figure 7) of the hysteresis loop with either a single Stoner−Wolfarth component or a mixture including a nonanisotropic component. Doing this, on the one hand, one gets a reduction of both M_r/M_s and H_c, and, on the other hand, the shape of the hysteresis curves of the C8 and C18 samples can be qualitatively reproduced. This means that we can interpret both the sharp reduction of H_c and the shoulder of the $M(h)$ curves for the C8 and C18 systems as a signature of the magnetic multiphase character of the corresponding NP assemblies. A similar interpretation was proposed for the behavior of the hysteresis curves of CoPt NP during annealing.[56,57]

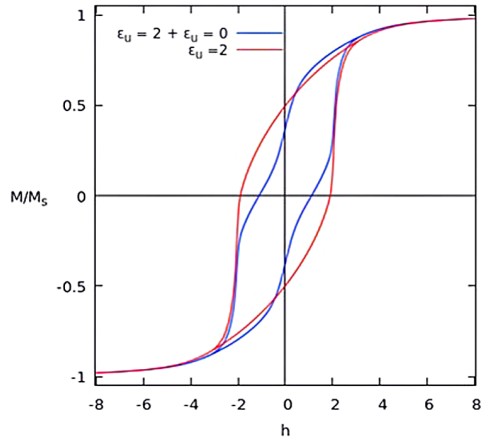

Figure 7. Monte Carlo simulation of the hysteresis curve of a single Stoner−Wolfarth model with reduced uniaxial anisotropy $e_u = 2$ and mixture including a nonanisotropic component ($e_u = 0$). This model is given only for a qualitative purpose, as the value chosen for the reduced anisotropy energy ($e_u = 2$) is not fitted to the experimental samples. The reduced field h is H/H_r where H_r is the reference field $H_r = H_k/(2e_u)$ and H_k is the usual anisotropy field ($2K/(\mu_0 \cdot M_s)$).

4. CONCLUSIONS

In this paper, we report the first example of low-size polydisperse spherical maghemite NPs synthesized by the thermal decomposition of an iron precursor with accurate control of both surface chemistry and diameter. The surface chemistry has been controlled by using three types of iron complexes, i.e., iron oleate (C18), iron dodecanoate (C12), and iron octanoate (C8) associated with the fatty acid ligands having the same alkyl chain length, i.e., oleic acid (C18), dodecanoic acid (C12), and octanoic acid (C8). The optimal conditions favoring the growth of diameters centered at 3.3, 7.5, and 12.0 nm, for the three types of ligands, have been established. It is worth noting that these conditions depend on the precursor length and its thermal decomposition behavior. Magnetic properties performed by SQUID magnetometry of the nine populations of maghemite NPs reflect accurate size control. A potential future direction for research in this field is to study the impact of the ligands differing by their chemical nature and chain length on the NP interactions with their environment (solvent, polymer, etc.). Controlling the ligand chain length of the maghemite NPs organized in supercrystals is of great importance to tune the structural characteristics of these nanomaterials, i.e., the interparticle distance and the 3D crystalline structure. Such magnetic superlattices provide a new horizon in fundamental physics and can be used as model systems for considering phenomena related to dipolar interactions within the solid and, in particular, the dipolar superferromagnetism (SFM), expected in highly dense supercrystals.

AUTHOR INFORMATION

Corresponding Author

Isabelle Lisiecki − *CNRS, De la Molécule aux Nano-Objets: Réactivité, Interactions Spectroscopies, MONARIS, Sorbonne Université, 75005 Paris, France;* orcid.org/0000-0001-7764-3125; Email: isabelle.lisiecki@sorbonne-universite.fr

Authors

Sakina Meftah − *CNRS, De la Molécule aux Nano-Objets: Réactivité, Interactions Spectroscopies, MONARIS, Sorbonne Université, 75005 Paris, France; Roberval (Mechanics, Energy and Electricity), Centre de recherche Royallieu—CS, Université de technologie de Compiègne, 60 319-60 203 Compiègne Cedex, France*

Anh-Tu Ngo − *CNRS, De la Molécule aux Nano-Objets: Réactivité, Interactions Spectroscopies, MONARIS, Sorbonne Université, 75005 Paris, France*

Laurent Bouteiller − *CNRS, Institut Parisien de Chimie Moléculaire, IPCM, Sorbonne Université, 75005 Paris, France;* orcid.org/0000-0001-7613-7028

Vincent Russier − *ICMPE UMR 7182 CNRS and Université UPE, 94320 Thiais, France*

David Hrabovsky − *Plateforme Mesures Physiques à Basses Températures (MPBT), Sorbonne Université, 75005 Paris, France*

https://doi.org/10.1021/acs.langmuir.4c02495
Langmuir 2024, 40, 22673−22683

Adama Konaté − *Service d'Analyse Physico-Chimique, Université de Technologie de Compiègne, Compiègne Cedex F-60205, France*
Djimédo Kondo − *CNRS, Institut Jean Le Rond D'Alembert, Sorbonne Université, 75005 Paris, France*
Fahmi Bedoui − *Roberval (Mechanics, Energy and Electricity), Centre de recherche Royallieu—CS, Université de technologie de Compiègne, 60 319-60 203 Compiègne Cedex, France; Materials and Process simulation Center, California institute of Technology, Pasadena 91106 California, United States;* orcid.org/0000-0002-2607-5209

Complete contact information is available at: https://pubs.acs.org/10.1021/acs.langmuir.4c02495

Notes

The authors declare no competing financial interest.

■ ACKNOWLEDGMENTS

The authors thank the ANR NanoHype "Temperature Profile in Nanomagnet-based Hyperthermia Devices" (contract number ANR-21-CE09-0043) and the LEEGO chair program for supporting this work. S.M. gratefully acknowledges the financial support from the Institut de science des matériaux (IMat) de Sorbonne Université for the Ph.D. Scholarship, contract number IMAT-DOCTORANT SORBR122RRO. Additionally, the authors thank François Oudet, Caroline Lefebvre, and Frédéric Nadaud from the Physico-Chemical Analysis Service (SAPC) for their contributions.

■ REFERENCES

(1) Sheng, S.; Liu, W.; Zhu, K.; Cheng, K.; Ye, K.; Wang, G.; Cao, D.; Yan, J. Fe3O4 Nanospheres in Situ Decorated Graphene as High-Performance Anode for Asymmetric Supercapacitor with Impressive Energy Density. *J. Colloid Interface Sci.* **2019**, *536*, 235−244.
(2) Rajabi, F.; Pineda, A.; Naserian, S.; Balu, A. M.; Luque, R.; Romero, A. A. Aqueous Oxidation of Alcohols Catalysed by Recoverable Iron Oxide Nanoparticles Supported on Aluminosilicates. *Green Chem.* **2013**, *15* (5), 1232.
(3) Nguyen, M. D.; Tran, H.-V.; Xu, S.; Lee, T. R. Fe3O4 Nanoparticles: Structures, Synthesis, Magnetic Properties, Surface Functionalization, and Emerging Applications. *Appl. Sci.* **2021**, *11* (23), 11301.
(4) Andrade, R. G. D.; Veloso, S. R. S.; Castanheira, E. M. S. Shape Anisotropic Iron Oxide-Based Magnetic Nanoparticles: Synthesis and Biomedical Applications. *Int. J. Mol. Sci.* **2020**, *21* (7), 2455.
(5) Rebodos, R. L.; Vikesland, P. J. Effects of Oxidation on the Magnetization of Nanoparticulate Magnetite. *Langmuir* **2010**, *26* (22), 16745−16753.
(6) Shokrollahi, H. A Review of the Magnetic Properties, Synthesis Methods and Applications of Maghemite. *J. Magn. Magn. Mater.* **2017**, *426*, 74−81.
(7) Ansari, S. A. M. K.; Ficiarà, E.; Ruffinatti, F. A.; Stura, I.; Argenziano, M.; Abollino, O.; Cavalli, R.; Guiot, C.; D'Agata, F. Magnetic Iron Oxide Nanoparticles: Synthesis, Characterization and Functionalization for Biomedical Applications in the Central Nervous System. *Mater. Basel Switz.* **2019**, *12* (3), 465.
(8) Sun, S.; Zeng, H. Size-Controlled Synthesis of Magnetite Nanoparticles. *J. Am. Chem. Soc.* **2002**, *124* (28), 8204−8205.
(9) Jana, N. R.; Chen, Y.; Peng, X. Size- and Shape-Controlled Magnetic (Cr, Mn, Fe, Co, Ni) Oxide Nanocrystals via a Simple and General Approach. *Chem. Mater.* **2004**, *16* (20), 3931−3935.
(10) Redl, F. X.; Black, C. T.; Papaefthymiou, G. C.; Sandstrom, R. L.; Yin, M.; Zeng, H.; Murray, C. B.; O'Brien, S. P. Magnetic, Electronic, and Structural Characterization of Nonstoichiometric Iron Oxides at the Nanoscale. *J. Am. Chem. Soc.* **2004**, *126* (44), 14583−14599.
(11) Park, J.; An, K.; Hwang, Y.; Park, J.-G.; Noh, H.-J.; Kim, J.-Y.; Park, J.-H.; Hwang, N.-M.; Hyeon, T. Ultra-Large-Scale Syntheses of Monodisperse Nanocrystals. *Nat. Mater.* **2004**, *3* (12), 891−895.
(12) Demortière, A.; Panissod, P.; Pichon, B. P.; Pourroy, G.; Guillon, D.; Donnio, B.; Bégin-Colin, S. Size-Dependent Properties of Magnetic Iron Oxide Nanocrystals. *Nanoscale* **2011**, *3* (1), 225−232.
(13) Pauly, M.; Pichon, B. P.; Panissod, P.; Fleutot, S.; Rodriguez, P.; Drillon, M.; Begin-Colin, S. Size Dependent Dipolar Interactions in Iron Oxide Nanoparticle Monolayer and Multilayer Langmuir−Blodgett Films. *J. Mater. Chem.* **2012**, *22* (13), 6343−6350.
(14) Baaziz, W.; Pichon, B. P.; Fleutot, S.; Liu, Y.; Lefevre, C.; Greneche, J.-M.; Toumi, M.; Mhiri, T.; Begin-Colin, S. Magnetic Iron Oxide Nanoparticles: Reproducible Tuning of the Size and Nanosized-Dependent Composition, Defects, and Spin Canting. *J. Phys. Chem. C* **2014**, *118* (7), 3795−3810.
(15) Baaziz, W.; Pichon, B. P.; Grenèche, J.-M.; Begin-Colin, S. Effect of Reaction Environment and in Situ Formation of the Precursor on the Composition and Shape of Iron Oxide Nanoparticles Synthesized by the Thermal Decomposition Method. *CrystEngComm* **2018**, *20* (44), 7206−7220.
(16) Kovalenko, M. V.; Bodnarchuk, M. I.; Lechner, R. T.; Hesser, G.; Schäffler, F.; Heiss, W. Fatty Acid Salts as Stabilizers in Size- and Shape-Controlled Nanocrystal Synthesis: The Case of Inverse Spinel Iron Oxide. *J. Am. Chem. Soc.* **2007**, *129* (20), 6352−6353.
(17) Yang, H.; Ogawa, T.; Hasegawa, D.; Takahashi, M. Synthesis and Magnetic Properties of Monodisperse Magnetite Nanocubes. *J. Appl. Phys.* **2008**, *103* (7), No. 07D526.
(18) Kim, D.; Lee, N.; Park, M.; Kim, B. H.; An, K.; Hyeon, T. Synthesis of Uniform Ferrimagnetic Magnetite Nanocubes. *J. Am. Chem. Soc.* **2009**, *131* (2), 454−455.
(19) Guardia, P.; Pérez, N.; Labarta, A.; Batlle, X. Controlled Synthesis of Iron Oxide Nanoparticles over a Wide Size Range. *Langmuir* **2010**, *26* (8), 5843−5847.
(20) Pauly, M.; Pichon, B. P.; Albouy, P.-A.; Fleutot, S.; Leuvrey, C.; Trassin, M.; Gallani, J.-L.; Begin-Colin, S. Monolayer and Multilayer Assemblies of Spherically and Cubic-Shaped Iron Oxide Nanoparticles. *J. Mater. Chem.* **2011**, *21* (40), 16018−16027.
(21) Zhang, L.; Wu, J.; Liao, H.; Hou, Y.; Gao, S. Octahedral Fe3O4nanoparticles and Their Assembled Structures. *Chem. Commun.* **2009**, *29*, 4378−4380.
(22) Zhao, Z.; Zhou, Z.; Bao, J.; Wang, Z.; Hu, J.; Chi, X.; Ni, K.; Wang, R.; Chen, X.; Chen, Z.; Gao, J. Octapod Iron Oxide Nanoparticles as High-Performance T2 Contrast Agents for Magnetic Resonance Imaging. *Nat. Commun.* **2013**, *4* (1), 2266.
(23) Zhou, Z.; Zhu, X.; Wu, D.; Chen, Q.; Huang, D.; Sun, C.; Xin, J.; Ni, K.; Gao, J. Anisotropic Shaped Iron Oxide Nanostructures: Controlled Synthesis and Proton Relaxation Shortening Effects. *Chem. Mater.* **2015**, *27* (9), 3505−3515.
(24) Roca, A. G.; Gutiérrez, L.; Gavilán, H.; Fortes Brollo, M. E.; Veintemillas-Verdaguer, S.; Morales, M. D. P. Design Strategies for Shape-Controlled Magnetic Iron Oxide Nanoparticles. *Adv. Drug Delivery Rev.* **2019**, *138*, 68−104.
(25) Park, J.; Joo, J.; Kwon, S. G.; Jang, Y.; Hyeon, T. Synthesis of Monodisperse Spherical Nanocrystals. *Angew. Chem., Int. Ed. Engl.* **2007**, *46* (25), 4630−4660.
(26) Wu, L.; Mendoza-Garcia, A.; Li, Q.; Sun, S. Organic Phase Syntheses of Magnetic Nanoparticles and Their Applications. *Chem. Rev.* **2016**, *116* (18), 10473−10512.
(27) Meftah, S.; Ngo, A.-T.; Shahmanesh, A.; Courty, A.; Kondo, D.; Bedoui, F.; Lisiecki, I. Striking Effect of the Iron Stearate Purity on the Shape and Size of Maghemite Nanoparticles. *Colloids Surf. Physicochem. Eng. Asp.* **2024**, *680*, No. 132689.
(28) Dehsari, H. S.; Ribeiro, A. H.; Ersöz, B.; Tremel, W.; Jakob, G.; Asadi, K. Effect of Precursor Concentration on Size Evolution of Iron Oxide Nanoparticles. *CrystEngComm* **2017**, *19* (44), 6694−6702.

(29) Henry, A.-I.; Courty, A.; Pileni, M.-P.; Albouy, P.-A.; Israelachvili, J. Tuning of Solid Phase in Supracrystals Made of Silver Nanocrystals. *Nano Lett.* **2008**, *8* (7), 2000−2005.
(30) Lee, S.; Ngo, A.-T.; Lisiecki, I.; Courty, A. Structural Diversity in Binary Superlattices from Au and γ-Fe2O3 Nanocrystals: Towards Fine Tuning of Dipolar Interactions. *Mater. Chem. Front.* **2022**, *6* (13), 1814−1823.
(31) Wan, Y.; Goubet, N.; Albouy, P.-A.; Schaeffer, N.; Pileni, M.-P. Hierarchy in Au Nanocrystal Ordering in a Supracrystal: II. Control of Interparticle Distances. *Langmuir ACS J. Surf. Colloids* **2013**, *29* (44), 13576−13581.
(32) Wan, Y. F.; Goubet, N.; Albouy, P. A.; Pileni, M. P. Hierarchy in Au Nanocrystal Ordering in Supracrystals: A Potential Approach to Detect New Physical Properties. *Langmuir ACS J. Surf. Colloids* **2013**, *29* (24), 7456−7463.
(33) Navarro Oliva, F. S.; Sahihi, M.; Lenglet, L.; Ospina, A.; Guenin, E.; Jaramillo-Botero, A.; Goddard, W. A.; Bedoui, F. Nanoparticle Size and Surface Chemistry Effects on Mechanical and Physical Properties of Nano-Reinforced Polymers: The Case of PVDF-Fe3O4 Nano-Composites. *Polym. Test.* **2023**, *117*, No. 107851.
(34) Bedoui, F.; Sahihi, M.; Jaramillo-Botero, A.; Goddard, W. A. I. Enhancing Multifunctionality: Optimal Properties of Iron-Oxide-Reinforced Polyvinylidene Difluoride Unveiled Through Full Atom Molecular Dynamics Simulations. *Langmuir* **2024**, *40* (15), 8067−8073.
(35) Bronstein, L. M.; Huang, X.; Retrum, J.; Schmucker, A.; Pink, M.; Stein, B. D.; Dragnea, B. Influence of Iron Oleate Complex Structure on Iron Oxide Nanoparticle Formation. *Chem. Mater.* **2007**, *19* (15), 3624−3632.
(36) Balakrishnan, T.; Lee, M.-J.; Dey, J.; Choi, S.-M. Sub-Nanometer Scale Size-Control of Iron Oxide Nanoparticles with Drying Time of Iron Oleate. *CrystEngComm* **2019**, *21* (27), 4063−4071.
(37) Hufschmid, R.; Arami, H.; Ferguson, R. M.; Gonzales, M.; Teeman, E.; Brush, L. N.; Browning, N. D.; Krishnan, K. M. Synthesis of Phase-Pure and Monodisperse Iron Oxide Nanoparticles by Thermal Decomposition. *Nanoscale* **2015**, *7* (25), 11142−11154.
(38) Vargas, J. M.; Zysler, R. D. Tailoring the Size in Colloidal Iron Oxide Magnetic Nanoparticles. *Nanotechnology* **2005**, *16* (9), 1474.
(39) Yu, W. W.; Falkner, J. C.; Yavuz, C. T.; Colvin, V. L. Synthesis of Monodisperse Iron Oxide Nanocrystals by Thermal Decomposition of Iron Carboxylate Salts. *Chem. Commun.* **2004**, *0* (20), 2306−2307.
(40) Zhu, Y.; Jiang, F. Y.; Chen, K.; Kang, F.; Tang, Z. K. Size-Controlled Synthesis of Monodisperse Superparamagnetic Iron Oxide Nanoparticles. *J. Alloys Compd.* **2011**, *509* (34), 8549−8553.
(41) Moya, C.; Batlle, X.; Labarta, A. The Effect of Oleic Acid on the Synthesis of Fe3−xO4 Nanoparticles over a Wide Size Range. *Phys. Chem. Chem. Phys.* **2015**, *17* (41), 27373−27379.
(42) Calvin, J. J.; Brewer, A. S.; Alivisatos, A. P. The Role of Organic Ligand Shell Structures in Colloidal Nanocrystal Synthesis. *Nat. Synth.* **2022**, *1* (2), 127−137.
(43) Tadmor, R.; Rosensweig, R. E.; Frey, J.; Klein, J. Resolving the Puzzle of Ferrofluid Dispersants. *Langmuir* **2000**, *16* (24), 9117−9120.
(44) Gupta, A. K.; Gupta, M. Synthesis and Surface Engineering of Iron Oxide Nanoparticles for Biomedical Applications. *Biomaterials* **2005**, *26* (18), 3995−4021.
(45) Costanzo, S.; Simon, G.; Richardi, J.; Colomban, Ph.; Lisiecki, I. Solvent Effects on Cobalt Nanocrystal Synthesis—A Facile Strategy To Control the Size of Co Nanocrystals. *J. Phys. Chem. C* **2016**, *120* (38), 22054−22061.
(46) Roca, A. G.; Marco, J. F.; Morales, M.; Del, P.; Serna, C. J. Effect of Nature and Particle Size on Properties of Uniform Magnetite and Maghemite Nanoparticles. *J. Phys. Chem. C* **2007**, *111* (50), 18577−18584.
(47) Patterson, A. L. The Scherrer Formula for X-Ray Particle Size Determination. *Phys. Rev.* **1939**, *56* (10), 978−982.
(48) Sappey, R.; Vincent, E.; Hadacek, N.; Chaput, F.; Boilot, J. P.; Zins, D. Nonmonotonic Field Dependence of the Zero-Field Cooled Magnetization Peak in Some Systems of Magnetic Nanoparticles. *Phys. Rev. B* **1997**, *56* (22), 14551−14559.
(49) Bruvera, I. J.; Mendoza Zélis, P.; Pilar Calatayud, M.; Goya, G. F.; Sánchez, F. H. Determination of the Blocking Temperature of Magnetic Nanoparticles: The Good, the Bad, and the Ugly. *J. Appl. Phys.* **2015**, *118* (18), 184304.
(50) Livesey, K. L.; Ruta, S.; Anderson, N. R.; Baldomir, D.; Chantrell, R. W.; Serantes, D. Beyond the Blocking Model to Fit Nanoparticle ZFC/FC Magnetisation Curves. *Sci. Rep.* **2018**, *8* (1), 11166.
(51) Schmitz-Antoniak, C. X-Ray Absorption Spectroscopy on Magnetic Nanoscale Systems for Modern Applications. *Rep. Prog. Phys.* **2015**, *78* (6), No. 062501.
(52) Tronc, E.; Prene, P.; Jolivet, J. P.; d'Orazio, F.; Lucari, F.; Fiorani, D.; Godinho, M.; Cherkaoui, R.; Nogues, M.; Dormann, J. L. Magnetic Behaviour of γ-Fe2O3 Nanoparticles by Mössbauer Spectroscopy and Magnetic Measurements. *Hyperfine Interact.* **1995**, *95* (1), 129−148.
(53) Kechrakos, D.; Trohidou, K. N. Magnetic Properties of Self-Assembled Interacting Nanoparticles. *Appl. Phys. Lett.* **2002**, *81* (24), 4574−4576.
(54) Stoner, E. C.; Wohlfarth, E. P. A Mechanism of Magnetic Hysteresis in Heterogeneous Alloys. *IEEE Trans. Magn.* **1991**, *27* (4), 3475−3518.
(55) Ngo, A. T.; Pileni, M. P. Assemblies of Ferrite Nanocrystals: Partial Orientation of the Easy Magnetic Axes. *J. Phys. Chem. B* **2001**, *105* (1), 53−58.
(56) Sehdev, N.; Medwal, R.; Annapoorni, S. Enhanced Phase Stabilization of CoPt in the Presence of Ag. *J. Appl. Phys.* **2011**, *110* (3), No. 033901.
(57) Kim, J. Fabrication of CoPt Nanoparticles with High Coercivity on a Polymer Film. *Colloids Surf., A* **2007**, *301*, 419.

https://doi.org/10.1021/acs.langmuir.4c02495
Langmuir 2024, 40, 22673−22683

Colloids and Surfaces A: Physicochemical and Engineering Aspects 680 (2024) 132689

Contents lists available at ScienceDirect

Colloids and Surfaces A: Physicochemical and Engineering Aspects

journal homepage: www.elsevier.com/locate/colsurfa

Striking effect of the iron stearate purity on the shape and size of maghemite nanoparticles

Sakina Meftah [a,b], Anh-Tu Ngo [a], Ashkan Shahmanesh [a], Alexa Courty [a], Djimédo Kondo [c], Fahmi Bedoui [b,d], Isabelle Lisiecki [a,*]

[a] Sorbonne Université, CNRS, De la Molécule aux Nano-Objets: Réactivité, Interactions Spectroscopies, MONARIS, 75005 Paris, France
[b] Centre de Recherche de Royallieu, Roberval Laboratory for Mechanics, CNRS, Université de Technologie de Compiègne, 60203 Compiègne, France
[c] Sorbonne Université, CNRS, Institut Jean Le Rond D'Alembert, 75005 Paris, France
[d] California Institute of Technology, Materials and Process Simulation Center, 91106 Pasadena, CA, USA

GRAPHICAL ABSTRACT

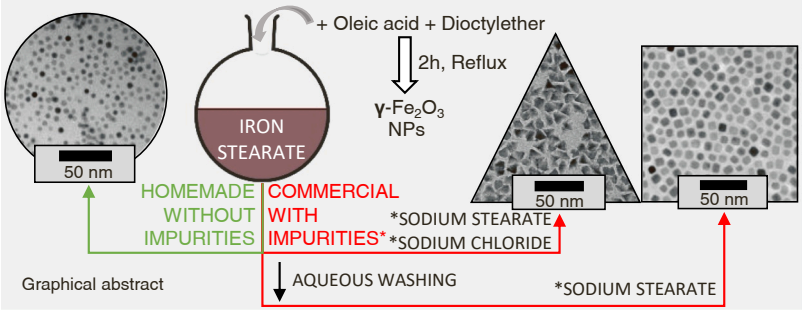

ARTICLE INFO

Keywords:
Maghemite nanoparticles
Thermal decomposition
Iron stearate
Impurities
Cubic
Triangular
And spherical shapes

ABSTRACT

In general, the synthesis of maghemite nanoparticles (NPs) by thermal decomposition of commercially available iron stearate precursors, in the presence of oleic acid, yields spherical nanoparticles. However, we show in this article that the synthesis of NPs from commercially available precursors (Commercial grade and washed) results in the formation of uniformly monodisperse triangular or cubic NPs. Spherical NPs result only from the precursors synthesized in the laboratory. The detailed Energy Dispersive X-ray spectrometry (EDS) and X-ray diffraction analysis performed on the commercial precursors (Commercial grade and washed) reveal the presence of impurities: sodium stearate and/or sodium chloride (NaCl). This result highlights the importance of iron stearate precursor origin (commercial grade or washed or home-made) in terms of reproducibility and growth of iron oxide NPs, giving rise to either monodisperse spherical, cubic, or triangular NPs. We emphasize that this finding majorly affects the development of NPs and also our understanding of the NP growth mechanisms, which can be biased if we do not account for this additional key parameter among all the ones involved in the colloidal synthesis. The formation of the triangular nanoparticles in the conditions we use has never been reported. Further, the formation of both cubic and triangular NPs has been discussed in terms of selective adsorption on the growing NP of sodium stearate, sodium, and chloride salts.

* Corresponding author.

https://doi.org/10.1016/j.colsurfa.2023.132689
Received 8 June 2023; Received in revised form 4 September 2023; Accepted 29 October 2023
Available online 3 November 2023

1. Introduction

In the last 20 years, iron oxide nanoparticles (NPs) have been extensively studied for their use in many technological applications such as energy storage [1], catalysis [2] and wastewater treatment [3]. In addition, thanks to their biocompatibility combined with their chemical stability, they are also widely used in biomedicine [4].

To continuously improve their performances, it is crucial to accurately control their structural characteristics (composition, nano crystallinity, size, geometry, and surface chemistry). Among the existing approaches to synthesizing NPs, the decomposition of metal precursors is more appropriate to favor uniform NPs. Using this strategy, uniform iron oxide NPs with controlled size [5–13] and shape [14–23] have been obtained. However, many key parameters must be controlled to successfully prepare well-defined populations. Hence, NP structural characteristics depend on the nature of the precursors, the ligands and the solvent, the heating rate, the reaction time, the reaction temperature, the precursor injection time, the surfactant to precursor ratio, and the presence of additives [24,25].

The reproducibility of these syntheses requires perfect control of all the key parameters playing a role in the formation of the NPs from the atomic scale (precursor decomposition, solvation of reactants, adsorption of ligands and salts …) to the nanoscale (nucleation, growth, aging steps …). In addition, a deep understanding of the nucleation and growth mechanisms of NPs is crucial, especially to highlight novel nanomaterials.

In this article, we report that one key parameter in the reproducibility of spherical iron oxide NPs by the thermal decomposition of iron stearate precursor is its origin. In the literature, it has been reported that the use of iron stearate precursors from the supplier Strem Chemicals [11,12] leads to spherical iron oxide NPs. Here, we show that the same synthesis approach using commercial iron (II) and iron (III) precursors provided by Strem chemicals and TCI, respectively, yields different anisotropic shape NPs, i.e., triangular and cubic ones, with different sizes. Besides, a washing step performed for the iron (II) precursor (Strem chemicals), induces a change from triangular to cubic NPs. Finally, the spherical NPs are recovered by using a precursor synthesized in the laboratory. Thanks to a qualitative and quantitative chemical analysis study performed by energy dispersive X-ray spectrometry (EDS) analysis and X-ray diffraction (XRD), we evidence the presence of various impurities (sodium stearate and/or sodium chloride) in the two commercial precursors (used as-received or washed), explaining, the formation of anisotropic shape NPs.

First, this study evidences the importance of the origin of the iron stearate precursor (as received commercially or washed, or homemade), i.e. its purity, on the growth of maghemite NPs as well as the role played by the detected impurities on the determination of the particle shape (spherical, cubic and triangular). Second, it highlights that the identification of the nature of the impurities, rarely proposed in the literature, is needed for the understanding of the NP growth mechanisms, which are still not totally elucidated. Third, the presence of the detected impurities in the commercial precursors is explained in terms of mistakes made in their fabrication. Fourth, triangular NPs are here formed using a strategy, that has never been reported previously.

2. Experimental section

2.1. Chemicals

Iron (III) chloride ($FeCl_3.6\ H_2O$, 99%, VWR), sodium stearate ($CH_3(CH_2)_{16}COONa$, 97%, TCI), iron (II) stearate (9% Fe, Strem Chemicals), iron (III) stearate (5.8–7% Fe, TCI), Oleic acid (99%, alpha aesar) and dioctyl ether (99%, sigma-aldrich).

2.2. Synthesis of iron (III) stearate precursor

Iron (III) stearate ($FeSt_3$) was prepared by reaction of sodium stearate (NaSt) and iron (III) chloride salts ($FeCl_3$) in an aqueous solution [13]. Sodium stearate (9.8 g, 32 mmol) is transferred into a two-necked round-bottomed flask (RBF) and solubilized in 320 mL of ultrapure water. The solution is heated to reflux at 120 °C and stirred for 30 min until complete dissolution of the stearate. Separately, $FeCl_3$ (2.9 g, 10.7 mmol) is dissolved in 160 mL of ultrapure water and added to the sodium stearate solution under vigorous stirring. A light orange precipitate formed immediately. The solution is kept under stirring at this temperature for 25 min. Thereafter the solution is allowed to cool to room temperature. The obtained precipitate is washed with 4 L of ultrapure water and filtrated with a Buchner funnel and oven-dried at 64 °C for 22 h.

2.3. Transmission electron microscopy (TEM)

TEM study is performed using a JEOL JEM-1011 microscope at 100 kV. For this study, some drops of the colloidal solution are deposited on an amorphous carbon-coated TEM grid. The average diameter and the polydispersity of NPs are determined from more than 500 NPs using ImageJ.

2.4. Microanalysis

The chemical compositions were determined by energy dispersive X-ray spectrometry (EDS) analysis using a scanning electron microscope (SEM, JEOL 5510 LV, Ltd, Tokyo, Japan) with IXRF Systems 500 digital processing.

2.5. X-ray diffraction

Powder X-ray diffraction (PXRD) diffractograms were recorded on a D8 DISCOVER of a Bruker XRD machine with a copper tube operating at 40 kV. All the samples were in the form of powder by which low background silicon sample holders were filled.

2.6. Synthesis of oleic acid-coated γ-Fe_2O_3 nanoparticles

Synthesis of oleic acid-coated γ-Fe_2O_3 nanoparticles is based on the thermal decomposition approach reported in a previous study by Begin-Colin et al., [10,11] however some with slight modification i.e., a smaller volume of dioctyl ether (10 mL instead of 20 mL) and a higher heating rate (45 °C/min instead of 5 °C/min).

0.69 g (1.1 mmol) of iron (II) stearate ($FeSt_2$) precursor (or 1 g (1.1 mmol) of iron (III) stearate ($FeSt_3$) precursor), and 0.63 g (2.2 mmol) of oleic acid are dissolved in 10 mL of dioctyl ether. This mixture is heated to the boiling point of dioctyl ether (287 °C) with a heating rate of 45 °C/min, refluxed for 2 h, and then cooled to room temperature. A black solution is formed and washed with a large excess of acetone followed by centrifugation (4900 rpm, 5 min). The oleic acid-coated NPs are finally dispersed in chloroform.

Five oleic acid-coated γ-Fe_2O_3 NP syntheses are performed with the same recipe described above with commercial iron (II) stearate precursor from Strem Chemicals, as received (P_1), *and* washed (P_1^w), *and* iron (III) stearate precursor from TCI, as received (P_2) and washed (P_2^w), and iron (III) stearate precursor synthesized in the laboratory, (P_3).

The commercial $FeSt_2$ and $FeSt_3$ precursors are washed as follows: 10 g of precursor in powder form is mixed with 150 mL of ultrapure water under vigorous stirring and is heated to 65 °C for 15 min. Then the mixture is cooled to room temperature. The precursor is then washed with 4 L of ultrapure water and filtrated with a Buchner funnel and oven-dried at 64 °C for 22 h.

3. Results and discussion

3.1. Synthesis of γ-Fe_2O_3 NPs using precursors P_1 and P_1^w

Fig. 1a and 1b show the TEM images of γ-Fe_2O_3 NPs synthesized using commercial grade iron (II) stearate ($FeSt_2$), P_1. Low and high-magnification images reveal a population composed of almost uniform NPs with triangular shape. The corresponding size histogram (Fig. 1d), shows a mean triangle height and a size polydispersity of 9.7 nm and 16% respectively. Surprisingly, the synthesis performed with the same

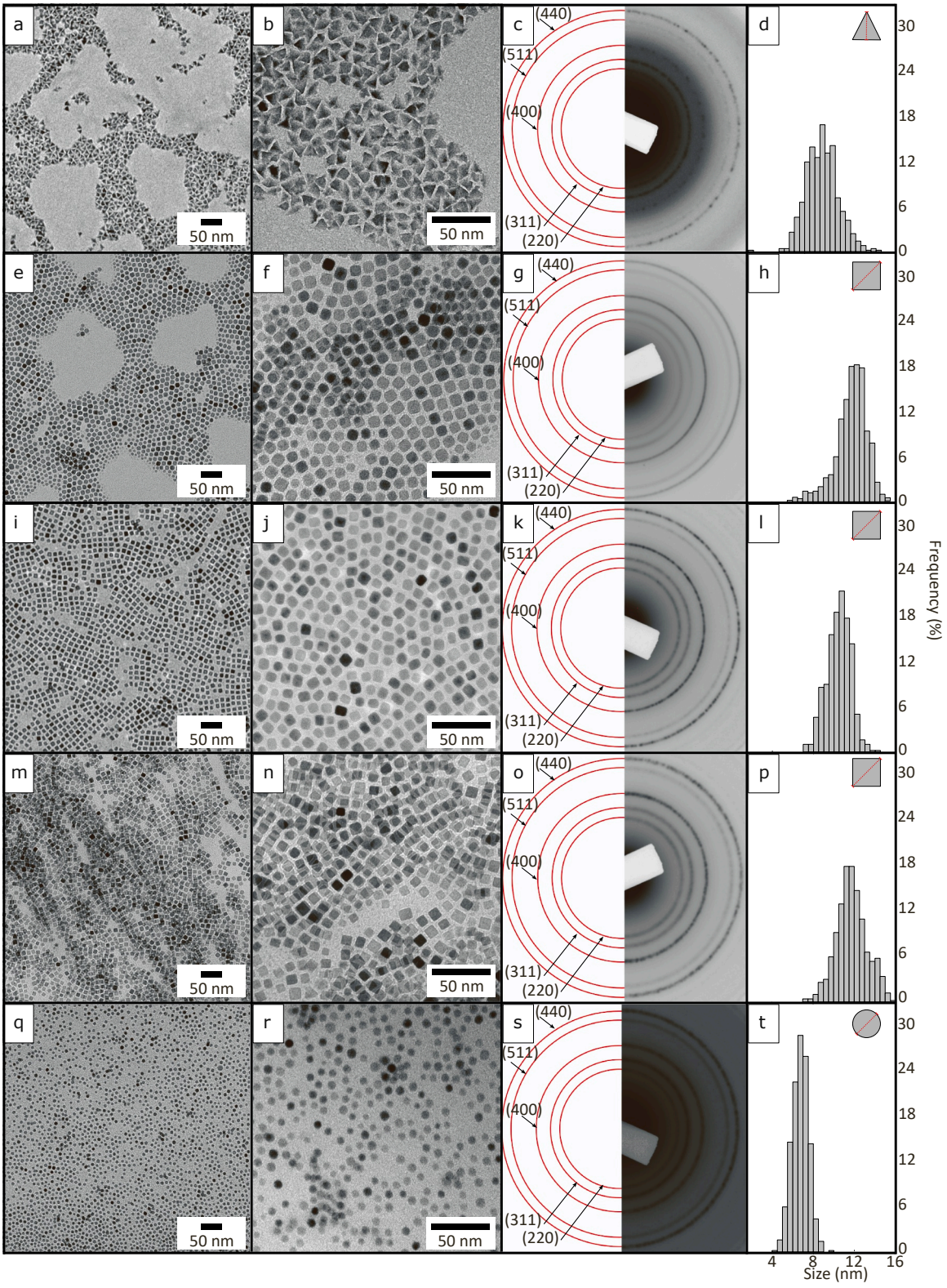

Fig. 1. TEM images, corresponding electron diffraction patterns, and size histograms of maghemite (γ-Fe_2O_3) nanoparticles synthesized with P_1 (a,b,c,d), P_1^w (e,f,g,h), P_2 (i,j,k,l), P_2^w (m,n,o,p) and P_3 (q,r,s,t) precursors.

precursor but after being washed, P_1^w, leads to a single population of nanocubes. As shown in Fig. 1e and 1f, they are characterized by flat facets and sharp edges and their mean side diagonal is 10.5 nm. Thanks to a very low size polydispersity, 11% (Fig. 1h), they tend to self-organize in 2D superlattices.

3.1.1. Synthesis of γ-Fe_2O_3 NPs using precursor P_2 and P_2^w

Replacing iron (II) stearate ($FeSt_2$) precursor P_1 with iron (III) stearate ($FeSt_3$) precursor P_2, while keeping other chemical components the same, results in a drastic change in the NP shape. Considering the as-received precursor (not washed), Fig. 1i and 1j clearly show that the population is made of nanocubes and not nanotriangles, which have rather similar characteristics compared to the sample prepared with the precursor P_1, i.e., a mean side diagonal and size polydispersity of 11.7 nm and 13% respectively (Fig. 1l). In this case, no washing effect on this precursor is observed as the population obtained with P_2^w, remains composed of nanocubes (Fig. 1m,1n) with similar mean side diagonal and size polydispersity of 11.7 nm and 11.7% respectively (Fig. 1p).

3.1.2. Synthesis of γ-Fe_2O_3 NPs using precursor P_3

Finally, using a precursor we synthesized in the laboratory iron (III) stearate ($FeSt_3$), P_3, a single population of spherical γ-Fe_2O_3 NPs form (Fig. 1q, 1r). The size histogram (Fig. 1t) shows a mean diameter of 6.7 nm with a size polydispersity of 12%.

From previous studies reported in the literature [9–13], a similar approach used to synthesize maghemite NPs induces the formation of spherical ones. In our study, we find that spherical NPs are only formed with the use of the home-made precursor P_3 and never with the commercial ones (as-received and washed). In addition, our results clearly evidence a drastic impact of both the supplier and the washing of the commercial product in the anisotropic shape of NPs. To understand this puzzling result, elemental analysis and X-ray diffraction studies have been performed for the different precursors to determine the possible impurities qualitatively and quantitatively, which could explain the differences we observe in the NP growth that in turn their final shape.

3.2. Study of the crystalline structure of the nanoparticles

3.2.1. Electron diffraction

The crystalline structure of the five populations of NPs obtained with P_1, P_2, P_1^w, and P_2^w and P_3 precursors have been investigated by the selected area electron diffraction (SAED). Whatever the precursor used and the shape of the NPs are, the electron diffraction patterns (Fig. 1c, 1g, 1k, 1o,1s) show five rather thin diffraction rings at 1.47, 1.60, 2.08, 1.51, and 2.95 Å corresponding to the (440), (511), (400), (311), and (220) planes of a maghemite iron oxide phase according to the JCPD 39–1346 database. However, it's important to note that the lattice spacings of the maghemite and magnetite phases are very close. This is thus difficult to conclude that our samples consist of pure maghemite. To address this uncertainty, the X-ray diffraction technique has been used to gain a more comprehensive understanding of the crystal structures of our NPs.

3.2.2. X-ray diffraction

To discriminate between magnetite and maghemite phases of the iron oxide nanoparticles synthesized by using the different precursors (P_1^w, P_2, P_2^w, P_3), we follow the method developed by Kim et al. [26] based on the X-ray analysis. The X-ray corresponding patterns are presented in Fig. 2. For all the samples, we detect the peaks characteristic of maghemite or magnetite, i.e., while peaks corresponding to hematite and wüstite are noticeably absent. The two peaks (210) and (211), which are the signature of exclusive maghemite are observed for the spherical and cubic NPs obtained with the precursors P_3 and P_2^W respectively. The cubic NPs synthesized with P_2 precursor show the (210) peak but not the (211) peak while the cubic NPs obtained with the P_1^W show the opposite trend. The presence of the (210) and/or (211)

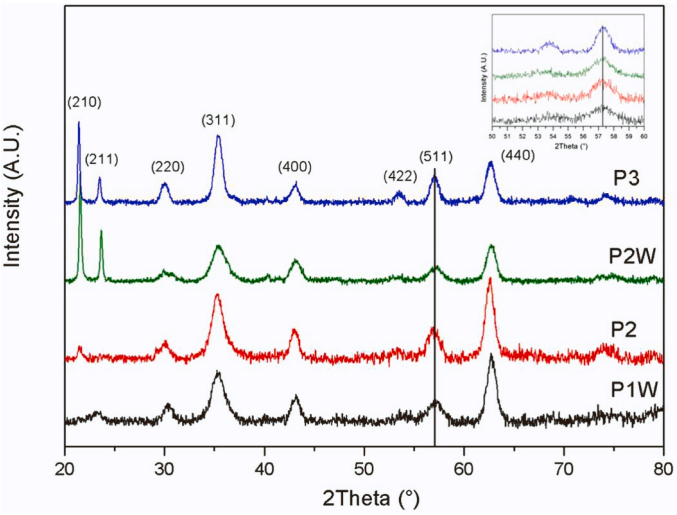

Fig. 2. XRD patterns of nanoparticles synthesized with P_1^w, P_2, P_2^w, and P_3 (e) precursors. Inset: magnified regions between 50° and 60° of the diffraction patterns.

peaks, coexisting with the others ((220), (311), (400), (422), (511), (440)), is indicative of either pure maghemite or a mixture of maghemite and magnetite. However, as reported by Kim et al. [26], the position of the peak (511) is essential as it allows to discriminate between magnetite and maghemite phases. Indeed, they show that the (511) peak shifts from 57° to 57.3° from pure magnetite to pure maghemite phase. In the case of a combination of both phases, they observe a larger peak, with a shoulder, composed of the lower and the higher angle peak [26]. As shown in the inset of Fig. 2, which represents the magnified regions between 50° and 60° of the diffraction patterns, all the (511) peaks are found at a value 2 Theta of 57.3° and appear symmetric. No shoulder characteristic of a mixture of maghemite and magnetite is observed. This feature, which agrees with the presence of the (210) and/or (211) peaks, allows us to conclude the formation of pure maghemite NPs for the spherical and cubic NPs obtained with the P_1^w, P_2, P_2^w, and P_3 precursors. Unfortunately, the triangular colloidal NP solution obtained with the P_1 precursor, could not be studied by XRD. This is explained by the too-low concentration of the colloidal solution. Indeed, we noticed that the triangular NP powder appears light red, in contrast to the black color of the other shape samples. This color variation is attributed to the presence of the precursor (color and texture). The low concentration of this population is explained by the low yield of this thermal decomposition reaction. However, the electron diffraction signature of the triangle NPs is like that of the spherical and cubic NPs. This permits us to conclude the formation of maghemite triangular NPs.

In summary, thanks to a comprehensive structural study with both electron and/or X-ray diffraction techniques, we conclude the formation of pure maghemite for the spherical, cubic, and triangular NPs synthesized with the P_1, P_1^w, P_2, P_2^w, and P_3 precursors. This result evidences that the impurities involved in the reaction, through the precursor, do not impact the crystalline structure of the iron oxide NPs. Conversely, it has a drastic effect on NP growth and therefore on the final shapes.

3.3. Characterization of P_1, P_2, P_1^w and P_2^w and P_3 precursors

3.3.1. Elemental analysis study on P_1, P_2, P_1^w and P_2^w and P_3 precursors

Elemental analysis spectra performed for the five precursors are shown in Fig. 3. In addition to the iron, and while not expected, sodium and chlorine elements are detected for the commercial precursors. The relative atomic composition of the three elements obtained by quantification of the spectra is reported in Table 1. If we focus on the precursor P_1 from Strem Chemicals, it appears that it contains a high atomic

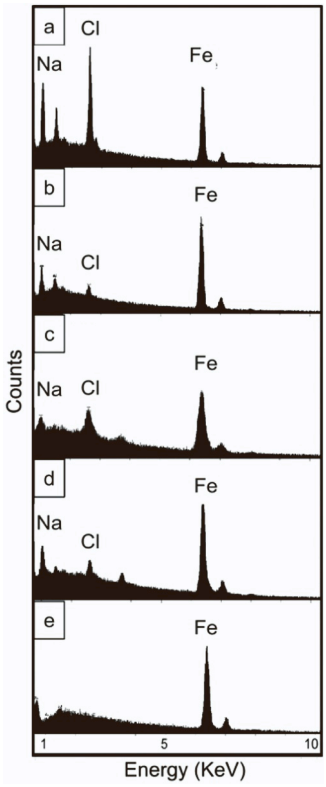

Fig. 3. EDX patterns of P_1 (a), P_1^w (b), P_2 (c), P_2^w (d), and P_3 (e) precursors.

Table 1
Relative atomic percentage of Fe, Na and Cl of the P_1, P_1^w, P_2, P_2^w and P_3 precursors.

Precursor	Atom%		
	Fe	Na	Cl
P_1	25	48	27
P_1^w	48	49	3
P_2	52	34	14
P_{2w}	58	38	4
P_3	100	0	0

percent of sodium elements, 48%. After its washing, (P_1^w), this value remains almost unchanged, 49%. Besides, 27% of chloride is detected on the as-received precursor while this value drops to 3% after its washing (P_1^w). Concerning the TCI commercial precursor, P_2, it also contains a high atomic percent of sodium elements, 34%, however only 14% of chloride is detected. P_2 washing mainly induces the drop of this last value to 4%. The same analysis performed on the home-made precursor (P_3) clearly shows that neither sodium nor chloride are detected.

3.3.2. *X-ray diffraction study on P_1, P_2, P_1^w and P_2^w and P_3 precursors*

To determine, the nature of the compounds present in the commercial P_1, P_2, P_1^w, and P_2^w precursors, an X-ray diffraction study has been performed. The XRD diffractograms are shown in Fig. 4.

For P_1 and P_2 precursors, one can detect two peaks at 31.7°, and 45.5° (marked with ∗) corresponding to the (200) and (220) plane reflections respectively, of NaCl salt [27]. After their washing, (P_1^w, P_2^w), these peaks are not anymore observed. If we focus on the smaller angle diffraction pattern, and for all the commercial precursors, P_1, P_2, P_1^w, and P_2^w, one intense peak at around 22° (marked with ◦) is observed. This peak is attributed to NaSt [28]. The XRD pattern of the home-made precursor (P_3) is characteristic of the pure lamellar structure $Fe(St)_3$ without any evidence of the presence of neither NaCl nor NaSt.

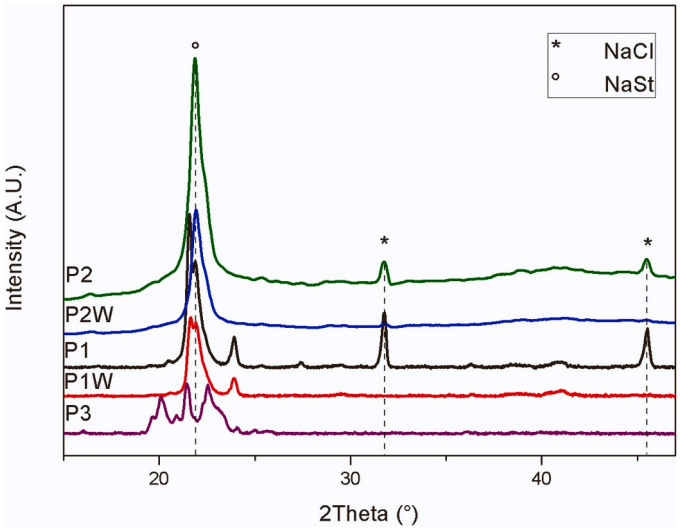

Fig. 4. XRD patterns of P_1, P_1^w, P_2, P_2^w, and P_3 precursors.

This XRD study is in good agreement with the elemental analysis. The presence of NaCl and NaSt is evidenced in the two as-received commercial precursors. After their washing, NaCl salt disappears. Finally, the home-made precursor is characterized by pure $FeSt_3$.

3.4. *How to explain the presence of the detected impurities in the commercial precursors?*

The results obtained by chemical and XRD analyses are interpreted as the following. The home-made precursor, P_3, has been synthesized in the stoichiometric conditions of the reaction:

$$FeCl_3 + 3\ NaSt => FeSt_3 + 3NaCl$$

i.e., 3 sodium stearates for 1 iron chloride (*see experimental section*). Once the iron precursor is obtained, the solution is washed with a large amount of ultrapure water (4 L) to remove the totality of the amount of sodium and chloride ions by-products. Considering the chemical analysis (Table 1), the absence of detection of these two by-products confirms that the iron precursor P_3 obtained is pure.

Conversely, for the as-received (not washed) commercial precursor P_1, a large amount of sodium and chloride ions are detected (Table 1). In addition, we note that the amount of sodium (48%) is higher compared to that of chloride ions (27%). This result makes us suggest that first, P_1 synthesis has not been performed in the stoichiometric conditions of the reaction but with a ratio of the sodium stearate to the chloride iron concentration higher than 3, leading to the presence of remaining sodium stearate and sodium chloride as by-products. Second, the washing step of the solution has not been optimal, otherwise, chloride ions would not be present. Our explanation is confirmed through the analysis of the precursor after its washing with 4 L of ultrapure water (P_1^w). The amount of detected chloride drops from 27% to 3%, while that of sodium ions remains high (49%) (Table 1). Conversely to the chloride ions, sodium ions cannot be removed during the washing with water as it forms the sodium stearate complex, which is not soluble in water. So, one can conclude that the P_1^w precursor contains a mixture of iron and sodium stearate in almost equal concentrations.

For the as-received commercial precursor P_2 (not washed), sodium (34%) and chloride (14%) are also detected. (Table 1). After its washing, the amount of chloride drops to 4%. Similar findings as for P_1 apply. However, the lower amount of sodium and chloride compared to P_1 suggests that P_2 has been produced in closer stoichiometric conditions compared to the synthesis of P_1.

3.5. Interpretation of the γ-Fe_2O_3 nanoparticle shape, in light of the nature of the impurities detected in the commercial iron stearate precursors

In light of the chemical and XRD analyses, the variety of maghemite NP shapes obtained can only be explained in terms of the purity of the iron precursors. All the other synthesis conditions are equal (ligand, solvent, heating rate, temperature, and reflux time).

When the synthesis is performed with the home-made iron stearate precursor (pure), oleic acid plays the role of universal stabilizer on each facet of the NPs, and the final NPs are spherical. In the literature, this behavior is well illustrated in several papers [10,11] reporting the formation of spherical iron oxide NPs by the thermal decomposition of iron stearate in the presence of oleic acid, without any additives. Begin-Colin et al. have evidenced that, regardless of the number of stearate chains of the iron precursor, $FeSt_2$ or $FeSt_3$ leads to spherical NPs [13,29]. It is noteworthy that spherical iron oxide NPs have also been obtained with oleate precursors, always in the presence of oleic acid and without any additives [6,8].

Conversely, when additives are present in the reaction medium, anisotropic NP growth can occur, resulting from their selective adsorption on the NP facets. For example, the addition of sodium oleate is expected to lead to cubic iron oxide NPs [14,18,21,30,31]. In this case, nanocubes are induced by the selective adsorption of the sodium oleate on the {100} facets of iron oxide. This induces the faster growth of the NP along the [111] direction over the [100] leading to surfaces composed of {100} facets. Comparative studies show, without any ambiguity, that the same approach performed in the absence and the presence of sodium oleate, gives rise to spherical and cubic NPs respectively [14,31]. Therefore, one can conclude that cubic NP growth formed by using the commercial precursors (P_1^w, P_2, and P_2^w), could be determined by the key role played by the sodium stearate.

The formation of the triangular NPs (tetrahedral geometry), is more puzzling. Chemical analysis indicates that the precursor P_1, yielding this shape, contains both sodium stearate and NaCl salt. Sodium stearate, here, is expected to bind to the {100} facets of iron oxide to form cubic NPs and then, does not seem to play a role in the formation of triangular NPs. However, it has been reported by Kovalenko et al. [14] that the thermal decomposition of iron oleate in the presence of sodium oleate gives rise to either nanocubes or a mixture of nanocubes and bipyramidal NPs. The first ones are obtained with a NaOL/$Fe(OL)_3$ molar ratio of 1 and a heating rate of 3.3 °C/min. The second ones are formed using similar growth conditions as for cubes, but by decreasing the NaOL/$Fe(OL)_3$ molar ratio to 0.67 and by reducing the heating rate to 1 °C/min. Besides, using the same approach with iron oleate precursor and sodium oleate ligand, Zhou et al. [21] observed, in mild conditions (with octadecene as solvent), the formation of Fe_3O_4 {111} facet exposed tetrahedrons, while in a higher boiling temperature solvent (tri-n-octylamine), they form nanocubes. These two examples indicate that sodium oleate may play various roles in different conditions. Concerning our study, the question is "Does the presence of NaCl in the commercial precursor P_1, could favor such a versatility of the role of sodium stearate?" At this moment, this question remains open. Otherwise, another question arises regarding the role played by Cl^- or Na^+ ions, in excess in the precursor P_1. Gao et al. [32] have shown that Cl^- adsorbs on the {100} facets of magnetite-yielding nanocubes. If we focus on the tetrahedral geometry, one hypothesis is that Na^+ ions selectively adsorb on the {111} facets of maghemite. This strategy is not excluded in a previous study reported by Liz-Marzan [31]. Besides, in a previous study performed in the laboratory, the use of Cl^- and Br^- ions has been shown to control the shape of copper NPs from nanorods to nanocubes [33]. Therefore, it is reasonable to think that either sodium stearate and/or Na^+, Cl^- ions, could be the key parameters in the growth of the triangular maghemite NPs.

3.6. Does the nature of the precursor, $FeSt_2$ and $FeSt_3$ play a role in the growth of cubic and triangular maghemite nanoparticles?

In recent papers, Begin-Colin et al. have reported the role played by the number of stearate chains (2 and 3) of the iron stearate precursors on the growth of iron oxide nanoparticles [13,29,34,35]. They have studied the influence of the ratio sodium oleate (NaOL) / oleic acid (OA) with $FeSt_2$ and $FeSt_3$ iron stearate precursors differing by their hydration state, on the shape of nanoparticles. The authors demonstrate clearly, the important role played by the presence of NaOL on the NP shape. Nanospheres are obtained in the absence of NaOL, i.e., with only OA. Facetted shapes are obtained, when NaOL is added, even at low concentration. They also show that the evolution of the shape with the amount of NaOL can depend on the nature of the precursor, $FeSt_2$ and $FeSt_3$, and on their hydration degree. For the NaOL/OA ratio (20/80), less-rounded NPs are obtained for all precursors. When this ratio increases, $FeSt_2$ and dehydrated $FeSt_2$ are allowed to obtain nanoplates while $FeSt_3$ and dehydrated $FeSt_3$ lead to nanocubes. The change in the NP shape is explained in terms of the thermal stability of the precursors, which differs from $FeSt_2$ to $FeSt_3$ iron stearate precursors.

In our study, we evidence that *maghemite nanocubes* are obtained with both $FeSt_2$ washed (P_1^w) and $FeSt_3$ washed and not washed (P_2^w, P_2) precursors. In addition, for all three cases, we identify a constant environment, i.e., the presence of sodium stearate (*see &3.4*), which is known to drive the nanoparticle growth toward the cubic shape. This result thus does not allow us to conclude an effect of the nature of the stearate precursor on the NP shape. However, it evidences the crucial role played by the presence of sodium stearate in the formation of maghemite nanocubes.

Focusing on the *triangular maghemite NPs*, we show in this paper that they are obtained with $FeSt_2$ not washed (P_1) precursor in the presence of NaSt, Na^+, and Cl^- ions. However, the same precursor, $FeSt_2$ washed (P_1^w) leads to nanocube growth. In addition, the triangular NPs are only obtained in the presence of NaSt, Na^+, and Cl^- while the nanocubes are obtained in the presence of NaSt. This behavior makes us conclude with the importance of the "impurities" in the formation of the triangles rather than the role played by the nature of the precursor.

Therefore, from the study presented in this paper, a possible impact of the nature of the precursor on the growth of anisotropic shape NPs cannot be evidenced.

This study clearly shows that the supplier, i.e., the purity of the iron stearate, must be considered in the reproducibility of maghemite NP syntheses. This constitutes another key parameter in the formation of NPs. Such finding has already been reported for other colloidal syntheses for example [36] and constitutes an impediment to the development of NPs as well as to the understanding of the growth mechanisms involved in these syntheses.

4. Conclusion

In the literature, the thermal decomposition of commercial iron stearate precursor in the presence of oleic acid surfactant (in the absence of additives) yields spherical iron oxide NPs. We show that the use of similar commercial iron precursors (used with and without a washing step) does not yield any more to the spherical but to a uniform and single population of cubic or triangular maghemite NPs. The presence of "impurities" identified as NaSt and NaCl by accurate chemical analysis and XRD study made on these precursors allow (1) to explain the cubic NP growth and (2) to highlight a new route to synthesize triangular maghemite NPs. Very few studies have been reported in the literature regarding triangular iron oxide NPs, whose growth remains unexplored. However, for highlighting novel magnetic properties, these NPs are very interesting. Further work will focus on the study of their formation mechanism to accurately control their structural properties and explore their magnetic properties.

Declaration of Competing Interest

We do not have any interest to declare.

Data availability

Data will be made available on request.

Acknowledgements

Authors thank (1) the “Institut de Sciences des Matériaux " (IMAT) of the ”Alliance Sorbonne Université ”, "Investigation of nanoparticle size effect on the properties of nano-reinforced polymers ", contract number IMAT – DOCTORANT SORBR122RRO, and (2) the ANR NanoHype " Temperature Profile in Nanomagnet based Hyperthermia Devices", contract number ANR-21-CE09–0043, for supporting this work. Thanks are also due to Mr Baptiste Roselli from the MONARIS laboratory (France) for his help with the X-ray diffraction measurements.

References

[1] S. Sheng, W. Liu, K. Zhu, K. Cheng, K. Ye, G. Wang, D. Cao, J. Yan, Fe_3O_4 nanospheres in situ decorated graphene as high-performance anode for asymmetric supercapacitor with impressive energy density, J. Colloid Interface Sci. 536 (2019) 235–244.
[2] Z.S. Wu, S. Yang, Y. Sun, K. Parvez, X. Feng, K. Müllen, 3D nitrogen-doped graphene aerogel-supported Fe_3O_4 nanoparticles as efficient electrocatalysts for the oxygen reduction reaction, J. Am. Chem. Soc. 134 (22) (2012) 9082–9085.
[3] S. Liu, B. Yu, S. Wang, Y. Shen, H. Cong, Preparation, surface functionalization and application of Fe_3O_4 magnetic nanoparticles, Adv. Colloid Interface Sci. 281 (2020), 102165.
[4] C. Blanco-Andujar, A. Walter, G. Cotin, C. Bordeianu, D. Mertz, D. Felder-Flesch, S. Begin-Colin, Design of iron oxide-based nanoparticles for MRI and magnetic hyperthermia, Nanomedicine 11 (14) (2016) 1889–1910.
[5] S. Sun, Shouheng, H. Zeng, Size-controlled synthesis of magnetite nanoparticles, J. Am. Chem. Soc. 124 (28) (2002) 8204–8205.
[6] N.R. Jana, Y. Chen, X. Peng, Size-and shape-controlled magnetic (Cr, Mn, Fe, Co, Ni) oxide nanocrystals via a simple and general approach, Chem. Mater. 16 (20) (2004) 3931–3935.
[7] F.X. Redl, C.T. Black, G.C. Papaefthymiou, R.L. Sandstrom, M. Yin, H. Zeng, C. B. Murray, S.P. O'Brien, Magnetic, electronic, and structural characterization of nonstoichiometric iron oxides at the nanoscale, J. Am. Chem. Soc. 126 (44) (2004) 14583–14599.
[8] J. Park, K. An, Y. Hwang, J.G. Park, H.J. Noh, J.Y. Kim, J.H. Park, N.M. Hwang, T. Hyeon, Ultra-large-scale syntheses of monodisperse nanocrystals, Nat. Mater. 3 (12) (2004) 891–895.
[9] A. Demortiere, P. Panissod, B. Pichon, D. Pourroy, D. Guillon, B. Donnio, S. Bégin-Colin, Size-dependent properties of magnetic iron oxide nanocrystals, Nanoscale 3 (1) (2011) 225–232.
[10] M. Pauly, B. Pichon, P. Panissod, S. Fleutot, P. Rodriguez, M. Drillon, S. Begin-Colin, Size dependent dipolar interactions in iron oxide nanoparticle monolayer and multilayer Langmuir–Blodgett films, J. Mater. Chem. 22 (13) (2012) 6343–6350.
[11] W. Baaziz, B. Pichon, S. Fleutot, Y. Liu, C. Lefevre, J.M. Greneche, M. Toumi, T. Mhiri, S. Begin-Colin, Magnetic iron oxide nanoparticles: reproducible tuning of the size and nanosized-dependent composition, defects, and spin canting, J. Phys. Chem. C. 118 (7) (2014) 3795–3810.
[12] W. Baaziz, B.P. Pichon, J.M. Grenèche, S. Begin-Colin, Effect of reaction environment and in situ formation of the precursor on the composition and shape of iron oxide nanoparticles synthesized by the thermal decomposition method, CrystEngComm 20 (44) (2018) 7206–7220.
[13] G. Cotin, C. Kiefer, F. Perton, M. Boero, B. Ozdamar, A. Bouzid, G. Ori, C. Massobrio, D. Begin, B. Pichon, D. Mertz, S. Begin-Colin, Evaluating the critical roles of precursor nature and water content when tailoring magnetic nanoparticles for specific applications, ACS Appl. Nano Mater. 1 (8) (2018) 4306–4316.
[14] M.V. Kovalenko, M.I. Bodnarchuk, R.T. Lechner, G. Hesser, F. Schäffler, W. Heiss, Fatty acid salts as stabilizers in size-and shape-controlled nanocrystal synthesis: the case of inverse spinel iron oxide, J. Am. Chem. Soc. 129 (20) (2007) 6352–6353.
[15] H. Yang, T. Ogawa, D. Hasegawa, M. Takahashi, Synthesis and magnetic properties of monodisperse magnetite nanocubes, J. Appl. Phys. 103 (7) (2008) 07D526.
[16] D. Kim, N. Lee, M. Park, B.H. Kim, K. An, T. Hyeon, Synthesis of uniform ferrimagnetic magnetite nanocubes, J. Am. Chem. Soc. 131 (2) (2009) 454–455.
[17] P. Guardia, N. Pérez, A. Labarta, X. Batlle, Controlled synthesis of iron oxide nanoparticles over a wide size range, Langmuir 26 (2010) 5843–5847.
[18] M. Pauly, B. Pichon, P. Albouy, S. Fleutot, C. Leuvrey, M. Trassin, J.L. Gallania, S. Begin-Colin, Monolayer and multilayer assemblies of spherically and cubic-shaped iron oxide nanoparticles, J. Mater. Chem. 21 (2011) 16018–16027.
[19] L.H. Zhang, J.J. Wu, H.B. Liao, Y.L. Hou, S. Gao, Octahedral Fe_3O_4 nanoparticles and their assembled structures, Commun 29 (2009) 4378–4380.
[20] Z. Zhao, Z. Zhou, J. Bao, Z. Wan, J. Hu, X. Chi, K. Ni, R. Wang, X. Chen, Z. Chen, J. Gao, Octapod iron oxide nanoparticles as high-performance T2 contrast agents for magnetic.
[21] Z. Zhou, X. Zhu, D. Wu, Q. Chen, D. Huang, C. Sun, J. Xin, K. Ni, J. Gao, Anisotropic shaped iron oxide nanostructures: controlled synthesis and proton relaxation shortening effects, Chem. Mater. 27 (2015) 3505–3515.
[22] A.G. Roca, L. Gutiérrez, H. Gavilán, M.E. Fortes Brollo, S. Veintemillas-Verdaguer, M. del Puerto, Morales, design strategies for shape-controlled magnetic iron oxide nanoparticles, Adv. Drug Deliv. Rev. 138 (2019) 68–104.
[23] M.D. Nguyen, H.V. Tran, S. Xu, T.R. Lee, Fe_3O_4 nanoparticles: structures, synthesis, magnetic properties, surface functionalization, and emerging applications, Appl. Sci. 11 (2021) 11301.
[24] J. Park, J. Joo, S.G. Kwon, Y. Jang, T. Hyeon, Synthesis of monodisperse spherical nanocrystals, Angew. Chem. 46 (2007) 4630–4660.
[25] L. Wu, A. Mendoza-Garcia, Q. Li, S. Sun, Organic phase syntheses of magnetic nanoparticles and their applications, Chem. Rev. 116 (2016) 10473–10512.
[26] W. Kim, C.Y. Suh, S.W. Cho, K.M. Roh, H. Kwon, K. Song, I.J. Shon, A new method for the identification and quantification of magnetite-maghemite mixture using conventional X-ray diffraction technique, Talanta 94 (2012) 348–352.
[27] M. Rabiei, A. Pelevicius, A. Dashti, S. Nasiri, A. Monshi, A. Vilkauskas, G. Janusas, Measurement modulus of elasticity related to the atomic density of planes in unit cell of crystal lattices, Materials 13 (19) (2020) 4380.
[28] J. Liang, Y. Ma, Y. Zheng, H.T. Davis, Solvent-induced crystal morphology transformation in a ternary soap system: sodium stearate crystalline fibers and platelets, Langmuir 17 (21) (2001) 6447–6454.
[29] F. Perton, G. Cotin, C. Kiefer, J.M. Strub, S. Cianferani, J.M. Greneche, N. Parizel, B. Heinrich, B. Pichon, D. Mertz, S. Begin-Colin, Iron stearate structures: an original tool for nanoparticles design, Inorg. Chem. 60 (2021) 12445–12456.
[30] A. Shavel, B. Rodríguez-González, M. Spasova, M. Farle, L.M. Liz-Marzán, Synthesis and characterization of iron/iron oxide core/shell nanocubes, Adv. Funct. Mater. 17 (2007) 3870–3876.
[31] A. Shavel, L.M. Liz-Marzán, Shape control of iron oxide nanoparticles, Phys. Chem. Chem. Phys. 11 (2009) 3762–3766.
[32] Z. Xu, C. Shen, Y. Tian, X. Shi, H.J. Gao, Organic phase synthesis of monodisperse iron oxide nanocrystals using iron chloride as precursor, Nanoscale 2 (2010) 1027–1032.
[33] A. Filankembo, S. Giorgio, I. Lisiecki, M.P. Pileni, Is the anion the major parameter in the shape control of nanocrystals? J. Phys. Chem. B 107 (2003) 7492–7500.
[34] G. Cotin, C. Kiefer, F. Perton, D. Ihiawakrim, C. Blanco-Andujar, S. Moldovan, C. Lefevre, O. Ersen, B. Pichon, D. Mertz, S. Begin-Colin, Unravelling the thermal decomposition parameters for the synthesis of anisotropic iron oxide nanoparticles, ACS Appl. Nano Mater. 8 (2018) 881.
[35] G. Cotin, F. Perton, C. Petit, S. Sall, C. Kiefer, V. Begin, B. Pichon, C. Lefevre, D. Mertz, J.M. Greneche, S. Begin-Colin, Chem. Mat. 32 (2020) 9245–9259.
[36] D.K. Smith, B.A. Korgel, The importance of the CTAB surfactant on the colloidal seed-mediated synthesis of gold nanorods, Langmuir 24 (2008) 644–649.

Part III

Polyisobutylene - Iron oxide Nanocomposites Synthesis

Chapter 5

In-situ Growth Kinetics of Iron Oxide Nanoparticles in a Polyisobutylene Matrix

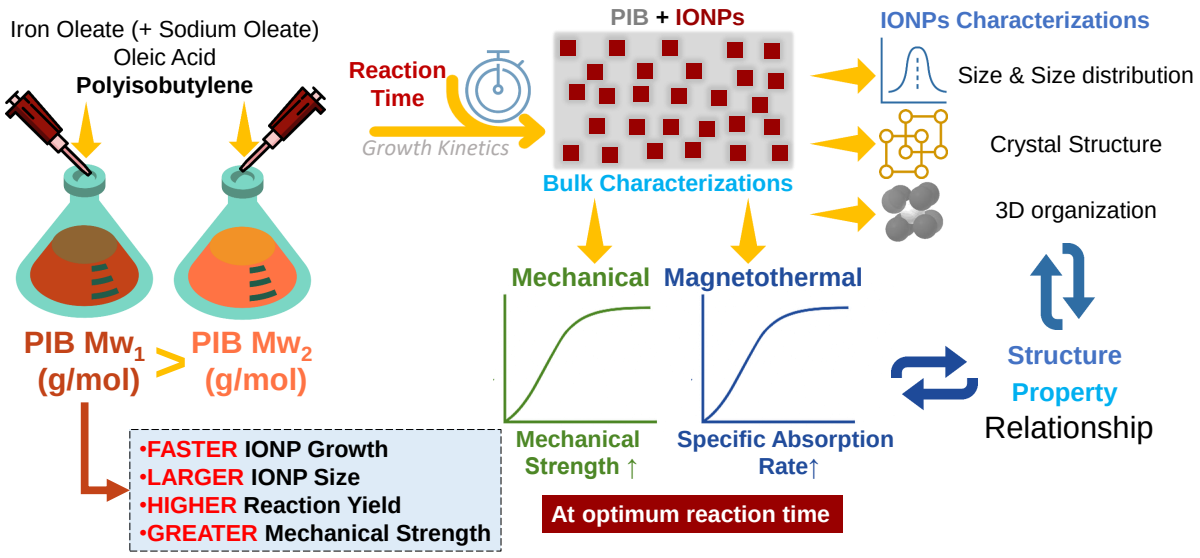

Contents

5.1 Introduction

In Chapter 2 of this PhD manuscript, we explored the development of polymer nanocomposites, highlighting the key factors that contribute to their enhanced multifunctional properties—mechanical, thermal, and electrical. A major challenge in fabricating high-performance nanocomposites lies in ensuring the homogeneous dispersion of nanoparticles within the polymer matrix. More broadly, it is essential to achieve homogeneity in terms of nanoparticle size, shape, surface chemistry, and spatial distribution within the polymer. Due to their high surface-to-volume ratio, nanoparticles have a strong tendency to agglomerate, which hinders their uniform dispersion and leads to inconsistent material properties, thereby compromising the overall performance of the nanocomposite.

Equally important is the establishment of optimal interactions at the interface between the nanoparticles and the polymer matrix. The interfacial region, which governs the transfer of stress from the matrix to the nanoparticles, plays a critical role in enhancing the mechanical behavior of the material. Without sufficient interfacial compatibility, the reinforcing potential of the nanoparticles cannot be fully exploited. Therefore, the successful fabrication of high-performance nanocomposites relies on both effective dispersion and well-matched chemical interactions, ensuring uniformity in nanoparticle characteristics through a carefully selected synthesis approach.

Despite progress in dispersion techniques, preventing nanoparticle agglomeration remains a persistent obstacle in nanocomposite processing. Conventional mixing methods—such as solution mixing or melt processing—often fail to achieve uniform nanoparticle dispersion and controlled distribution in terms of size and spatial arrangement. This results in heterogeneous materials with poorly reproducible and non-optimized properties.

To address these limitations, we have adopted in-situ synthesis methods, wherein the nanoparticles are formed directly within the polymer matrix. This approach offers two major advantages: it significantly reduces nanoparticle agglomeration and promotes strong polymer–nanoparticle interactions at the molecular level. Furthermore, it facilitates more uniform nanoparticle growth, thereby improving control over their size and morphology. These benefits were already introduced in Section 2.5.3 of Chapter 2 and will be further elaborated in the present chapter.

Building upon the knowledge and methodologies developed in our previous studies (Chapters 3 and 4), which centered on the synthesis of iron oxide nanoparticles via the thermal decomposition of carboxylate iron precursors in solution, the present chapter takes a step further by exploring the in-situ synthesis of iron oxide-based polymer nanocomposites. This approach involves the synthesis of nanoparticles directly within the polymer matrix, rather than in a separate solvent phase, thereby aiming to achieve better control over

nanoparticle dispersion, strengthen interfacial interactions, and ultimately enhance the mechanical performance of the resulting nanocomposite materials. Moreover, this method reduces direct handling of nanoparticles, thus limiting exposure and minimizing health and safety risks associated with nanoparticle manipulation.

Despite the extensive literature on nanoparticle synthesis in solvent-based systems, the mechanisms governing the growth of nanoparticles—particularly under thermal decomposition conditions—remain incompletely understood. When this process is transposed into a viscous polymer medium, the complexity increases significantly. The viscous nature of the polymer matrix introduces additional constraints and variables, such as limited diffusivity, altered thermal conductivity, and possible matrix–precursor interactions, all of which can profoundly influence the nucleation and growth mechanisms of nanoparticles. Consequently, in-situ nanoparticle synthesis within polymers remains a relatively unexplored and challenging area.

In this chapter, we present a systematic methodology to explore and optimize the in-situ synthesis of iron oxide nanoparticles in polyisobutylene, building upon the synthesis protocol previously studied. We investigate the influence of key parameters such as reaction time and the molecular weight of the polymer matrix, both of which are hypothesized to critically affect the size, distribution, and structural organization of the resulting nanoparticles. Through this investigation, we aim not only to refine the synthesis strategy but also to gain deeper insights into the physicochemical factors that govern nanoparticle formation and evolution in complex, highly viscous polymer environments.

To ensure compatibility between the nanoparticles and the polymer matrix, we employed the Hansen Solubility Parameter (HSP) method to identify a suitable polymer for this study. Specifically, we evaluated the solubility between various polymers and the synthesis mixture (including the solvents and ligands used for the samples produced in Chapter 3) using the HSP approach [1]. As a reminder from Section 2.6 in Chapter 2, this method characterizes materials using three key solubility parameters:

1. Dispersion forces (δ_d)
2. Polar forces (δ_p)
3. Hydrogen bonding (δ_h)

Together, these parameters define solubility behavior within the three-dimensional Hansen sphere framework.

As illustrated in Figure 5.1, polyisobutylene was identified as the most compatible polymer, positioned at the center of the Hansen sphere. The interaction radius (R_0) delineates the region of compatibility, within which both hexadecene and oleic acid are located. This confirms their compatibility and validates PIB's solubility with the synthesis mixture developed

in Chapter 3. Ensuring solvent and ligand compatibility minimizes risks of phase separation, aggregation, or unwanted side reactions. This synergy between PIB's intrinsic properties and the synthesis protocol, hopefully, enables precise control over nanoparticle formation, ultimately enhancing composite performance.

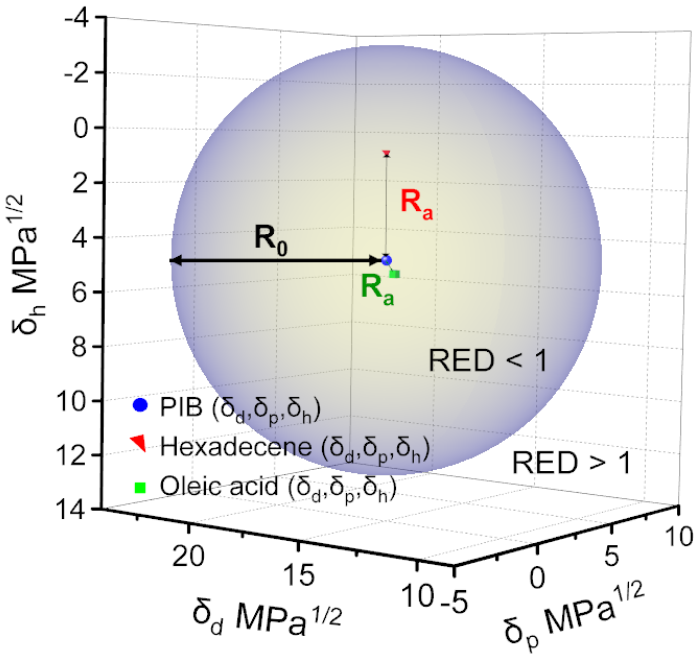

Figure 5.1 – *HSP sphere of PIB, demonstrating the solubility of hexadecene and oleic acid within the polymer matrix. The HSP values of PIB were obtained from the Diversified Enterprises database [2], and the HSP values of hexadecene and oleic acid were calculated using the Stefanis-Panayiotou method [3].*

PIB is a suitable elastomer for this nanoreinforced polymer study not only because of its strong chemical compatibility with the synthesis environment (Solvent and Ligand) but also due to its ability to be synthesized across a wide range of molecular weights. This molecular weight variety provides a broad spectrum of mechanical properties, from thermoplastics to elastomers. These characteristics make PIB highly prevalent in the market and ideal for various applications. With the chemical formula $(C_4H_8)_n$, PIB is a vinyl polymer synthesized from the monomer isobutylene (IB) via cationic polymerization. Although its structure is linear, PIB with high molecular weight is classified as a synthetic rubber or elastomer despite the absence of crosslinking. Its key properties include:

- **Chemical Stability:** PIB is a non-polar polymer that exhibits excellent thermal and chemical stability, making it resistant to degradation in harsh environments. Its structure, which lacks tertiary hydrogen atoms, contributes to its resistance to oxidation compared to other polymers like polypropylene [4].
- **Low Permeability:** One of the standout features of PIB is its remarkably low perme-

ability to gases and moisture. This property makes it highly effective in applications requiring barrier materials, such as in food packaging, pharmaceutical blisters, and protective coatings for electronics [4].

- **Viscoelasticity:** PIB possesses viscoelastic properties, allowing it to exhibit both viscous and elastic characteristics. This makes it suitable for applications such as adhesives and sealants where flexibility and durability are required [5].
- **Mechanical Properties:** The mechanical properties of PIB can vary significantly with molecular weight. Lower molecular weight PIBs are sticky and viscous, while those with higher molecular weights resemble rubber, offering good tensile strength and elongation capabilities [4].
- **Tackiness:** PIB's inherent tackiness makes it an ideal candidate for pressure-sensitive adhesives and hot melt adhesives, enhancing bonding capabilities in various applications [6].

These properties make PIB a versatile material with a variety of applications, as shown in Table 5.1, among others.

Table 5.1 – *Applications of Polyisobutylene [4] [7] [8] [9]*

Application	**Description**
Adhesives	Used in pressure-sensitive adhesives for tapes and labels, as well as hot melt adhesives for packaging due to its tackiness and low permeability.
Sealants	Popular choice for sealants in construction and automotive applications, providing effective barriers against moisture and air infiltration.
Lubricants	Serves as a viscosity modifier in automotive lubricants and greases, enhancing performance under varying temperature conditions.
Coatings	Utilized in coatings for fabrics and papers due to excellent adhesion properties and moisture resistance, suitable for outdoor applications.
Personal Care Products	Found in personal care items such as chewing gum and cosmetics, contributing to texture and stability.

5.2 Nanocomposite Processing

To optimize nanocomposite synthesis, we systematically investigated the growth kinetics of iron oxide nanoparticles within polyisobutylene matrices, building upon established protocols for stable colloidal iron oxide nanoparticle preparation (Chapters 3 and 4). This study bridges the gap between nanoparticle and nanocomposite synthesis, providing a deeper understanding of nanoparticle formation.

Adapting these conditions for PIB and varying reaction time, we aim to monitor nanoparticle size and distribution changes. This should allow us to directly correlate reaction time with the different steps of the nanoparticle synthesis protocol (precursor decomposition, nucleation, and growth).

The following sections explain our synthesis parameter choices, specific process conditions, and the characterization techniques used to evaluate the resulting nanocomposite properties.

The transition from a solvent system to a polymer system introduces key differences in the synthesis process. In a solvent system, nanoparticles are more mobile, allowing for a more homogeneous distribution. In contrast, in a polymer matrix such as PIB, the highly viscous environment limits particle movement and can affect the nucleation and growth kinetics. According to LaMer's model, nanoparticle formation typically follows a three-step process: precursor decomposition, nucleation, and growth. In the polymer matrix, heterogeneous nucleation may occur due to localized areas of higher precursor concentration, which can lead to the formation of different-sized nanoparticle clusters. Furthermore, the slower movement of nanoparticles in the polymer may result in slower growth kinetics compared to a solvent-based system. Key parameters that may change in the polymer system include reaction time, temperature, molecular weight of the polymer, and the polymer's viscosity, all of which affect the nucleation and growth stages. The interaction between the polymer matrix and precursor is another critical factor influencing nanoparticle formation.

5.2.1 Synthesis Composition

We evaluated different samples and synthesis conditions, presented in Chapter 3 for spherical particles and in Chapter 4 for other morphologies. After considering various factors, we selected the conditions that yielded medium-sized iron oxide nanoparticles coated with oleic acid. These parameters were chosen to meet the specific requirements of this study, taking into account the physical and chemical properties of both the polymer matrix and the reagents used, as detailed below.

1. **Precursor and Ligand**: Oleic acid is widely recognized as one of the most stable and effective ligands for stabilizing IONPs. Its robust interaction with nanoparticle surfaces

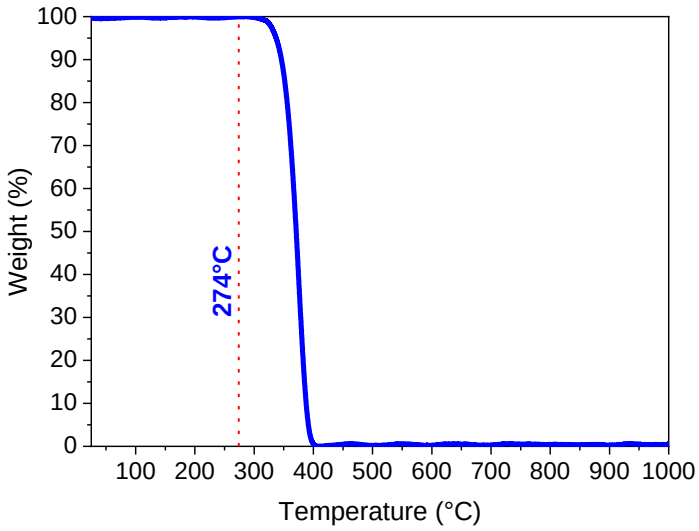

Figure 5.2 – *TGA curve showing the weight loss of PIB polymer as a function of temperature. The weight loss is observed at temperatures above 274°C, corresponding to the boiling point of hexadecene, which is also the reaction temperature of the synthesis. This indicates that the reaction synthesis occurs at a lower temperature than the degradation temperature of the PIB polymer.*

ensures a consistent and high-quality coating.

2. **Solvent**: Hexadecene was selected as the synthesis solvent due to its favorable boiling point, which is sufficiently lower than the degradation temperature of PIB. This compatibility was confirmed through thermogravimetric analysis, as illustrated in Figure 5.2. By choosing hexadecene over other solvents such as octadecene, we ensured that the synthesis conditions remained within safe thermal limits, preserving the integrity of the PIB matrix.
3. **Nanoparticle size**: We targeted 7 nm oleic acid-coated nanoparticles synthesized in hexadecene over 3 nm particles. While both met initial requirements, the 7 nm size was preferred for tracking growth kinetics; 3 nm particles risked rapid size saturation, hindering accurate measurement.

Concerning the iron oleate precursor used, we performed energy-dispersive X-ray analysis and detected a small amount of sodium, as shown in the EDX spectrum in Figure 5.3. This sodium promotes the formation of the cubic morphology of the iron oxide nanoparticles, as expected for the synthesis conditions outlined in Chapter 4. It acts as a capping agent for the 111 crystal face, selectively promoting the formation of cubic structures, as was anticipated in our study [10].

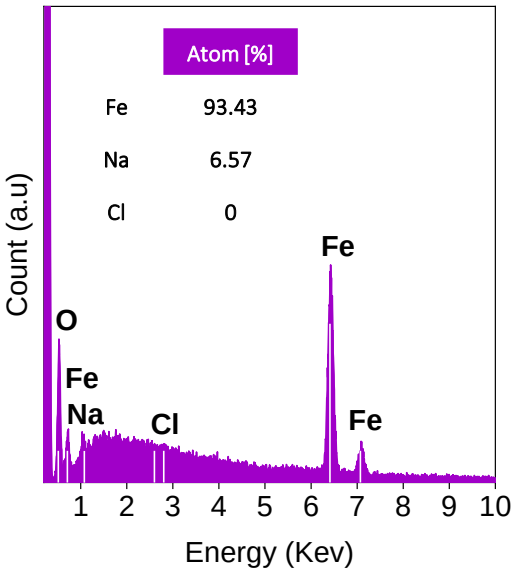

Figure 5.3 – *EDX spectrum of the iron oxide nanoparticles used for this study. The spectrum reveals the presence of residual sodium, which acts as a capping agent for the 111 crystal face of the nanoparticles, promoting the formation of cubic iron oxide nanoparticles.*

5.2.2 Synthesis Protocol

The synthesis of oleic acid-coated iron oxide nanoparticles within a PIB matrix was adapted and carried out through a two-stage process, illustrated in Figure 5.4 and detailed below. Two key variables were studied: variations in reaction time to investigate growth kinetics, and the molecular weight of PIB to assess how chain length impacts nanoparticle growth. The specific synthesis procedure is as follows:

1. **Preparation of PIB solution:** 0.46 g (0.5 mL) of polyisobutylene (PIB) was dissolved in 8 mL of hexadecene in a 250 mL round-bottom flask and stirred for 72 h to ensure complete dissolution. Two types of PIB were used in this study: **PIB1**, with a weight-average molecular weight $M_w \sim 1\,000\,000$, and **PIB2**, with $M_w \sim 500\,000$. Subsequently, 1.6 mmol of iron oleate and 0.8 mmol of oleic acid were added to the PIB-hexadecene solution, along with an additional 2 mL of hexadecene. This mixture was stirred for another 72 h to allow thorough dispersion of the iron precursors and surfactants. We used 0.5 mL of PIB dissolved in 10 mL of hexadecene to achieve a solution with an optimal viscosity for the first analysis, referred to as 5%. This amount was chosen to ensure the solution was neither too viscous, which could complicate handling, nor too dilute, which might hinder accurate characterization of the nanocomposite.
2. **Thermal decomposition:** The resulting solution was heated under reflux to 274°C.

The thermal decomposition was carried out for **various reflux durations (15, 20, 25, 30, 45, or 60 minutes)** to investigate the effect of reaction time on nanoparticle formation. The progress of the reaction was evidenced by the solution turning black, indicating the formation of iron oxide nanoparticles.

Figure 5.4 – *Synthesis process of PIB - IONPs composites incorporating*

Upon cooling, acetone was added to disrupt the interactions between the nonpolar PIB and hexadecene, promoting precipitation. Given that PIB is hydrophobic and nonpolar, and that the IONPs are coated with oleic acid (also hydrophobic), the addition of acetone effectively reduces solubility and facilitates the separation of these components from the solution. The obtained nanocomposite was collected using a magnet to validate its magnetic properties for effective separation.

5.3 Monitoring Nanoparticle Growth and Nanocomposite Characterization

12 samples were generated from 6 synthesis reaction times and 2 molecular weight variations. Each sample was then analyzed in both solution and solid form, the latter obtained after solvent removal and polymer precipitation. This procedure yielded a total of 24 nanocomposites to be studied : 12 in solution and 12 in solid form following precipitation. These nanocomposites would present variations in size, shape, and organization, leading to differences in their mechanical, thermal, and magnetic properties. Consequently, it was essential to employ an appropriate characterization approach capable of revealing the macro-properties of these samples. Therefore, a comprehensive characterization approach was crucial for revealing the macro-properties of these samples. A multiscale approach, as detailed in Chapter 2, was necessary to study these nanocomposites, with time incorporated as a third dimension to monitor growth kinetics.

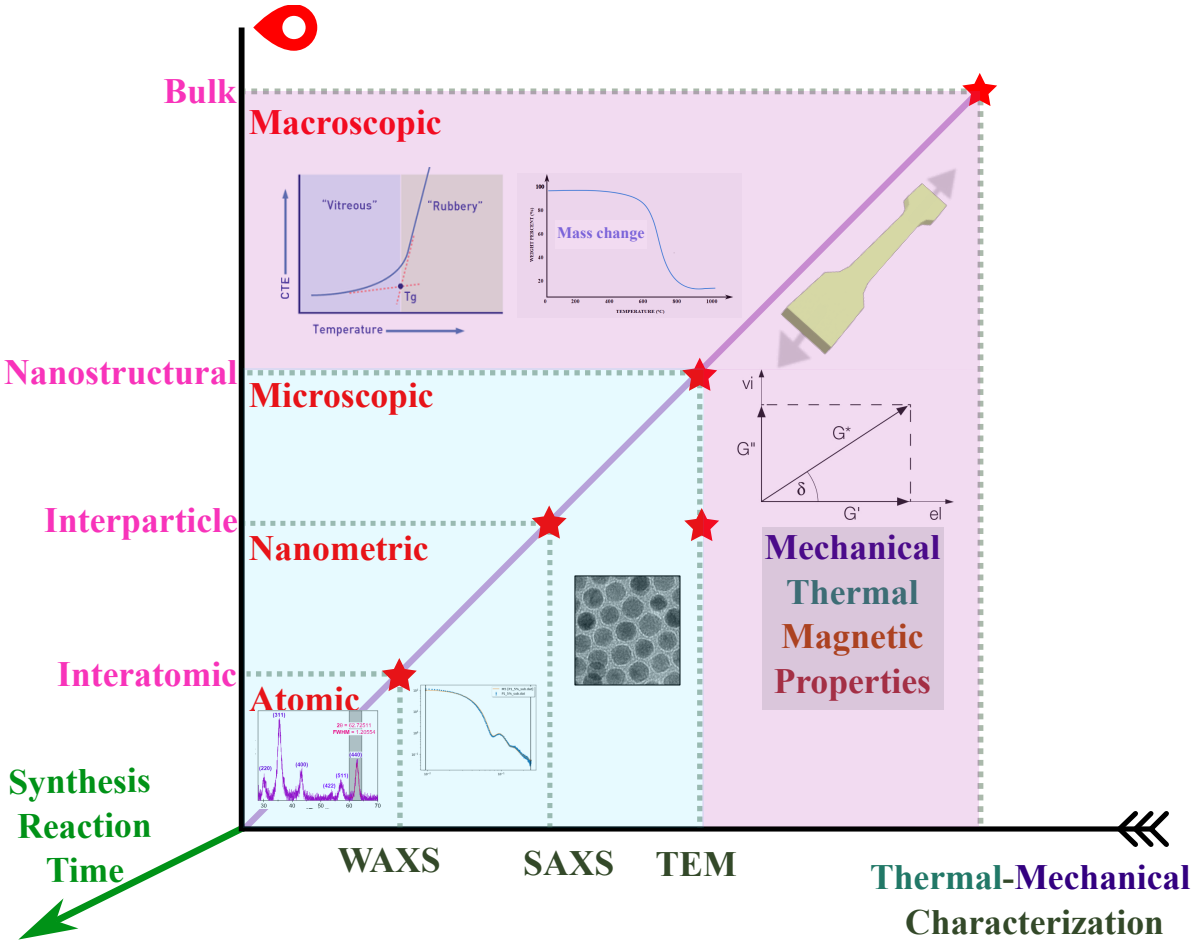

Figure 5.5 – *The multi-scale approach, as discussed in Chapter 2, is used to characterize the resulting properties as a function of synthesis time, molecular weight, and the final macro-properties of the samples.*

5.4 Growth of Nanoparticle Size and Morphology in PIB

Nanoparticle size and morphology was characterized using TEM (JEOL 2100F, 200 kV) for different synthesis times. Samples were prepared by direct deposition of the synthesis solution onto TEM grids without washing, and particle analysis followed previously described methods. SAXS was used to complement TEM and provide information on nanoparticle shape, size, and spatial organization in both solution and precipitate states. SAXS measurements were conducted using a Xenocs Xeuss 2.0 system with Cu Kα radiation ($\lambda = 1.54189$ Å). Solution samples were loaded into capillary tubes, while precipitates were affixed to a sample holder. The sample-to-detector distance was 0.698 m.

5.4.1 Early Reaction Stage: 15 Minutes

After 15 minutes of reaction, TEM images of PIB1 and PIB2 reveal only a few very small, sparsely distributed nuclei. Combined with charging effects from the polymer matrix, this limits the direct visualization of individual nanoparticles. However, several large, high-contrast domains are observed within the matrix (Figure 5.6a,b), suggesting localized enrichment of the iron precursor. Upon higher magnification (Figure 5.6c,d), these regions reveal nascent nanoparticle aggregates, confirming their role as active nucleation sites. This marks the onset of precursor decomposition and phase separation, likely driven by local supersaturation. These observations are consistent with an early stage of iron oxide nucleation, prior to the development of significant particle growth.

The SAXS profiles of PIB1 and PIB2 at 15 minutes (Figure 5.6e,f) show a featureless, monotonically decreasing intensity, indicating insufficient contrast for detecting particles or precursor complexes in solution. In contrast, the SAXS patterns of the precipitated material (Figure 5.6g,h) display a pronounced peak at low–mid q. Comparison with reference patterns for pure iron oleate and sodium oleate confirms two key findings: (i) the presence of sodium oleate in the precursor mixture (as evidenced by the characteristic sodium oleate peak) corroborates EDX analysis and explains the later formation of cubic morphologies; (ii) the peak position matching iron oleate indicates that the precursor remains largely undecomposed at this early stage. The emergence of this peak only in the precipitate is due to the higher local concentration of precursor, which enhances scattering contrast. Importantly, the PIB2 sample shows a sharper peak, implying a more ordered arrangement of precursor molecules in its nucleation domains.

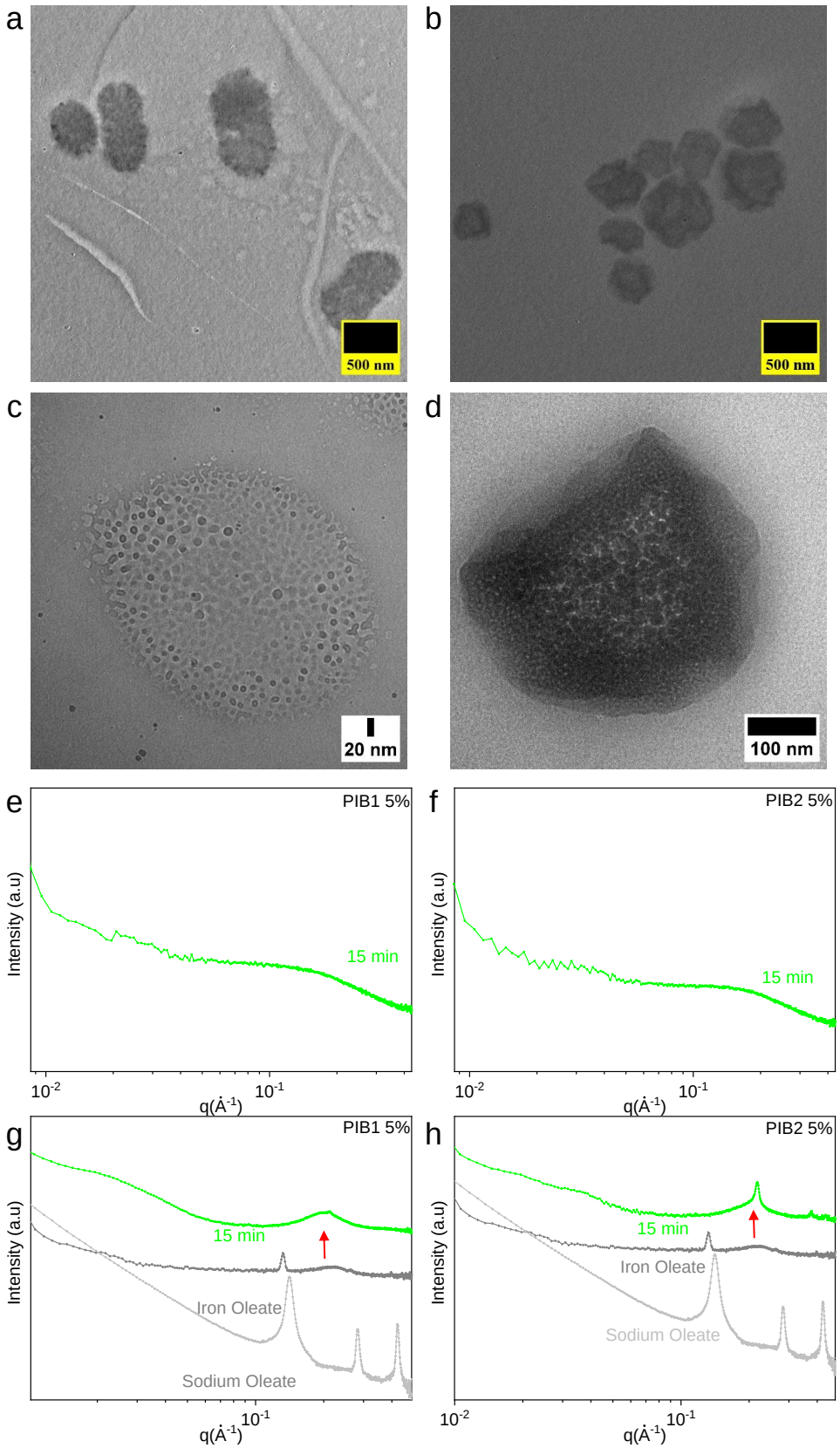

Figure 5.6 – *(a, b) TEM images of PIB nanocomposites; (c, d) corresponding magnified views; (e, f) SAXS patterns of the nanocomposites in solution; (g, h) SAXS patterns of the precipitates, compared with those of the precursor and sodium oleate, for PIB1 and PIB2, respectively.*

5.4.2 Starting from 20 min

Starting from 20 minutes, the nanoparticles begin to appear. Figures 5.7 and 5.8 show TEM images and size distribution histograms for PIB1 and PIB2 nanocomposites at reaction times of 20, 25, 30, 45, and 60 minutes, revealing the evolution of nanoparticle size and morphology from the onset of the reaction.

Nanoparticles were discernible after 20 minutes, with PIB1 averaging 6.8 nm and PIB2 averaging 3.3 nm, suggesting faster growth kinetics for the longer chain (PIB1). These nanoparticles exhibited a cubic, rather than spherical, morphology as expected from the sodium detected in the precursors. At 25 minutes, PIB2 experienced rapid growth, resulting in similar edge lengths for PIB1 (7.6 nm) and PIB2 (7.2 nm). From 30 to 60 minutes, nanoparticle sizes stabilized, with PIB1 averaging 8.4 nm and PIB2 7.7 nm.

Overall, TEM analysis reveals the successive formation of uniform nanoparticles within the polymer solution and shows that nanoparticle growth follows a distinct kinetics in each system. In PIB1, it occurs between 15 and 20 minutes, while in PIB2, it is delayed until between 20 and 25 minutes. Both systems reach a stabilization phase starting at 30 minutes, with PIB1 stabilizing at larger nanoparticles compared to PIB2. This rapid increase in nanoparticle size during the initial 20–30 minutes highlights a high nucleation and growth rate, while the subsequent plateau suggests a shift in reaction dynamics—possibly due to precursor depletion or nanoparticle surface stabilization. Moreover, the larger nanoparticle sizes observed in the PIB1 system compared to PIB2 suggest that variations in factors such as polymer chain length or precursor concentration distribution may play a role, as observed for the samples at the 15-minute reaction time.

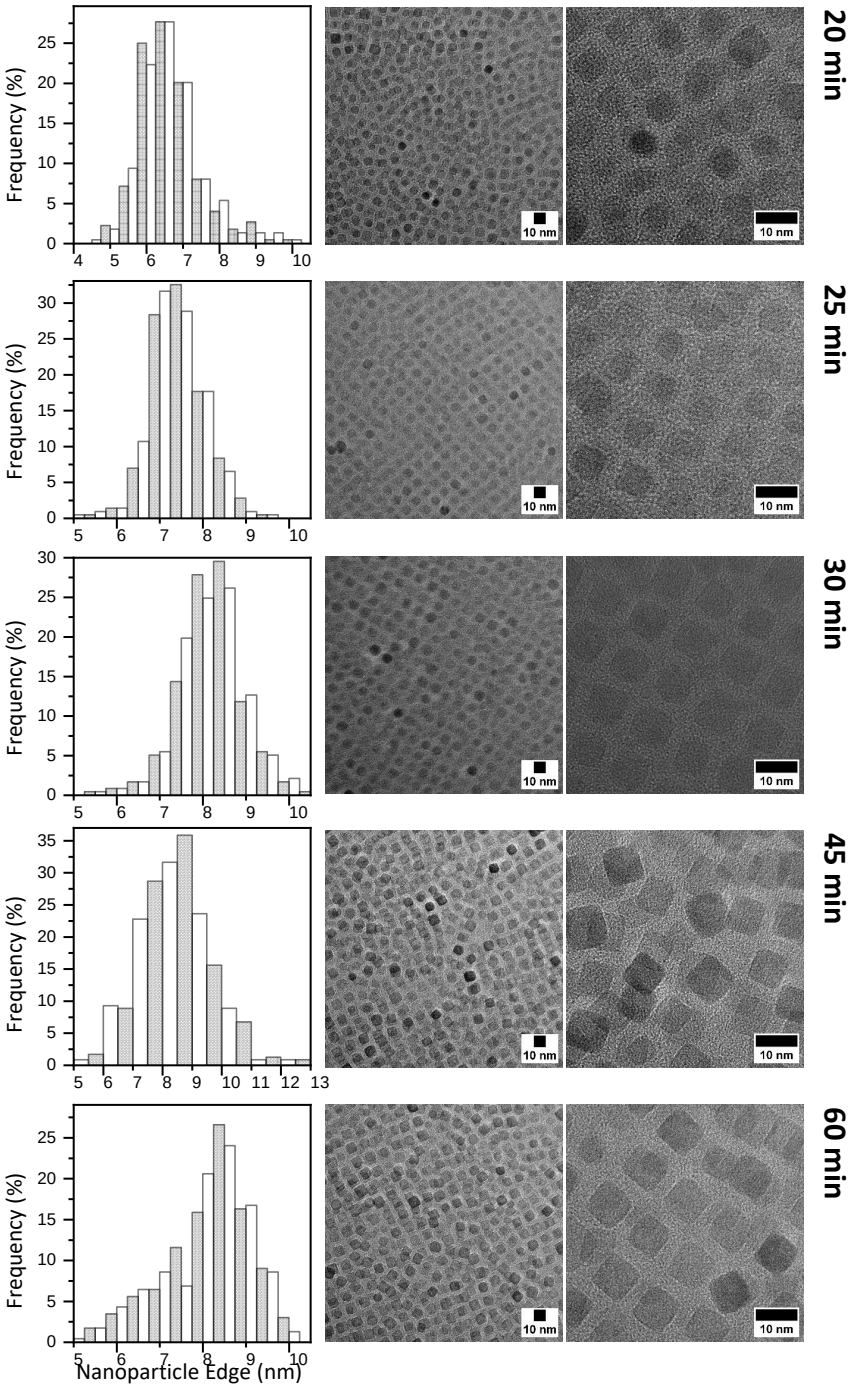

Figure 5.7 – *TEM images of iron oxide nanoparticles synthesized in PIB1 matrix at various reaction times (20, 25, 30, 45, and 60 minutes).*

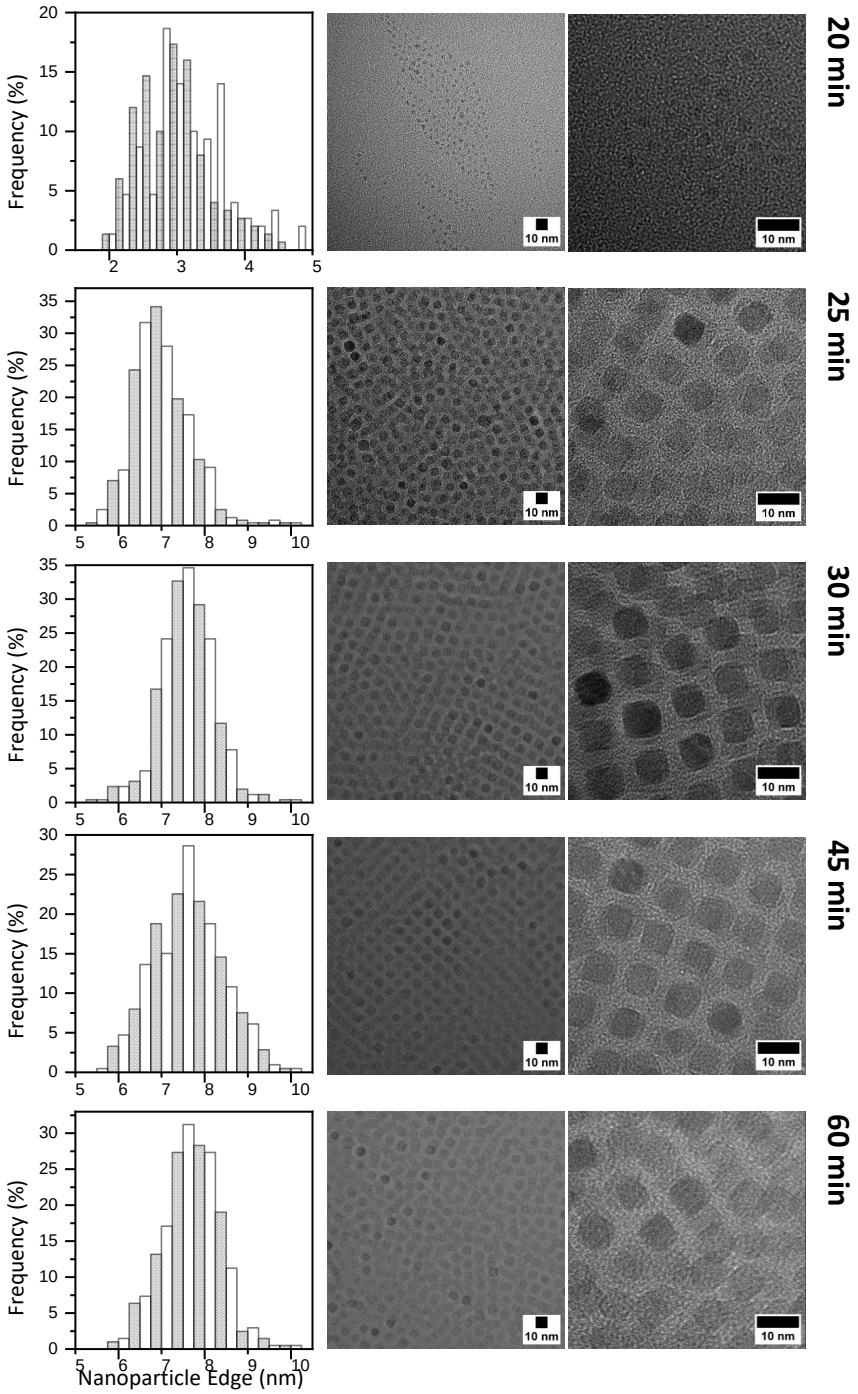

Figure 5.8 – *TEM images of iron oxide nanoparticles synthesized in PIB2 matrix at various reaction times (20, 25, 30, 45, and 60 minutes).*

Table 5.2 presents TEM-derived size statistics (long edge, a, and short edge, b) for PIB1 and PIB2 nanoparticles. Figure 5.9 shows the evolution of these edge sizes over reaction time.

Table 5.2 – *TEM-derived size statistics of cubic nanoparticles synthesized within the PIB1 and PIB2 matrices, with a denoting the longer edge and b the shorter edge. Values are presented as mean ± standard deviation.*

	PIB1			
	a		b	
Reflux Time	Mean (nm)	Standard Deviation	Mean (nm)	Standard Deviation
20 min	6.8	0.85	6.4	0.84
25 min	7.6	0.62	7.2	0.63
30 min	8.4	0.76	7.9	0.75
45 min	8.6	1.24	8.3	1.19
60 min	8.3	1.00	7.9	0.98
	PIB2			
	a		b	
Reflux Time	Mean (nm)	Standard Deviation	Mean (nm)	Standard Deviation
20 min	3.3	0.59	2.9	0.53
25 min	7.2	0.67	6.8	0.64
30 min	7.7	0.59	7.4	0.61
45 min	7.8	0.80	7.4	0.78
60 min	7.8	0.64	7.5	0.65

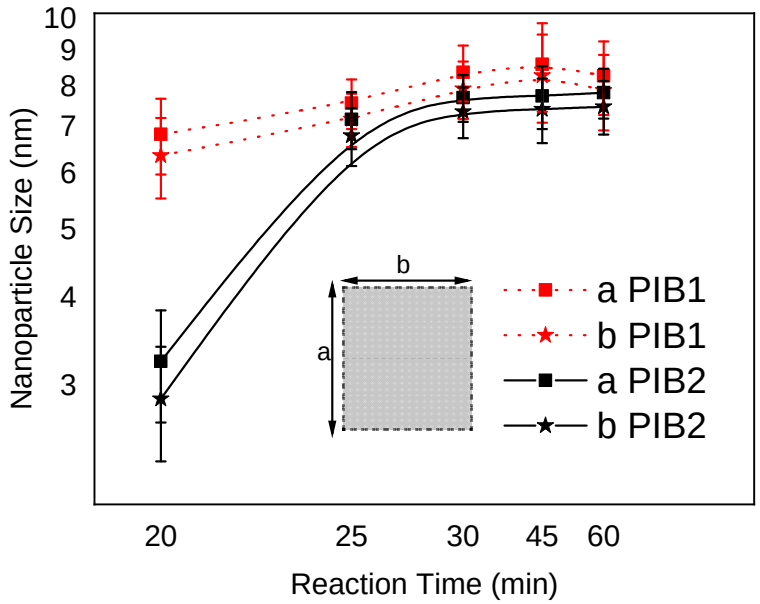

Figure 5.9 – *Evolution of cubic nanoparticle size in PIB1 and PIB2 matrices as a function of reaction time, determined by TEM. The long edge (a) and shorter edge (b) are shown for both matrices, with PIB1 in red and PIB2 in black. Error bars represent the standard deviation.*

SAXS Patterns

For a more global analysis, SAXS analysis was conducted as a complement to TEM to gain further information about the structure of the PIB-based nanocomposites in both the synthesis solution and precipitated states. The SAXS patterns of the samples in solution (Figure 5.10) reveal two main features: (1) the pattern exhibits characteristics indicative of inter-particle interactions, suggesting that the nanoparticles are sufficiently close to interact even in solution, and (2) the first peak of the pattern, which correlates with the nanoparticle size, shows an evolution similar to that observed via TEM. The position of this peak shifts to lower values (indicating larger particle sizes) at 20 and 25 minutes and then stabilizes at 30, 45, and 60 minutes. Moreover, as the reaction time increases, the structure factor peak becomes more intense and additional peaks emerge, reflecting the development of short/long-range ordering in the nanocomposites. Specifically, the increasing intensity of these features with reaction time suggests a progressive evolution of the nanoparticle structure and organization within the solution. For PIB1, evidence of this structural organization is apparent as early as 25 minutes, while for PIB2, it emerges around 45 minutes.

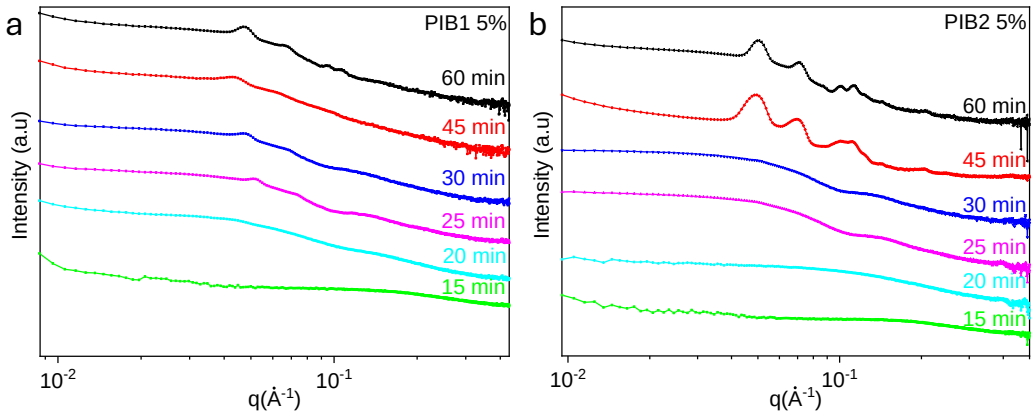

Figure 5.10 – *SAXS patterns of PIB nanocomposites in solution state: (a) PIB1, (b) PIB2.*

Guinier Analysis

The Guinier plot, derived from the SAXS patterns of the nanocomposite solutions, enables the determination of the radius of gyration (R_g). The radius of gyration provides information about the spatial extent of the scattering objects, reflecting the overall size and shape of the nanoparticles or their agglomerates. Although R_g can be related to the dimensions of simple geometric shapes, the relationship to the cube edge (a) using the formula $R_g = a/2$ is only valid for homogeneous cubes [11] [12]. This relationship simplifies the characterization of

cubic nanoparticles. The calculated R_g and corresponding cube edge (a) values for all the samples, PIB1 and PIB2, are summarized in Table 5.3 below.

Table 5.3 – *Radius of gyration (R_g) and equivalent cube edge length (a) for different samples of PIB1 and PIB2.*

	PIB1		**PIB2**	
Sample (min)	R_g **(nm)**	a **(nm)**	R_g **(nm)**	a **(nm)**
20	3.28	6.56	1.44	2.88
25	3.86	7.72	3.41	6.82
30	2.63	5.26	3.45	6.90
45	2.53	5.00	2.53	5.00
60	2.89	5.78	2.76	5.52

From the nanoparticle sizes calculated from the R_g values presented in the table, we can observe the following: For PIB1, at 20 minutes, the particle size is 6.56 nm, which is similar to the size obtained by TEM. At 25 minutes, there is a further increase in size, consistent with the TEM data, reaching 7.72 nm. Suddenly, at 30 minutes, a decrease in nanoparticle size to 5.26 nm is observed, and it continues to fluctuate around this value at 45 and 60 minutes.

Concerning PIB2 nanocomposites, at 20 minutes, nanoparticle sizes of 2.88 nm are observed, which is in agreement with TEM. At 25 minutes, the size is 6.82 nm, also consistent with TEM, followed by stabilization at 30 minutes with a size of 6.30 nm. Similarly to PIB1, we observe a decrease in size to 5 nm at 45 minutes, with the size remaining stable at 60 minutes.

The observed decrease in the R_g at higher reaction times can be explained by the appearance of more intense structure factor peaks, which indicate stronger interparticle interactions. These interactions, often arising from increased particle concentration or changes in surface properties, significantly influence the scattering intensity profile in small-angle scattering experiments.

In small-angle scattering, the total scattering intensity $I(q)$ is described as the product of the particle form factor $P(q)$ and the structure factor $S(q)$:

$$I(q) = P(q) \cdot S(q) \tag{5.1}$$

The form factor $P(q)$ reflects the size, shape, and internal structure of individual particles, while the structure factor $S(q)$ accounts for interparticle correlations. When interparticle interactions become significant, $S(q)$ deviates from unity, particularly at low q values where the Guinier region lies. This deviation alters the scattering profile and can lead to an underestimation of the radius of gyration (R_g), as the Guinier approximation assumes

non-interacting particles.

At higher reaction times, stronger interparticle interactions occur, and the modification of $I(q)$ by these peaks can obscure the contribution of $P(q)$, making it challenging to isolate the true particle size. As a result, the calculated R_g appears smaller than expected.

Core-Shell Sphere Fit

SAXS data for the PIB nanocomposite samples in solution were fitted using a core-shell sphere model in SasView. While TEM confirms the cubic morphology of the nanocomposite particles, the core-shell sphere model was employed to obtain a global size estimation for several key reasons. Firstly, the superball model, which more accurately represents intermediate shapes between spheres and cubes, failed to converge during fitting, likely due to its inability to incorporate a core-shell structure required to model the nanocomposites. Secondly, the core-shell sphere model provided a reasonable initial approximation of the particle size. The samples fitted were those corresponding to 20, 25, and 30-minute reaction times for both PIB1 and PIB2, as illustrated in Figure 5.11a and 5.11b, respectively. At longer reaction times, the peaks arising from the structure factor become more prominent, indicating increased inter-particle correlations and higher-order organization. To minimize the impact of inter-particle effects, the fitting procedure was restricted to data where the form factor predominated.

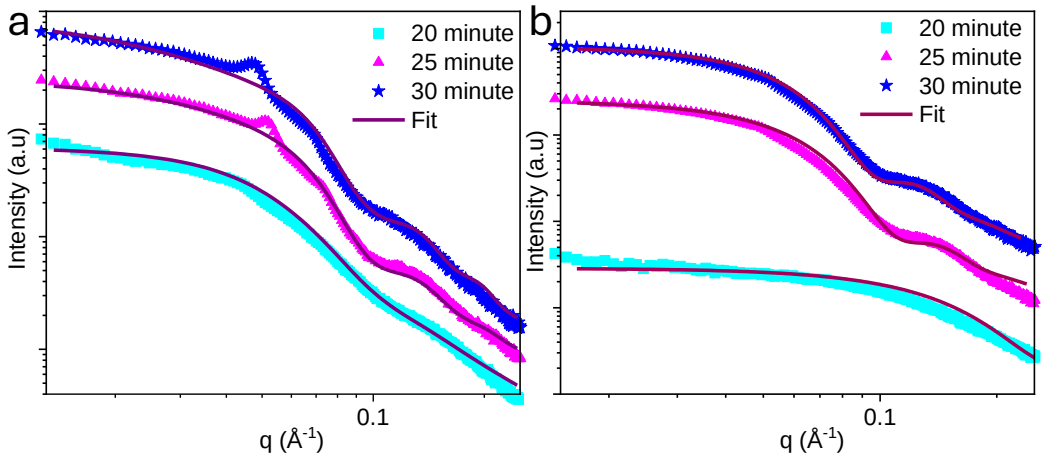

Figure 5.11 – *Fitted with core-shell sphere model*

Table 5.4 summarizes the fitting parameters obtained for the PIB1 and PIB2 nanocomposite samples at reaction times of 20, 25, and 30 minutes in their solution state. The parameters include the radius and thickness of the nanoparticles, as well as their respective distributions. For PIB1, the radius values show no significant change, with measurements of

Table 5.4 – *Parameters for the fitting of the SAXS pattern of the PIB nanocomposite*

	PIB1			
	Core Shell Sphere		Core Shell Sphere @ sticky Hard Sphere	
	20 min	25 min	25 min	30 min
Radius (nm)	4.50	4.66	4.80	5.00
Thickness (nm)	0.80	0.81	0.86	0.87
Distribution of Radius	0.25	0.17	0.18	0.20
Distribution of Thickness	0.10	≈ 0.00	≈ 0.00	0.10
Sld Core ($10^{-6}\,nm^{-2}$)	0.81	0.81	0.81	0.81
Sld Shell ($10^{-6}\,nm^{-2}$)	1.06	1.05	1.05	1.05
Sld Solvent ($10^{-6}\,nm^{-2}$)	0.92	0.94	0.94	0.93
Radius_effective (nm)		4.88	4.88	5.10
Volfraction		0.05	0.05	0.10
	PIB2			
	Core Shell Sphere			
	20 min	25 min	30 min	
Radius (nm)	1.47	4.19	4.78	
Thickness (nm)	0.22	0.87	1.10	
Distribution of Radius	0.10	0.16	0.16	
Distribution of Thickness	0.10	0.18	0.18	
Sld Core ($5 \times 10^{-6} nm^{-2}$)	0.79	0.80	0.80	
Sld Shell ($5 \times 10^{-6} nm^{-2}$)	1.04	1.01	1.01	
Sld Solvent ($5 \times 10^{-6} nm^{-2}$)	1.00	0.93	0.93	

4.5 nm at 20 minutes, between 4.66 and 4.8 nm at 25 minutes, and 5 nm at 30 minutes. In contrast, for PIB2, the radius values indicate a significant increase in particle size with longer reaction times, with measurements of 1.47 nm at 20 minutes, rising to 4.19 nm at 25 minutes, and reaching 4.78 nm at 30 minutes. This trend aligns with previous findings, where PIB1 grows faster between 15 and 20 minutes before stabilizing, while PIB2 grows more rapidly between 20 and 25 minutes. The thickness values also show an increasing trend over time, indicating that as the particles grow in size, the shell thickness around the core also increases. The thickness is around 1 nm, most likely corresponding to the oleic acid coating. The distribution of both radius and thickness reflects the variability in particle size and shell uniformity across the samples. The relatively low distribution values (ranging from 0.10 to 0.18) suggest a reasonably narrow size distribution for these nanoparticles, indicating the successful formation of small, well-dispersed nanoparticles within the PIB matrix.

To estimate the edge length of a cube from the radius r of a fitted sphere, we used an equivalent volume approach. This approach assumes that the volume of the sphere is approximately equal to the volume of the cube. Consequently, the edge length of the cube can be estimated using the following relationship:

$$a = \left(\frac{6}{\pi}\right)^{\frac{1}{3}} r \approx 1.61r \tag{5.2}$$

The uncertainty in the cube edge length (σ_a) was calculated by propagating the distribution of the radius (σ_r). The formula for uncertainty propagation in this case, where a is directly proportional to r, is given by:

$$\sigma_a = 1.61\sigma_r \tag{5.3}$$

Here, σ_a represents the uncertainty in the cube edge length, and σ_r is the distribution of the radius obtained from the fitting process. This relationship indicates that any variation in the radius will directly affect the calculated edge length, scaled by a factor of approximately 1.61. The calculated cube edge lengths a are summarized in Table 5.5 and are aligned with the TEM measurements.

Table 5.5 – *Estimated cube edge length (a) and uncertainty for PIB nanocomposite samples.*

Sample	r (nm)	$a \pm \sigma_a$ (nm)
PIB1 - 20 min	4.499	7.252 ± 0.041
PIB1 - 25 min	4.655	7.504 ± 0.027
PIB1 - 25 min (with Structure Factor)	4.800	7.738 ± 0.029
PIB1 - 30 min (with Structure Factor)	5.000	8.060 ± 0.033
PIB2 - 20 min	1.47	2.37 ± 0.16
PIB2 - 25 min	4.19	6.75 ± 0.26
PIB2 - 30 min	4.78	7.32 ± 0.26

These size and morphological analyses indicate that growth follows a logistic model, characterized by rapid initial growth that decelerates as equilibrium is approached. This growth pattern aligns well with experimental observations: nanoparticles experience rapid growth during the early stages and gradually stabilize as the reaction progresses. The growth kinetics of the cubic nanoparticles can be summarized as follows:

- **Rapid growth phase** (15–20 minutes for PIB1 and 20–30 minutes for PIB2): driven by precursor decomposition.
- **Slower growth phase** (around 30 minutes): the system begins to approach equilibrium, and the growth rate decreases.
- **Stabilization phase** (45–60 minutes): Nanoparticles reach their maximum stable size and start to develop long-range order.

Interestingly, the formation of cubic nanoparticles even in the absence of PIB (data not shown) suggests that PIB does not play a role in determining particle shape. In contrast,

the presence of sodium, even at low concentrations, appears to exert a strong influence on morphology: the nanoparticles initially adopt intermediate "superball" shapes, which progressively evolve into well-defined cubes as the synthesis proceeds.

5.5 Self-Assembly and 3D Packing in PIB Nanocomposites

5.5.1 Inter-Particle Distance

To gain insights into the arrangement and distribution of particles within the polymer, we analyzed the positions of the first peaks in the SAXS data for samples in their precipitated state (see Figures 5.12aa and 5.13aa for PIB1 and PIB2, respectively). The position of the first peak (q_{peak}) provides information about the average center-to-center distance between neighboring nanoparticles embedded in the polymer matrix. This inter-particle distance (D) indicates the degree of spatial separation between the particles and is inversely proportional to the peak position, as described by the following relationship:, as described by the following relationship:

$$D = \frac{2\pi}{q_{\text{peak}}} \tag{5.4}$$

where:

- D is the average center-to-center inter-particle distance, and
- q_{peak} is the scattering vector at which the first structure-related peak occurs.

Using this expression, we calculated the inter-particle distances for each sample and tracked how these values evolved with reaction time. The results are summarized in Table 5.6.

From the data in Table 5.6, we observe that the inter-particle distance increases up to 30 minutes of reaction time and then plateaus between 30 and 60 minutes. Importantly, the calculated inter-particle distances are significantly larger than the nanoparticle edge lengths, indicating that the nanoparticles remain well-dispersed and do not form dense agglomerates within the polymer matrix. This suggests a relatively homogeneous spatial distribution of the nanoparticles throughout the nanocomposite precipitate.

Although the inter-particle distance stabilizes after 30 minutes, the increasing intensity of the structure factor peak suggests enhanced spatial correlations between particles. This could indicate a higher degree of local ordering or increased particle concentration within correlated domains, without necessarily reducing the average center-to-center distance. Such behavior is consistent with a scenario where nanoparticles stop growing in size but continue to interact more strongly, leading to a more structured organization within the matrix.

Table 5.6 – *Peak Positions and Inter-Particle Distances for PIB1 and PIB2 at Different Reaction Times*

	PIB1		PIB2	
	q (nm^{-1})	D (nm)	q (nm^{-1})	D (nm)
20 min	0.69	9.11	-	-
25 min	0.54	11.55	0.68	9.31
30 min	0.48	13.17	0.52	12.18
45 min	0.46	13.72	0.50	12.67
60 min	0.48	13.02	0.51	12.27

5.5.2 3D Packing

We conducted further analysis on the SAXS patterns of the precipitated nanocomposites. These SAXS patterns reveal the emergence of additional peaks following the first peak, which corresponds to the intermediate inter-particle distance. These additional peaks, highlighted by thin segments in Figures 5.12aa and 5.12ab, provide evidence of structural organization within the nanocomposite matrix. For both PIB1 and PIB2, starting from a reaction time of 25 minutes, at least three well-defined peaks appear in the low-angle region of the SAXS patterns. This observation suggests that the nanoparticles undergo self-assembly, leading to the formation of an ordered 3D packing structure within the matrix.

Both PIB1 and PIB2 nanocomposites demonstrate a trend of self-assembly; however, their SAXS patterns show notable differences in the positions of the lattice peaks. These variations indicate differences in the packing arrangements or inter-particle distances between the two systems. To analyze these structural differences systematically, we designate q_1 as the position of the first peak in the SAXS pattern, which corresponds to the primary inter-particle distance. The positions of subsequent peaks are expressed as ratios relative to q_1. These ratios provide valuable insights into the symmetry and type of three-dimensional packing present in each sample, such as cubic or hexagonal arrangements.

From the SAXS patterns, it is evident that nanoparticles within the polymer matrix are organized in a cubic arrangement. According to the literature, the relative values of q_{n+1}/q_1 follow distinct patterns for different cubic symmetries. For a body-centered cubic (BCC) structure, these ratios are given as follows [13]:

$$1 : \sqrt{2} : \sqrt{3} : \sqrt{4} : \sqrt{5} : \sqrt{6} : \ldots$$

For a face-centered cubic (FCC) structure, the corresponding ratios are:

$$1 : \sqrt{\frac{4}{3}} : \sqrt{\frac{8}{3}} : \sqrt{\frac{11}{3}} : \sqrt{4} : \sqrt{\frac{16}{3}} : \sqrt{\frac{19}{3}} : \sqrt{\frac{20}{3}} : \ldots$$

To investigate the self-assembly process over time, the peak positions and their relative ratios to the first peak were plotted for the PIB1 sample (from a 20-minute reaction) and the PIB2 sample (from a 25-minute reaction). These were then compared to the ideal ratios for FCC and BCC structures, as shown in Figure 5.12a for PIB1 and Figure 5.13a for PIB2.

Structural Evolution in PIB1

Figure 5.12aa presents the SAXS pattern of the PIB1 nanocomposites. Starting from a reaction time of 20 minutes, the relative peak positions in Figure 5.12ab are compared to the theoretical values for a FCC arrangement, which are included in the graph for reference. The relative positions of the sample peaks are also shown in Figure 5.12ac, with the BCC reference included for comparison. From the graph, a transition from an FCC to a BCC arrangement can be observed, which is more evident when tracking the evolution of the second peak. Notably, the position of this peak relative to the primary peak follows a ratio of $(2)^{1/2}$, which differs from the position of any higher-order peaks typically observed in an FCC lattice ($(4/3)^{1/2}$). Initially, this peak appeared as a shoulder in the FCC phase, but as the system transitions to the BCC phase, it becomes a distinct and well-defined peak. This change further supports the identification of the BCC phase, clearly highlighting the structural evolution in the system as the reaction progresses. The Figure 5.12b gives insight into the composites' high order organization at 60 min reaction time.

Structural Evolution in PIB2

Regarding PIB2 nanocomposites (see Figure 5.13a), a form factor peak begins to emerge after 20 minutes, although no interparticle distance peak is observed during this time. Starting from 25 minutes, the SAXS pattern exhibits a sudden and pronounced appearance of peaks. These peaks are not only more numerous but also better defined than those in the PIB1 sample, indicating a more advanced structural organization in PIB2. Similarly to PIB1, the relative peak positions compared to FCC and BCC structures are shown in Figure 5.13ab and Figure 5.13ae, respectively. A similar trend to PIB1 is observed, with a transition from an FCC organization to a BCC organization. However, in the case of PIB2, more peaks are observed, indicating a higher degree of structural organization (see Figure 5.13b).

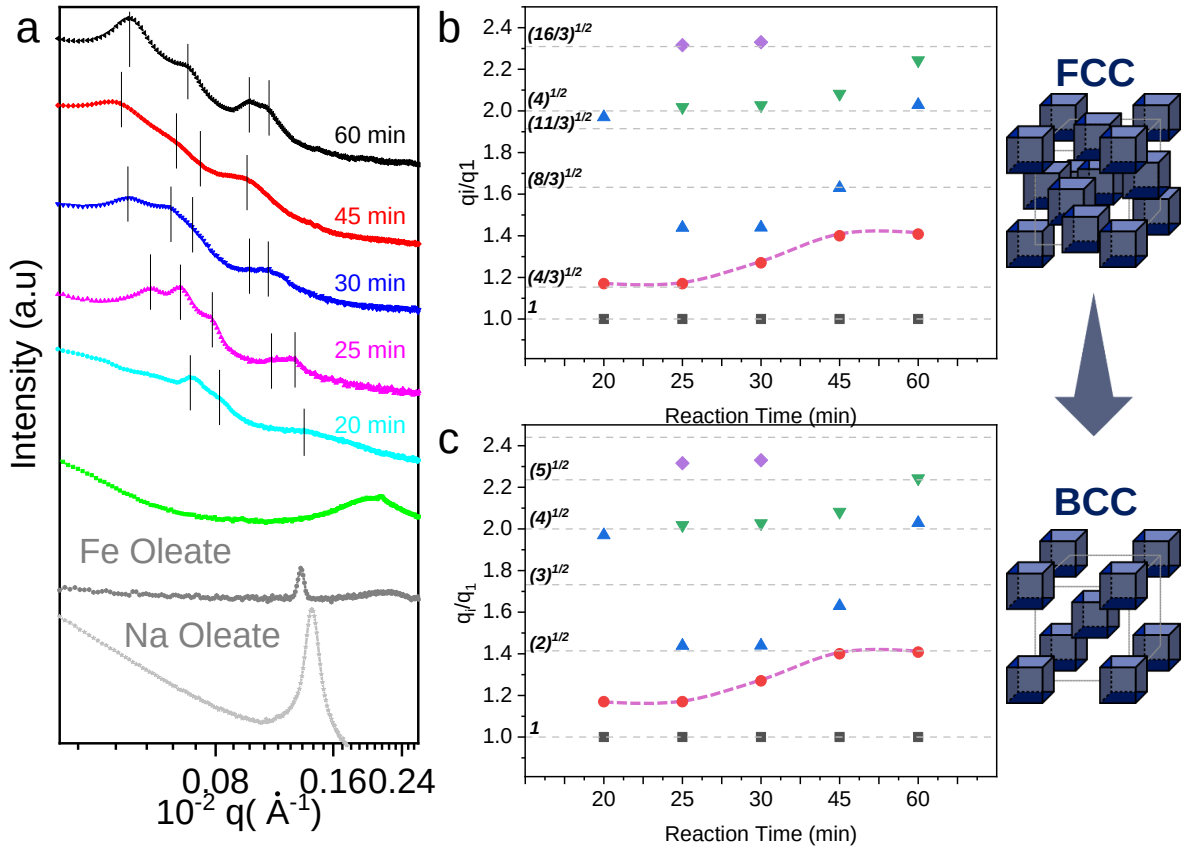

(a) *(a) SAXS patterns of iron oxide nanoparticles in the PIB1 matrix in precipitated form, with peak positions marked (Samples from 20 to 60 min reaction time). (b) Ratio of peak positions in PIB1 nanocomposites compared with FCC packing. (c) Same analysis for PIB1, but compared with BCC packing.*

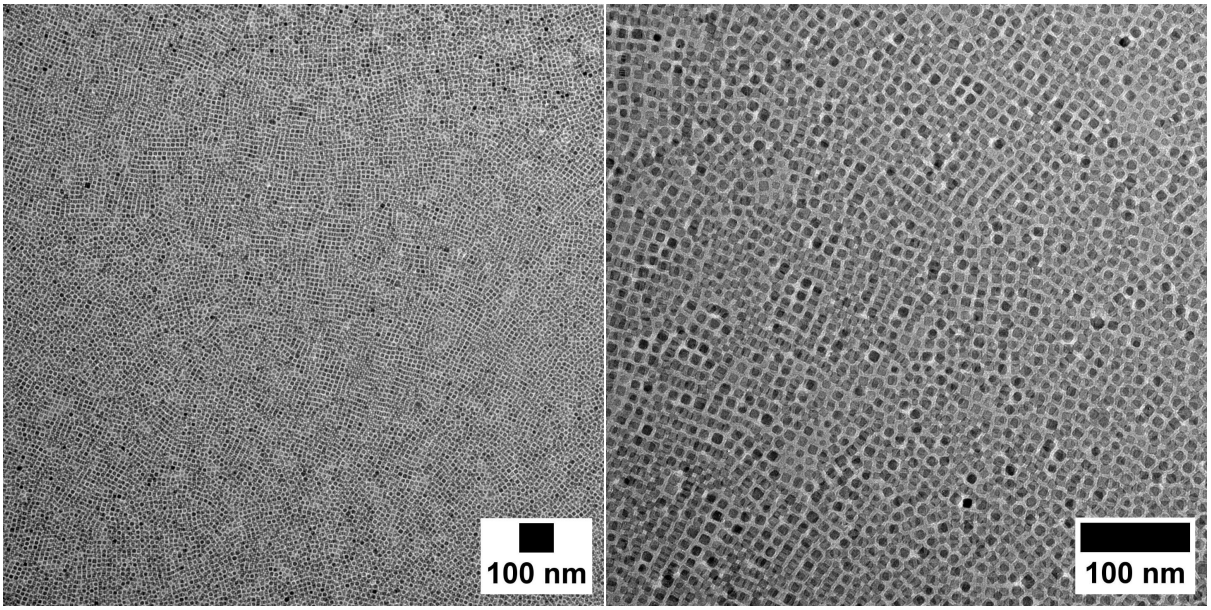

(b) *Low magnification TEM images of nanoparticles from PIB1 nanocomposites at a 60-minute reaction time, showing highly ordered organization.*

Figure 5.12 – *Structural and morphological analysis of PIB1 nanocomposites.*

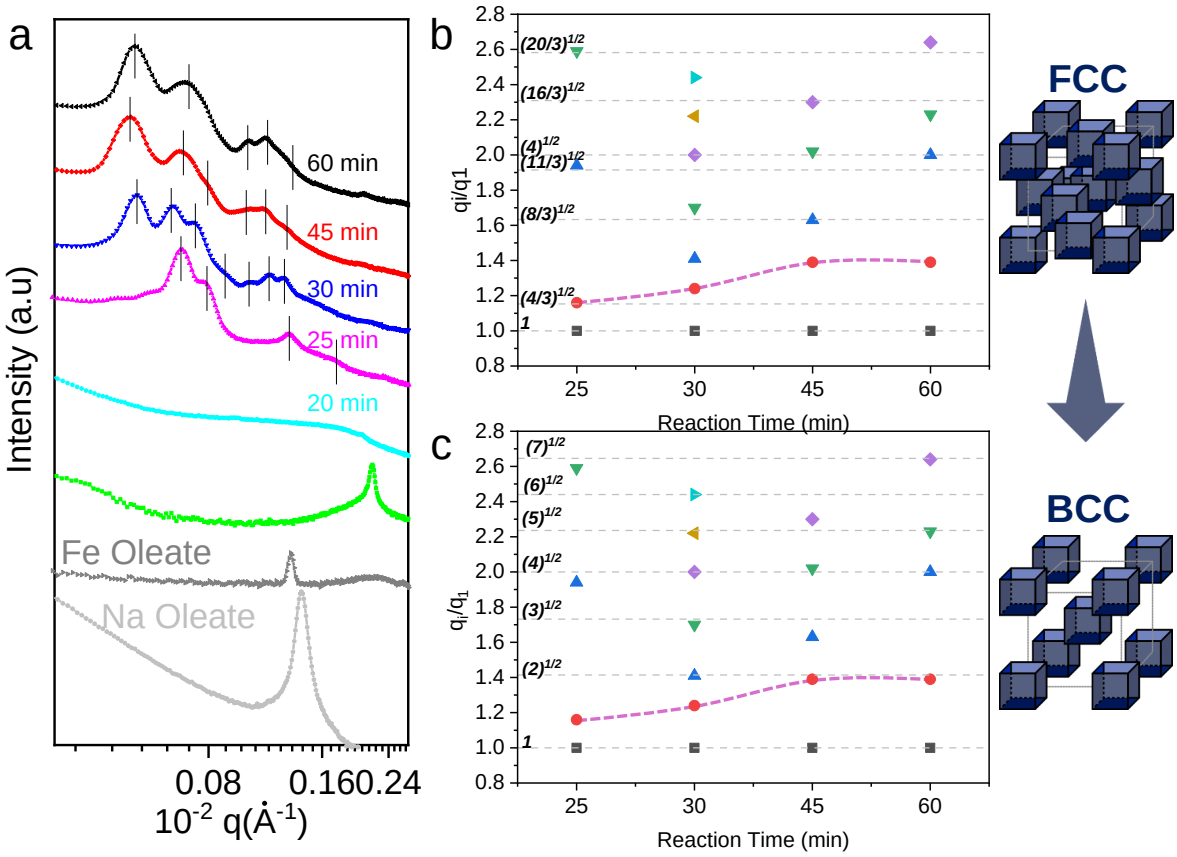

(a) *(a) SAXS patterns of iron oxide nanoparticles in the PIB2 matrix in precipitated form, with peak positions marked (Samples from 25 to 60 min reaction time) (b) Ratio of peak positions in PIB2 nanocomposites compared with FCC packing. (c) Same analysis for PIB2, but compared with BCC packing.*

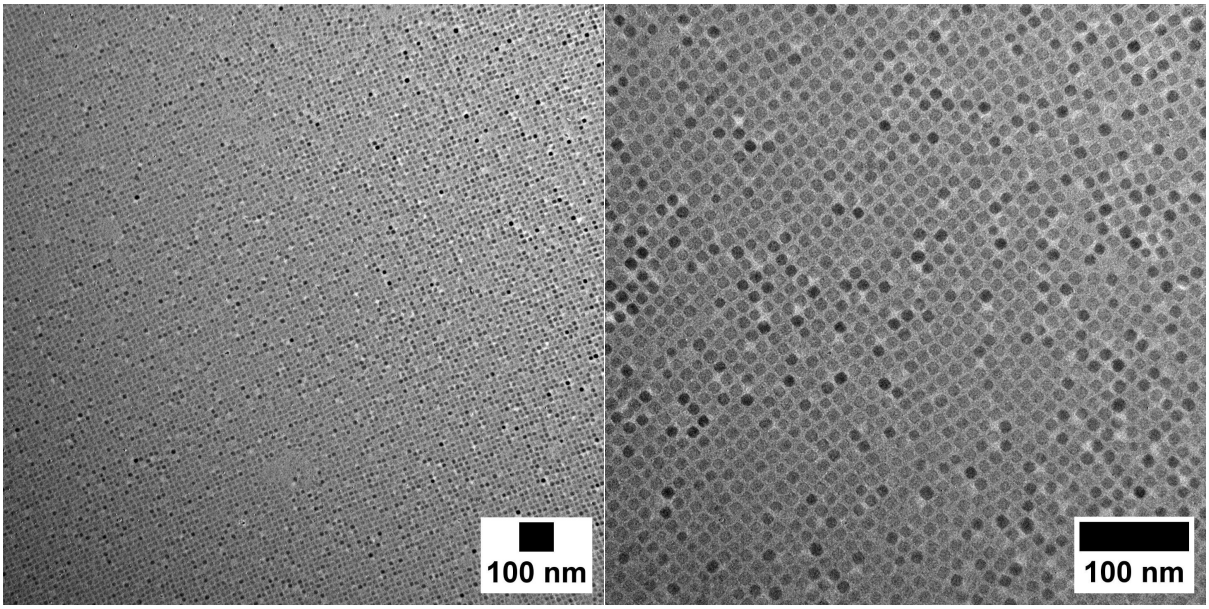

(b) *Low magnification TEM images of nanoparticles from PIB2 nanocomposites at a 60-minute reaction time, showing highly ordered organization.*

Figure 5.13 – *Structural and morphological analysis of PIB2 nanocomposites.*

Reported FCC–BCC 3D Packing Transitions

Both PIB1 and PIB2 nanocomposites exhibit a transition from an FCC to a BCC arrangement of nanoparticles within the matrix as the reaction time increases. This transition is accompanied by an increase in particle size and the development of a more defined cubic morphology. From the literature, two aspects have been identified that can influence the 3D organization: (1) the coating ligand and (2) the nanoparticle shape.

a. Influence of surface ligands

The literature shows that in a typical system where spherical particles (referred to as "hard spheres") are packed together, they tend to form the most efficient and densely packed structure to maximize free volume entropy, known as the face-centered cubic lattice. This lattice is highly ordered, with each particle surrounded by 12 others in a symmetrical arrangement [14] [15] [16]. Sterically stabilized, uniform colloidal nanocrystals—with their relatively short-range repulsive interactions—also tend to form FCC self-assemblies [17] [18].

However, ligand frustration can occur, leading to the formation of a BCC arrangement. The literature suggests that ligands prefer to maintain uniform lengths around the nanoparticle core. However, spatial constraints in ordered superlattices force ligands to stretch or compress, creating an entropic penalty. This mismatch between ideal ligand behavior and geometric constraints is termed *packing frustration* [19].

In an FCC lattice, the fundamental Wigner-Seitz cells are rhombic dodecahedra, characterized by high symmetry but limited spatial adaptability. Due to the high packing density (74%), ligands experience uneven compression or extension, amplifying frustration. Conversely, in a BCC arrangement, the Wigner-Seitz cells are truncated octahedra with a lower packing density (68%), allowing ligands to distribute more uniformly, thereby reducing strain.

When ligands from adjacent nanoparticles overlap (*interpenetration*), the larger interstitial spaces in the BCC structure accommodate this behavior more effectively, minimizing excessive compression. In contrast, FCC's tighter packing restricts ligand interpenetration, increasing entropic penalties. Consequently, BCC superlattices consistently emerge when ligand interpenetration is feasible, as observed with oleic acid ligands [19].

From these studies, we can hypothesize that the transition from FCC to BCC structures during nanoparticle synthesis is driven by ligand interpenetration and steric constraints as reaction time increases and nanoparticles grow larger. Initially, smaller and more spherical nanoparticles favor FCC packing due to minimal ligand frustration and the high packing density of the FCC arrangement, which maximizes free volume entropy. However, as nanopar-

ticles increase in size, ligands on their surfaces experience greater steric constraints and frustration due to the geometric incompatibility of densely packed FCC structures. This leads to entropic penalties as ligands are forced into unfavorable configurations. The lower packing density of the BCC arrangement provides larger interstitial spaces, allowing ligands to distribute more uniformly and reducing strain caused by compression or extension. Consequently, the transition to BCC becomes energetically favorable as particle size increases, aligning with the observed structural evolution over longer synthesis times.

b. Influence of particle geometry

In addition to the role of the ligand, the morphology of the particles also contributes to their preferential organization. Previous studies have emphasized the profound influence of particle geometry on the formation of self-assembled superstructures [20]. Two key principles govern this process. First, flat faces promote alignment with neighboring particles and other planar surfaces, leading to highly ordered arrangements. Second, sharp edges and corners act as spatial constraints that help maintain separation between particles, preventing excessive overlap. Even minor rounding of these edges can destabilize the phase, altering packing behavior and potentially inducing structural transitions.

These principles align closely with the observations in this study. At early stages, the nanoparticles exhibit a rounded cubic morphology, naturally favoring an FCC arrangement due to its higher packing density. The smooth edges and quasi-spherical nature of the particles facilitate close packing and efficient spatial organization. However, as the reaction progresses, the particles evolve into well-defined cubes with sharper edges and flatter faces. This morphological transformation disrupts the conditions necessary for FCC packing and induces a transition to a BCC arrangement. The BCC structure, with its lower packing factor, reflects a less dense but more anisotropic organization, consistent with the increasing geometric definition of the particles.

Overall, the cubic morphology is a major factor, alongside nanoparticle size, in determining their 3D order.

5.6 Time-resolved WAXS for Crystal Structure Analysis

WAXS analysis using a Bruker D8 Advance X-ray diffractometer (conditions as previously described) was conducted on the precipitated nanocomposites to investigate crystal structure formation during nanoparticle growth. Figure 5.14a (PIB1-based nanocomposites) and Figure 5.14b (PIB2-based nanocomposites) present WAXS patterns for PIB-iron oxide nanocomposites synthesized at various reaction times (15-60 minutes). These patterns

illustrate the evolution of iron oxide nanoparticle crystallization within the PIB matrix, corroborating the size evolution observed via TEM and SAXS.

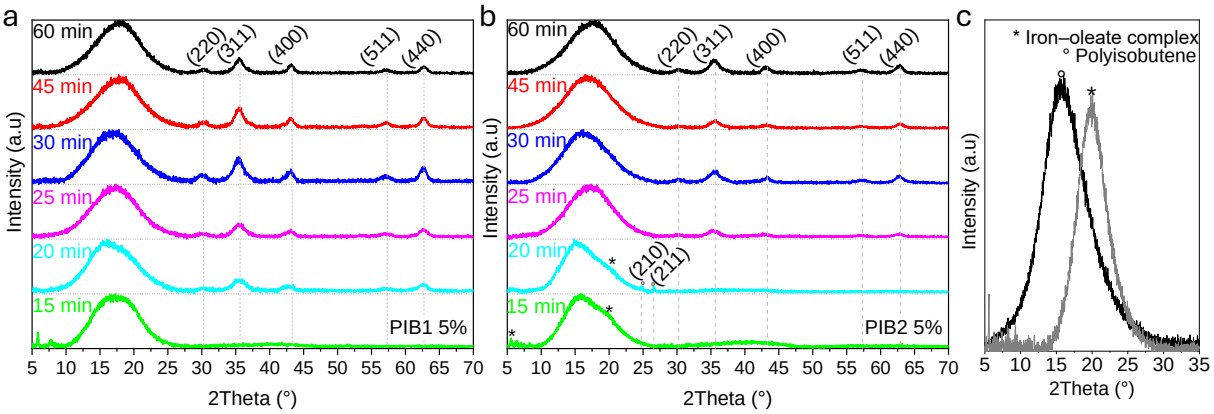

Figure 5.14 – *WAXS patterns of (a) PIB1 and (b) PIB2 nanocomposites, each at synthesis reaction times of 15, 20, 25, 30, 45, and 60 minutes. (c) Iron oleate and the treated PIB*

The XRD patterns reveal the following:

5.6.1 Early Reaction Stage: 15 Minutes

At 15 min, the XRD patterns for both PIB1 and PIB2 samples do not exhibit distinct crystalline peaks, except for a broad amorphous peak centered around **16°**, characteristic of the PIB matrix (Figure 5.14c). However, a subtle shoulder is observed in the diffraction pattern, particularly in the PIB2 sample, as indicated by an asterisk (*) in Figure 5.14b. This shoulder is attributed to the presence of the iron oleate precursor, which has not yet fully decomposed at this early stage of the reaction. The more pronounced shoulder in PIB2 suggests a slower decomposition rate of the precursor in this system compared to PIB1.

5.6.2 Starting from 20 min

By the 20-minute mark, the crystallization process begins to manifest differently in the two systems. For PIB1, the characteristic peaks of maghemite (γ-Fe_2O_3) start to emerge, indicating the onset of nanoparticle formation. In contrast, for PIB2, the precursor shoulder diminishes, but the maghemite peaks remain less defined, suggesting that the crystallization process is still in its early stages. This difference highlights the influence of the polymer matrix on the nucleation and growth kinetics of the iron oxide nanoparticles. The intensity of these peaks increases with reaction time for PIB2, indicating progressive growth and crystallization of the nanoparticles, although this is not as apparent for PIB1.

The XRD analysis reveals that the crystallization of iron oxide nanoparticles within the

PIB matrix is strongly influenced by the reaction time and the properties of the polymer matrix. While both PIB1 and PIB2 eventually lead to the formation of well-crystallized maghemite nanoparticles, the crystallization process occurs more rapidly in the presence of PIB1. This difference highlights the influence of the polymer chain length on synthesis kinetics and structural properties of the resulting nanocomposites.

5.7 Nanocomposites Densities and Nanoparticle Mass Fractions

The mass fraction of nanoparticles within the PIB matrix was determined by comparing the density of the nanocomposites with that of the corresponding treated PIB samples synthesized under identical thermal conditions. The treated PIB refers to PIB dissolved in hexadecene and subjected to the same heating cycle and reaction time as the nanocomposites (15, 20, 25, 30, 45, and 60 minutes), but without the addition of the nanoparticle precursors, thereby accounting for any thermal degradation of the polymer.

For each sample, the mass was measured three times in air and three times in ethanol. The density (ρ) was calculated using the following equation:

$$\rho = \frac{\text{average mass in air} \times \text{density of ethanol}}{\text{average mass in air} - \text{average mass in ethanol}} \tag{5.5}$$

The density of the oleic acid-coated maghemite nanoparticles was estimated using TEM measurements to determine the core radius, combined with the shell thickness obtained from SAXS data. Using the density of the treated PIB as a reference, along with the estimated density of the oleic acid-coated maghemite and the measured density of the nanocomposites, the mass fraction of nanoparticles (w_m) was calculated using the following equation:

$$w_m = \frac{\left(\frac{1}{\rho_c} - \frac{1}{\rho_p}\right)}{\left(\frac{1}{\rho_m} - \frac{1}{\rho_p}\right)} \tag{5.6}$$

where ρ_c is the density of the nanocomposite, ρ_p is the density of the treated PIB, and ρ_m is the estimated density of the oleic acid-coated maghemite.

5.7.1 Nanoparticle Mass Fractions in the PIB matrix

The densities of nanocomposites and their corresponding treated polymer matrices were measured over varying reaction times to evaluate how in situ nanoparticle synthesis influences material structure (Figure 5.15).

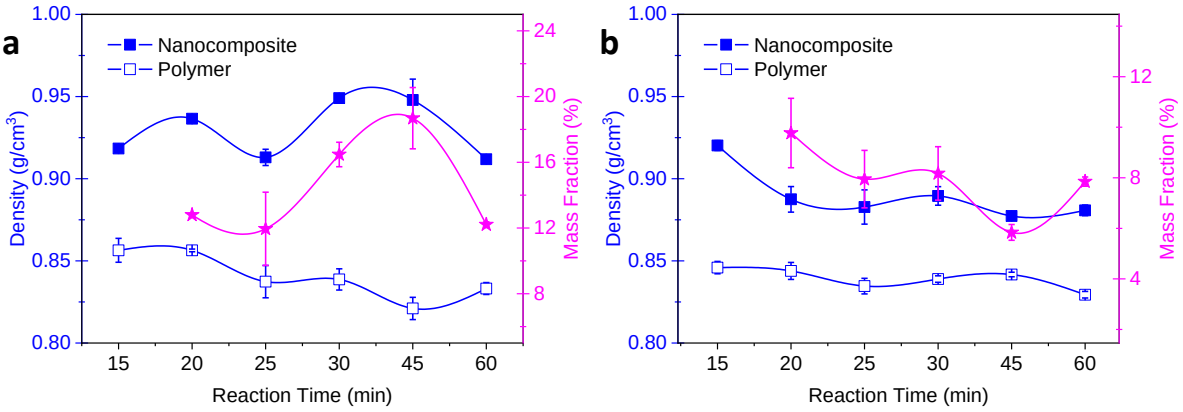

Figure 5.15 – *Density evolution of the nanocomposites (solid squares) and treated polymers (open squares) as a function of reaction time, measured in the precipitated state (left axis). The corresponding mass fraction of inorganic content (pink stars) is shown (right axis). Panels (a) and (b) represent the results for PIB1 and PIB2 composites, respectively.*

PIB1 nanocomposites

Focusing first on the PIB1 system (Figure 5.15a), the polymer density remained stable between 15 and 20 minutes, indicating minimal thermal degradation in this initial phase. In contrast, the nanocomposite density increased during this interval, reflecting the formation and incorporation of inorganic nanoparticles within the polymer matrix.

From 20 to 25 minutes, a slight decrease in polymer density was observed, likely signaling the onset of thermal degradation. The concurrent decrease in nanocomposite density suggests that nanoparticle formation was insufficient to offset matrix degradation, or that nanoparticle incorporation was still limited.

Between 25 and 30 minutes, the polymer density stabilized, while the nanocomposite density rose further. This trend points to more efficient nanoparticle formation and dispersion, resulting in increased bulk density. The mass fraction of inorganic content also increased during this period, supporting the conclusion that nanoparticle loading was rising.

From 30 to 45 minutes, the polymer density progressively decreased, consistent with ongoing thermal degradation. However, the nanocomposite density remained stable, indicating that the growing inorganic content partially compensated for the loss in polymer

matrix density. The continued increase in mass fraction during this stage confirms ongoing nanoparticle growth and incorporation into the polymer.

An unexpected increase in polymer density was observed between 45 and 60 minutes, potentially due to partial matrix reorganization, such as localized densification or chain rearrangement, which may have temporarily counteracted thermal degradation. Alternatively, accelerated degradation could have released low-molecular-weight fragments, increasing the composite's free volume, while the formation of denser, shorter polymer chains may have contributed to a higher density in the pure polymer phase.

The decrease in composite density suggests that the particles may have aggregated during this reaction time. As a result, a significant number of particles could have been lost during the precipitation step. Another possibility is that the polymer matrix may have embedded the particles less effectively after this heat treatment, which would explain the drop in the mass fraction.

PIB2 Nanocomposites

The density evolution of the treated PIB2 polymer and the synthesized nanocomposites shows a trend comparable to PIB1. Qualitatively, there is an initial increase in mass fraction between 20 and 25 minutes, followed by a rise between 25 and 30 minutes. However, the decrease occurs earlier in PIB2, between 30 and 45 minutes, whereas for PIB1 it occurs later. In contrast, PIB2 exhibits an additional increase in mass fraction between 45 and 60 minutes. Quantitatively, the mass fractions are significantly lower for PIB1 (between 7% and 10%) compared to PIB2 (between 12% and 19%), despite using the same amount of molecular precursors.

5.7.2 Hypothesis for Reduced Reaction Yield in Low-Molecular-Weight Polyisobutylene in the Presence of Sodium Oleate

The reduced reaction yield observed when using low-molecular-weight polyisobutylene (PIB2) in the presence of sodium oleate can be understood through the lens of fundamental physicochemical interactions. Notably, spherical nanoparticles were obtained in systems without sodium oleate (as discussed in the next chapter), and the reaction yield was comparable across different the two PIB molecular weights (PIB1 & PIB2). However, in sodium oleate's presence, yield drop is consistently observed when low-MW PIB is used.

This behavior can be rationalized by considering three interconnected factors: (1) the limited direct affinity between PIB and sodium oleate, (2) the role of polymer chain length in modulating precursor distribution, and (3) the downstream effects on nanoparticle nucleation and growth mechanisms.

1. Limited Direct Affinity Between PIB and Sodium Oleate PIB is a completely nonpolar polymer, lacking polar or ionic functionalities. As such, it exhibits only weak van der Waals interactions with sodium oleate, whose amphiphilic structure includes a charged carboxylate headgroup and a hydrophobic C18 tail. This lack of chemical compatibility limits any meaningful molecular association or miscibility between the two components. In nonpolar media such as hexadecene, PIB does not stabilize Na-oleate on the molecular level. This is consistent with established chemical principles regarding the immiscibility of ionic surfactants in nonpolar matrices [21].

2. Polymer Chain Length Modulates Precursor Distribution The polymer chain length influences the spatial organization of precursors during synthesis. Higher-MW PIB provides greater steric hindrance and forms more entangled or viscous environments, thereby creating microdomains where local concentrations of iron oleate and sodium oleate remain relatively balanced. In contrast, shorter PIB chains allow for increased mobility of the surfactants and precursors, potentially resulting in phase separation or Na-oleate-rich domains if diffusion outpaces local reaction kinetics [22].

This concept aligns with literature from surfactant and polymer sciences, which shows that reduced steric confinement can facilitate micellar segregation or domain formation in soft materials [23]. Additionally, micelle formation and domain stability are sensitive to the molecular environment, particularly in systems involving co-surfactants or polymer matrices [21] [22] [23].

3. Effects on Nucleation, Growth, and Reaction Yield The presence of Na-oleate-rich regions can significantly influence the nucleation and growth of nanoparticles. These regions may alter the local critical micelle concentration (CMC), change the aggregation behavior of the precursors, and disrupt controlled nucleation. High local concentrations of sodium oleate have been shown to affect micelle morphology and dynamic behavior—e.g., transforming spherical micelles into ellipsoids as ionic strength increases [21]. Furthermore, salt-induced changes in CMC in aqueous systems may have analogous effects in nonpolar media, affecting the availability of active precursor species during nucleation.

These phenomena can hinder nucleation, reducing overall reaction yield or triggering secondary nucleation at later stages (explaining the mass fraction increase at 60 min), particularly in low-molecular-weight PIB systems, where rapid mixing dilutes the precursors faster than they are consumed, delaying nucleation and favoring secondary events at later stages.

5.8 Mechanical Properties: Viscoelastic Behavior

The morphological analysis of the nanocomposites confirms the successful formation of iron oxide nanoparticles with uniform size and shape. However, the synthesis process involves high temperatures, which may alter the properties of the polymer matrix. To assess the thermal effect, untreated polyisobutylene was compared with PIB samples subjected to the same thermal treatment for 30 minutes.

In parallel with this thermal evaluation, the role of nanoparticles in reinforcing the polymer matrix is also addressed. Nanoparticles are known to significantly enhance the mechanical properties of polymer matrices. In earlier studies, achieving optimal nanoparticle dispersion was a major challenge. With uniform dispersion now ensured, the size effect of the nanoparticles can be investigated. The mechanical response of the nanocomposite is evaluated as a function of nanoparticle size, concentration, and growth stage, while also accounting for matrix degradation due to heating. This approach enables the correlation of the mechanical behavior of the samples with the nanoparticle growth kinetics discussed in the previous sections.

Overall, the mechanical behavior captures the interplay between two competing processes:

(1) The formation, increasing concentration, and progressive organization of larger nanoparticles, which—through stronger interfacial interactions and network structuring—enhance stiffness and contribute to mechanical reinforcement;
(2) Thermal degradation of the polymer matrix, which potentially reduces chain length, and the presence of residual solvent, which may hinder chain entanglement and slippage—thereby weakening the intrinsic viscoelastic network of the material.

To quantify the mechanical properties, frequency sweep tests were conducted using a *Physica MRC 301* rheometer (Anton Paar) equipped with a parallel plate geometry (2 mm gap) at 298.15 K. The linear viscoelastic region was first determined via an amplitude sweep at 1 Hz, using a deformation range from 1×10^{-5} to 0.01. Subsequently, frequency sweep tests in the range of 0.01 to 10 Hz were conducted at a constant deformation of 0.1%. Each 0.1 g sample was analyzed in triplicate to ensure repeatability.

5.8.1 Comparison of Mechanical Behavior Before and After Treatment

The frequency sweep results in Figure 5.16 reveal a distinct reduction in both storage (G') and loss (G'') moduli following the thermal treatment of PIB1 and PIB2. Untreated samples exhibit more solid-like behavior, with G' consistently higher than G'' across the measured frequency range and no crossover observed. In contrast, thermally treated samples display a crossover point between G' and G'', indicating a shift toward more liquid-like behavior. This transition reflects a significant deterioration of the viscoelastic network. The observed softening is attributed to thermal degradation of the polymer matrix, which likely reduces chain length, as well as to the presence of residual solvent, which may disrupt chain entanglement and promote slippage-both factors that weaken the material's mechanical integrity. While the treated samples maintain the general trend of increasing moduli with frequency, the decrease in absolute values confirms a substantial loss in viscoelastic performance.

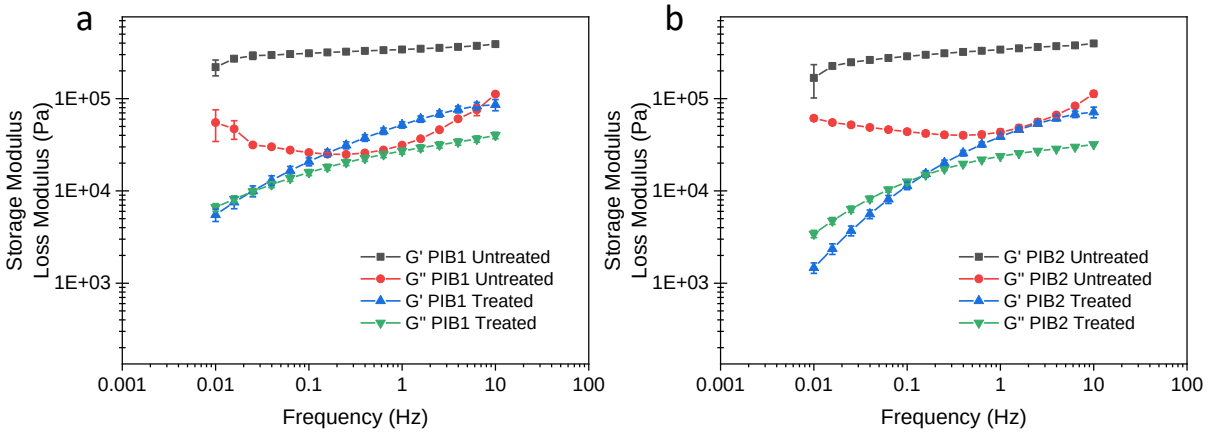

Figure 5.16 – *Frequency dependence of storage and loss moduli for untreated (raw) and thermally treated PIB samples: (a) PIB1; (b) PIB2.*

For PIB1, untreated samples show high stiffness, with G' increasing from 219 kPa to 390 kPa and G'' from 55 kPa to 112 kPa across the frequency range. Thermal treatment reduces G' to 5.5–85.9 kPa and G'' to 6.6–40 kPa, with a crossover at approximately 0.025 Hz ($G'' > G'$ at low frequencies), indicating a transition to more fluid-like behavior. Untreated PIB1 remains elastic throughout the frequency range.

PIB2 follows the same trend: untreated samples show G' rising from 168 to 397 kPa and G'' from 61.2 to 113 kPa. After heating, G' drops to 1.5–71.4 kPa and G'' to 3.4–31.9 kPa, again with $G'' > G'$ at low frequencies. The thermal treatment clearly softens both materials and induces a frequency-dependent mechanical response.

It is worth mentioning that the untreated PIB samples exhibit a non-monotonic trend in their loss modulus G'', showing an initial decrease at low frequencies followed by an

increase at higher frequencies. This behavior is characteristic of high-molecular-weight polymers in the rubbery regime. At low frequencies, chain relaxation processes dominate, resulting in reduced energy dissipation. As the frequency increases, segmental motions and entanglement dynamics become more significant, causing G'' to rise. The observed minimum likely corresponds to a transition between terminal flow behavior and the onset of entanglement-controlled viscoelasticity.

5.8.2 Frequency-Dependent Storage Modulus (G')

Figure 5.17 shows frequency sweep tests for PIB1 and PIB2 nanocomposites. These results highlight how the evolving nanoparticle structure and the corresponding changes in the polymer matrix jointly govern the viscoelastic performance of the nanocomposites. Based on these graphs, the frequency-dependent storage modulus (G') is analyzed to track its evolution across six reaction times for both molecular weights of PIB. This analysis is correlated with the synthesis process (nucleation and growth), as well as with nanoparticle size, concentration, and 3D packing.

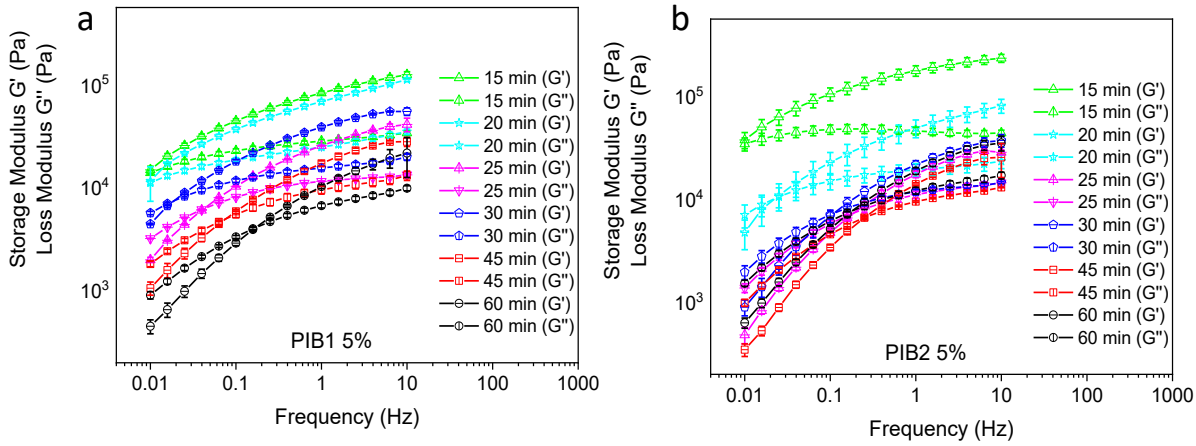

Figure 5.17 – *Frequency sweep of storage modulus and loss modulus: (a) PIB1 nanocomposites, (b) PIB2 nanocomposites.*

For direct comparison, Figures 5.18a and b replot data at identical frequencies for both systems. G' increases monotonically with frequency across all synthesis durations, exhibiting typical frequency-stiffening behavior indicative of enhanced energy storage and dominant elastic responses under rapid deformation.

Early Reaction Times (15 Minutes) At 15 minutes of reaction time, both PIB1 and PIB2 nanocomposites exhibit their highest storage modulus values. This behavior corresponds to a dense and well-organized polymer network that remains intact at this stage. Nanoparticles are still in their nucleation phase (Early growth), contributing minimally to reinforcement

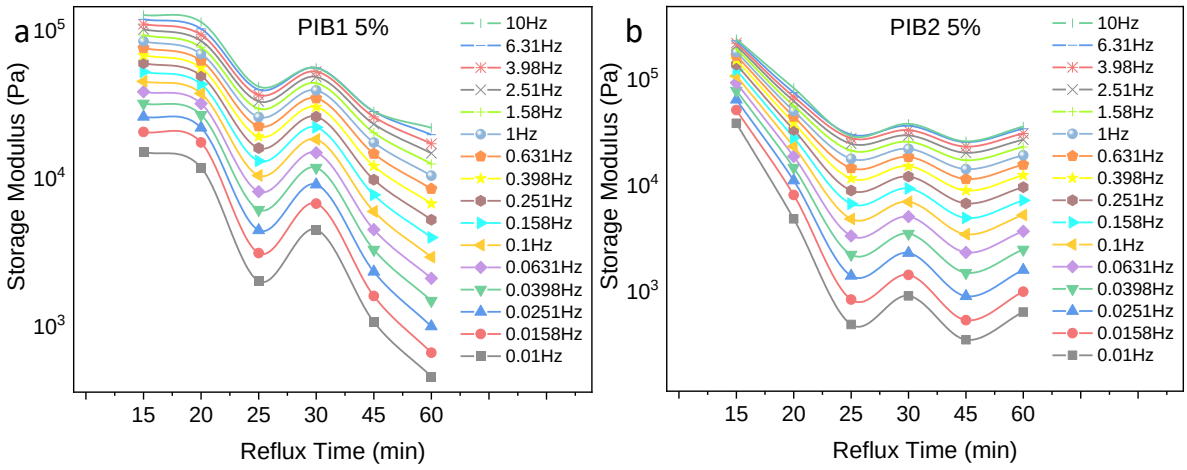

Figure 5.18 – *Frequency-dependent storage modulus (G') for (a) PIB1 and (b) PIB2 nanocomposites*

effects.

Intermediate Reaction Times (20–25 Minutes) By 20 minutes, a decrease in G' is observed for both PIB1 and PIB2 nanocomposites. However, this decrease is more pronounced for PIB2 compared to PIB1. For PIB1, nanoparticles have already grown to approximately 6.8 nm—nearing their final size—while PIB2 nanoparticles remain smaller (around 3.3 nm) and less defined.

At 25 minutes, both systems still show decreasing G', but their trends diverge.

- PIB1 shows a significant drop, whereas PIB2 exhibits only a slight decrease.
- PIB1 nanoparticles grow modestly from 6.8 nm to 7.6 nm.
- PIB2 nanoparticles undergo rapid growth from 3.3 nm to 7.2 nm.

The contrasting behavior suggests that while PIB1 nanoparticles are stabilizing, PIB2 nanoparticles are still in an active growth phase.

Stabilization Phase (25–30 Minutes) Around 25-30 minutes, both nanocomposites show a sharp rise in G', which is more significant for PIB1 than PIB2. This stabilization phase, where nanoparticles form and effectively interact with the polymer matrix, enhances the storage modulus. PIB1's earlier stabilization explains its superior reinforcement over PIB2 during this period, particularly considering its higher nanoparticle mass fraction.

Late Reaction Times (30–45 Minutes) Between 30 and 45 minutes, G' decreases in both systems as thermal degradation outweighs nanoparticle reinforcement. Prolonged heat exposure diminishes reinforcement effectiveness and degrades the matrix's molecular weight, resulting in poorer viscoelastic properties.

Final Reaction Time (60 Minutes) After 60 minutes, PIB1's G' continues to decline as matrix degradation outweighs nanoparticle reinforcement. Conversely, PIB2 shows a slight

G' increase, correlating with its earlier observed mass fraction increase.

From these evolutions, the rheological behavior of PIB nanocomposites reveals a dynamic balance between nanoparticle growth/stabilization and polymer degradation:

- Early synthesis stages favor matrix integrity over nanoparticle reinforcement.
- Intermediate stages show competitive interactions between nanoparticle growth and matrix deterioration.
- Late stages highlight thermal degradation as the dominant factor.

While potentially reducing mechanical properties, this process offers significant improvements in nanoparticle dispersion and morphological control, enabling homogeneous nanoparticle distribution and uniform particle size and shape within the polymer matrix. This control, difficult to achieve using conventional methods that often lead to aggregation or polydispersity, makes the resulting nanocomposites promising for soft robotics, where flexibility and functional integration are key [24], and biomedical applications like magnetic hyperthermia, where precise nanoparticle control is vital for targeted therapeutic efficacy [25].

5.8.3 Liquid-Like Behavior to Solid-Like Behavior

From Figure 5.17, we observe that from the G' and G'' curves for each sample, G'' is initially higher than G'. Then, we observe a crossover point where G' exceeds G''. The crossover frequencies for each sample were plotted to track their evolution across the reaction time in Figure 5.19.

The reaction occurs at 274°C, a temperature that facilitates molecular rearrangements, and nanoparticle formation within the polymer matrix. For PIB1, which has a higher molecular weight than PIB2, the crossover frequency generally increases with reaction time, starting at 0.0083 Hz at 15 minutes and reaching 0.1678 Hz at 60 minutes. This trend suggests that PIB1 transitions to elastic behavior at progressively higher deformation rates as the reaction proceeds, indicating weaker network formation or reduced elasticity over time. However, there is a significant drop in crossover frequency at 30 minutes (0.0188 Hz compared to 0.042 Hz at 25 minutes). This drop suggests that PIB1 becomes more solid-like at this stage, transitioning to elastic behavior at lower deformation rates. The drop is likely due to **forced reinforcement** caused by the formation of nanoparticles within the polymer matrix, which temporarily enhances structural organization and solid-like properties.

PIB2, with its lower molecular weight, exhibits a similar trend but with more pronounced fluctuations in its crossover frequencies. It starts at 0.0077 Hz at 15 minutes and peaks sharply at 25 minutes (0.1899 Hz), then drops significantly to 0.108 Hz at 30 minutes. As

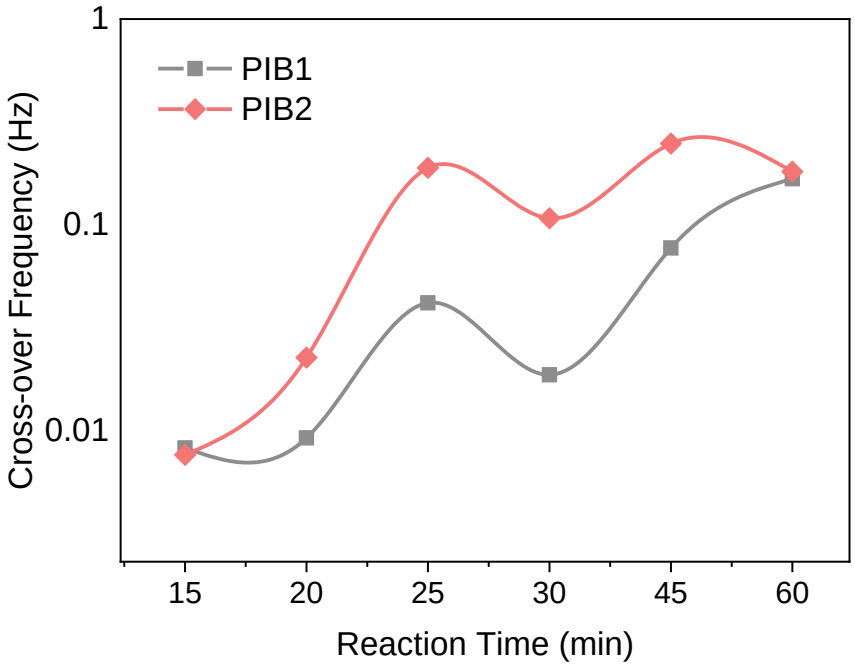

Figure 5.19 – *Evolution of crossover frequencies for PIB1 and PIB2, where G' exceeds G''. The plot tracks the progression of the viscoelastic transition across reaction time.*

with PIB1, this drop reflects an increase in solid-like behavior due to **nanoparticle-induced reinforcement**, which strengthens the material's elastic response by increasing molecular entanglement or crosslink density. After recovering to its highest crossover frequency of 0.249 Hz at 45 minutes, PIB2 again shows a decline in crossover frequency to 0.1819 Hz at 60 minutes. This second drop indicates that PIB2 regains solid-like behavior as it transitions to elastic dominance at lower deformation rates once more. The gain in solid-like properties at this stage may be attributed to further nanoparticle formation or additional crosslinking within the polymer matrix.

Comparing the two polymers, PIB1 consistently exhibits lower crossover frequencies than PIB2 across most reaction times. This difference can be attributed to its **higher molecular weight**, which facilitates greater chain entanglement and earlier gelation (solid-like behavior) at lower deformation rates. In contrast, PIB2's lower molecular weight results in weaker chain interactions and delayed gelation, requiring higher deformation rates for elastic behavior to dominate. The dips in crossover frequency observed for both polymers—at 30 minutes for both and again at 60 minutes for PIB2—highlight critical stages where nanoparticle formation or structural reorganization reinforces their internal structures, temporarily enhancing solid-like properties before further curing alters their mechanical response.

Overall, while both polymers show similar trends in their viscoelastic transitions, PIB1 demonstrates relatively stable behavior after its initial dip at 30 minutes, whereas PIB2 shows greater volatility due to its lower molecular weight and sensitivity to curing dynamics.

The drops in crossover frequency observed for both materials suggest important stages of nanoparticle-induced reinforcement, where elasticity temporarily dominates as structural organization increases within the polymer matrix.

5.9 Magneto-Thermal Properties

Beyond their role in reinforcing mechanical properties, iron oxide nanoparticles embedded in the polymer matrix also exhibit magneto-thermal behavior when exposed to an alternating magnetic field. This phenomenon, primarily driven by Néel and Brownian relaxation mechanisms (as discussed in Chapter 2), can be exploited for magnetic hyperthermia applications.

To evaluate the heating efficiency of the nanocomposites, alternating magnetic field measurements were performed using a DM100 system (nanoScale Biomagnetics, Spain) with a water-cooled copper coil. A 1.5 mL dispersion of nanoparticles was sealed in glass vials and placed at the center of the coil. The temperature was recorded using a fluoroptic fiber-optic probe. The magnetic field was applied at a frequency of 776.30 kHz and an amplitude of 300 G (30 mT), and heating was terminated once the sample reached 45°C.

Figures 5.20 and 5.21 show the magneto-thermal responses of PIB1- and PIB2-based nanocomposites under AMF exposure, synthesized with reaction times of 20, 25, 30, 45, and 60 minutes. The heating profiles indicate the influence of nanoparticle size, crystallinity, and distribution within the polymer matrices.

5.9.1 Data Analysis and Mathematical Modeling

The experimental heating curves were analyzed using a Python-based fitting script developed by Dr. Felix Gautier, implementing the Box-Lucas method to account for non-adiabatic thermal losses [26]. This approach overcomes limitations of traditional initial slope analysis by modeling the complete temperature evolution [27] [28]. The goal was to extract the specific absorption rate (SAR) of the nanocomposites, which quantifies the power dissipated per gram of magnetic material:

$$\mathrm{SAR}_{NP} = \frac{P}{m_{NP}} \tag{5.7}$$

Here, m_{NP} is the mass of the magnetic nanoparticle core, and P is the power generated by the hyperthermia process. Under the assumption of adiabatic conditions (no heat exchange with the environment), the power is estimated using the initial slope of the temperature curve:

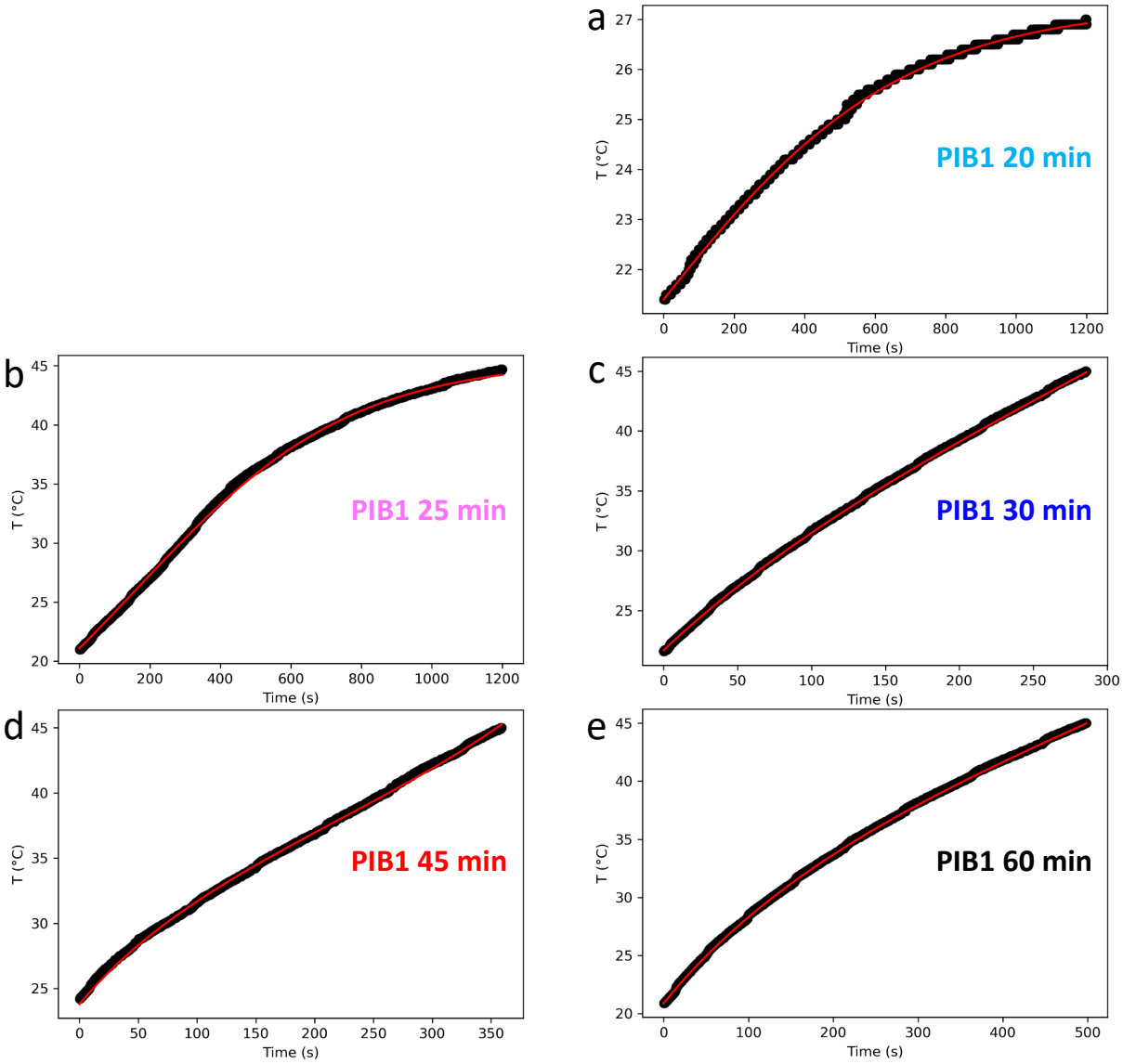

Figure 5.20 – *Magnetic heating behavior of PIB nanocomposites under an alternating magnetic field of 300 Gauss, with heating continued until a target temperature of 45°C was reached. Linear fits were applied to the temperature profiles to extract heating rates. (a–e) PIB1 nanocomposite measured at 20, 25, 30, 45, and 60 minutes.*

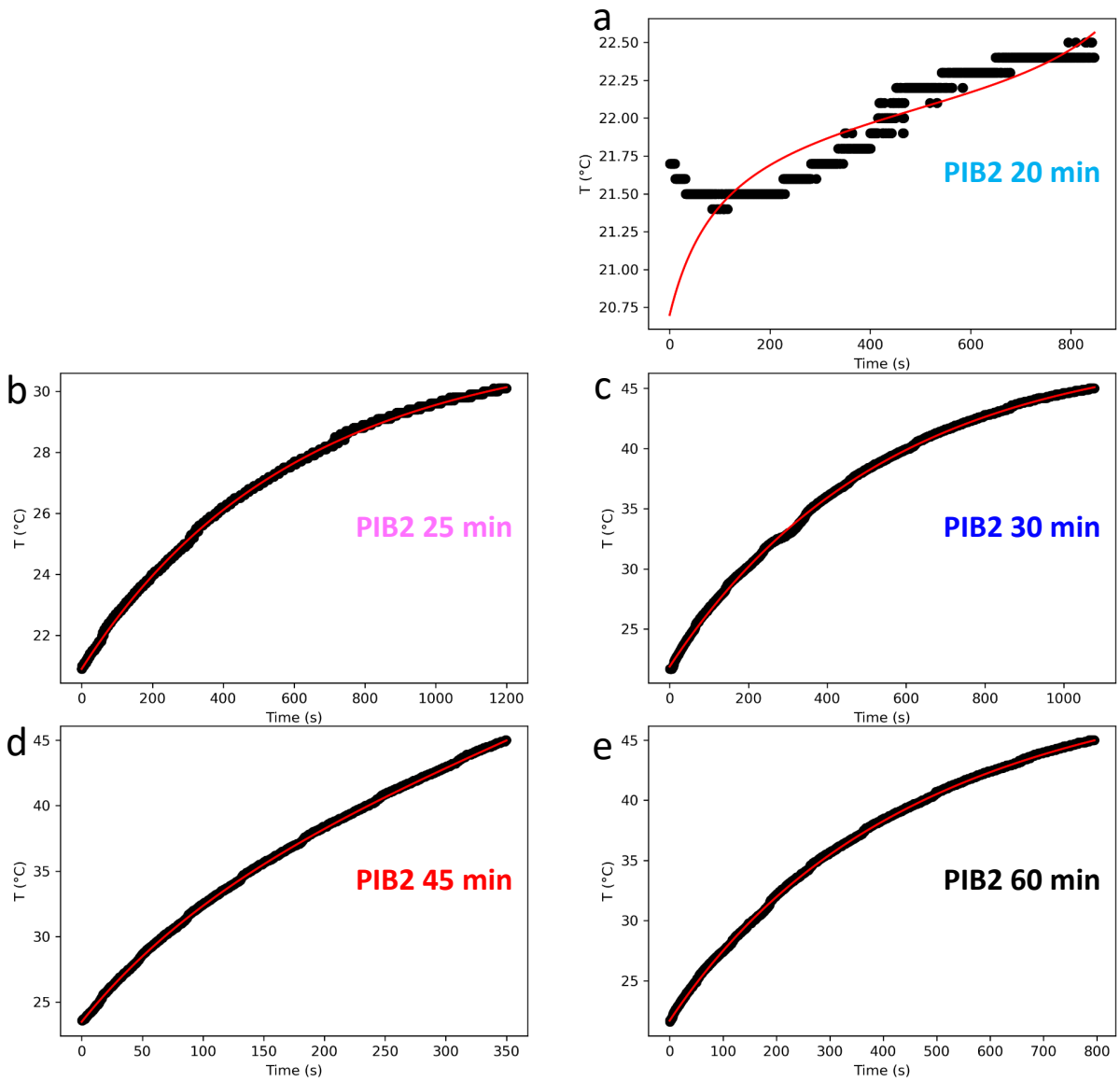

Figure 5.21 – *Magnetic heating behavior of PIB nanocomposites under an alternating magnetic field of 300 Gauss, with heating continued until a target temperature of 45°C was reached. Linear fits were applied to the temperature profiles to extract heating rates. (a–e) PIB2 nanocomposite measured at 20, 25, 30, 45, and 60 minutes.*

$$P = m_f c_f \cdot \frac{dT}{dt} \tag{5.8}$$

$$\mathrm{SAR}_{NP} = \frac{m_f c_f}{m_{NP}} \cdot \frac{dT}{dt} \tag{5.9}$$

However, in real conditions, heat losses to the environment must be taken into account. In this case, Equation 5.8 is modified to include a phenomenological energy loss term, based on Newton's law of cooling:

$$m_f c_f \cdot \frac{dT}{dt} = P - h \cdot A \cdot (T - T_0) \tag{5.10}$$

Here, h is the heat transfer coefficient, A is the surface area through which heat is exchanged, and T_0 is the ambient temperature. The solution of this differential equation yields the time evolution of temperature:

$$T(t) = \frac{P}{hA} + T_0 - \frac{P}{hA} \cdot \exp\left(-\frac{hA}{m_f c_f} t\right) \tag{5.11}$$

While this approach can model moderate heat loss scenarios, it may not always suffice for complex systems (e.g., polymer nanocomposites or inhomogeneous systems). A more general approach considers the energy loss term as an unknown function of T and T_0, denoted $f(T, T_0)$:

$$m_f c_f \cdot \frac{dT}{dt} = P - f(T, T_0) \tag{5.12}$$

Assuming T_0 is constant and the temperature difference $(T - T_0)$ remains small, a Taylor expansion of $f(T)$ can be used. The first-order approximation recovers Newton's law:

$$m_f c_f \cdot \frac{dT}{dt} = P - (T - T_0) \cdot \frac{\partial f(T_0)}{\partial T} \tag{5.13}$$

If this linear approximation does not accurately capture the system's behavior, a second-order expansion can be considered:

$$m_f c_f \cdot \frac{dT}{dt} = P - (T - T_0) \cdot \frac{\partial f(T_0)}{\partial T} - \frac{(T - T_0)^2}{2} \cdot \frac{\partial^2 f(T_0)}{\partial T^2} \tag{5.14}$$

This differential equation exhibits greater complexity; therefore, it has been addressed numerically by employing the finite difference method :

$$T(t + \Delta t) = T(t) + \frac{\Delta t}{m_f c_f} \cdot \Big(P - (T(t) - T_0) \cdot A - (T(t) - T_0)^2 \cdot B\Big) \tag{5.15}$$

with:

$$A = \frac{\partial f(T_0)}{\partial T} \tag{5.16}$$

$$B = \frac{1}{2} \cdot \frac{\partial^2 f(T_0)}{\partial T^2} \tag{5.17}$$

Lastly, it is worth noting that the effective heat capacity of the system can be expressed as:

$$m_f c_f = \frac{m_{NP} \cdot c_{V,f}}{C_{NP}} \tag{5.18}$$

where $c_{V,f}$ is the volumetric heat capacity of the fluid, and C_{NP} is the nanoparticle concentration.

This numerical approach enables a more accurate description of the heating dynamics, especially when experimental data deviate from idealized models.

5.9.2 Thermal Response Analysis

The second-order Taylor series model (Equation 5.14) was used to numerically fit the experimental magnetothermia data through the Python-based program. This approach allows for accurate modeling of non-adiabatic heat losses by accounting for both first- and second-order contributions to thermal dissipation. The corresponding fits are shown in red on the magneto-thermal response curves of PIB1- and PIB2-based nanocomposites in Figures 5.20 and 5.21, respectively. The SAR values were directly extracted from the program and are provided in Table 5.7.

The measured SAR values fall within the expected range for maghemite/magnetite nanoparticles [29]. However, a direct comparison of SAR values with those reported in the literature is not straightforward. This is because SAR depends on various factors, including the equipment used for testing, the method applied for SAR evaluation—especially in non-adiabatic environments where multiple methods exist—the concentration and aggregation state of the sample, particle size, particle material, and the effect of the dispersant [30] [31] [27]. In our case, the dispersant is a viscous polymer solution. Additionally, heating is not measured directly at the nanoparticle surface, as an optical fiber probe is used. Therefore, for our data, we focus on commenting on the relative efficiency of our samples and comparing them with each other.

In both PIB1 and PIB2 matrices, the specific absorption rate (SAR) non-linearly depends on reaction time and nanoparticle size. The PIB1 series reaches a maximum SAR of 26 W g^{-1} at 30 minutes with nanoparticles averaging 8.4 nm (long edge) and 7.9 nm (short edge). Although

Table 5.7 – *SAR values of PIB1 and PIB2 nanocomposites calculated using derivative-based Box–Lucas fitting. The mass fractions (W_m%) correspond to the estimated mass percentage of nanoparticles in the diluted hexadecene solution before the preparation of the nanocomposite.*

Reaction Time (min)	Massic Fraction (%)	Concentration ($g.mL^{-1}$)	Concentration ($mg.mL^{-1}$)	SAR ($W.g^{-1}$)
	PIB1			
20	0.81	0.0063	6.326	2
25	0.75	0.0059	5.858	9
30	1.09	0.0085	8.513	**26**
45	1.26	0.0098	9.841	19
60	0.77	0.0060	6.014	25
	PIB2			
20	0.60	0.0047	4.678	0
25	0.48	0.0037	3.733	8
30	0.50	0.0039	3.850	22
45	0.35	0.0027	2.687	62
60	0.50	0.0039	3.928	29

these dimensions are within the superparamagnetic regime, they are suboptimal for magnetic hyperthermia, as literature suggests peak SAR values occur with larger nanoparticles (18-23 nm) where superparamagnetic relaxation and magnetic moment are optimally balanced for enhanced heating.

After 30 minutes, particle size remains relatively stable, while SAR decreases to $19\,W\,g^{-1}$ at 45 minutes before increasing slightly to $25\,W\,g^{-1}$ at 60 minutes. This later increase could be attributed to dispersity changes, evidenced by the broader size distribution at 45 minutes, or alterations in interparticle magnetic interactions. Thus, nanoparticle size alone is not the sole determinant of heating efficiency; structural or microenvironmental factors, like particle arrangement, dipolar coupling, or local viscosity, significantly impact SAR values.

PIB2 nanocomposites exhibit a SAR response distinct from PIB1. Initially (20-25 minutes), PIB2 shows low SAR values (0-$8\,W\,g^{-1}$) associated with smaller nanoparticles (3.3-7.2 nm). PIB1, at the same early time points, yields slightly larger particles (6.8-7.8 nm) with similar SAR values (2-$9\,W\,g^{-1}$). Subsequently, the PIB2 SAR increases to $22\,W\,g^{-1}$ at 30 minutes, matching the PIB1 SAR at that time. At this stage, both materials exhibit comparable average particle sizes: 8.4 nm for PIB1 and 7.7 nm for PIB2.

PIB2 exhibits a sharp SAR increase at 45 minutes, peaking at $62\,W\,g^{-1}$, exceeding PIB1's maximum by more than twofold. This is unexpected because, at this time, both PIB1 and PIB2 have similar average particle sizes (8 nm), yet higher SAR values are typically observed with larger particles (18-23 nm for iron oxide nanoparticles). This suggests that factors beyond average particle size, such as particle dispersity, crystallinity, interparticle interactions, or the local microenvironment, likely influence heating efficiency.

Interestingly, the SAR drops to $29\,W\,g^{-1}$ at 60 minutes, a value similar to those observed in PIB1 between 30 and 60 minutes and in PIB2 at 30 minutes, despite no significant change in particle size compared to PIB2 at 45 minutes. This further supports the idea that subtle changes in particle arrangement, magnetic coupling, or matrix properties can have a pronounced effect on SAR, independent of average nanoparticle size.

5.10 Conclusion

This study presents a novel approach for synthesizing magnetic nanocomposites by forming IONPs within a polyisobutylene PIB matrix. Our method effectively addresses common challenges such as achieving uniform dispersion and minimizing the polydispersity in nanoparticle size and shape. By carefully monitoring the growth kinetics of IONPs in two PIBs with different molecular weights, we succeeded in producing nanoparticles with a consistent size distribution that were well-dispersed within the matrix.

A major focus was placed on understanding the growth kinetics of the nanoparticles. By monitoring the synthesis process at various reaction times, we elucidated the evolution of particle size, size distribution, and crystalline structure. This kinetic study revealed that the nucleation and growth phases are strongly influenced by the polymer's molecular weight.

To assess the quality of the resulting nanocomposites, we employed a range of multiscale analytical techniques, including TEM, SAXS, and WAXS, all of which provided valuable insights into their morphological properties.

We used density measurements to quantify the amount of formed nanoparticles. The mechanical behavior was evaluated through rheological analysis, where we observed changes in mechanical properties before and after nanoparticle reinforcement. Alternating magnetic field measurements were also performed to assess the magnetothermal behavior.

Based on the morphological, compositional, and bulk properties evaluated for the two molecular weights across six reaction times, we identified 30 minutes as the optimal reaction time. This duration allowed us to balance the rapid formation of nanoparticles with the need to maintain controlled morphology and limit polymer degradation. Under these conditions, both molecular weights produced IONPs with a narrow size distribution and well-defined crystalline structure, which are essential for achieving desirable magnetic properties, mechanical reinforcement, and specific absorption rate.

Chapter 6

Influence of Polyisobutylene Concentration and Molecular Weight on the Synthesis and Properties of Iron Oxide Nanoparticle Nanocomposites

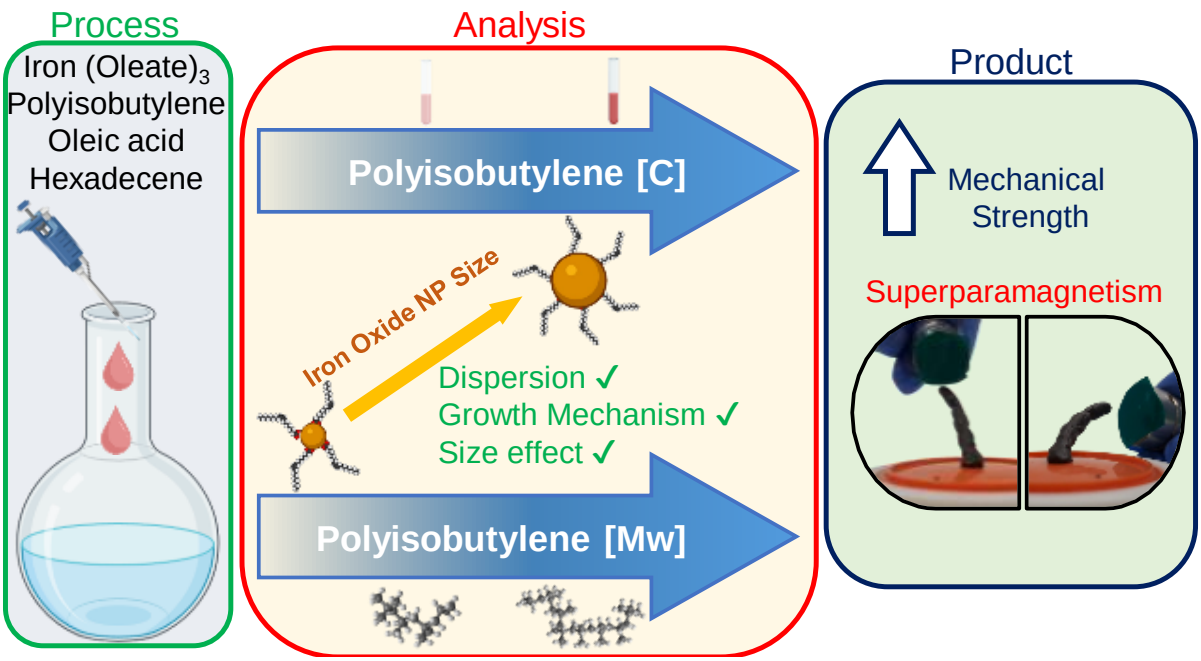

Contents

6.1 Introduction

Building upon our previous work, this chapter presents a systematic investigation into the effect of polyisobutylene concentration on the *in-situ* synthesis of iron oxide nanoparticles within a PIB matrix. We maintain the previously established optimal reaction time of 30 minutes, which was found to yield favorable nanoparticle characteristics—including size, crystallinity, 3D organization, as well as mechanical and magnetothermal performance—for both molecular weights of PIB, as summarized in Figure 6.1. Our goal is to explore how varying the PIB concentration influences the nanoparticle formation process and, consequently, the properties of the resulting nanocomposites.

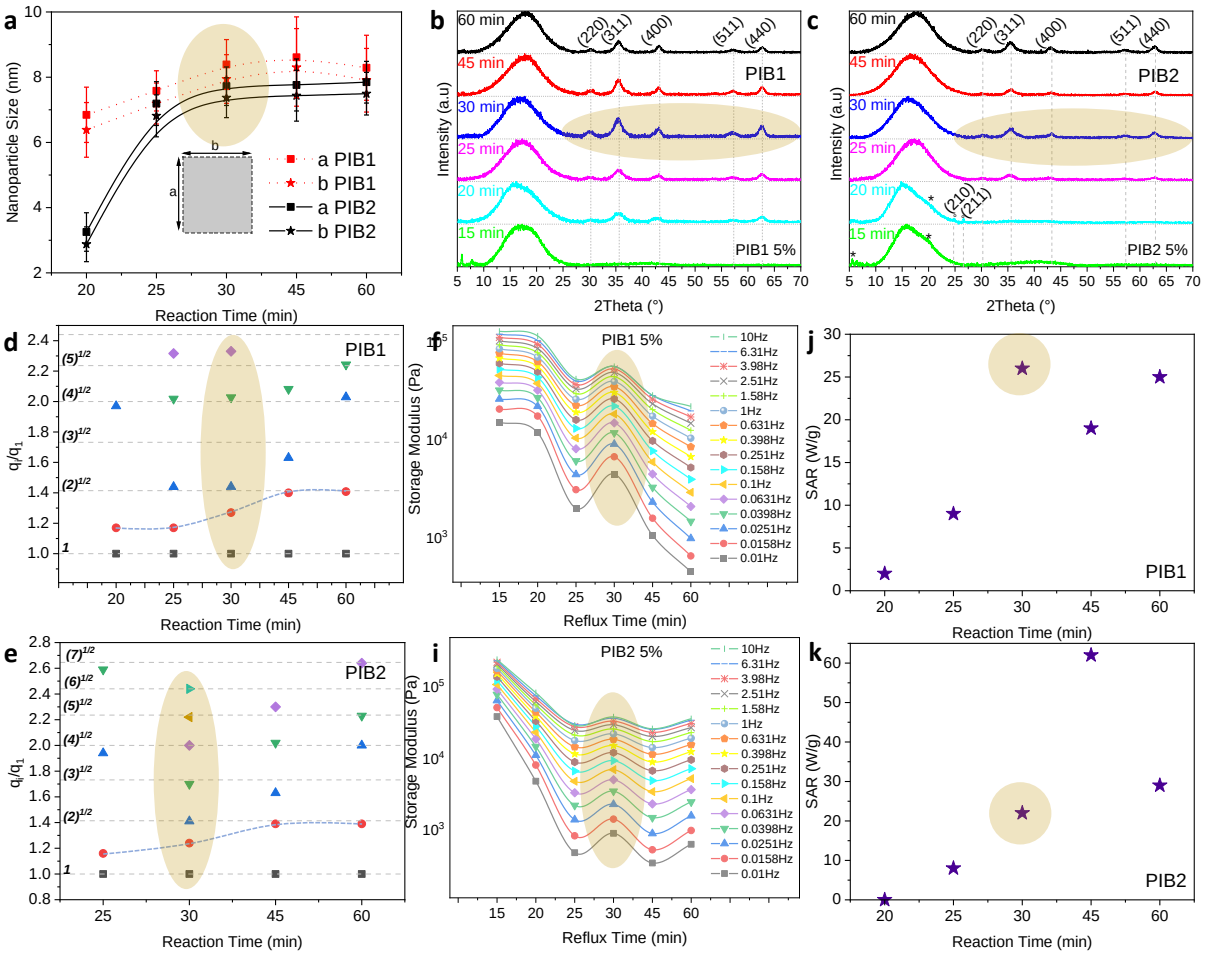

Figure 6.1 – *Summary of the rationale for selecting a 30-minute reaction time as optimal for the in-situ synthesis of IONPs in PIB matrices. This duration was found to yield nanoparticles with favorable characteristics: controlled (a) size, (b,c) enhanced crystallinity, (d,e) well-defined 3D packing, and improved (f,i) mechanical and (j,k) magnetothermal properties, across both PIB1 and PIB2, respectively.*

The central hypothesis of this study is that the concentration of the polymer significantly

modulates the physicochemical environment during synthesis. Specifically, increasing the PIB concentration is expected to raise the solution viscosity, thereby altering precursor diffusion and affecting the kinetics of nucleation and growth. These changes in reaction dynamics are likely to impact not only nanoparticle size and size distribution but also their morphology. Gaining insight into these effects is essential for optimizing the synthesis protocol and tailoring the final nanocomposite properties.

In addition, this chapter investigates how variations in nanoparticle features translate into the multifunctional performance of the final IONP-PIB system. The incorporation of IONPs is expected to enhance properties such as magnetic responsiveness and mechanical robustness—features that are particularly valuable for applications in soft robotics activated via magnetothermal stimuli, and in advanced sensor technologies. In this context, we pay special attention to the interplay between the polymer matrix and the nanoparticles, focusing on how PIB concentration modulates interfacial interactions and governs overall material performance.

Through a combination of kinetic analysis, structural characterization, and functional testing, this chapter aims to establish clear correlations between synthesis parameters, nanoparticle characteristics, and the final performance of the nanocomposite. These findings will not only deepen our understanding of IONP formation within PIB matrices but also offer valuable guidelines for designing and optimizing other polymer-based nanocomposite systems.

6.2 Samples Preparation

6.2.1 Synthesis Process

The *in-situ* synthesis of IONP-PIB nanocomposites was conducted as outlined in the previous chapter, with a few modifications. (1) The reaction time was consistently set at 30 minutes for all samples, as this was determined to be the optimal duration. (2) Three new concentrations were examined alongside the previously mentioned 5% concentration for each molecular weight. (3) A pure iron oleate precursor was used.

Specifically, a given volume of PIB was dissolved in 8 mL of hexadecene in a 250 mL round-bottom flask and stirred for 72 hours to ensure complete dissolution. Following this, 1.6 mmol of iron oleate and 0.8 mmol of oleic acid were introduced into the PIB-hexadecene solution, along with an additional 2 mL of hexadecene. The mixture was stirred for another 72 hours to ensure the thorough dispersion of the iron precursors and surfactants. Afterward, the solution was heated under reflux at 274°C for 30 minutes. Once cooled, acetone was added to the solution to precipitate the nanoparticles, forming a hydrophobic gel layer

around the nanoparticles due to the PIB content by diluting the total PIB in hexadecene.

6.2.2 Samples Variety

To control the size and distribution of the nanoparticles, we varied both the dilution ratio (i.e., PIB concentration) and the molecular weight of PIB. Dilution ratios of 1%, 2.5%, 5%, and 10% were tested using the two PIB molecular weights: 1000 kDa (PIB1) and 500 kDa (PIB2) (Table 6.1). By adjusting these parameters, we demonstrate how nanoparticle size, chemical composition, and dispersion within the PIB matrix are influenced. After completing these characterizations, we assessed the mechanical properties of the nanocomposites to evaluate the impact of nanoparticle size and dispersion on the overall material performance.

Table 6.1 – *PIB molecular weights and concentrations in Hexadecene*

PIB MW	Concentration	Volume	Mass	W_m
kg/mol	%	ml	g	%
PIB1 1000	1	0.1	0.092	23.1
	2.5	0.25	0.23	18.4
	5	0.5	0.46	15
	10	1	0.92	6.7
PIB2 500	1	0.1	0.092	44.4
	2.5	0.25	0.23	16.8
	5	0.5	0.46	14.8
	10	1	0.92	9.6

6.3 Size & Morphology Analysis

6.3.1 Hydrodynamic Diameter

Dynamic Light Scattering technique revealed the hydrodynamic diameter of the IONPs in colloidal suspension. For the PIB1 sample (Figure 6.2a), the size range spanned from 13 nm to 43.6 nm, while the PIB2 sample (Figure 6.2b) exhibited a narrower range of 13.06 nm to 23.8 nm. DLS analysis revealed a Gaussian size distribution indicative of uniform nanoparticles and a stable colloidal system in both samples, suggesting well-controlled synthesis. The hydrodynamic diameter of PIB1 and PIB2 nanocomposites increased with increasing polymer concentration in the synthesis mixture.

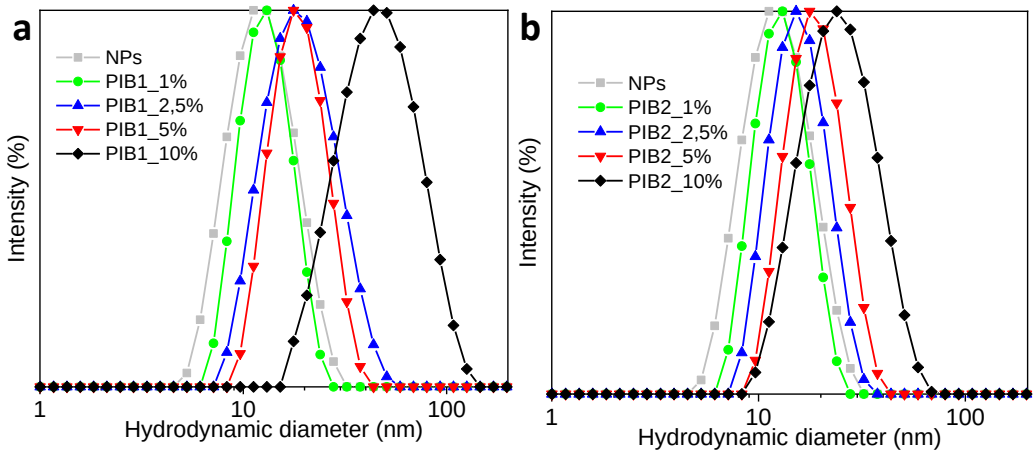

Figure 6.2 – *DLS curves comparing the hydrodynamic size distribution of neat iron oxide nanoparticles and their size evolution in the presence of PIB during synthesis with dilution ratios of 1%, 2.5%, 5%, and 10% using (a) PIB1 and (b) PIB2.*

6.3.2 TEM-Based Particle Size Analysis

To complement the DLS measurements and gain further insights into the morphology and size of the nanoparticles, we employed Transmission Electron Microscopy for direct visualization of the IONPs. The TEM analysis of the IONPs revealed spherical nanoparticles with high uniformity, arranged in a long-range ordered assembly. The spherical morphology results from the lack of shape-directing capping agents, allowing unrestricted nanoparticle formation. For PIB1, the particle diameters ranged from 7.5 nm to 10.8 nm (Figure 6.3a), while PIB2 showed diameters between 7.5 nm and 9.1 nm (Figure 6.3b). In comparison, neat IONPs synthesized without PIB exhibited the smallest size at 7.3 nm (Figure 6.3c). The results corroborate hydrodynamic diameter analysis, confirming that increased PIB concentration or molecular weight yields larger IONP sizes. This finding, consistent with the previous chapter, reinforces the correlation between polymer molecular weight and particle size. Notably, all samples maintained low polydispersity, with values ranging from 7% to 12% (Figure 6.3d), indicating a consistent particle size distribution across different synthesis conditions.

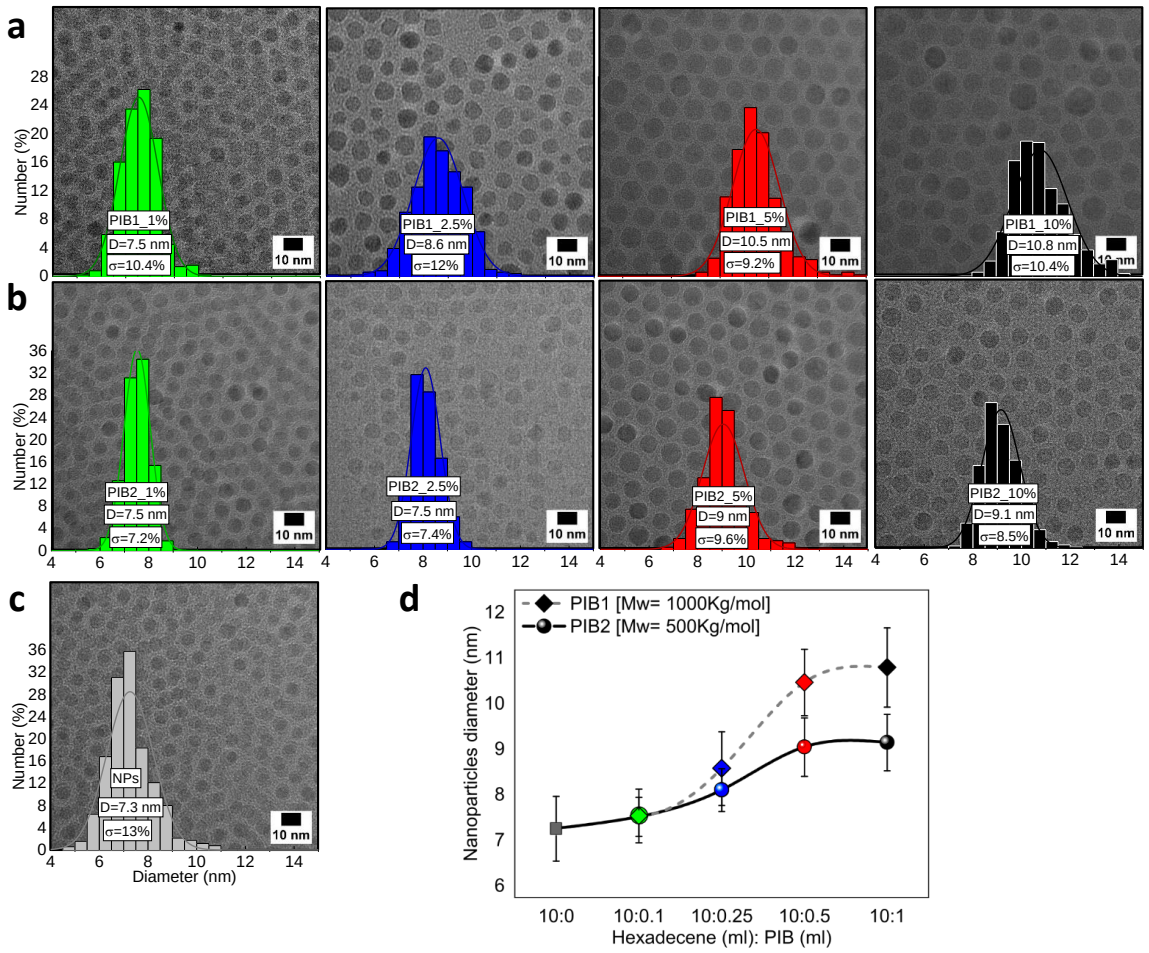

Figure 6.3 – *TEM images and size distributions of IONPs: (a) synthesized in the PIB1 matrix, (b) synthesized in the PIB2 matrix, (c) synthesized in solvent-only conditions, and (d) size evolution as a function of PIB dilution in hexadecene.*

6.3.3 Size Characterization via Small-Angle X-Ray Scattering

To further investigate size and morphology, SAXS measurements were performed on IONP-PIB1 (Figure 6.4a) and IONP-PIB2 (Figure 6.4b). These measurements were conducted on 1%, 2.5%, 5%, and 10% solutions (as-synthesized), precipitated nanocomposites, and a reference solution.

The scattering patterns observed in the diluted regime confirmed the presence of spherical particles, as evidenced by the shape of the intensity curve showing characteristic form factor oscillations specific to spheres.

Analysis of the SAXS curves also revealed a consistent trend in the position of the first minimum. As the concentration increased from neat NPs to 10% IONP-PIB, the first minimum systematically shifted towards lower q values [32]. The observed progression of the first minimum followed a clear order: neat NPs > IONP-PIB 1% > IONP-PIB 2.5% > IONP-PIB 5%

> IONP-PIB 10%. This gradual shift towards lower q values with increasing concentration provides strong evidence for the growth in particle core size as the polymer content increases.

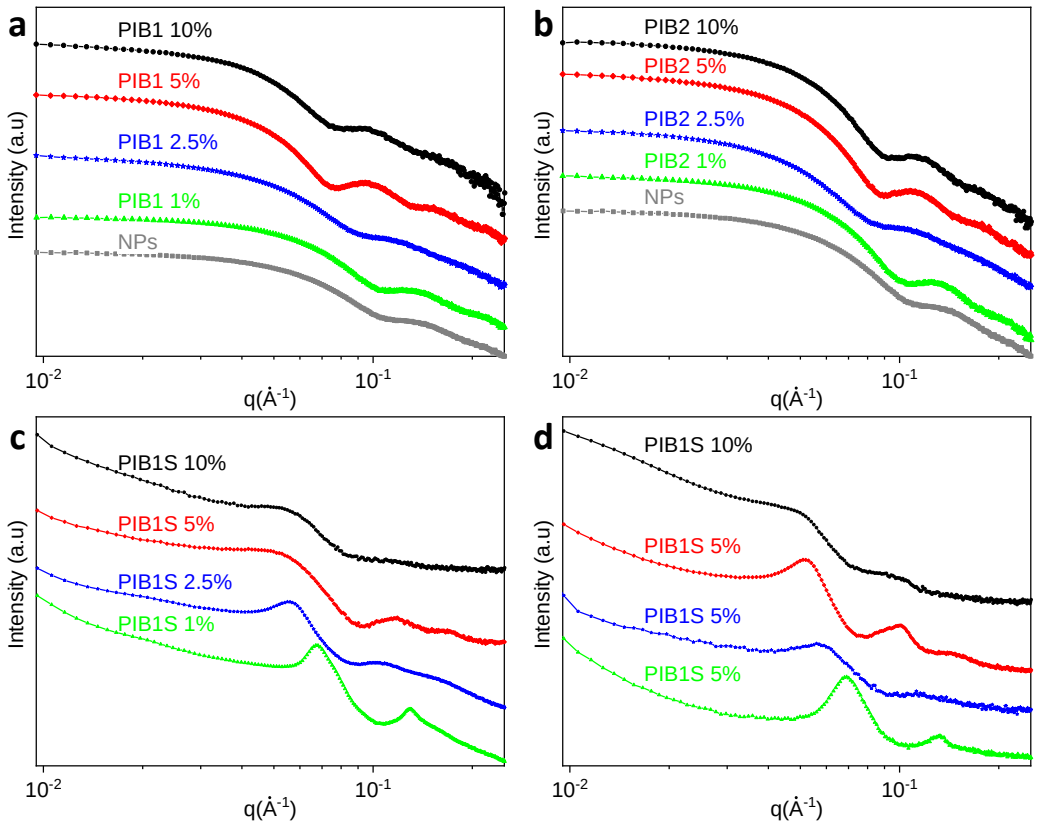

Figure 6.4 – *SAXS patterns of PIB nanocomposites: (a) PIB1 in solution, (b) PIB1 precipitate, (c) PIB2 in solution, and (d) PIB2 precipitate.*

Guinier Plot

Using the Guinier approximation shown in Figure 6.5 for the lower q-range, the radius of gyration (R_g) was determined to range from 33.2 Å to 55.76 Å for PIB1 and from 34.7 Å to 58.8 Å for PIB2 (see Table 6.2). Assuming a homogeneous distribution of spherical particles, as observed from TEM, the radius calculated using the formula (6.1) [33] aligns well with the values previously obtained from TEM measurements.

$$D = 2\sqrt{\frac{5}{3}}R_g \tag{6.1}$$

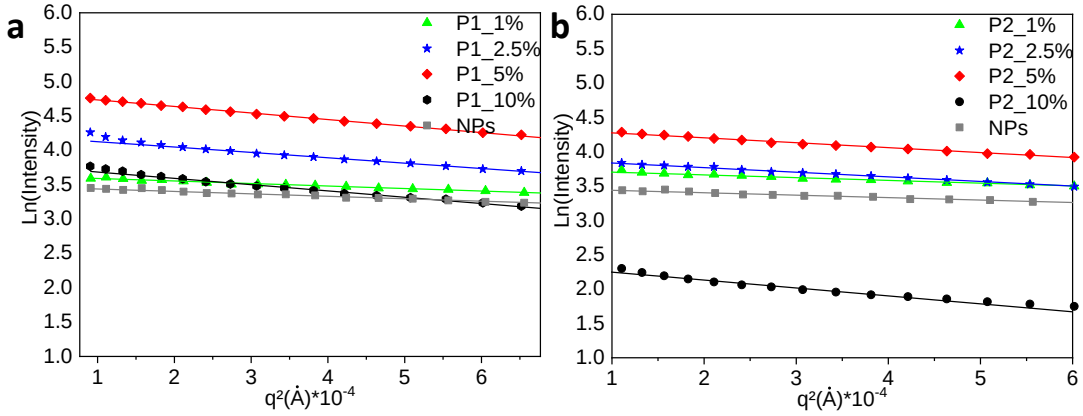

Figure 6.5 – *Guinier plot of (a) PIB1 and (b) PIB2 nanocomposites.*

Table 6.2 – *Summary of R_g and D for PIB1 and PIB2 nanocomposites at different concentrations.*

%	R_g (Å)	D (nm)
IONPs	32.6 ± 0.31	8.41
PIB1 1%	33.2 ± 0.13	8.57
PIB1 2.5%	48.4 ± 0.15	12.46
PIB1 5%	53.8 ± 0.19	13.9
PIB1 10%	55.7 ± 0.26	14.4

%	R_g (Å)	D (nm)
IONPs	32.6 ± 0.31	8.41
PIB2 1%	34.7 ± 0.13	9.84
PIB2 2.5%	44.8 ± 0.15	11.58
PIB2 5%	46.2 ± 0.21	12.15
PIB2 10%	58.8 ± 0.26	15.2

SASView Fitting

SAXS patterns of the IONP-PIB solutions were also analyzed using SASView to investigate the structural properties of oleic acid-coated iron oxide nanoparticles and their distribution within the PIB matrix. The data were fitted to a core-shell sphere form factor model. The fitting results are presented in Figure 6.6a for the PIB1 solution and in Figure 6.6b for both composites in their solution states.

The table 6.3 below summarizes the fitting parameters used in SASView for PIB1 and PIB2 nanocomposites in solution, and the neat nanoparticles, using the spherical core-shell form factor model. The derived parameters confirmed that the average nanoparticle radius increased with PIB concentration and/or molecular weight. Core radius values agreed with TEM results, and the oleic acid coating (shell thickness) ranged from 1 to 1.23 nm.

For precipitate samples (Figure 6.6c,d), where IONP interactions are important, we included a structure factor S(q). The sticky hard sphere model with Percus-Yevick closure provided the best fit [34]. Importantly, the results for the nanoparticle size and shell thickness are closely aligned with those obtained for the PIB nanocomposite in solution (Table 6.3). This consistency suggests that there is no significant variation in size distribution when extracting IONPs with PIB using acetone, indicating that the extraction process effectively

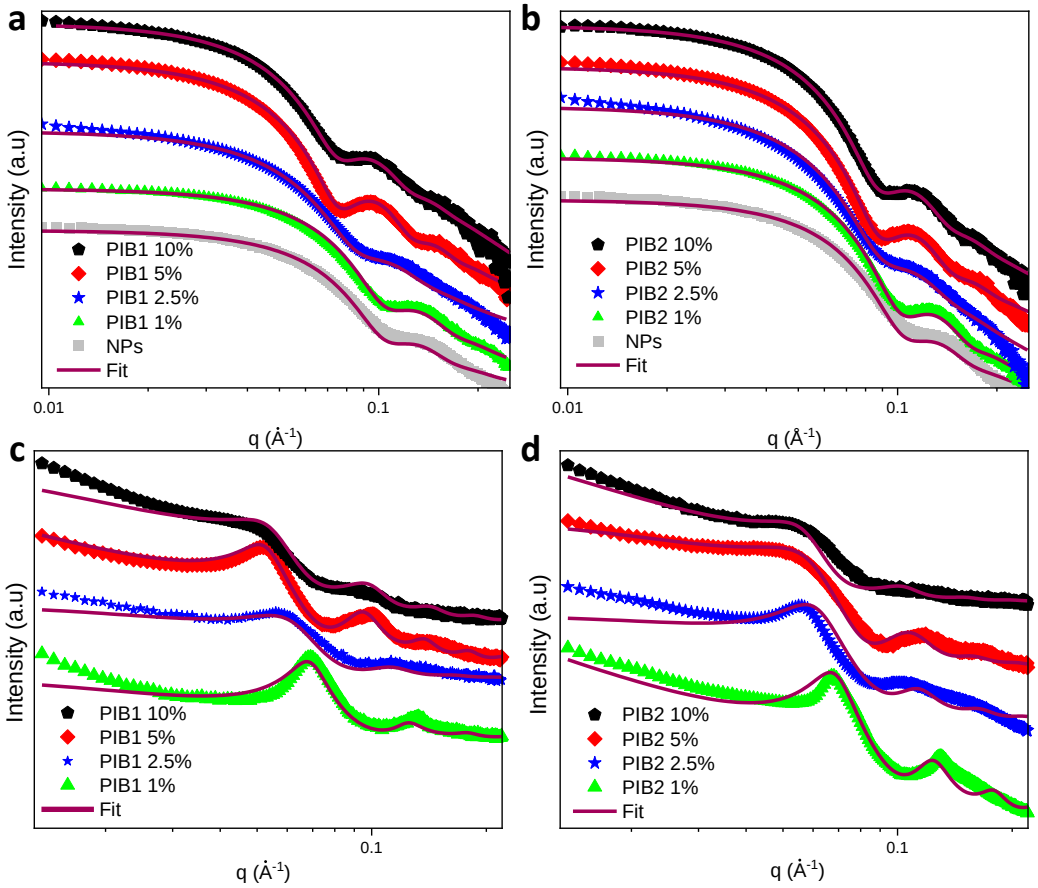

Figure 6.6 – *Fitting curves for SAXS data using the spherical core-shell form factor: (a) PIB1 solution and (b) PIB2 solution. Fitting curves incorporating the spherical core-shell form factor with a sticky-hard sphere structure factor: (c) PIB1 precipitate and (d) PIB2 precipitate.*

preserves the nanoparticle characteristics.

Nanoparticles Spatial Arrangement

The SAXS patterns provided valuable insights into the spatial arrangement of IONPs within the PIB matrix. Specifically, we analyzed the peak positions in the SAXS curves of the PIB1 nanocomposite at 5% concentration (Figure 6.7). The ratios of the peak positions (q_1, q_2, q_3, etc.) relative to the first peak were determined (Figure 6.7). Ratios of $\sqrt{1}$, $\sqrt{4}$, and $\sqrt{9}$ suggested a dominant lamellar arrangement. However, the presence of additional hidden peaks (shoulders) at $\sqrt{3}$, $\sqrt{6}$, and $\sqrt{19}$ hinted at a possible hexagonal arrangement superimposed on the lamellar structure. The observed shoulders, particularly in q_2, further reinforced this interpretation.

To further investigate the hexagonal arrangement, we calculated the lattice parameter a,

Table 6.3 – *SAXS fitting models and parameters: core-shell sphere model applied for solution nanocomposites, with an additional Sticky Hard Sphere interaction model included for precipitated nanocomposites.*

		PIB1_NPs Solution					PIB1_NPs Precipitate			
	PIB concentration	NPs	1%	2.5%	5%	10%	1%	2.5%	5%	10%
Form Factor	*NP radius (nm)*	*4.1*	4.33	4.88	6	6	4.1	4.8	5.8	6.1
	Shell thickness (nm)	*1*	1	1.15	1	1.23	1	1	1	1.2
	Core SLD (10^-7 nm)	7.99	7.99	7.99	7.99	7.99	7.99	7.99	7.99	7.99
	Shell SLD (10^-7 nm)	10.4	10.4	10.4	10.4	10.4	10.4	10.4	10.4	10.4
	Solvent SLD (10^-7 nm)	9.8	9.8	9.8	9.8	9.8	9.8	9.8	9.8	9.8
Structure Factor	*Effective radius (nm)*	/	/	/	/	/	5.1	5.8	6.8	7
	Volumic fraction	/	/	/	/	/	0.4	0.3	0.34	0.33
	Stickeness	/	/	/	/	/	0.01	0.2	0.015	0.15
		PIB2_NPs Solution					PIB2_NPs Precipitate			
	PIB concentration	NPs	1%	2.5%	5%	10%	1%	2.5%	5%	10%
Form Factor	*NP radius (nm)*	*4.21*	4.4	4.75	5.1	5.1	4.1	4.5	5.35	5.4
	Shell thickness (nm)	*1.2*	1.3	1.4	1.4	1.5	1.1	1.2	1.5	1.5
	Core SLD (10^-7 nm)	7.98	7.98	7.98	7.98	7.98	7.98	7.98	7.98	7.98
	Shell SLD (10^-7 nm)	10.4	10.4	10.4	10.4	10.4	10.4	10.4	10.4	10.4
	Solvent SLD (10^-7 nm)	9.8	9.8	9.8	9.8	9.8	9.8	9.8	9.8	9.8
Structure Factor	*Effective radius (nm)*	/	/	/	/	/	5.3	5.8	6.2	6.3
	Volumic fraction	/	/	/	/	/	0.4	0.4	0.34	0.34
	Stickeness	/	/	/	/	/	0.01	0.1	0.02	0.05

representing the center-to-center distance between adjacent cylinders, using the scattering vector q_{100} (corresponding to q_1) as shown in Eq. 6.2 [35]:

$$a = \frac{4\pi}{\sqrt{3}q_1} \tag{6.2}$$

The calculated lattice parameter for the PIB1 sample at 5% concentration was 14.51 nm. This value was consistent with measurements from TEM images, which revealed an average center-to-center distance of 14.85 nm between adjacent nanoparticles arranged in hexagonal patterns. The close agreement between the SAXS-derived lattice parameter and the TEM-measured distance highlights the consistency of the nanoparticle arrangement as observed through these two techniques. While TEM provides a two-dimensional projection of local arrangements, SAXS offers insight into the three-dimensional structure of the sample.

The observation of hexagonal patterns in the TEM images aligns with the SAXS data, suggesting that a hexagonal arrangement is superimposed on the lamellar structure. Although the quantitative analysis was conducted specifically for the PIB1 sample, qualitative assessments of TEM micrographs and SAXS patterns across all samples revealed similar structural organization. The consistent presence of hexagonal-like arrangements in the TEM images, combined with comparable SAXS scattering profiles, strongly suggests that this

ordered nanostructure is a characteristic feature across the entire series of nanocomposites.

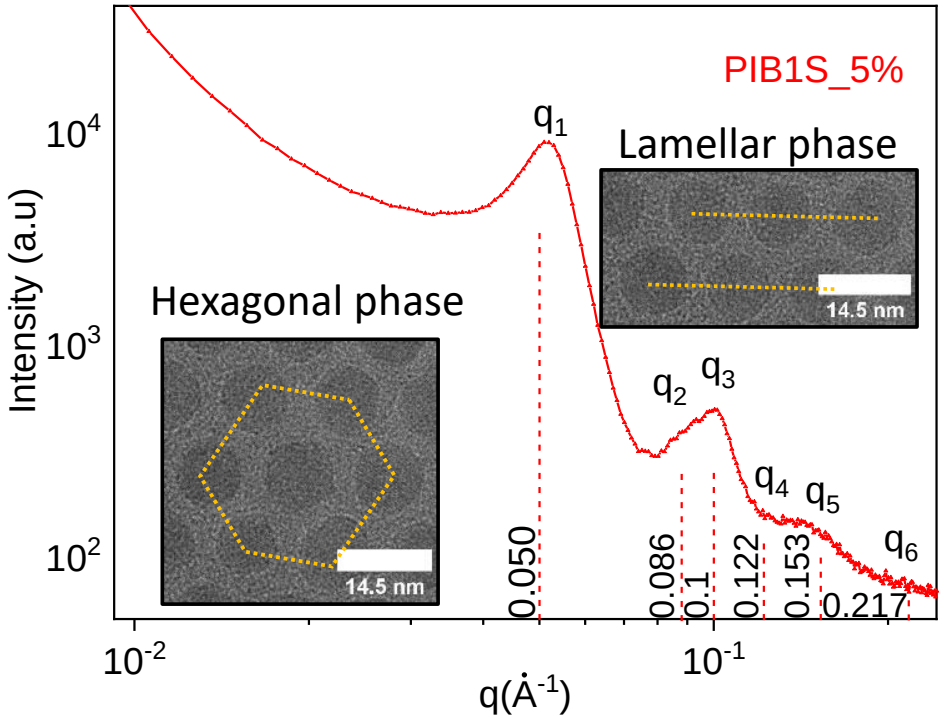

Figure 6.7 – *The SAXS pattern for PIB1 5% after precipitation displays both lamellar and hexagonal phases. The observed peaks indicate the presence of different ordered structures. The left inset image shows the hexagonal phase while the right inset image shows the lamellar phase*

An important point is that, from the previous chapter findings, the 3D packing of cubic IONPs within the polyisobutylene matrix was BCC under the same concentration and reaction time. However, in a spherical system, the IONPs followed a hexagonal close-packed (HCP) arrangement. According to the literature [19] [36], this difference in packing can be attributed primarily to the shape of the nanoparticles and the resulting entropic and geometric considerations.

Packing of Cubic IONPs (BCC Structure): For cubic nanoparticles, the BCC structure is often favored because the cubic geometry does not allow for the efficient close packing seen in spherical particles. The BCC lattice, with its lower packing density and larger interstitial spaces, accommodates the edges and corners of cubic particles more effectively. This arrangement also provides larger voids, which can be beneficial for the polymer chains in the matrix, reducing conformational strain and allowing for better dispersion [19].

Packing of Spherical IONPs (HCP Structure): In contrast, spherical nanoparticles

naturally tend to maximize packing efficiency, leading to either HCP or face-centered cubic (FCC) structures. Hard spheres can theoretically form both FCC and HCP lattices [36], but HCP is frequently observed in polymer nanocomposites because the interconnected octahedral voids in this lattice allow the PIB chains to explore a larger, continuous volume, increasing the entropy of the polymer matrix. This entropic gain is thermodynamically favorable, as supported by studies on block copolymer and homopolymer blends, which show that the polymer can more easily occupy the interconnected voids in HCP structures, thus promoting this packing mode [37].

6.4 Structure and Crystallization

To fully grasp the physicochemical properties of nanoparticles, it is important to consider their crystalline structure and phase composition along with their morphology. The WAXS patterns showed the presence of maghemite (γ-Fe_2O_3), the fully oxidized form of the IONPs, in all PIB1 and PIB2 nanocomposite samples at concentrations of 1%, 2.5%, 5%, and 10%, as well as in the IONPs synthesized without PIB, as seen in Figure 6.8a and c. Characteristic peaks at (220), (311), (400), (511), and (440) were identified, in line with ICDD PDF card no. 04-025-0576. A prominent amorphous peak at 16° was observed for all nanocomposite samples at low 2θ angles (below 25°), representing the characteristic feature of amorphous PIB. For IONPs without PIB, however, this peak shifted from 16° to 20°, corresponding to the peak of ordered iron(oleate) molecules.

In the highly concentrated PIB samples (PIB1 and PIB2 at 10%), WAXS patterns revealed additional closely spaced peaks, notably at the (400) plane (Figure. 6.8b and d). This suggests the coexistence of magnetite (Fe_3O_4) alongside maghemite [38], indicating that the IONPs were not fully oxidized at high polymer concentrations. This incomplete oxidation could be attributed to limitations in oxygen diffusion at higher polymer concentrations and longer chain lengths, with the appearance of magnetite peaks being more pronounced in PIB1 than in PIB2.

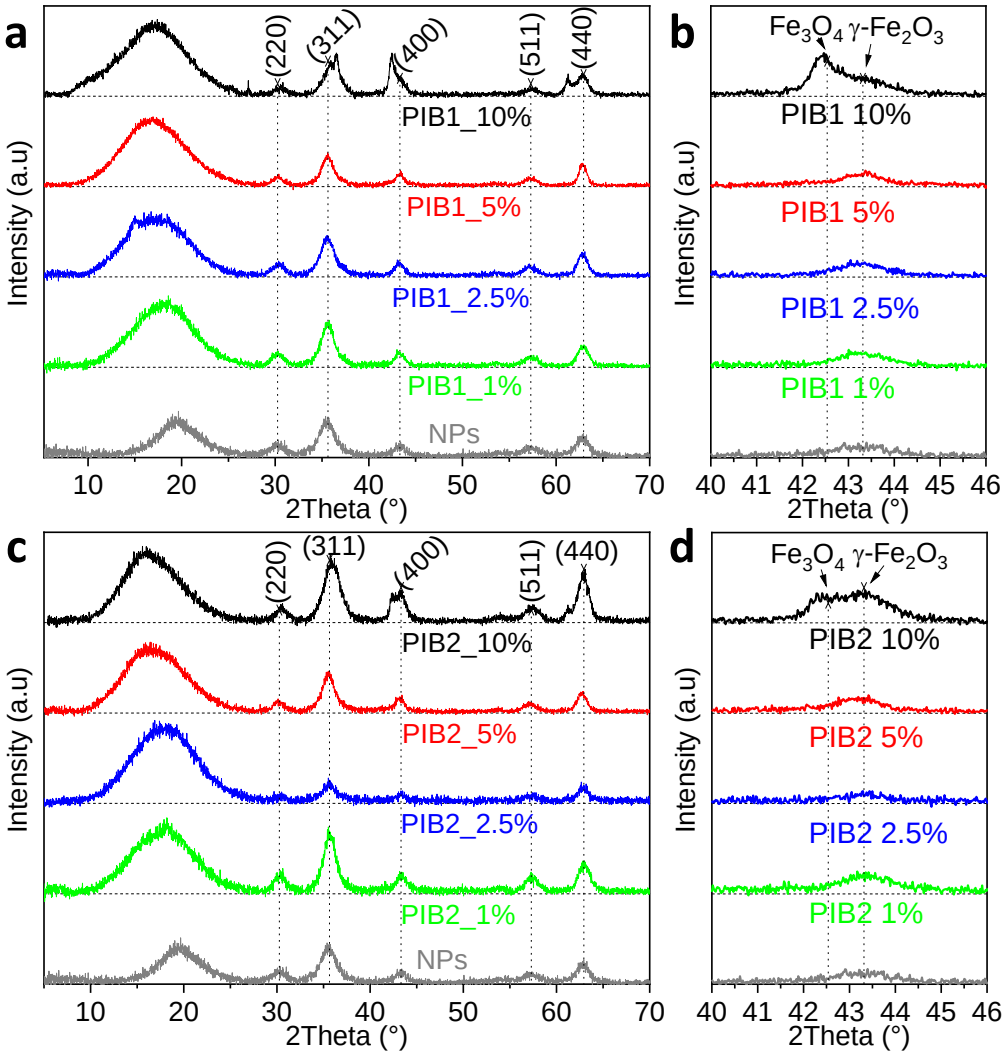

Figure 6.8 – *WAXS patterns of PIB nanocomposites compared to XRD patterns of nanoparticles synthesized without PIB: (a) PIB1 nanocomposite, (b) zoom-in on the (400) peak, (c) PIB2 nanocomposite, and (d) zoom-in on the (400) peak.*

How is it possible to obtain magnetite (Fe_3O_4), which contains both Fe(II) and Fe(III), when only Fe(III) oleate is used as a precursor? Although iron(III) oleate ($Fe(oleate)_3$) is the initial precursor, magnetite formation involves partial *in situ* reduction of Fe(III) to Fe(II) during the thermal decomposition process. This reduction is facilitated by the reaction conditions: elevated temperatures, the presence of excess oleic acid, and organic solvents like hexadecene, which can act as mild reducing agents. These conditions create a mildly reducing environment that enables the formation of the mixed-valence oxide Fe_3O_4. Similar mechanisms have been reported in the literature for thermal decomposition synthesis of iron oxide nanoparticles [39, 40, 41].

6.5 Composition Analysis

6.5.1 Nanocomposites Density

With the nanoparticle size and composition determined, we assessed reaction yields to evaluate the efficiency of nanoparticle synthesis and the effects of PIB concentration and molecular weight. Starting with 1.6 mmol of iron oleate as the precursor, the theoretical yield was calculated to produce 127 mg of maghemite ($Fe_{2.67}O_4$). This corresponds to maximum mass fractions of IONPs of 57.9%, 35.5%, 21.6%, and 12.1% for PIB concentrations of 1%, 2.5%, 5%, and 10%, respectively.

Figure 6.9 presents a radar chart comparing the densities of PIB nanocomposites synthesized with two different molecular weights: PIB1 (red) and PIB2 (blue). The chart spans five axes, each representing a specific nanocomposite concentration. The data reveal that, at all concentrations, PIB2 nanocomposites consistently displayed higher density values compared to PIB1. This trend indicates that the synthesis of nanoparticles in the PIB2 matrix results in a greater number of particles at identical PIB concentrations, leading to a denser polymer matrix. The larger area covered by PIB2 on the radar chart visually underscores this observation.

6.5.2 Nanoparticles Mass Fraction

Experimentally determined mass fractions, shown in Figure 6.9 and Table 6.1, were lower than theoretical predictions, likely due to incomplete reactions or material loss during synthesis. For PIB2, the measured fractions were 44.4%, 16.8%, 14.8%, and 9.6% for PIB concentrations of 1%, 2.5%, 5%, and 10%, respectively. In contrast, PIB1 yielded 23.1%, 18.4%, 15%, and 6.7% under identical conditions. Notably, at a 1% PIB concentration, PIB1 produced significantly fewer nanoparticles (23.1%) than PIB2 (44.4%).

Despite the discrepancy between theoretical and experimental values, these results remain reasonable and highlight the challenges of nanoparticle synthesis, including incomplete reactions and unavoidable material losses. The comparative analysis emphasizes the influence of molecular weight and concentration on the efficiency of nanoparticle synthesis and the resulting nanocomposite density.

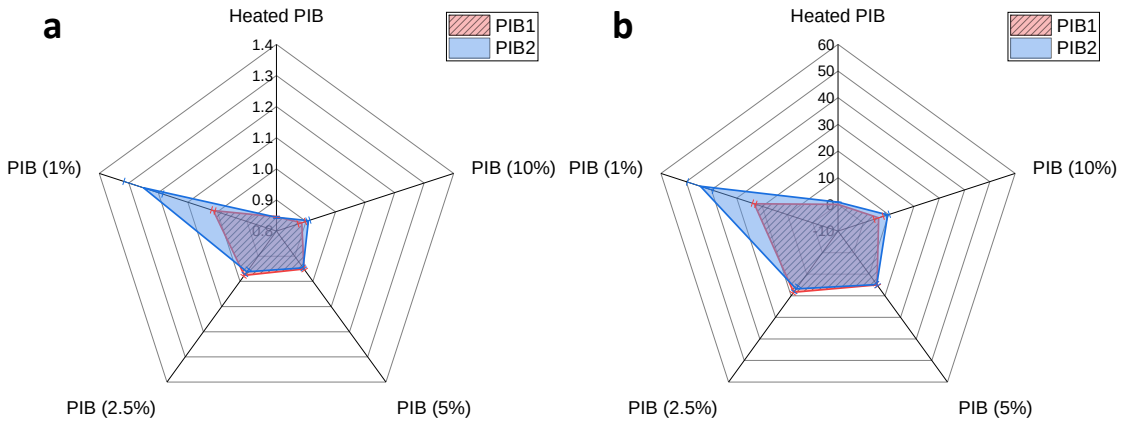

Figure 6.9 – *Radar chart comparing (a) densities and (b) IONPs mass fractions of PIB nanocomposites, PIB1 and PIB2, across four different nanocomposite concentrations (1, 2.5, 5, and 10%).*

6.6 Physical Characterization

6.6.1 Rheological properties

After establishing the synthesis parameters and compositional profile of our nanocomposite, we focused on evaluating its performance, starting with an analysis of its rheological properties. The frequency sweep test (Figure 6.10) highlighted notable changes in rheological behavior resulting from the incorporation of IONPs into the PIB matrices. These tests were conducted on PIB1 and PIB2 nanocomposites at concentrations of 2.5%, 5%, and 10%, as shown in Figure 6.10. To quantify the effects of nanoreinforcement, the storage modulus over the frequency range was compared with that of heat-treated PIB (PIB H), which was prepared by diluting 0.5 mL of PIB in 10 mL of hexadecene and mixing for 144 hours before refluxing for 30 minutes, as illustrated in Figure 6.11. This assessment aimed to investigate how IONP concentration, dispersion, and size influence the storage modulus (G') and loss modulus (G'') in samples subjected to the same heating process, which could improve chain mobility, lower viscosity, and possibly lead to degradation. Tests at the 1% concentration were excluded due to insufficient sample volume.

From Figure 6.11, the ratio of G' of the nanocomposites to that of the heat-treated PIB revealed significant improvements, especially at a low frequency of 0.01 Hz. At this frequency, PIB1 nanocomposites exhibited increases in G' by factors of 22, 13, and 3 at IONP concentrations of 2.5%, 5%, and 10%, respectively. PIB2 nanocomposites showed even greater enhancements, with G' increasing by factors of 30, 16, and 13 at the same concentrations

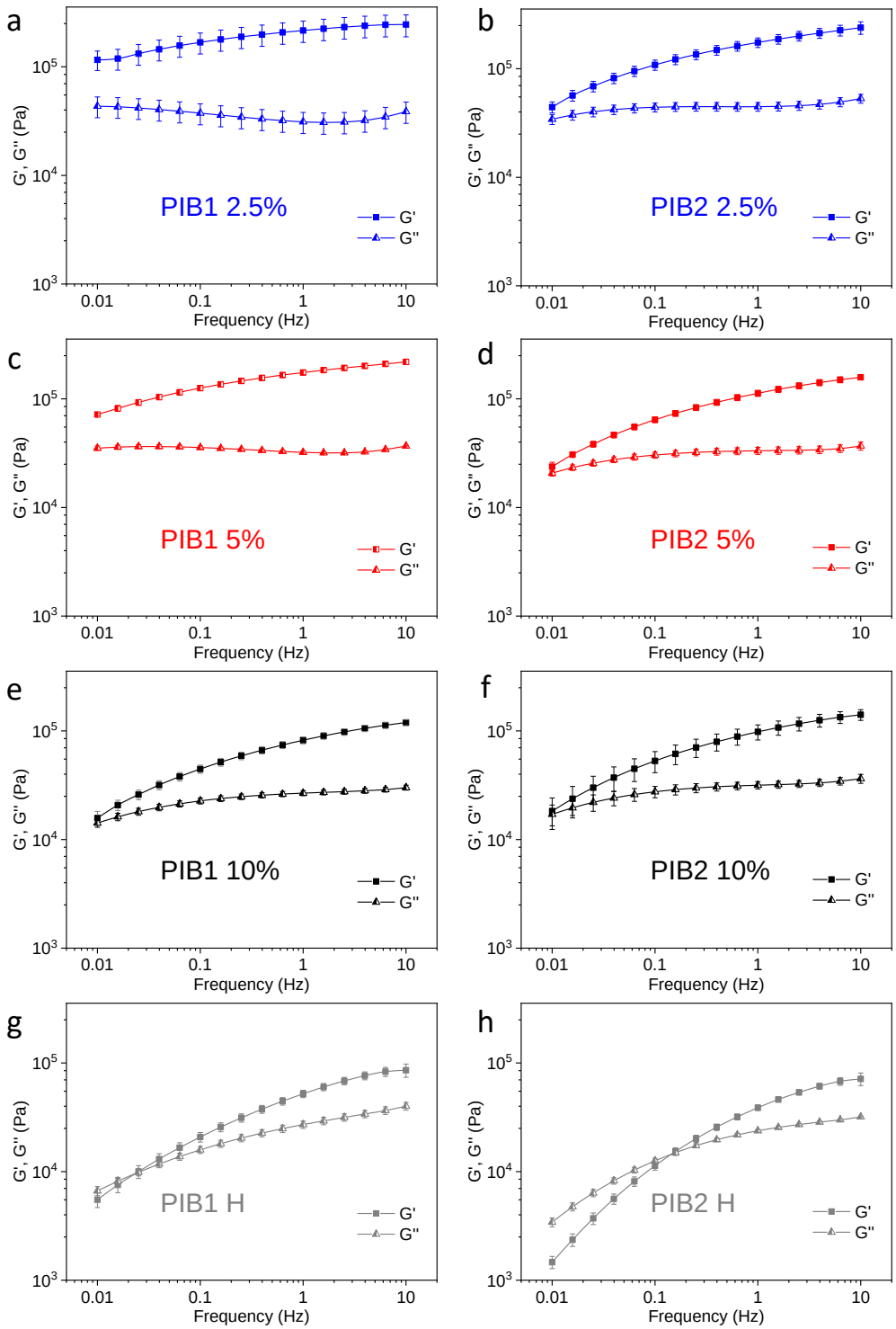

Figure 6.10 – *Frequency sweeps illustrating the storage and loss moduli for PIB1 and PIB2 nanocomposites*

(see Figure 6.11b). While the impact of IONPs diminished at higher frequencies due to faster molecular dynamics, substantial increases in modulus were still observed. For PIB1, G' rose by factors of 3, 2.5, and 1.4 for the 2.5%, 5%, and 10% IONP concentrations, respectively. PIB2 exhibited similar trends, with comparable improvements.

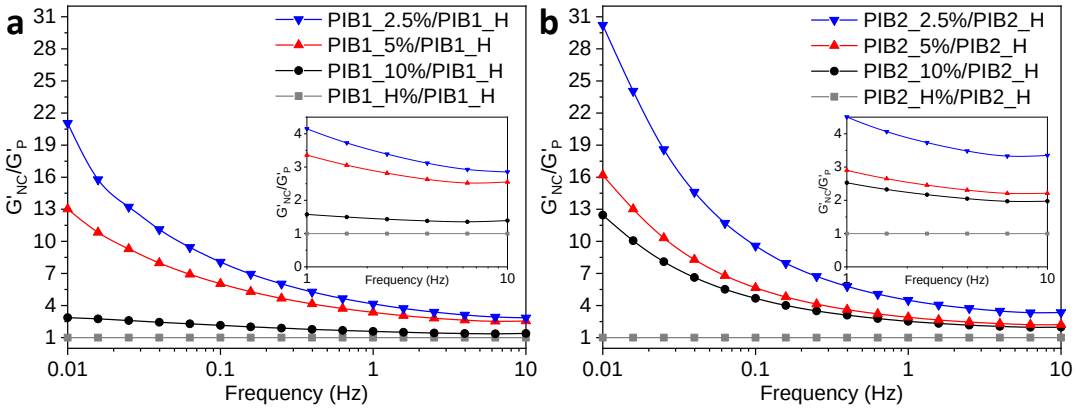

Figure 6.11 – *Rheological properties of PIB nanocomposites. Comparison of storage modulus (G') between PIB nanocomposites and heat-treated PIB for (a) PIB1 and (b) PIB2 at various IONP concentrations.*

6.6.2 Glass transition temperature

In addition to their mechanical properties, nanoparticles are known to affect the thermal properties of polymers, including their glass transition temperatures [42]. To evaluate this effect, we employed differential scanning calorimetry to observe the changes in the Tg of the polymer matrix upon nanoparticle addition. This phenomenon, often referred to as a nano-effect, can manifest as either an increase or decrease in Tg, depending on the specific interactions between the matrix and particles [42]. In the case of polyisobutylenes (PIB1 and PIB2), the DSC curves obtained between -80°C and 80°C, as presented in Figure 6.12, revealed no sharp transitions. The most notable feature observed was a subtle step in the heat flow at -68°C, which corresponded to Tg. This value aligns well with previously reported data for these materials [43].

For the heated PIBs processed with hexadecene, DSC analysis revealed alterations in the thermal behavior. The observed Tg at -79°C was lower than that typical for PIB, which may suggest the process thermally degrades the PIB by reducing polymer chain length, therefore increasing their mobility. Additionally, a sharp endothermic peak between 0 and 10°C is attributed to the melting of residual hexadecene, which has a melting point of 4-5°C. For the PIB nanocomposites, Tg remained unchanged compared to that of the heated PIB,

indicating that the IONPs did not have a significant effect. However, a sharp endothermic peak appeared between -10°C and 0°C, which was lower than the melting points of both pure oleic acid (13-14°C) and hexadecene (4-5°C). The absence of distinct melting peaks for these components, combined with the appearance of a new peak at a lower temperature, strongly suggested the formation of a eutectic mixture between oleic acid (from the IONP coating) and residual hexadecene. This has been observed in similar cases involving alkenes combined with fatty acids [44]. A repeatable, unexpected peak was observed at -30°C in the DSC analysis of PIB2 1%. This peak may be attributed to trace impurities within the sample, although its precise origin remains unclear.

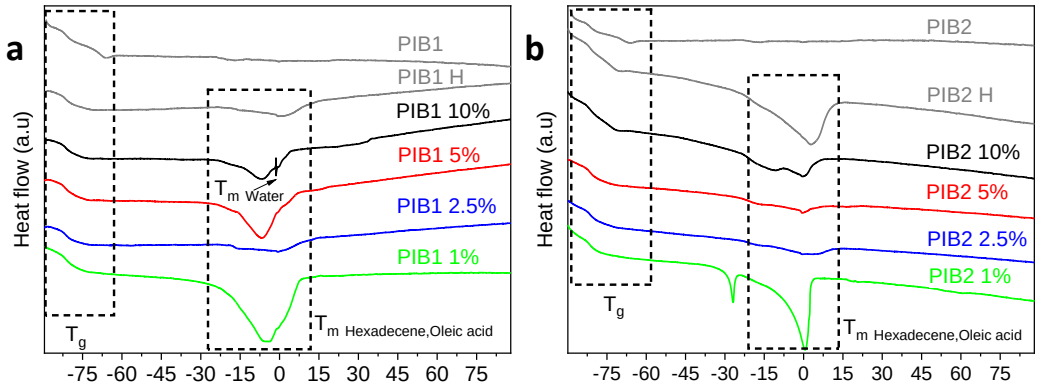

Figure 6.12 – *DSC curves of (a) PIB1 et (b) PIB2 nanocomposites*

6.6.3 Magnetic Behavior

Beyond enhancing the intrinsic properties of PIB, the inclusion of IONPs imparts magnetic characteristics to the nanocomposite. Both the isolated nanoparticles and the resulting nanocomposites exhibited superparamagnetic behavior at room temperature. This phenomenon was characterized by magnetization curves for all samples, as shown in Figure 6.13, with panels (a) and (b) illustrating the results for PIB1 and PIB2, respectively. The magnetization curves displayed no remanence or coercivity, which are key indicators of superparamagnetism at room temperature. These results are consistent with previously reported properties of 10 nm maghemite particles [45] and magnetite particles [46] observed at 300 K. The maintenance of superparamagnetic behavior in the nanocomposites suggests that the IONPs preserved their individual magnetic properties within the PIB matrix.

To explore the practical applications of these nanocomposites, their actuation behavior under magnetic stimuli was evaluated. A time-lapse sequence illustrating the response of the PIB2–10% nanocomposite to a magnetic field is shown in Figure 6.14, with the full video

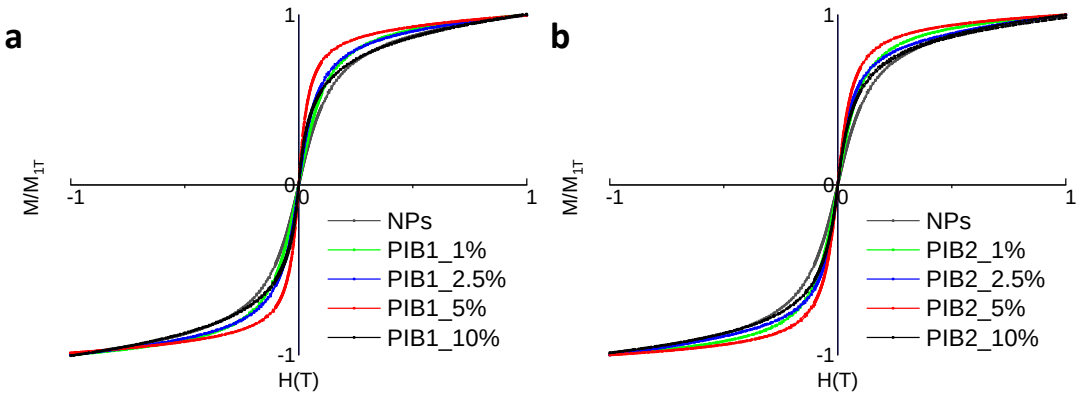

Figure 6.13 – *Hysteresis loop of (a) PIB1 and (b) PIB2 nanocomposites, all showing superparamagnetic behavior at room temperature.*

provided in the Supporting Information of the published article.

This video provides visual evidence of the nanocomposite's ability to follow the movement of an external magnet, highlighting its potential for use in smart materials and actuator technologies. The observed superparamagnetic behavior and magnetic responsiveness of these PIB-based nanocomposites open exciting opportunities for their integration into magnetic field sensors and magnetically actuated soft robotics.

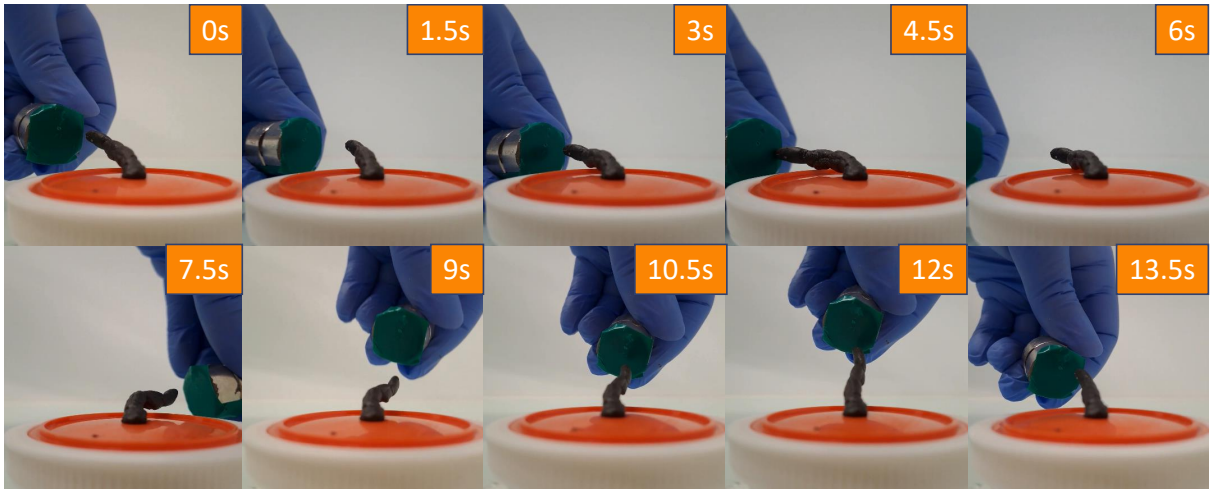

Figure 6.14 – *Sequential images showing the magnetic field-induced flow of the PIB2–10% nanocomposite. The 10 frames were extracted every 1.5 seconds, capturing the material's gradual movement in response to the magnetic stimulus.*

6.7 Growth Mechanism as a Function of PIB Molecular Weight and Concentration

6.7.1 Polymer Chain Segregation and Nanoparticle Size

From the previous observations, a connection can be made between the size of the IONPs, PIB concentration, molecular weight, and the evolution of the storage modulus, all influenced by the growth mechanism. We suggest that polymer chain segregation further impacts this process. Specifically, when the synthesis solution has higher PIB concentrations and molecular weights, larger IONPs are generated due to the thermal decomposition of iron oleate. This occurs because of an increased tendency for polymer chain segregation under these conditions. At higher concentrations and with longer chains, PIB molecules are more likely to segregate, resulting in a less homogeneous distribution of precursor molecules throughout the reaction medium.

Based on this hypothesis, an increase in PIB concentration and molecular weight likely leads to a higher concentration of growth species (nuclei) in the medium. This is similar to the effects seen with solvent volume, where a higher concentration of nuclei at the interface shortens the diffusion distance, enhancing mass transfer and increasing the growth rate. As a result, larger nanoparticles are formed within the same growth period [47], as shown in Figure 6.15. In contrast, with lower polymer concentration and molecular weight, the precursor molecules are more evenly dispersed in the medium. The reduced tendency for chain segregation favors this uniform distribution, as shorter polymer chains and lower concentrations are less likely to aggregate or form distinct domains. This homogeneous environment minimizes the formation of localized nuclei, thereby limiting the availability of growth species at nucleation sites. Consequently, the growth process becomes more controlled and gradual, leading to the formation of smaller nanoparticles.

In a previous study of the nanoparticle growth kinetics, samples collected at different reaction times (from 15 to 60 minutes) showed structural organization consistent with our current hypothesis. At 15 minutes, the system displayed a network-like structure, where nanoparticles were already forming within localized regions enriched with precursors. When comparing samples synthesized in PIB1 and PIB2, the nanoparticles in PIB1 appear larger and more spaced apart, as illustrated in Figure 6.16. This observation supports the idea that higher PIB concentration and molecular weight promote localized precursor segregation and larger nucleation sites, consistent with faster or less controlled growth.

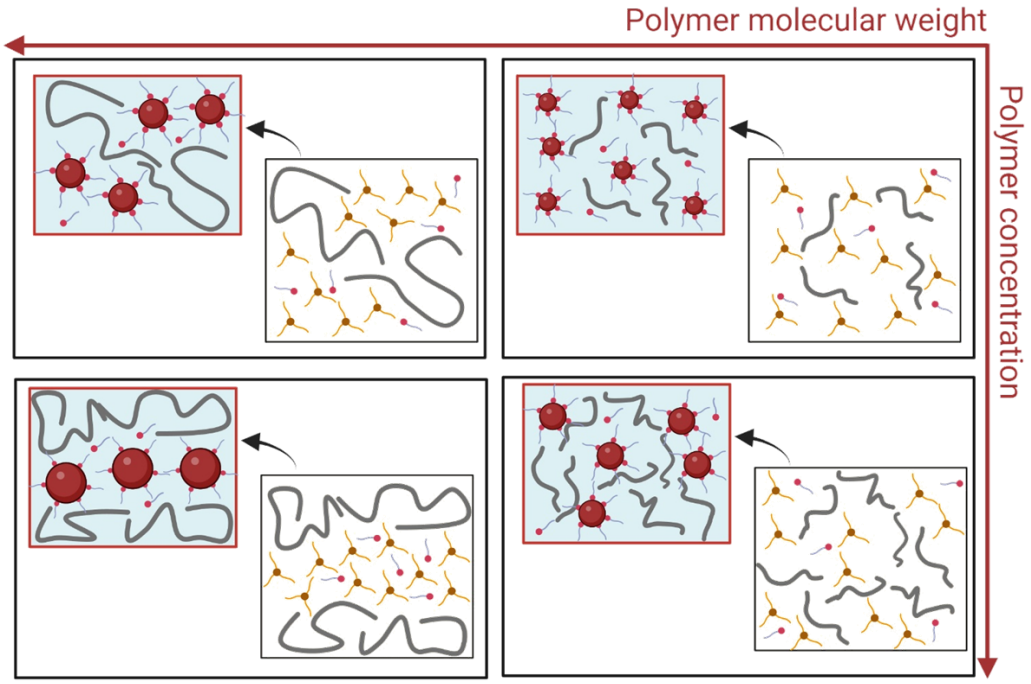

Figure 6.15 – *IONP size and dispersion as a function of PIB chain length (horizontal) and concentration (vertical). The four sections illustrate that the smallest IONPs were produced at the lowest PIB concentration and molecular weight, while higher PIB concentrations and molecular weights yielded larger nanoparticles. Intermediate conditions result in nanoparticles of intermediate sizes.*

6.7.2 Polymer Chain Segregation and Nanoparticle Oxidation

This explanation also accounts for why the nanoparticles did not undergo complete oxidation when the polymer concentration and molecular weight were high. We hypothesize that, under these conditions, localized regions of nuclei accumulation are formed due to chain segregation, which hinders the diffusion of oxygen. As a result, the nanoparticles are not fully oxidized, leading to the coexistence of maghemite and magnetite phases, as observed in the XRD pattern previously discussed (Figure 6.8). Moreover, the oxidation behavior of IONPs is inherently linked to their size and surface characteristics. Fe^{2+} ions at the nanoparticle surface are highly prone to oxidation, with this susceptibility inversely related to particle size. In nanoparticles synthesized via coprecipitation, those smaller than 20 nm are typically fully oxidized to maghemite (γ-Fe_2O_3), while larger particles often form a core-shell structure, with a magnetite (Fe_3O_4) core and an oxidized maghemite shell [48].

The thermal decomposition synthesis method, however, introduces additional factors that influence oxidation. The oleic acid coating and organic solvent likely play a dual role:

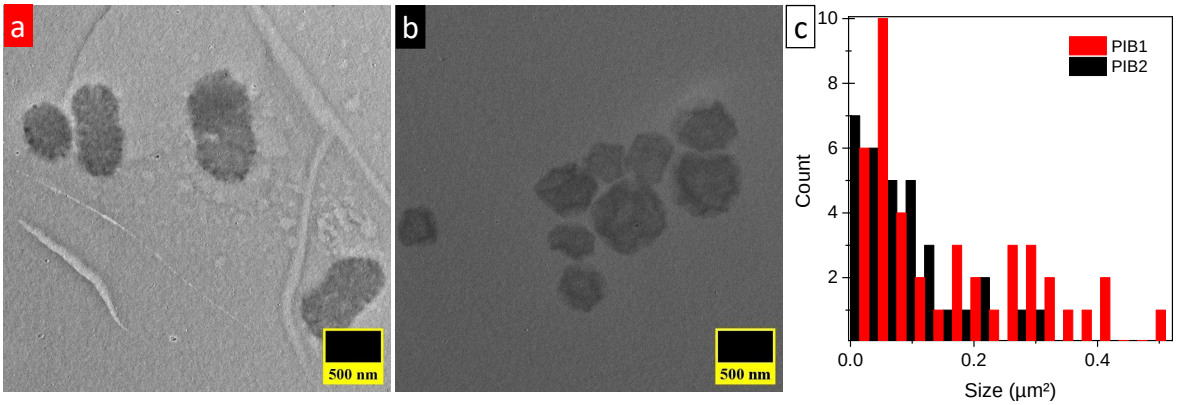

Figure 6.16 – *Low-magnification TEM images of (a) PIB1 and (b) PIB2 nanocomposites at an early reaction stage (15 min). The zoomed-in image highlights the smaller nanoparticles forming a network within the organic matrix (sample from the previous chapter). (c) Comparison of the mean size of the organic nucleation sites.*

regulating the growth kinetics and providing a protective barrier against oxidation and coalescence. Consequently, nanoparticles around 11 nm in size tend to preserve a lattice structure that more closely resembles magnetite, indicating the formation of a core-shell configuration. This protective effect is especially notable when compared to coprecipitation-synthesized nanoparticles, which lack such coatings and are more susceptible to oxidation in aqueous environments [48].

In particular, for IONPs synthesized at high PIB concentrations, an intriguing phenomenon was observed. At higher PIB concentrations (10%), a more oxygen-restrictive environment seemed to be created, possibly due to increased solution viscosity or the formation of a physical barrier around the growing nanoparticles. This limitation on oxygen diffusion, coupled with the protective effects of oleic acid and the organic solvent, leads to nanoparticles that undergo incomplete oxidation. Notably, when comparing IONPs synthesized at 5% and 10% PIB concentrations, the particle sizes were nearly identical, as shown by the plateau in Figure 6.3d. Despite the similarity in size, the 10% PIB sample exhibited incomplete oxidation, while the 5% sample was fully oxidized. This finding allowed us to associate the PIB concentration and molecular weight on the oxidation process, separating it from the effects of oleic acid and organic solvent.

6.7.3 Polymer Chain Segregation and Storage Modulus

The increase in G' in PIB nanocomposites, relative to heat-treated PIB, indicates a complex interaction between polymer molecular weight, nanoparticle size, and the nanoparticle-polymer interface. In theory, polymers with higher molecular weights should exhibit higher G' due to increased chain entanglements, which result in a stiffer network. Indeed, PIB1, with a higher entanglement factor (95), shows a significant advantage over PIB2 (500 kDa, entanglement factor 48), even after heat treatment, as demonstrated in Figure 6.10g and h. Despite this, PIB2, in the presence of IONPs at identical concentrations, shows a substantially greater increase in G'.

This unexpected behavior can be attributed to the effect of nanoparticle size. In PIB2, the smaller nanoparticles offer a larger surface area for polymer-nanoparticle interactions, which strengthens these interactions and forms a denser polymer-particle network. This compensates for PIB2's lower entanglement density. Conversely, the larger nanoparticles in PIB1 provide less surface area for interaction, thereby limiting the reinforcement from the nanoparticles, despite the higher polymer entanglement. Therefore, the greater increase in G' observed in PIB2 is mainly driven by the size effect of the smaller nanoparticles, which enhance the polymer-nanoparticle interactions.

Additionally, when samples with a constant molecular weight are examined, variations in mass fraction have a notable impact on the mechanical properties. As the nanoparticle mass fraction increases (which corresponds to lower polymer concentrations), a greater enhancement in G' is typically observed. This can be attributed to a higher number of polymer-nanoparticle interfaces and an increased probability of forming interconnected networks within the polymer matrix.

6.7.4 Polymer Chain Segregation and Glass Transition Temperature

The substantial increase in the storage modulus of PIB upon the addition of oleic-acid-coated IONPs, without a corresponding change in T_g, presents an interesting observation. The rise in the storage modulus indicates that the IONPs effectively reinforce the PIB matrix by introducing physical constraints within the polymer structure. The well-dispersed nanoparticles restrict the large-scale motion of the polymer chains under stress, enhancing stiffness and mechanical properties. However, the lack of change in T_g suggests that the local segmental mobility of the PIB chains remains largely unaffected. This can be attributed to the oleic acid coating on the IONPs, which ensures good nanoparticle dispersion while creating a barrier that limits direct interactions between the iron oxide core and the polymer chains, thereby preserving the short-range dynamics responsible for the glass transition in this amorphous polymer.

6.8 Conclusion

This chapter complements the findings of the previous one by investigating the effect of PIB concentration on the synthesis and properties of iron oxide nanoparticle (IONP)–PIB composites.

We found that higher molecular weight PIB leads to the formation of larger nanoparticles, confirming and generalizing the results from the previous chapter across both cubic and spherical nanoparticle systems. The polymer concentration was also shown to influence nanoparticle size: more concentrated synthesis solutions yielded larger IONPs. Moreover, high polymer concentrations appeared to inhibit complete oxidation of the IONPs.

The resulting nanoparticles were highly homogeneous and uniform in both size and shape, and they formed lamellar hexagonal arrangements within the PIB matrix.

The reaction yield was comparable between the two PIB molecular weights, reinforcing the conclusion from the previous chapter that the lower yield observed with low molecular weight PIB was more likely due to the presence of sodium oleate rather than the polymer itself.

At similar nanoparticle mass fractions (reinforcement levels), we observed an enhancement in mechanical stiffness, demonstrating the reinforcing effect and the influence of nanoparticle size on the composite's mechanical properties.

Our DSC results indicated that the shifts in glass transition temperature (T_g) observed in the nanocomposites were primarily due to the heating process, rather than the presence of IONPs. This suggests that the nanoparticles have little influence on the molecular mobility of the PIB chains, further confirming their minimal effect on the bulk polymer dynamics. Additionally, the enhanced storage modulus (G') observed in rheological measurements supports the conclusion that well-dispersed nanoparticles can significantly improve the mechanical performance of the composite material.

VSM measurements confirmed the superparamagnetic behavior of the IONPs within the PIB matrix. Although magnetothermal properties were not studied here, they may be explored in future work.

Ultimately, we hope that this research contributes to the broader understanding of polymer nanocomposite processing by elucidating the relationship between nanoparticle characteristics (size, dispersion, and concentration) and the resulting physical properties of the composite. This study lays the groundwork for future advancements in the design of functional materials with tailored properties, opening new opportunities for applications across diverse technological fields.

Bibliography

[1] J. Ma and R. M. Larsen, "Comparative study on dispersion and interfacial properties of single walled carbon nanotube/polymer composites using hansen solubility parameters," *ACS Applied Materials & Interfaces*, vol. 5, no. 4, pp. 1287–1293, 2013.

[2] Accudyne Test, "Polymeric materials table of hansen solubility parameters," n.d. Accessed: 2024-06-09.

[3] E. Stefanis and C. Panayiotou, "A new expanded solubility parameter approach," *International journal of pharmaceutics*, vol. 426, no. 1-2, pp. 29–43, 2012.

[4] N. Lebedeva, "Polyisobutene-based pressure-sensitive adhesives," *Technology of Pressure-Sensitive Adhesives and Products*, 2008.

[5] U. G. Centa, A. Oseli, M. Mihelčič, A. Kralj, M. Žnidaršič, M. Halilovič, and L. S. Perše, "Long-term viscoelastic behavior of polyisobutylene sealants before and after thermal stabilization," *Polymers*, vol. 16, no. 1, p. 22, 2023.

[6] N. Willenbacher and O. V. Lebedeva, "Polyisobutene-based pressure-sensitive adhesives," in *Technology of Pressure-Sensitive Adhesives and Products*, pp. 4–1, CRC Press, 2008.

[7] I. E. Nifant'ev, S. A. Korchagina, M. S. Chinova, and A. N. Tavtorkin, "Polyisobutylenes with controlled molecular weight and chain-end structure: Synthesis and actual applications," *Polymers*, vol. 15, no. 16, p. 3415, 2023.

[8] J. Zigmond, A. Gray, and J. Moore, "Chemical and temperature resistance of pib-based temporary adhesives," in *2019 IEEE 21st Electronics Packaging Technology Conference (EPTC)*, pp. 217–223, IEEE, 2019.

[9] N. Dayan, R. Sivalenka, and J. Chase, "Skin moisturization by hydrogenated polyisobutene—quantitative and visual evaluation," *International Journal of Cosmetic Science*, vol. 32, no. 1, pp. 81–82, 2010.

[10] S. Meftah, A.-T. Ngo, A. Shahmanesh, A. Courty, D. Kondo, F. Bedoui, and I. Lisiecki, "Striking effect of the iron stearate purity on the shape and size of maghemite nanoparticles," *Colloids and Surfaces A: Physicochemical and Engineering Aspects*, vol. 680, p. 132689, 2024.

[11] S. Disch, E. Wetterskog, R. P. Hermann, A. Wiedenmann, U. Vainio, G. Salazar-Alvarez, L. Bergström, and T. Brückel, "Quantitative spatial magnetization distribution in iron oxide nanocubes and nanospheres by polarized small-angle neutron scattering," *New Journal of Physics*, vol. 14, no. 1, p. 013025, 2012.

[12] M. Agthe, K. Høydalsvik, A. Mayence, P. Karvinen, M. Liebi, L. Bergstrom, and K. Nygard, "Controlling orientational and translational order of iron oxide nanocubes by assembly in nanofluidic containers," *Langmuir*, vol. 31, no. 45, pp. 12537–12543, 2015.

[13] Y.-Y. Huang, H.-L. Chen, and T. Hashimoto, "Face-centered cubic lattice of spherical micelles in block copolymer/homopolymer blends," *Macromolecules*, vol. 36, no. 3, pp. 764–770, 2003.

[14] P. Pusey, W. Van Megen, P. Bartlett, B. Ackerson, J. Rarity, and S. Underwood, "Structure of crystals of hard colloidal spheres," *Physical review letters*, vol. 63, no. 25, p. 2753, 1989.

[15] M. Eldridge, P. Madden, and D. Frenkel, "Entropy-driven formation of a superlattice in a hard-sphere binary mixture," *Nature*, vol. 365, no. 6441, pp. 35–37, 1993.

[16] B. J. Alder, T. E. Wainwright, *et al.*, "Phase transition for a hard sphere system," *The Journal of chemical physics*, vol. 27, no. 5, p. 1208, 1957.

[17] C. Murray, C. Kagan, and M. Bawendi, "Self-organization of cdse nanocrystallites into three-dimensional quantum dot superlattices," *Science*, vol. 270, no. 5240, pp. 1335–1338, 1995.

[18] M. B. Sigman, A. E. Saunders, and B. A. Korgel, "Metal nanocrystal superlattice nucleation and growth," *Langmuir*, vol. 20, no. 3, pp. 978–983, 2004.

[19] B. W. Goodfellow, Y. Yu, C. A. Bosoy, D.-M. Smilgies, and B. A. Korgel, "The role of ligand packing frustration in body-centered cubic (bcc) superlattices of colloidal nanocrystals," *The journal of physical chemistry letters*, vol. 6, no. 13, pp. 2406–2412, 2015.

[20] D. Wang, M. Hermes, R. Kotni, Y. Wu, N. Tasios, Y. Liu, B. De Nijs, E. B. Van Der Wee, C. B. Murray, M. Dijkstra, *et al.*, "Interplay between spherical confinement and particle

shape on the self-assembly of rounded cubes," *Nature communications*, vol. 9, no. 1, p. 2228, 2018.

[21] K. Utriainen, "Soap micelles in nonpolar media," 2018.

[22] N. Petersen, M. Girard, A. Riedinger, and O. Valsson, "The crucial role of solvation forces in the steric stabilization of nanoplatelets," *Nano Letters*, vol. 22, no. 24, pp. 9847–9853, 2022.

[23] S. Llanos, L. J. Giraldo, O. Santamaria, C. A. Franco, and F. B. Cortés, "Effect of sodium oleate surfactant concentration grafted onto sio2 nanoparticles in polymer flooding processes," *ACS omega*, vol. 3, no. 12, pp. 18673–18684, 2018.

[24] R. Nasseri, N. Bouzari, J. Huang, H. Golzar, S. Jankhani, X. Tang, T. H. Mekonnen, A. Aghakhani, and H. Shahsavan, "Programmable nanocomposites of cellulose nanocrystals and zwitterionic hydrogels for soft robotics," *Nature Communications*, vol. 14, no. 1, p. 6108, 2023.

[25] R. Eivazzadeh-Keihan, A. Mohammadi, H. Aghamirza Moghim Aliabadi, A. Kashtiaray, M. S. Bani, A. H. Karimi, A. Maleki, and M. Mahdavi, "A novel ternary magnetic nanobiocomposite based on tragacanth-silk fibroin hydrogel for hyperthermia and biological properties," *Scientific Reports*, vol. 14, no. 1, p. 8166, 2024.

[26] B. Bouvet, *Conception de nano-plateformes multifonctionnelles à base de nanoparticules inorganiques pour des applications de théranostique et de détection*. Thèse de doctorat, Université de Montpellier, Montpellier, France, 2024.

[27] R. Wildeboer, P. Southern, and Q. Pankhurst, "On the reliable measurement of specific absorption rates and intrinsic loss parameters in magnetic hyperthermia materials," *Journal of Physics D: Applied Physics*, vol. 47, no. 49, p. 495003, 2014.

[28] H. L. Ring, A. Sharma, R. Ivkov, and J. C. Bischof, "The impact of data selection and fitting on sar estimation for magnetic nanoparticle heating," *International journal of hyperthermia*, vol. 37, no. 3, pp. 100–107, 2020.

[29] D. Shi, M. Sadat, A. W. Dunn, and D. B. Mast, "Photo-fluorescent and magnetic properties of iron oxide nanoparticles for biomedical applications," *Nanoscale*, vol. 7, no. 18, pp. 8209–8232, 2015.

[30] I. Andreu and E. Natividad, "Accuracy of available methods for quantifying the heat power generation of nanoparticles for magnetic hyperthermia," *International Journal of Hyperthermia*, vol. 29, no. 8, pp. 739–751, 2013.

[31] A. Drayton, J. Zehner, J. Timmis, V. Patel, G. Vallejo-Fernandez, and K. O'Grady, "A comparative measurement technique of nanoparticle heating for magnetic hyperthermia applications," *Journal of Physics D: Applied Physics*, vol. 50, no. 49, p. 495003, 2017.

[32] M. Bonini, E. Fratini, and P. Baglioni, "Saxs study of chain-like structures formed by magnetic nanoparticles," *Materials Science and Engineering: C*, vol. 27, no. 5-8, pp. 1377–1381, 2007.

[33] A. Guinier, G. Fournet, C. B. Walker, and G. H. Vineyard, "Small-angle scattering of x-rays," 1956.

[34] S. Menon, C. Manohar, and K. S. Rao, "A new interpretation of the sticky hard sphere model," *The Journal of chemical physics*, vol. 95, no. 12, pp. 9186–9190, 1991.

[35] W. Ruland and B. Smarsly, "Saxs of self-assembled nanocomposite films with oriented two-dimensional cylinder arrays: an advanced method of evaluation," *Journal of applied crystallography*, vol. 38, no. 1, pp. 78–86, 2005.

[36] W. Ouyang, J. Han, and W. Wang, "Nanofluidic crystals: nanofluidics in a close-packed nanoparticle array," *Lab on a Chip*, vol. 17, no. 18, pp. 3006–3025, 2017.

[37] N. A. Mahynski, S. K. Kumar, and A. Z. Panagiotopoulos, "Relative stability of the fcc and hcp polymorphs with interacting polymers," *Soft Matter*, vol. 11, no. 2, pp. 280–289, 2015.

[38] W. Kim, C.-Y. Suh, S.-W. Cho, K.-M. Roh, H. Kwon, K. Song, and I.-J. Shon, "A new method for the identification and quantification of magnetite–maghemite mixture using conventional x-ray diffraction technique," *Talanta*, vol. 94, pp. 348–352, 2012.

[39] J. Park, K. An, Y. Hwang, J.-G. Park, H.-J. Noh, J.-Y. Kim, J.-H. Park, N.-M. Hwang, and T. Hyeon, "Ultra-large-scale syntheses of monodisperse nanocrystals," *Nature materials*, vol. 3, no. 12, pp. 891–895, 2004.

[40] K. Nader, I. Castellanos-Rubio, I. Orue, D. Iglesias-Rojas, A. Barón, I. G. de Muro, L. Lezama, and M. Insausti, "Getting insight into how iron (iii) oleate precursors affect the features of magnetite nanoparticles," *Journal of Solid State Chemistry*, vol. 316, p. 123619, 2022.

[41] L. M. Bronstein, X. Huang, J. Retrum, A. Schmucker, M. Pink, B. D. Stein, and B. Dragnea, "Influence of iron oleate complex structure on iron oxide nanoparticle formation," *Chemistry of materials*, vol. 19, no. 15, pp. 3624–3632, 2007.

[42] P. Rittigstein and J. M. Torkelson, "Polymer–nanoparticle interfacial interactions in polymer nanocomposites: confinement effects on glass transition temperature and suppression of physical aging," *Journal of Polymer Science Part B: Polymer Physics*, vol. 44, no. 20, pp. 2935–2943, 2006.

[43] NETZSCH, "Polymer characterization methods." Accessed: 2024-09-30.

[44] M. Wieckowski and M. Królikowski, "Designing and characterization of low-temperature eutectic phase change materials based on alkanes," *Journal of Chemical & Engineering Data*, vol. 67, no. 3, pp. 727–738, 2022.

[45] Y. Mizukoshi, T. Shuto, N. Masahashi, and S. Tanabe, "Preparation of superparamagnetic magnetite nanoparticles by reverse precipitation method: contribution of sonochemically generated oxidants," *Ultrasonics sonochemistry*, vol. 16, no. 4, pp. 525–531, 2009.

[46] D. Vollath, D. Szabo, R. Taylor, and J. Willis, "Synthesis and magnetic properties of nanostructured maghemite," *Journal of materials research*, vol. 12, no. 8, pp. 2175–2182, 1997.

[47] H. S. Dehsari, A. H. Ribeiro, B. Ersöz, W. Tremel, G. Jakob, and K. Asadi, "Effect of precursor concentration on size evolution of iron oxide nanoparticles," *CrystEngComm*, vol. 19, no. 44, pp. 6694–6702, 2017.

[48] W. Baaziz, B. P. Pichon, S. Fleutot, Y. Liu, C. Lefevre, J.-M. Greneche, M. Toumi, T. Mhiri, and S. Begin-Colin, "Magnetic iron oxide nanoparticles: reproducible tuning of the size and nanosized-dependent composition, defects, and spin canting," *The Journal of Physical Chemistry C*, vol. 118, no. 7, pp. 3795–3810, 2014.

ACS APPLIED POLYMER MATERIALS

pubs.acs.org/acsapm Article

In Situ Synthesis of Iron Oxide-Polyisobutylene Multifunctional Nanocomposites: Size Control, Magnetic and Mechanical Properties Enhancement

Sakina Meftah, Nadine Aydi, Lohitha R. Hegde, Mohamed Selman, Jinkai Yuan, Laurent Bouteiller, Caroline Lefebvre, Anh-tu Ngo, Djimedo Kondo, Andres Jaramillo-Botero, William A. Goddard, III, Isabelle Lisiecki, and Fahmi Bedoui*

Cite This: https://doi.org/10.1021/acsapm.5c00457 Read Online

ACCESS | Metrics & More | Article Recommendations | Supporting Information

ABSTRACT: Polymer nanocomposites with precisely controlled nanoparticle size and narrow polydispersity offer substantial potential for multifunctional applications, particularly in energy and healthcare. In this study, we introduce an *in situ* synthesis approach for creating iron oxide nanoparticle-polyisobutylene nanocomposites, where the nanoparticle size distribution and spatial dispersion are finely tuned by adjusting the polymer concentration and molecular weight. This method allows us to investigate and control the growth dynamics of nanoparticles within the polymer solution, providing insights into how the polymer molecular weight and concentration influence nucleation, growth, and assembly. Beyond achieving precise size control, our approach enables the rational design of nanocomposites with significantly enhanced mechanical strength, evidenced by an increased storage modulus, while preserving their superparamagnetic behavior. This strategy advances the development of high-performance magnetic polymer nanocomposites and opens up possibilities for applications that require both robust mechanical properties and responsive magnetic features, marking a significant step forward in nanocomposite design and functionality.

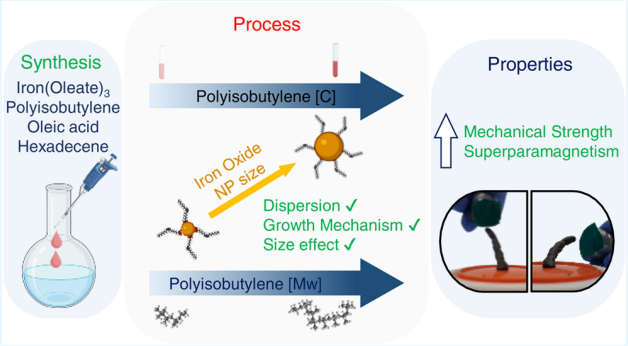

KEYWORDS: *polymer nanocomposites, iron oxide nanoparticles, in situ synthesis, superparamagnetism, mechanical strength, growth mechanism, polymer concentration, molecular weight*

INTRODUCTION

Polymer nanocomposites are advanced materials that combine nanofillers within a polymer matrix, resulting in functional materials with enhanced mechanical, thermal, and electrical properties.[1−3] The high surface-to-volume ratio of nanoparticles significantly enhances these properties.[2,4−11] However, nanoparticle agglomeration, primarily due to their high surface energy, can diminish these enhancements.[12−14] Additionally, potential hazards associated with nanomaterials and the challenges of large-scale fabrication further complicate the production of nanocomposites with consistent performance.

This paper presents an innovative synthesis procedure for polymer nanocomposites using polyisobutylene (PIB) as the matrix and iron oxide nanoparticles (IONPs) as the nanofillers. PIB, a material widely used in tire tubes, adhesives, sealants, lubricants, plasticizers, fuel additives, and electrical insulation, is known for its high flexibility, chemical resistance, and low gas permeability, all of which enhance the stability and durability of the resulting nanocomposite.[15] For this study, polyisobutylene sourced from Sigma-Aldrich was used as the matrix material. PIB is also produced under the OPPANOL brand, with BASF's production facilities for this product certified under ISO 14001:2015 for environmental management and ISO 50001:2018 for energy management. These certifications reflect the ongoing shift toward more sustainable manufacturing practices in the industry. Although not directly utilized in this study, the availability of such environmentally certified options highlights potential opportunities for incorporating sustainability into future nanocomposite research.

For IONPs, magnetite (Fe_3O_4) and maghemite (γ-Fe_2O_3) were selected mainly for their advantages, like precise control over their size, surface coating,[16−18] morphology,[19] etc. These properties are essential for tuning the mechanical and thermal

Received: February 6, 2025
Revised: April 7, 2025
Accepted: April 9, 2025

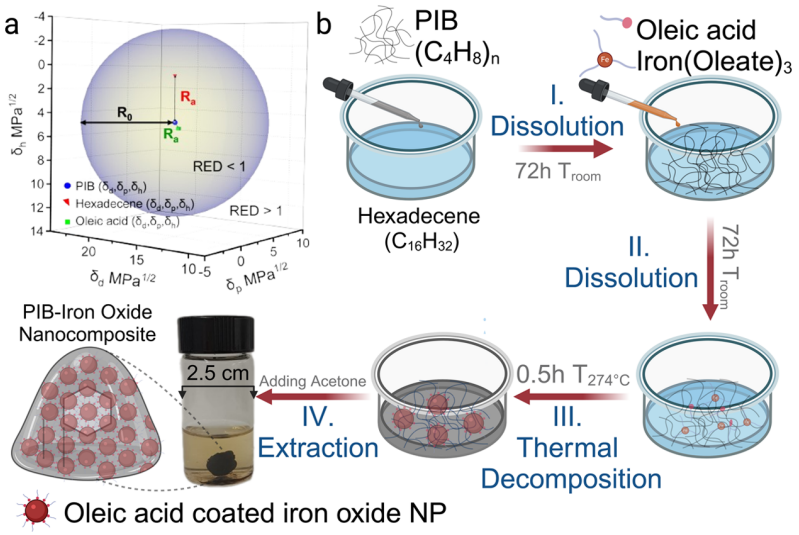

Figure 1. (a) HSP sphere of PIB, demonstrating the solubility of hexadecene and oleic acid within the polymer matrix. The HSPs values of PIB were obtained from the Diversified Enterprises database,[32] and the HSPs of hexadecene and oleic acid were calculated using the Stefanis Panayiotou method.[33] (b) Synthesis process of PIB-IONPs composites. Created in BioRender. Meftah, S. (2025) https://BioRender.com/c77k851.

properties. In addition, IONPs are also well known for their remarkable magnetic properties. The IONPs dispersed within a polymer matrix result in functional magnetic nanocomposites with tunable properties that respond to external stimuli, such as magnetic fields.[20] Thus, these materials are extensively utilized in many applications requiring precise control of the magnetic behavior, such as energy storage,[21] environmental sensing,[22,23] and biomedicine.[24] Moreover, incorporating magnetic nanoparticles enhances the performance of drug delivery systems, in which targeted therapy is crucial for maximizing treatment efficacy while minimizing side effects.[25]

Large-scale manufacturing of polymer nanocomposites traditionally involves incorporating presynthesized nanoparticles (in solution or powder) into a molten or predissolved polymer matrix. In this context, the synthesis of IONPs via thermal decomposition of organometallic precursors exemplified by Park et al. is renowned for its ability to produce monodisperse nanocrystals with precise size control and has been demonstrated at large scales (up to 40 g per batch) without the need for postsynthetic size sorting.[16] This method, governed by the LaMer model,[26,27] involves supersaturation, nucleation, and growth stages, with critical parameters such as precursor concentration, temperature, surfactant ratio, and reaction time dictating the final nanoparticle characteristics.[17,19] However, when it comes to nanocomposite production, nanoparticles are formed, and the solution containing them is mixed with the polymer to create a nanocomposite material. This process aims to uniformly incorporate nanoparticles into the polymer matrix. However, achieving a homogeneous dispersion of nanoparticles within the polymer is not always guaranteed. Indeed, it can be influenced by various factors, including the affinity between the coated nanoparticles and the polymer, the mixing method employed, and the processing conditions.

In this study, we explore the *in situ* synthesis of iron oxide nanoparticles directly within a polyisobutylene matrix by adapting a thermal decomposition strategy originally developed for producing IONPs in organic solvents.[16] By dissolving the iron oleate precursor in a PIB solution, our method eliminates the need for pre-synthesized nanoparticles and subsequent dispersion steps, resulting in a more uniform distribution throughout the polymer. We maintain precise control over nanoparticle size, consistently keeping them under 12 nm, which is essential for preserving their superparamagnetic behavior. While leveraging prior insights about PIB oligomers in nanoparticle stabilization,[28] our approach also offers the advantage of forming nanoparticles directly within the matrix.

Park's original synthesis has demonstrated its effectiveness at a large scale by producing high-quality nanoparticles. Our adaptation of this method to a nanocomposite system albeit at a smaller scale, allowed us to thoroughly investigate the growth mechanisms. The successful reproduction of key aspects of the synthesis at this reduced scale strongly suggests that our nanocomposite system could be scaled up for larger production. Although such scalability would likely require further optimization of heat and mass transfer processes, the underlying principles remain consistent across scales. This scalability holds promise for overcoming challenges related to nanoparticle agglomeration and dispersion in industrial-scale nanocomposite fabrication.

This study also examines how nanoparticle size affects the mechanical properties of the nanocomposites, providing further insight into polymer−nanoparticle interactions at the nanoscale. In doing so, our work builds on prior research in *in situ* nanoparticle synthesis within polymers[29] and contributes to ongoing efforts to develop multifunctional nanocomposites with enhanced structural and magnetic performance.

PIB was dissolved in hexadecene to obtain a polymer solution, a choice supported by Hansen solubility parameters (HSP) analysis.[30,31] The HSP method, which characterizes materials using dispersion, polarity, and hydrogen bonding parameters, confirms the chemical compatibility of PIB and hexadecene (Figure 1a). Due to the high viscosity of the solution, the preparation was performed in several steps to ensure thorough mixing (Figure 1b). Initially, PIB was solubilized in hexadecene under continuous stirring for 72 h at room temperature. Subsequently, iron oleate and oleic acid

https://doi.org/10.1021/acsapm.5c00457
ACS Appl. Polym. Mater. XXXX, XXX, XXX−XXX

were added, and the mixture was stirred for an additional 72 h to ensure uniform distribution of the iron precursor throughout the polymer solution. Finally, the entire solution was refluxed to induce nanoparticle formation. A fraction of the oleic acid-coated IONPs-PIB nanocomposite was isolated by adding acetone, which precipitated the hydrophobic PIB and coated IONPs from the solvent and unreacted materials.

To control nanoparticle size and distribution, we varied the dilution ratio and molecular weight of PIB. We tested dilution ratios of 1, 2.5, 5, and 10% with two molecular weights, 1000 kDa (PIB1) and 500 kDa (PIB2) (Table 1). By adjusting these

Table 1. PIB Molecular Weights and Concentrations in Hexadecene

PIB MW (kg/mol)	concentration (%)	volume (mL)	mass (g)	W_m (%)
PIB1 1000	1	0.1	0.092	23.1
	2.5	0.25	0.23	18.4
	5	0.5	0.46	15
	10	1	0.92	6.7
PIB2 500	1	0.1	0.092	44.4
	2.5	0.25	0.23	16.8
	5	0.5	0.46	14.8
	10	1	0.92	9.6

two parameters, we illustrate how the size and chemical composition of the nanoparticles are influenced and how they disperse within the PIB matrix. After completing these characterizations, we examined the mechanical properties of the nanocomposite to determine how variations in size and dispersion affect the overall performance of the material.

RESULTS

Reaction Yields. We assessed reaction yields to evaluate the nanoparticle synthesis efficiency and the effects of PIB concentration and molecular weight. Using 1.6 mmol of iron oleate, we theoretically expected to produce 127 mg of maghemite ($Fe_{2.67}O_4$), corresponding to maximum mass fractions of IONPs of 57.9, 35.5, 21.6, and 12.1% for PIB concentrations of 1, 2.5, 5, and 10%. Experimental results showed lower mass fractions (Figure S1 and Table 1). For PIB2, the measured fractions were 44.4, 16.8, 14.8, and 9.6% at the same concentrations, while PIB1 yielded 23.1, 18.4, 15, and 6.7%. Notably, at 1% PIB concentration, PIB1 formed significantly fewer nanoparticles (23.1%) compared with PIB2 (44.4%). Although experimental values were lower than theoretical predictions, they remained reasonable considering incomplete reactions and material loss.

Nanoparticle Size Distribution. The nanoparticle size distribution measurements obtained by the Dynamic Light Scattering (DLS) technique showed the hydrodynamic diameter of the IONPs ranged between 13 and 43.6 nm for PIB1 (Figure 2b), and from 13.06 to 23.8 nm for PIB2 (Figure 2c). The DLS analysis suggests a normal size distribution of one nanoparticle-sized population with a relatively uniform particle size. Furthermore, Transmission Electron Microscopy (TEM) images of the IONPs revealed highly uniform nanoparticles with spherical morphology forming a long-range order assembly. The diameter ranged between 7.5 and 10.8 nm for PIB1 (Figure 2d) and between 7.5 and 9.1 nm for PIB2, respectively (Figure 2e), whereas neat IONPs synthesized without PIB showed the smallest size of 7.3 nm (Figure 2a), indicating the increase in the concentration or molecular weight of PIB leads to the increase in size for IONPs while keeping the low polydispersity (ranging from 7 to 12% for all samples), as shown in Figure 2f.

Small-Angle X-ray Scattering (SAXS) was employed to statistically evaluate the particle size, shape, and aggregation behavior on a larger observable scale. SAXS was performed on IONP-PIB1 and IONP-PIB2 in dilute hexadecene solutions (1, 2.5, 5, and 10%) and the precipitated regime revealed scattering patterns consistent with spherical particles (Figure 3).

When examining the first minimum of each SAXS curve, we observed a systematic shift toward lower q values as the concentration increased from neat NPs to IONP-PIB at 10% concentration.[34] Specifically, the first minimum progression followed the order IONP-PIB10% < IONP-PIB5% < IONP-PIB2.5% < IONP-PIB1% < neat NPs. This shift is indicative of the increase in particle core size with increasing concentration.

From the Guinier approximation in the lower q-range, the radius of gyration (R_g) obtained was between 33.2 and 55.76 Å for PIB1, and between 34.7 and 58.8 Å for PIB2 (see Figure S2 and Table S1).

Assuming a homogeneous distribution of spherical particles based on TEM, the radius calculated using formula 1[35] shows a radius in the range of the previously obtained values from the TEM.

$$D = 2\sqrt{\frac{5}{3}}R_g \tag{1}$$

To determine the nanoparticle size in the samples in the solution (Figure 3a,b), we evaluated the form factor $F(q)$ by fitting the scattering data with a spherical core−shell model[35] (Figure S3). The parameters obtained from the fitted curves are listed in Table S2. Our analysis confirmed an increase in the average radius of nanoparticles with increasing PIB concentration and/or molecular weight. The core radius values were consistent with the sizes determined by TEM analysis. The shell thickness, attributed to the oleic acid coating, varied slightly between 1 and 1.23 nm.

For precipitate samples (Figure 3c,d), where IONP interactions are important, we included structure factor $S(q)$. The sticky hard sphere model with Percus−Yevick closure provided the best fit[36] (Figure S4). Importantly, the results for the nanoparticle size and shell thickness are closely aligned with those obtained for the PIB nanocomposite in solution (Table S2). This consistency suggests that there is no significant variation in size distribution when extracting IONPs with PIB using acetone, indicating that the extraction process effectively preserves the nanoparticle characteristics.

Nanoparticles Spatial Arrangement. SAXS patterns also provided insights into the spatial arrangement of IONPs within the PIB matrix. We analyzed peak positions in the SAXS curves of the PIB1 5% precipitate nanocomposite (Figure 3e). The ratios of peak positions (q_1, q_2, q_3, etc.) relative to the first peak were calculated. The ratios of $\sqrt{1}$, $\sqrt{4}$, and $\sqrt{9}$ suggested a prominent lamellar arrangement. However, additional hidden peaks (shoulders) at $\sqrt{3}$, $\sqrt{6}$, and $\sqrt{19}$ indicated a potential hexagonal arrangement superimposed on the lamellar structure. The observed shoulders, especially those in q_2, further supported this hypothesis. To investigate the hexagonal arrangement, we calculated the lattice parameter a, represent-

https://doi.org/10.1021/acsapm.5c00457
ACS Appl. Polym. Mater. XXXX, XXX, XXX−XXX

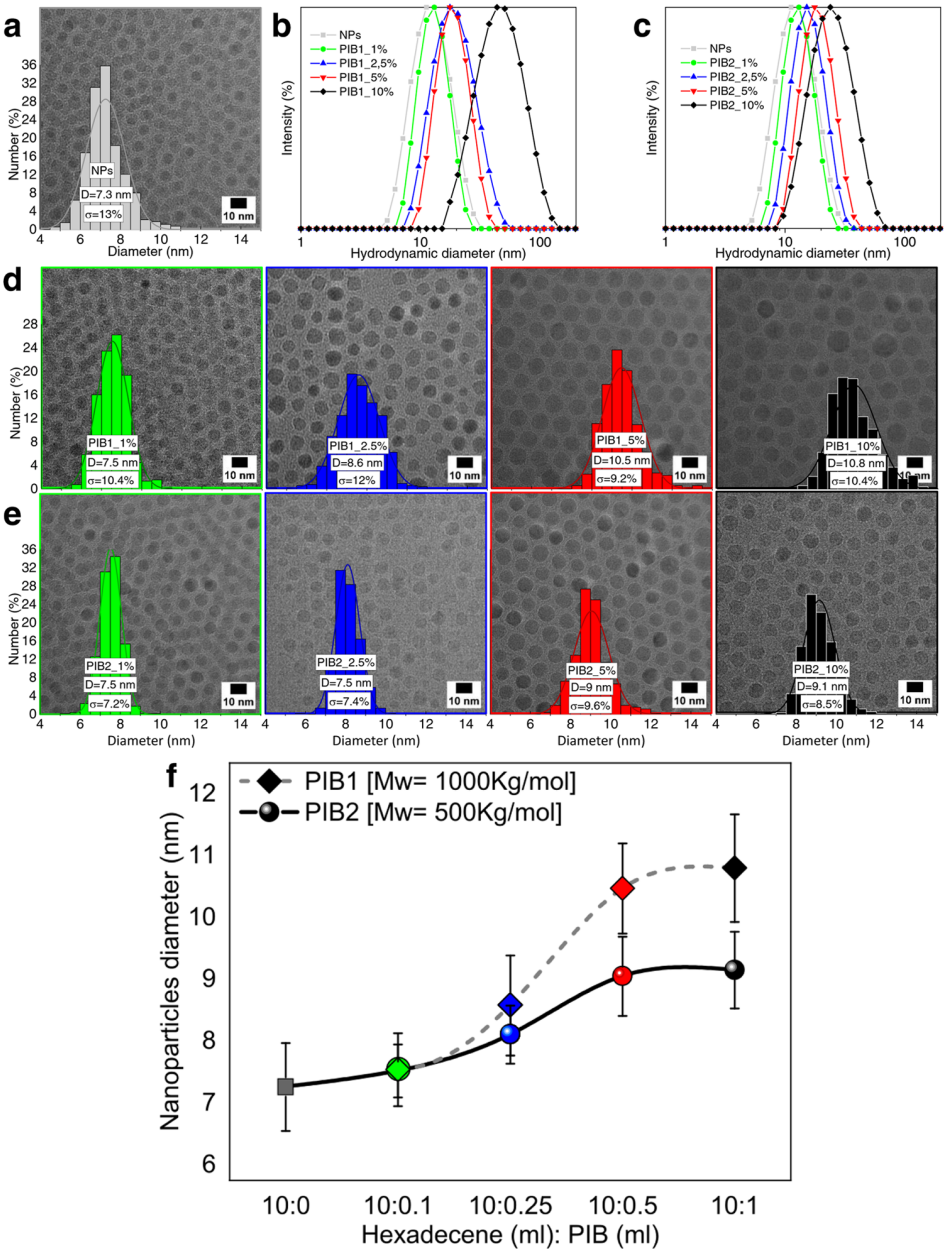

Figure 2. (a) TEM image and size distribution of IONPs synthesized in solvent, (b) DLS curves of the neat IONPs and the PIB1/IONPs, (c) DLS curves of the neat IONPs and the PIB2/IONPs, (d) TEM images and size distribution of PIB1/IONPs, (e) TEM images and size distribution of PIB2/IONPs, and (f) nanoparticle size evolution as a function of PIB dilution in hexadecene and its molecular weight.

ing the center-to-center distance between adjacent cylinders, using the scattering vector q_{100} (2) (corresponding to q_1):[37]

$$a = \frac{4\pi}{\sqrt{3}\, q_1} \tag{2}$$

The calculated lattice parameter was 14.51 nm for PIB2 at a 5% concentration. In comparison, measurements from TEM images revealed an average distance of 14.85 nm between the centers of adjacent nanoparticles, which appeared to be arranged in hexagonal patterns. The close agreement between the SAXS-derived lattice parameter and the TEM-measured distance supports the consistency of the nanoparticle arrangement across these different techniques. While TEM provides a two-dimensional projection, revealing local arrangements, SAXS offers insight into the three-dimensional structure of the entire sample. The observation of hexagonal patterns in the TEM images aligns with the SAXS data, suggesting a hexagonal arrangement superimposed on a lamellar structure. While this quantitative analysis was performed on the PIB2 sample, qualitative examination of TEM micrographs and SAXS patterns across all samples revealed similarities in structural organization. The consistent presence of hexagonal-like arrangements in TEM images, coupled with comparable SAXS scattering profiles, strongly suggests that this ordered nanostructure is a characteristic feature across the entire sample series.

Chemical Composition and Crystallization. To fully understand the physicochemical properties of nanoparticles, it is essential to examine their crystalline structure and phase

https://doi.org/10.1021/acsapm.5c00457
ACS Appl. Polym. Mater. XXXX, XXX, XXX−XXX

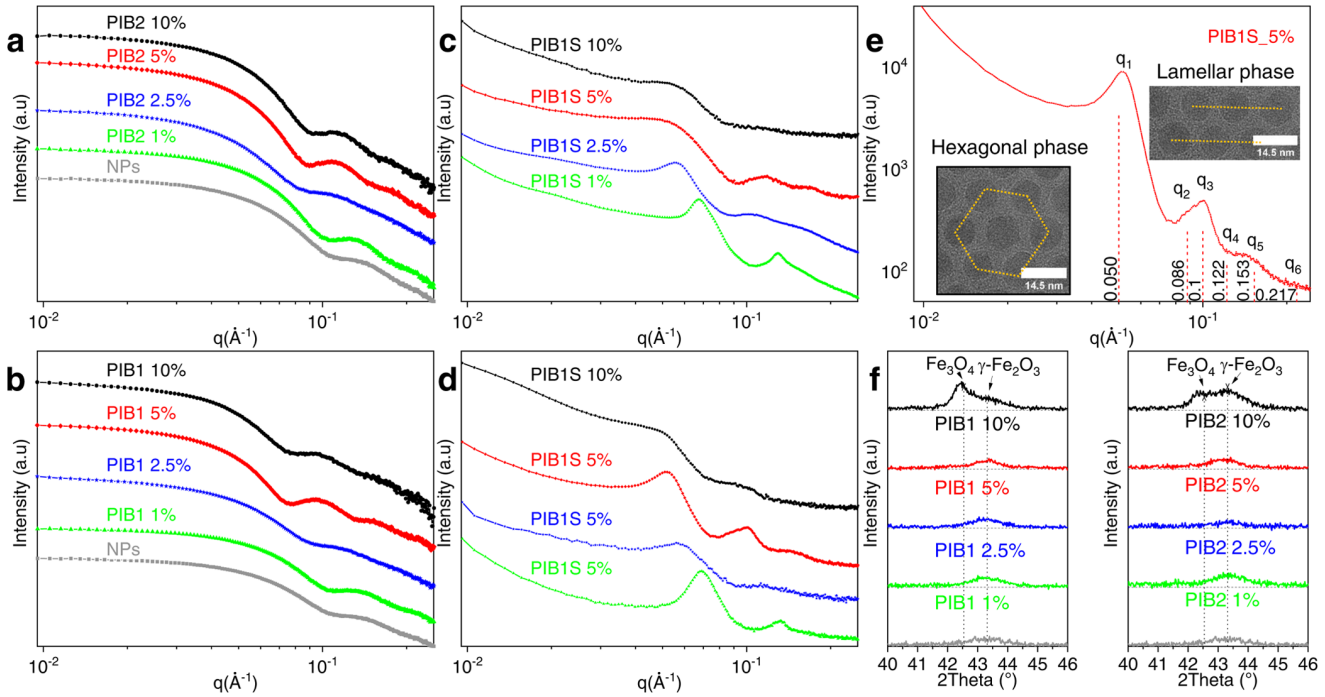

Figure 3. SAXS patterns of PIB nanocomposites: PIB1 in (a) solution and (c) precipitate, PIB2 in (b) solution and (d) precipitate. (e) Lamellar and hexagonal indexing on the PIB2 5%. (f) WAXS pattern of the peak of the plane (400) showing the coexistence of maghemite and magnetite at higher concentrations.

composition alongside their morphological characteristics. The Wide-Angle X-ray Scattering (WAXS) patterns indicated the presence of maghemite (γ-Fe_2O_3), which represents the fully oxidized state of the IONPs. This composition was observed in all samples of PIB1 and PIB2 nanocomposites at concentrations of 1, 2.5, 5, and 10%, as well as in IONPs synthesized without PIB, as shown in Figure S5a,b. This was confirmed by the detection of characteristic peaks at (220), (311), (400), (511), and (440), as identified by ICDD PDF card no. 04-025-0576. At low 2θ angles (below 25°), a prominent amorphous peak was observed for all of the nanocomposite samples, representing the characteristic peak of amorphous PIB centered at 16°. Notably, for IONPs without PIB, this peak shifted from 16 to 20°, corresponding to the peak of ordered iron(oleate) molecules, as shown in Figure S5c. However, in the highly concentrated PIB samples (PIB1 and PIB2 at 10%), WAXS patterns revealed additional closely spaced peaks, notably the (400) plane peak (Figure 3f). This indicates the coexistence of magnetite (Fe_3O_4) alongside maghemite.[38] The coexistence of maghemite and magnetite indicates that IONPs were not fully oxidized at high polymer concentrations. This incomplete oxidation can be explained by the oxygen diffusion limitation at higher polymer concentrations and longer chains, as the appearance of magnetite peaks is more pronounced in PIB1 than in PIB2.

Rheological Properties. Having established the synthesis parameters and compositional profile of our nanocomposite, we investigated its performance, starting with its rheological properties. From the frequency sweep test (Figure S6), the presence of IONPs within the PIB matrices led to remarkable changes in the rheological behavior. These tests were conducted on PIB1 and PIB2 nanocomposites at concentrations of 2.5, 5, and 10%, and were compared to heat-treated PIB (PIB H), which was achieved by diluting 0.5 mL PIB in 10 mL of hexadecene and mixing it for 144 h before refluxing for 30 min. This assessment aimed to evaluate the influence of IONP concentration, dispersion, and size on the storage modulus (G') and loss modulus (G'') for samples that underwent the same heating process, which may improve chain mobility, reduce viscosity, and potentially cause degradation.

Tests at 1% concentration were omitted because of an insufficient sample volume. Figure 4a shows a comparison of the storage moduli of the PIB1 nanocomposites and heat-treated PIB1. The ratio of G' of the nanocomposite to that of the heat-treated PIB revealed substantial enhancements, particularly at a low frequency of 0.01 Hz. At this frequency, the PIB1 nanocomposites showed increases in G' by factors of 22, 13, and 3 at IONP concentrations of 2.5, 5, and 10%, respectively. PIB2 nanocomposites exhibited even greater enhancements, with G' increasing by factors of 30, 16, and 13 at the same concentrations (see Figure 4b). Although the influence of IONPs diminishes at higher frequencies owing to accelerated molecular dynamics, significant modulus increases are still observed. For PIB1, G' increased by factors of 3, 2.5, and 1.4 for the 2.5, 5, and 10% IONP concentrations, respectively. PIB2 demonstrated similar trends with comparable enhancement.

Glass Transition Temperature. In addition to their mechanical properties, nanoparticles are known to affect the thermal properties of polymers, including their glass transition temperatures (T_g).[39] To evaluate this effect, we employed differential scanning calorimetry (DSC) to observe the changes in the T_g of the polymer matrix upon nanoparticle addition. This phenomenon, often referred to as a nanoeffect, can manifest as either an increase or decrease in T_g, depending on the specific interactions between the matrix and particles.[39] In the case of polyisobutylenes (PIB1 and PIB2), the DSC curves

https://doi.org/10.1021/acsapm.5c00457
ACS Appl. Polym. Mater. XXXX, XXX, XXX−XXX

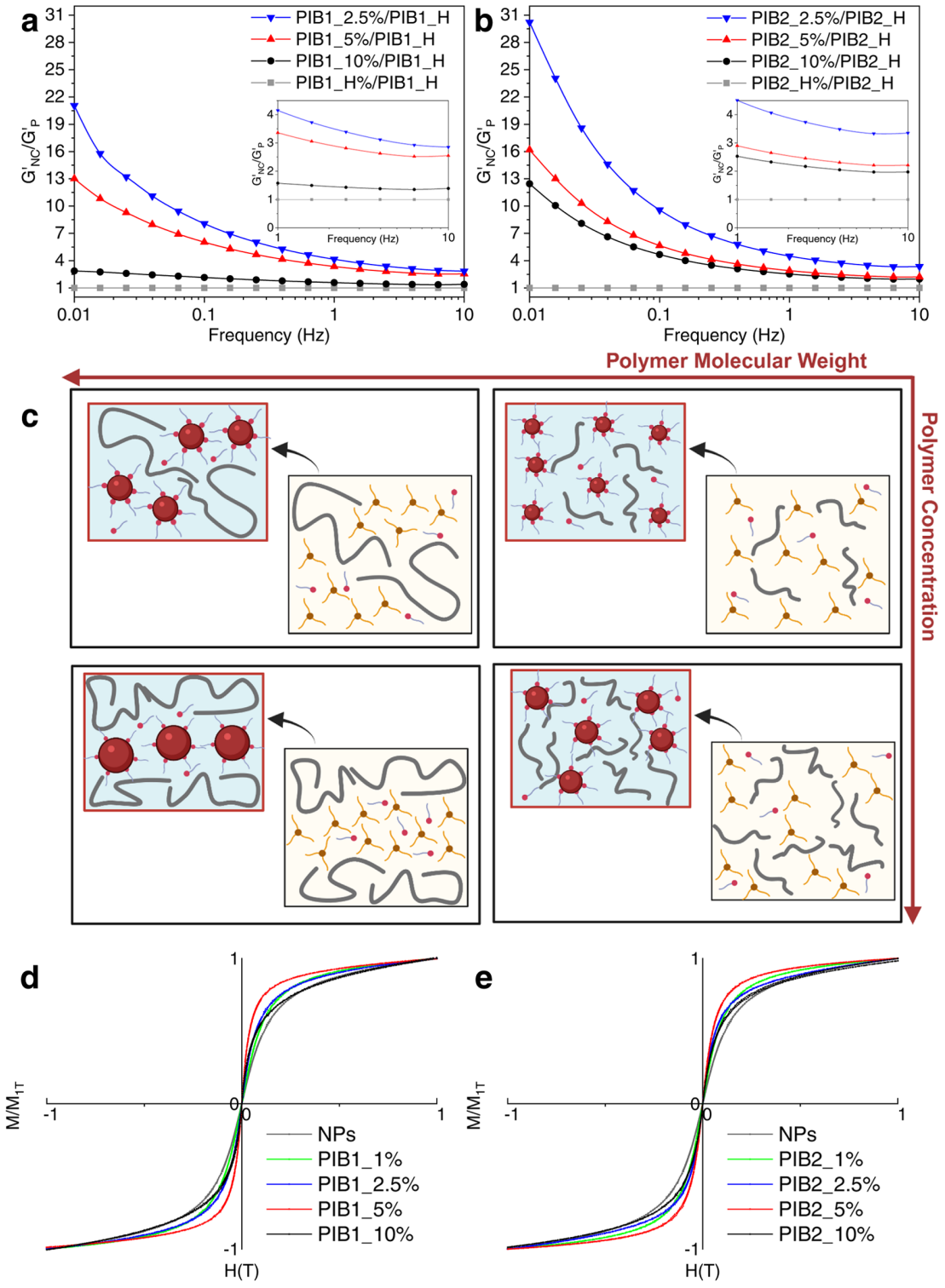

Figure 4. Rheological properties of the PIB nanocomposites. Comparison of storage modulus (G') between PIB nanocomposites and heat-treated PIB for (a) PIB1 and (b) PIB2 at various IONP concentrations. (c) IONP size and dispersion as a function of PIB chain length (horizontal) and concentration (vertical). The four sections illustrate that the smallest IONPs were produced at the lowest PIB concentration and molecular weight, while higher PIB concentrations and molecular weights yielded larger nanoparticles. Intermediate conditions result in nanoparticles of intermediate sizes [Created in BioRender. Meftah, S. (2025) https://BioRender.com/c77k851]. All samples exhibit (d, e) a superparamagnetic behavior at 300 K.

obtained between −80 and 80 °C, as presented in Figure S7, revealed no sharp transitions. The most notable feature observed was a subtle step in the heat flow at −68 °C, which corresponded to T_g. This value aligns well with previously reported data for these materials.[40] For the heated PIBs processed with hexadecene, DSC analysis revealed

https://doi.org/10.1021/acsapm.5c00457
ACS Appl. Polym. Mater. XXXX, XXX, XXX−XXX

alterations in the thermal behavior. The observed T_g at −79 °C was lower than that typical for PIB, which may suggest that our process thermally degrades the PIB by reducing polymer chain length, therefore increasing their mobility. Additionally, a sharp endothermic peak between 0 and 10 °C is attributed to the melting of residual hexadecene, which has a melting point of 4−5 °C. For the PIB nanocomposites, T_g remained unchanged compared to that of the heated PIB, indicating that the IONPs did not have a significant effect. However, a sharp endothermic peak appeared between −10 and 0 °C, which was lower than the melting points of both pure oleic acid (13−14 °C) and hexadecene (4−5 °C). The absence of distinct melting peaks for these components, combined with the appearance of a new peak at a lower temperature, strongly suggested the formation of a eutectic mixture between oleic acid (from the IONP coating) and residual hexadecene. This has been observed in similar cases involving alkenes combined with fatty acids.[41]

Magnetic Properties. In addition to enhancing the intrinsic properties of PIB, IONPs impart magnetic characteristics to the nanocomposite. Both the isolated nanoparticles and the resulting nanocomposites exhibited superparamagnetic behavior at room temperature. This phenomenon was characterized through the magnetization curves for all samples, as depicted in Figure 4d,e, with panels (a) and (b) illustrating the results for PIB1 and PIB2, respectively. The magnetization curves revealed a lack of remanence and coercivity, which are hallmark indicators of superparamagnetism at room temperature. These findings are consistent with previously reported properties of 10 nm maghemite particles[42] and magnetite particles[43] observed at 300 K. The preservation of superparamagnetic behavior in the nanocomposites suggests that the IONPs maintained their individual magnetic characteristics within the PIB matrix, effectively transferring their unique magnetic properties to the composite material. To further investigate the practical applications of these nanocomposites, their actuation behavior under magnetic stimuli was examined. A video demonstration of the PIB2−10% nanocomposite's response to magnetic fields is provided in the Supporting Information.

This video provides visual evidence of the nanocomposite's ability to respond to external magnetic fields, showcasing its potential for various applications in smart materials and actuator technologies. The observed superparamagnetic behavior and magnetic actuation capabilities of these PIB nanocomposites open up exciting possibilities for their use in magnetic field sensors, magnetically controlled drug delivery systems, magnetic separation technologies, magnetic resonance imaging (MRI) contrast agents, and magnetically actuated soft robotics.

DISCUSSION

Based on our previous observations, we can establish a relationship between the size of IONPs, PIB concentration, molecular weight, and evolution of the storage modulus, all based on the growth mechanism. We hypothesize that polymer chain segregation further influences this relationship. Specifically, when the synthesis solution contained higher PIB concentrations and molecular weights, larger IONPs were produced following the thermal decomposition of iron oleate. This can be attributed to the increased tendency of polymer chain segregation under these conditions. PIB molecules are more likely to segregate at higher concentrations and longer chains, leading to a less uniform distribution of precursor molecules throughout the reaction medium. According to this reasoning, an increase in the PIB concentration and molecular weight likely results in a higher concentration of growth species (nuclei) in the reaction medium. Similar to the effects observed with the solvent volume, higher nuclei concentrations at the interface of the nuclei resulted in a shorter diffusion distance and enhanced mass transfer, ultimately leading to a higher growth rate. This scenario promoted the formation of larger nanoparticles within the same growth period,[44] as illustrated in Figure 4c. In the case of low polymer concentrations and low molecular weights, the precursor molecules were more evenly dispersed throughout the reaction medium. The reduced tendency for chain segregation further enhances this uniform distribution because shorter polymer chains with lower concentrations are less likely to aggregate or form distinct domains. The resulting homogeneous environment reduces the likelihood of localized nucleus accumulation, which in turn limits the availability of the growth species at any given nucleation site. Consequently, the growth process becomes more controlled and gradual, leading to the formation of smaller nanoparticles.

This reasoning may also explain why the nanoparticles did not oxidize completely when the concentration and molecular weight of the polymer were high. We believe that under conditions where localized nuclei accumulation regions are formed from chain segregation, the diffusion of oxygen is hindered. As a result, the nanoparticles are not fully oxidized, leading to the coexistence of maghemite and magnetite phases, as observed in the XRD pattern discussed previously (Figure 3f). Furthermore, the oxidation behavior of IONPs is intrinsically linked to their size and surface properties. Fe^{2+} ions at the nanoparticle surface are highly susceptible to oxidation, and this susceptibility is inversely proportional to the particle size. In coprecipitation-synthesized nanoparticles, particles smaller than 20 nm tend to be fully oxidized to maghemite (γ-Fe_2O_3), while larger particles often exhibit a core−shell structure with a magnetite (Fe_3O_4) core and an oxidized maghemite shell.[45]

However, the thermal decomposition synthesis method introduces additional factors that modulate oxidation. The oleic acid coating and organic solvent likely serve a dual purpose: they control the growth kinetics and provide a protective barrier against oxidation. As a result, nanoparticles with sizes of approximately 11 nm still tend to maintain a lattice structure that more closely resembles that of magnetite, suggesting the formation of a core−shell configuration. This protection is particularly significant when compared to coprecipitation-synthesized nanoparticles, which lack such coatings and are more vulnerable to oxidation in aqueous environments.[45] Specifically, for IONPs synthesized at high PIB concentrations, we observed an interesting phenomenon. Higher PIB concentrations (10%) appeared to create a more oxygen-restrictive environment, potentially through increased solution viscosity or by the formation of a physical barrier around the growing nanoparticles. This restriction of oxygen diffusion, combined with the protective effects of oleic acid and organic solvent, results in nanoparticles with incomplete oxidation. Importantly, when comparing IONPs synthesized at 5 and 10% PIB concentrations, we observed that the particle sizes were close, as evidenced by the plateau in Figure 3f. Despite this similarity in size, the 10% PIB sample showed incomplete oxidation, whereas the 5% sample was fully oxidized. This observation allowed us to isolate the effect of

https://doi.org/10.1021/acsapm.5c00457
ACS Appl. Polym. Mater. XXXX, XXX, XXX−XXX

the PIB concentration or molecular weight on the oxidation process, distinguishing it from the effects of oleic acid, organic solvent, and nanoparticle size.

The enhancement of G' in PIB nanocomposites, compared to heat-treated PIB, reveals an interplay among polymer molecular weight, nanoparticle size, and nanoparticle−polymer interactions. Theoretically, higher-molecular-weight polymers are expected to exhibit higher G' due to their increased chain entanglements, which contribute to a stiffer network. Indeed, PIB1 has a significantly higher entanglement factor (∼95) compared to PIB2 (500 kDa, entanglement factor of ∼48), even after heat treatment, as shown in Figure S6g,h. However, with the presence of IONPs at identical concentrations, PIB2 demonstrated a much larger increase in G'.

This unexpected behavior can be explained by considering the effect of the nanoparticle size. In PIB2, the nanoparticles are smaller than those in PIB1, leading to a larger surface area for polymer−nanoparticle interactions. This increased surface area enhances the strength of these interactions, creating a denser polymer−particle network that compensates for PIB2's lower entanglement density. In contrast, the larger nanoparticles in PIB1 provide less surface area for interaction, limiting the reinforcement provided by the nanoparticles, despite the higher polymer entanglement. Thus, the superior increase in G' observed in PIB2 is primarily driven by the size effect of the smaller nanoparticles, which leads to stronger polymer−nanoparticle interactions.

Furthermore, when samples with constant molecular weight are examined, variations in mass fraction significantly influence the mechanical properties. As the mass fraction of nanoparticles increases (corresponding to lower polymer concentrations), a greater enhancement in G' is often observed. This is attributed to a higher number of polymer−nanoparticle interfaces and an increased likelihood of forming interconnected networks within the polymer matrix.

The significant enhancement in the storage modulus of PIB upon the incorporation of oleic acid-coated IONPs without a corresponding change in T_g presents an intriguing phenomenon. The increase in the storage modulus suggests that IONPs effectively reinforce the PIB matrix by creating physical constraints within the polymer structure. These well-dispersed nanoparticles restrict the large-scale motion of the polymer chains under stress, leading to improved stiffness and mechanical properties. However, the unchanged T_g indicates that the local segmental mobility of the PIB chains remained largely unaffected. This can be attributed to the oleic acid coating on the IONPs, which ensures good nanoparticle dispersion but creates a barrier that limits the direct interactions between the iron oxide core and polymer chains, thereby preserving the short-range dynamics responsible for the glass transition in this amorphous polymer.

CONCLUSIONS

In summary, this study presents a method for synthesizing magnetic nanocomposites by embedding IONPs in a PIB matrix. Our approach addresses the challenges associated with achieving uniform dispersion and low polydispersity in nanoparticle size and shape. By optimizing synthesis parameters, such as PIB concentration and molecular weight, we successfully produced IONPs with consistent size distribution and satisfactory dispersion within the PIB matrix. The application of various analytical techniques, including DLS, TEM, SAXS, and WAXS, has provided valuable insights into the quality of the resulting nanocomposites. These analyses indicated that our method can produce well-dispersed nanoparticles with minimal variation in size and shape. Our DSC results suggested that the observed shift in T_g was primarily influenced by the heating process rather than the presence of IONPs, indicating that the nanoparticles do not significantly affect the molecular mobility of the PIB matrix. Additionally, the enhancement in G' observed in our rheological studies supports the notion that effective nanoparticle dispersion can contribute to a drastic improvement in mechanical strength. Future efforts could consider incorporating poly(ethylene oxide)-*block*-poly(isobutylene) (PEO-*b*-PIB) into nanocomposite systems to further enhance material properties. Previous studies have shown that PEO-*b*-PIB can interact with hydrophobically modified Fe_2O_3 nanoparticles to form hierarchical structures at interfaces.[46] This strategy holds the potential for improving properties, such as water resistance and mechanical durability. However, further investigation is required to assess the feasibility and long-term impact of such approaches. Overall, we hope that our research contributes to the ongoing exploration of polymer nanocomposites processing.

MATERIALS AND METHODS

Materials. All of the materials were used as purchased without further purification. Iron(III) chloride ($FeCl_3{\cdot}6H_2O$, 99%, VWR), sodium oleate (97.0%, TCI), 1-hexadecene (for synthesis, Sigma-Aldrich), oleic acid (technical grade, 90%, Sigma-Aldrich), polyisobutylene (average M_w ∼ 1,000,000, M_n ∼ 600,000, PDI ∼ 1.67, Sigma-Aldrich), and polyisobutylene (average M_w ∼ 500,000, M_n ∼ 200,000, PDI ∼ 2.5, Sigma-Aldrich) were used.

Iron(Oleate)$_3$ Precursor Synthesis. The synthesis, as explained in previous papers,[16,17] involves a double-displacement reaction between sodium oleate and iron(III) chloride.

Iron Oxide Nanoparticles Synthesis. 7 nm oleic acid-coated iron oxide nanoparticles were synthesized by the thermal decomposition of iron(oleate)$_3$, as reported previously.[17] Briefly, 1.6 mmol of iron oleate (Fe-oleate) and 0.8 mmol of oleic acid were dissolved in hexadecene (10 mL) in a 250 mL round-bottom flask, and the mixture was stirred for 10 min. The solution was then heated under reflux at 274 °C for 30 min to promote the thermal decomposition of iron(oleate)$_3$. This thermal treatment caused the solution to turn black, indicating the formation of iron oxide nanoparticles. Upon completion of heating, the solution was allowed to cool to room temperature, during which it remained black. Acetone was added to the cooled solution to precipitate the nanoparticles. The oleic acid-coated iron oxide nanoparticles were then collected using a magnet to separate them from the solution. This magnetic separation method is effective because of the magnetic properties of the iron oxide nanoparticles.

Polyisobutylene/Iron Oxide Nanocomposite Synthesis. Polyisobutylene incorporated with oleic acid-coated iron oxide nanoparticles was synthesized using a method similar to that used for the nanoparticles alone, with the addition of PIB dissolved in hexadecene. x mL of PIB was dissolved in 8 mL of hexadecene in a 250 mL round-bottom flask, and the mixture was stirred for 72 h to ensure complete dissolution. Subsequently, 1.6 mmol of iron oleate and 0.8 mmol of oleic acid were added to the PIB-hexadecene solution, along with an additional 2 mL of hexadecene. The mixture was stirred for an additional 72 h to allow for thorough dispersion of the iron precursors and surfactants. The solution was then heated under reflux at 274 °C for 30 min. When acetone was added to the cooled solution to precipitate the nanoparticles, a hydrophobic gel layer was formed around the nanoparticles owing to the presence of the PIB.

Studied Samples. Eleven samples were prepared to comprehensively investigate the synthesis and properties of polyisobutylene

https://doi.org/10.1021/acsapm.5c00457
ACS Appl. Polym. Mater. XXXX, XXX, XXX−XXX

(PIB) and iron oxide nanoparticle (IONP) nanocomposites; (1) IONPs without PIB synthesized as a reference, without polyisobutylene in the solution. (4 × 2) of PIB concentrations in hexadecene. Two PIBs, PIB1 with a molecular weight of 1000 kg/mol and PIB2 with a molecular weight of 500 kg/mol, were each used at the following concentrations in 10 mL of hexadecene (see Table 1). (2) Heat-treated PIB samples PIB1 (PIB1 H%) and PIB2 (PIB2 H) were subjected to reflux conditions in hexadecene to simulate the thermal treatment used during nanoparticle synthesis.

Density and Mass Fraction. The mass fraction of the nanoparticles within the PIB matrix was determined by measuring the density of the treated PIB and that of the corresponding nanocomposites. For each sample, the mass was measured three times in air and three times in ethanol. The density (ρ) was calculated using formula 3:

$$\rho = \frac{\text{average mass in air} \times \text{density of ethanol}}{\text{average mass in air} - \text{average mass in ethanol}} \quad (3)$$

The density of the oleic acid-coated maghemite nanoparticles was estimated using small-angle X-ray scattering data, which provided the particle radius and shell thickness. Using the density of treated PIB as a reference, along with the estimated density of oleic acid-coated maghemite and the measured density of the nanocomposites, the mass fraction of nanoparticles (w_m) was calculated according to eq 4:

$$w_m = \frac{\left(\frac{1}{\rho_c} - \frac{1}{\rho_p}\right)}{\left(\frac{1}{\rho_m} - \frac{1}{\rho_p}\right)} \quad (4)$$

where ρ_c is the density of the nanocomposite, ρ_p is the density of the treated PIB, and ρ_m is the estimated density of the oleic acid-coated maghemite (more details are provided in Section SI 1).

Dynamic Light Scattering (DLS). Dynamic Light Scattering measurements were conducted by using a Litesizer 500 Anton Paar particle size analyzer (Anton Paar France, Courtabeouf, France) to determine the average hydrodynamic diameter of iron oxide nanoparticles in polyisobutylene. The synthesis solution was diluted with toluene in a ratio of 1:100 (100 μL synthesis solution in 10,000 μL toluene). Measurements were performed in a PCS1115 glass cuvette at a temperature of 273.15 K. The instrument was operated with a laser wavelength of 658 nm (single-frequency laser diode) and a detection angle of 175°. The medium viscosity and refractive index are 0.8903 mPa·s and 1.3303, respectively.

Transmission Electron Microscopy (TEM). Transmission Electron Microscopy was performed using a JEOL 2100F instrument operated at an acceleration voltage of 200 kV. Carbon-coated 200 mesh grids were used to collect the samples for analysis. A drop of the synthesis solution was deposited onto the TEM grid without washing to analyze the actual size distribution without any selection bias. Particle sizes were determined by measuring at least 500 nanoparticles per sample using the ImageJ software.[47]

Wide-Anglea X-ray Scattering (WAXS). Wide-Angle X-ray Scattering studies were conducted using a Bruker D8 Advance X-ray diffractometer to investigate the crystallization of iron oxide nanoparticles within polyisobutylene. The X-ray wavelength was 0.1542 nm, and the instrument was operated at 30 kV and 40 mA. Scanning was performed over the 2θ range of 10−70° with increments of 0.02°.

Small-Angle X-ray Scattering (SAXS). Small-Angle X-ray Scattering measurements were performed to determine the shape, size, and organization of the polyisobutylene/iron oxide nanocomposite samples in the solution and Semi-gel states. SAXS experiments were conducted using a Xenocs Xeuss 2.0 SAXS instrument with Cu Kα radiation source (λ = 1.54189 Å). For the solution samples, the material was placed in a capillary tube, whereas for the semi-gel samples, a small portion was affixed to a sample holder. The measurements were performed at room temperature with an exposure time of 150 s for each sample. Scattering data were collected over a q-range of 0.01−0.3 Å^{-1}. The sample-to-detector distance was set at 0.698 m. Data analysis, including background correction with a constant of 0.00015 and reduction using a factor of 0.1, was performed using the SASView software package to extract information about particle size, shape, and distribution.

Differential Scanning Calorimetry (DSC). Differential scanning calorimetry was conducted to investigate the glass transition temperature of the synthesized polyisobutylene/iron oxide nanocomposites. The analysis used a DSC Q200 instrument with the version 24.11 Build 124 software. DSC thermograms were recorded in the temperature range 183−363 K at a heating rate of 2 K/min. For sample preparation, approximately 1.3 mg of the product was placed in a Tzero Aluminum Hermetic pan, and measurements were carried out under a nitrogen atmosphere.

Rheological Measurements. Rheological measurements were performed by using a Physica MRC 301 rheometer with parallel plate geometry, maintaining a 2 mm gap between the plates. The tests were performed at a constant temperature of 298.15 K. An amplitude sweep test was first conducted at a frequency of 1 Hz with deformations ranging from 1 × 10^{-5} to 0.01, to determine the linear viscoelastic region. Subsequently, a frequency sweep test was performed for all samples from 0.01 to 10 Hz with a constant deformation of 0.1%. Each sample, weighing 0.1 g, was analyzed three times by testing three different portions of the sample. The tested materials included polyisobutylene and a polyisobutylene/iron oxide nanocomposite.

Vibrating Sample Magnetometer (VSM). Magnetic measurements were conducted by using a vibrating sample magnetometer from Quantum Design with fields up to 1 T to measure the magnetization curves at 300 K for all samples. The magnetic properties of the nanocrystals were measured at room temperature.

■ ASSOCIATED CONTENT

Supporting Information

The Supporting Information is available free of charge at https://pubs.acs.org/doi/10.1021/acsapm.5c00457.

PIB2−10% nanocomposite's response to magnetic fields, showing its flow behavior when exposed to a magnet (MP4)

Density mass fraction, Guinier plot, SAXS fitting, XRD, rheology frequency sweep, and DSC analysis (PDF)

■ AUTHOR INFORMATION

Corresponding Author

Fahmi Bedoui − *Université de technologie de Compiègne, Roberval (Mechanics, energy and electricity), Centre de recherche Royallieu, CS 60 319, 60 203 Compiègne Cedex, France; Materials and Process Simulation Center, California Institute of Technology, Pasadena, California 91125, United States;* orcid.org/0000-0002-2607-5209; Email: fahmi.bedoui@utc.fr

Authors

Sakina Meftah − *Université de technologie de Compiègne, Roberval (Mechanics, energy and electricity), Centre de recherche Royallieu, CS 60 319, 60 203 Compiègne Cedex, France; Sorbonne Université, CNRS, De la Molécule aux Nano-Objets: Réactivité, Interactions Spectroscopies, MONARIS, 75005 Paris, France*

Nadine Aydi − *Université de technologie de Compiègne, Roberval (Mechanics, energy and electricity), Centre de recherche Royallieu, CS 60 319, 60 203 Compiègne Cedex, France*

Lohitha R. Hegde − *Université de technologie de Compiègne, Roberval (Mechanics, energy and electricity), Centre de recherche Royallieu, CS 60 319, 60 203 Compiègne Cedex,*

https://doi.org/10.1021/acsapm.5c00457
ACS Appl. Polym. Mater. XXXX, XXX, XXX−XXX

France; Laboratory for Biomaterials, Rutgers University, Piscataway, New Jersey 08854, United States

Mohamed Selman − *Sorbonne Université, Laboratoire de Chimie de la Matière Condensée de Paris, LCMCP, 75005 Paris, France*

Jinkai Yuan − *Sorbonne Université, Laboratoire de Chimie de la Matière Condensée de Paris, LCMCP, 75005 Paris, France*

Laurent Bouteiller − *Sorbonne Université, CNRS, Institut Parisien de Chimie Moléculaire, IPCM, 75005 Paris, France;* orcid.org/0000-0001-7613-7028

Caroline Lefebvre − *Service d'Analyse Physico-Chimique, Université de Technologie de Compiègne, F-60205 Compiègne Cedex, France*

Anh-tu Ngo − *Sorbonne Université, CNRS, De la Molécule aux Nano-Objets: Réactivité, Interactions Spectroscopies, MONARIS, 75005 Paris, France*

Djimedo Kondo − *Sorbonne Université, CNRS, Institut Jean Le Rond D'Alembert, 75005 Paris, France*

Andres Jaramillo-Botero − *Materials and Process Simulation Center, California Institute of Technology, Pasadena, California 91125, United States;* orcid.org/0000-0003-2844-0756

William A. Goddard, III − *Materials and Process Simulation Center, California Institute of Technology, Pasadena, California 91125, United States;* orcid.org/0000-0003-0097-5716

Isabelle Lisiecki − *Sorbonne Université, CNRS, De la Molécule aux Nano-Objets: Réactivité, Interactions Spectroscopies, MONARIS, 75005 Paris, France*

Complete contact information is available at: https://pubs.acs.org/10.1021/acsapm.5c00457

Notes

The authors declare no competing financial interest.

■ ACKNOWLEDGMENTS

The authors gratefully acknowledge the support of the LEEGO "chalLEnges and opportunities of connecting lenGth scales in nanO-structuredmaterials" chair program, and the ANR NanoHype project "Temperature Profile in Nanomagnetbased Hyperthermia Devices" (ANR-21-CE09-0043). S.M. extends sincere appreciation to the Materials Institute for the Ph.D. scholarship (IMAT-DOCTORANT SORBR122RRO). The authors thank Dr. Sanjeeva Murthy (Rutgers University) and Jacques Jestin (Institut Laue-Langevin) for the fruitful discussion about the SAXS data analysis. They also express their gratitude to Dr. Erwann Guénin, Dr. Layella Ziyani, and Isabelle Velluet for providing access to essential instrumentation. The authors also thank Dr. David Hrabovsky from the Plateforme Mesures Physiques a Basses Temperatures (MPBT), Sorbonne Université, 75005 Paris, France, for his support in VSM measurements.

■ REFERENCES

(1) Liu, L.; Chang, D.; Gao, C. *Adv. Fiber Mater.* **2024**, *6*, 68−105.
(2) Lin, Y.; Li, P.; Liu, W.; Chen, J.; Liu, X.; Jiang, P.; Huang, X. *ACS Nano* **2024**, *18*, 3851−3870.
(3) Omana, L.; Chandran, A.; John, R. E.; Wilson, R.; George, K. C.; Unnikrishnan, N. V.; Varghese, S. S.; George, G.; Simon, S. M.; Paul, I. *ACS Omega* **2022**, *7*, 25921−25947.
(4) Thostenson, E. T.; Li, C.; Chou, T.-W. *Compos. Sci. Technol.* **2005**, *65*, 491−516.
(5) Montes, H.; Lequeux, F. *C. R. Phys.* **2021**, *22*, 33−50.
(6) Papon, A.; Montes, H.; Lequeux, F.; Oberdisse, J.; Saalwächter, K.; Guy, L. *Soft Matter* **2012**, *8*, 4090−4096.
(7) Schweizer, K. S.; Simmons, D. S. *J. Chem. Phys.* **2019**, *151*, No. 240901.
(8) Bailey, E. J.; Winey, K. I. *Prog. Polym. Sci.* **2020**, *105*, No. 101242.
(9) Wei, T.; Torkelson, J. M. *Macromolecules* **2020**, *53*, 8725−8736.
(10) Mutiso, R. M.; Winey, K. I. *Prog. Polym. Sci.* **2015**, *40*, 63−84.
(11) Toor, A.; So, H.; Pisano, A. P. *ACS Appl. Mater. Interfaces* **2017**, *9*, 6369−6375.
(12) Colijn, I.; Postma, E.; Fix, R.; van der Kooij, H. M.; Schroën, K. *J. Colloid Interface Sci.* **2024**, *658*, 354−361.
(13) ByKabir, G. *Applications of Nanocomposites*; CRC Press eBooks, 2022; pp 1−33.
(14) Ashraf, M. A.; Peng, W.; Zare, Y.; Rhee, K. Y. *Nanoscale Res. Lett.* **2018**, *13*, 1−7.
(15) Sangalov, Y. A.; Minsker, K. S.; Zaikov, G. E. *Polymers Derived from Isobutylene: Synthesis, Properties, Application*; CRC Press, 2023.
(16) Park, J.; An, K.; Hwang, Y.; Park, J.-G.; Noh, H.-J.; Kim, J.-Y.; Park, J.-H.; Hwang, N.-M.; Hyeon, T. *Nat. Mater.* **2004**, *3*, 891−895.
(17) Meftah, S.; Ngo, A.-T.; Bouteiller, L.; Russier, V.; Hrabovsky, D.; Konaté, A.; Kondo, D.; Bedoui, F.; Lisiecki, I. *Langmuir* **2024**, *40*, 22673−22683.
(18) Baaziz, W.; Pichon, B. P.; Grenèche, J.-M.; Begin-Colin, S. *CrystEngComm* **2018**, *20*, 7206−7220.
(19) Meftah, S.; Ngo, A.-T.; Shahmanesh, A.; Courty, A.; Kondo, D.; Bedoui, F.; Lisiecki, I. *Colloids Surf., A* **2024**, *680*, No. 132689.
(20) Behrens, S.; Appel, I. *Curr. Opin. Biotechnol.* **2016**, *39*, 89−96.
(21) Arun, T.; Dhanabalan, S. S.; Udayabhaskar, R.; Ravichandran, K.; Akbari-Fakhrabadi, A.; Morel, M. J. *Inorganic Materials for Energy, Medicine and Environmental Remediation*; Springer, 2022; Vol. *69*, pp 131−150.
(22) Tajik, S.; Beitollahi, H.; Nejad, F. G.; Dourandish, Z.; Khalilzadeh, M. A.; Jang, H. W.; Venditti, R. A.; Varma, R. S.; Shokouhimehr, M. *Ind. Eng. Chem. Res.* **2019**, *74*, 1112−1136.
(23) Marcelo, L. R.; de Gois, J. S.; da Silva, A. A.; Cesar, D. V. *Environ. Chem. Lett.* **2021**, *19*, 1229−1274.
(24) Naghdi, M.; Ghovvati, M.; Rabiee, N.; Ahmadi, S.; Abbariki, N.; Sojdeh, S.; Ojaghi, A.; Bagherzadeh, M.; Akhavan, O.; Sharifi, E.; et al. *Adv. Colloid Interface Sci.* **2022**, *308*, No. 102771.
(25) Ma, X.; Tao, H.; Yang, K.; Feng, L.; Cheng, L.; Shi, X.; Li, Y.; Guo, L.; Liu, Z. *Nano Res.* **2012**, *5*, 199−212.
(26) LaMer, V. K.; Dinegar, R. H. *J. Am. Chem. Soc.* **1950**, *72*, 4847−4854.
(27) Thanh, N. T.; Maclean, N.; Mahiddine, S. *Chem. Rev.* **2014**, *114*, 7610−7630.
(28) Chao, C.-G.; Kumar, M. P.; Riaz, N.; Khanoyan, R. T.; Madrahimov, S. T.; Bergbreiter, D. E. *Macromolecules* **2017**, *50*, 1494−1502.
(29) Lewis, E. A.; McNaughter, P. D.; Yin, Z.; Chen, Y.; Brent, J. R.; Saah, S. A.; Raftery, J.; Awudza, J. A.; Malik, M. A.; O'Brien, P.; et al. *Chem. Mater.* **2015**, *27*, 2127−2136.
(30) Ma, J.; Larsen, R. M. *ACS Appl. Mater. Interfaces* **2013**, *5*, 1287−1293.
(31) Hansen, C. M. *The Three Dimensional Solubility Parameter*; Danish Technical: Copenhagen, 1967; Vol. *14*.
(32) Test, A. Accudyne Test, 2024. https://www.accudynetest.com/polytable_02.html.
(33) Stefanis, E.; Panayiotou, C. *Int. J. Pharm.* **2012**, *426*, 29−43.
(34) Bonini, M.; Fratini, E.; Baglioni, P. *Mater. Sci. Eng., C* **2007**, *27*, 1377−1381.
(35) Guinier, A.; Fournet, G.; Walker, C. B.; Vineyard, G. H. Small-angle scattering of X-rays. *Phys. Today* **1956**, *9*, No. 38, DOI: 10.1063/1.3060069.
(36) Menon, S.; Manohar, C.; Rao, K. S. *J. Chem. Phys.* **1991**, *95*, 9186−9190.
(37) Ruland, W.; Smarsly, B. *J. Appl. Crystallogr.* **2005**, *38*, 78−86.
(38) Kim, W.; Suh, C.-Y.; Cho, S.-W.; Roh, K.-M.; Kwon, H.; Song, K.; Shon, I.-J. *Talanta* **2012**, *94*, 348−352.

(39) Rittigstein, P.; Torkelson, J. M. *J. Polym. Sci., Part B: Polym. Phys.* **2006**, *44*, 2935−2943.
(40) NETZSCH Polymer characterization methods, accessed: 2024-09-30.
(41) Wieckowski, M.; Królikowski, M. *J. Chem. Eng. Data* **2022**, *67*, 727−738.
(42) Mizukoshi, Y.; Shuto, T.; Masahashi, N.; Tanabe, S. *Ultrason. Sonochem.* **2009**, *16*, 525−531.
(43) Vollath, D.; Szabo, D.; Taylor, R.; Willis, J. *J. Mater. Res.* **1997**, *12*, 2175−2182.
(44) Dehsari, H. S.; Ribeiro, A. H.; Ersöz, B.; Tremel, W.; Jakob, G.; Asadi, K. *CrystEngComm* **2017**, *19*, 6694−6702.
(45) Baaziz, W.; Pichon, B. P.; Fleutot, S.; Liu, Y.; Lefevre, C.; Greneche, J.-M.; Toumi, M.; Mhiri, T.; Begin-Colin, S. *J. Phys. Chem. C* **2014**, *118*, 3795−3810.
(46) Li, H.; Sachsenhofer, R.; Binder, W. H.; Henze, T.; Thurn-Albrecht, T.; Busse, K.; Kressler, J. *Langmuir* **2009**, *25*, 8320−8329.
(47) Schneider, C. A.; Rasband, W. S.; Eliceiri, K. W. *Nat. Methods* **2012**, *9*, 671−675.

https://doi.org/10.1021/acsapm.5c00457
ACS Appl. Polym. Mater. XXXX, XXX, XXX−XXX

Conclusions and Perspectives

Conclusion

This PhD research has delved into the intricate interplay between the synthesis, properties, and applications of iron oxide nanoparticles, and their incorporation into polymer nanocomposites, particularly with a polyisobutylene matrix. The overarching aim has been to achieve precise control over nanoparticle characteristics while ensuring effective integration into the polymer matrix to address challenges in modern materials science and engineering.

At the heart of this work lies the exploration of IONPs, from their crystalline structure and magnetic properties to their synthesis and functionalization. The study underscores the critical relationship between structural attributes—such as size, shape, and surface chemistry—and their functionality in diverse applications. Through a systematic evaluation of various synthesis methods, including thermal decomposition and modifications involving tailored precursors and ligands, this research achieved significant control over nanoparticle size and dispersion. These findings highlight the impact of precursor and ligand chemistry on nanoparticle formation, demonstrating the ability to produce particles with specific diameters and properties. Moreover, novel nanoparticle shapes, such as triangular maghemite, were synthesized, providing insights into the mechanisms governing their growth and presenting new opportunities to investigate their unique magnetic behaviors.

In parallel, this study has advanced the understanding of polymer nanocomposites, emphasizing the complex interactions between matrix materials, nanofillers, and their interfaces. By embedding IONPs into a PIB matrix, a novel approach was developed to overcome persistent challenges such as nanoparticle agglomeration and polydispersity. The optimized synthesis protocol ensured uniform dispersion and consistent nanoparticle size within the matrix. Analytical techniques such as transmission electron microscopy, dynamic light scattering, and X-ray scattering revealed the effectiveness of this approach, providing insights into the structural and morphological properties of the resulting nanocomposites.

The mechanical and thermal properties of the nanocomposites were rigorously evaluated to elucidate the role of nanoparticles in enhancing polymer performance. Rheological studies revealed an increase in the storage modulus, demonstrating improved mechanical strength due to effective nanoparticle dispersion. Interestingly, differential scanning calorimetry results suggested that the nanoparticles had minimal impact on the molecular mobility of the PIB matrix, as evidenced by the lack of significant changes in the glass transition temperature. These findings reinforce the importance of achieving a balance between nanoparticle dispersion and matrix integrity to optimize composite performance.

This work also sheds light on the potential of nanoparticle-functionalized polymers for advanced applications. The study's exploration of ligand chain lengths and their impact on nanoparticle interactions within the polymer matrix offers valuable insights for tailoring

interparticle distances and achieving ordered superstructures. Such advancements open new avenues for designing materials with tunable properties, particularly in fields requiring lightweight and strong materials, controlled magnetic behavior, or enhanced thermal and mechanical properties.

In conclusion, this research bridges the gap between nanoparticle synthesis and polymer nanocomposite design, providing a comprehensive understanding of how synthesis parameters, nanoparticle properties, and polymer interactions influence the final material's performance. The findings not only contribute to the fundamental understanding of nanoparticle growth and polymer nanocomposite processing but also lay the groundwork for future developments in nanotechnology and materials science. By addressing key challenges and proposing innovative solutions, this work paves the way for the development of advanced materials tailored to meet the evolving demands of modern technologies.

Perspectives

Opportunities for Further Exploration

While our work demonstrates the successful synthesis of oleic acid-coated iron oxide nanoparticles uniformly dispersed in a polyisobutylene matrix, there remain several promising avenues for further exploration to deepen our understanding of nanocomposite behavior and improve synthesis methods. These efforts could provide valuable insights into structure–property relationships and enable the development of tailored materials for advanced applications.

One particularly intriguing direction is the *in-situ* synthesis of iron oxide nanoparticles directly within the PIB matrix using surface chemistries with alternative ligands, such as octanoic and dodecanoic acids, as discussed in Chapter 3. Ligand chain length plays a critical role in determining nanoparticle dispersion, interfacial adhesion, and interphase properties. Shorter-chain ligands, such as octanoic acid, may promote stronger interfacial adhesion between the nanoparticles and the polymer matrix due to reduced steric hindrance, potentially enhancing mechanical properties such as stiffness and toughness. Conversely, longer-chain ligands like dodecanoic acid could introduce steric effects or increase flexibility at the interphase, influencing nanoparticle packing density and overall composite behavior. By systematically varying ligand chain length during synthesis, it would be possible to investigate how these structural changes impact key material properties, such as load transfer efficiency, fracture toughness, and magnetic behavior.

In addition to ligand chemistry, there is significant potential to refine the synthesis process itself. The current method relies on precursors that decompose at elevated temperatures, which can lead to polymer degradation during nanoparticle formation. Exploring alternative precursors that decompose at lower temperatures could minimize this degradation and preserve the integrity of the polymer matrix. For example, precursor systems designed for mild thermal decomposition or chemical reduction could be investigated to reduce thermal stress on PIB during nanoparticle formation. Alternatively, employing polymers with higher thermal stability could expand the range of processing conditions while maintaining matrix compatibility. This approach would allow for greater flexibility in tailoring nanocomposite properties without compromising polymer performance.

Furthermore, combining these advancements—optimized ligand chemistries and improved synthesis methods—could enable deeper exploration of interphase phenomena in nanocomposites. The interphase region is often considered a "third material" distinct from both the nanoparticle core and polymer matrix, with unique mechanical and chemical properties that dominate overall composite behavior. By systematically tuning ligand chain length

and synthesis conditions, future studies could investigate how interphase thickness, stiffness gradients, or chemical composition influence macroscale properties such as toughness, elasticity, or magnetic response.

Numerical Modeling of Nanocomposites: A Roadmap for Interphase Decoding

The nanocomposites we have developed represent an exciting experimental achievement that could serve as a model system for understanding interphase phenomena. By addressing key challenges such as nanoparticle agglomeration and polydispersity, we have created a reproducible nanocomposite system with well-defined parameters. This system could form the foundation for future theoretical and computational studies. While our work primarily focuses on the experimental synthesis and characterization of these nanocomposites, their unique features open the door for numerical modeling approaches that link nanoscale interactions to macroscopic properties.

Because of the complexity of the interphase region, a complete understanding of nanocomposites requires both macro- and nanoscale analyses [1]. Experimental techniques are generally effective at capturing macroscopic properties, but they often lack the resolution needed to fully characterize the intricate nanoscale features of the interphase. These limitations in spatial and temporal resolution make numerical modeling a crucial tool for bridging the gap. Multiscale modeling, which integrates different numerical approaches across multiple length and time scales (Figure 6.17, provides a more detailed view of the interphase and its effect on the overall properties of nanocomposites [2] [3].

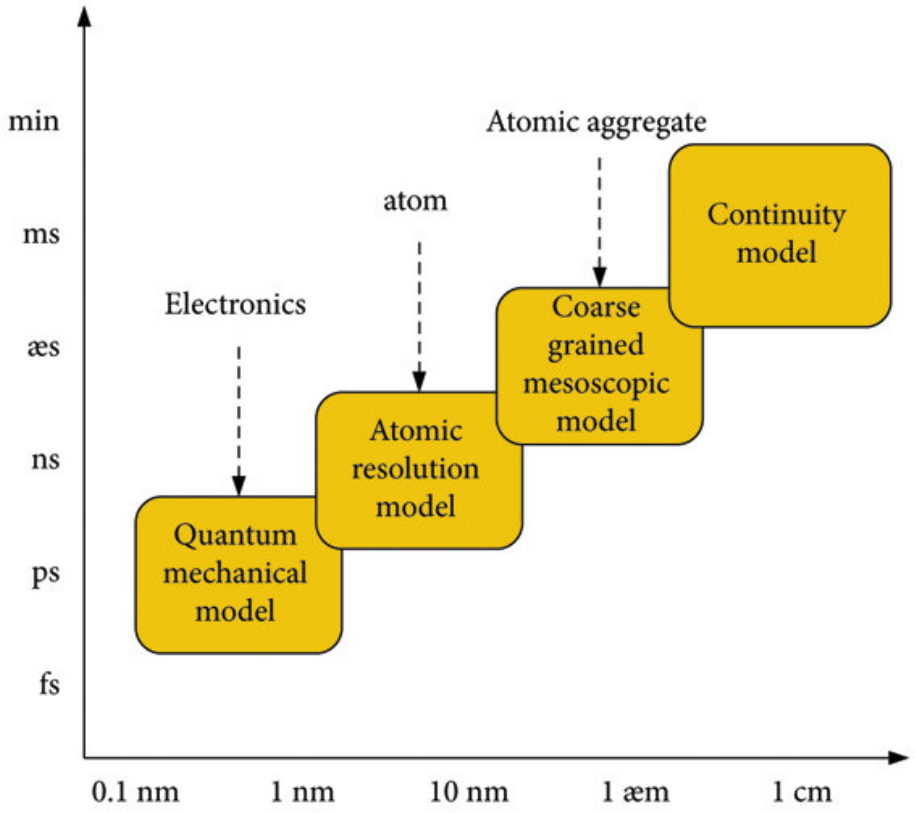

Figure 6.17 – *Multiscale Modeling Hierarchy in Materials Science: Time and Length Scales [4].*

At the atomic scale, quantum mechanics (QM) simulations can help elucidate the bonding mechanisms between functionalized nanoparticle surfaces and polymer chains, shedding light on interfacial adhesion. Molecular dynamics (MD) simulations offer insights into polymer chain mobility and packing density near nanoparticle surfaces, helping to understand how interphase stiffness and thickness emerge from nanoscale interactions. By using parameters derived from our experimentally synthesized nanocomposite system, such as nanoparticle size, shape, and dispersion quality, these simulations can closely mirror real-world conditions.

To bridge the gap between atomic and macroscopic scales, coarse-grained (CG) models can be used to efficiently simulate nanoparticle-polymer interactions while retaining essential physical behaviors. These models can predict stress distribution, dispersion stability, and the impact of nanoparticle geometry on mechanical performance. Finite element modeling (FEM) further extends these insights by incorporating interphase properties from MD and CG simulations into a continuum mechanics framework, enabling the study of stress transfer and deformation behavior at the macroscale.

By systematically varying parameters such as nanoparticle spacing relative to interphase thickness, numerical modeling can help establish design rules for optimizing nanocomposite

performance. Our ability to produce nanocomposites with controlled nanoparticle geometry, size uniformity, and agglomeration-free dispersion makes them an ideal experimental benchmark for validating theoretical predictions. Combining precise experimental systems with advanced numerical modeling could lead to a deeper understanding of how interphase regions influence properties such as stiffness, toughness, and load transfer efficiency.

While much remains to be explored, this integrated approach holds significant potential for advancing the field of nanocomposites. By leveraging both experimental and computational insights, we can develop new design strategies for nanocomposites optimized for applications in structural materials, magnetic systems, and beyond.

Bibliography

[1] F. Zaccardi, M. G. Santonicola, and S. Laurenzi, "Role of interface bonding on the elastic properties of epoxy-based nanocomposites with carbon nanotubes using multiscale analysis," *Composite Structures*, vol. 255, p. 113050, 2021.

[2] A. Muhammad, R. Srivastava, N. Koutroumanis, D. Semitekolos, E. Chiavazzo, P.-N. Pappas, C. Galiotis, P. Asinari, C. A. Charitidis, and M. Fasano, "Mesoscopic modeling and experimental validation of thermal and mechanical properties of polypropylene nanocomposites reinforced by graphene-based fillers," *Macromolecules*, vol. 56, no. 24, pp. 9969–9982, 2023.

[3] Q. Zeng, A. Yu, and G. Lu, "Multiscale modeling and simulation of polymer nanocomposites," *Progress in polymer science*, vol. 33, no. 2, pp. 191–269, 2008.

[4] S. Saini, "Designing clusters for efficient catalytic activity at a realistic condition from first-principles simulation," 2020.

List of Figures

List of Tables

Résumé

Comprendre les mécanismes de synthèse et de croissance des nanoparticules est crucial pour obtenir un contrôle précis de leur taille, de leur forme et de leur chimie de surface, qui sont essentiels pour leur intégration dans des nanocomposites polymères. Ce travail explore la synthèse par décomposition thermique des nanoparticules d'oxyde de fer (IONPs), en mettant l'accent sur le rôle des différents précurseurs (oléate, dodécanoate, octanoate) dans l'ajustement des propriétés des nanoparticules. Une attention particulière est portée aux défis de robustesse, en soulignant comment la sélection des précurseurs et les conditions de synthèse influencent la morphologie et le contrôle de la forme des nanoparticules. Parallèlement, la synthèse in situ des IONPs au sein d'une matrice de polyisobutylène (PIB) est étudiée, en examinant l'auto-assemblage des nanoparticules, leur dispersion et leur impact sur les propriétés mécaniques et fonctionnelles du nanocomposite résultant. La combinaison de la nature hydrophobe du PIB et du comportement superparamagnétique des IONPs ouvre des perspectives d'applications dans la détection et l'actionnement. En apportant des éclairages fondamentaux sur la croissance des nanoparticules, le contrôle de leur forme et les interactions polymère-nanoparticules, cette étude contribue à l'avancement du développement de nanocomposites polymères robustes et à haute performance.

Mots clés:Nanoparticules d'oxyde de fer, Mécanismes de synthèse, Contrôle de taille, Défis de robustesse, Nanocomposites polymères, Propriétés mécaniques.

Abstract

Understanding the synthesis and growth mechanisms of nanoparticles is crucial for achieving controlled size, shape, and surface chemistry, all of which are essential for their integration into polymer nanocomposites. This work investigates the thermal decomposition synthesis of iron oxide nanoparticles (IONPs), focusing on the role of different precursors (oleate, dodecanoate, octanoate) in tailoring nanoparticle properties. Particular attention is given to robustness challenges, highlighting how precursor selection and synthesis conditions influence nanoparticle morphology and shape control. In parallel, the in situ synthesis of IONPs within a polyisobutylene (PIB) matrix is explored, examining nanoparticle self-assembly, dispersion, and their impact on the mechanical and functional properties of the resulting nanocomposite. The combination of PIB's hydrophobic nature and the superparamagnetic behavior of IONPs offers potential applications in sensing and actuation. By bridging fundamental insights into nanoparticle growth, shape control, and polymer-nanoparticle interactions, this study advances the development of robust, high-performance polymer nanocomposites.

Keywords: Iron oxide nanoparticles, Synthesis mechanisms, Size control, Robustness challenges, Polymer nanocomposites, Mechanical properties.